

The Eigenvalues of Quantized Spin Waves and the Uniaxial Anisotropy in a Biferromagnetic System

Xiao Juan Hou^{1,2}, Guo Hong Yun^{1,3}, Yu Hao Bai¹, and Narsu Bai³

¹College of Physical Science and Technology, Inner Mongolia University, Hohhot 010021, China

²Department of Applied Physics, School of Mathematics, Physics and Biological Engineering
Inner Mongolia University of Science and Technology, Baotou 014030, China

³Inner Mongolia Key Laboratory of Physics and Chemistry of Functional Materials
College of Physics and Electronic Information, Inner Mongolia Normal University, Hohhot 010022, China

Abstract— The eigenproblems of quantized spin waves in a (100) ferromagnetic bilayer system have been investigated theoretically by using the interface rescaling approach. The energy-band structure of the system has been obtained and the effect of the uniaxial bulk anisotropy field of easy-axis type on the energy bands are explored thoroughly. It is found that all kinds of eigenmodes of the spin waves in the biferromagnetic system are determined by the bulk exchange coupling constant, the interface exchange coupling constant, the spin of lattice, the number of atomic layers and the uniaxial bulk anisotropy. Especially, we explored the effect of the uniaxial bulk anisotropy field of easy-axis type on the energy band of first Brillouin zone and the existence of all kinds of the eigenmodes.

1. INTRODUCTION

Magnetic multilayers have been increasing interest in the areas of magnetism and spintronic devices [1], due to their potential applications to solid-state data-storage and data-processing devices. At the beginning of magnetic data storage it is important to understand spin waves to reduce their harmful influence or their assistance for the magnetization reversal [2]. More recent publications have shown that it is impossible to use spin waves for logic devices [3]. To make a first step towards future devices minimizing magnons' disturbing influence or using magnons, spin waves and their properties have to be understood [4]. With experiment techniques developing, several methods such as Ferromagnetic Resonance and Brillouin Light Scattering [5] have been used to explore spin waves. These have greatly stimulated physicists' interest in studying magnetic multilayers [6]. Many authors also have researched the spin-wave excitations using a variety of theory methods, such as Green Function Method [7], the Transfer-matrix Method [8] and Monte Carlo Method [9]. However, a direct numerical analysis by use of these methods would lead to huge numerical computations. Therefore, it is difficult to get exact solutions of the eigenvalue problems of such a multilayer system even at low temperature because of the interface coupling. Puzskarski and his cooperators [10] have introduced an interface-rescaling approach (IRA) to decompose a coupling system into independent subsystems and to form interface-rescaling equations. Moreover, this method has been widely used to investigate many magnetic properties of layered magnetic materials [11–13]. But these are mainly classical or quasi-classical theories. In this paper we use the IRA to explore the quantized spin waves in a ferromagnetic bilayer system. We obtain the exact solutions of the spin waves and five kinds of eigenmodes, and particularly we analyze the influence of the uniaxial bulk anisotropy on the spin-wave eigenvalues.

2. THE MODEL

We study a bilayer system composed of two ferromagnetic layers (sublayers A and B) of the different magnetic material, coupled by exchange interactions at their interface through a nonmagnetic spacer. We thus include the effects of modified exchange interaction and intrinsic bulk anisotropy. For the sake of simplicity, we assume the two ferromagnets still have the periodicity in the atomic planes parallel to interface and the two outer surfaces. Moreover, we neglect the anisotropy in the interface and on the surfaces. So the Heisenberg Hamiltonian of the system was written as:

$$\hat{H} = -\frac{1}{2} \sum_{n,m} \sum_{i,j} J(n,i;m,j) \hat{S}(n,i) \cdot \hat{S}(m,j) - \sum_{n,i} D(n) \left[\hat{S}^z(n,i) \right]^2 \quad (1)$$

with terms accounting successively for exchange interaction and the uniaxial bulk anisotropy energy. Where n, m are the indices of the lattice planes and i, j are the sites in the atomic planes n and

m , respectively. We write for the nearest neighbor exchange terms $J(n, i; m, j) = J_A$ if both spins belong to the A sublayer, $J(n, i; m, j) = J_B$ if both spins belong to the B sublayer and $J(n, i; m, j) = J_{AB}$ if the spins are coupled across the interface between the sublayers A and B . The second term of (1) comprises the bulk anisotropy effect, favoring the z direction as the easy axis of the system, specially, $D(n) = D_A$ for A sublayer and $D(n) = D_B$ for B sublayer. The spin operators satisfy the following equation:

$$\hat{S}(n, i) \cdot \hat{S}(n, i) = S(n) [S(n) + 1] \quad (2)$$

where the spin $S(n) = S_A$ if the site belongs to the A sublayer and $S(n) = S_B$ if the site belongs to the B sublayer.

We only consider the ferromagnetic case with $J(n, i; m, j) > 0$ and assume $D(n) > 0$. The ground state of the system is all spin parallel. Above we have chosen the same theory model as the paper [13], but we use the different boundary condition — aperiodic boundary condition. Moreover we'll expose the effect of the uniaxial bulk anisotropy field of easy-axis type on energy bands theoretically. Using the method in the paper [12] and only take quadratic terms, the Hamiltonian can be easily diagonalized as

$$\hat{H} = H_0 + \sum_{p,k} \varepsilon_{pk} \hat{a}^+(p, k) \cdot \hat{a}(p, k) \quad (3)$$

where $\hat{a}^+(p, k)$ is the creation operator of magnons, $\hat{a}(p, k)$ is the annihilation operator of magnons and ε_{pk} is the excitation energy of spin waves which satisfies the eigenequations as follows,

$$\begin{aligned} \varepsilon_{pk} f(n, p) = & \{J(n, n)S(n) + J(n, n-1)S(n-1) + J(n, n+1)S(n+1) + D(n)[2S(n) + 1]\} f(n, p) \\ & - \left[J(n, n+1)\sqrt{S(n)S(n+1)}f(n+1, p) + J(n, n-1)\sqrt{S(n)S(n-1)}f(n-1, p) \right] \end{aligned} \quad (4)$$

where $J(n, n) = 2(2 - \cos k_x - \cos k_y) = 2\gamma J_n$, γ is the wave vector parallel to the interface, $f(n, p)$ is the orthonormalized wave function and $J(n, n \pm 1) = J(n \pm 1, n)$. We choose the lattice constants in both sublayers as unit length and neglect the index p of $f(n, p)$ for simplicity, and let N_A and N_B denote the numbers of atomic planes of the two ferromagnets A and B , respectively. We assume the atomic planes $n = 1, 2, \dots, N_A$ are occupied by A spins, whereas $n = N_A + 1, N_A + 2, \dots, N_A + N_B$ are occupied by B spins. In this way, one hand the interface is formed between the planes $n = N_A$ and $n = N_A + 1$, on the other hand, the two surfaces are the planes at $n = 1$ and $n = N_A + N_B$, moreover, we set $f(n) = f_A(n)$ when the spin belongs to sublayer A and $f(n) = f_B(n)$ when the spin belongs to sublayer B .

We apply the IRA to Equation (4) and get two independent subsets of eigenequations which have the general solutions as follows

$$\begin{aligned} f_A(n) = & C\rho[\exp(-ink_A) - \theta_A \exp(ink_A)], \\ \theta_A = & -\exp[i(2N_A + 1)k_A], \quad 1 \leq n \leq N_A, \end{aligned} \quad (5a)$$

$$\begin{aligned} f_B(n) = & C[\exp(ink_B) - \theta_B \exp(-ink_B)], \\ \theta_B = & -\exp[i(2N_B - 1)k_B], \quad N_A + 1 \leq n \leq N_A + N_B, \end{aligned} \quad (5b)$$

where k_A and k_B are the wave vectors of the spin waves in A and B perpendicular to the interface; C is the normalization coefficient and ρ is a constant with respect to n . At the same time, we define the interface-rescaling coefficient R similar to [10] as follows

$$Rf_A(N_A) = f_B(N_A + 1) \quad (6)$$

Inserting Equation (6) into Equation (4), we consider that the surfaces are free, then obtain

$$\varepsilon_{pk} = 2J_A S_A (\gamma + 1 - \cos k_A) + D_A (2S_A + 1) = 2J_B S_B (\gamma + 1 - \cos k_B) + D_B (2S_B + 1) \quad (7)$$

and

$$\mu_i(k) = \frac{\sin(N_i + 1)k_i - \sin N_i k_i}{\sin N_i k_i - \sin(N_i - 1)k_i} \quad (8)$$

where the index i represents A or B , and the parameters μ_A and μ_B are given by

$$\mu_A = 1 - \frac{J_{AB}S_B}{J_A S_A} (1 - \alpha^{-1}R) \quad (9)$$

$$\mu_B = 1 - \frac{J_{AB}S_A}{J_B S_B} (1 - \alpha R^{-1}) \quad (10)$$

where

$$\alpha = \sqrt{S_B/S_A} \quad (11)$$

By canceling R from the Equations (9) and (10) we can get the other constrained equation of k_A and k_B

$$\left[1 - \frac{J_A S_A}{J_{AB} S_B} (1 - \mu_A) \right] \left[1 - \frac{J_B S_B}{J_{AB} S_A} (1 - \mu_B) \right] = 1 \quad (12)$$

The eigenvectors k_A and k_B can be derived from the Equations (7) and (12) when the material parameters of the system are given.

3. EIGENMODES AND ENERGY BANDS

In this section we turn to analyze in detail the eigenvalues of spin waves with the longitudinal spin waves with transverse wave vector γ varying along the high-symmetry paths of two dimensional (2D) Brillouin zone. When $J_{AB} \neq J_A$, $J_A = J_B$ and $S_A = S_B$, the energy band only consists of bulk modes (BMs) and interface modes (IMs). The results resemble to Ref. [11]. So we only discuss the case of $J_A S_A \neq J_B S_B$. Without any loss of the generality, we assume $J_A S_A > J_B S_B$ and the gap appears at the site M . In order to thoroughly explore the properties of the spin waves in the system, we choose the parameters J_A , J_B , J_{AB} , S_A , S_B , N_A and N_B as, respectively, 1.0, 1.0, 2.0, 1/2, 1/2, 31 and 15. The results show that there are five types of eigenmodes which are bulk mode (BM), the perfectly confined mode in sublayer A (PCMA), the perfectly confined mode in sublayer B (PCMB), the optic-optic type interface mode (OOIM) and the acoustic-optic type interface mode (AOIM), respectively, corresponding to k_A and k_B being both real, k_A being real and k_B being $\pi + iq_B$, k_B being real and k_A being iq_A , k_A and k_B being $\pi + iq_A$ and $\pi + iq_B$, and k_A being iq_A and k_B being $\pi + iq_B$ (i is imaginary unit and q_A (or q_B) is real). BMs are all standing waves that can freely propagate both in sublayers A and B ; PCMAs are standing waves in sublayer A , while in sublayer B they are surface optic decaying waves; PCMBs are standing waves in sublayer B , while in sublayer A they are surface acoustic decaying waves; OOIM and AOIM are surface decaying waves that can only exist near the interface in both sublayers. The higher subband whose width is 4 ($4J_A S_A$) is composed of PCMAs, the lower subband whose width is 1 ($4J_B S_B$) consist of PCMBs, and the overlap of the subbands is made of BMs. The highest branch (dotted line) is OOIM, and the branch (dotted line) within the gap is AOIM (see Fig. 1). For $\gamma = 0$, the number of BMs is 25, the number of PCAMs is 20 and the number of OIM is 1. Along Δ path, with γ increasing, the energy of all modes increases, moreover, the highest dotted line changing into a PCMA whose energy is maximum and the BMs gradually changing into PCMA and PCMBs. Along Y path, the gap becomes wide. At the position M, the number of PCMA is 31, the number of PCMB is 14 and the number of AOIM is 1, moreover, the maximum gap Δ_g appearing which equals to $8J_A S_A - 12J_B S_B$.

4. ANISOTROPY AND THE ENERGY BANDS

At last, we'll consider the effect of the uniaxial bulk anisotropy constant and take D_A as variable and D_B as a definite value. For simplicity, we define D_B as 0.

The numerical calculations are performed as above. The change of the energy bands with respect to D_A are somewhat different from γ . Comparing Fig. 2 with Fig. 1, we indicate that the higher subband moves up globally with D_A increasing, however, the lower subband is fixed. Moreover, the overlap branches are reduced with D_A increasing (see Fig. 2). When $D_A \geq \frac{4J_B S_B}{2S_A - 1}$, all the overlap branches vanish and the AOIM appears in the whole first Brillouin zone between two subbands (see Fig. 2). At the same time, the gap become larger with D_A enlarging and the maximum gap yet lies at the site M (for $\gamma = 0$). So when $D_A > 0$, the maximum gap located at the point M, moreover, its width getting greater with D_A increasing. Anyway, the number of the eigenmodes equals to the number of the atomic layers.

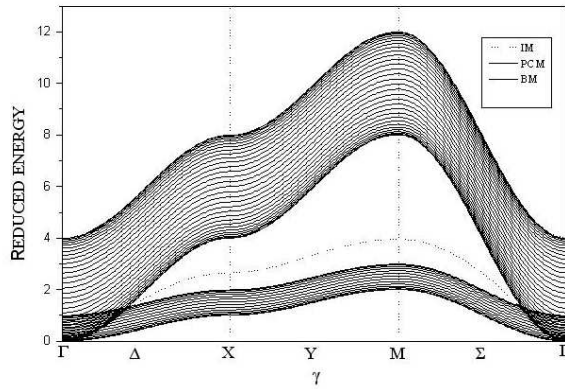


Figure 1: The energy band structure (EBS) of 2D Brillouin zone of the biferromagnetic layer corresponding to D_A , D_B , J_{AB} , J_A , J_B , S_A , S_B , N_A and N_B are, respectively, 0, 0, 2.0, 1.0, 1.0, 0.5, 1/2, 31 and 15. The highest dotted line denotes the OOIM, and the dotted line inside the gap denotes the AOIM. Δ line, Y line and Σ line are three high symmetry paths.

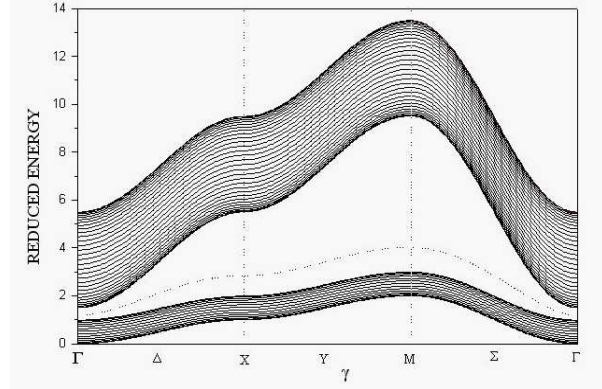


Figure 2: The EBS of 2D Brillouin zone of the biferromagnetic layer corresponding to D_A is 1.5 and the other parameters are same as Fig. 1. The higher subband moves up globally and the overlap branches decrease.

5. CONCLUSION

In summary, all kinds of eigenmodes of the spin waves of the biferromagnetic system relates not only to the bulk exchange coupling, the interface exchange coupling, the spin of lattice and the number of atomic layers, but also to the uniaxial bulk anisotropy. Moreover, the uniaxial bulk anisotropy affects the width of the gap. When D_A is greater than 0, the maximum gap lies in the site M and the width of two subbands is invariant. In any case, the total number of the spin-wave modes of the system equals to the number of atomic layers.

ACKNOWLEDGMENT

This work was supported by the National Natural Science Foundation of China under Grant No. 10762001, the NCET under Grant No. 05-0272, the Ph.D Progress Foundation of higher education institutions of China under Grant No. 200801260003, and Inner Mongolia Natural Science Foundation under Grant No. 200711020115.

REFERENCES

1. Smith, D., C. E. S. Khizroev, and D. Litvinov, "Magnetoresistive playback heads for bit-patterned medium recording applications," *J. Appl. Phys.*, Vol. 99, 014503, 2006.
2. Nembach, H. T., P. M. Pimentel, S. J. Hermsdoerfer, B. Leven, B. Hillebrands, and S. O. Demokritov, "Microwave-assisted magnetization switching of $\text{Ni}_{80}\text{Fe}_{20}$ in magnetic tunnel junctions," *Appl. Phys. Lett.*, Vol. 90, 062503, 2007.
3. Khitun, A., D. E. Nikonov, and B. Mingqiang, "Feasibility study of logic circuits with a spin wave bus," *Nanotechnology*, Vol. 18, No. 46, 465202(1–9), 2007.
4. Wieser, R., E. Y. Vedmedenko, and R. Wiesenganger, "Quantized spin waves in ferromagnetic and anti ferromagnetic structures with domain walls," *Phys. Rev. B*, Vol. 79, 144412, 2009.
5. Grünberg, P., *Light Scattering in Solids V*, M. Cardona, G. Güntherodt (Eds.), Springer, Berlin, 1989.
6. Livesey, K. L., D. C. Crew, and R. L. Stamps, "Spin wave valve in an exchange spring bilayer," *Phys. Rev. B*, Vol. 73, 184432, 2006.
7. Müller, W. and W. Nolting, "Temperature-dependent quasiparticle band structure of the ferromagnetic semiconductor EuS," *Phys. Rev. B*, Vol. 66, 085205, 2002.
8. Mercier, D., J. C. S. Levy, M. L. Watson, J. S. S. Whiting, and A. Chamber, "Spin-wave modes in layered magnetic sandwich structures," *Phys. Rev. B*, Vol. 43, 3311, 1991.
9. Dobrzynski, L. and H. Puzkarski, "Eigenvectors of composite systems. I. General theory," *J. Phys.: Condens. Matter*, Vol. 1, 1239, 1989.

10. Henelius, P., P. Frobrich, P. J. Kuntz, C. Timm, and P. J. Jensen, “Quantum Monte Carlo simulation of thin magnetic films,” *Phys. Rev. B*, Vol. 66, 094407, 2002.
11. Puzkarski, H., “Ferromagnetic-bilayer spin-wave resonance. Effects of surface-interface-mode bilocalization,” *Phys. Rev. B*, Vol. 49, 6718, 1994.
12. Yun, G. H., et al., *Theories of the Electron-phonon Interaction and Spin Waves in Layered Materials*, Inner Mongolia University Press, Chapter 5, 1995.
13. Zhou, W. P. and G. H. Yun, “The energy bands and the dispersion relations of the spin waves in a ferromagnetic bilayer system,” *Surf. Sci.*, Vol. 553, 75, 2004.

Structure Optimization for Magnetic Equipment of Permanent Magnet Retarder Using ANSYS

B. F. Jiao, D. S. Li, Y. K. Sui, and L. Z. Ye

School of Mechanical Engineering and Applied Electronics Technology
Beijing University of Technology, China

Abstract— The main purpose of this research is to perform a magnetic analysis on magnetic equipment of permanent magnet retarder (PMR) and optimize the structure of magnetic equipment with ANSYS, finite element analysis software and its design optimization module. The physical model is built as axisymmetric model according to the characteristics of the structure in magnetic equipment. Using this model, the magnetic field distribution and magnetic force is calculated by ANSYS. Mathematical model of structure optimization is also built. The design variables are structural parameters including the dimensions of permanent magnets and magnetic yoke; the objective function is the magnetic force. The unconstrained optimization model takes the maximum value of magnetic force as the objective. First order optimization method is used to determine the optimum design of this problem. The optimization process works entirely with the ANSYS Parametric Design Language (APDL). The ANSYS optimization module offers several tools that attempt to address the mathematical model in different ways. The design tools are used to understand design space and the behavior of the dependent variables. It is showed that designing a structure with ANSYS optimization module and its design tools is an effective means to make improvements of structure.

1. INTRODUCTION

Conventional friction braking system suffering loss of torque and severe damage at high temperature [1] result in decreasing the lifespan of braking system, increasing the cost of vehicle operation and even influence the safety. Permanent magnet retarder (PMR) can resolve the problem mentioned above as a kind of braking assistant device.

According to the disadvantages of existing PMR, our previous work proposed a novel PMR (Figure 1) and confirmed the linear relationship between magnetic force of magnetic equipment and brake torque under some conditions [2]. In order to improve the performance of the novel PMR, a magnetic analysis on magnetic equipment is performed and the structure of magnetic equipment is optimized using ANSYS.

2. PHYSICAL MODEL

Figure 2 shows the principle structure of magnetic equipment. According to the structure, the simplified physical model and design parameters is showed in Figure 3. It is an axisymmetric model and the short-circuit ring is neglected.

Rotor and shell yoke is made of steel 10. Magnetic yoke is made of iron DT4. Permanent magnet is made of Ne-Fe-B. Steel 10 and iron DT4 need to consider the $B-H$ curve. Air magnetic relative permeability is 1. Nd-Fe-B magnetic relative permeability is 1.0936 and axis magnetic coercive

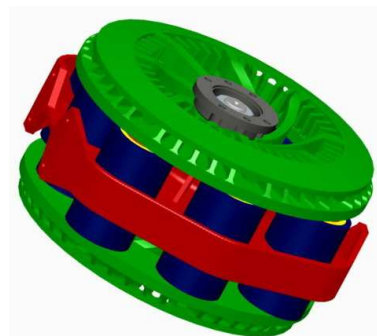


Figure 1: Disk type PMR structure.

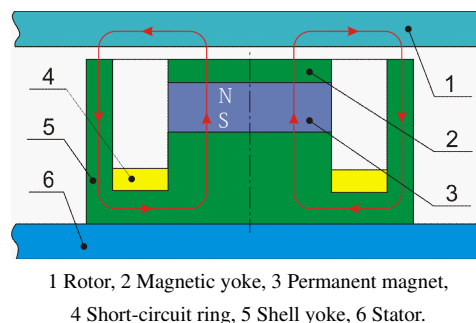


Figure 2: Principle structure of magnetic equipment.

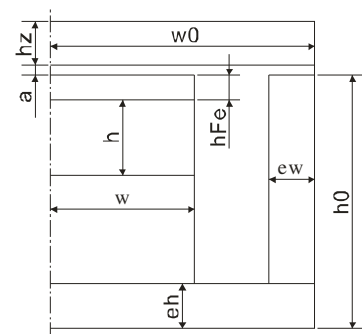


Figure 3: Physical model of magnetic equipment.

forces is 895 kA/m. This magnetic equipment model doesn't consider magnetic leak at boundary. The initial value of design parameters shows in Table 1. According to the magnetic equipment size of the eddy current retarder DHB20A (High 140 mm and Diameter 140 mm) which produced by CAMA (Luoyang) Electromechanic Equipment Co., Ltd, parameters w_0 , h_0 , a and h_z are constant. Others are design variables.

3. OPTIMIZATION DESIGN USING ANSYS

3.1. Optimization Model

Our purpose is maximizing the magnetic force under the structure size limitations. The optimization model is:

$$\begin{cases} hFe, w, h, eh, ew \\ f(hFe, w, h, ew, eh) \rightarrow \min \\ s.t. \\ 5 \leq hFe \leq 10, 5 \leq w \leq 50, \\ 5 \leq h \leq 50, 5 \leq ew \leq 20, \\ 5 \leq eh \leq 20. \end{cases}$$

3.2. Process for Optimization and Analysis Results

3.2.1. Create the Analysis File with the ANSYS Parametric Design Language (APDL)

In the process for optimization using ANSYS, many problems may intermit the analysis loop [3], especially creating the analysis file. This file includes the entire analysis: create geometry model parametrically with the initial value of parameters, obtain the solution, retrieve the value of magnetic force and assign the parameter of objective function.

Initial Model is meshed with element plane 53. Air gap need tidy mesh, so the global element edge length is 0.001 and air gap mesh is mapped. The other parts are free meshed. Figure 4 shows the meshed model and Figure 5 shows the distribution of flux lines.

ANSYS software only makes the objective function (OF) minimum. So magnetic force (its value is defined as FVW_Y) must be transform to OF (its value is defined as FOBJ) form to satisfy the need of ANSYS software. In this paper, the OF form is $FOBJ = 10000 + FVW_Y$. The magnetic force is -2764.6 N with initial value of design parameters by numerical computation using ANSYS.

3.2.2. Use the Optimization Module

The progress is:

- Specify the analysis file.
- Declare the optimization variables and keep the convergence tolerance as default values.
- Choose optimization methods or tools.
- Execute optimization.
- Review the optimization results.

Firstly, first order method is used. After computation converged, 3 optimization sets is obtained, showed in Table 2 and the optimization design is annotated with *. Distribution of flux lines for optimized model showed in Figure 6.

Table 1: Design parameters.

Parameters	Value (mm)
w_0	70
h_0	70
a	1.5
h_z	10
hFe	5
w	40
h	15
eh	5
ew	5

Table 2: Optimization sets.

	SET 1	SET 2	*SET 3*
HFE	5.0000	5.0000	5.0000
W	40.000	50.000	50.000
H	25.000	27.311	28.206
EW	5.0000	9.9470	9.4632
EH	5.0000	5.7686	5.9625
FOBJ	7235.4	5100.7	5075.8
Feasibility	FEASIBLE	FEASIBLE	FEASIBLE

Table 2 showed that parameters hFe and w reach the boundary value. Then, sweep tool is used to show the relationship between design variables and OF . The analysis of relationship between parameter w and OF is execute as parameter h is set to 28, ew is set to 9.5, eh is set to 6 and hFe is set to 5, and Figure 7 shows the relationship. It is showed that parameter w has significant influence to OF . Therefore, w is set to 50 and analysis of relationship $hFe-OF$ is executed and showed in Figure 8.

Figure 8 showed that the relationship between parameter hFe and OF is linear and setting hFe to 5 as optimization value is reasonable.

3.3. Comparison between Preliminary Design and Optimized Design

Table 3 shows the comparison between preliminary design and optimized design. Magnetic force increased 78.11%.

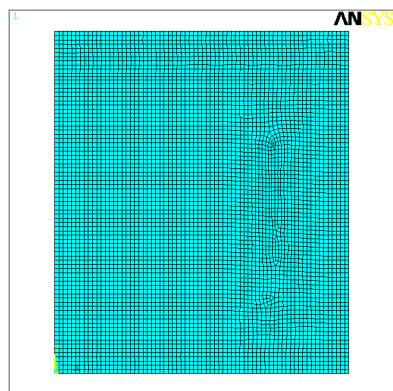


Figure 4: Meshed model.

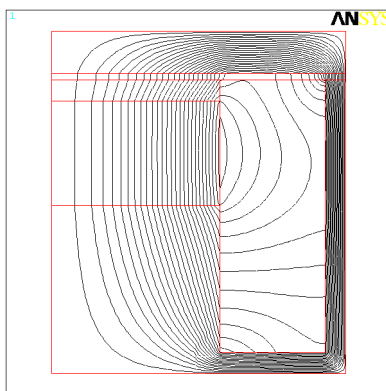


Figure 5: Distribution of flux lines.

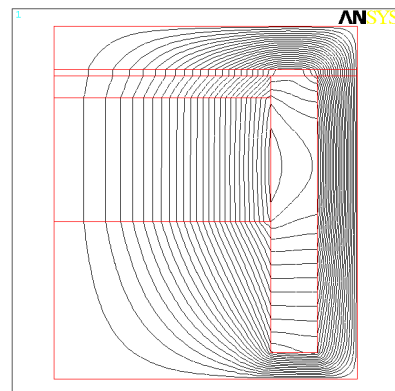


Figure 6: Distribution of flux lines for optimized model.

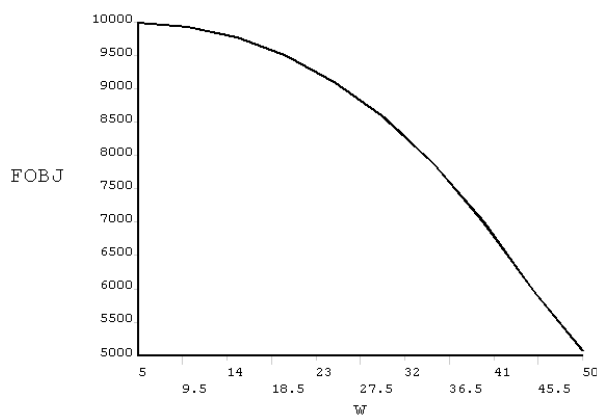


Figure 7: $w-OF$ curve.

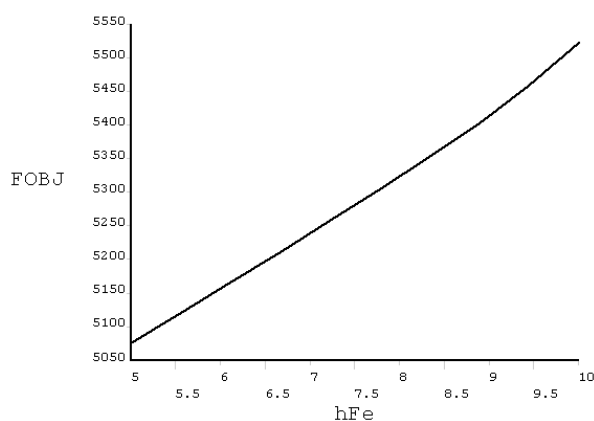


Figure 8: $hFe-OF$ curve.

Table 3: Comparison between preliminary design and optimized design.

Optimization variables	Preliminary design	Optimized design
hFe	5 mm	5 mm
w	40 mm	50 mm
h	15 mm	28 mm
ew	5 mm	9.5 mm
eh	5 mm	6 mm
FOBJ	7235.4N	5075.9N
Magnetic force	2764.6 N	4924.1 N

4. CONCLUSIONS

(1) ANSYS software is a efficient tool to analysis and optimize the structure. It is showed the significant influence of ANSYS in optimal design of structure.

(2) The best magnetic equipment design parameters are $hFe = 5$ mm, $w = 50$ mm, $h = 28$ mm, $ew = 9.5$ mm and $eh=6$ mm. As the best design, value of magnetic force is 4924.1 N and magnetic force is 78.11% higher than that of preliminary design.

(3) Both parameters hFe and w have significant influence to magnetic force.

REFERENCES

1. Gay, S. E. and M. Ehsani, "Analysis and experimental testing of a permanent magnet eddy-current brake," *2005 IEEE Vehicle Power and Propulsion Conference, VPPC*, 756–765, Chicago, IL, United States, September 2005.
2. Ye, L. Z., D. S. Li, Z. Y. Lu, and Q. H. Guo, "Study on a novel permanent magnet retarder for vehicles," *PIERS Proceedings*, 531–535, Hangzhou, China, March 24–28, 2008.
3. Wang, X., Z. Yang, and L. Duan, "About some optimization design problems of ANSYS," *Su Xing Gong Cheng Xue Bao/Journal of Plasticity Engineering*, Vol. 14, No. 6, 181–184, 2007.

Analysis of Drilling Parallel Horizontal Twin Wells Rotating Magnetic Beacons Magnetic Field Strength Size in SAGD

B. Tu, D. S. Li, E. H. Lin, B. Luo, J. He, L. Z. Ye, J. L. Liu, and Y. Z. Wang

School of Mechanical Engineering and Applied Electronics Technology

Beijing University of Technology, China

Abstract—Rotating magnetic beacons magnetic field strength size is very important to drilling parallel horizontal twin wells in Steam Assisted Gravity Drainage (SAGD). This paper analyzes a small magnet by made of diameter is 25.4 mm at both ends when a single length of 12.6 mm by permanent magnet and in the middle of the length is 78 mm magnetic materials. Analysis the magnetic material composition of 1J12, 1J50, 1J79 generated magnetic field strength size. Use ANSOFT software simulation the magnetic field strength to different magnetic materials and build experimental methods to a specific experimental test. According to the simulation results and experimental results compared and analyzed 1J12, 1J50, 1J79 three kinds of magnetic materials generated magnetic field strength size. Experimental results and simulation results are basically consistent and the results show that the magnetic material 1J50 that applied to the rotating magnetic beacon generated magnetic field strength that fluxgate can effective collect rotating magnetic beacon generated magnetic field strength in the horizontal distance of 55.5 m and it can to meet the specific requirements of engineering applications.

1. INTRODUCTION

In recent years, super-heavy to open has gradually attracted people's attention because of super-heavy crude oil viscosity is high and flow is poor and relying on any pressure differential-driven approach is difficult to succeed in this reservoir. This requires people to get such new technologies in order get heavy oil. SAGD (Steam Assisted Gravity Drainage) technology is suitable for mining very high viscosity of crude oil or natural asphalt extra-heavy oil reservoir. The process is steam as the heat source, relying on condensate liquid asphalt and heavy oil gravity. It can be two kinds of ways to achieve. The first one is a pair of upper and lower parallel well. The second one is a combination of vertical wells and parallel well. Steam is injection into the reservoir wells from the above and injection of steam upward and lateral movement. The heated viscosity of crude oil and condensate in the gravity-driven downstream into the production wells. With the crude oil recovery, steam room gradually expanding. The Figure 1 is the structure mining process of SAGD and the above is injection wells and the below is production wells [1–4].

SAGD called for two parallel wells up and down vertical distance is about 5 m. SAGD use the RMRS (Rotating Magnet Ranging Service) rotating magnetic ranging system to control the vertical distance between two wells and analyzed different magnetic materials RMRS rotation magnetic beacons in this paper. The rotating magnetic beacons installed in the motor the output shaft, which connected the end of drill bit. Magnetic beacons and drill bit together rotation in the mud motor driven, producing a dynamic rotating magnetic field. MWD uses logging winch into the target under the target depth of wells, which collect the rotating magnetic beacon generated signals and transmission to the surface interface box. Surface interface box is used to hole at the end of MWD to provide power supply and with the data communication between the MWD will eventually send the signal via mud pulse signal transmission to the laptop computer for data collection (Figure 2) [1–4]. The magnetic structure of this beacon be made of 12 individual magnets and each individual composition of the small magnets in diameter from 2-side 25.4 mm height 12.6 mm NdFe35 the composition of the permanent magnet, the middle is straight through the 25.4 mm height of 78 mm of lead magnetic material composition (Figure 3). Study 1J12, 1J79, 1J50 3 in different magnetic materials magnetic field strength.

2. ANSOFT MODELING AND SIMULATION

ANSOFT HFSS Maxwell2D/3D can design and analysis variety of products electromagnetic phenomena. It has a powerful and user-friendliness analysis module, such as static magnetic field and eddy current field and transient field and temperature field analysis. It can be used to analyze static and steady-state and transient and normal operating conditions and fault conditions of the properties of motors and transformers and sensors and electromagnetic devices. It contains a

top-down implementation of the user interface and lead adaptive mesh separation technology and user-defined materials and libraries and other characteristics. Maxwell2D/3D can increase speed of the fastest solution because it have a high-performance matrix solver and multi-CPU processing capability [5].

Maxwell 2D/3D use graphical input interface and AutoCAD input conversion interface and draw graphics is extremely easy. You can create a variety of models. Maxwell2D/3D use adaptive finite element method and graphic input is completed and given dielectric material and problems of the correct boundary conditions. It can automatically analyze and calculated without human interference as long as you give solution accuracy and dielectric material.

Building model accord the design of magnetic beacons size and the Figure 4 is three-dimensional

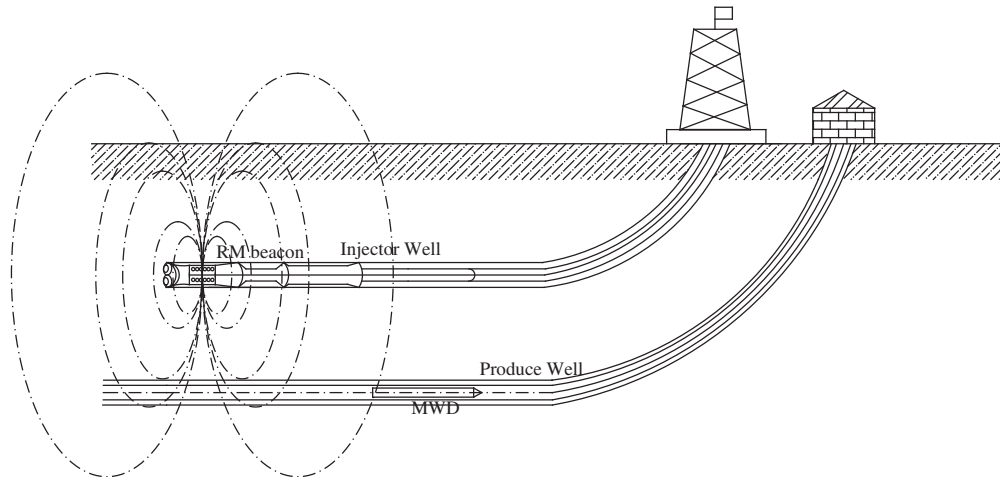


Figure 1: The structure of mining process SAGD.

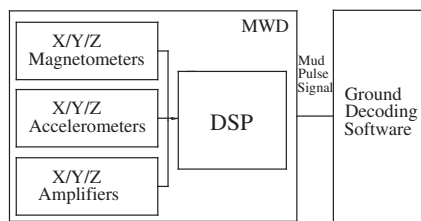


Figure 2: The signal transmission process of mining process SAGD.

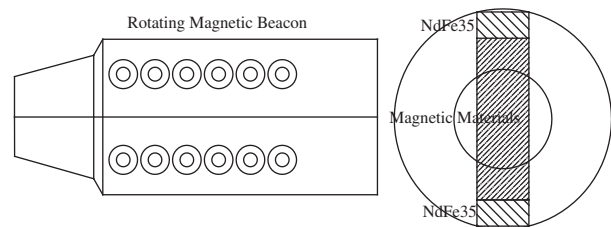


Figure 3: The structure of RM beacons.

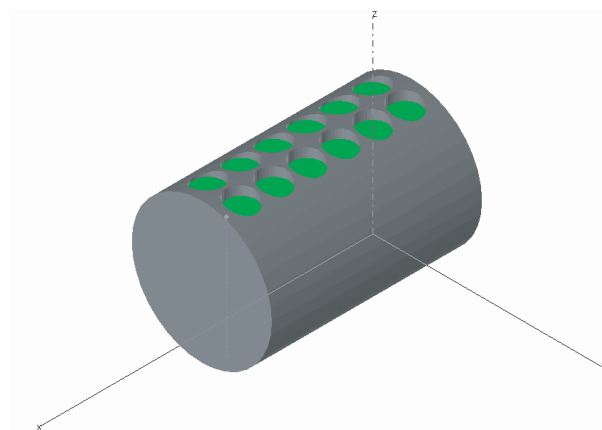


Figure 4: The three-dimensional model of RM beacon.

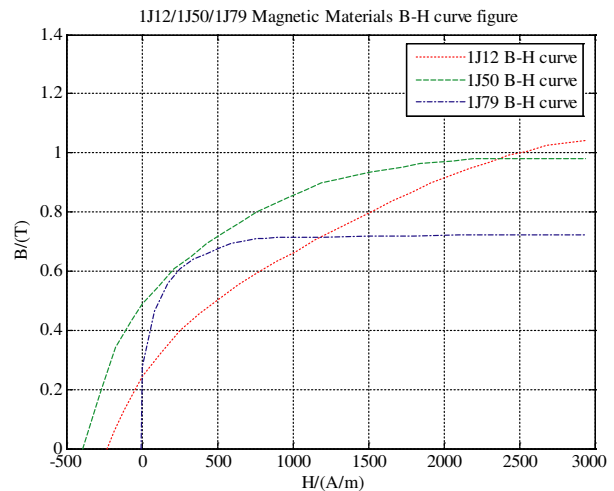


Figure 5: 1J12/1J50/1J79 magnetic materials B-H curve.

model diagram.

Determine the magnetic material properties. Maxwell2D/3D allowed to add their own material besides have built-in library of materials. This paper researched 1J12/1J50/1J79 three different magnetic materials magnetic field strength. The Figure 5 show three different magnetic materials BH curves. 1J79 permalloy soft magnetic material is a series of iron-nickel soft magnetic alloy with high magnetic permeability and low coercivity and so on. 1J12 have a high saturation magnetic flux density and so on. 1J50 is low-nickel and middle-nickel iron-nickel alloy and magnetic permeability and coercivity range of between high magnetic saturation materials and high magnetic material [6–8].

Finally, according to the design requirements calculation statistics in the Y axis and the statistics results are shown in Table 1.

Table 1: ANSOFT simulation statistic data.

	(0, 50, 0)	(0, 100, 0)	(0, 150, 0)	(0, 200, 0)
1J12 (T)	(-0.025, 0.102, 0.059)	(-0.005, 0.012, 0.009)	(-0.005, 0.012, 0.009)	$(-2, 4, 8) \times 10^{-4}$
1J79 (T)	(-0.028, 0.101, 0.023)	(-0.004, 0.011, 0.001)	(-0.001, 0.002, 0.003)	$(-1, 5, 9) \times 10^{-4}$
1J50 (T)	(-0.066, 0.179, 0.062)	(-0.013, 0.031, 0.015)	(-0.001, 0.004, 0.005)	$(-2, 8, 18) \times 10^{-4}$

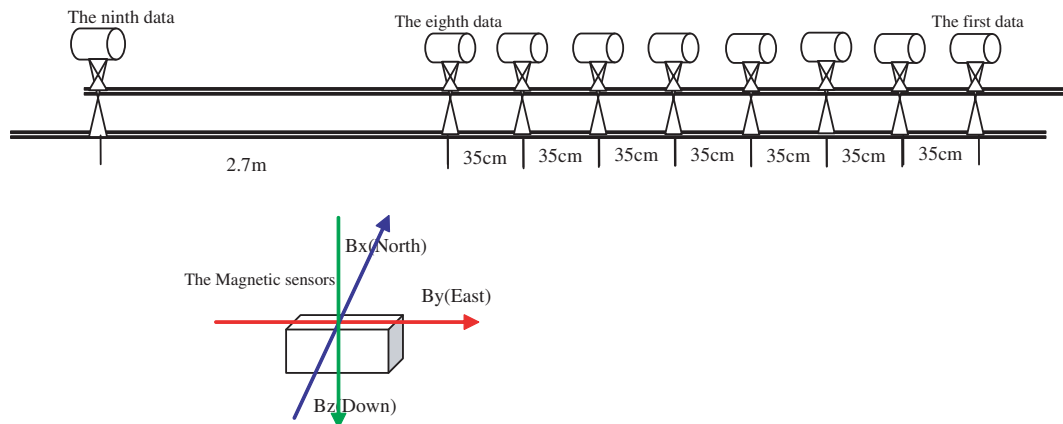


Figure 6: The engineering test scenario structure.

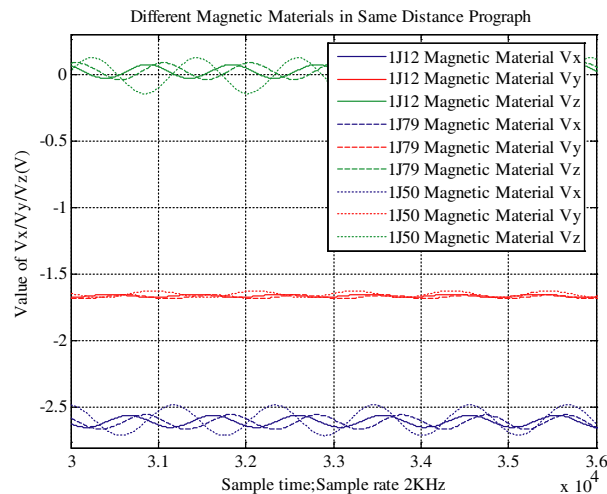


Figure 7: Magnetic sensor acquisition voltage value.

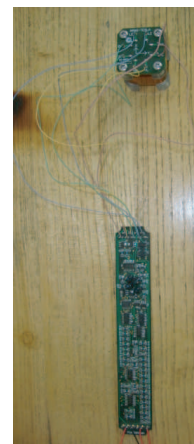


Figure 8: Magnetic sensor photo.

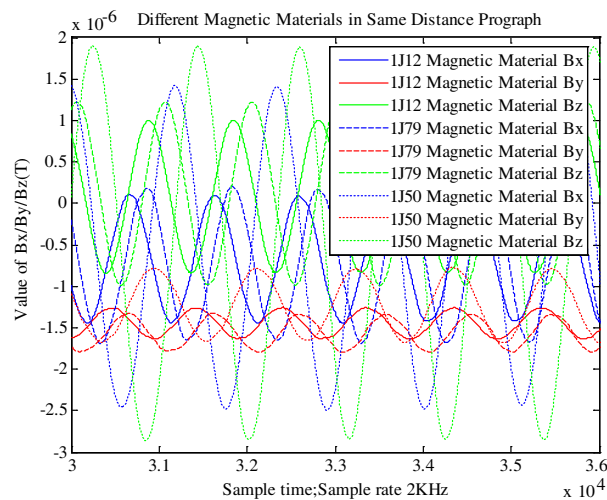


Figure 9: Voltage converted to magnetic field strength values.

Figure 10: Rotating Magnetic Beacon photo.

Table 2: 1J12/1J79/1J50 statistical results.

		1	2	3	4	5	6	7	8
V _{max} (V)	V _x (1J12)	1.921	1.945	1.976	2.031	2.213	2.450	2.674	2.768
	V _x (1J79)	1.970	2.014	2.034	2.161	2.307	2.440	2.664	2.717
	V _x (1J50)	2.019	2.023	2.030	2.438	2.602	3.075	3.555	3.756
	V _y (1J12)	0.056	0.112	0.177	0.255	0.313	0.297	0.161	0
	V _y (1J79)	0.042	0.096	0.152	0.210	0.269	0.284	0.157	0
	V _y (1J50)	0.028	0.317	0.458	0.667	0.721	0.688	0.426	0
	V _z (1J12)	2.717	2.783	2.894	2.902	2.853	2.949	3.021	3.035
	V _z (1J79)	2.684	2.823	2.845	2.864	2.845	2.904	2.973	3.016
	V _z (1J50)	2.903	3.003	2.890	3.002	3.217	3.589	2.462	3.507
V _{min} (V)	V _x (1J12)	0	0	0	0	0	0	0	0
	V _x (1J79)	0	0	0	0	0	0	0	0
	V _x (1J50)	0	0	0	0	0	0	0	0
	V _y (1J12)	-0.24	-0.27	-0.36	-0.41	-0.47	-0.49	-0.34	-0.09
	V _y (1J79)	-0.22	-0.27	-0.34	-0.42	-0.46	-0.45	-0.32	-0.10
	V _y (1J60)	-0.42	-0.45	-0.60	-0.74	-0.87	-0.84	-0.60	-0.08
	V _z (1J12)	0	0	0	0	0	0	0	0
	V _z (1J79)	0	0	0	0	0	0	0	0
	V _z (1J50)	0	0	0	0	0	0	0	0

3. EXPERIMENTS

In this paper, the simulation is also built on the basis of engineering test methods, test scenario structure, as shown in Figure 6.

This paper built engineering test methods basis on the ANSOFT simulation and the test scenario structure is shown in Figure 6. The engineering experimentation tested nine points of data through magnetic sensors and the ninth point measured voltage value is shown in Figure 7. The Figure 8 is the magnetic sensor actual photo. The magnetic sensor output data is voltage value and through the Equations (1)–(3) converted to magnetic field strength value: The Figure 10 is the Rotating Magnetic beacons actual photo.

$$B_x = V_x * 0.54 / SF_x - Bias_{Fx} * 0.54 \tag{1}$$

$$B_y = V_y * 0.54 / SF_y - Bias_{Fy} * 0.54 \tag{2}$$

$$B_z = V_z * 0.54 / SF_z - Bias_{Fz} * 0.54 \tag{3}$$

where, $SFx/SFy/SFz/$ and $BiasFx/BiasFy/BiasFz/$ is the calibration factor. The Figure 9 is the ninth point data converted to magnetic field strength values.

The measured data from the first data to the eighth data statistical results are shown in Table 2 according to the above build project test method.

4. CONCLUSION

This paper analyzes 1J12/1J50/1J79 different magnetic materials use measure the parallel wells distance applications of SAGD. This paper using ANSOFT software simulation to different magnetic materials and built an experimental method has been actual test. The test results show that 1J50 magnetic material able to meet the requirements of engineering applications and through the practical engineering test that is satisfactory.

REFERENCES

1. Kuckes, A. F. and J. McMathon, "New electromagnetic surveying/ranging method for drilling parallel horizontal twin wells," *IADC/SPE27466 Drilling Conference*, 322–333, 1994.
2. Kuckes, A. F. and R. G. Pitezer, *Relative Drill Bit Direction Measurement*, United States Patent Application Publication, Pub. No.: 2003/0085059A1, May 8, 2003.
3. Hu, H. Y. and Q. S. Chen, "RMRS application on target-hitting of horizontal drilling," *Geology and Prospecting*, Vol. 6, 89–92, 2008.
4. Xiang, J. W. and C. S. Liu, "New developments of directional opposite joints in the connected brine wells," *China Well and Rock Salf*, Vol. 33, 20–22, 2002.
5. Liu, G. Q. and L. Z. Zhao, *The Finite Element Analysis of Ansoft Engineering Electromagnetic Field*, Publishing House of Electronics Industry, Beijing, 2005.
6. Ye, X. Y. and C. S. Yang, "Determination of content of Mn, Si, Ni, Cu, V in 1J12 soft magnetic alloys by ICP-AES," *Chemistry Analysis Measure*, Vol. 18, 19–21, 2009.
7. Zhang, Q. and R. Zhang, "Study about process of electroplating nickel on 1J50 material," *Scrawl Act and Electroplate*, Vol. 6, 39–41, 2008.
8. Cao, J. and Y. F. Wang, "Influence of annealing process on magnetic properties of 1J79 alloy," *Material & Heat Treatment*, Vol. 10, 82–89, 2008.

Full-wave Equivalent Circuit of Planar Multilayer Structures for Remote Sensing Applications

D. B. Ferreira¹, S. J. S. Sant'Anna^{1,2}, and J. C. da S. Lacava¹

¹Laboratório de Antenas e Propagação, Instituto Tecnológico de Aeronáutica, Brazil

²Divisão de Processamento de Imagem, Instituto Nacional de Pesquisas Espaciais, Brazil

Abstract— An elegant procedure, based on auxiliary potential functions and the transmission ($ABCD$) matrix, for obtaining the full-wave equivalent circuit of planar multilayer structures is presented. Green's functions are derived in a straightforward way by using the symbolic capability of the *Mathematica* software. Their applicability is shown through the calculation of the polarimetric response for a simple target embedded in a particular configuration of the multilayer planar structure.

1. INTRODUCTION

Multilayer structures have been the subject of intensive studies during the last decades. They can be applied, for instance, to optics in filter development, to microwave engineering in microstrip antenna design, or to remote sensing in natural target modeling, among other areas. Although the planar geometry is the most widely employed configuration for these distinct applications, cylindrical [1] and spherical [2] geometries can also be found in the microstrip antenna literature. Regardless of the application or the geometry, knowledge of the electromagnetic fields behavior in the structure layers is crucial for its correct modeling and usage. In the remote sensing context, a new electromagnetic methodology for the simulation of polarimetric SAR images has recently been proposed in [3]. Starting from Maxwell's equations, it applies the spectral domain full-wave technique and the moment method to evaluate the electromagnetic fields scattered by a multilayer planar structure excited by plane waves. However, the calculations of spectral fields and the related Green's functions in multilayer structures are usually tedious and error-prone when done by hand, so a circuital model has been devised to minimize these limitations. Following [4, 5], but using a different approach, a new elegant and straightforward procedure for obtaining the full-wave equivalent circuit of a planar multilayer structure based on auxiliary potential functions and the transmission ($ABCD$) matrix is presented. The electromagnetic characteristics of each confined layer are incorporated into the transmission matrix and the circuital parameters are evaluated by using the symbolic capability of the *Mathematica* package. Therefore, the use of such circuital model to generate the Green's functions of a multilayer structure can be extremely helpful in the determination of a simple target's scattering matrix and consequently of its related polarimetric features.

2. TARGET GEOMETRY

A multilayer planar structure composed of $N + 2$ isotropic, linear and homogenous layers stacked up in the z -direction is shown in Fig. 1. The layers are assumed to be unbounded along the x - and y -directions. The lower layer, having complex permittivity ε_g and complex permeability μ_g , is denoted as the ground layer and occupies the negative- z region. The next N layers are characterized by thickness ℓ_n , complex permittivity ε_n and complex permeability μ_n , where $1 \leq n \leq N$. The planar interface $z = d_N$ separates the N -th layer from free space (the upper layer). Metallic patches, which behave as scattering elements, are printed at arbitrary positions on each one of the $N + 1$ interfaces of the structure. The surface electric current densities on the scatterers located at the interfaces are induced by an illuminating elliptically polarized plane wave at oblique incidence.

3. ELECTROMAGNETIC FIELDS

The analytical development is based on a global rectangular coordinate system located atop the ground layer ($z = 0$). The electromagnetic fields in each of the $N + 2$ layers are determined by using the auxiliary vector potential approach. According to [6], by superposing the expressions for the fields of the TM^z and TE^z modes in the n -th layer, calculated from the magnetic (A_{mzn}) and electric (A_{ezn}) potentials, the total field in that layer can be determined. Working in the Fourier

domain, the following expressions are obtained for the transversal components of the spectral fields in the n -th layer:

$$E_{xn} = i\{[k_y A_n + (k_x \gamma_n / \omega \mu_n) C_n] e^{-i\gamma_n z} + [k_y B_n - (k_x \gamma_n / \omega \mu_n) D_n] e^{i\gamma_n z}\} / \varepsilon_n, \quad (1)$$

$$E_{yn} = i\{[-k_x A_n + (k_y \gamma_n / \omega \mu_n) C_n] e^{-i\gamma_n z} + [k_x B_n + (k_y \gamma_n / \omega \mu_n) D_n] e^{i\gamma_n z}\} / \varepsilon_n, \quad (2)$$

$$H_{xn} = i\{[(k_x \gamma_n / \omega \varepsilon_n) A_n - k_y C_n] e^{-i\gamma_n z} - [(k_x \gamma_n / \omega \varepsilon_n) B_n + k_y D_n] e^{i\gamma_n z}\} / \mu_n, \quad (3)$$

$$H_{yn} = i\{[(k_y \gamma_n / \omega \varepsilon_n) A_n + k_x C_n] e^{-i\gamma_n z} - [(k_y \gamma_n / \omega \varepsilon_n) B_n - k_x D_n] e^{i\gamma_n z}\} / \mu_n, \quad (4)$$

where $\gamma_n = [k_n^2 - (k_x^2 + k_y^2)]^{1/2}$, k_x and k_y are the spectral variables and A_n , B_n , C_n and D_n are functions of k_x and k_y to be determined.

The next step consists of obtaining the transmission ($ABCD$) matrix for the n -th layer located between the interfaces $z = d_{n-1}$ and $z = d_n$. First, Equations (1)–(4) are solved for A_n , B_n , C_n and D_n , at the $z = d_n$ interface. Then, these functions are replaced into the same set of equations, which is now re-calculated at $z = d_{n-1}$. Consequently, the two-port transmission network, shown in Fig. 2, can be established in order to characterize the relationship between the transversal components of the spectral fields at the n -th layer interfaces. In Fig. 2, $\mathbf{E}_n(z)$ and $\mathbf{H}_n(z)$ denote the transversal components of the spectral fields in the n -th layer at coordinate z (italic bold letters represent vectors); expressions for the \mathbf{V}_n , \mathbf{Z}_n , \mathbf{Y}_n and \mathbf{B}_n matrices are available in [2]. An equivalent procedure is employed to evaluate the fields at the free space and ground layer interfaces. The boundary conditions are then applied for each planar interface, resulting in the circuit elements presented in Table 1. Consequently, the multilayer target (Fig. 1) can be modeled by the circuit illustrated in Fig. 3 and the spectral Green's functions can then be obtained directly from this circuit's equations.

As an example, the Green's functions for a structure composed of a single confined layer ($N = 1$), with a surface electric current density (\mathbf{J}_1) located at the interface between the confined layer and

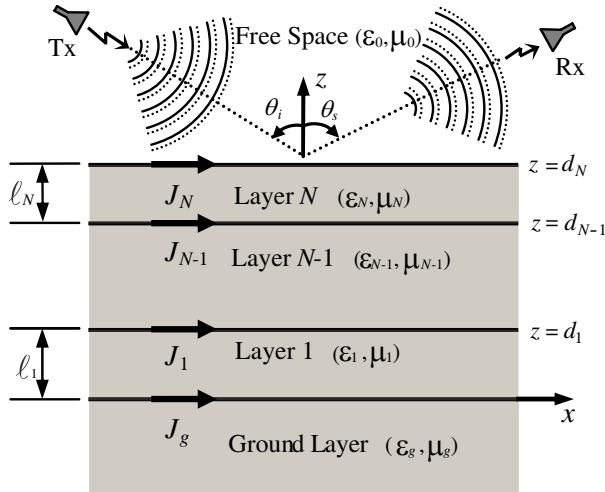


Figure 1: Target geometry.

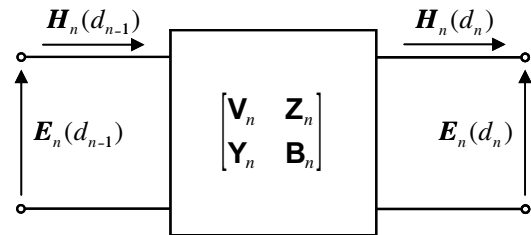


Figure 2: Transmission ($ABCD$) network.

Table 1: Return loss of a circular corrugated horn.

Ground interface	Free space interface	Surface electric current density

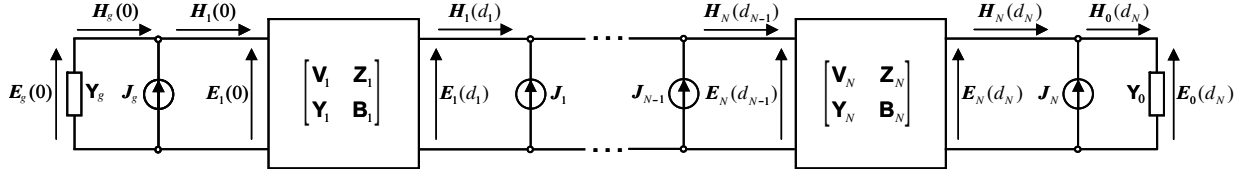


Figure 3: Circuitual representation of a planar multilayer structure.

free space, are evaluated next. In this case it was considered that $\mu_g = \mu_1 = \mu_0$. Solving the respective equivalent circuit, the Green's functions at the interface $z = d_1$ are given by

$$\mathbf{G} = \begin{bmatrix} G_{xy} & -G_{xx} \\ G_{yy} & -G_{yx} \end{bmatrix} = \left[\mathbf{Y}_0 + (\mathbf{B}_1 - \mathbf{Y}_g \cdot \mathbf{Z}_1)^{-1} \cdot (\mathbf{Y}_1 - \mathbf{Y}_g \cdot \mathbf{V}_1) \right]^{-1}. \quad (5)$$

Using the symbolic capability of *Mathematica* for evaluating Equation (5), the following expressions can be derived

$$G_{xx}(k_x, k_y, d_1) = -4\omega^2 \left(k_x^2 \gamma_0 \Omega_0^e \Delta_m + k_y^2 \omega \mu_0 \Omega_0^h \Delta_e \right) e^{-i\gamma_0 d_1} / (u^2 \Delta_m \Delta_e), \quad (6)$$

$$G_{xy}(k_x, k_y, d_1) = G_{yx}(k_x, k_y, d_1) = -4\omega^2 k_x k_y \left(\gamma_0 \Omega_0^e \Delta_m - \omega \mu_0 \Omega_0^h \Delta_e \right) e^{-i\gamma_0 d_1} / (u^2 \Delta_m \Delta_e), \quad (7)$$

$$G_{yy}(k_x, k_y, d_1) = G_{xx}(k_y, k_x, d_1), \quad (8)$$

where $u^2 = k_x^2 + k_y^2$,

$$\begin{aligned} \Delta_e &= -4\omega^3 \varepsilon_1 \gamma_1 \{ \varepsilon_g \gamma_1 [\varepsilon_1 \gamma_0 \cos(\gamma_1 d_1) + i \varepsilon_0 \gamma_1 \sin(\gamma_1 d_1)] \\ &\quad + \varepsilon_1 \gamma_g [\varepsilon_0 \gamma_1 \cos(\gamma_1 d_1) + i \varepsilon_1 \gamma_0 \sin(\gamma_1 d_1)] \} e^{-i\gamma_0 d_1}, \end{aligned} \quad (9)$$

$$\Delta_m = 4\omega^3 \mu_0^3 \gamma_1 \{ \gamma_1 [\gamma_0 \cos(\gamma_1 d_1) + i \gamma_1 \sin(\gamma_1 d_1)] + \gamma_g [\gamma_1 \cos(\gamma_1 d_1) + i \gamma_0 \sin(\gamma_1 d_1)] \} e^{-i\gamma_0 d_1}, \quad (10)$$

$$\Omega_0^e = -\varepsilon_1 \gamma_1^2 [\varepsilon_1 \gamma_g \cos(\gamma_1 d_1) + i \varepsilon_g \gamma_1 \sin(\gamma_1 d_1)], \quad (11)$$

$$\Omega_0^h = \omega \mu_0^3 \gamma_1 [\gamma_1 \cos(\gamma_1 d_1) + i \gamma_g \sin(\gamma_1 d_1)]. \quad (12)$$

4. SCATERING ATTRIBUTES

The scattering matrix is considered the most important parameter in polarimetric SAR image analysis, since it provides complete information about the scattering mechanism and from which other polarimetric features that describe the scattering target can be derived. Therefore, the scattering matrix can be regarded as the mathematical signature of a scattering target, as it relates the scattered wave's electric field to the incident one. Using the proposed methodology and applying the stationary phase method, asymptotic expressions for the far electromagnetic fields scattered by the structure into free space are obtained. From these expressions and the knowledge of the electric current densities on the interfaces, the scattering matrix elements can then be completely determined for any incidence and scattering direction. However, for a simple target such as an electric dipole, the electric current densities become a multiplicative factor of the scattering matrix so its elements can be obtained directly from the Green's functions terms, as described in [7–9]. Consequently, for this kind of target, several polarimetric attributes, such as the polarimetric response and the radar cross section, among others, can be readily derived.

The polarimetric response is typically used in remote sensing to characterize the scattering properties of a target. It is a graphical representation of the target's scattering cross section as a function of the ellipticity and the orientation angles of the transmitted electromagnetic wave [10], and it can be straightforwardly computed from the target's scattering matrix. Based on the circuitual parameters, the polarimetric response of a particular structure having a single confined layer and a single electric dipole printed on the interface $z = d_1$ is derived. Assuming an L-band frequency (1.25 GHz) and monostatic configuration, i.e., $\theta_i = \theta_s$ e $\phi_i = \phi_s$, the response was generated for a structure characterized by the following parameters: $\varepsilon_{r1} = 2.33$, $\tan \delta_1 = 1.2 \times 10^{-1}$, $d_1 = 0.5$ m, $\varepsilon_{rg} = 5.0$ and $\tan \delta_g = 2.0 \times 10^{-1}$. The co-polarized response is presented in Fig. 4 for three different azimuth angles ($\phi_i = 0^\circ$, 60° and 120°). The representative surface of the polarimetric response, as well as its respective contour graphic, are depicted. The coordinates of the peak value of the

co-polarized response are marked in the contour graphic by the crossing point of the two dashed lines.

From Fig. 4 it can be noted that the polarimetric response must be carefully used as an attribute for target discrimination, since for the same target an azimuth angle variation can lead to different responses. This kind of variation was not observed when the orientation angle is varied. It is worth mentioning that the developed methodology permits the quick and precise evaluation of the target's scattering behavior by varying, for instance, the operating frequency as well as the structure's characteristic parameters.

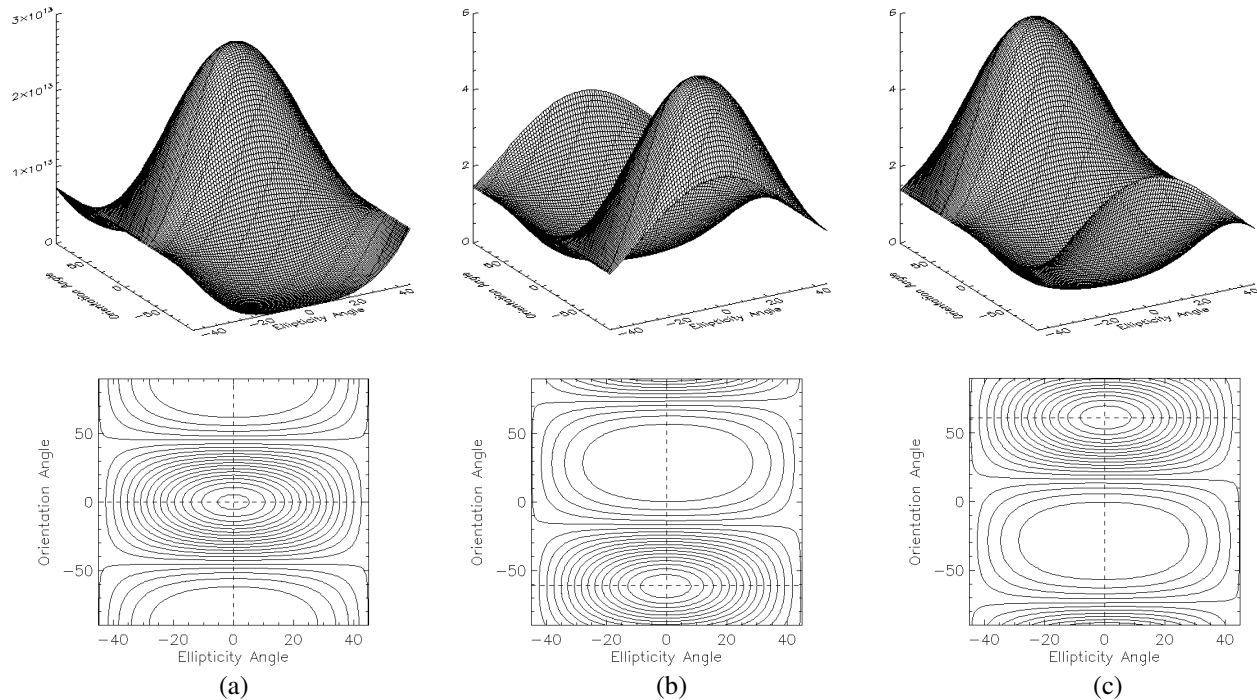


Figure 4: Co-polarized case of the polarimetric response of an electric dipole on top of the confined layer: (a) $\phi_i = 0^\circ$, (b) $\phi_i = 60^\circ$, (c) $\phi_i = 120^\circ$.

5. CONCLUSIONS

The spectral Green's functions of multilayer planar structures were obtained by an elegant and straightforward procedure: it consists of calculating a full-wave equivalent circuit, which is based on auxiliary potential functions and the transmission ($ABCD$) matrix. A particular structure configuration having a single electric dipole printed at the interface between free space and the single confined layer is used to demonstrate the great versatility and potentiality of the proposed methodology in the remote sensing framework. Using this insight the target's scattering analysis can be promptly evaluated for several distinct structures. The electric dipole's polarimetric response is also computed and analyzed, showing that its use as a discriminating measure must be done carefully.

ACKNOWLEDGMENT

The authors are grateful to FAPESP and FINEP-CAPTAER project for the partial support.

REFERENCES

1. Tinoco S., A. F. and J. C. S. Lacava, "Symbolic calculation of closed-form spectral Green's functions for cylindrically stratified media," *Proceedings of 9th International Mathematica Symposium*, Maastricht, Netherlands, June 2008.
2. Ferreira, D. B., "Microstrip antennas conformed onto spherical surfaces," Graduation thesis, Technological Institute of Aeronautics, São José dos Campos, Brazil, 2009 (in Portuguese).
3. Sant'Anna, S. J. S., J. C. S. Lacava, and D. Fernandes, "From Maxwell's equations to polarimetric SAR images: A simulation approach," *Sensors*, Vol. 8, No. 11, 7380–7409, 2008.

4. Itoh, T., *Numerical Techniques for Microwave and Millimeter-Wave Passive Structures*, John Wiley, New York, 1989.
5. Dreher, A., “A new approach to dyadic Green’s function in spectral domain,” *IEEE Trans. Antennas and Propag.*, Vol. 43, No. 11, 1297–1302, 1995.
6. Balanis, C. A., *Advanced Engineering Electromagnetics*, John Wiley, New York, 1989.
7. Sant’Anna, S. J. S., J. C. S. Lacava, and D. Fernandes, “Closed form expressions for scattering matrix of simple targets in multilayer structures,” *Proceedings of International Geoscience and Remote Sensing Symposium*, 714–717, Barcelona, Spain, July 2007.
8. Sant’Anna, S. J. S., J. C. S. Lacava, and D. Fernandes, “Evaluation of scattering matrix of flat dipoles embedded in multilayer structures,” *PIERS Online*, Vol. 4, No. 5, 536–540, 2008.
9. Rabelo, N. R., S. J. S. Sant’Anna, J. C. S. Lacava, and D. Fernandes, “Scattering analysis of flat electric dipoles on multilayer chiral structures,” to appear in *Proceedings of European Conference on Antenna Propagation*, Barcelona, Spain, April 2010.
10. Van Zyl, J. J., H. A. Zebcker, and C. Elachi, “Imaging radar polarization signature: Theory and observations,” *Radio Science*, Vol. 22, No. 4, 529–543, 1987.

Tumor Classification Using Radar Target Signatures

R. C. Conceição, M. O'Halloran, D. Byrne, E. Jones, and M. Glavin

Electronic and Electrical Engineering, College of Engineering and Informatics
National University of Ireland Galway, Ireland

Abstract— The use of Ultra Wideband (UWB) radar to detect early-stage breast cancer has been extensively investigated. The basis for this imaging modality is the significant dielectric contrast between normal and cancerous breast tissue at microwave frequencies.

However, based on the recently-established dielectric similarities between malignant, benign and fibroglandular tissue within the breast, differentiating between these types of tissues in microwave images may be problematic. Therefore, it is important to investigate alternative methods to analyse and classify dielectric scatterers within the breast. One such approach is to classify scatterers based on their radar target signature, which carries information about scatterer size and shape.

Benign tumors tend to have smooth surfaces and are compact and oval in shape. Conversely, malignant tumors tend to have rough and complex surfaces with spicules or microlobules. These properties can significantly influence the radar target signature, potentially allowing for dielectric scatterer classification.

This paper presents a method to model the growth pattern of benign and malignant tumors, based on the use of Gaussian Random Spheres (ranging between smooth, macrolobulated, microlobulated and spiculated shapes), while classification algorithms that attempt to define the nature of tumors based on radar target signatures are also examined.

1. INTRODUCTION

Microwave imaging has been comprehensively investigated as a means to detect possible tumors within the breast, and is based on the dielectric contrast between different types of tissues.

When the breast is illuminated by a UWB pulse, significant reflections are generated by dielectric scatterers, such as tumors. These reflections can be processed to produce a UWB image of the breast, where high energy regions suggest the possible presence of tumor tissue. Historical studies such as those taken by Joines et al. [1] and Surowiec et al. [2] found significant dielectric contrast between normal tissue and tumors found in the breast.

Recent findings by Lazebnik et al. [3, 4] have supported earlier research that there is a high dielectric contrast between normal adipose tissue and tumors within the breast, suggesting that UWB radar may be sufficient to isolate tumors, particularly in breasts that are primarily composed of adipose tissue. However, it was also found that the dielectric contrast between normal fibroglandular and tumor tissues, as well as between benign and malignant tumor, may not be sufficient to identify tumors in more dense breasts where the fibroglandular content is much more significant or to differentiate between benign and malignant tumors.

This has highlighted the need to further analyse data to help characterise the type of tissues within the breast. In previous work, Davis et al. [5] investigated the radar target signature of objects in order to characterise tumors. In her paper, Davis created tumor models based on Gaussian Random Spheres (firstly introduced by Muinonen [6]) which can represent the different stages of growth of a tumor through varying shapes and sizes.

This paper investigates the development of a classifier which distinguishes between malignant and benign tumors, using a coarse size classifier. Compared to [5], our size classifier attempts to divide the models into two size groups, instead of the four size groups included in the testing group. Also in our study, a fourth tumor model is introduced: the microlobulated Gaussian Random Spheres which represents a malignant tumor. Similarly, our shape classifier attempts to classify the tumors into benign or malignant tumors instead of fully classifying the four different shapes included in the testing group.

The remainder of the paper is organized as follows: Section 2 introduces the experimental set, Section 3 presents the results, and in Section 4 the conclusions are drawn.

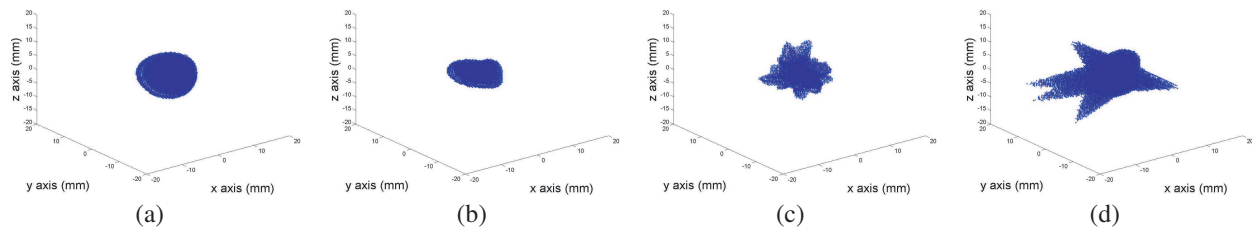


Figure 1: Samples of different Gaussian Random Spheres. From left to right (a) smooth, (b) macrolobulated, (c) microlobulated and (d) spiculated (5 spicules) models, with an average radius size of 5 mm.

2. EXPERIMENT

2.1. Models

A 3D Finite-Difference Time-Domain (FDTD) model of the breast was developed which incorporates the different dielectric properties of the breast tissues. A resolution of half millimeter cubic grid is used for the FDTD model. In order to analyse the target signature of the tumors, the backscattered data was generated by means of a Total-Field/Scattered-Field (TF/SF) simulation. A plane wave impinged on the target from four different equidistant angles and the resulting cross-polarized backscatter was recorded and analysed from each point where the plane wave originated from. The tumors were modeled with the dielectric properties of malignant tumor tissue whereas the surrounding tissue was modeled with homogeneous adipose tissue, using the same Debye parameters as in [5].

The models for tumors are based on the Gaussian Random Spheres approach [5, 6]. Four different shapes and four different sizes are used. Malignant tumors include spiculated and microlobulated Gaussian Random Spheres, whereas benign tumors include macrolobulated and smooth Gaussian Random Spheres. Microlobulated, macrolobulated and smooth Gaussian Random Spheres can be obtained by varying the correlation angle from low to high. Spiculated Gaussian Random Spheres are obtained by adding 3, 5 or 10 spicules to smooth Gaussian Random Spheres. The average size of the radius of all types of spheres took values of 2.5, 5, 7.5 or 10 mm. Between all sizes and shapes, the testing group for the present experiment consists of 240 different tumor models.

2.2. Signal Analysis and Classification

The algorithm for classification of the different tumor models involves four steps, and is based on the work in [5]. The sequence is as follows:

- The backscattered recorded signals are downsampled by a factor of 16;
- Principal Component Analysis (PCA) is carried out on each recorded backscattered signal;
- Dimensionality reduction is carried out;
- Classification is carried out using both linear [5, 7, 8] and quadratic discriminant approaches [7, 8].

3. RESULTS

The results section is divided in two parts. Firstly, the results of separate size and shape classifiers, and in particular, the determination of a suitable value of dimensionality used for classification, are presented. The second part shows results for a combined size-then-shape cascade classifier.

3.1. Performance of Size and Shape Classification

The objective of this experiment is twofold: Firstly, to determine the performance of size and shape classifiers as a function of the dimensionality, and therefore, to determine a suitable value for dimensionality that can be used in practice (providing a good compromise between accuracy and computational load); and secondly, to analyse the performance of each classifier and to compare linear and quadratic classification approaches.

Two classifiers were created: the first classifies the tumor models according to their size and the second according to their shape. The size classifier assigns each tumor model either to a radius size below or equal to 5 mm (2.5 and 5 mm) or to a radius size above 5 mm (7.5 and 10 mm). The shape classifier assigns each tumor either to a malignant shape (spiculated and microlobulated) or to a benign shape (macrolobulated and smooth). For these experiments, the accuracy of each classifier is expressed in terms of classification accuracy (i.e., the proportion of models correctly classified). For training the size and the shape classifiers, a database of 960 models was used. The size of the test sets were 240 for both size and shape classifiers.

For both size and shape classifier, a graph was obtained showing the accuracy of the linear and quadratic classifications against the number of PCA components, from 2 to 100. The results are shown in Figure 2.

Looking at both graphs in Figure 2, a dimensionality in the range of 25–30 appears to be a reasonable compromise between computational complexity and performance; for both cases, the classification performance starts to saturate at this level. A dimensionality of 30 was used in [5].

Using 30 principal components as the value for the dimensionality for the classification algorithm, the size and shape classifiers were analysed. Table 1 presents the accuracy of both classifiers using a linear and a quadratic classifier.

From Table 1, it is clear that for a dimensionality of 30, the size classifier outputs higher results than the shape classifier. Classification on the basis of shape alone gives poorer performance. However, as the final aim of the classification of tumors is to be able to distinguish between malignant and benign tumors (and not just obtain information on the size of tumors), it is reasonable to assume that a cascade of a size classifier followed by a shape classifier will provide more accurate classification. The size classifier provides higher accuracy in producing groups, to which a shape classifier can be applied. This approach was also used in [5].

3.2. Results for Combined Size/Shape Classifiers

Here, each of the two size groups, to which models were assigned using the size classifier, are individually classified using separate classifiers for shape, in which tumor models are classified into two shape categories: malignant and benign. The accuracy of these two individual shape classifiers

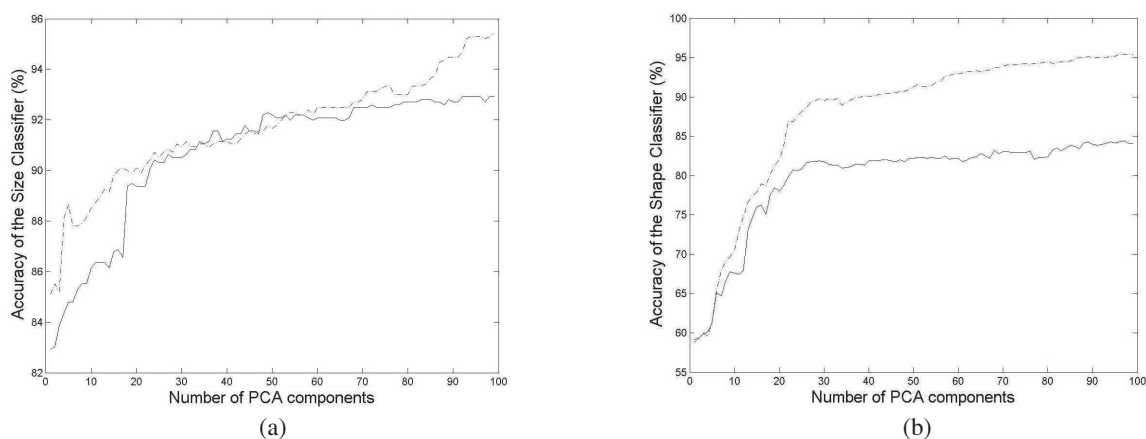


Figure 2: Graph with accuracy of linear (solid line) and quadratic (dashed line) classifiers versus the number of principal components used. Figure 2(a) shows the results for the size classifier and 2(b) for the shape classifier.

Table 1: Accuracy for size and shape classifiers using both linear and quadratic classifications with 30 principal components.

	Size classifier	Shape classifier
Groups to which models are assigned	- Radius size less than or equal to 5 mm - Radius size greater than 5 mm	- Malignant shape - Benign shape
Accuracy using the linear classification	90.52%	81.87%
Accuracy using the quadratic classification	91.04%	89.79%

Table 2: Accuracy for the shape classifier (when applied to pre-classified size groups) and the size-then-shape cascade classifier using both linear and quadratic classifications with 30 principal components.

	Shape classifier	Size-then-shape cascade classifier
Groups to which models are assigned	- Malignant shape - Benign shape	- Malignant shape - Benign shape
Accuracy using the linear classification	86.35%	78.17%
Accuracy using the quadratic classification	87.81%	79.95%

is expressed in terms of the proportion of tumors correctly identified, each using a training set which only includes tumors belonging to a pre-classified size group. The results are averaged for these two shape classifiers and are presented in the first column of Table 2. The overall accuracy for the size-then-shape cascade classifier is calculated by multiplying the partial accuracies for the size classifier and the shape classifier. The overall classification results for the size-then-shape classifier are presented in the second column of Table 2.

For this two-stage approach, the quadratic approach provides better performance. In particular, for the shape classifier (first column in Table 2), the quadratic approach provides an absolute performance improvement of almost 1.5% compared to the linear classifier (relative improvement of 1.7%). For the size-then-shape classifier (second column in Table 2), the quadratic approach gives an absolute performance level 1.8% better than the linear classifier (relative improvement of 2.3%).

4. CONCLUSION

This paper has described experiments conducted on the analysis of UWB radar backscatter signals, with the aim of classifying tumors as either malignant or benign. A set of 240 tumor models of different sizes and shapes is classified through a 4-step classification algorithm. PCA was used for feature extraction, while both linear and quadratic approaches were used for classification. The number of principal components for use in the classification was chosen as 30, offering a good compromise between classification accuracy and computational time.

Without any prior knowledge of any of the groups of all tumor models, the size classifier offers higher accuracy (90.52 and 91.04% for linear and quadratic classifiers, respectively) than the shape classifier (81.87 and 89.79% for linear and quadratic classifiers, respectively).

Using the prior results for the size classifier, the shape classifier is applied and classification accuracies of 86.35 and 87.81% were achieved (for linear and quadratic classifications, respectively). For completion of this study the overall accuracies for the size-then-shape cascade classifier are calculated and the accuracy for detecting whether a tumor was benign or malignant is 78.17% for the linear classifier and 79.95% for the quadratic classifier.

ACKNOWLEDGMENT

This work is supported by Science Foundation Ireland (SFI) under grant number 07/RFP/ENEF420. It is also supported by the Irish Research Council for Science, Engineering and Technology (IRCSET) Enterprise Partnership Fellowship Scheme with Hewlett Packard (HP).

REFERENCES

1. Joines, W. T., Y. Zhang, C. Li, and R. L. Jirtle, "The measured electrical properties of normal and malignant human tissues from 50 to 900 MHz," *Med. Phys.*, Vol. 21, No. 4, 547–550, 1994.
2. Surowiec, A. J., S. S. Stuchly, J. R. Barr, and A. Swarup, "Dielectric properties of breast carcinoma and the surrounding tissues," *IEEE Trans. Biomed. Eng.*, Vol. 35, No. 4, 257–263, 1988.
3. Lazebnik, M., L. McCartney, D. Popovic, C. B. Watkins, M. J. Lindstrom, J. Harter, S. Sewall, A. Magliocco, J. H. Booske, M. Okoniewski, and S. C. Hagness, "A large-scale study of the ultrawideband microwave dielectric properties of normal breast tissue obtained from reduction surgeries," *Phys. Med. Biol.*, Vol. 52, 2637–2656, 2007.
4. Lazebnik, M., D. Popovic, L. McCartney, C. B. Watkins, M. J. Lindstrom, J. Harter, S. Sewall, T. Ogilvie, A. Magliocco, T. M. Breslin, W. Temple, D. Mew, J. H. Booske, M. Okoniewski, and S. C. Hagness, "A large-scale study of the ultrawideband microwave dielectric properties of normal, benign and malignant breast tissues obtained from cancer surgeries," *Phys. Med. Biol.*, Vol. 52, 6093–6115, 2007.
5. Davis, S. K., B. D. V. Veen, S. C. Hagness, and F. Kelcz, "Breast tumor characterization based on ultrawideband microwave backscatter," *IEEE Trans. Biomed. Eng.*, Vol. 55, No. 1, 237–246, 2008.
6. Muinonen, K., "Introducing the Gaussian shape hypothesis for asteroids and comets," *Astron. Astrophys.*, Vol. 332, No. 3, 1087–1098, 1998.
7. Krzanowski, W. J., *Principles of Multivariate Analysis: A User's Perspective*, Oxford University Press, New York, 1988.
8. Seber, G. A. F., *Multivariate Observations*, John Wiley & Sons, Inc., Hoboken, New Jersey, 1984.

Optimizing Windows Security Features to Block Malware and Hack Tools on USB Storage Devices

Dung Vu Pham¹, Malka N. Halgamuge², Ali Syed¹, and Priyan Mendis²

¹School of Computing and Mathematics, Charles Sturt University, Victoria 3000, Australia

²The Department of Civil and Environmental Engineering, The University of Melbourne
Victoria 3010, Australia

Abstract— Malware replicating via USB storage devices including worms, virus, Trojan horses and other malicious codes together with USB based hack tools such as Pod Slurp and USB Switchblade have accounted for many serious security issues for the last few years. The majority of these malicious codes exploit Windows Autoplay features to automatically launch attacks on host computers transparently to the users. In this paper, we will analyze the vulnerabilities in the default settings of the latest Windows operating systems which allow malware from attached USB storage devices to launch attacks on the computers. We will also propose solutions and patches for the vulnerabilities in form of ready-to-deploy scripts which can be run by any computer users. The solutions will focus on the latest Windows operating systems including Windows XP SP2, Windows Vista, Windows 7, and Windows 2008.

1. INTRODUCTION

Universal Serial Bus (USB) storage devices have been one of the most common means of malware and hack tools attacks on computers for the last few years. This has been possible due to some factors involving the lack of security mechanisms for Windows Autoplay features, and the communication channel between computer and USB drives, and the popularity of USB storage devices such as compact flash cards, flash drives, external HDDs, digital cameras, iPods, and USB phones. Malware that exploits Windows Autoplay features to replicate via USB drives and automatically activate itself is commonly known as Autorun malware. This threat vector represented the largest single category of malware for the first two quarters of 2008 which, accounted for 17.7% of the total infection detected by Microsoft [1], and from June 13 to July 13, 2009, over 27 million infections by this type of malware were detected by McAfee [2]. Moreover, there are also various USB based hack tools, especially on U3 drives, such as USB Switchblade, Pod Slurp, and USB Pocket Knife which exploit the Autoplay features to automatically launch attacks on host computers transparently. Microsoft and security firms such as McAfee, Symantec, ESET, Trend Micro Inc, and BitDefender have invested a lot of effort in re-engineering their products to reduce the impacts of Autorun malware. Recently, Microsoft had to make a decision to disable the Autoplay feature for USB drives on Windows 7, their latest operating system, in an effort to reduce the impact of Autorun malware [1]. However, such a solution only helps prevent malware from activating via Autoplay features on USB drive insertion. There have been some work on the risks of USB devices to information security in corporate environments with proposed solutions involving *data access control, USB port access control, and security policies* [3–5]. However, the most common type of risks from USB drives which was not mentioned in the previous papers is malware on USB which are supposed to be accounted for the majority of all USB based software attacks. This threat vector has not received enough attention and further work on this type of attacks is necessary. Moreover, there are important factors which were not considered in the solutions proposed in the previous papers which are personal computers and their users. Solutions proposed in previous papers are only applicable for corporate environments which require license costs, technical configurations and maintenance cost, and corporate policies [6]. In this paper, we will propose a solution package in form of ready-to-deploy scripts which helps optimize Windows security features to mitigate attacks by malware and hack tools on USB storage devices. Here, we target for a solution which does not require license costs or complex technical configuration and suits both personal and corporate computer environment.

2. MALWARE AND HACK TOOLS ON USB STORAGE DEVICES

The term *malware* in this paper refers to computer worms, viruses, Trojan horses, root kits, spyware, and adware. Malware uses two main techniques to spread via USB storage devices, executable file

infections and by exploiting Autorun.inf file and Windows Autoplay feature [6]. Malware presenting on USB drives are capable of self-replicating themselves via many means of media under the forms of executable files and scripts. Such executable files typically involve .exe, .dll, .prg, .ocx, .ovl, and .sys, and scripting files with .bat, .js, .pl, .vbs, and .wsh extension.

USB based hack tool refers to non-self-replicable malicious tools deployed on USB drives, especially U3 drives, and can be triggered from USB drives [6]. Many of these tools involve the use of scripting files and are specially designed to exploit Windows Autoplay features to trigger themselves on USB drive insertion [3–5]. USB based hack tools generally provides attackers with ultimate payloads varying from *data theft, information exploits, accounts and password exploits, data recovery, to privilege escalation* [6]. Although the number of incidents caused by USB based hack tools is limited because these tools cannot self-replicate and are not fully automated, they do cause fear in corporate environments where information security is critical.

3. WINDOWS VULNERABILITIES EXPLOITED BY MALWARE AND HACK TOOLS ON USB DEVICES

3.1. No Security Mechanism for Windows Autoplay Features

Windows Autoplay features automatically launch the content on removable media at the very moment when the media are inserted. The Autoplay process is activated with parameters specified in Autorun.inf located in the root folder of a USB drive which specifies the path to executable files to be run. Attackers exploit this benign feature to auto launch malware without any user interaction when a USB device is inserted. The computer detects newly inserted USB drive, reads the Autorun.inf file and loads the malware. Unfortunately, Windows does not provide any security mechanism, which prevents activation of malware specified in Autorun.inf files.

3.2. U3 USB Drives Remain a Major Threat Vector

U3 is an open standard developed to provide users with application mobility through an application platform available in U3 drives whereby U3 applications can be installed on and run from U3 drives *independently from host computers*. In a U3 drive, a small partition located at the beginning of the drive is marked as a CDFS (CD file system) partition so that Windows recognizes it as a CD rather than a USB drives. U3 applications are self-contained applications run from the CDFS partition. While the Autoplay features for USB drives are disabled on Windows 7, they are still enabled for the CDFS partition. U3 technology is supported on all Windows x86 and x64 platform from Windows 2000 SP. Attackers can customize their own ISO images with necessary hack tools and malware to install in the CDFS partitions to exploit the Autoplay feature available for CDFS partitions or directly run the hack tools from the U3 Launchpad [6]. The CDFS partition contains irremovable Autorun.inf file and malware which cannot be removed by Antivirus software even when they are detected.

3.3. Driver Signing Is Not Enforced on 32 Bit Platform

Digital signatures allow users to know whether a legitimate publisher has provided the software package. The x64 families of Windows Vista and Windows Server 2008 require Kernel Mode Code Signing (KMCS) in order to load kernel-mode software. Kernel Mode Code Signing (KMCS) policy requires kernel-mode code to be signed with a valid Authenticode certificate rooted by a famous code signing authorities, such as VeriSign. However, The 32 bit family does not provide any protection to private read/write system memory used by components running in kernel mode and, therefore, once in kernel mode the software has complete access to all operating system data [7]. This was the reason why attackers could craft their own driver for their USB drives to cause buffer overflow attacks on Windows 32 bit operating systems [8].

3.4. Vulnerabilities in User Account Control (UAC)

Windows operating systems including Vista and the later are still vulnerable to unsigned code execution. Although UAC does warn users when there is an unsigned application activated and try to make changes to system settings or system files, these warning messages are not always effective as users can simply allow the execution of the unsigned code. This is due to the lack of standardization in the software industry where a lot of software is released without digital certificates which make it difficult to make the decision of allowing only signed code execution on Windows computers. Figure 1 illustrates an alert by UAC created when an unidentified (unsigned) application which is trying to make changes the computer. In this situation, if the user chooses “Allow”, the unsigned code gets the full permissions to make changes to the operating system files

and settings. Unfortunately, in many cases, users feel UAC alerts annoying and immediately allow the unsigned application to execute.

Moreover, information gathering tools which collect user's information left in temporary files and Windows registry are generally not blocked because UAC only alert users when there is a process trying to *make changes* to the computers. Therefore, in many situations, malware and hack tools on USB drives can still successfully execute their payload under the monitor of UAC. Figure 2 shows the UAC setting options under Windows 7 where it shows that only application which try to modify or make changes to the current settings and system files will generate an alert. This explains why some spyware and information gathering tools can still successfully exploit user's private information such as online accounts, credit card information from windows temporary files under the UAC monitor.

3.5. In Effective Malware Detection Based on Behavior Patterns by Microsoft Antimalware

The recent test by AV-Test.org, independent anti-virus testing lab, showed that Microsoft Security Essentials (MSE) achieved 98.44 per cent detection rate using signature based detection but it does not have any effective dynamic detection features which can analyze malware based on malicious behaviors. Detection and cleaning of infected computers worked but in many cases MSE does not correct the problem left behind after malware attacks [9]. Therefore, MSE is not effective to malware whose signatures are yet not there in malware definition database and chances for stopping malware on activation is lower than a thorough scan over all the files before the malware gets triggered.

In Figure 3, the drivers for USB devices provided by hardware vendors are located in User Mode layer where access to system resources is limited to user right and privileges only. This model is generally applied to Windows Vista and the later. However, in previous Windows version such as Windows XP and 2003, USB driver was located in Kernel Mode layer where it has unlimited access to system resources. Thus, attackers who successfully commit USB drivers can have system rights and privileges. Moreover, attackers were able to craft drivers for USB drives and successfully injected the drivers into Windows possibly due to the lack of driver signing enforcement in Windows XP and other 32 bit editions. The enforcement of signed drivers will prevent unsigned drivers from being injected to Windows kernel and thus help mitigate this threat vector effectively.

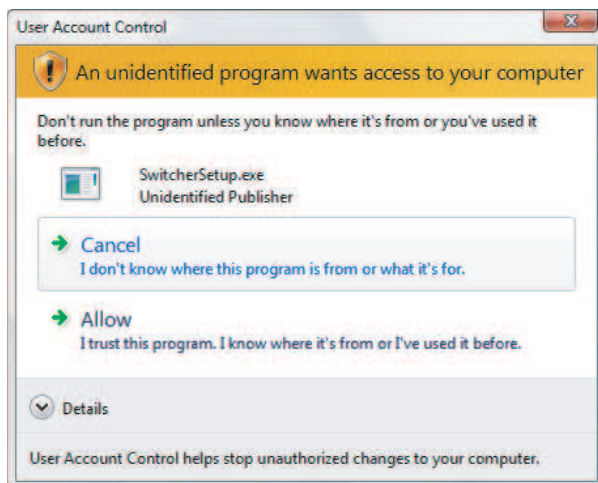


Figure 1: UAC alert on unsigned code execution.

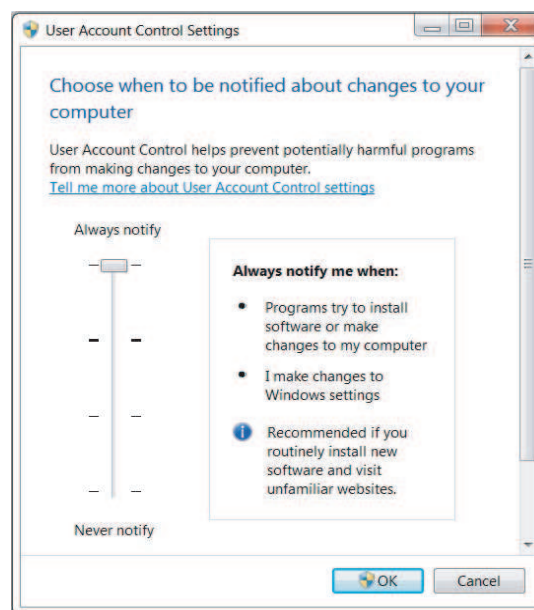


Figure 2: User account control settings.

4. SOLUTIONS

4.1. Block “Untrusted” Executable Files on USB Drive from Being Executed

A *trusted executable files* must be a *valid executable file signed with a non-expired digital signature by a trusted publisher or a reputable certificate authority* such as VeriSign. Viruses and worms

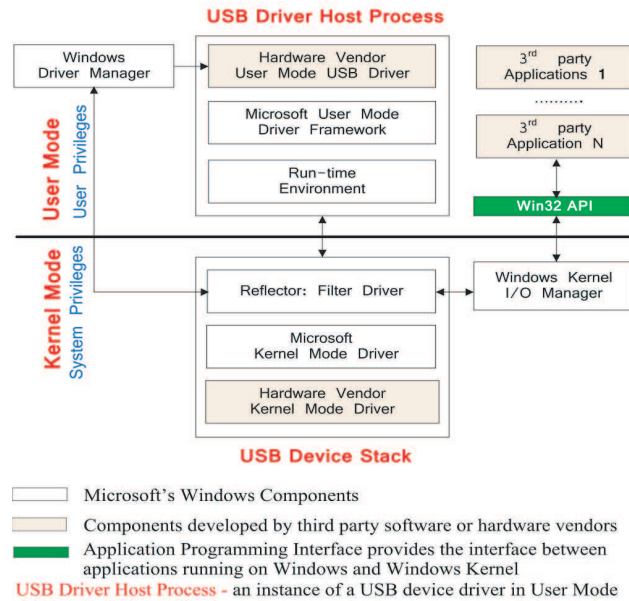


Figure 3: Windows USB driver architecture [6].

are often deployed with social engineering technique to trick users into triggering them. Therefore, allowing only trusted executable files on USB drive to be executed will help blocking any potentially dangerous code from executing even by users. This can be done via either software restriction policies or AppLocker feature. While software restriction policies feature is first introduced in Windows XP and 2003, AppLocker is a new advanced feature first introduced in Windows 7 Ultimate/Enterprise, and Windows 2008 R2.

The implementation of *software restriction policies* for executable files on USB drives are handled by certificates rules *specifying a code-signing, software publisher certificate and path rules specifying a fully qualified path to the USB drives* using wildcards to address all executable and script files. AppLocker is the more flexible option where we can specify only files belonging to trusted publishers can be executed from USB drives on specific user or users groups. Our ready-to-deploy script package allows users to choose to implement either software restriction policies or AppLocker based on their needs and their own operating systems.

4.2. Enforcement of Driver Signing

Under Windows XP, the driver signing option must be set to “block — never install unsigned driver software” under system property console. This will prevents crafted USB drivers to be installed on computers. While under the later 64 bit versions of Vista, Windows 2008, and Windows 7, driver signing enforcement is enabled by default, their 32 bit versions still allows users to force unsigned driver installation [7]. Therefore, manually enforcement of driver signing option must be done through *Local policy/security options* with *Devices: Unsigned driver installation behavior* option set to “do not allow installation”. We also provides a script which automatically checks on the integrity check option for driver to make sure the driver signing option is enabled.

4.3. Prevent Autorun File from Being Created on Drive Root Folders

The most common feature of Autorun viruses and worms is Autorun.inf file creation on any drives to which they replicate as this is a part of the strategy on which they replicate and launch attacks on the next computer [10]. If the malware cannot create Autorun.inf on the next drives, it cannot automatically trigger itself and the chances for replication are much lower. The script that we provides here will automatically create Read-only Autorun.inf folder on USB drives and any connected drives on the host computer and thus preventing Autorun malware from overwrite Autorun.inf file to complete an attack cycle.

4.4. Enforcement of UAC and updated Microsoft Antimalware

The most common infection methods by malware involve through bundling (packaged with legitimate software) and social engineering (tricking users into activate the malware). UAC, Windows Defender and MSE offer significant protection against both bundling and social engineering. UAC

will always alert users on any process which try to make changes to system files and settings which helps users aware of what is going on and take necessary actions. Windows Defender and MSE provide real-time protection and scans executable files before they are activated. However, the detection mechanism of MSE relies solely on malware signatures [8] and therefore, enforcing malware definition update will provide the best protection results. Our script package is provides self check for UAC and automatically update the malware definition database for Windows Defender as well as MSE on daily basis.

5. RESULTS

Table 1 summarizes the changes made to Windows operating system after implementing the solutions. This generally shows how the security features in Windows operating systems are utilized to protect computers from malware on external USB drives.

Table 1: Changes applied to Windows after implementing the solution.

Setting & Features	Default Settings	Changes in Settings
Execution files running from USB drive	Yes	Trusted signed applications only
Autoplay feature on USB devices	Yes: Before Windows 7; No: Windows 7	Yes
Unsigned USB driver installation	Yes: 32 bit; No: 64 bit	No: Signed driver only
Executable files copied to System locations	Yes	No
Group Policy: Software Restriction Policy	Not implemented	Yes, block untrusted codes on USB drives
User Account Control	Yes by default, can be turned off	Yes, checked and turned on at system booting
AppLocker	Not implemented	Yes, block untrusted codes on USB drives
Windows Defender	Available on Windows Vista, 7, 2008	Installed on all versions from Windows XP
Microsoft Security Essentials	Not implemented	Installed on all versions from Windows XP
Windows Update	Not enforced	Enforced, malware definition update
Windows security features utilized	UAC, Windows Defender (Vista & Win 7 only), Windows Firewall	AppLocker, MSE, Windows Defender, UAC, Windows Firewall, Windows Update, GPO

6. DISCUSSION

The solution package helps to optimize and maximize the effectiveness of all currently available security features on Windows operating systems to mitigate the threats from malware and hack tools on USB drives. The solution does not require complex configuration or additional software license costs and the most complex processes are automated via script packages which make the solution suitable for all computer users in both office and home environment. Moreover, the enforcement of signed applications and trust is just another step towards a secure computing environment which is currently the common trend in the computing industry. However, this solution does not directly address and remove un-activated or “sleeping” malware and hack tools inside USB storage devices. Therefore, we suggest a more comprehensive solution which involves a new Windows

security service architecture with new Windows security services and features which coordinate the available Windows security services and features to provide a scheme based real time scanning on USB drives for malware and hack tools right at the time of USB drive insertion in our next paper.

REFERENCES

1. Cohen, A., “Improvement to autoPlay,” Engineering Windows 7, Microsoft Developer Network Blog, Microsoft Corporation, 2009 (accessed November 2009), <http://blogs.msdn.com/e7/archive/2009/04/27/improvements-to-autoplay.aspx>.
2. McAfee Avert Labs., “McAfee threats report: Second quarter 2009,” *McAfee, Inc.*, 2009.
3. Alzarouni, M., “The reality of risks from consented use of USB devices,” *Proceedings of the 4th Australian Information Security Conference*, 2006.
4. Fabian, M., “Endpoint security: Managing USB-based removable devices with the advent of portable applications,” *Information Security Curriculum Development Conference*, 2007.
5. Wong, S., “Risk associated with USB memory sticks and high capacity storage devices,” *Siemens Insight Consulting*, 2007 (access January 2010), [http://www.insight.co.uk/files/whitepapers/Risks%20Associated%20with%20USB%20Memory%20Stick%20\(White%20paper\).pdf](http://www.insight.co.uk/files/whitepapers/Risks%20Associated%20with%20USB%20Memory%20Stick%20(White%20paper).pdf).
6. Pham, V. D., A. Syed, and M. N. Halgamuge, “Universal Serial Bus based software attacks and protection solutions,” Unpublished Result.
7. Russinovich, M. E. and D. A. Solomon, *Windows Internals*, 5th Edition, Microsoft Press, 2009.
8. Roberts, P. F., “USB devices can crack windows,” *Eweek*, 2005 (accessed February 12, 2010), <http://www.eweek.com/c/a/Security/USB-Devices-Can-Crack-Windows/>.
9. Leyden, J., “One thumb up for MS security essentials in early tests,” *The Register*, 2009 (accessed January 2010), http://www.theregister.co.uk/2009/10/01/ms_security_essentials_review/.
10. Thomas, V., P. Ramagopal, and R. Mohandas, “The rise of autorun- based malware,” *McAfee Avert Labs., McAfee Inc.*, 2009.

Evaluated the High Rang Resolution Profile Identifying Simulation by Laser Radar of the Rotation Targets

M.-J. Wang^{1,2}, Z.-S Wu³, Y.-L. Li¹, and J.-D. Xu²

¹Institute of E.M. Wave Propagation & Scattering, Xianyang Normal College, Box 103, 712000, China

²The School of Electronic Information, Northwestern Polytechnical University
Xi'an, Shaanxi 710076, China

³Science School, Xidian University, Box 273, 710071, China

Abstract— Recently, we presented a study of pulse beam scattering from a rigid body on the estimation by used with laser high-range resolution profile (LHRRP) simulations. However, there has been an increased interest in study of the LHRRP of a moving object. The LHRRP of rigid bodies are tightly connected with their posture and sensitive to the angle of their rotation. This paper presents a line of sight (LOS) method for analyzed the influence of a rotation angle of the targets, and compare the difference between their LOS projection and LHRRP simulations.

1. INTRODUCTION

There has been an increased interest which needs to understand the laser scattering from the complex targets and utilize these theories to simulate in the laser radar imaging. The laser high-range resolution profile (LHRRP) as one of laser radar imaging technologies will play more and more important roles in target recognition and battle sense. As compared to HRRP radar image, LHRRP is easy to offer enough and precise data on attitude characteristic determination of target such as ground-base, spacecraft and airplane [1–3]. Actually, the tomographic method of filtered back-projection was the earliest technologies to obtain high-resolution two-dimensional images, which represented an extension of radar imaging used at microwave wavelengths into the optical regime [4]. Due to range resolution is the ability to distinguish between two or more closely spaced objects, Reference [5] developed to increase the range resolving ability of a long pulse laser radar system. On the basis of an analysis of the autocovariance of the complex heterodyne signal, Reference [6] derived and investigated some novel algorithms to estimate the velocity of the targets. As a result, Laser high range resolution imaging radar is a novel technology has particularly attracted the attention of a great many institutes [7–9].

We have recently presented a study of an innovative technique of rigid body estimation by using of laser high-range resolution profile (LHRRP) simulations, and the theoretical simulated models are based on the of pulse beam scattering from random rough surfaces [10]. Because the LHRRP is very sensitivity to the change of the target's posture, according to the technologies, it is offered simulated methods to further study the influence on the LHRRP in different postures in order to conveniently discriminate them.

So this paper will be combined the LOS and LHRRP simulations to discuss the difference between the laser imaging and the actual geometrical dimension of the detected target. The body of this paper proceeds as follows. In Section 2, the briefly theoretical principle for the determination of the laser radar of a pulse beam by an arbitrary scatterer is given. Section 3 LHRRP is analyzed by projection of LOS an arbitrary rotated body. Section 4 provides comparison between the geometrical projection of LOS and the LHRRP characteristics by the numerical simulation and estimation of LHRRP properties of a typical target. The work is summarized in Section 5.

2. THE BRIEF THEORITICAL MODEL OF LASER SCATTERING FROM AN ARBITRARY ROTATION BODY

The laser radar equation of pulse beam scattering from arbitrary scattered body can be expressed [14–16]

$$P(t) = \int dS' \frac{P_i T_{A1} \eta_t}{\pi \phi^2 \rho_0^2} \pi w_0^2 \exp \left[-\frac{2g_0(\vec{r}')}{\phi^2 \rho_0^2} \right] \sigma(\vec{r}') \frac{T_{A2}}{4\pi \rho_0^2} \frac{\pi D^2 \eta_r}{4} \quad (1)$$

where dS' is cell rough surface in the scattering target, P_i is the incidence power, T_{A1} , T_{A2} is the rate of the average atmospheric transmission from the laser illumination and the receiver to

scattered body, respectively. η_t, η_r is the Equivalent optical efficiency the emission and receiver system, $\phi = 2/k_0 w_0$ is the width of pulse, $g_0(\vec{r}')$ is the zero order approximation of stationary phase point, $\sigma(\vec{r}')$ is the differential cross section, D is the aperture of detector, ρ_0 is the detected distance and w_0 is beam waist radius.

3. LASER HIGH RANGE RESOLUTION PROFILE ANALYZED BY PROJECTION OF LOS AN ARBITRARY ROTATION BODY

LHRRP can recognize some important characteristics from the detected targets. When the targets translate along a line, the characteristics of LHRRP don't change with their movements, which are as same as that of the static targets [16]. However, these imaging technologies have stronger response of their rotated posture. The high range resolution profiles (HRRP) is the amplitude of the coherent summations of the complex time returns from scattering points in each range cell, which represents the projection of the complex returned echoes from the target scattering centers onto the radar line-of-sight (LOS). Now, the analysis of LOS will be utilized to discuss the LHRRP in this section.

3.1. The Analyzed Methods of LOS in LHRRP

A coordinate frame of target is built and shown in Fig. 1. Coordinate system $OXYZ$ is the reference coordinate and the one of $O'X'Y'Z'$ is a coordinate frame of target, where the original point O' is the complex body center of gravity. Let us suppose that the coordinate of O' is (x_0, y_0, z_0) in reference coordinate $OXYZ$, and in the same time the surface of complex body's configuration will be expressed a function $f(x, y, z) = 0$. It is supposed that the area S' is illuminated by laser pulse, $\Delta s'$ is the illuminated cell whose positional vector and direction cosine of the unit vector normal correspond to \vec{r}' , $\vec{e}'_r = (\cos \alpha'_r, \cos \beta'_r, \cos \gamma'_r)$ in the coordinate frame of target, and ζ is the angle between the LOS direction and the positional vector \vec{r}' . So it is can compute the geometric range profile of illuminated unit $\Delta s'$ in the LOS direction

$$\text{Range profile} = |\vec{r}'| \cos \zeta = |\vec{r}'| \vec{e}'_{sr} \cdot \vec{e}'_r = |\vec{r}'| (\cos \alpha_{sr} \cdot \cos \alpha'_r + \cos \beta_{sr} \cdot \cos \beta'_r + \cos \gamma_{sr} \cdot \cos \gamma'_r) \quad (2)$$

Based on the Equation (1), the power signal of laser scattering from $\Delta s'$ can be obtained

$$\Delta P(t) = \frac{P_i T_{A1} \eta_t}{\pi \phi^2 \rho_0^2} \pi w_0^2 \exp \left[-\frac{2g_0(\vec{r}')}{\phi^2 \rho_0^2} \right] \frac{T_{A2}}{4\pi \rho_0^2} \frac{\pi D^2 \eta_r}{4} \sigma(\vec{r}') \Delta s' \quad (3)$$

where $\sigma(\vec{r}')$ is the laser radar cross section (LRCS) including the coherent and incoherent scattering part.

In some applications, the detected target will be acted by external force to move its locus alone. We find that translational slip can not make the LHRRP characteristic of the target significant changes, and the rotation has the important influence on their LHRRP. If the target is rotated around their center of gravity, the coordinate frame of target $O'X'Y'Z'$ will be changed in $O'X''Y''Z''$, ζ, ξ, δ are the angle between all of axis in Fig. 2. The positional vector of illuminated

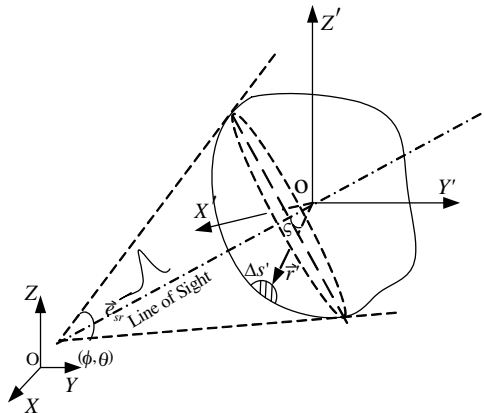


Figure 1: The analyzed methods of LOS in LHRRP simulation.

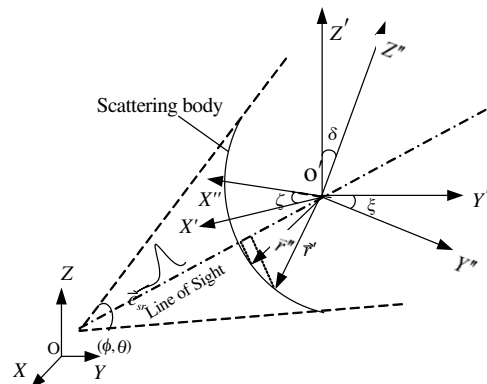


Figure 2: The change of LOS projection on the rotated.

area cell also changes correspondingly $\vec{r}' \rightarrow \vec{r}''$. Geometric range profile of illuminated unit $\Delta s'$ in the LOS direction can be obtained by

$$\begin{aligned} \text{Range profile} &= \left| \vec{r}'' \right| \cos \zeta = \left| \vec{r}'' \right| \vec{e}_{sr}'' \cdot \vec{e}_r'' \\ &= \left| \vec{r}'' \right| [\cos \alpha_{sr} \cdot \cos(\alpha'_r + \zeta) + \cos \beta_{sr} \cdot \cos(\beta'_r + \xi) + \cos \gamma_{sr} \cdot \cos(\gamma'_r + \delta)] \end{aligned} \quad (4)$$

The power signal of laser scattering from target can be computed by Equation (1) and the algorithms are as following in the next section.

4. NUMERICAL ESTIMATIONS OF LHRRP ON TYPICAL TARGET

In order to certify our algorithms and estimated the numerical simulations, we emphasis on the discussion of the influence on the LHRRP of a rotated cone in this section. If we suppose that the cone is rotated with the coordinate axis Y' , the axis X' and Z' will be turned into X'' and Z'' . The analyzed methods of LOS in LHRRP simulation of a rotated cone are shown in Fig. 3. δ is the angle between the axis Z' and Z'' . As the rotation of a cone, the projection on the geometric range profile in the direction of LOS also changes correspondingly $AB \rightarrow A'B'$ from Fig. 3.

Table 1: Compare the data between the LHRRP image of a cone in different rotated angles and the analyzed methods of LOS on the cone.

Rot. angle	$\delta = 0^\circ$	$\delta = 15^\circ$	$\delta = 30^\circ$	$\delta = 45^\circ$
LHRRP	0.936 m	0.9152 m	0.871 m	0.843 m
LOS projection	1.0 m	0.9447 m	0.8202 m	0.6967 m
Relative error	6.4%	3.1%	6.19%	20.4%

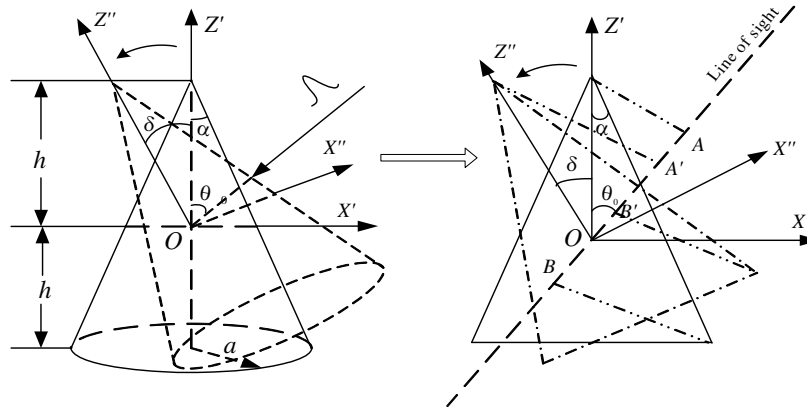


Figure 3: The LHRRP simulation of rotated cone and its analysis of LOS.

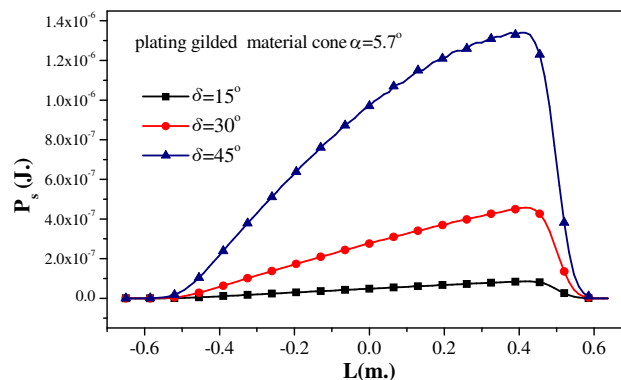


Figure 4: LHRRP image of a cone in different rotated angles.

LHRRP image of a cone in different rotated angles $\delta = 15^\circ, 30^\circ, 45^\circ$ is shown in Fig. 4, with the incidence wavelength $\lambda = 1.06 \mu\text{m}$, width of laser pulse $wP = 2 \text{ ns}$, the height root mean square $\sigma = 0.04 \mu\text{m}$, correlation length of rough surface $l = 10.7 \mu\text{m}$ the complex refractive index of the rough surface materials $n = 1.51 + 0.003i$, the radii $a = 100 \text{ mm}$, and the half-cone angle $\alpha = 5.7^\circ$.

Comparison between the LHRRP image of a cone in different rotated angles and the analyzed methods of LOS on the cone are shown in Table 1.

From the analyzed results in Table 1 we find two main reasons have influence on identifying the rotated cone, this is the physical characteristics of rough surface materials and the speed of rotation. The projection of LOS is a geometrical relation which is indicated the actual distinctive shape of the cone. If the rough surface is more smooth there are more different between the characteristics of LHRRP and the shape of cone in big rotated angle δ , and in the same time the backscattering are stronger. On the contra, if the rotated angle δ is more smaller, the characteristics of LHRRP is more similar with its geometrical dimension.

5. CONCLUSION

The LHRRP characteristics of detected targets will be widely applied in aerospace, national defence, and some other industry fields, due to the imaging technologies can discriminate geometrical and physical characteristics of the targets. However, the LHRRP is sensitivity to the change of the target's posture. So, based on the pulse beam scattering characteristics of LHRRP identifying simulation, it is discussed the influence on the LHRRP of the detected cone in different rotated angle in this paper. Some difference is analyzed between the geometrical projection of LOS and the LHRRP characteristics in detail. The results are shown a basic theories and methods to discuss the LHRRP of the target during in rotated state. Of course, it is finished the recognized technologies and systems of LHRRP, there are a great many works which must be presented, such as a great deal of signal acquisition on laser scattering from detected target, database building and matching ect. Our research of LHRRP will be further developed to build a base in detected fields of laser radar.

ACKNOWLEDGMENT

This works is supported by the National Natural Science Foundation of China (Grant No. 60801047, 60771038, 60971079), China Postdoctoral Science Foundation funded project (Grant No. 200904613-08). The Natural Science and Education Reform Project of Xianyan Teacher's college (Grant No. 08XSYK304, 200702027).

REFERENCES

1. Matson, C. L., E. P. Magee, and D. H. Stone, "Reflective tomography for space object imaging using a short-pulse length laser," *Proc. SPIE*, Vol. 2302, 73–82, 1994.
2. Jacques, G. V. and L. D. Richard, "Model-based automatic target recognition system for forwardlooking groundbased and airborne imaging laser radars (LADAR)," *Proceedings of the IEEE*, Vol. 84, 126–1634, 1996.
3. Yano, T., T. Tsujimura, and K. Yoshida, "Vehicle identification technique using active laser radar system," *IEEE Conference on Multisensor Fusion and Integration for Intelligent Systems*, 2003.
4. Parker, J. K., E. B. Craig, D. L. Klick, et al., "Reflective tomography images from range-resolved laser radar measurements," *Applied Optics*, Vol. 27, 2642–2643, 1988.
5. Masters, L. T., M. B. Mark, and B. D. Duncan, "Range resolution enhancements for laser radar by phase modulation," *Aerospace and Electronics Proceedings of the IEEE*, 129–133, 1995.
6. Gurdev, L. L., T. N. Dreischuh, and D. V. Stoyanov, "High-range-resolution velocity-estimation techniques for coherent Doppler lidars with exponentially shaped laser pulses," *Applied Optics*, Vol. 41, 1741–1749, 2002.
7. Haridim, M., H. Matzner, Y. Ben-Ezra, and J. Gavan, "Cooperative targets detection and tracking range maximization using multimode lidar/radar and transponders," *Progress In Electromagnetics Research*, PIER 44, 217–229, 2004.
8. Chen, H., "Scattering of Gaussian beam by object with rough surface and its application on laser one-dimensional range profile," A Doctoral Dissertation Submitted by Xidian University, 2004.

9. Wang, M.-J., “Research on scattering of pulse beam by target with rough surface and its laser range Doppler imaging,” A Doctoral Dissertation Submitted by Xidian University, 2008.
10. Wang, M.-J., Z.-S. Wu, Y.-L. Li, and G. Zhang, “High resolution range profile identifying simulation of laser radar based on pulse beam scattering characteristics of targets,” *Progress In Electromagnetics Research*, PIER 96, 193–204, 2009.

Problems of Statistical Decisions in Ocean Monitoring

F. A. Mkrtchyan

Department of Informatics, V. A. Kotelnikov's Institute of Radioengineering and Electronics
Russian Academy of Science, Fryazino 141190, Russia

Abstract— Application of means of geoinformation monitoring in many cases is connected to acceptance of the statistical decision on presence on a surveyed part Terrestrial surface of this or that phenomenon. One of features of a condition of gathering of the information for such decision is the impossibility of reception the big statistical samples.

Therefore, development and research of optimum algorithms of distinction of the casual signals characterized by samples of limited volume, in conditions of parametrical aprioristic uncertainty are necessary.

In the present work, the generalized adaptive algorithm of training to acceptance of statistical decisions for exponential classes of distributions is developed at aprioristic parametrical uncertainty of conditions small samples. Numerical examples are shown. Efficiency of the developed optimum procedure for small samples is shown.

1. INTRODUCTION

Development of systems of geoinformation monitoring demands the decision of some problems of the organisation of data flows of measurements. Among these problems of one of important the problem of acceptance of the statistical decision on presence on a surveyed part of a terrestrial surface of this or that phenomenon is. One of features of conditions of gathering of the information for such decision is the impossibility of reception statistical samples small volumes. Therefore working out and research of optimum algorithms of acceptance of statistical decisions for sample small volume are necessary at informational restrictions.

For a case when the number of supervision is great enough, the problem dares a method of an estimation of parameters of likelihood distributions which is effective at unlimited growth of volumes sample on which basis the estimation of parameters is made. At the limited volumes sample, received by a method of an estimation of the parameters, the solving rule does not satisfy to necessary conditions of an optimality: to a constancy of average probability of an error of first kind and unbiasedness.

In the present work, the generalised adaptive algorithm of training to acceptance of statistical decisions for exponential groups of distributions is developed at aprioristic parametrical uncertainty of conditions samples small volume [1, 2].

2. PROBLEM DEFINITION

Very often there is a problem: to what of two classes to carry a measured random variable, and the full likelihood description of these classes is not known that does not allow to use classical results of the theory of statistical decisions for the decision of this problem. The decision can be received only by means of training sampling.

Let ξ, η, ζ independent random variables, $f_\xi(x/\omega_0), f_\eta(y/\omega_1), f_\zeta(z/\omega)$ distribution of probabilities, $\omega_0, \omega_1, \omega \in \Omega$. For parameter ω two alternatives: $H_0: \omega = \omega_0$ and $H_1: \omega = \omega_1$. The problem consists in construction of a solving rule on n_0, n_1, n to supervision of random variables

$$\begin{aligned}\xi &: x^* = (x_1, x_2, \dots, x_{n_0}) \\ \eta &: y^* = (y_1, y_2, \dots, y_{n_1}) \\ \zeta &: z^* = (z_1, z_2, \dots, z_n)\end{aligned}$$

to specify, what alternative H_0 or H_1 is accepted.

The solving rule can be set by means of function $\varphi(x^*, y^*, z^*)$.

If $\varphi = 0$: $H = H_0$, $\varphi = 1$: $H = H_1$. Errors of first and second kind:

$$\begin{aligned}\alpha(\varphi, \omega_0, x^*, y^*) &= \int \varphi(x^*, y^*, z^*) f_{\omega_0}(z^*) dz^* \\ \beta(\varphi, \omega_0, x^*, y^*) &= \int [1 - \varphi(x^*, y^*, z^*)] f_{\omega_1}(z^*) dz^*\end{aligned}$$

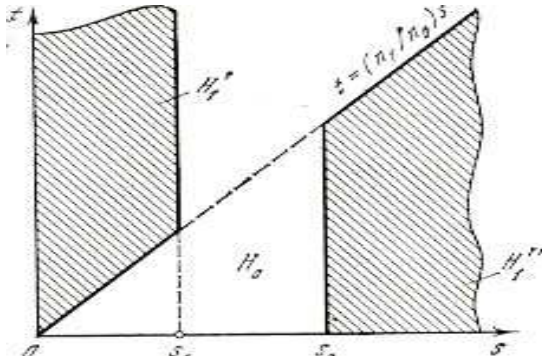


Figure 1: Areas of acceptance of hypotheses for a classical solving rule.

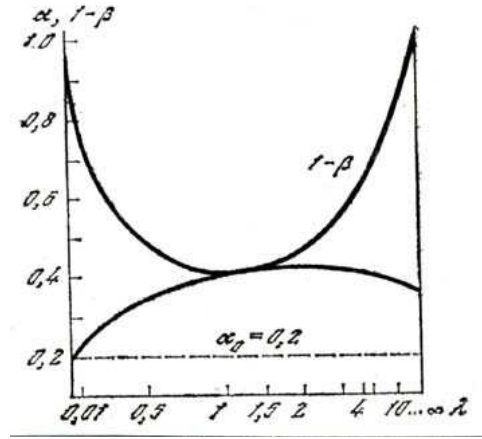


Figure 2: Probabilities of acceptance of correct solution and error of first kind.

An optimality condition: 1. $\hat{\alpha} = \alpha_0$, (a constancy of an error of first kind); 2. $1 - \beta > \hat{\alpha}$ (unbiasedness).

In the present work, it is developed a mathematical apparatus and the generalized adaptive procedure for the decision of a problem of training to distinction of random variables from exponential group distributions with unknown parameters for sampling small volume is offered at information restrictions.

It is shown that, procedures of training applied now to distinction in which the estimation of parameters at first is resulted, and then a choice between hypotheses, do not meet the above-stated requirements shown to optimum procedures.

For a case when the number of supervision is great enough, the problem dares a method of an estimation of parameters of likelihood distributions which is effective at unlimited growth of volumes sampling on which basis the parameter estimation is made. At the limited volumes sampling, received by a method of an estimation of the parameters, the solving rule does not satisfy to necessary conditions of an optimality: to a constancy of average probability of an error of the first kind and unibasendness.

3. THE SOLVING RULE BASED ON ESTIMATION OF UNKNOWN PARAMETERS OF DISTRIBUTIONS

The classic method of the decision of a considered problem is based on enough developed theory of dot estimations of unknown parameters of likelihood distributions. In a considered problem for unknown parameters ω_0, ω_1 , starting with n_0 sequence $x^* = (x_1, x_2, \dots, x_{n_0})$ and n_1 sequence $y^* = (y_1, y_2, \dots, y_{n_1})$ random variables ξ and η estimations of parameters $\omega_0, \omega_1, \theta_1, \theta_0$ accordingly turn out.

Further, the way of construction of a solving rule is based on fundamental lemma Neyman-Pearson: the credibility relation is under construction:

$$L(z^*/\theta_1, \theta_0) = [f(z_1, z_2, \dots, z_n/\theta_1)/f(z_1, z_2, \dots, z_n/\theta_0)] > C(\theta_1, \theta_0)$$

Also, threshold $C(\theta_1, \theta_0)$ gets out.

$$1. \theta_1 > \theta_0 \{s < t(n_0/n_1), s < n_0/G_n^{-1}(1 - \alpha_0)$$

$$2. \theta_1 < \theta_0 \{s > t(n_0/n_1), s > n_0/G_n^{-1}(1 - \alpha_0)$$

$s = x/z, t = y/z, G_n^{-1} = [1/(n - 1)!] \int \exp(-z)z^{n-1}dz$, θ_1 and θ_0 — dot estimations for ω_1 and ω_0 .

Areas of acceptance of hypothesis H_1 it is resulted on Figure 1.

Apparently from Figure 2. The probability of an error of the first sort two from half of time exceeds admissible volume α_0 .

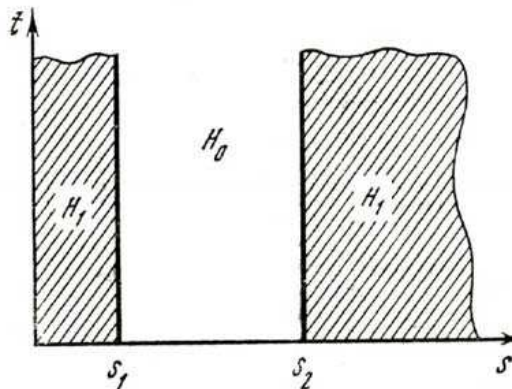


Figure 3: Areas of acceptance of hypotheses for the optimal inference engine.

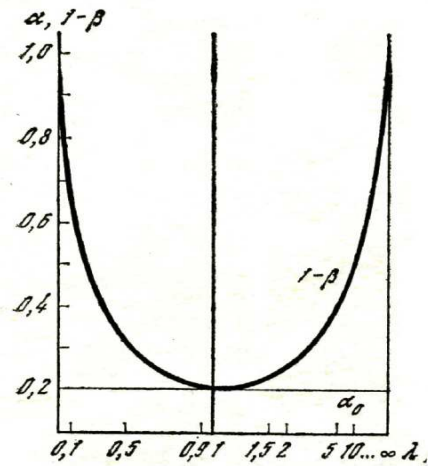


Figure 4: Probabilities of acceptance of correct solution and error of first kind.

4. THE SOLVING RULE SATISFYING NECESSARY CONDITIONS OF AN OPTIMALITY

Optimum solving rule in a class of solving rules shown on Figure 3.

$$\begin{aligned}
 &1) \max \alpha(s_1, s_2/\lambda) = \alpha_0, \quad (0 < \lambda < \infty). \\
 &2) \max \min D(s_1, s_2/\lambda) \quad ((s_1, s_2) \quad 0 < \lambda < \infty). \\
 &\quad D(s_1, s_2/\lambda) = 1 - \beta(s_1, s_2/\lambda) \\
 &\quad \alpha(s_1, s_2/\lambda) = P_0(s_1) + [P_0(\infty) - P_0(s_1)] \\
 &\quad D(s_1, s_2/\lambda) = P_1(s_1) + [P_1(\infty) - P_1(s_2)] \\
 &\quad P_i(k) = \iint f_i(s, t) ds dt, \quad \text{where } i = 0, 1.
 \end{aligned}$$

Applying a method of uncertain multipliers of Lagrange to optimum thresholds s_1 and s_2 , we receive system of the equations:

$$\begin{aligned}
 &1) (s_1/s_2)_0^n = [(s_1 + 1)/(s_2 + 1)]_0^{(n+n)} n_0 - 1 \\
 &2) 1 - \sum_{j=0} [(n_0 + j)/n!] \left[\left[(n_0 + n - 1)!(s_1 + 1)_0^{(n-1)} - n \right] / (s_1 + 1)_0^{(n+n-1)} \right] \\
 &\quad - \left[\left[(n_0 + n - 1)!(s_2 + 1)_0^{(n-1)} - n \right] / (s_2 + 1)_0^{(n+n-1)} \right] - \alpha_0 = 0
 \end{aligned}$$

The offered procedure satisfies following imperative conditions: 1) to a constancy of average probability of an error of the first kind α and 2) unbiasedness $(1 - \beta) < \alpha$.

5. APPLICATION

Analysis of statistical characteristics of “spottiness” for three types of areas of Atlantic and Pacific oceans was conducted. These statistical characteristics were determined for the most informative thresholds. At that time, statistical characteristics of “spottiness” for the same areas, selected using criteria of minimal value of coefficient of correlation for joint sample of positive and negative spots. Analysis of these characteristics showed, that the statistical characteristics of “spottiness” coincide for areas with temperate sea roughness and storm zones. Minimum for the coefficient of correlation ρ_{\min} is run down for a case of most informative thresholds. But for quiet area the situation is different [2].

On Figure 5, the example of work of the automated system in a mode of monitoring of temperature of a surface of Northern Atlantic on data Space Satellite “Cosmos-1151” (8-April, 14, 1980) is given. The system allows to receive maps of temperatures on enough rarefied grid of trajectory SS. Points on a map designate areas of realization of ship measurements. The analysis of satellite and

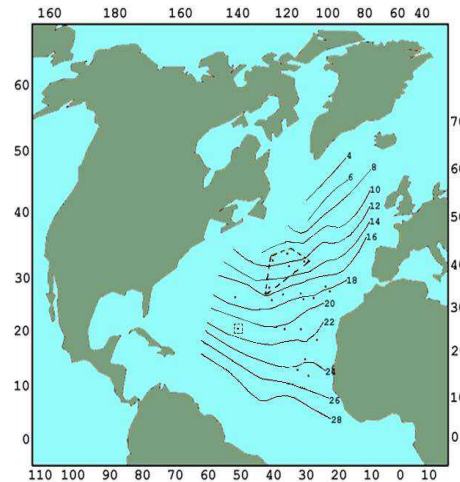


Figure 5: Map of temperature of Northern Atlantic.

contact measurements shows, that there is an appreciable regular understating satellite estimations of temperature of ocean concerning ship which on the average makes 1.6 K. The root-mean-square deviation (rejection) of satellite estimations T from ship measuring on all given sample makes 3.3 K. The dotted line on a map designates areas where the difference between ship and satellite measurements exceeds 4 K. It is typical, that high overcast is registered in all these points (on the data weather forecasters). The root-mean-square deviation of satellite measurements of temperature from ship, designed without taking into account the allocated points, makes 1.4 K.

From the aforesaid follows, that statistical characteristics for “spottiness” of brightness temperatures in microwaves can be used for detection and classification of the phenomena on a surface of the ocean, that was caused by a degree of sea roughness.

6. CONCLUSION

The analysis of empirical histograms for spottiness of “brightness temperatures in microwaves” shows that, in most cases (l^+ , l^-), characteristics will be coordinated with exponential distribution, and amplitude characteristics will be coordinated with normal distribution. Therefore for detection and classification of the phenomena on a surface of ocean it is necessary to apply optimal algorithms for the COMPUTER training to taking statistical decisions for the aforesaid distributions.

REFERENCES

1. Mkrtchyan, F. A., *Optimal Distinguish of Signals and Monitoring Problems*, 182, Nauka, Moscow, 1982, (in Russian).
2. Armand, N. A., V. F. Krapivin, and F. A. Mkrtchyan, *Methods of Data Processing of Radio Physical Research of an Environment*, 270, Nauka, Moscow, 1987, (in Russian).

An Adaptive Spectroellipsometric Identifier for Ecological Monitoring of the Aquatic Environment

F. A. Mkrtchyan, V. F. Krapivin, V. I. Kovalev, and V. V. Klimov
Institute of Radioengineering and Electronics, Russian Academy of Sciences
1 Vvedensky Square, Fryazino, Moscow Region 141190, Russia

Abstract— Spectroellipsometry is a peak of polarization optics. The creation of multichannel polarization optical instrumentation and use of spectroellipsometric technology are very important for the real-time ecological control of aquatic environment. Spectroellipsometric devices give us high precision of measurements. Spectroellipsometric multichannel measurements in an aquatic environment provide an information basis for the application of modern algorithms for the recognition and identification of pollutants. New original elements (coaxial polarization switchers and achromatic compensators), developed in IRE RAS, allow to design cheap polarization systems (for example, spectroscopic ellipsometers, polarization spectrometers, polarimeters, dichrometers, polarization microscopes and interferometers, sensitive photometers, differential reflectometers) without expensive standard polarization elements.

1. INTRODUCTION

The creation of multichannel polarization optical instrumentation and use of spectroellipsometric technology are very important for the real-time ecological control of aquatic environment. It should be mentioned that efficient solution of this multiparametric problem greatly depends on the precision and simplicity of ellipsometric devices.

This report is aimed to describe.

A technology of combined use of spectroellipsometry and algorithms of identification and recognition that allowed the creation of a standard integral complex of instrumental, algorithmic, modular and software tools for the collection and processing of data on the aquatic environment quality with forecasting and decision-making functions.

A compact measuring-information multichannel spectroellipsometric system (device) for monitoring the quality of aquatic environment, that is based on the combined use of spectroellipsometry and training, classification, and identification algorithms.

This spectroellipsometric system will differ from modern foreign analogues by the use of a new and very promising method of ellipsometric measurements, an original element base of polarization optics and a complex mathematical approach to estimating the quality of a water object subjected to anthropogenic influence.

Unlike foreign analogues, the system has no rotating polarization elements. This allows one to increase the signal-to-noise ratio and the long-term stability of measurements, to simplify and reduce the price of multichannel spectroellipsometers.

The system will be trainable to the recognition of the pollutants of aquatic environment.

2. MEASURING COMPLEXES

A spectroellipsometer in laboratories of V. A. Kotelnikov's IRE RAS is designed for in-situ real time measurements of spectra of ellipsometric parameters Ψ and Δ with consequent change-over to spectra of transmitted and reflected signal from water media in frames of used physical model of water environment [1].

A compact measuring-information multichannel spectroellipsometric system (Figure 1) (device) is applied for monitoring the quality of natural and waste water, that is based on the combined use of spectroellipsometry and training, classification, and identification algorithms.

Device composition:

- Polarizer block;
- Analyzer block;
- Power supply unit;
- Illuminator;
- Fiber-optic cabel;



Figure 1: High precision real-time multi-wavelengths spectroellipsometer with binary polarization modulation.

Notebook with interface unit;

Wide-band filters.

Features of high precision real time multi-wavelengths spectroscopic ellipsometers created for monitoring the quality of natural and waste waters:

New approach in ellipsometry, based on binary polarization modulation;

New low cost effective polarization elements;

No rotating polarization elements;

Excellent signal-to-noise ratio and the long-term stability of measurements makes possible to simplify and reduce the price of the multichannel spectroellipsometers;

One of the key element of the systems is a polarization switch which transforms unpolarized light from a source into highly linearly polarized light with alternate (up to kHz or more) and orthogonal polarizations;

Sets of silicon photodiodes with arbitrary access to them;

Flexibility, simple design, low cost, high precision, long term stability.

Specifications of some spectroellipsometers used:

a) Specification of portable 128-channel spectroellipsometer:

Spectral range 280–600 nm.

Minimal measurement time 0.5 sec.

Precision and stability 0.01 and 0.02 degree in Psi and Delta, respectively, polarization rotation angle — 0.001 degree.

Sources: miniature pulsed xenon lamp PX-2 with high resource and laser diode.

Micro spot focus 300 μm with PX-2 and 30 μm with laser diode.

Achromatic compensator.

User-friendly software.

A weight of measuring device — about 4 kg.

b) Specification of compact 128-channel spectroellipsometer with halogen lamp.

Spectral ranges — 380–740 nm and 650–930 nm.

Minimal measurement time 0.6 sec.

Precision to 0.003 and 0.01 degree in Psi and Delta, respectively, polarization rotation angle — 0.001 degree.

Sources: halogen lamp KGM 9–70.

Long-term stability 0.01 degree.

Use of achromatic compensator on the basis of Fresnel rhomb made of fused quartz enhances precision of measurements.

A weight of measuring device — about 4 kg.

Polarization block 2 kg.

Analyzer block 2 kg.

For the first time the combined use of real-time spectroellipsometry measurements and data processing methods has been realized in an **Adaptive Identifier**.

3. STRUCTURE OF THE ADAPTIVE IDENTIFIER

The algorithmic support of the Adaptive Identifier is based on a complex application of recognition and classification algorithms on the basis of 128 spectra images registered during a fixed period of time.

A time interval of 1 second is usually established and provides about 30 value of brightness for each of the 128 optical channels.

The spectra obtained are sources of set of statistical parameters and different characteristics united into vector spaces for their comparison with the standard samples of famous pollutants stored on the computer.

The technology of this comparison depends on the diversity of identification methods.

Learning procedure description.

The system is trainable to the recognition of the pollutants of aquatic environment.

Learning procedure includes: The Adaptive Identifier is designed to learn from the measurements of spectral characteristics and the simultaneous independent measurement of the content of chemical elements in the aquatic environment.

As a result, a standard data bank is created in the knowledge base, comparison with which provides the solution of the identification problem. The software of the Adaptive Identifier provides different algorithms for the solution of this problem, and cluster analysis is among of them [2, 3].

There are some specific features of measurements of the quality of natural and waste water using spectroellipsometric technology:

1. Measurements of natural and waste water quality may be performed using: a) **Transmission** scheme when quality of sample is measured during inserting the fused quartz cuvette with water analyzed into spectroellipsometer device. b). **Reflection** scheme when quality of water is measured by inserting of spectroellipsometer sensor into water media examined.

2. Because of high accuracy of measurements with the spectroellipsometers it is not possible to use whole potential of method for remote measurements of natural and waste water quality (Even small waves, ripples, foam can influence on quality of measurements).

The Adaptive Identifier can be used in different fields where the quality of water should be estimated or the presence of a particular set of chemical elements should be revealed. The Adaptive Identifier solves these problems by real-time monitoring of the aquatic environment. In the stationary version it allows the tracking of the dynamics of water quality in a stream, and when placed on a ship, it allows the measurement of water parameters along the route.

The functionality of the Adaptive Identifier can be extended by increasing the volume of standards in the knowledge base. The use of a natural light source allows the examination of soils, the indication of oil products on a water surface, the determination of the degree of the pollution of atmospheric air and the estimation of the conditions of other objects of the environment, whose spectral images may change.

An adaptive spectroellipsometric technology may be applied to following areas:

- Estimation of natural and wastewater quality;

- Analysis of liquids in medicine, biochemistry, food industry.

- Measurement of the mineralization level and chemical pollution of reservoir depending on the pollution type.

- Estimation of water salinity variations.

- Ellipsometrically based biosensor and gas sensor systems.

- Testing the organic pollution clots in water environment.

The Adaptive Identifier was tested under expeditionary conditions on board of the research vessel "Dmitry Mendeleev" in the Japanese Sea and in central areas of the Pacific Ocean and also during the investigation of aqueous systems of South Vietnam and Siberia (lake Baikal, Angara and Yenisey river) within the framework of the Russian-American and Russian-Vietnamese ecological expeditions.

A Russian-Vietnamese scientific and engineering laboratory has been created to create a standards base and to prepare the Adaptive Identifier for full-scale production.

The main objective of work is to create in future the compact information systems for monitoring the quality of aquatic environment and to investigate their potential efficiency. These systems are based on the combined application of methods of the spectroellipsometry, and algorithms of training, classification, and identification [2, 3].

4. CONCLUSION

The technology of combined use of spectroellipsometry and the algorithms of detection and classification will allow the creation of an original system of instrumental, algorithmic, modular and software tools for the collection and processing of data on the aquatic environment with forecasting and decision-making functions.

The theoretical part of the work will include the use of methods of polarization optics, mathematical statistics, the theory of pattern recognition and mathematical modeling.

Creation of a new element base for polarization optics with simple and efficient switches of the polarization state (SPS), that successfully substitutes for the conventional expensive polarizer — Modulators of polarization state with rotating polarization elements.

Optimization of the spectrum of the ellipsometric method concerning the change of the amplitudes and phases of mutually orthogonal components of electromagnetic radiation for measuring the thickness of thin films on a water surface. Determination of sensitivity and precision limits of adaptive spectroellipsometers in different operating regime.

Creation of methods for investigating the water surface, determination of statistical characteristics of “spottiness” as informative signs for solving detection, classification, and identification problems. Elaboration and optimization of algorithms for the detection, classification, and identification of the characteristics of the aquatic environment for adaptive spectroellipsometers. Creation of a bank of standards on the basis of the measurement of the pollution level of the aquatic environment for training the adaptive spectroellipsometer.

The experimental part of the work described in report will include description.

The laboratory and on-site measurements of absorption, scattering, and reflection of electromagnetic waves from aquatic objects under local and structural adaptation of the model estimation of the efficiency of the technique, algorithms and models for specific aquatic objects.

REFERENCES

1. Perov, P. I., V. I. Kovalev, A. I. Rukovishnikov, N. M. Rossukanyi, and W. H. Johnson, “Hydrogensensitive palladium film study with precise and fast ellipsometers,” *Int. J. Electronics*, Vol. 78, No. 5, 797–803, 1999.
2. Armand, N. A., V. F. Krapivin, and F. A. Mkrtchyan, *Methods of Processing Radiophysical Exploration of Environment*, Moscow, Nauka, 1987, (in Russian).
3. Mkrtchyan, F. A., V. F. Krapivin, V. I. Kovalev, and V. V. Klimov, “An adaptive spectroellipsometer for ecological monitoring,” *Microwave and Optical Technology Letters*, Vol. 51, No. 11, 2792–2795, 2009.

A Uniform Asymptotic Solution for Diffraction by a Right-angled Dielectric Wedge

G. Gennarelli and G. Riccio

D.I.I.I.E., University of Salerno, Via Ponte Don Melillo, 84084 Fisciano (Salerno), Italy

Abstract— The aim of this work is to propose an approximate asymptotic solution for the field diffracted by a lossless right-angled dielectric wedge in the case of a plane wave having normal incidence with respect to the edge. The diffraction problem is tackled by considering two observation regions: the inner region of the wedge and the surrounding free-space. For each of them, the electric and magnetic surface currents involved in the radiation integrals are determined in the Physical Optics approximation. Useful analytical manipulations and uniform asymptotic evaluations allow one to obtain the diffracted field in terms of the Fresnel’s reflection and transmission coefficients of the structure and the transition function of the Uniform Geometrical Theory of Diffraction. The proposed solution for the diffracted field compensates the Geometrical Optics field discontinuities and its accuracy is well-assessed by using Finite Difference Time Domain results.

1. INTRODUCTION

Diffraction by a wedge is a well-covered research topic due to its relevance for practical applications, but the results available in the scientific literature mainly concern impenetrable structures. This is due to difficulties encountered by researchers in the case of penetrable materials, where a complex coupling between the external and the internal region arises. The existing approaches can be characterized by either trying to provide analytical or heuristic approximate solutions, or trying to solve the problem in an exact sense using combined analytical-numerical techniques. With reference to the diffraction by a dielectric wedge, significant but not conclusive contributions can be found in [1–4].

A Uniform Asymptotic Physical Optics (UAPO) solution for predicting the field diffracted by a lossless right-angled dielectric wedge when illuminated by a uniform plane wave at normal incidence (see Fig. 1) is proposed in this paper. The considered problem is splitted into two sub-problems concerning the regions external and internal to the wedge. With reference to the outer problem, equivalent electric and magnetic PO surface currents lying on the external faces of the wedge are assumed as sources in the standard radiation integral. Useful analytical manipulations and uniform asymptotic evaluations of the resulting integrals give the field diffracted in the space surrounding the wedge in terms of the Fresnel’s reflection coefficients of the structure and the transition function of the Uniform Geometrical Theory of Diffraction (UTD) [5]. The inner problem is solved by determining equivalent electric and magnetic PO surface currents on the internal faces of the wedge. They are related to the field transmitted into the structure. Once such currents are known, the diffracted field is evaluated by an approach like that used for the outer problem. Numerical results show that the here derived solution for the diffracted field compensates the discontinuities of the Geometrical Optics (GO) field at the shadow boundaries in the external and internal regions. Moreover, it results to be very accurate as confirmed by comparisons between the

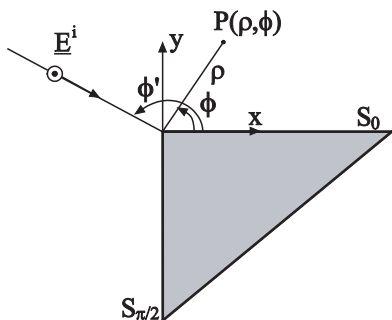


Figure 1: Geometry of the problem.

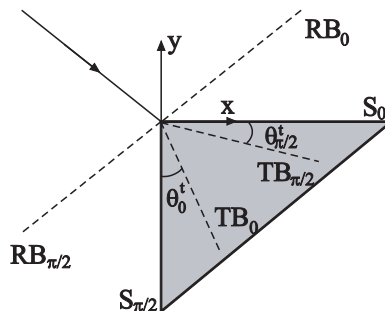


Figure 2: Shadow boundaries.

UAPO-based approach results and those obtained via the reliable Finite Difference Time Domain (FDTD) technique.

2. DIFFRACTED FIELD: UAPO SOLUTION

Let us consider the problem of plane-wave diffraction by the edge of a lossless right-angled dielectric wedge illuminated at normal incidence (see Fig. 1). The surface S_0 is located at $\phi = 0$ whereas $S_{\pi/2}$ corresponds to $\phi = 3\pi/2$. They divide the space into the outer region ($0 < \phi < 3\pi/2$) and the inner region ($3\pi/2 < \phi < 2\pi$). The incident plane wave is linearly polarized along the z -axis and propagates in the direction fixed by ϕ' so as both surfaces result to be illuminated ($\pi/2 < \phi' < \pi$). Accordingly, there are two reflection boundaries in the region surrounding the wedge and two transmission boundaries in the internal region (see Fig. 2).

It is convenient to split the original problem in accordance to the equivalence theorem, and to consider two sub-problems relevant to the regions external and internal to the wedge.

2.1. Outer Region

The electric field scattered by the wedge can be represented by the well-known radiation integral:

$$E_{out}^s \cong -jk_0 \iint_S \left[\left(\underline{\underline{I}} - \hat{R}\hat{R} \right) (\zeta_0 \underline{J}_s) + \underline{J}_{ms} \times \hat{R} \right] G(\underline{r}, \underline{r}') dS \quad (1)$$

wherein $S = S_{0,out} \cup S_{\pi/2,out}$, \underline{J}_s and \underline{J}_{ms} are the equivalent electric and magnetic surface currents over S , $G(\underline{r}, \underline{r}')$ is the Green's function, ζ_0 and k_0 are the impedance and propagation constant for the free-space, \underline{r} and \underline{r}' denote the observation and source points, respectively, \hat{R} is the unit vector from the radiating element at \underline{r}' to the observation point, and $\underline{\underline{I}}$ is the (3×3) identity matrix. Due to the linearity of the operator in (1), $S_{0,out}$ and $S_{\pi/2,out}$ contribute separately to the scattered field, so that $\underline{E}_{out}^s = \underline{E}_{0,out}^s + \underline{E}_{\pi/2,out}^s$. The key steps of the proposed approach are presented only with reference to the diffracted field $\underline{E}_{0,out}^d$ related to $\underline{E}_{0,out}^s$. For this contribution, the corresponding PO surface currents can be so expressed:

$$\zeta_0 \underline{J}_{s,0}^{out} = E_0 (1 - R_0) \sin \phi' e^{jk_0 x \cos \phi'} \hat{z} \quad (2)$$

$$\underline{J}_{ms,0}^{out} = -E_0 (1 + R_0) e^{jk_0 x \cos \phi'} \hat{x} \quad (3)$$

in which E_0 denotes the incident field at the origin and R_0 is the Fresnel's reflection coefficient associated to S_0 . Since diffraction is confined to the Keller's cone, the approximation $\hat{R} \cong \hat{s}$ (\hat{s} is the diffraction direction) is permitted for evaluating the edge diffracted field. As a consequence, after analytical manipulations, the radiation integral associated to $S_{0,out}$ can be written as follows:

$$E_{0,out}^s \cong \hat{z} E_0 \left[(1 - R_0) \sin \phi' - (1 + R_0) \sin \phi \right] \frac{1}{4\pi j} \int_C \frac{e^{-jk_0 \rho \cos(\alpha \mp \phi)}}{\cos \alpha + \cos \phi'} d\alpha \quad (4)$$

The integration path C in (4) is shown in Fig. 3. The application of the Steepest Descent Method allows one to write the integral in (4) as a typical diffraction integral, and a uniform asymptotic evaluation of this last gives the diffraction contribution:

$$E_{0,out}^d = \hat{z} E_0 \left[(1 - R_0) \sin \phi' - (1 + R_0) \sin \phi \right] \frac{e^{-j\pi/4}}{2\sqrt{2\pi k_0}} \frac{F_t \left[2k_0 \rho \cos^2 \left(\frac{\phi \pm \phi'}{2} \right) \right]}{\cos \phi + \cos \phi'} \frac{e^{-jk_0 \rho}}{\sqrt{\rho}} \quad (5)$$

where $F_t(\cdot)$ is the UTD transition function [5], and $+$ ($-$) sign applies when $0 < \phi < \pi$ ($\pi < \phi < 3\pi/2$).

With reference to the diffracted field $\underline{E}_{\pi/2,out}^d$ related to $\underline{E}_{\pi/2,out}^s$, the corresponding PO surface currents

$$\zeta_0 \underline{J}_{s,\pi/2}^{out} = -E_0 (1 - R_{\pi/2}) \cos \phi' e^{jk_0 y \sin \phi'} \hat{z} \quad (6)$$

$$\underline{J}_{ms,\pi/2}^{out} = -E_0 (1 + R_{\pi/2}) e^{jk_0 y \sin \phi'} \hat{y} \quad (7)$$

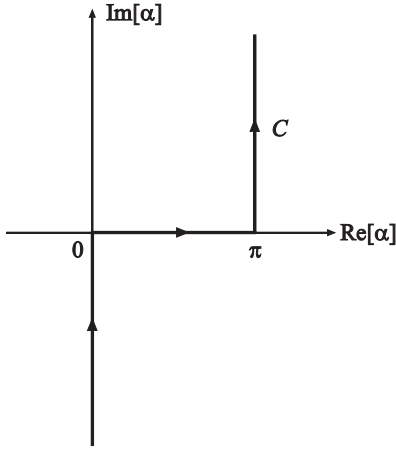
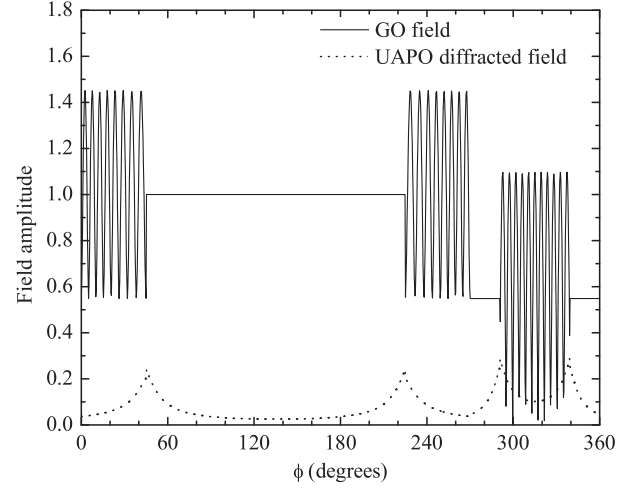

 Figure 3: Integration path C .


Figure 4: GO field and UAPO diffracted field.

provide

$$E_{\pi/2,out}^d = \hat{z} E_0 \left[(1 + R_{\pi/2}) \cos \phi - (1 - R_{\pi/2}) \cos \phi' \right] \frac{e^{-j\pi/4}}{2\sqrt{2\pi k_0}} \\ \frac{F_t \left[2k_0 \rho \cos^2 \left(\frac{(3\pi/2 - \phi) \pm (3\pi/2 - \phi')}{2} \right) \right]}{\cos(3\pi/2 - \phi) + \cos(3\pi/2 - \phi')} \frac{e^{-jk_0 \rho}}{\sqrt{\rho}} \quad (8)$$

where $+$ ($-$) sign applies when $\pi/2 < \phi < 3\pi/2$ ($0 < \phi < \pi/2$).

2.2. Inner Region

The inner problem is solved by using an approach like that adopted for the outer problem. Accordingly, the resulting UAPO field diffracted in the internal region of the wedge is given by $\underline{E}_{in}^d = \underline{E}_{0,in}^d + \underline{E}_{\pi/2,in}^d$, where

$$\underline{E}_{0,in}^d = \hat{z} E_0 T_0 \sqrt{\varepsilon_r} \left[\sin \phi - \cos \theta_0^t \right] \frac{e^{-j\pi/4}}{2\sqrt{2\pi k_d}} \frac{F_t \left[2k_d \rho \cos^2 \left(\frac{\pi - \phi - \cos^{-1}(|\cos \phi'|/\sqrt{\varepsilon_r})}{2} \right) \right]}{\cos \phi' + \sqrt{\varepsilon_r} \cos \phi} \frac{e^{-jk_d \rho}}{\sqrt{\rho}} \quad (9)$$

$$\underline{E}_{\pi/2,in}^d = \hat{z} E_0 T_{\pi/2} \sqrt{\varepsilon_r} \left[\cos \phi + \cos \theta_{\pi/2}^t \right] \frac{e^{-j\pi/4}}{2\sqrt{2\pi k_d}} \frac{F_t \left[2k_d \rho \cos^2 \left(\frac{\pi/2 - \phi + \cos^{-1}(\sin \phi'/\sqrt{\varepsilon_r})}{2} \right) \right]}{\sin \phi' + \sqrt{\varepsilon_r} \sin \phi} \frac{e^{-jk_d \rho}}{\sqrt{\rho}} \quad (10)$$

In (9) and (10), T_0 ($T_{\pi/2}$) and θ_0^t ($\theta_{\pi/2}^t$) are the transmission coefficient and the transmission angle (see Fig. 2) related to S_0 ($S_{\pi/2}$), and $k_d = k_0 \sqrt{\varepsilon_r}$ is the propagation constant in the wedge region by assuming a non-magnetic dielectric having relative permittivity ε_r .

3. NUMERICAL RESULTS

Numerical results are provided to assess the correctness and effectiveness of the proposed solution. They are relevant to a wedge characterized by $\varepsilon_r = 4$ and a plane wave propagating in the direction $\phi' = 135^\circ$. The field is evaluated over a circular path with radius $\rho = 8\lambda_0$, λ_0 being the free-space wavelength. Fig. 4 shows the GO field and the proposed UAPO diffracted field. As expected, the GO field has four discontinuities at the shadow boundaries RB_0 ($\phi = 45^\circ$), $RB_{\pi/2}$ ($\phi = 225^\circ$), TB_0 ($\phi = 291^\circ$) and $TB_{\pi/2}$ ($\phi = 339^\circ$). On the other hand, the diffracted field presents peaks at such boundaries. It ensures the continuity of the total field into the wedge and in the surrounding space (see Fig. 5). The accuracy of the here derived solution has been proved by means of comparisons with the results obtained via an “ad hoc” developed FDTD code. The comparison relevant to the considered case is reported in Fig. 6 and confirms this statement.

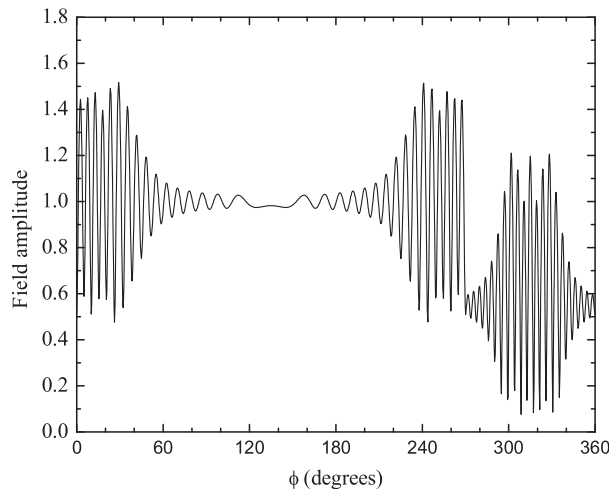


Figure 5: Total field.

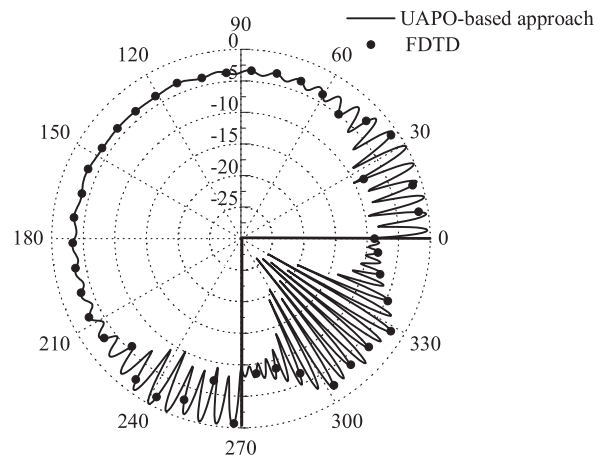


Figure 6: Comparison between UAPO-based approach results and FDTD results.

4. CONCLUSIONS

Uniform asymptotic solutions for evaluating the field diffracted by a right-angled dielectric wedge in the inner and outer regions have been presented in this paper. They are expressed in terms of the standard Fresnel's coefficients and the UTD transition function, are easy to handle, compensate the GO field discontinuities at the shadow boundaries and give accurate results.

REFERENCES

1. Berntsen, S., "Diffraction of an electric polarized wave by a dielectric wedge," *SIAM J. Appl. Math.*, Vol. 43, 186–211, 1983.
2. Joo, C. S., J. W. Ra, and S. Y. Shin, "Scattering by a right angle dielectric wedge," *IEEE Trans. Antennas Propagat.*, Vol. 32, 61–69, 1984.
3. Burge, R. E., et al., "Microwave scattering from dielectric wedges with planar surfaces: A diffraction coefficient based on a physical optics version of GTD," *IEEE Trans. Antennas Propagat.*, Vol. 47, 1515–1527, 1999.
4. Rouviere, J. F., N. Douchin, and P. F. Combes, "Diffraction by lossy dielectric wedges using both heuristic UTD formulations and FDTD," *IEEE Trans. Antennas Propagat.*, Vol. 47, 1702–1708, 1999.
5. Kouyoumjian, R. G. and P. H. Pathak, "A uniform geometrical theory of diffraction for an edge in a perfectly conducting surface," *Proc. IEEE*, Vol. 62, 1448–1461, 1974.

Diffraction by a Double-negative Metamaterial Layer with PEC Backing

G. Gennarelli and G. Riccio

D.I.I.I.E., University of Salerno, Via Ponte Don Melillo, 84084 Fisciano (Salerno), Italy

Abstract— This work deals with the diffraction problem originated by a plane wave normally impinging on the edge of a lossy, isotropic and homogeneous double-negative metamaterial layer with a perfect electric conductor backing. The here proposed solution is obtained by using a Physical Optics approximation of the electric and magnetic surface currents in the radiation integral and by performing a uniform asymptotic evaluation of this last. The resulting diffraction coefficients contain the Geometrical Optics response of the structure and the transition function of the Uniform Theory of Diffraction. The accuracy of the solution is well assessed by comparisons with Comsol Multiphysics[®] results.

1. INTRODUCTION

Double-Negative (DNG) metamaterials (MTMs) are characterized by negative permittivity and permeability simultaneously. This may lead to new physically realizable response functions opening the way to novel applications at microwave and optics frequencies [1–3].

A Uniform Asymptotic Physical Optics (UAPO) solution has been recently proposed in closed form by the authors for determining the field diffracted by the edge of a lossless, isotropic and homogeneous DNG MTM layer [4]. It has resulted to be accurate, easy to handle and apply. The peculiarities of the UAPO solution suggest to work in this context also for solving the problem concerning the evaluation of the field diffracted by a truncated lossy, isotropic and homogeneous DNG MTM layer with a perfect electric conductor (PEC) backing when illuminated by a plane wave at normal incidence (see Fig. 1). The starting point is that of considering the radiation integral with a PO approximation of the equivalent electric and magnetic surface current densities assumed as sources of the scattered electric field. Such currents lie on the half-plane representing the structure and are expressed in terms of the incident field and the reflection coefficient, which is here evaluated by considering the Equivalent Transmission Line (ETL) circuit. A useful approximation and a uniform asymptotic evaluation of the resulting radiation integral allow one to obtain the UAPO diffraction coefficients in terms of the Geometrical Optics (GO) response of the structure and the standard transition function of the Uniform Geometrical Theory of Diffraction (UTD) [5]. The proposed solution fulfils expectations since it perfectly compensates the GO field discontinuities at the reflection and incident field shadow boundaries. Moreover, its accuracy is demonstrated by the good agreement obtained in comparisons with the RF module of Comsol Multiphysics[®], a commercial tool based on the Finite Element Method.

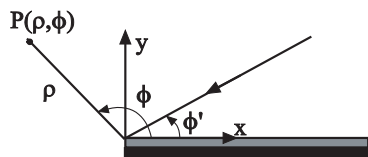


Figure 1: Geometry of the problem.

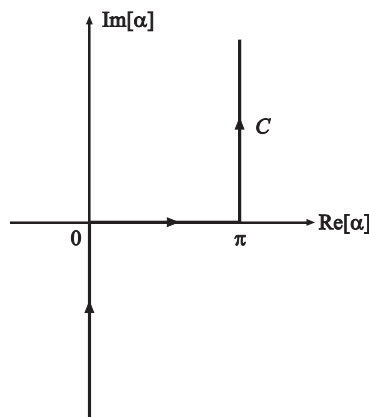


Figure 2: Integration path C .

2. GO FIELD RESPONSE

Let us consider a thin lossy, isotropic and homogeneous DNG MTM layer placed on a PEC ground plane. The layer is characterized by thickness d , permittivity $\varepsilon = \varepsilon_0(-\varepsilon' - j\varepsilon'')$ and permeability $\mu = \mu_0(-\mu' - j\mu'')$, where ε_0 and μ_0 are the free-space permittivity and permeability, respectively. A linearly polarized plane wave impinges on the structure, which reflects it in the specular direction. The related electric field is assumed to have components parallel and perpendicular to the ordinary plane of incidence, so that the GO response is determined by the corresponding reflection coefficients $R_{\parallel, \perp}$ here evaluated by considering the ETL circuit:

$$R_{\parallel, \perp} = \frac{Z_{\parallel, \perp}^{in} - Z_{\parallel, \perp}^0}{Z_{\parallel, \perp}^{in} + Z_{\parallel, \perp}^0} \quad (1)$$

wherein the subscripts \parallel, \perp refer to the parallel and perpendicular polarization, respectively. If ζ_0 is the free-space impedance and θ^i is the angle between the unit vector \hat{n} normal to the illuminated surface and the incidence direction, $Z_{\parallel}^0 = \zeta_0 \cos \theta^i$ and $Z_{\perp}^0 = \zeta_0 / \cos \theta^i$ are the ETL characteristic impedances related to the free-space surrounding the structure. The ETL input impedances concerning the grounded layer are given by:

$$Z_{\parallel, \perp}^{in} = jZ_{\parallel, \perp}^l \tan(k_{z''}d) \quad (2)$$

$$Z_{\parallel}^l = \frac{k_{z''}}{\omega\varepsilon}; \quad Z_{\perp}^l = \frac{\omega\mu}{k_{z''}}; \quad k_{z''} = -\beta_{z''} - j\alpha_{z''} \quad (3)$$

$$\beta_{z''} = \sqrt{\frac{B - (k_0 \sin \theta^i)^2 + \sqrt{A^2 + [B - (k_0 \sin \theta^i)^2]^2}}{2}} \quad \alpha_{z''} = \sqrt{\frac{(k_0 \sin \theta^i)^2 - B + \sqrt{A^2 + [B - (k_0 \sin \theta^i)^2]^2}}{2}} \quad (4)$$

$$A = k_0^2 (\varepsilon' \mu'' + \varepsilon'' \mu') \quad B = k_0^2 (\varepsilon' \mu' - \varepsilon'' \mu'') \quad (5)$$

in which k_0 is the free-space propagation constant.

3. UAPO DIFFRACTION COEFFICIENTS

The truncated structure is modeled by an equivalent half-plane and a PO approximation is adopted for the electric and magnetic equivalent surface currents, so that they can be expressed in terms of the incident field:

$$\zeta_0 \underline{J}_s^{PO} = \zeta_0 \tilde{\underline{J}}_s^{PO} e^{jk_0 x \cos \phi'} = \left\{ [1 - R_{\perp}] E_{\perp}^i \sin \phi' \hat{e}_{\perp} + [1 + R_{\parallel}] E_{\parallel}^i \hat{t} \right\} e^{jk_0 x \cos \phi'} \quad (6)$$

$$\underline{J}_{ms}^{PO} = \tilde{\underline{J}}_{ms}^{PO} e^{jk_0 x \cos \phi'} = \left\{ [1 - R_{\parallel}] E_{\parallel}^i \sin \phi' \hat{e}_{\perp} + [1 + R_{\perp}] E_{\perp}^i \hat{t} \right\} e^{jk_0 x \cos \phi'} \quad (7)$$

where the angle ϕ' fixes the incidence direction, $\hat{t} = \hat{y} \times \hat{e}_{\perp}$ and $\hat{e}_{\perp} = \hat{s}' \times \hat{y} / |\hat{s}' \times \hat{y}|$, \hat{s}' being the unit vector in the incidence direction. In the far-field approximation, the scattered field generated by these currents can be expressed by means of the well-known radiation integral:

$$\underline{E}^s \cong -jk_0 \iint_S \left[(\underline{I} - \hat{R}\hat{R}) (\zeta_0 \underline{J}_s^{PO}) + \underline{J}_{ms}^{PO} \times \hat{R} \right] G(\underline{r}, \underline{r}') dS \quad (8)$$

in which $G(\underline{r}, \underline{r}')$ is the Green's function, \underline{r} and \underline{r}' denote the observation and source points, respectively, \hat{R} is the unit vector from the radiating element at \underline{r}' to the observation point, and \underline{I} is the (3×3) identity matrix. The approximation $\hat{R} \cong \hat{s}$ (\hat{s} is the diffraction direction) is permitted for evaluating the edge diffracted field, so that analytical manipulations transform (8) into:

$$\underline{E}^s \cong \left[(\underline{I} - \hat{s}\hat{s}) (\zeta_0 \tilde{\underline{J}}_s^{PO}) + \tilde{\underline{J}}_{ms}^{PO} \times \hat{s} \right] \frac{1}{4\pi j} \int_C \frac{e^{-jk_0 \rho \cos(\alpha \mp \phi)}}{\cos \alpha + \cos \phi'} d\alpha = \left[(\underline{I} - \hat{s}\hat{s}) (\zeta_0 \tilde{\underline{J}}_s^{PO}) + \tilde{\underline{J}}_{ms}^{PO} \times \hat{s} \right] I_s \quad (9)$$

The curve C is shown in Fig. 2, (ρ, ϕ) denotes the observation point, and $- (+)$ sign applies if $0 < \phi < \pi$ ($\pi < \phi < 2\pi$).

The integration term I_s can be reduced to a typical diffraction integral and evaluated by using the Steepest Descent Method in the high frequency approximation. The resulting diffraction term is:

$$I_s^d = \frac{e^{-j\pi/4}}{2\sqrt{2\pi k_0}(\cos \phi + \cos \phi')} F_t \left(2k_0 \rho \cos^2 \left(\frac{\phi \pm \phi'}{2} \right) \right) \frac{e^{-jk_0 \rho}}{\sqrt{\rho}} \quad (10)$$

where $F_t(\cdot)$ is the UTD transition function [5], and $+$ ($-$) sign applies when $0 < \phi < \pi$ ($\pi < \phi < 2\pi$). The above analytic results define the UAPO diffracted field to be added to the GO field:

$$\underline{E}^d = \begin{pmatrix} E_z^d \\ E_\phi^d \end{pmatrix} = \begin{pmatrix} D_{zz}^{UAPO} & 0 \\ 0 & D_{\phi\phi'}^{UAPO} \end{pmatrix} \begin{pmatrix} E_z^i \\ E_{\phi'}^i \end{pmatrix} \frac{e^{-jk_0 \rho}}{\sqrt{\rho}} \quad (11)$$

in which the UAPO diffraction coefficients are so expressed:

$$D_{zz}^{UAPO} = [(1 - R_\perp) \sin \phi' - (1 + R_\perp) \sin \phi] \frac{e^{-j\pi/4}}{2\sqrt{2\pi k_0}(\cos \phi + \cos \phi')} F_t \left(2k_0 \rho \cos^2 \left(\frac{\phi \pm \phi'}{2} \right) \right) \quad (12)$$

$$D_{\phi\phi'}^{UAPO} = [(1 + R_\parallel) \sin \phi - (1 - R_\parallel) \sin \phi'] \frac{e^{-j\pi/4}}{2\sqrt{2\pi k_0}(\cos \phi + \cos \phi')} F_t \left(2k_0 \rho \cos^2 \left(\frac{\phi \pm \phi'}{2} \right) \right) \quad (13)$$

4. NUMERICAL RESULTS

The validity of the UAPO-based approach is demonstrated by numerical tests. They refer to a lossy DNG MTM layer having thickness $d = 0.125\lambda_0$, λ_0 being the free-space wavelength, $\varepsilon =$

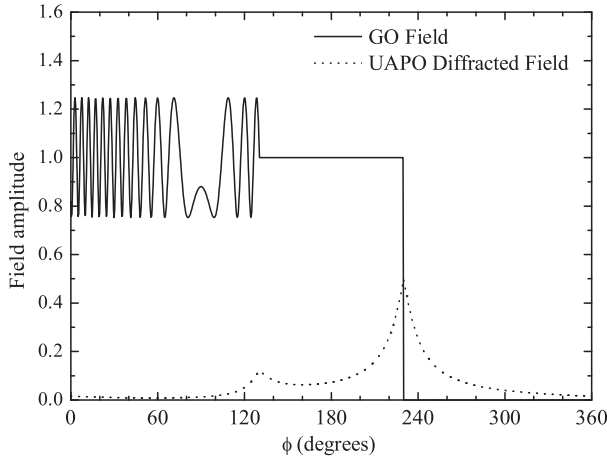


Figure 3: z -component of GO field and UAPO diffracted field. Incident field: $E_z^i = 1$, $E_{\phi'}^i = 0$.

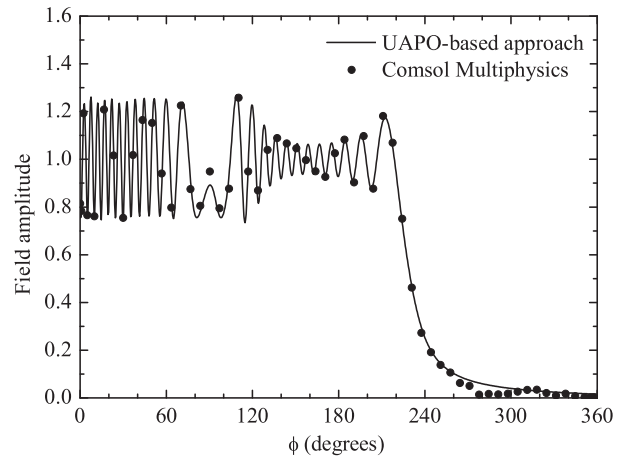


Figure 4: z -component of the total field. Incident field: $E_z^i = 1$, $E_{\phi'}^i = 0$.

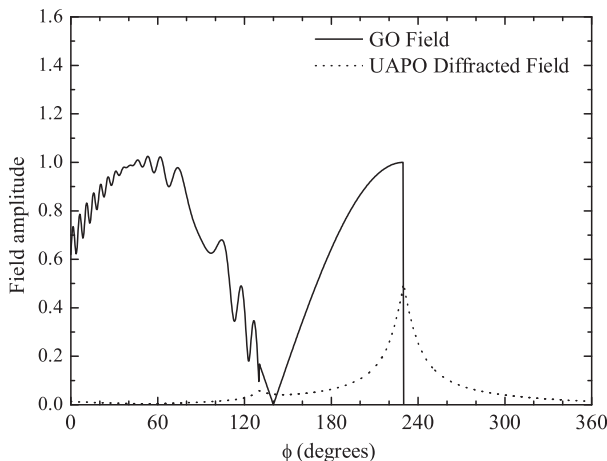


Figure 5: ϕ -component of GO field and UAPO diffracted field. Incident field: $E_z^i = 0$, $E_{\phi'}^i = 1$.

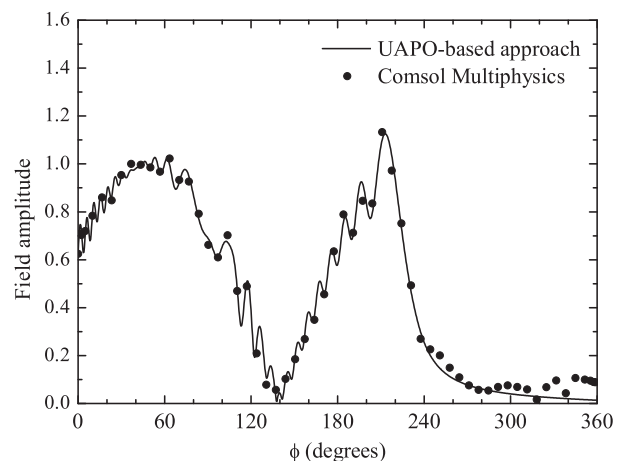


Figure 6: ϕ -component of the total field. Incident field: $E_z^i = 0$, $E_{\phi'}^i = 1$.

$(-3 - j1.5)\epsilon_0$ and $\mu = (-1 - j0.5)\mu_0$. The incident plane wave propagates in the direction $\phi' = 50^\circ$ and the field is observed over a circular path having radius $\rho = 8\lambda_0$. Fig. 3 shows the amplitude of the electric field z -component related to GO field and UAPO diffracted field contributions. As expected, the GO field exhibits two discontinuities at the reflection and incident field shadow boundaries ($\phi = 130^\circ$ and $\phi = 230^\circ$). On the other hand, the UAPO diffracted field is not negligible in the neighbourhood of such boundaries and guarantees the continuity of the total field as reported in Fig. 4, where the comparison with Comsol Multiphysics[®] results is also shown. The good agreement demonstrates the correctness and the accuracy of the proposed approach. According to the results reported in Figs. 5 and 6, same conclusions hold when considering the electric field ϕ -component.

5. CONCLUSION

A closed form UAPO-based solution has been here proposed for evaluating the field diffracted by a DNG MTM layer with a PEC backing when illuminated by an incident plane wave at normal incidence. It has been derived by using a PO approximation for the equivalent electric and magnetic surface currents in the radiation integral. A useful approximation and a uniform asymptotic evaluation of the resulting integral has allowed to obtain the UAPO diffraction coefficients in terms of the standard UTD transition function and the reflection coefficient of the considered structure. As demonstrated by numerical simulations, the proposed solution perfectly compensates the GO field discontinuities at the reflection and incident field shadow boundaries, it is simple and easy to handle. Moreover, its accuracy is well assessed by the good agreement obtained in comparisons with Comsol Multiphysics[®], a commercial tool based on the Finite Element Method.

REFERENCES

1. Engheta, N. and R. W. Ziolkowski, "A positive future for double-negative metamaterials," *IEEE Trans. Microwave Theory Tech.*, Vol. 53, 1535–1556, 2005.
2. Engheta, N. and R. W. Ziolkowski, *Metamaterials: Physics and Engineering Explorations*, Wiley-Interscience, 2006.
3. Caloz, C. and T. Itoh, *Electromagnetic Metamaterials: Transmission Line Theory and Microwave Applications*, Wiley-Interscience, Hoboken, 2006.
4. Gennarelli, G. and G. Riccio, "A UAPO-based solution for the scattering by a lossless double-negative metamaterial slab," *Progress In Electromagnetics Research M*, Vol. 8, 207–220, 2009.
5. Kouyoumjian, R. G. and P. H. Pathak, "A uniform geometrical theory of diffraction for an edge in a perfectly conducting surface," *Proc. IEEE*, Vol. 62, 1448–1461, 1974.

A Novel Four-port De-embedding Method and the Parametric Extraction of MOSFETs

C. I. Lee, W. C. Lin, C. C. Chen, Y. T. Lin, and Y. T. Lee

Department of Electrical Engineering, National Sun Yat-Sen University, Taiwan, R.O.C.

Abstract— A new four-port de-embedding procedure based on the transmission-line theory for on wafer S -parameter measurement is demonstrated in this paper for the first time. Although the traditional open and short test structures can characterize the resistive and inductive properties of the parasitic effects of the metal interconnect lines, the conductive and capacitive characteristics are hardly eliminated only with lumped equivalent circuit models in high substrate loss CMOS process. In this paper, we employed the transmission-line based technique to accurately remove not only the resistive and inductive parasitic effects but also the conductive and capacitive ones in the four-port measurement. We only used one simple open and one through test structures to remove the unwanted parasitic effects from pads and interconnects. In addition, the poly ground-shielded technology was adopted underneath the pads to reduce the parallel parasitic capacitance of shielded-based test structures without influencing the isolation between the signal ports in this work. This de-embedding methodology for extracting the four-port MOSFET parameters including the substrate network can be realized up to 10 GHz operating frequency in this work. In addition, in comparison with the traditional four-port open-short de-embedding procedure, the greatest advantage of our proposed method is the significant chip area reduction, and we expect to construct equivalent circuit models for different dimensions and bias through our proposed de-embedding method for future rf circuit designers.

1. INTRODUCTION

In recent years, the operating frequency of MOSFETs implemented in integrated circuit (IC) process increases due to the downscaling technology improvement. In order to acquire the precise high frequency characteristics and establish the device model, an accurate de-embedding method must be performed to remove the unnecessary parasitics of test structures. However, when the operating frequency increases, the parasitic effects caused from the pads, metal interconnect lines and silicon substrates are difficult to be eliminated by the traditional physics-based model of parasitic network due to the distributed features instead of lumped ones. Therefore, a de-embedding procedure which can eliminate all the parasitic effects induced at microwave frequency for the MOSFETs implemented in lossy silicon substrate is significant [1, 2].

At microwave frequencies, the effective length of the interconnect lines becomes considerable and the conductance and capacitance effects are difficult to be determined by the lumped equivalent-circuit model. Therefore, a de-embedding procedure based on the transmission-line theory is reported [3]. One open and one through test structures are required to remove the parasitic effects at microwave frequencies in [3]. Previously, most transmission-line de-embedding procedures are performed in the two-port network [3–7]. However, the source and body terminals of MOSFETs are not always connected to each other in the circuit design, for example, cascaded amplifiers or switch stage of mixers. Traditional common-source two-port test structures are incapable of extracting the impedance of the source and body terminals independently because of the connection between the source and body terminals. Many research efforts focus on the four-port measurement to extract the high frequency characteristics of MOSFETs for each port [8–11]. In [11], the de-embedding method based on the transmission-line theory is developed with the utilization of a through dummy and a four-port type open dummy. However, this method will suffer from the large chip area due to the four-port type open dummy.

In this paper, we propose a novel four-port de-embedding procedure which are based on two-port cascade structure de-embedding procedure and combined of metal and polysilicon ground-shielded technology [12, 13]. This method only employs a simple open test structure and a through one which is the most chip area saving de-embedding method according to our knowledge.

2. DE-EMBEDDING METHOD

Figure 1 shows the proposed four-port de-embedding dummy structures. The layout of the MOSFETs is designed to connect to four signal pads, which are gate, source, drain and body. Based

on cascade-based de-embedding method [3], we only use one through and one simple open dummy structure for eliminating the parasitic effects as shown in Figure 1(b) and Figure 1(c), respectively.

First, extracting the propagation constants and characteristic impedances of the interconnect lines was carried out by the simple open and through test structures. Next, the four-port MOSFET characteristics can be determined directly after removing the pad parasitic effects and the interconnect line ones calculated from the extracted transmission line parameters. To reduce the substrate-carried and port-to-port coupling, the ground-shielded technology is utilized. The equivalent representation of device under test (DUT) dummy structure is shown in Figure 2.

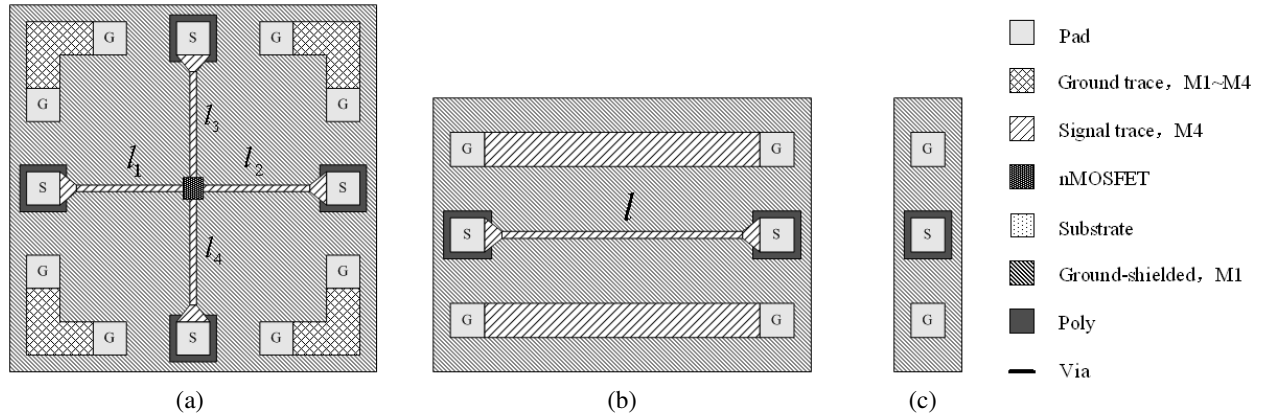


Figure 1: Dummy structures. (a) DUT. (b) Open. (c) Simple open.

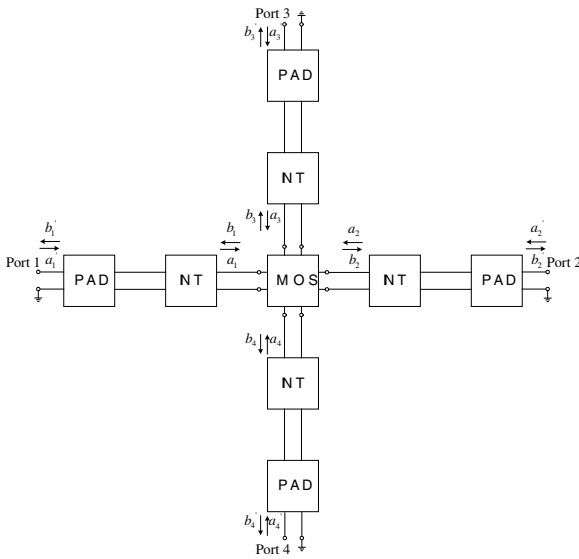


Figure 2: Equivalent representation of DUT dummy structure.

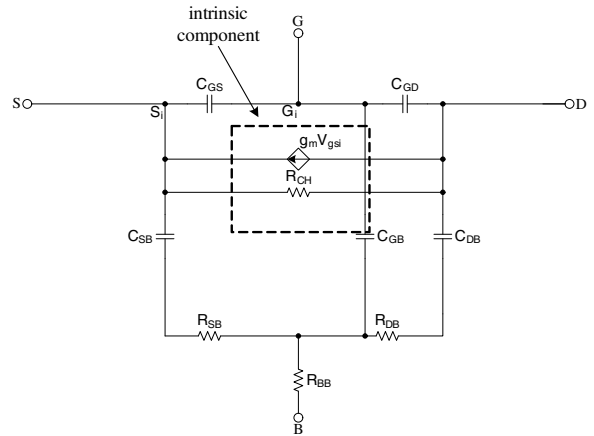


Figure 3: The small signal equivalent circuit for MOSFETs.

In the following section, we only show the significant equations of the de-embedding method. The corresponding matrixes are similar to ones listed in [14], but we extend the matrixes from three-port form to four-port one. According to the definition of each matrix in the literature [14], we can calculate the de-embedded S -parameter of MOSFETs $[S]$ from the measured one $[S']$ as

$$[S] = \left([G] \cdot ([S'] - [E])^{-1} \cdot [F] + [H] \right)^{-1} \quad (1)$$

where $[G]$, $[E]$, $[F]$, and $[H]$ are the modified four-port matrixes which are related to the three-port ones listed in [14].

3. MODEL VALIDATION RESULTS

The proposed and validated dummy structures were fabricated using 0.35 μm CMOS process. The width and channel length of the DUT are 12 and 0.35 μm , respectively. The finger numbers are 5. Figure 3 shows the equivalent circuit model that we use to extract and validate between measurement and simulation.

In order to validate the extrinsic parameters extracted from MOSFETs as shown in Tables 1 and 2, we compare simulated results with measured data biased in the active region ($V_g = V_d = 2\text{ V}$, $V_s = V_b = 0\text{ V}$), as shown in Figures 4(a) to (d). Good agreements are achieved between behavior of simulated results and measured data.

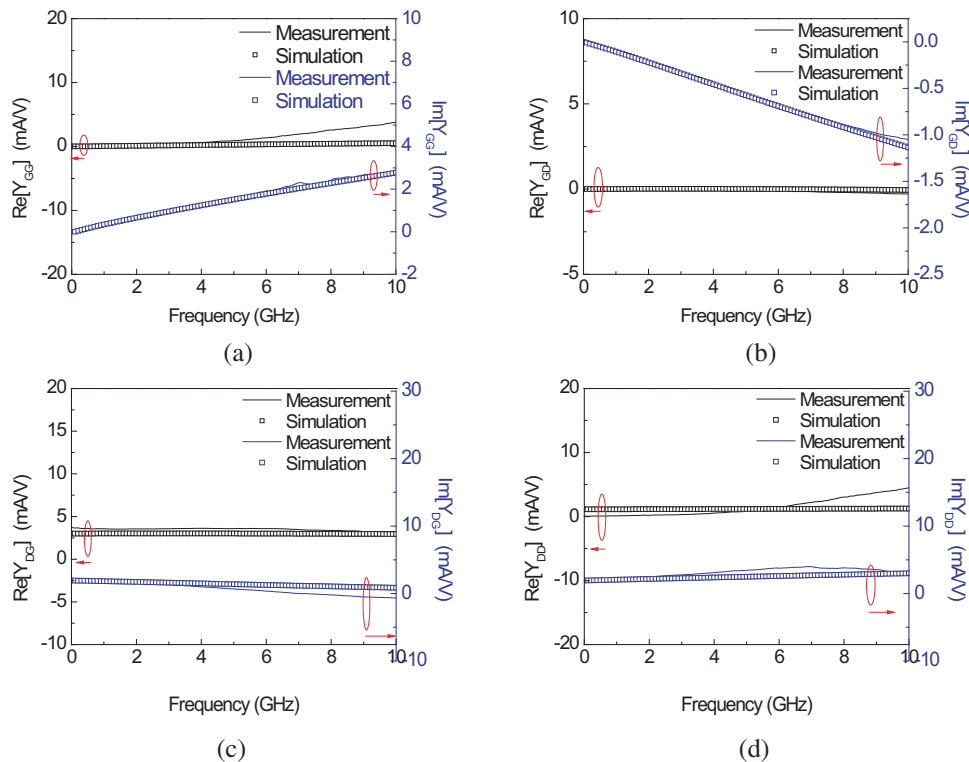


Figure 4: The comparison of measured and simulated data in active region. (a) $\text{Re}[Y_{GG}]$ and $\text{Im}[Y_{GG}]$. (b) $\text{Re}[Y_{GD}]$ and $\text{Im}[Y_{GD}]$. (c) $\text{Re}[Y_{DG}]$ and $\text{Im}[Y_{DG}]$. (d) $\text{Re}[Y_{DD}]$ and $\text{Im}[Y_{DD}]$.

Table 1: The extraction parameters of substrate resistance in cold bias.

	R_{SB0} (Ω)	R_{DB0} (Ω)	R_{BB0} (Ω)
Value	3337	3806	2567

Table 2: The extraction parameters of capacitance and transconductance in active region.

	C_{GS} (fF)	C_{GD} (fF)	C_{SB} (fF)	C_{DB} (fF)	C_{GB} (fF)	R_{CH} (Ω)	g_m (mS)
Value	22	15	12	4	26	887	3

4. CONCLUSIONS

A novel four-port de-embedding method based on transmission-line theory is demonstrated in this paper. The proposed de-embedding method is utilized to remove unwanted parasitics including the conductive and capacitive effects for a MOSFET device. The greatest advantage of our proposed method is significantly chip area reduction due to the only usage of simple open and through test structures. After removing unwanted parasitic parameters, the extrinsic parameters have

been demonstrated through simulated results and measured data. For future RF circuit designers, we expect to construct the model with different dimensions and bias through our de-embedding method.

ACKNOWLEDGMENT

The authors would like to thank National Chip Implementation Center (CIC) for chip fabrication, the National Nano Device Laboratories (NDL) for the high frequency measurement support, and the Wireless Communication Antenna Research Center for the support. This work is also supported in part by the National Science Council of Taiwan, R.O.C. under Grant NSC98-2221-E-110-032-MY2 and under Grant NSC97-2221-E-110-036-MY3.

REFERENCES

1. Koolen, M. C. A. M., J. A. M. Geelen, and M. P. J. G. Versleijen, "An improved de-embedding technique for on-wafer high-frequency characterization," *Proceedings Bipolar Circuits and Technology Meeting*, 188–191, Minneapolis, September 1991.
2. Kolding, T. E., "A four-step method for de-embedding gigahertz on-wafer CMOS measurements," *IEEE Trans. Electron Devices*, Vol. 47, No. 4, 734–740, 2000.
3. Chen, C. H. and M. J. Deen, "A general noise and S -parameter deembedding procedure for on-wafer high-frequency noise measurements of MOSFETs," *IEEE Trans. Microwave Theory Tech.*, Vol. 49, No. 5, 1004–1005, 2001.
4. Cho, M. H., G. W. Huang, C. S. Chiu, K. M. Chen, A. S. Peng, and Y. M. Teng, "A cascade open-short-thru (COST) de-embedding method for microwave on-wafer characterization and automatic measurement," *IEICE Trans. on Electronics*, Vol. E88C, No. 5, 845–850, 2005.
5. Cho, M. H., G. W. Huang, K. M. Chen, and A. S. Peng, "A novel cascade-based de-embedding method for on-wafer microwave characterization and automatic measurement," *IEEE MTT-S Int. Microwave Symp. Dig.*, Vol. 2, 1237–1240, 2004.
6. Cho, M. H., G. W. Huang, Y. H. Wang, and L. K. Wu, "A scalable noise de-embedding technique for on-wafer microwave device characterization," *IEEE Microw. Wireless Compon. Lett.*, Vol. 15, No. 10, 649–651, 2005.
7. Cho, M.-H., D. Chen, R. Lee, A.-S. Peng, L.-K. Wu, and C.-S. Yeh, "Geometry-scalable parasitic deembedding methodology for on-wafer microwave characterization of MOSFETs," *IEEE Trans. Electron Devices*, Vol. 56, No. 2, 299–305, 2009.
8. Wu, S.-D., G.-W. Huang, K.-M. Chen, H.-C. Tseng, and T.-L. Hsu, "Extraction of substrate parameters for RF MOSFETs based on four-port measurement," *IEEE Microw. Wireless Compon. Lett.*, Vol. 15, No. 6, 437–439, 2005.
9. Brinkhoff, J., S. C. Rustagi, J. Shi, and F. Lin, "MOSFET model extraction using 50 GHz four-port measurements," *RFIC Symp.*, 647–650, Honolulu, June 2007.
10. Wu, S. D., G. W. Huang, K. M. Chen, H. C. Tseng, T. L. Hsu, and C. Y. Chang, "RF MOSFET characterization by four-port measurement," *IEICE Trans. on Electronics*, Vol. E88C, No. 5, 851–856, 2005.
11. Cho, M.-H., G.-W. Huang, C.-S. Chiu, and K.-M. Chen, "Unified parasitic de-embedding methodology of on-wafer multi-port device characterization," *IEEE MTT-S Int. Microwave Symp. Dig.*, 1307–1310, 2005.
12. Kolding, T. E., O. K. Jensen, and T. Larsen, "Ground-shielded measuring technique for accurate on-wafer characterization of RF CMOS devices," *Proceedings ICMTS*, 246–251, Monterey, March 2000.
13. Kaija, T. and P. Heino, "Shield-based on-wafer CMOS test fixture employing polysilicon shield plane," *NORCHIP Conference*, 118–121, November 2005.
14. Chen, M.-H., G.-H. Huang, L.-K. Wu, C.-S. Chiu, Y.-H. Wang, K.-M. Chen, H.-C. Tseng, and T.-L. Hsu, "A shield-based three-port de-embedding method for microwave on-wafer characterization of deep-submicrometer silicon MOSFETs," *IEEE Trans. Microwave Theory Tech.*, Vol. 53, No. 9, 2926–2934, 2005.

The RF I-V Curve for PHEMT through the Small Signal S -parameter Extraction Method

C. I. Lee, W. C. Lin, Y. T. Lee, and Y. T. Lin

Microwave Circuit and Device Lab, Department of Electrical Engineering, National Sun Yat-Sen University
Kaohsiung, Taiwan, R.O.C.

Abstract— In this paper, the rf (radio frequency) I-V (current-voltage) curve and its equivalent circuit for a 0.15 μm gate length GaAs (Gallium Arsenide) pHEMT (pseudomorphic High Electron Mobility Transistors) with four fingers up to 26 GHz is presented for the first time. The traditional dc I-V curve obtained by dc measurement was unable to provide sufficient information. In this paper, the rf I-V curve was determined by high-frequency measurement and each element of the equivalent circuit was extracted directly using the measured S -parameters. Through the above measurement and mathematical calculation, the rf I-V curve has been established by integrating the extracted element g_m and g_{ds} . It can be observed that the knee voltages in dc and rf I-V curve are different. Due to the surface state effect and slow deep level traps surface state effect, the rf I-V curve shows the higher transconductance than the dc I-V curve. Furthermore, under high drain-source bias conditions, the hot carrier effect observed in the rf I-V curve is weaker than the dc I-V curve. The above phenomena explain the significant difference between the rf and dc I-V curve. The rf I-V curve does reveal the high-frequency characteristics of the transistor. The information from the rf I-V curve will provide the circuit designers to predict the transistor performance more precisely.

1. INTRODUCTION

With the development of wireless communication technology, high-frequency integrated circuit design will be more important. For this reason, to predict the high-frequency characteristics of the device is the major agenda. In recent years, to model the characteristics of the transistors under static or large signal condition is an important topic, and many research efforts focus on the development of different kinds of small signal and large signal models [1]. Some models demonstrate great prediction about output performance and the nonlinearity characteristics and also show the agreement of the I-V curve between the model and dc measurement. It is notable that even the model can predict the performance but still a controversial issue needs to be clarified. The I-V curve in the dc situation would not be the same as in high-frequency situation. In this paper, we demonstrate the difference between the I-V curve measured under the dc condition and the rf I-V curve implemented by high-frequency measurement. In addition, the reasons for the difference between these two conditions will be explained in the following section.

pHEMTs have excellent noise characteristics and great power performance, and it is more suitable for front-end circuits for the wireless communication system design. According to the application of the high-frequency integrated circuit design, this work emphasizes the high-frequency characteristics of the pHEMTs. The traditional current-voltage curve obtained by dc measurement was unable to provide sufficient high-frequency performance information. In this paper, the rf I-V curve of pHEMTs was determined by high-frequency measurement for the first time, and each element of the equivalent circuit was extracted directly using the measured high-frequency S -parameters. Through the above measurement and mathematical calculation, the rf I-V curve has been established by integrating the extracted equivalent circuit element g_m and g_{ds} . It is useful to determine the high-frequency characteristics of the device for circuit design.

2. DETERMINATION OF SMALL-SIGNAL EQUIVALENT CIRCUIT PARAMETERS AND VERIFICATION

The equivalent circuit parameters can be extracted by biasing the device in cold-device, pinch-off and active region. To eliminate the effect caused by pad and signal interconnect lines to obtain the device performance, a two step de-embedding method [2] was used to accomplish the de-embedding process. Its equivalent small signal model can be divided into extrinsic and intrinsic parts. The extrinsic element (resistance and inductance) value can be extracted under the cold condition [3].

Similarly, the extraction of the extrinsic parasitic capacitance could be done by means of biasing the transistor slightly below the pinch-off condition. After eliminating the series extrinsic inductance and resistance, the parasitic capacitance can also be determined [4].

The completed equivalent circuit model of the GaAs pHEMT is shown in [3]. To analyze the intrinsic elements, the transistor was biased in the active region by the utilization of the de-embedding process to eliminate the extrinsic parasitic elements [5]. In accordance with the above steps, we can obtain each intrinsic Y -parameters of the device at different bias voltages. Through the mathematical analysis described in [6], the intrinsic element values can be extracted. Therefore, all the element of the equivalent circuit have been determined, and the extracted element values are listed in Table 1.

Table 1: The element values of the equivalent circuit of GaAs pHEMT biased at $V_{gs} = -0.5$ V and $V_{ds} = 2$ V.

Element	L_g	L_d	L_s	R_g	R_d	R_s	C_{pg}	C_{pd}	C_{gs}	C_{gd}	C_{ds}	R_{ds}	R_i	g_m	Tau
Value	57.41 (pH)	1.69 (pH)	3.63 (pH)	1.69 (Ohm)	1.21 (Ohm)	1.19 (Ohm)	6.36 (fF)	18.61 (fF)	0.41 (pF)	30.91 (fF)	86.68 (fF)	97.05 (Ohm)	0.02 (Ohm)	240 (mS)	1.01 (pSec)

The transistor dependence current source at drain terminal is a nonlinear source, and its current characteristics depends on V_{gs} (gate-source) and V_{ds} (drain-source) bias voltage. The bias dependent intrinsic elements extracted from high-frequency measurement are determined. The rf output conductances (g_{ds}) decrease with the increasing of drain voltage as shown in Figure 1. And the transconductances (g_m) relate to the transfer characteristics as shown in Figure 2. Another nonlinear source of the transistor is nonlinear input impedance caused by the nonlinear variation of the capacitance C_{gs} and C_{gd} are shown in Figures 3 and 4. Through the mathematical calculations and integration of the extracted intrinsic elements, transconductances and output conductances, the currents characteristics corresponding to each bias voltage can be evaluated and form the rf I-V curve. Finally, the performance and I-V characteristics of the transistors under the high-frequency operation can be obtained.

3. EXPERIMENTAL RESULT ANALYSIS

In this paper, the GaAs based pHEMTs 0.15 μm process is provided by WIN Semiconductors Corporation. The device has four fingers and its total gate width is $4 \times 100 \mu\text{m}$. The S -parameters were obtained by on wafer measurement through the Cascade microwave probe and Agilent E8364B network analyzer. The gate-source was biased from -1 V to 0 V with a step of 0.1 V and drain-source from 0 V to 5 V with a step of 0.25 V. The measurement frequency ranges from 1 GHz to 26 GHz.

The model and measured S -parameter have excellent agreement as shown in Figure 5. From the experimental results, the significant difference between the rf I-V curve implemented by the integration and the traditional dc I-V curve obtained by dc measurement can be found in Figure 6. When the transistors operate in the high-frequency region, the output characteristics and currents are significantly higher. The knee voltages relating to the gain compression phenomenon [7] are different in the dc and rf I-V curve. As the result of the slow deep level traps [8] and surface state effect [9], the frequency dispersion behavior [10] makes the rf I-V curve show higher transconductances and currents on output characteristics. Moreover, the hot carrier effect observed in the rf I-V curve

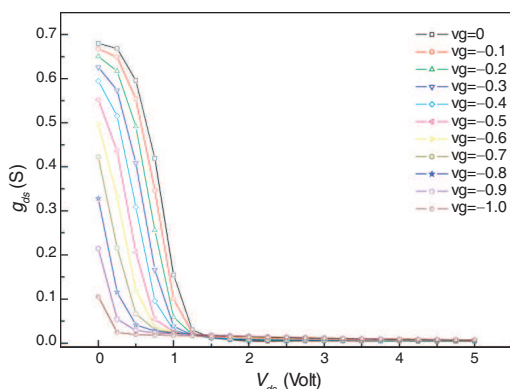


Figure 1: The relation between output conductances and drain voltage as a function of gate voltage.

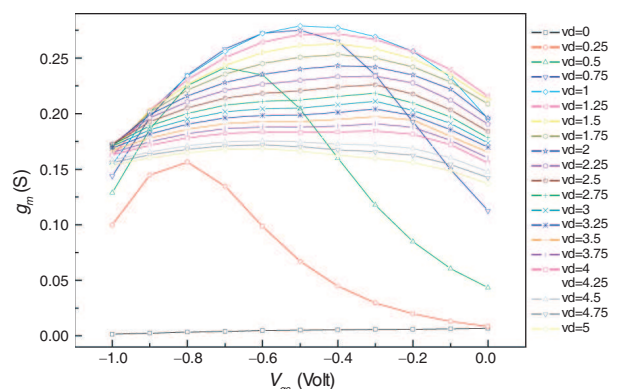


Figure 2: The relation between transconductances and gate voltage as a function of drain voltage.

is relatively weaker than in the dc I-V curve when biasing the transistor under high drain-source conditions. In addition, during the high-frequency operation, the self-heating effect [11] is not noticeable because this phenomenon appears only in the low-frequency region not in high-frequency measurement. In this work, we observe that the rf I-V curve has higher currents than dc I-V curve at the same drain-source bias. According to the above results and explanations, the obtained high-frequency characteristics of transistors from rf I-V curve is suitable for the application of the transistors in the high-frequency circuit design.

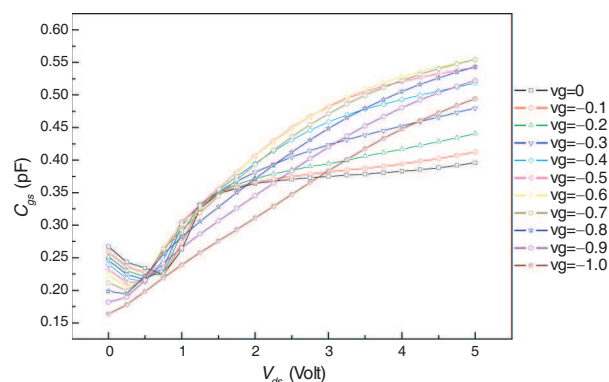


Figure 3: The relation between intrinsic gate-source capacitance and drain voltage as a function of gate voltage.

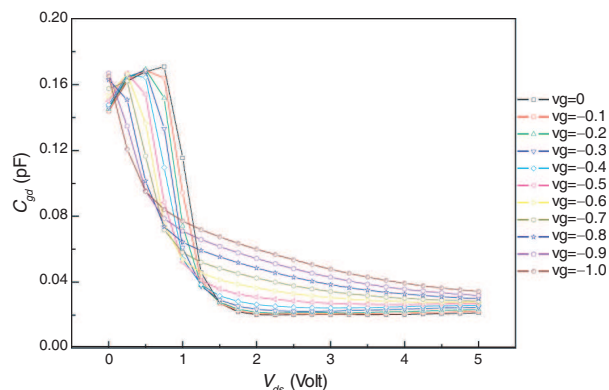


Figure 4: The relation between intrinsic gate-drain capacitance and drain voltage as a function of gate voltage.

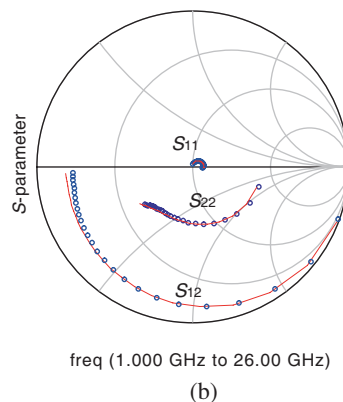
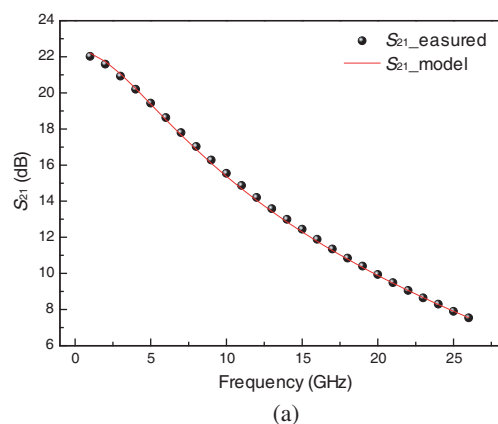


Figure 5: Comparison between measured (open circles) and modeled (solid line) S -parameter at $V_{ds} = 2\text{ V}$, $V_{gs} = -0.5\text{ V}$, and the frequency range from 1 GHz to 26 GHz. (a) S_{21} (b) S_{11} , S_{12} and S_{22} .

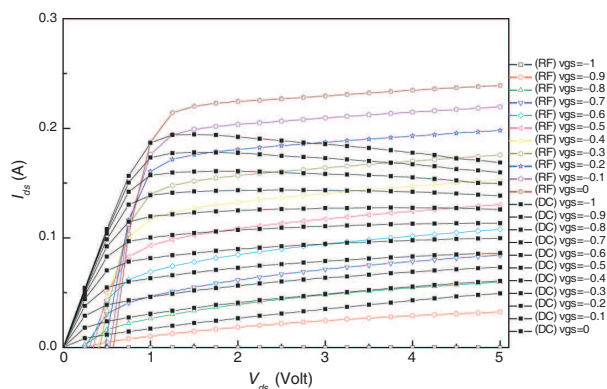


Figure 6: The measured dc I-V curves and rf I-V curves for $100 \times 4 \times 0.15\text{ }\mu\text{m}$ pHEMT transistor.

4. CONCLUSION

In this study, the small-signal model of GaAs pHEMTs and its completed rf I-V curve calculated from the high-frequency measurement data are demonstrated for the first time, and the obtained rf I-V curve can accurately describe the high-frequency characteristics of the transistors. For the front-end circuits of wireless communication systems, the selection of the bias point has a key influence on the performance of the power amplifiers, and its operation mode also depends on transistor bias voltage. The information from the rf I-V curve will provide circuit designers a more accurate way to select the appropriate bias point for the high-frequency operation and then bias the transistor in the suitable operation region. The rf I-V curve provides more accurate information than the dc I-V curve to describe the transistor high-frequency characteristics and can be applied to the high-frequency integrated circuit design.

ACKNOWLEDGMENT

The authors would like to thank National Chip Implementation Center (CIC) for chip fabrication and the Wireless Communication Antenna Research Center for the support. This work is also supported in part by the National Science Council of Taiwan, R.O.C. under Grant NSC98-2221-E-110-032-MY2 and under Grant NSC97-2221-E-110-036-MY3.

REFERENCES

1. Angelov, I., H. Zirath, and N. Rosman, "A new empirical nonlinear model for HEMT and MESFET devices," *IEEE Trans. Microwave Theory Tech.*, Vol. 40, 2258–2266, 1992.
2. Koolen, M. C. A. M., J. A. M. Geelen, and M. P. J. G. Versleijen, "An improved de-embedding technique for on-wafer high-frequency characterization," *Proceedings of the 1991 Bipolar Circuits and Technology Meeting*, 188–191, 1991.
3. Jeon, M.-Y., B.-G. Kim, Y.-J. Jeon, and Y.-H. Jeong, "A technique for extracting small-signal equivalent-circuit elements of HEMTs," *IEICE Trans. on Electronics*, Vol. 82, 1968–1976, 1999.
4. Andreas, P., G. Markus, and W. Dirk, "Small-signal and temperature noise model for MOS-FETs," *IEEE Trans. Microwave Theory Tech.*, 1927–1934, 2002.
5. Dambrine, G., A. Cappy, F. Heliodore, and E. Playez, "A new method for determining the FET small-signal equivalent circuit," *IEEE Trans. Microwave Theory Tech.*, Vol. 36, 1151–1159, 1988.
6. Berroth, M. and R. Bosch, "Broad-band determination of the FET small-signal equivalent circuit," *IEEE Trans. Microwave Theory Tech.*, Vol. 38, 891–895, 1990.
7. Meng, C. C. and G. H. Huang, "High frequency I-V curves for GaAs MESFETs through unique determination of small signal circuit parameters at multiple bias points," *Asia-Pacific Microwave Conference*, Vol. 702, 709–711, 2001.
8. Ladbroke, P. H. and S. R. Blight, "Low-field low-frequency dispersion of transconductance in GaAs MESFETs with implications for other rate-dependent anomalies," *IEEE Trans. Electron. Devices*, Vol. 35, 257–267, 1988.
9. Kyoung Jin, C. and L. Jong-Lam, "Interpretation of transconductance dispersion in GaAs MESFET using deep level transient spectroscopy," *IEEE Trans. Electron. Devices*, Vol. 48, 190–195, 2001.
10. Hasumi, Y., N. Matsunaga, T. Oshima, and H. Kodera, "Characterization of the frequency dispersion of transconductance and drain conductance of GaAs MESFET," *IEEE Trans. Electron. Devices*, Vol. 50, 2032–2038, 2003.
11. Chigaeva, E., N. Wieser, W. Walthes, M. GrÖZing, M. Berroth, H. Roll, O. Breitschädel, J. Off, B. Kuhn, F. Scholz, and H. Schweizer, "Dynamic large-signal I-V analysis and non-linear modelling of AlGaIn/GaN HEMTs," *The European Gallium Arsenide and Related III-V Compounds Application Symposium*, London, 631–634, 2001.

A Novel H-shaped Slot-coupled Antenna for the Integration of Power Amplifier

C. I. Lee, W. C. Lin, Y. T. Lin, and Y. T. Lee

Microwave Circuit and Device Lab, Department of Electrical Engineering
National Sun Yat-Sen University, Kaohsiung, Taiwan, R.O.C.

Abstract— This paper presents a novel H-shaped structure with the bow-tie shaped meander slot to integrate the class AB power amplifier. This compact structure is appropriate to apply to the wireless communication system. The novel H-shaped antenna has many excellent advantages over the conventional rectangular microstrip antenna such as the harmonic mode suppression, bandwidth enhancement, and the increase of the whole transmitter efficiency. This H-shaped antenna adopts slot-coupled microstrip patch structure to achieve the harmonic termination and good wideband matching. Due to the reduction of the surplus harmonic content from the nonlinear circuits, the improvement of the whole performance of the transmitter is achieved. The advantage of our novel structure is effective to decrease the additional area for the harmonic tuning network and suitable to obtain maximum output power.

1. INTRODUCTION

Low harmonic distortion and high efficiency are crucial factors in the wireless communication system. The power amplifier of the transmitter generally converts the power to the antenna through antenna matching network and interconnect cables [1]. The significant loss caused from the additional components will lower the whole performance and increase the cost. Therefore, many efforts focus on the investigation of the active integrated antenna (AIA) [1]. The component number of the harmonic tuning network and the interconnect line can be reduced with the realization of the AIA technique. The interface of the antenna and power amplifier is an important issue to satisfy optimum matching at the fundamental resonant frequency and meets the optimum output matching condition.

Many research efforts have been made to investigate the modified methods for decreasing whole area and maintaining the initial performance. Previous methods have focused on increasing the electrical field on the open end for the uniform field on the aperture [2, 3]. Hence, the associated studies with the H-shaped slot coupled antenna, dumbbell shaped slot coupled antenna, and bow-tie shaped slot coupled antenna [4–6] are adopted to improve the amount of electromagnetic coupling. This paper describes a modified meander slot coupled H-shaped antenna to reduce the area of antenna and achieve the termination of high order harmonic component behaviors. It also exhibits excellent efficiency and linearity.

2. ANTENNA DESIGN

In this work, the bow-tie shaped meander slot coupled H-shaped patch antenna shown in Figure 1 is presented. The ground of the antenna is printed on the upper surface of lower substrate composed of bow-tie profile with four meander segments and the feed line on the other side of lower substrate. The bow-tie shaped meander slot is extended as theta, θ , and the numbers of meander segments are added to modify the resonant frequency. In addition, the quality factor, Q , of the ground plane is decreased for the advantages of low profile and the wide band characterization is obtained. The H-shaped patch is attached on the upper substrate [7]. The novel H-shaped patch is inserted a pair of parallel slots into radiation edge vicinity to modify the surface current at the harmonic frequency response. The benefit of this topology is significant in changing the harmonic mode to exhibit the harmonic compression. The depth of the slits mounted on the center of H-shaped patch is modified to obtain appropriate coupling amount.

The 0.8 mm thick glass fiber board substrate is employed. The simulation has been carried out using 3-D EM simulator tool, Ansoft HFSS, which is convenient to predict the behavior of the passive circuit. The antenna is designed at 2.4 GHz operation frequency, and the parameters of the physical dimensions are presented in Table 1.

To integrate the power amplifier, the harmonic compression behavior is a good choice to isolate the inherent characteristics of non-demanded harmonics of active circuits. Furthermore, the

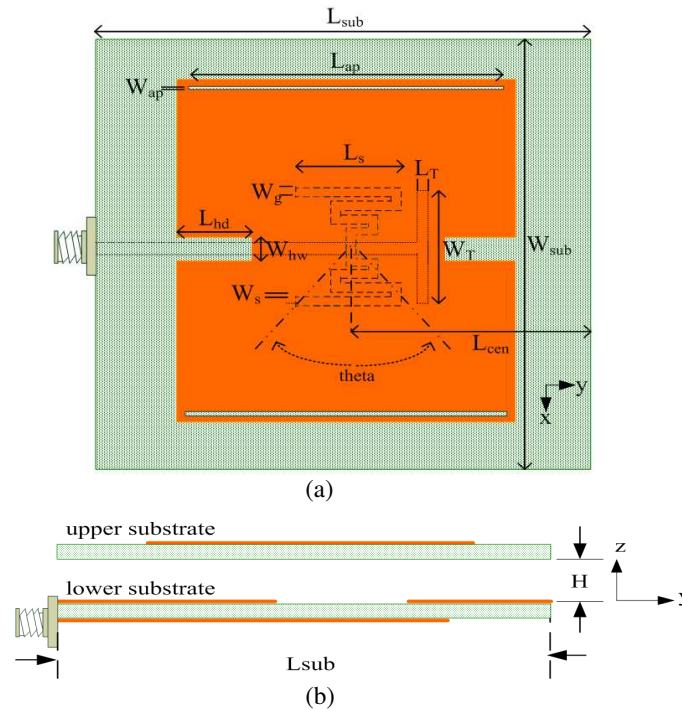


Figure 1: Configuration of presented antenna. (a) top view, and (b) side view.

Table 1: Physical dimensions of the presented antenna.

W_{sub} (mm)	L_{sub} (mm)	θ (degree)	W_g (mm)	L_s (mm)
68	60	45	1.2	12
W_s (mm)	L_{cen} (mm)	L_T (mm)	W_T (mm)	W_{ap} (mm)
0.5	0.95	3	14.4	0.7
L_{ap} (mm)	W_{hw} (mm)	L_{hd} (mm)	H (mm)	
42	3	12.5	4	

impedance of antenna must be integrated to meet the optimum output power matching. In addition, the linearity and PAE (power added efficiency) are taken in the application of the front-end design. The class-AB power amplifier is described as following.

3. CLASS-AB POWER AMPLIFIER DESIGN

The output stage network is the most crucial in the whole transmitter. In order to maintain the good linearity and efficiency, the class-AB power amplifier is employed in this work [8]. Because of the harmonic tuning characteristics and the input impedance of the antenna as the load of the class-AB power amplifier, the input impedance of the antenna should be designed to achieve to the optimum power matching. The power amplifier is performed as the feed plane which is attached on the bottom layer of lower substrate. This approach can significantly decrease the electromagnetic interference generated from the high output power by the ground shield between radiation space and the feed level. The packaged transistor, FPD 3000SOT89 is fabricated by RFMD company with GaAs technology in this power amplifier design. The operating DC bias is selected from the IV curve and the load pull method is utilized as shown in Figure 2. The gain matching is employed in the input matching network. First, the optimum output power is determined with power counter and large signal analysis with V_{GS} and V_{DS} at -0.9 V and 5.4 V respectively. The tuner is carried out to convert the output reference plane to the output DC-block under the optimum output power condition. Second, the input matching network is performed with lumped components, and the source pull has been taken to analyze using small signal analysis. The final topology is carried out with the lumped components and the transmission line as shown in Figure 3, and the photos in each metallic plane have been shown in Figure 4. These lumped components have been listed in

Table 2.

Table 2: Lumped components of the AIA.

C_1 (pF)	C_2 (pF)	C_3 (pF)	C_4 (pF)	C_5 (pF)
2.2	1.2	10	1.2	2.7
C_{DC} (uF)	L_1 (nH)	L_2 (nH)	L_3 (nH)	L_4 (nH)
22	2.7	15	15	5.6

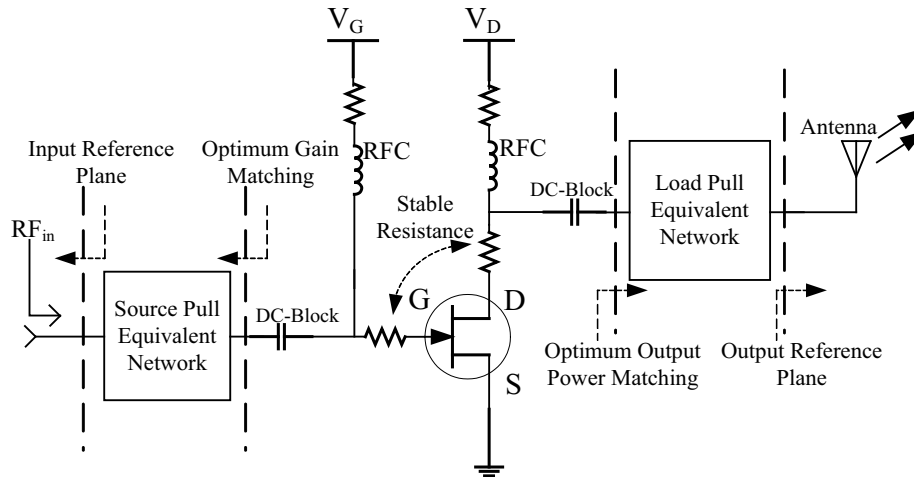


Figure 2: The schematic of class-AB power amplifier which is accounted to the concept and design process.

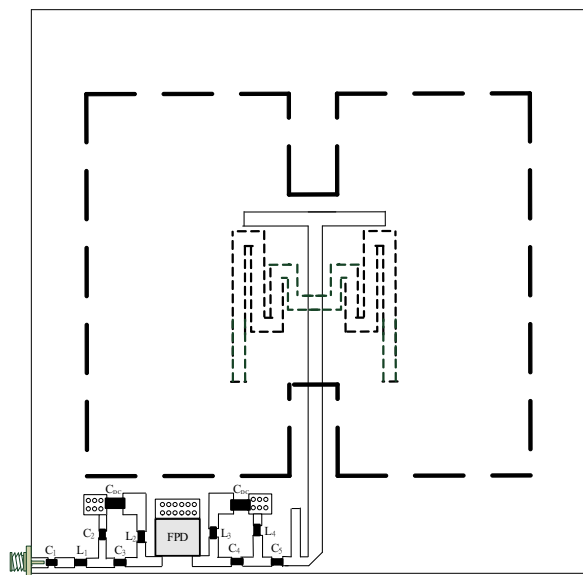


Figure 3: The whole structure of the presented AIA.

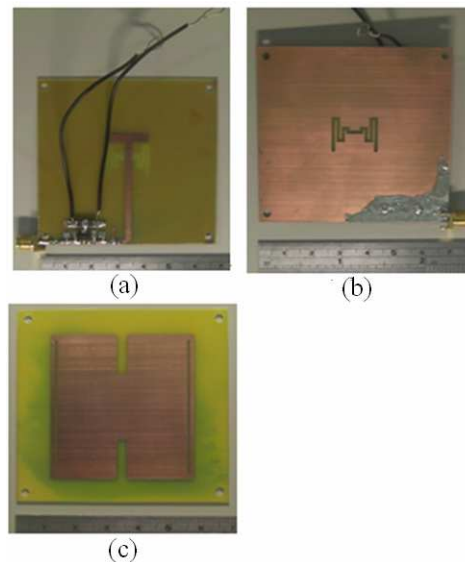


Figure 4: The three planes of the active integrated antenna are associated to Figure 3, respectively. These are photos of (a) feed layer circuit, (b) ground, and (c) patch.

4. EXPERIMENT RESULT OF AIA

This radiation pattern of the AIA has been measured in anechoic chamber. In addition, the structure which the center frequency is 2.4 GHz has been measured with 19 dBm input power. Figure 5

shows good agreement in the measurement and simulation. The measured 10-dB bandwidth of the antenna is 150 MHz at the resonant frequency of 2.4 GHz. The return loss of the resonant frequency has been described as -23 dB, -1.1 dB, and -2.3 dB at the fundamental, second order and third order frequency, respectively. In addition, the associated impedance characterization reveals the pure resistance at the fundamental frequency. The measured maximum gain of the antenna is 6.3 dBi. Furthermore, this AIA has the lowest return loss, -26 dB at the resonant frequency and 500 MHz bandwidth from 2.14 GHz to 2.64 GHz. The gain, drain efficiency and PAE as a function of input power at 2.4 GHz operating frequency is shown in Figure 6. The linear gain is 11.5 dB and the peak value of PAE and drain efficiency is up to 66 and 72 percent, respectively. $OP_{1\text{dB}}$ achieves to about 1 W. The normalized results of measurement and simulation in the E -plane radiation pattern and H -plane radiation pattern have been exhibited in Figure 7 and Figure 8, respectively. The measurement radiation pattern in Figure 7 and Figure 8 has shown that there is good agreement in the measurement and simulation. The cross polarization in E -plane and H -plane are well below at least 20 dB in the main radiation direction.

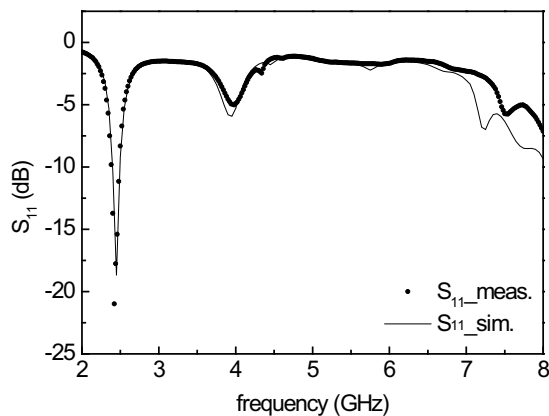


Figure 5: Simulated and measured return loss at frequency sweeping from 2 GHz to 8 GHz.

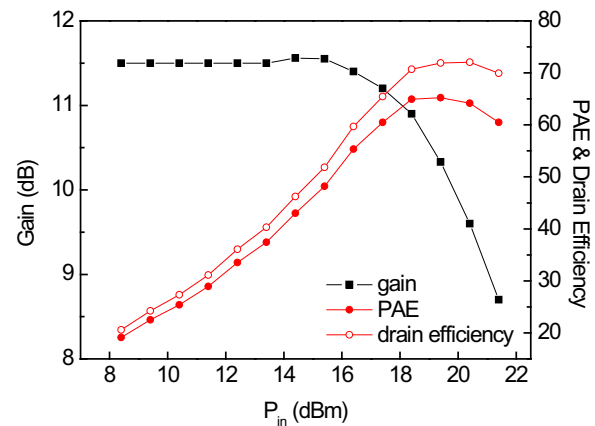


Figure 6: The maximum PAE and drain efficiency are 66% and 72% respectively. In addition, the gain is 11.5 dB.

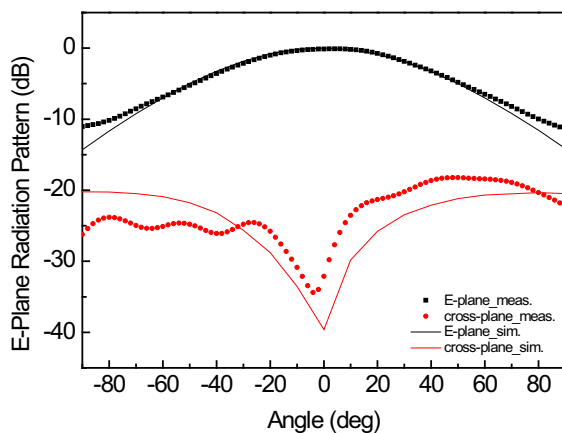


Figure 7: Measured and normalized E -plane radiation pattern of the presented AIA.

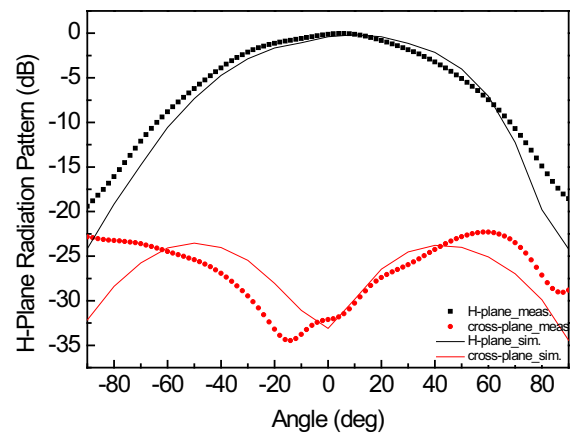


Figure 8: Measured and normalized H -plane radiation pattern of presented AIA.

5. CONCLUSIONS

In this paper, the novel bow-tie shaped meander slot coupled H-shaped patch antenna designed for the 2.4GHz application has been presented. The harmonic termination has been achieved to apply in AIA, which successfully enhance the return loss at the second and third order resonant frequency by modifying the resonant frequency. The stepped width feed line is applied for the bent feed line structure, which the L_T is experimented at the interested resonant frequency. The

harmonic termination level is presented in -20 dB, -1.1 dB, and -2.3 dB, which are associated at fundamental, the second, and the third order frequency, respectively. The peak PAE and the drain efficiency of 66% and 72% for the class-AB power amplifier have been measured at the 2.4 GHz resonant frequency, and the $OP_{1\text{dB}}$ is 1 W. The gain can reach to 11.5 dB. The active integrated antenna has 20.8% bandwidth ranged from 2.14 GHz to 2.64 GHz.

ACKNOWLEDGMENT

The authors would like to thank the Wireless Communication Antenna Research Center for the support. This work is also supported in part by the National Science Council of Taiwan, R.O.C. under Grant NSC98-2221-E-110-032-MY2 and under Grant NSC97-2221-E-110-036-MY3.

REFERENCES

1. Radisic, V., Y. Qian, and T. Itoh, "Novel architectures for high-efficiency amplifiers for wireless applications," *IEEE Trans. on Microwave Theory and Techniques*, Vol. 46, 1901–1909, 1998.
2. Rathi, V., G. Kumar, and K. P. Ray, "Improved coupling for aperture coupled microstrip antennas," *IEEE Trans. on Antennas and Propagation*, Vol. 44, 1196–1198, 1996.
3. Shin, H. S. and N. Kim, "Wideband and high-gain one-patch microstrip antenna coupled with H-shaped aperture," *Electronics Letts.*, Vol. 38, 1072–1073, 2002.
4. Wi, S.-H., J.-M. Kim, and J.-G. Yook, "Microstrip-fed bow-tie-shaped meander slot antenna with compact and broadband characteristics," *Microwave Opt. Tech. Letts.*, Vol. 45, 3, 2005.
5. Wang, H. Y. and M. J. Lancaster, "Aperture-coupled thin-film superconducting meander antennas," *IEEE Trans. on Antennas and Propagation*, Vol. 47, 829–836, 1999.
6. Tsutomu, E., S. Yonehiko, S. Shinichi, and K. Takashi, "Resonant frequency and radiation efficiency of meander line antennas," *Electronics and Communications in Japan*, Vol. 83, 52–58, 2000.
7. Hyungrak, K., H. Kwang Sun, C. Kihun, and Y. Young Joong, "Novel slot antennas for harmonic suppression," *IEEE Microwave and Wireless Components Letts*, Vol. 14, 286–288, 2004.
8. Qin, Y., S. Gao, A. Sambell, E. Korolkiewicz, and M. Elsdon, "Broadband patch antenna with ring slot coupling," *Electronics Letts*, Vol. 40, 5–6, 2004.

Review of 3D EM Modeling and Interpretation Methods for Triaxial Induction and Propagation Resistivity Well Logging Tools

S. Davydycheva¹ and M. A. Frenkel²

¹3DEM Consulting, Texas, USA

²EMGS Americas, Texas, USA

Abstract— The 3D electromagnetic (EM) modeling and inversion techniques for the geological formation evaluation have been experiencing significant progress since the early 90s. There are three main 3D EM numerical techniques: finite-difference (FD), finite element (FE), and integral equation (IE). They have been used for simulating arbitrary 3D media as well as for development of 3D inversion-based interpretation of well log data acquired by the conventional and new-generation logging tools. We present a brief review of these three techniques as to their ability to simulate and interpret the new-generation of triaxial tensor wireline and logging-while-drilling (LWD) measurements. The new EM tools provide full triaxial tensor measurement, in addition to the conventional axial measurement, when the formation is excited by an axial z -directed magnetic dipole transmitter, and the response of axial receivers is analyzed. Due to full 3D sensitivities, the new tools allow significantly enhanced formation resistivity interpretation. We present synthetic logs for four different new-generation tools: both triaxial induction and directional propagation resistivity LWD tools. We also consider new features in the new tool responses and discuss various post-acquisition processing techniques. These approaches allow to better visualize tool responses and enable efficient application of fast stable inversion schemes for resistivity interpretation.

1. INTRODUCTION

At least five new EM logging tools have been introduced in the last decade. In addition to the conventional axial ZZ measurement, they provide triaxial measurements, i.e., XX , XY , XZ , YX , YY , YZ , ZX , and ZY components (notation used: transmitter direction, receiver direction) that allow performing enhanced geological formation interpretation. However, extracting the formation geometry and properties out of the new tool data requires application of advanced 3D modeling and interpretation methods. 3D EM numerical modeling and inversion lately experienced significant progress. Three basic numerical techniques have been known to simulate EM measurements: the finite-difference (FD), the finite element (FE) and the integral equation (IE) methods. These techniques have been successfully applied to 3D modeling and interpretation of conventional resistivity logging [2]. In this paper, we review these techniques based on their ability to handle new-generation triaxial measurements, leaving aside the material related to the conventional EM logging tools.

2. NEW-GENERATION TENSOR RESISTIVITY MEASUREMENTS

In a vertical well with horizontal bedding, there is no coupling between vertical transmitters and transverse receivers and vice versa. Coupling only exists between transmitters and receivers of the same orientation. Any azimuthal asymmetry (dipping beds, dipping anisotropy, fractures, faults, asymmetric invasion zones, etc.) generates cross-terms XY , XZ , YX , YZ , ZX , and ZY .

Two different concepts of triaxial induction measurements have been developed. Fig. 1(a) presents a simplified scheme of single-spacing tool 3DEX, including triaxial transmitter and receivers [16]. This tool is operating at ten frequencies ranging from 20 to 220 kHz. To reduce effects caused by the borehole, the invaded zone, and the tool eccentricity, the Multi-Frequency Focusing (MFF) method was introduced. It is based on calculation of a linear combination of 3DEX data acquired in the main and bucking receivers at two or more frequencies. The processed data can be interpreted using a uniform-medium model [16]. This approach is fast, but it leads to a reduction of the spatial resolution of anisotropy interpretation using 3DEX data.

Spatial resolution of anisotropy interpretation is improved via the application of raw log data inversion. For example, the rapid inversion of 3DEX logs can be used to accurately determine the parameters of both invaded and uncontaminated zones [12]. The rapid inversion method also demonstrates the potential for substantially reducing computing time by partitioning the 2D inverse problem into a sequence of smaller 1D problems, thereby enabling the delivery of interpretation in run times comparable to run times for other familiar well-site deliverables.

To expand the operational range of 3DEX technology for use in wells drilled with very conductive waterbased muds, it was proposed logging 3DEX in combination with a galvanic tool and using 2D/3D inversion-based interpretation procedures [13]. Such an approach enables the determination of the formation resistivity anisotropy using 3DEX in boreholes with diameter ≤ 12 in., muds $R_m \geq 0.02 \Omega\text{m}$, and a relatively deep invasion of up to 18 in.

Another concept implies multi-spacing triaxial measurements. The new tool (RtScanner, Fig. 1(b)) includes six balanced triaxial arrays [9]. This tool’s short spacings allow high spatial resolution, whereas the longer spacings and relatively low frequencies (13 and 27 kHz) enable high depth of investigation. Data symmetrization and rotation techniques allow separation of the borehole effect from the effects of dipping bed boundaries and the formation anisotropy, resulting in enhanced sensitivity to wanted formation properties [6]. Separation of the invasion zone effect from the formation response requires full 3D inversion [1].

New-generation LWD propagation resistivity measurements used for geo-steering purposes are also based on the multi-frequency, multi-spacing tilted [5, 15] or transverse [11] antenna concept. These tools take advantage of the tool rotation, providing directional measurement — as a ratio (or attenuation and phase shift) of the voltages measured at two positions of the tilted or transverse antenna, up and down. Such a measurement provides high sensitivity to dipping anisotropy, dipping bed boundaries and other azimuthal asymmetries. Transmitters’ and receivers’ configurations of two directional LWD tools, Azimuthal Deep-reading Resistivity (ADR [5]) and PeriScope [15], are depicted in Figs. 1(b) and 1(c), respectively. A detailed review of these tools is given in [21]. Full 2D or 3D inversions of directional resistivity LWD measurements are not yet common. Instead, the trial-and-error forward modeling is used to interpret 2D or 3D data [15].

3. NUMERICAL MODELING METHODS: FE, FD AND IE

In FD and FE approaches, Maxwell’s differential equations with respect to the EM field (or its potentials) are discretized on a FD or FE mesh or grid. This leads to the resulting system of linear equations with respect to the approximate EM field/potentials, which is typically solved iteratively. The grid cells in the FD approach (which is nothing but a particular case of the FE approach) are typically conformal to the coordinate system; in Cartesian coordinates the grid boxes are rectangular blocks. This allows for relative simplicity of the FD numerical implementation. In the FE approach the grid elements may have almost arbitrary shapes (prisms, tetrahedrons, etc.). This apparent flexibility allows modeling non-trivial shapes, but it is counterbalanced by a nontrivial and usually time-consuming construction of the finite elements themselves. This is why the FD method is used more commonly than the FE method.

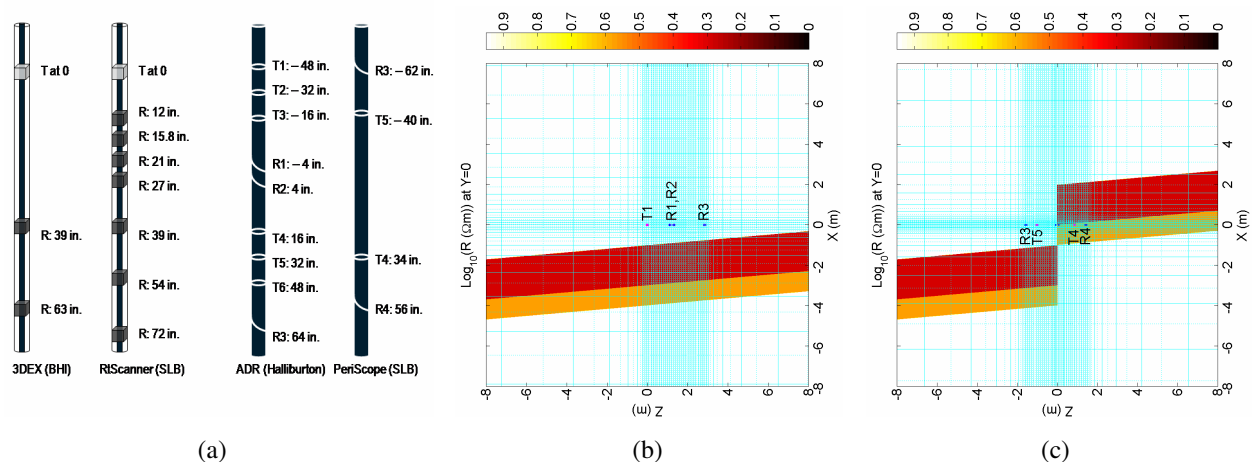


Figure 1: (a) Configuration of transmitters and receivers in two triaxial induction and two directional LWD resistivity tools (only long spacings of PeriScope are shown); (b) 1D, (c) 2D FD models of the tools and the geological formation; the tool trajectory coincides with z -axis; transmitters and receivers are shown: (b) ADR; (c) PeriScope; the solid/dotted cyan lines depict primary/dual Lebedev subgrids.

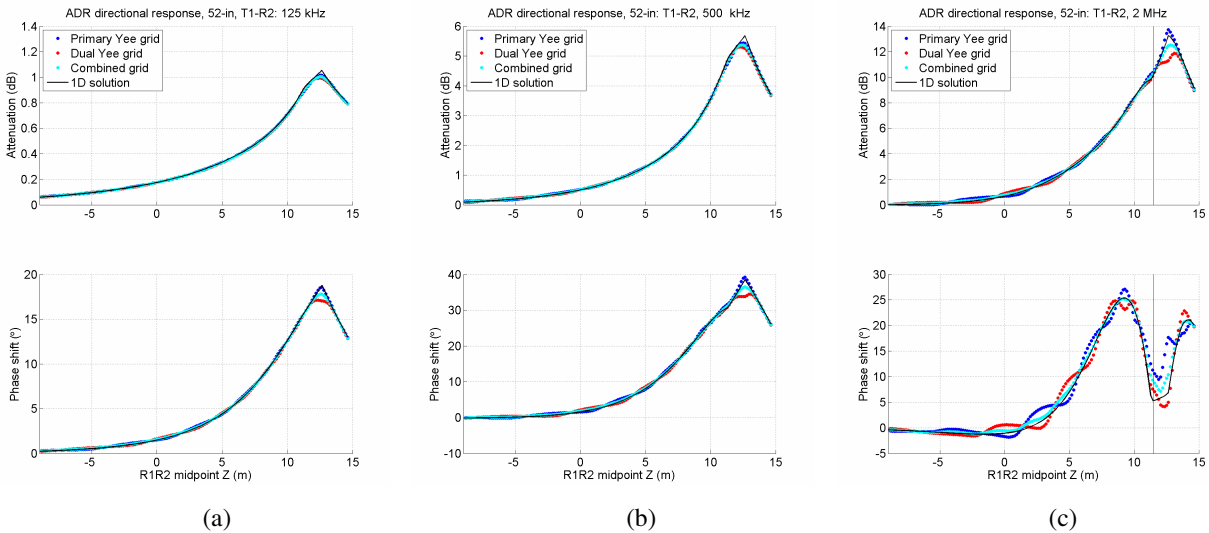


Figure 2: ADR synthetic response to the 85° -dipping layered 1D formation: (a) 125-kHz, (b) 500-kHz and (c) 2-MHz directional response of T1-R2 pair. A thin vertical line signifies the bed boundary.

3.1. The FD Method

Most FD software developers use the so-called staggered Yee FD grid (named after Yee, who introduced it in 1966), which was initially designed for isotropic media. The different components of the FD electric field and of the FD current density are determined at different edges of the grid boxes, and the different components of the FD magnetic field — at different faces of the grid boxes. Such a grid produces coercive approximation i.e. the current conservation law is satisfied. However, such a staggered grid does not easily allow applying the general anisotropic Ohm’s law, $\mathbf{J} = \boldsymbol{\sigma}\mathbf{E}$, with arbitrary non-diagonal conductivity tensor $\boldsymbol{\sigma}$ connecting all components of the current density \mathbf{J} and the electric field \mathbf{E} taken at the same spatial points. Recently, many authors have extended the Yee approach to arbitrary anisotropic media (see [19, 20, 14] among others). They use interpolation to obtain the different components of \mathbf{J} and \mathbf{E} at the same spatial points. This may lead to a loss of the current conservation property and, in the presence of the arbitrary dipping anisotropy, to the appearance of “parasitic” currents on the FD grid that may significantly reduce the accuracy of the FD scheme. When applying straightforward interpolation, the ingoing and outgoing grid currents (in those grid cells where the anisotropy tensor is non-diagonal) may not be equal anymore, since the differential identities $\mathbf{curl\ grad} \equiv 0$ and $\mathbf{div\ curl} \equiv 0$ may be broken for the interpolated fields on the FD grid. Circumventing this difficulty requires special efforts. This may result in inefficiently dense and large FD grids.

Another approach to handle the arbitrary dipping anisotropy on the FD grid is the so-called Lebedev grid [7, 8]. It includes a combination of two (in the 2D case) or four (in the 3D case) subgrids—Yee grids shifted in space with respect to each other so that all the components of the electric field E_x , E_y and E_z , and the electric current density, J_x , J_y and J_z are determined at the same spatial nodes. The Lebedev grid provides the current conservation property automatically and allows simple implementation of the anisotropic Ohm’s law. Moreover, even in trivial isotropic media the Lebedev grid demonstrates the FD error cancellation property at medium interfaces and at grid domain boundaries, which allows for a reduced grid domain size and density compared to the standard Yee grid.

We illustrate this statement on an example of synthetic directional ADR response. Fig. 1(b) depicts a vertical cross-section of 1D 85° -dipping layered medium. We consider the synthetic ADR tool “moving” through this medium: from the isotropic $10\text{-}\Omega\text{m}$ bed into the more conductive 2-m thick anisotropic bed having horizontal and vertical resistivities $R_h = 1$ and $R_v = 2\text{ }\Omega\text{m}$, respectively. Since the conductive bed approaches the tool from below, its directional response is positive, smoothly elevating from 0 at a distance from the boundary, reaching a maximum value when the tool intersects the boundary, and then decreasing (a general rule: the directional response is positive when intersecting a dipping resistive/conductive bed boundary with a positive dip in xz -plane). Colored symbols show numerical FD modeling on the FD grid. It becomes evident that

the standard Yee grid (blue and red symbols) hardly allows accurate modeling of the directional tool response, especially at higher frequencies. Both primary and dual Yee subgrids generate strong oscillating errors due to fictitious “reflections” from the grid cell walls. Grid refining would be the only way to suppress these errors on the standard Yee. When using the Lebedev grid the errors mostly cancel. Thus, the fictitious “reflections” make the computational cost of the conventional Yee grid approach not very efficient for modeling the cross-terms, especially at higher frequencies or on targets with complex non-conformal geometries and large contrasts in conductivities. On the contrary, the Lebedev grid allows handling complex 3D geometries on a relatively coarse FD grid.

The described FD scheme allows handling both frequency- and time-domain EM problems. The solution of the scheme can be obtained using various iterative solvers. Moreover, the Spectral Lanczos Decomposition Method (SLDM) [7, 10] allows computing multi-spacing and multi-frequency (or multi-time) responses in one run, practically at the cost of a single spacing and a single frequency (or a single time moment). The CPU time for this test was 30 seconds per logging point on a 2-GHz laptop; all three frequency responses were computed simultaneously using the SLDM solver.

3.2. The FE Method

has also been proven to be capable at modeling the new-generation tool responses to complex 3D formations [4, 15, 18]. The FE method is believed to account for geometry more accurately than the FD method. Flexibility of the finite elements allows including complex tool and formation geometry into the model. In general, the FE method may be more capable than the FD method if complex tool details need to be accounted for, including insulators and metal parts having very high contrast in conductivity. When using the FE method, building simple model-independent rectangular grids is not practical. Due to complicated and model-dependent grid construction and large resulting FE grids, the FE method requires at least several minutes per logging point to model the new-generation resistivity logging tools. Because of this, the FE method can hardly be used for fast 3D inversion as a forward engine. On the contrary, the FD method with its simple model-independent gridding is typically faster and so more suitable for 3D inversion: FD modeling, when used as a forward engine for the 3D inversion of new-generation triaxial measurements, takes seconds per logging point [17]. A comparison of the FE versus the FD method for RtScanner response to a borehole drilled through a dipping anisotropic space is presented in [7]. The two methods agree within 1–3%.

3.3. The IE Method

Unlike FE and FD methods, which require a large volume of the medium to be discretized, the IE method allows only discretization of an anomalous body: for example, the borehole and invasion zones around it. This reduces the size of the resulting system of linear equations dramatically. However, accurate computation of the Green functions of the background medium needed for the discretization (for example, of the layered anisotropic space) is a tedious and nontrivial problem itself. This imposes restrictions on the complexity of the background model: for example, only a moderate number of beds can be included. This is why the IE method is not very common for the resistivity logging applications. A review of the IE method applications based on research and publications by D. Avdeev, V. Dmitriev, B. Singer, M. Zhdanov and other authors can be found in [2]. An example of application of the IE method to model XX , YY and ZZ responses of a generic triaxial tool for the case of a borehole drilled through a homogeneous dipping anisotropic medium is given in [3]. No cross-component measurement simulations using IE method have been reported.

4. MODELING PRACTICAL EM TOOL RESPONSES

Figure 3 depicts PeriScope (a) and ADR ((b), (c)) synthetic directional logs through the fault zone (Fig. 1(c)). PeriScope’s 96-inch 400-kHz directional measurements “see” the approaching fault at ~ 2 – 3 m from the fault line: at such a distance a clear difference between the 1D solution (lines) without the fault (as in Fig. 1(b)) and 3D solution (dots) for the faulted model (Fig. 1(c)) can be observed. Obviously, in the framework of the 1D modeling/inversion scheme the fault effect could easily be misinterpreted. Indeed, the tool response becomes non-trivial when approaching the fault line: first T5-R4 (black dots) attenuation undergoes some increase, and then, at ~ 1 – 1.5 m from the fault line, a sharp decrease and sign change due to the fault happens.

For geo-steering purposes, this may be too late to alert the driller and to change the tool trajectory in time. Thus, drilling stop and more careful interpretation (for example, running a full 3D inversion scheme) would be necessary for reliable prediction of the approaching fault. Fast

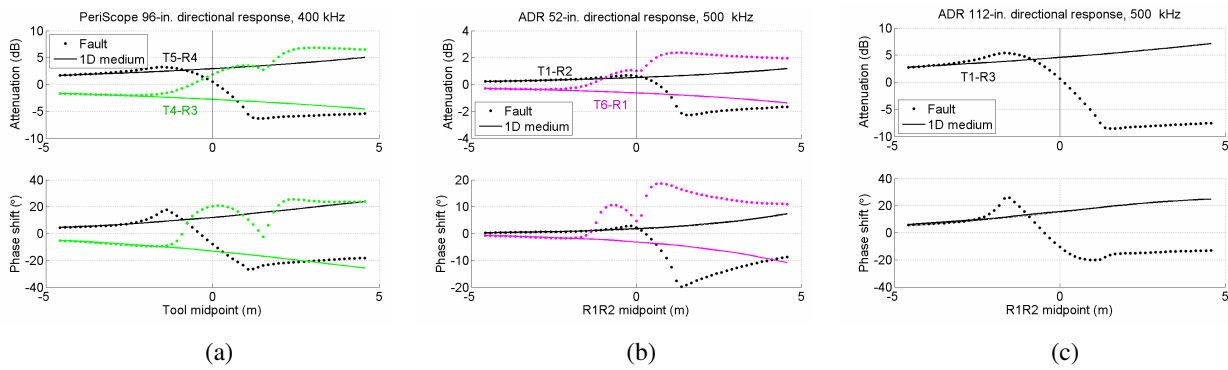


Figure 3: (a) PeriScope and (b)–(c) ADR synthetic directional logs through fault line (thin vertical line).

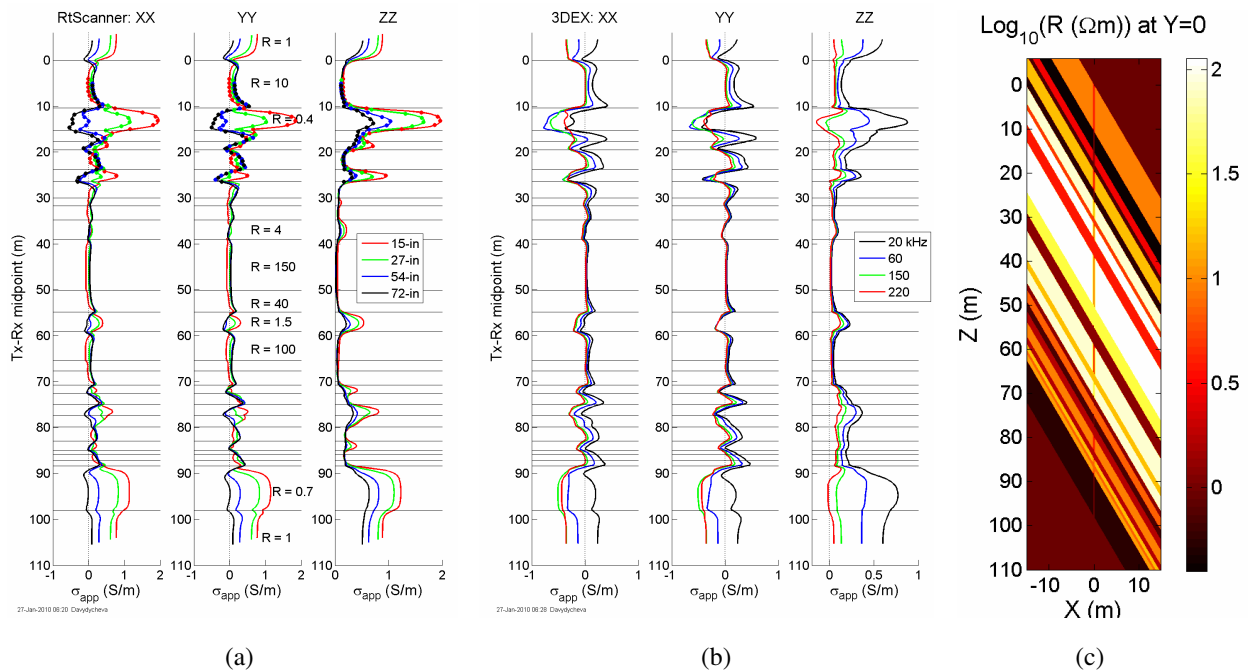


Figure 4: (a) RtScanner and (b) 3DEX responses to invaded isotropic Oklahoma formation model with (c) a 60° -dipping borehole. Circles in (a): FD modeling in cylindrical coordinates; lines: Cartesian FD modeling.

running numerical models for various possible scenarios (in advance or while drilling) could be helpful. The ADR 52-inch directional measurement “sees” the approaching fault at ~ 2 m from the fault line (T6-R1 coupling, magenta dots). The other 52-inch coupling (T1-R2, black dots) “sees” the fault only in its close vicinity, since the T1-R2 midpoint is situated significantly closer to the up-hole end of the tool than the T6-R1 midpoint. The ADR longest 112-inch directional measurement, T1-R3, “sees” the approaching fault at ~ 3 m from the fault line. But since this pair has no transmitter-receiver pair counterpart with equal spacing, unlike 52-inch pairs T1-R6 and T2-R1, this array data do not allow symmetrisation and may have a restricted application (being affected by the electronic temperature drift, borehole, eccentricity effects, etc.).

Figure 4 shows RtScanner (a) and 3DEX (b) synthetic responses to a FD model of invaded dipping Oklahoma formation (c). The borehole resistivity is $1 \Omega\text{m}$, its radius is 0.127 m, and the radii of the invasion zones are 0.3048 m. This Oklahoma benchmark formation is considered one of the most challenging to model and handle even with conventional logging tools. Conventional ZZ-coupling of RtScanner does allow resolving all the beds whose thickness is greater than 1.5 – 2 m (the tool vertical resolution). It allows some visual interpretation, which would be very challenging for the transverse XX- and YY-couplings due to the multiple horns at the bed boundaries and sometimes negative readings of the apparent conductivity. 3DEX, whose single spacing is relatively long (1.6 m), has lower spatial resolution. Its unprocessed responses generally do not allow any

simple visual interpretation. The cross-coil responses of the both tools will be shown during the presentation.

5. CONCLUSIONS

A review of three different numerical techniques for modeling new-generation resistivity measurements was given. The new EM tools provide a full triaxial tensor measurement, which allows significantly enhanced formation evaluation. Their complex 3D sensitivities open the possibilities for interpreting complex 3D structures. Fast and reliable 3D modeling is the key to evaluating the new measurements, to exploring their full potential, and to further development of new interpretation techniques. Accurate and easy-to-use 3D modeling numerical techniques are capable of modeling and handling the new tool responses in complex 3D scenarios.

REFERENCES

1. Abubakar A., T. M. Habashy, V. Druskin, L. Knizhnerman, and S. Davydycheva, "A 3D parametric inversion algorithm for triaxial induction data," *Geophysics*, Vol. 71, No. 1, G1–G9, 2006.
2. Avdeev, D., "Three-dimensional electromagnetic modeling and inversion from theory to application," *Survey in Geophysics*, Vol. 26, 767–799, 2005.
3. Avdeev, D. and S. Knizhnik, "3D integral equation method with a linear dependence on dimensions," *Geophysics*, Vol. 74, No. 5, F89–F94, 2009.
4. Bachinger, F., U. Langer, and J. Schöberl, "Efficient solvers for nonlinear time-periodic eddy current problem," *Computing and Visualization in Science*, Vol. 9, No. 4, 197–207, 2006.
5. Bittar, M., J. Klein., R. Beste, G. Hu, M. Wu, J. Pitcher, G. Golla, G. Althoff, M. Sitka, V. Minosyam, and M. Paulk, "A new azimuthal deep-reading resistivity tool for geosteering and advanced formation evaluation," *Proceedings of SPE ATC*, Paper #09971, 2007.
6. Davydycheva, S., "Separation of azimuthal effects for new-generation resistivity logging tools — Part I," *Geophysics*, Vol. 75, No. 1, E31–E40, 2010.
7. Davydycheva, S. and V. Druskin, "Staggered grid for Maxwell's equations in arbitrary 3-D inhomogeneous anisotropic media," *Three-Dimensional Electromagnetics*, M. Oristaglio and B. Spies, Eds., 119–137, SEG, 1999.
8. Davydycheva, S., V. Druskin, and T. Habashy, "An efficient finite-difference scheme for electromagnetic logging in 3D anisotropic inhomogeneous media," *Geophysics*, Vol. 68, 1525–1536, 2003.
9. Davydycheva, S., D. Homan, and G. Minerbo, "Triaxial induction tool with electrode sleeve. FD modeling in 3D geometries," *J. Appl. Geophys.*, Vol. 67, No. 1, 98–108, 2009.
10. Druskin, V. and L. Knizhnerman, "Spectral approach to solving three-dimensional Maxwell's equations in the time and frequency domains," *Radio Science*, Vol. 29, 937–953, 1994.
11. Fang, S., A. Merchant, E. Hart, and A. Kirkwood, "Determination of structural dip and azimuth from LWD azimuthal propagation resistivity measurements in anisotropic formations," *Proceedings of SPE ATC*, SPE paper #116123, 2008.
12. Frenkel, M. A., "Well-site resistivity anisotropy interpretation: a 2-D method and a case study from the Gulf of Mexico," *Proceedings of SPE ATC*, SPE paper #77793, 2002.
13. Frenkel, M. A. and I. M. Geldmacher, "Method for resistivity anisotropy determination in conductive borehole environments," US Patent 6, 925, 384, 2005.
14. Hou, J., R. K. Mallan, and C. Torres-Verdin, "Finite-difference simulation of borehole EM measurements in 3D anisotropic media using coupled scalar-vector potentials," *Geophysics*, Vol. 71, No. 5, G225–G233, 2006.
15. Omeragic, D., T. Habashy, Y.-H. Chen, V. Polyakov, C. Kuo, R. Altman, D. Hupp, and C. Maeso, "Reservoir characterization and well placement in complex scenarios using LWD directional EM measurements," *Petrophysics*, Vol. 50, No. 5, 396–415, 2009.
16. Rabinovich, M., L. Tabarovsky, B. Corley, J. van der Horst, and M. Epov, "Processing multi-component induction data for formation dips and anisotropy," *Petrophysics*, Vol. 47, No. 6, 506–526, 2006.
17. Wang, H., S. Davydycheva, J. Zhou, M. Frey, T. Barber, A. Abubakar, and T. Habashy, "Sensitivity study and inversion of the fully-triaxial induction logging in cross-bedded anisotropic formation," SEG paper, 2008.

18. Wang, H., P. Wu, R. Rosthal, G. Minerbo, and T. Barber, “Modeling and understanding the triaxial induction logging in borehole environment with dip anisotropic formation,” SEG paper, 2008b.
19. Wang, T. and S. Fang, “3D electromagnetic anisotropy modeling using finite differences,” *Geophysics*, Vol. 66, 1386–1398, 2001.
20. Weiss, C. J. and G. A. Newman, “Electromagnetic induction in a fully 3D anisotropic earth,” *Geophysics*, Vol. 67, 1104–1114, 2002.
21. Zhang, Z., C. Gonguet, V. Rajani, and R. Roeterding, “Directional LWD resistivity tool and their business impacts,” *Proceedings of 49th Annual Logging Symposium (SPWLA)*, Edinburg, 2008.

Nitsche-type Mortaring for Maxwell’s Equations

K. Hollaus¹, D. Feldengut¹, J. Schöberl², M. Wabro³, and D. Omeragic⁴

¹RWTH Aachen University, Germany

²Vienna University of Technology, Austria

³CST AG, Germany

⁴Schlumberger-Doll Research, USA

Abstract— We propose a new method for treating transmission conditions on non-matching meshes. The basic method is a hybrid version of Nitsche’s method. By introducing a scalar potential on the interface we obtain a robust method for the low frequency limit. In order to simplify numerical integration, we use smooth B-spline basis functions on the interface. We present the formulation for scalar potential problems and for time-harmonic Maxwell’s equations. A simple well logging example is used to benchmark the algorithm.

1. INTRODUCTION

The finite element modeling can often be simplified by allowing independent meshes for different parts. Typical examples are rotating parts in electric machines, or a logging while drilling (LWD) tool moving through the bore-hole. The difficulty is an accurate discretization of the transmission conditions on the interface. Since interpolation methods lose accuracy, mortar methods became popular in recent years [3, 11]. Here, the continuity of the primal field is enforced by an additional equation, and a Lagrange parameter at the interface must be added. The resulting linear system has saddle point structure. In theory, it is tricky to prove stability, and finite element spaces must be chosen carefully. In practice, it’s non-trivial to implement the numerical integration over nonmatching meshes, in particular for 3D applications. The Nitsche method is an alternative to the mortar method. Here, no additional Lagrange parameter comes in, and the saddle point problem can be avoided [2, 8]. The price to pay are additional boundary terms in the variational formulation. We choose a hybrid formulation with additional variables at the interface as in [6]. We propose to use smooth B-spline basis functions on the interface to simplify numerical integration.

2. THE POISSON EQUATION

We decompose the domain Ω into non-overlapping sub-domains Ω_1 and Ω_2 , and call the common interface γ . For introducing the method, we start with the Dirichlet problem for the Poisson equation

$$\begin{aligned} -\Delta u &= f && \text{in } \Omega_1 \cup \Omega_2, \\ u &= 0 && \text{on } \partial\Omega, \end{aligned}$$

and the transmission conditions

$$u|_{\Omega_1} = u|_{\Omega_2}, \tag{1}$$

$$\frac{\partial u}{\partial n_1}|_{\Omega_1} = \frac{\partial u}{\partial n_2}|_{\Omega_2} \quad \text{on } \gamma. \tag{2}$$

The idea of the Nitsche method is to multiply by test-functions v , and integrate by parts on the sub-domains:

$$\int_{\Omega_i} \nabla u \cdot \nabla v - \int_{\partial\Omega_i} \frac{\partial u}{\partial n} v = \int_{\Omega_i} f v \quad \text{for } i \in \{1, 2\}$$

Next, we introduce an additional independent variable λ on the interface, which shall be the restriction of $u_1 = u_2$ on the interface. We define the function spaces

$$\begin{aligned} V &:= \{v \in H^1(\Omega_1) \times H^1(\Omega_2) : v = 0 \quad \text{on } \partial\Omega\}, \\ W &:= \{\mu \in L_2(\partial\Omega_1 \cup \partial\Omega_2) : \mu = 0 \quad \text{on } \partial\Omega\}. \end{aligned}$$

Note that functions form V are piece-wise in H^1 , but may be discontinuous across the interface. Functions in W are single-valued on the interface. The solution (u, λ) satisfies the variational equation: find $u \in V$ and $\lambda \in W$ such that

$$\sum_{i=1}^2 \left\{ \int_{\Omega_i} \nabla u \cdot \nabla v - \int_{\partial\Omega_i} \frac{\partial u}{\partial n} (v - \mu) - \int_{\partial\Omega_i} \frac{\partial v}{\partial n} (u - \lambda) + \frac{\alpha p^2}{h} \int_{\partial\Omega_i} (u - \lambda)(v - \mu) \right\} = \int_{\Omega} f v$$

for $v \in V$ and $\mu \in W$. For the true solution the terms involving $\mu - \lambda$ vanish. Furthermore, $\sum_i \int_{\partial\Omega_i} \frac{\partial u}{\partial n} \mu$ cancel due to the transmission condition (2) and the essential boundary condition on the test function μ .

The left hand side defines the bilinear-form $A(., .)$, which depends on the chosen finite element space. Here, p denotes the polynomial degree, and h is the mesh size. The parameter α must be chosen sufficiently large, and is typically set as $\alpha = 10$. The bilinear-form is symmetric and coercive with respect to the norm defined by

$$|||(u, \lambda)|||^2 = \sum_{i=1}^2 \left\{ \|\nabla u\|_{\Omega_i}^2 + \frac{p^2}{h} \|u - \lambda\|_{\partial\Omega_i}^2 \right\}.$$

The key to prove coercivity is to bound the mixed term by the diagonal terms, i.e., the inequality

$$\sum_{i=1}^2 \int_{\partial\Omega_i} \frac{\partial u}{\partial n} (v - \mu) \leq c(|||(u, \lambda)|||^2 + |||(v, \mu)|||^2)$$

on the finite element space. This is standard in discontinuous Galerkin methods [1].

The formulation allows to use independent meshes in both sub-domains, and another discrete space on the interface. It requires to integrate basis functions on the boundary of the domain meshes against basis functions defined on an interface mesh. Gauss integration rules are exact for piecewise polynomials on the mesh, but converge very slowly if the interface functions are not smooth or even not continuous. Then an intersection mesh should be used. But, this is difficult to generate, in particular for curved 3D domains. We propose a different strategy: Since the interface domain is often simple, e.g., a cylinder, we can use a structured mesh and high order B-spline basis functions [5]. The use of Gauss integration on the boundary mesh is not exact, but still of high order for the smooth basis functions on the interface.

3. MAXWELL'S EQUATIONS

We consider the time harmonic Maxwell's equations in vector potential formulation

$$\text{curl } \mu^{-1} \text{curl } u + \kappa u = j \quad \text{in } \Omega_i, \tag{3}$$

with $\kappa = i\omega\sigma - \omega^2\epsilon$, and

$$E = -i\omega u, \quad H = \mu^{-1} \text{curl } u.$$

The transmission conditions for the tangential components of the electric and magnetic field are

$$\begin{aligned} u_1 \times n_1 &= -u_2 \times n_2, \\ \mu_1^{-1} \text{curl } u_1 \times n_1 &= -\mu_2^{-1} \text{curl } u_2 \times n_2. \end{aligned}$$

Proceeding as in the scalar case, one obtains

$$\int_{\Omega_i} \{ \mu^{-1} \text{curl } u \cdot \text{curl } v + \kappa u \cdot v \} + \int_{\partial\Omega_i} \mu^{-1} \text{curl } u \cdot (v \times n) \int_{\Omega_i} j \cdot v \tag{4}$$

and the variational formulation: find (u, λ) such that

$$\begin{aligned} &\sum_{i=1}^2 \left\{ \int_{\Omega_i} \mu^{-1} \{ \text{curl } u \cdot \text{curl } v + \kappa u \cdot v \} + \int_{\partial\Omega_i} \mu^{-1} \text{curl } u \cdot [(v - \mu) \times n] \right. \\ &\left. + \int_{\partial\Omega_i} \mu^{-1} \text{curl } v \cdot [(v - \lambda) \times n] + \frac{\alpha p^2}{\mu h} \int_{\partial\Omega_i} [(v - \lambda) \times n] \cdot [(v - \mu) \times n] \right\} = \int_{\Omega} j \cdot v, \end{aligned}$$

where $u, v \in H(\text{curl}, \Omega_1) \times H(\text{curl}, \Omega_2)$, and λ, μ are tangential vector valued fields on the interface. For simplification let us assume $\kappa \in \mathbb{R}^+$ and small. Then, the bilinear-form is coercive with respect to the norm

$$\| (u, \lambda) \|^2 = \sum_{i=1}^2 \left\{ \mu^{-1} \|\text{curl } u\|_{\Omega_i}^2 + \kappa \|u\|_{\Omega_i}^2 + \frac{p^2}{\mu h} \|(u - \lambda) \times n\|_{\partial\Omega_i}^2 \right\}.$$

An important point for discretizing low frequency problems with small κ is to treat the gradient sub-space. Let $u = \nabla\phi$; the energy norm of u should scale as

$$\|u\|^2 = \mu^{-1} \|\text{curl } u\|^2 + \kappa \|u\|^2 = \kappa \|\nabla\phi\|^2 = O(\kappa).$$

But, the penalty term $\|(u - \lambda) \times n\|$ scales like $O(1)$ and thus is an over-penalization for gradient fields. The goal is now to modify the formulation to have separate penalization terms for gradient and rotational components.

First, we derive a relation for scalar test functions on the boundary. Set $v = \nabla\psi$ in (4) and obtain

$$\int_{\Omega_i} \kappa u \cdot \nabla\psi = \int_{\partial\Omega_i} \mu^{-1} \text{curl } u \cdot (\nabla\psi \times n) = \int_{\Omega} j \cdot \nabla\psi. \tag{5}$$

Apply the div operator on the sub-domains Ω_i to Equation (3), and test by ψ to obtain

$$\int_{\Omega_i} \text{div}(\kappa u)\psi = \int_{\Omega_i} \text{div } j\psi.$$

Integration by parts on the sub-domains leads to

$$-\int_{\Omega_i} \kappa u \cdot \nabla\psi + \int_{\partial\Omega_i} \kappa u_n \psi = -\int_{\Omega_i} j \cdot \nabla\psi + \int_{\partial\Omega_i} j_n \psi \tag{6}$$

Adding Equations (5) and (6) we obtain

$$\sum_{i=1}^2 \left\{ \int_{\partial\Omega_i} \mu^{-1} \text{curl } u \cdot (\nabla\psi \times n) + \int_{\partial\Omega_i} \kappa u_n \psi \right\} = \sum_{i=1}^2 \int_{\partial\Omega_i} j_n \psi \tag{7}$$

Note that ψ is evaluated only on the boundary of the sub-domains Ω_i , and thus it is enough to define ψ only on the boundary.

We introduce a new scalar field variable $\phi_\gamma \in W$ on the interface, which shall be the scalar potential of a Helmholtz-type decomposition of u on the interface. We set $\phi_i = \phi_\gamma|_{\partial\Omega_i}$ on the sub-domain boundaries. Instead of posing continuity for $u \times n$, we pose it for $(u - \nabla\phi) \times n$ and ϕ separately. This allows different scalings for the gradient part and the rotational part. In a first step, we redefine the interface vector variable as the rotational part, i.e., $\lambda \times n = (u - \nabla\phi) \times n$, and add a penalty term also for $\phi = \phi_\gamma$:

$$\begin{aligned} & \sum_{i=1}^2 \left\{ \int_{\Omega_i} \{ \mu^{-1} \text{curl } u \cdot \text{curl } v + \kappa uv \} + \int_{\partial\Omega_i} \mu^{-1} \text{curl } u [(v - \mu) \times n] + \int_{\partial\Omega_i} \mu^{-1} \text{curl } v [(u - \nabla\phi - \lambda) \times n] \right. \\ & \left. + \frac{\alpha p^2}{\mu h} \int_{\partial\Omega_i} [(u - \nabla\phi - \lambda) \times n][(v - \nabla\psi - \mu) \times n] + \frac{\alpha p^2}{h} \int_{\partial\Omega_i} \kappa(\phi - \phi_\gamma)(\psi - \psi_\gamma) \right\} = \int_{\Omega} jv \end{aligned}$$

The skew terms do not lead to a symmetric bilinear-form. Now, we subtract relation (7), and use $\kappa u_n - j_n$ continuous following from the transmission conditions to obtain

$$\begin{aligned} & \sum_{i=1}^2 \left\{ \int_{\Omega_i} \{ \mu^{-1} \text{curl } u \cdot \text{curl } v + \kappa uv \} + \int_{\partial\Omega_i} \mu^{-1} \text{curl } u [(v - \nabla\psi - \mu) \times n] + \int_{\partial\Omega_i} \mu^{-1} \text{curl } v [(u - \nabla\phi - \lambda) \times n] \right. \\ & \left. + \frac{\alpha p^2}{\mu h} \int_{\partial\Omega_i} [(u - \nabla\phi - \lambda) \times n][(v - \nabla\psi - \mu) \times n] - \int_{\partial\Omega_i} \kappa u_n (\psi - \psi_\gamma) - \int_{\partial\Omega_i} \kappa u_n (\phi - \phi_\gamma) \right. \\ & \left. + \frac{\alpha p^2}{h} \int_{\partial\Omega_i} \kappa(\phi - \phi_\gamma)(\psi - \psi_\gamma) \right\} = \sum_{i=1}^2 \left\{ \int_{\Omega_i} jv - \int_{\partial\Omega_i} j_n \psi \right\} \end{aligned}$$

As in the scalar case, one can easily show coercivity on the finite element space with respect to the semi-norm

$$\| (u, \lambda, \phi, \phi_\gamma) \|^2 := \sum_{i=1}^2 \left\{ \mu^{-1} \|\operatorname{curl} u\|_{\Omega_i}^2 + \kappa \|u\|_{\Omega_i}^2 + \frac{p^2}{\mu h} \|(u - \nabla \phi - \lambda) \times n\|_{\partial \Omega_i}^2 + \frac{\kappa p^2}{h} \|\phi - \phi_\gamma\|_{\partial \Omega_i}^2 \right\}.$$

Now, the penalization of the gradient field ϕ is of order κ , and only the rotational part $u - \nabla \phi$ is penalized of order 1.

We propose to discretize u by Nedelec finite elements [7] of order p , ϕ by continuous, scalar finite elements of order $p + 1$ on $\partial \Omega_i$, ϕ_γ by tensor product B-splines of order m , and λ by Nedelec-type B-splines satisfying an exact sequence [4]. The full finite element error analysis will be given in a subsequent paper.

4. A NUMERICAL EXAMPLE

To demonstrate the feasibility of the proposed method the simplified logging-while-drilling (LWD) tool shown in Fig. 1 has been analyzed numerically. Two identical conducting loops, i.e., a sending and a receiving antenna, represent the sensor. In general several finite element meshes might be created of both the sensor and the surrounding mud and formation to simulate the LWD tool in use. The present formulation avoids repeated complete modeling of all domains by means of separate non matching meshes which can be merged together with the Nitsche method.

Although the geometry of the problem is rotational symmetric, the problem was modeled in 3D. All dimensions are given in inches. The transmitter-receiver spacing is 46", and the operating frequency ranges from 20 kHz to 2.0 MHz. The electric conductivities of the tool body, the borehole mud and the formation have been selected with $1.0 \cdot 10^6$ S/m, 1.0 S/m and 0.01 S/m, respectively. A relative electric permittivity of $\epsilon_r = 26.67$ for 2 MHz has been considered for the borehole mud and the formation. The relative electric permittivity was determined with $\epsilon_r = 38.63$ for 400 kHz and all smaller frequencies. The relative permeability was chosen with $\mu_r = 1.0$ throughout the problem region. Due to the high conductivity of the tool body, it has been eliminated in the model by using a proper surface impedance boundary condition. The transmitter is excited by an electric current of 1.0 A, and the induced voltage in the receiver is computed.

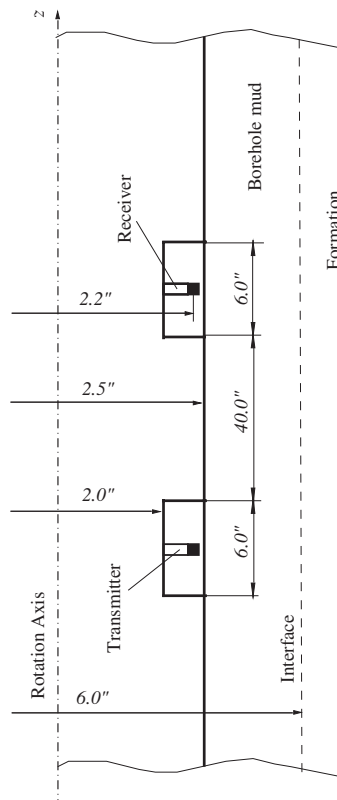


Figure 1: Sketch of a two-coil LWD tool used to benchmark the method.

For that, we have performed computations with first and second order Nédélec elements of the second type, see Table 1 and Table 2. Once we used a standard method with a conforming mesh across the interface. Then we used the proposed Nitsche method, with 5 B-splines of order 5 in azimuthal direction, and 150 B-splines of order 5 in axial direction. We can observe that the difference between the standard method and the Nitsche method is much less than the difference between first and second order elements. We conclude that the error due to the proposed Nitsche method is small for LWD tool simulations of this type.

Table 1: Numerical results for first order elements.

frequency [kHz]	standard, rec volt [nV] 185 810 dofs	Nitsche, rec volt [nV] 195 383 dofs
20	25.44 – i 18.38	25.43 – i 18.37
100	71.68 – i 197.5	71.65 – i 197.3
400	124.9 – i 963.0	124.9 – i 962.3
2000	–635.9 – i 5295	–634.8 – i 5255

Table 2: Numerical results for second order elements.

frequency [kHz]	standard, rec volt [nV] 733 881 dofs	Nitsche, rec volt [nV] 736 939 dofs
20	24.99 – i 18.47	24.98 – i 18.47
100	70.25 – i 196.7	70.23 – i 196.7
400	121.7 – i 957.9	121.7 – i 957.7
2000	–648.1 – i 5256	–647.9 – i 5255

5. CONCLUSION

We have developed domain decomposition techniques based on Nitsche’s method to discretize transmission conditions on non-matching meshes. Due to the use of a scalar potential on the interface, the method is robust at low frequencies. The algorithm was tested on a simple well logging application, where independent meshes for the tool-borehole volume and the formation were used.

ACKNOWLEDGMENT

The first three authors would like to thank Schlumberger Technology corporation for financial support of this work. The authors are especially grateful to colleagues in Schlumberger Research and Technology Centers for their help and many useful discussion and suggestions during the course of this work.

REFERENCES

1. Arnold, D. N., F. Brezzi, B. Cockburn, and D. Marini, “Unified analysis of discontinuous Galerkin methods for elliptic problems,” *SIAM J. Numer. Anal.*, Vol. 39, No. 5, 1749–1779, 2002.
2. Becker, R., P. Hansbo, and R. Stenberg, “A finite element method for domain decomposition with non-matching grids,” *M2AN Math. Model. Numer. Anal.*, Vol. 37, No. 2, 209–225, 2003.
3. Ben Belgacem, F., A. Buffa, and Y. Maday, “The mortar finite element method for 3D Maxwell equations: First results,” *SIAM J. Numer. Anal.*, Vol. 39, No. 3, 880–901, 2001.
4. Buffa, A., G. Sangalli, and R. Vazquez, “Isogeometric analysis in electromagnetics: B-splines approximation,” *Comput. Methods Appl. Mech. Engrg.*, doi:10.1016/j.cma.2009.12.002, 2009.
5. De Boor, C., *A Practical Guide to Splines*, Revised Edition, Springer-Verlag, New York, 2001.
6. Egger, H., “A class of hybrid mortar finite element methods for interface problems with non-matching meshes,” Preprint AICES-2009-2, Aachen Institute for Advanced Study in Computational Engineering Science, 2009.
7. Nédélec, J.-C., “A new family of mixed finite elements in \mathbb{R}^3 ,” *Numer. Math.*, Vol. 50, No. 1, 57–81, 1986.

8. Nitsche, J., “Über ein Variationsprinzip zur Lösung von Dirichlet-Problemen bei Verwendung von Teilräumen, die keinen Randbedingungen unterworfen sind,” *Abh. Math. Sem. Univ. Hamburg*, Vol. 36, 915, 1971.
9. Omeragic, D., “EM modeling of logging-while drilling resistivity tool responses: State of art and challenges,” *Proceedings of Mathematics of Finite Elements and Application (MAFELAP) Conference 2003*, Brunel University, Uxbridge, June 2003.
10. Pardo, D., M. J. Nam, C. Torres-Verdin, and M. Paszynski, “A parallel, fourier finite-element formulation with an iterative solver for the simulation of 3D LWD measurements acquired in deviated wells,” *PIERS Online*, Vol. 4, No. 5, 551–555, 2008.
11. Wohlmuth, B., “A mortar finite element method using dual spaces for the Lagrange multiplier,” *SIAM J. Numer. Anal.*, Vol. 38, No. 3, 989–1012, 2000.

Correction for the Borehole Effect of Multi-component Array Induction Log Data

Junsheng Hou and Michael Bittar

Halliburton Energy Services, Inc.
3000 N Sam Houston Parkway E, Houston, TX 77302, USA

Abstract— This paper presents a new real-time borehole effect correction scheme designed specifically for processing multi-component array induction logging data. This algorithm consists of the following steps: reading raw data and preprocessing, estimating tool eccentricity azimuthal angle, inverting the unknown model parameters, correcting the borehole effects, and generating the borehole corrected results. The inversion of the modeled parameters is the key component of the correction scheme. The inversion algorithm converts the inversion problem of one high-dimensional unknown vector into several lower-dimension vectors, this separation is based on their sensitivity to various components of the measured conductivity tensor for the different sub-arrays. This dimensionality reduction makes the borehole correction inversion simpler, and more reliable. Because the three-dimensional simulation of a multi-component induction is a very time consuming process, the forward modeling used in the inversion is based on a pre-calculated look-up table. Hence, the inversion is fast, and the borehole correction processing can be applied in real time or at the well site. To validate the new borehole correction scheme, synthetic multi-component induction log data is processed using this new scheme. The obtained borehole corrected log results demonstrate its reliability and effectiveness.

1. INTRODUCTION

Multi-component array induction logging has been used to evaluate anisotropic formations in the oil and gas exploration industry for almost ten years [4–6, 8]. In addition to conventional induction logs, multi-component induction sensors provide information about formation horizontal and vertical resistivities, relative dip angle, and azimuthal angle for a wide range of borehole and formation environments. This additional information is very important for improving the analyses of low resistivity and thin-bed laminated reservoirs; however, the presence of a borehole strongly affects the multi-component induction measurements in both water-based and oil-based mud borehole environments. The borehole effects on the transverse couplings of multi-component induction logging tools are much greater than those that occur during conventional array induction logging. Consequently, the raw multi-component induction log data must be corrected for these effects before they can be applied to determine all of the formation properties previously described.

During the last several years, some developments related to the borehole effect correction issue for multi-component induction measurements were published in the literature. [1] reported their findings studies of the borehole effects and the borehole correction algorithm of triaxial logging data for a vertical well. They focus on determining the formation resistivity anisotropy in the presence of invasion. [10] developed a borehole correction algorithm of triaxial induction log data in oil-based mud with dip and anisotropy; however, this borehole correction algorithm is based on the simultaneous inversion of all unknown parameters. [7] discussed the borehole effects and presented a borehole correction algorithm of direct couplings for a generic two-coil multi-component logging tool in a vertical well, but this algorithm is not applicable for deviated wells. Because of the complexity of the multi-component induction borehole correction, inversion includes many free parameters with various units and scales and a fully three-dimensional electromagnetic forward simulation. The borehole correction issue provides a major challenge in the processing and interpretation of multi-component induction log data.

This paper presents a new real-time borehole correction scheme based on a new inversion algorithm for processing multi-component induction log data. This scheme is applicable in both a vertical and deviated borehole.

2. FORWARD MODEL AND BOREHOLE CORRECTION ALGORITHM

For the development of the new borehole correction algorithm, we use a three-coil collocated triaxial induction sonde; the equivalent dipole model of this sonde is shown in Fig. 1. The sonde consists of three mutually orthogonal transmitters, three mutually orthogonal main receivers, and three

mutually orthogonal bucking receivers. This configuration enables the measurement of the nine-component tensor of apparent conductivities in the rectangular coordinate system at every logging depth: XX , XY , XZ , YY , YX , YZ , ZX , ZY , and ZZ . In this designation, the first letter indicates the direction of the magnetic moment of the transmitter and the second letter indicates the direction of the receiver. Most modern multi-component induction logging use several of these arrays at different spacings and operating at different frequencies.

As a forward model must be built to develop the new borehole correction schemes. It is customary to ignore shoulder-bed or boundary effects for the borehole correction forward modeling, the model consists of a circular borehole surrounded by an infinitely thick homogeneous formation (Fig. 2). The borehole may be vertical or deviated, and the multi-component induction logging tool can be centered or eccentric in the borehole. Formation resistivity can be isotropic or anisotropic. The numerical simulation of the multi-component induction log response is calculated using a three-dimensional electromagnetic forward model. Extensive simulations of the multi-component induction response have been performed using this model, which show that for a given sub-array and frequency, the nine-component multi-component induction apparent conductivity tensor depends on the following eight parameters:

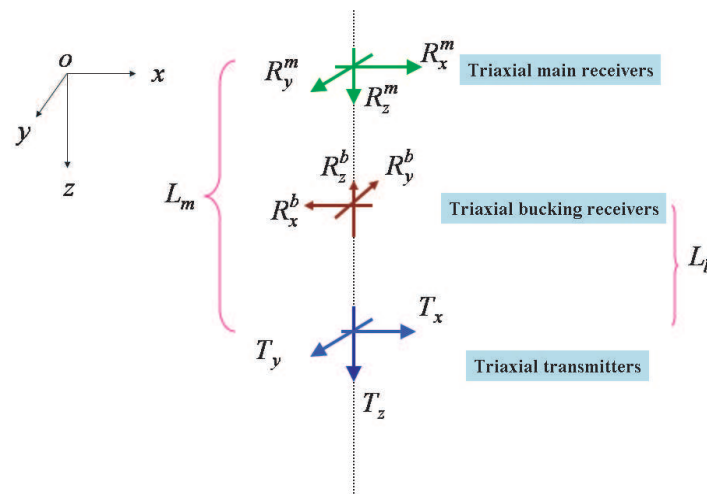


Figure 1: Configuration of a three-coil triaxial induction sonde in the rectangular coordinate system (equivalent dipole model) in which L_m and L_b are the transmitter-receiver spacings of the main and bucking receivers.

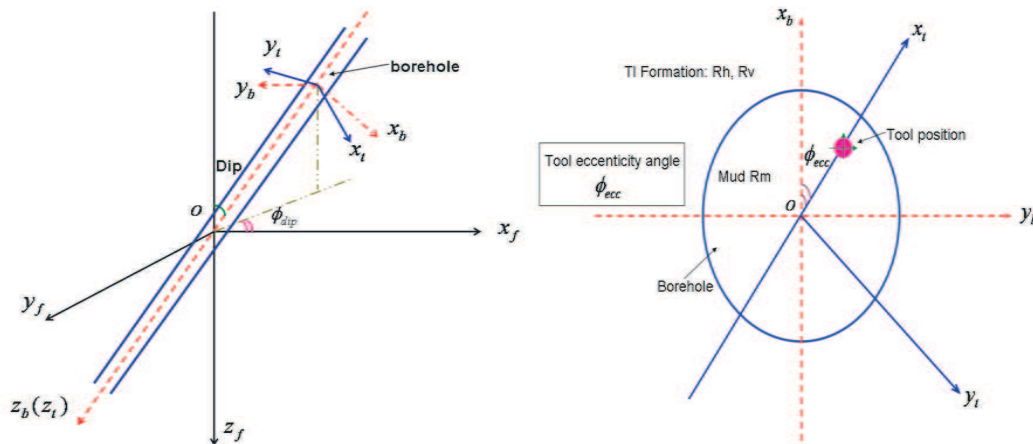


Figure 2: Borehole-formation forward model. The left panel is the 3D view and the right one is the top 2D view in the x_b - y_b plane. Here, (x_b, y_b, z_b) is the borehole coordinate system, (x_f, y_f, z_f) is the formation coordinate system, and (x_t, y_t, z_t) is the tool coordinate system.

- R_h — formation horizontal resistivity
- R_v — formation vertical resistivity
- cal — borehole diameter
- Rm — borehole mud resistivity
- d_{ecc} — tool eccentric distance (or standoff)
- ϕ_{ecc} — tool orientation/eccentricity azimuthal angle
- Dip — borehole dip angle
- ϕ_{dip} — borehole dip azimuthal angle

Three coordinate systems come into play:

1. Borehole coordinate system (x_b, y_b, z_b) ,
2. Formation coordinate system (x_f, y_f, z_f) ,
3. Tool coordinate system (x_t, y_t, z_t) .

The ZZ component should be independent of the two azimuthal angles of ϕ_{ecc} and ϕ_{dip} ; consequently, it depends only on the six model parameter: R_h , R_v , cal, Rm, d_{ecc} , and dip. Moreover, as in anisotropic media, the formation true conductivity tensor has two equal horizontal components; there is no preferred or unique choice of axes in the x_f - y_f horizontal plane. As a result, there is no loss of generality if the x_f - z_f plane is defined as the plane containing the σ_v principal axis and borehole axis [12]. Therefore, we can always assume $\phi_{dip} = 0$ for the multi-component induction forward model.

The new borehole correction processing system consists of the following steps:

- Read the measured log data, borehole correction look-up table, and other control processing parameters.
- Preprocess the log data (e.g., an adaptive low-pass filtering technique is developed for removal of high-frequency noise in raw log data).
- Estimate the eccentricity azimuth angle.
- Invert the unknown multi-component induction borehole correction parameters (e.g., R_h , R_v , dip, and d_{ecc}).
- Compute the multi-component induction borehole effects.
- Compute the final borehole corrected results $\overline{\overline{\sigma_{BHC}}}$.
- Generate the final borehole corrected results $\overline{\overline{\sigma_{BHC}}}$ for other applications, such as the correction of shoulder-bed effect and vertical one-dimensional inversion.

The inversion of the modeled parameters is the key component of the entire borehole correction system. Generally, the fewer unknowns in the inversion, the faster the inversion converges, and the less ambiguity is present in the inverted results. For example, assuming that the borehole size and mud resistivity can be obtained from the caliper and mud resistivity measurements, only the six remaining unknowns (R_h , R_v , dip, d_{ecc} , ϕ_{ecc} , and ϕ_{dip}) must be determined by the inversion. In conventional inversion of induction logs, all unknown parameters are inverted simultaneously, which minimizes problems of poor convergence and inverted results of large uncertainty. These complications largely affect the efficiency of the inversion methods and reliability of the inverted results.

Because the borehole correction inversion involves many unknown parameters with various units and scales, the new inversion algorithm is implemented by dividing the inversion problem of one high-dimension unknown vector into a few lower-dimension vectors. This division is based on their sensitivity to various components of the measured conductivity tensor for various sub-arrays operated at various frequencies. For example, in a vertical borehole (in which the dip is known), the ZZ component is insensitive to R_v ; all long-spacing direct couplings (ZZ , XX , and YY) are practically unaffected by tool eccentricity, and the XZ and ZX are almost linear with respect to the tool eccentricity. The azimuthal angles of ϕ_{ecc} can be independently solved by a coordinate rotation. Consequently, the borehole correction inversion algorithm is implemented by using the following steps:

1. R_h is inverted by only using the ZZ component.
2. R_v is solved by only using the direct couplings (XX , and/or YY).

3. d_{ecc} is obtained by only using the XZ and/or ZX and solving a quadratic programming problem.

In a deviated borehole, the ZZ component is unaffected by the two azimuthal angles of ϕ_{ecc} and ϕ_{dip} , and all long-spacing ZZ components are slightly affected by the tool eccentric distance parameter, especially in oil-based mud and fresh water-based mud; we can ignore the effect of this parameter on the long-spacing ZZ components. In oil-based mud and fresh water-based mud, we can ignore the effect of the tool eccentricity parameter on the long-spacing XX and YY components. Therefore, the borehole correction inversion algorithm is implemented by using the following steps in deviated boreholes:

1. Unknown parameters of R_h , R_v , and dip are determined by using only the ZZ component.
2. After R_h , R_v , and dip become known, the unknowns of ϕ_{ecc} , ϕ_{dip} , and d_{ecc} can be inverted by using the XX and/or YY components and the XZ and/or ZX components.
3. In oil-based mud and fresh water-based mud, ϕ_{ecc} and ϕ_{dip} can be solved by using only the XX and/or YY components.
4. d_{ecc} is inverted by using only the cross couplings XZ and/or ZX .

Many practical optimization techniques [2] can be used to solve the constrained inversion problems. In this paper, a constrained Gauss-Newton based method is used to minimize the object function.

Another critical issue for the inversion and real-time borehole correction processing is fast forward modeling. Because the three-dimensional multi-component induction simulation is a very time consuming process, the three-dimensional forward modeling used in the inversion is not implemented in a real-time manner; instead it is based on the pre-built look-up table. This table comprises pre-calculated tool responses at the grid points addressing all possible ranges of borehole-formation model parameters. In addition, we also developed a fast high-dimensional spline interpolation to compute the tool responses at arbitrary model parameters using the look-up table. The novel inversion algorithm, combined with the application of the pre-built look-up table, enhances the stability and speed of the borehole correction inversion and enables the borehole correction processing to be performed in real-time or at the wellsite.

3. APPLICATION

To test the new borehole correction scheme, a three-dimensional finite-difference electromagnetic potential algorithm [3] was developed. With this code we created the look-up table and modeled some multi-component induction logging measurements (XX , XY , XZ , YY , YX , YZ , ZX , ZY , and ZZ) in vertical and deviated boreholes. The model consisted of multi-layered anisotropic formations without invasion. Next, these synthetic multi-component induction log data were processed by using this new scheme for the borehole effect correction. For comparison with the borehole corrected logs, the multi-component induction logs without borehole were computed by using the

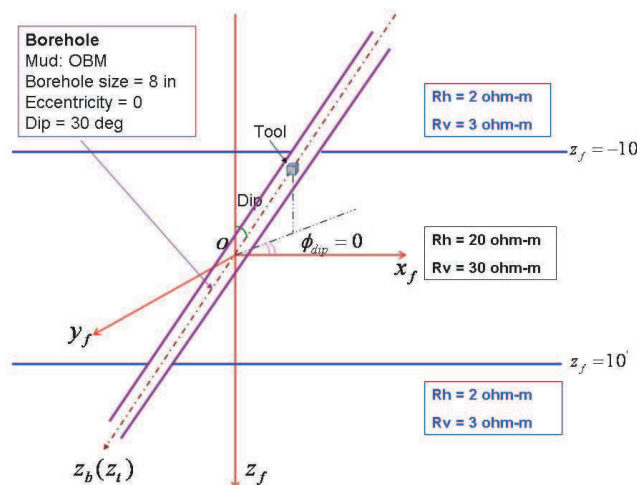


Figure 3: Three-dimensional model comprised 3-layer TI anisotropic formation with a 30-degree deviated borehole; here, R_h and R_v are the formation true horizontal and vertical resistivities.

electromagnetic semi-analytical solution for one-dimensional layered anisotropic media [13]. The borehole corrected log results are compared with the multi-component induction log data in the same multi-layered formations without borehole. The results of all comparisons were consistent and correlated well with one another. In all forward modeling computations, both the mandrel and tool coil size are disregarded, and point dipoles are used to model the finite-sized tool coils.

Figure 3 provides an example of the synthetic formation models. In this example, the model is a three-layer anisotropic formation with a 30 degree deviated borehole, making it a full three-dimensional model. Its upper and lower layers have the same horizontal and vertical resistivities of 2 ohm-m and 3 ohm-m. The middle layer has horizontal and vertical resistivities of 20 ohm-m and 30 ohm-m, and its thickness is 20 ft. The borehole diameter is 8 in., and the mud resistivity is 1000 ohm-m.. The multi-component induction logging tool includes four multi-component sub-arrays operated at three frequencies of 12 kHz, 36 kHz, and 72 kHz, and the tool is centered in the borehole. Fig. 3 shows other model parameters. Fig. 4, Fig. 5, and Fig. 6 show the borehole corrected nine-component logs at the frequencies of 12 kHz, 36 kHz, and 72 kHz for this three-dimensional model, and their comparisons with the vertical one-dimensional multi-component induction logs. All comparisons were consistent and showed good agreements.

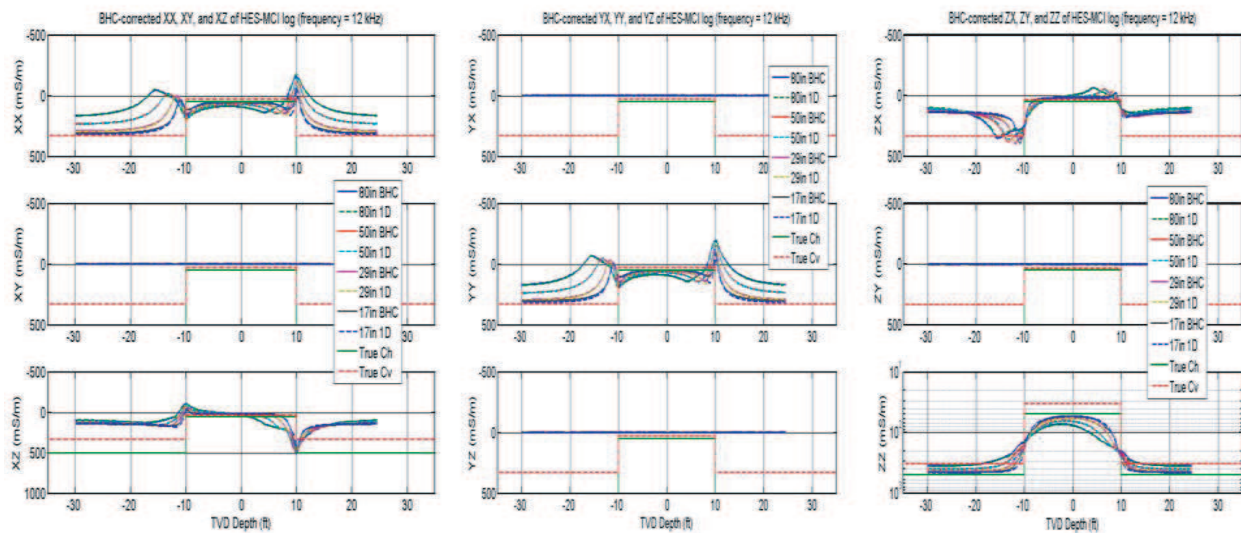


Figure 4: Borehole corrected nine-component logs at frequency of 12 kHz for 3D model.

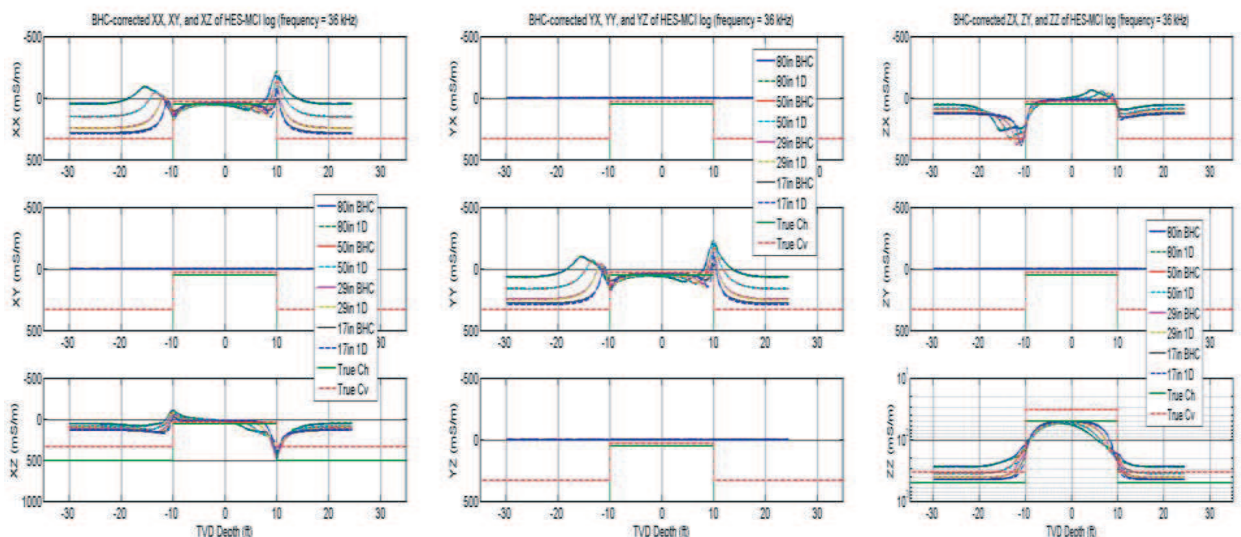


Figure 5: Borehole corrected nine-component logs at frequency of 36 kHz for 3D model.

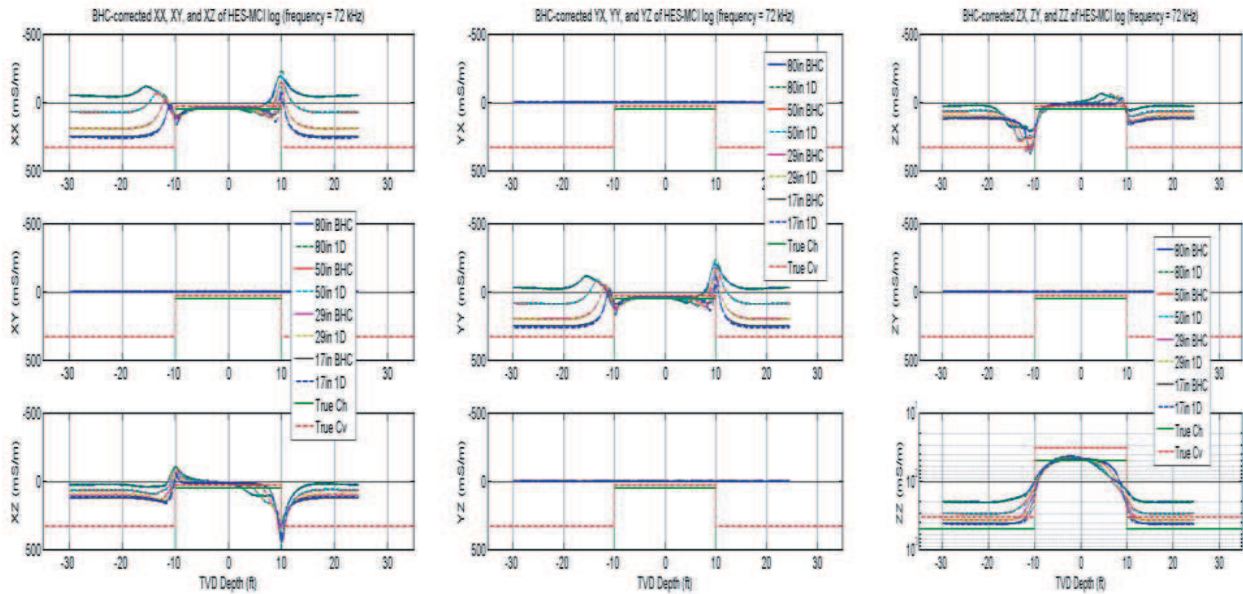


Figure 6: Borehole corrected nine-component logs at frequency of 72 kHz for 3D model.

4. CONCLUSION

We have developed a new real-time borehole correction system for processing multi-component induction logging data. This novel inversion algorithm is implemented by dividing the original inversion problem of one high-dimension unknown vector into a few lower-dimension vectors, based on their sensitivity of various model parameters to various components of the measured conductivity tensor for different sub-arrays. Numerical tests show that this dimensionality reduction makes the complicated borehole correction inversion overall easier and more reliable. Because the three-dimensional multi-component induction simulation is a very time consuming process, the forward modeling used in the inversion is based on the pre-calculated look-up table on a grid addressing all possible ranges of borehole-formation model parameters. This makes the borehole correction inversion very fast and enables the borehole correction processing to be performed in real-time or at the wellsite. To validate the new borehole correction scheme, synthetic multi-component induction data are generated and then processed by using this new scheme. The final borehole corrected results demonstrate that multi-component induction logs can be accurately corrected for the borehole effects.

ACKNOWLEDGMENT

The authors would like to thank Halliburton management for their support throughout the project and for permission to publish the results.

REFERENCES

1. Barber, T., B. Anderson, A. Abubakar, T. Broussard, K. Chen, S. Davydycheva, V. Druskin, T. Habashy, D. Homan, G. Minerbo, R. Rosthal, R. Schlein, and H. Wang, "Determining formation resistivity anisotropy in the presence of invasion," *SPE 80th Annual Technical Conference and Exhibition*, Houston, Texas, USA, September 26–29, 2004.
2. Gill, P., W. Murray, and M. Wright, *Practical Optimization*, Academic Press, 1981.
3. Hou, J. and M. Bittar, "Fast finite-difference simulation of 3D borehole EM fields using scattered potentials," *SEG 79th Annual Technical Conference*, Houston, Texas, USA, October 35–30, 2009.
4. Kriegshauser, B., O. Fanini, S. Forgang, G. Itskovich, M. Rabinovich, L. Tabarovsky, L. Yu, and M. Epov, "A new multi-component induction logging tool to resolve anisotropic formations," *SPWLA 41st Annual Logging Symposium*, Dallas, Texas, USA, June 4–7, 2000.
5. Rabinovich, M., L. Tabarovsky, B. Corley, and J. Horst, "Processing multicomponent induction data for formation dip and azimuth in anisotropic formations," *SPWLA 46th Annual Logging Symposium*, New Orleans, Louisiana, USA, June 26–29, 2005.

6. Rosthal, R., T. Barber, S. Bonner, K. C. Chen, S. Davydcheva, and G. Hazen, “Field test results of an experimental fully-triaxial induction tool,” *SPWLA 44th Annual Logging Symposium*, Galveston, Texas, USA, June 6–9, 2003.
7. Sun, X. Y., Z.-P. Nie, A. Li, and X. Luo, “Analysis and correction of borehole effect of the responses of multicomponent induction logging tools,” *Progress In Electromagnetic Research*, PIER 85, 211–226, 2008.
8. Wang, H., T. Barber, C. Morriss, R. Rosthal, R. Hayden, and M. Markley, “Determining anisotropic formation resistivity at any relative dip using a multiarray triaxial induction tool,” *SPE 82nd Annual Technical Conference and Exhibition*, San Antonio, Texas, USA, September 24–27, 2006.
9. Wang, H., P. Wu, R. Rosthal, G. Minerbo, and T. Barber, “Modeling and understanding the triaxial induction logging in borehole environment with dip anisotropic formation,” *SEG 78th Annual Technical Conference*, Las Vegas, Nevada, USA, November 9–14, 2008.
10. Wu, P., H. Wang, G. Minerbo, D. Homan, T. Barber, and M. Frey, “Borehole effects and correction in OBM with dip and anisotropy for triaxial induction tools,” *SPE 83rd Annual Technical Conference and Exhibition*, Anaheim, California, USA, November 11–14, 2007.
11. Xue, D., M. Rabinovich, B. Corley, A. Bespalov, and L. Pelegri, “Solutions to near zone effects on multi-component induction measurements,” *SPWLA 48th Annual Logging Symposium*, Austin, Texas, USA, June 5–6, 2007.
12. Zhdanov, M., D. Kennedy, and E. Peksen, “Foundations of tensor induction well-logging,” *Petrophysics*, Vol. 42, No. 6, 588–610, 2001.
13. Zhong, L., L. Shen, S. Li, R. Liu, M. Bittar, and G. Hu, “Simulation of tri-axial induction logging tools in layered anisotropic dipping formations,” *SEG 76th Annual Technical Conference*, New Orleans, Louisiana, USA, October 1–6, 2006.

Determination of Dip and Anisotropy from Multi-frequency Tri-axial Induction Measurements

Teruhiko Hagiwara

Aramco Service Company, Houston, Texas, USA

Abstract— The tri-axial (or multi-component) induction log is used to measure not only the resistivity anisotropy of an anisotropic formation but also the relative dip of the tool with respect to the formation. When the tri-axial induction log is run at multiple frequencies, multi-frequency focusing can be applied to the measurements. The apparent dip and the apparent anisotropy are algebraically defined from the frequency-focused tri-axial induction measurements. The apparent dip gives the true dip in thinly bedded formations, but a smaller dip than the true dip in a thick anisotropic bed when the anisotropy is small (the anisotropy effect). The apparent anisotropy gives the true anisotropy in thick anisotropic formations but is affected by the shoulder bed anisotropy when the formation is not thick (the shoulder bed effect).

1. INTRODUCTION

The tri-axial (or multi-component) induction log was developed to measure the formation anisotropy in vertical wells [1, 2] and to help interpretation of thinly laminated formations [3, 4]. It has been also recognized that a dip-meter in oil-base mud can be made out of tri-axial induction measurements and that the relative dip of the tool with respect to the formation is determined [5–8]. The anisotropic resistivity and the relative dip of layered formations are generally determined by inversion, namely by assuming a homogeneous or layered formation model and borehole dip and by fitting the tri-axial induction data to the model response in the earth model [9–11].

It is possible to compute the dip from the tri-axial induction data at a depth in homogeneous anisotropic formations [12] using the multi-frequency focusing method [13]. In the previous study [14], I showed that the apparent dip is less accurate in low resistivity formations and in thick isotropic formations while the apparent dip was remarkably useful in general. The accuracy of the apparent dip can be improved somewhat by using lower frequencies and/or shorter transmitter-receiver offsets. In reality, a thick formation may always be slightly anisotropic. Then, can the apparent dip be more accurate?

I will show in this paper that not only the dip but also the anisotropy is algebraically determined at a depth in homogeneous anisotropic formations using the multi-frequency focusing. The apparent dip and the apparent anisotropy can be applied to layered formations. The dip and the anisotropy can be algebraically computed without inversion. I model the multi-frequency tri-axial induction responses in thinly layered, macroscopically anisotropic, formations and examine how accurate the apparent dip and the apparent anisotropy are. I will show that the apparent dip needs the anisotropy correction in thick formations when the formation anisotropy is small, the formation resistivity is low, and the high frequency data are used. I will also show that the apparent anisotropy needs the shoulder bed correction in thin formations when the low frequency data are used.

2. DIP AND ANISOTROPY IN ANISOTROPIC FORMATIONS

Consider a tri-axial induction tool in a layered formation. See Fig. 1(a). The logging tool and the borehole are deviated from the vertical direction toward the x -axis direction by the dip angle ϑ . The formation (TI: transverse isotropic) anisotropy is defined in relative to the layering; namely, the horizontal conductivity is the conductivity in the direction parallel to the layers, by $\alpha^2 = \sigma_V / \sigma_H$ in this paper. The anisotropy factor β by $\beta = \sqrt{1 + (\alpha^2 - 1) \sin^2 \vartheta}$.

The tri-axial induction responses (the magnetic field strength vector) are noted as H_j^i ($i, j = x, y, z$) in the earth-bound coordinates (x, y, z), where a superscript i and a subscript j specifies the directions of a transmitter and a receiver. The actually measured tri-axial tool response are the magnetic field vector defined in the tool-bound coordinates (t, u, l) as H_b^a ($a, b = t, u, l$) where a and b are the transmitter's and receiver's polarity. Note that the l -axis is the tool's longitudinal direction, t the transverse direction in the xz -plane, and u the transverse direction perpendicular to the xz -plane. See Fig. 1(b).

The tri-axial responses in two coordinate systems are related by the axis rotation matrix $P(\vartheta)$ as

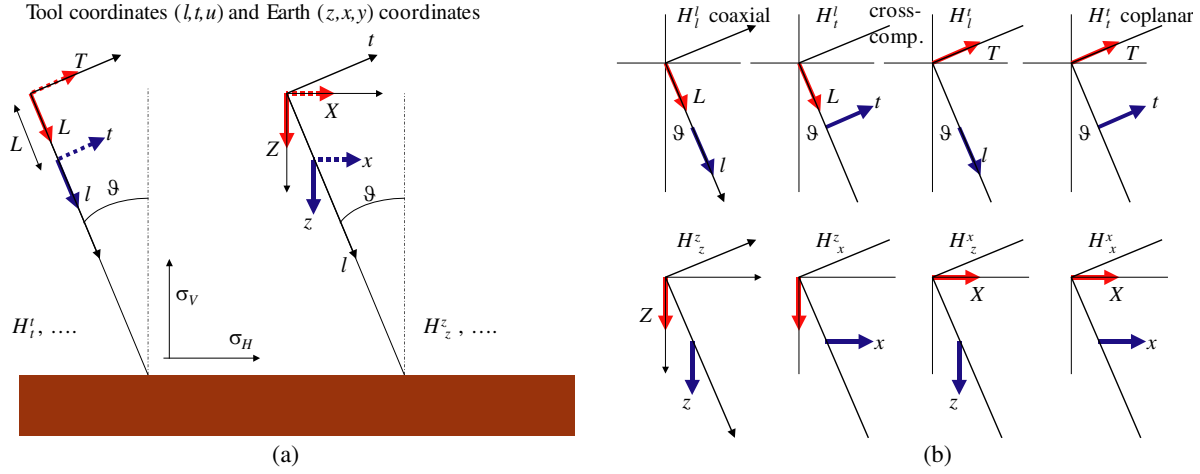


Figure 1: (a) Tool coordinates and earth coordinates. (b) Tri-axial transmitter-receiver configurations.

$$\begin{bmatrix} H_t^t & H_u^t & H_l^t \\ H_t^u & H_u^u & H_l^u \\ H_t^l & H_u^l & H_l^l \end{bmatrix} = P(\vartheta)^{tr} \begin{bmatrix} H_x^x & H_y^x & H_z^x \\ H_x^y & H_y^y & H_z^y \\ H_x^z & H_y^z & H_z^z \end{bmatrix} P(\vartheta) \quad \text{where} \quad P(\vartheta) = \begin{bmatrix} \cos \vartheta & 0 & -\sin \vartheta \\ 0 & 1 & 0 \\ \sin \vartheta & 0 & \cos \vartheta \end{bmatrix} \quad (1)$$

Hence, the following relations exist from the coordinate transformation.

$$H_l^l - H_t^t = (\cos^2 \vartheta - \sin^2 \vartheta) (H_z^z - H_x^x) - 2 \cos \vartheta \sin \vartheta (H_x^z + H_z^x) \quad (2)$$

$$H_t^t + H_l^l = -2 \cos \vartheta \sin \vartheta (H_z^z - H_x^x) - (\cos^2 \vartheta - \sin^2 \vartheta) (H_x^z + H_z^x) \quad (3)$$

$$H_l^l + H_t^t = H_z^z + H_x^x \quad (3)$$

The apparent dip may be defined by the ratio of measured tri-axial induction responses [7–9] as

$$\tan(2\vartheta_{app}) = -\frac{H_t^l + H_l^t}{H_l^l - H_t^t} \quad (4)$$

However, this apparent dip is not the true dip ϑ unless $H_x^z + H_z^x = 0$, according to Eq. (2) [14].

$$\tan(\vartheta_{app}) = \frac{H_t^l + H_l^t}{H_l^l - H_t^t} = \tan(2\vartheta + 2\psi); \quad \tan(2\psi) = \frac{H_x^z + H_z^x}{H_z^z - H_x^x} \quad (5)$$

The cross-components is calculated in a homogeneous TI anisotropic formation in the earth coordinates as

$$H_x^z = H_z^x = \frac{M_0}{4\pi L^3} \cos \vartheta \sin \vartheta (3(1-u) + u^2) e^u \quad (6)$$

where L is the transmitter-receiver spacing, σ_H the horizontal conductivity, and k_H the wave number in the horizontal direction: $u = ik_H L$ and $u^2 = -k_H^2 L^2 = -i\omega\mu\sigma_H L^2$, with $\omega = 2\pi f$ the angular frequency and μ the magnetic permeability. As the cross-component is not zero, the apparent dip ϑ_{app} of Eq. (4) does not give the true dip ϑ .

In the long wave expansion for $|u|^2 = \omega\mu\sigma_H L^2 \ll 1$,

$$H_x^z = H_z^x \approx \frac{M_0}{4\pi L^3} \cos \vartheta \sin \vartheta \left(3 - \frac{1}{2}u^2 + 0^*u^3 + \frac{1}{8}u^4 + O(u^5) \right) \quad (7)$$

When each tri-axial response is defined in the long wavelength expansion as,

$$H_x^z = H_z^x = H_{Zx}^{(0)} + H_{Zx}^{(2)}u^2 + H_{Zx}^{(3)}u^3 + H_{Zx}^{(4)}u^4 + O(u^5) \quad (8)$$

then, $H_{Zx}^{(2)} = -\frac{1}{2}\frac{M_0}{4\pi L^3} \cos \vartheta \sin \vartheta$ $H_{Zx}^{(3)} = 0$.

Note that $H_x^{z(3)} + H_z^{x(3)} = 0$ for the 3rd order terms (u^3) in the expansion. If the third order terms can be measured using the frequency focusing [12, 13], then

$$\begin{aligned} H_l^{l(3)} - H_t^{t(3)} &= (\cos^2 \vartheta - \sin^2 \vartheta) (H_z^{z(3)} - H_x^{x(3)}) \\ H_t^{t(3)} + H_l^{l(3)} &= -2 \cos \vartheta \sin \vartheta (H_z^{z(3)} - H_x^{x(3)}) \end{aligned} \quad (9)$$

And, the dip is algebraically determined by the 3rd order tri-axial induction responses by,

$$\tan(2\vartheta) = -\frac{H_t^{l(3)} + H_l^{t(3)}}{H_l^{l(3)} - H_t^{t(3)}} \quad (10)$$

The coaxial and coplanar responses are also calculated in the earth coordinates to give:

$$H_l^{l(3)} - H_t^{t(3)} = \cos 2\vartheta \left[H_z^{z(3)} - H_x^{x(3)} \right] = \cos 2\vartheta \frac{M_0}{4\pi L^3} \frac{\alpha^2 - 1}{2} \quad (11)$$

$$H_l^{l(3)} + H_t^{t(3)} = H_z^{z(3)} + H_x^{x(3)} = -\frac{M_0}{4\pi L^3} \left[\frac{4}{3} + \frac{\alpha^2 - 1}{2} \right] = -\frac{M_0}{4\pi L^3} \frac{3\alpha^2 + 5}{6} \quad (12)$$

From these, the formation anisotropy $\alpha^2 = \sigma_V/\sigma_H$ is algebraically determined from the measured tri-axial induction measurements and the dip angle ϑ (Eq. (10)), by the equation

$$\frac{H_l^{l(3)} - H_t^{t(3)}}{H_l^{l(3)} + H_t^{t(3)}} = -\frac{\alpha^2 - 1}{\alpha^2 + \frac{5}{3}} \cos 2\vartheta \quad (13)$$

$$\alpha^2 = \frac{\sigma_V}{\sigma_H} = \frac{y - \frac{5}{3}}{y + 1} \quad \text{where} \quad y = \frac{1 + x}{1 - x} \cos(2\vartheta) \quad \text{and} \quad x = \frac{H_t^{t(3)}}{H_l^{l(3)}}. \quad (14)$$

Note that the 3rd order in u is the $\omega^{3/2}$ -order in the frequency expansion. The 3rd order terms are separately determined for each of the tri-axial responses using frequency focusing in the low frequency expansion if the tri-axial measurements are made at multiple frequencies [12, 13].

3. APPARENT DIP AND ANISOTROPY IN LAYERED FORMATIONS

The apparent dip and the apparent anisotropy are algebraically defined at a depth from the frequency-focused 3rd order terms of tri-axial induction responses, respectively, by

$$\tan(2\vartheta_{app}) = -\frac{H_t^{l(3)} + H_l^{t(3)}}{H_l^{l(3)} - H_t^{t(3)}} \quad (15)$$

$$\alpha_{app}^2 = \frac{\sigma_V}{\sigma_H} = \frac{y - \frac{5}{3}}{y + 1} \quad \text{where} \quad y = \frac{1 + x}{1 - x} \cos(2\vartheta_{app}) \quad \text{and} \quad x = \frac{H_t^{t(3)}}{H_l^{l(3)}} \quad (16)$$

To investigate how close the apparent dip and the apparent anisotropy are to the true dip and the true anisotropy, I compute the tri-axial induction responses in an anisotropic formation model where the horizontal resistivity is 10 Ohm-m and its vertical resistivity is varied. The shoulder beds are isotropic and 10 Ohm-m. The tool deviation (dip) is 30 degrees. The transmitter-receiver offset is 1 meter. The frequency focusing is applied in three different ranges of frequencies: 100 Hz to 1 kHz, 1 kHz to 10 kHz, and 10 kHz to 100 kHz.

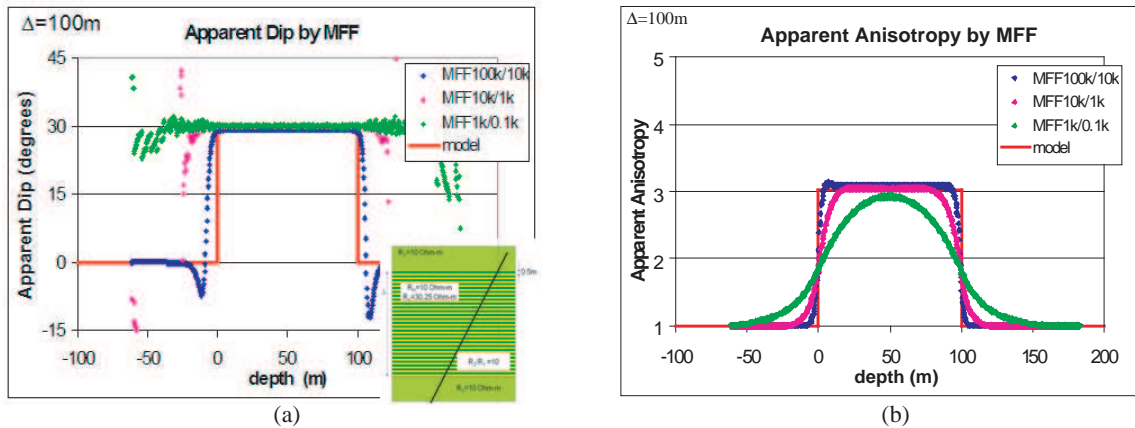


Figure 2: (a) The apparent dip in a 100 m thick formation. (b) The apparent dip in a 100 m thick formation.

4. THE EFFECT OF FREQUENCY

Shown in Figs. 2(a) and (b) are the apparent dip and the apparent anisotropy at the 100 m thick anisotropic formation for the 30 degree dip angle and the formation anisotropy of 3.025. The apparent dip reads the correct deviation angle of 30° in the three frequency ranges. On the other hand, the apparent anisotropy reads the true anisotropy only at higher frequency. The apparent anisotropy using the frequency focusing with the lower frequency is affected by the shoulder bed effect.

5. THE EFFECT OF FORMATION THICKNESS

The effect of the anisotropic formation thickness was studied by varying the thickness of an anisotropic formation from 100-m, 50-m, 25-m, to 13-m. Shown in Figs. 3(a) and 3(b) are the apparent dip and the apparent anisotropy for the 13-m thick anisotropic formation ($R_V/R_H = 3$). It is evident that the apparent dip reads the same (and true) dip for any formation thickness, but the apparent anisotropy is significantly affected by the shoulder bed, especially at lower frequencies.

6. THE EFFECT OF FORMATION ANISOTROPY

The effect of the anisotropic formation anisotropy was studied where the horizontal resistivity is 10 Ohm-m while its vertical resistivity are varied for the anisotropy of 3.025, 1.125, 1.04, and 1.01. Shown in Fig. 4(a) is effect of formation anisotropy on the apparent dip from MFF (110 kHz/10 kHz) at different bed thickness. Fig. 4(b) shows the effect of bed thickness on the apparent anisotropy from MFF (10 kHz/1 kHz) at different bed anisotropy. The apparent dip is close to the true dip at the lower frequencies, 1 kHz–0.1 kHz, but it is close to the true dip only in the highly anisotropic formation at the higher frequencies when the anisotropy is small.

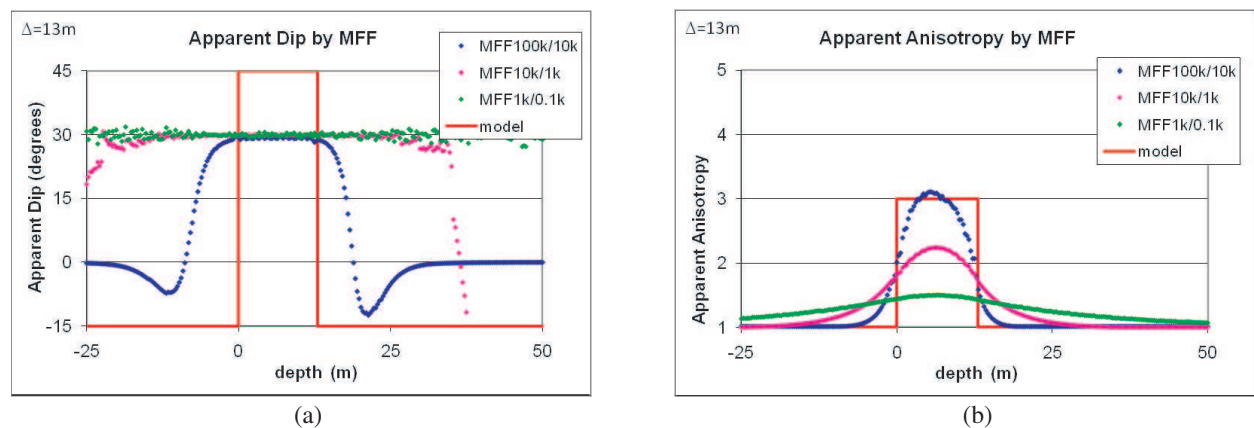


Figure 3: (a) The apparent dip in a 13 m thick formation. (b) The apparent anisotropy in a 13 m thick formation.

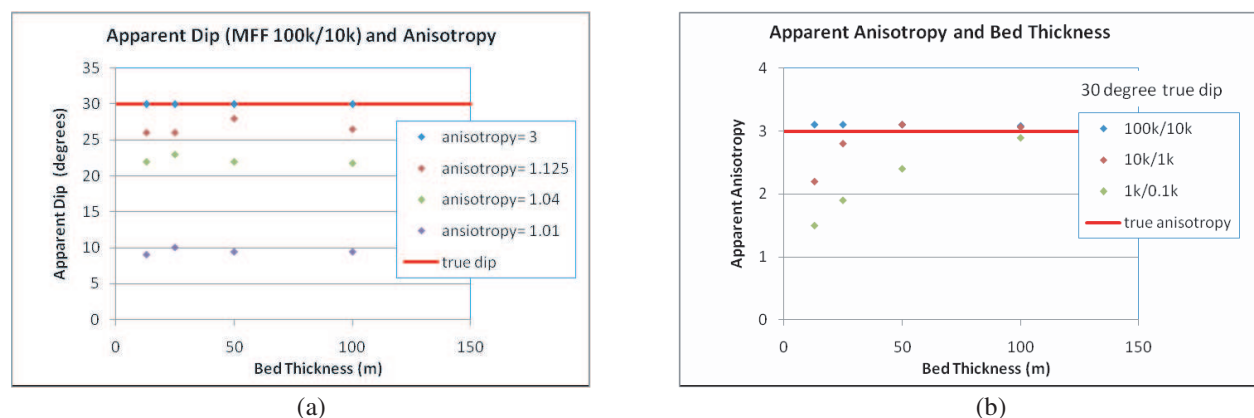


Figure 4: (a) The apparent dip and formation anisotropy. (b) The apparent anisotropy and formation thickness.

Though not presented here, the effect of resistivity is also studied: The apparent dip reads less correctly even in an anisotropic formation if the resistivity is smaller. The apparent anisotropy reads also incorrectly in the anisotropic low resistivity formation, particularly at the higher frequency.

7. CONCLUSION

Using the tri-axial induction log, one can measure not only the formation resistivity and the formation anisotropy but also the relative dip of the formation. When the tri-axial induction log is run at multiple frequencies, the apparent dip and the apparent anisotropy can be algebraically calculated at a depth using the frequency-focused tri-axial induction log responses.

The apparent anisotropy can read the true anisotropy in thick formations. However, there is shoulder bed effect for the apparent anisotropy: The apparent anisotropy does not read a constant anisotropy value in a thinly laminated formation if the formation is not thick.

The apparent dip can read the true dip in thick anisotropic formations. However, there is anisotropy effect for the apparent dip: The apparent dip reads inaccurately small dip even in an anisotropic formation if the anisotropy is smaller.

REFERENCES

1. Kriegshauser, B., O. Fanini, S. Forgang, G. Itskovich, M. Rabinovich, L. Tabarovsky, L. Yu, M. Epov, and J. Van Der Horst, "A new multicomponent induction logging tool to resolve anisotropic formations," *40th Annual Symposium, SPWLA*, Paper D, 1999.
2. Rosthal, R., T. Barber, S. Bonner, K.-C. Chen, S. Davydycheva, G. Hazen, D. Homan, C. Kibbe, G. Minerbo, R. Schlein, L. Villegas, H. Wang, and F. Zhou, "Field test results of an experimental fully-triaxial induction tool," *44th Annual Symposium, SPWLA*, Paper QQ, 2003.
3. Hagiwara, T., "Macroscopic anisotropy model: Analysis of thinly laminated sand/shale binary formations," *The 3rd Archie Conference, SEG/SPE/SPWLA/AAPG*, 1992.
4. Klein, J., P. Martin, and D. Allen, "The petrophysics of electrically anisotropic reservoirs," *36th Annual Symposium, SPWLA*, Paper HH, 1995.
5. Hungerford, E. T. and C. H. Fay, "Electromagnetic earth surveying apparatus," US Patent 3,014,177, 1957.
6. Runge, R., "Triple coil induction logging method for determining dip, anisotropy and true resistivity," US Patent 3,808,520, 1974.
7. Moran, J. H. and S. Gianzero, "Effects of formation anisotropy on resistivity measurements," *Geophysics*, Vol. 44, 1266–1286, 1979.
8. Gianzero, S., "Virtual induction sonde for steering transmitted and received signals," US Patent 5,757,191, 1998.
9. Zhang, Z., L. Yu, B. Kriegshäuser, and R. Chunduru, "Simultaneous determination of relative angles and anisotropic resistivity using multi-component induction logging data," *42nd Annual Symposium, SPWLA*, Paper Q, 2001.
10. Wang, H., T. Barber, R. Rosthal, J. Tabanou, B. Anderson, and T. Habashy, "Fast and rigorous inversion of triaxial induction data to determine formation resistivity anisotropy, bed boundary position, relative dip and azimuth angles," *73rd Annual Meeting, SEG*, Expanded Abstracts ER 1.1, 2003.
11. Rabinovich, M., L. Tabarovsky, B. Corley, J. Van Der Horst, and M. Epov, "Processing multi component induction data for formation dip and anisotropy," *Petrophysics*, Vol. 47, No. 6, 506–526, 2006.
12. Tabarovsky, L., M. Epov, and M. Rabinovich, "Measuring formation anisotropy using multi-frequency processing of transverse induction measurements," *SPE71706*, 2001.
13. Kaufman, A. and Y. A. Dashevsky, "Principles of induction logging," *Method of Geochemistry and Geophysics 38 Elsevier Science BV, Amsterdam, The Netherlands*.
14. Hagiwara, T., "Directionality and tri-axial induction log," *49th Annual Symposium, SPWLA*, Paper OOOO, 2008.

Measuring the Soil Water Content of a Sandy Soil with a Frequency Cross-hole Radar: Antenna Design and Experiments

F. Rejiba¹, F. Sagnard², C. Schamper¹, M. Froumentin³, and Guérin¹

¹Université Pierre et Marie Curie, Paris 6, UMR Sisyphe, Boite 105
4 place Jussieu, 75252 Paris cedex 05, France

²LRPC Rouen, ERA 23, 10 chemin de la Poudrière, 76120 Le Grand Quevilly, France

³CER Rouen, ERA 23, 10 chemin de la Poudrière, 76120 Le Grand Quevilly, France

Abstract— Road surface quality is very sensitive to mechanical properties of the underground structure, and particularly to its water content. Electromagnetic frequency cross-hole radar associated with a Zero Offset Profiling (ZOP) acquisition mode has been used as a non destructive technique to evaluate the vertical distribution of the water content inside a multi-layered clay sand embankment test site. In order to fit two borehole diameters (40 and 67 mm), that are used for civil engineering monitoring, two specific radar transmission links (with a distance less than 1 m) have been developed to work in the frequency band [0.5; 1.5] GHz. These borehole transmission links have led to the design of two types of ultra-wideband symmetric antennas: a 3D “folded dipole” made of thin wire elements, and a planar “blade dipole”. Numerical electromagnetic modeling associated with both antenna geometries, and their integration in a transmission link have been performed using two complementary FDTD softwares: a commercial software EMPIRE based on an adaptative grid, and a laboratory-made software which relies on parallel calculation and can consider a soil made of a random dielectric distribution. The comparison of measurement and simulation results with both folded and blade dipoles, has allowed to highlight contrasts of real permittivities induced by water content and soil compaction level.

1. INTRODUCTION

The quality of foundation in road construction or rehabilitation is crucial to obtain satisfying load-bearing strength. Those foundations generally consist in earthfill which optimal mechanical property are inversely correlated with its water content. Therefore, the measurement of the water content distribution in embankments is crucial to plan any structural consolidation or additional drain. The monitoring of embankments (or any natural soil) water content could be made using Zero Offset Profiling (ZOP) radar tomography in standard and narrow boreholes previously digged for geotechnical purpose during the road construction. A example involving crosshole GPR for vertical water content profiling, in a ZOP acquisition, is described by Rucker and Ferre [1]. In order to obtain an accurate profile of water content using crosshole GPR in such specific boreholes, two geometrically optimal, wideband and dipole shaped antenna have been designed: a thin wire folded dipole and a planar blade dipole. Each dipole geometry has been designed using EMPIRE FDTD modeler (distributed by IMST) including the entire transmission link. Experimental results have been made using each type of dipole on a real-size embankment in laboratory LRPC, Rouen and have been compared to simulations. The real dielectric permittivity have been estimated from first arrivals times and then converted in volumetric water content using Malicki’s empirical law [2].

2. ANTENNA DESIGN AND EXPERIMENTAL RESULTS

The test site (Figure 1) presented is an embankment (22.5 m × 2.8 m) made of two layers of a wet clay sand B2 (methylene blue value 5.6) characterized by 80% of grains below 600 μm, 10% of grains below 100 μm, and a maximum grain diameter close to 20 mm. The two major layers (upper layer 1 and lower layer 2) are characterized by two different moisture contents with layer 2 having the highest moisture content. The bottom of the embankment is made of natural soil that is very dry. The variation of the compaction level (percentage of the Optimum Proctor) as a function of the depth z presented on Figure 2 highlights that a wetter layer can be more easily compacted.

The two pairs of boreholes used for the experiments are at a distance of 44 cm and 122 cm respectively. In order to match the two different borehole diameters (inner diameter of 34 mm and 63 mm respectively), we have designed two antenna, a folded (Figure 3) and a blade dipole (Figure 4), in the frequency band [0.5; 1.5] GHz which leads to the desired spatial resolution in addition to a limited scattering attenuation. Comparing to folded dipole, the blade dipole has the



Figure 1: General view of the embankment test site.

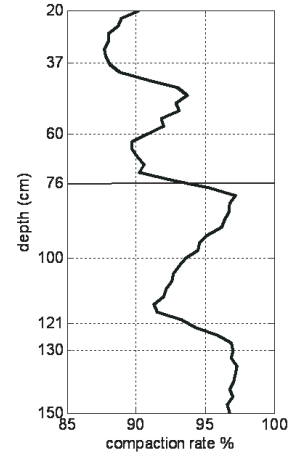


Figure 2: Of the compaction level (% of the optimum proctor) as a function of the depth.

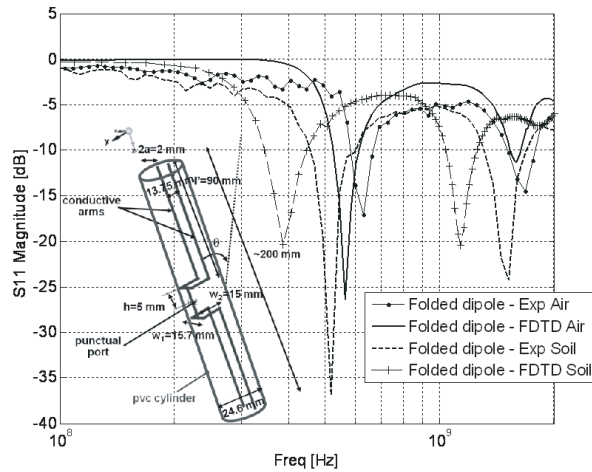


Figure 3: Theoretical and experimental reflection coefficients $S_{11}(f)$ recorded in air during the calibration process and at a depth $z = 40$ cm inside the boreholes in the case of the folded dipole.

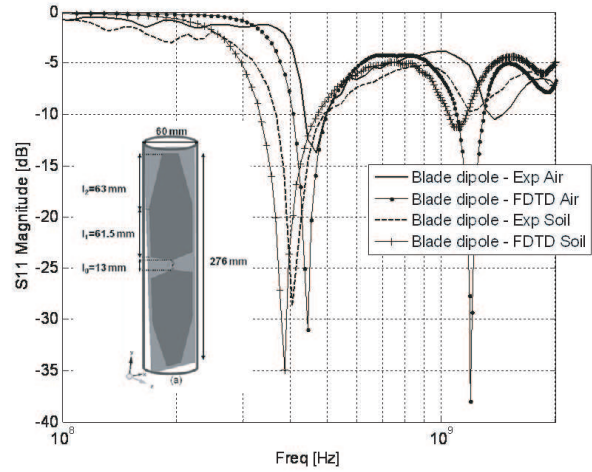


Figure 4: Theoretical and experimental reflection coefficients $S_{11}(f)$ recorded in air during the calibration process and at a depth $z = 40$ cm inside the boreholes in the case of the blade dipole.

advantage to produce a better horizontal directivity at 800 MHz (Figure 5) which limits the effect of refracted waves that could leads to errors during the picking process of direct wavefronts.

The effective real permittivity $\epsilon_b(z)$ of the soil between the boreholes as a function of the depth has been evaluated from first arrival time picking of the direct waves observed in the radargrams associated with both types of boreholes. The $S_{21}(\omega)$ conversion in time domain (for emitter and receiver located at the same depth) has been performed using a frequency-domain convolution with a gaussian spectrum centered at 800 MHz followed by an inverse fourier transform.

The volumetric water content has been therefore evaluated from the effective real permittivity and the dry soil bulk density ($\rho_s(z)$) measured (for depth step size equal to 20 cm), according to Malicki's empirical relation as follows:

$$\theta = \frac{\sqrt{\epsilon_b} - 0.82 + 0.17\rho_s - 0.16\rho_s^2}{7.17 + 1.8\rho_s} \quad (1)$$

Figure 6, shows the vertical variations of volumetric water content from folded and blade dipole measurements, in addition to geotechnical measurements. The two major layers are “visible” with both transmission links. The “folded dipole” results agree accurately with oven drying measurements associated with double gamma probe density records, while the “blade dipole” results are

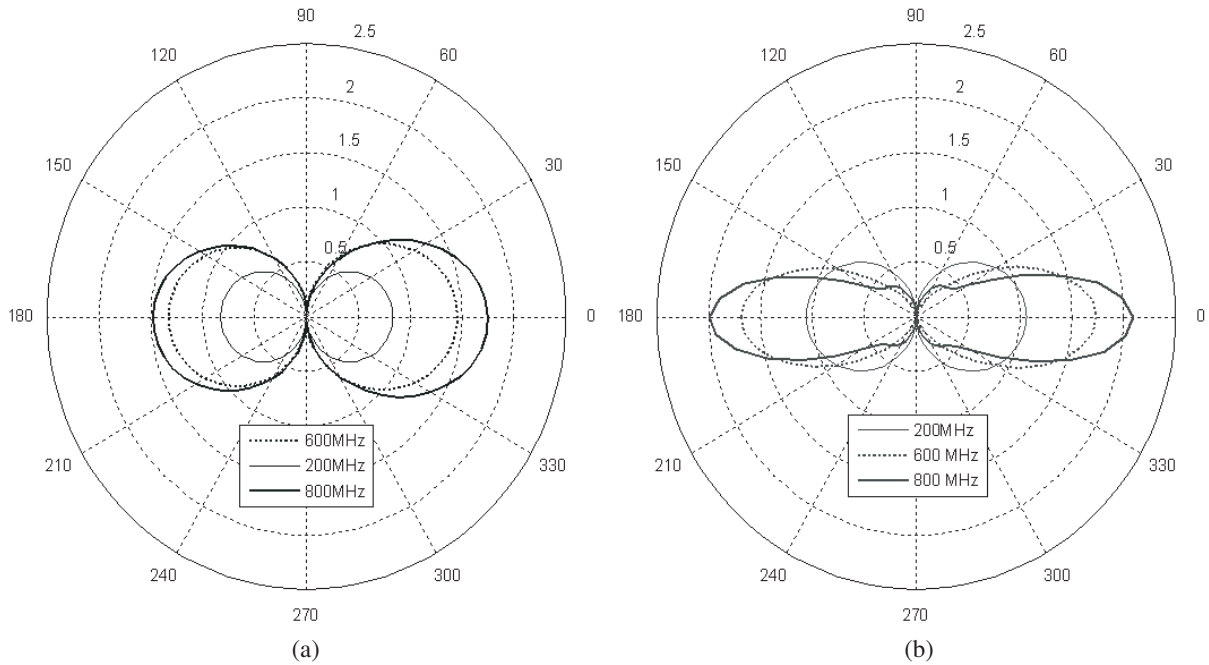


Figure 5: Amplitude radiation patterns in the vertical containing the boreholes at three frequencies 200, 600 and 800 MHz of (a) the folded dipole, and (b) the blade dipole. The magnitude presented are in the linear scale.

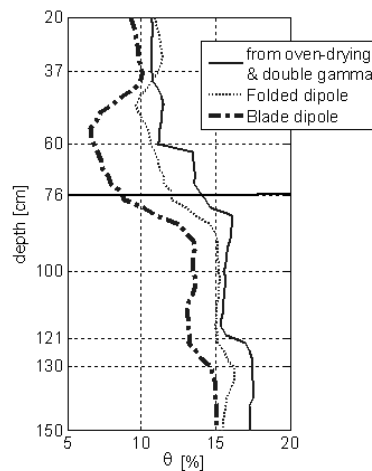


Figure 6: Volumetric water content curves obtained with the folded and blade dipoles (the distance between boreholes is 44 cm and 122 cm respectively) compared to the oven drying/double-gamma probe measurements.

more sensitive to compaction levels, and underestimate slightly the volumetric water content.

3. CONCLUSION

Two radar crosshole transmission links, which differ from the diameter of their boreholes and dedicated to in-situ measurements of the volumetric water content, have been designed and tested successfully. The main technical constraint was the design of the antennas (pairs of folded and blade dipoles) with a narrow width (inner diameter of 34 mm and 63 mm respectively) in the frequency band ranging from 0.5 to 1.5 GHz. Volumetric water content measurements using both transmission links, have been sufficiently accurate to even discriminate the compaction level induced by the construction of the embankment test site. In the near future, accurate electrical conductivities profile should be evaluated from cross hole measurements with the dipoles designed.

ACKNOWLEDGMENT

The authors are grateful to the National Laboratory of Civil Engineering (LCPC) for funding this research associated with the project SOLEM.

REFERENCES

1. Rucker, D. F. and T. Ferre, “Parameter estimation for soil hydraulic properties using zero-offset borehole radar: Analytical method,” *Soil Science Society of America Journal*, Vol. 68, No. 5, 1560, 2004.
2. Malicki, M. A., R. Plagge, and C. H. Roth, “Improving the calibration of dielectric TDR soil moisture determination taking into account the solid soil,” *European Journal of Soil Science*, Vol. 47, No. 3, 357–366, 1996.

Focusing Microprobes Based on Integrated Chains of Microspheres

Vasily N. Astratov, Arash Darafsheh, Matthew D. Kerr, Kenneth W. Allen,
and Nathaniel M. Fried

Department of Physics and Optical Science, Center for Optoelectronics and Optical Communication
University of North Carolina at Charlotte, Charlotte, North Carolina 28223-0001, USA

Abstract— The concept of nanoscale photonic jets has emerged as a novel way of focusing light with subwavelength spatial resolution. Practical focusing systems are, however, limited in their resolution by the multimodal structure of beams delivered by flexible waveguides or fibers. In this work, by using numerical modeling, we show that the chains of microspheres assembled inside the bores of the hollow waveguides or microcapillaries provide significant advantages over single lenses in such applications. It is also shown that the chains of microspheres are capable of focusing light in contact with tissue. Experimental studies are performed for spheres with sizes from 10 to 300 μm with different indices of refraction ranging from 1.47 to 1.9. The focusing and transport properties of such chains are found to be in good agreement with numerical modeling results.

1. INTRODUCTION

Recently it has been demonstrated that a small wavelength-scale microsphere with a refractive index of about 1.6 produces a narrow focused beam, termed a ‘nanoscale photonic jet’ [1–7]. The photonic nanojet propagates with little divergence for several wavelengths into the surrounding medium, while maintaining a sub-wavelength transverse beam width. A fundamental principle in diffraction-limited optics [8] requires that the spatial resolution of focusing devices be limited by the wavelength of the incident light (λ) and by the numerical aperture of the objective lens systems. Microspheres allow obtaining focused beams with effective volumes of the order of $(\lambda/n)^3$, where n is the sphere’s refractive index [7]. The concept of nanojets is attractive for designing focusing microprobes that can be used for detecting nanoparticles [1], dry laser cleaning [9], multiplexed imaging [10], nanopatterning [11], Raman spectroscopy [12], and optical data storage [13]. It should be noted, however, that photonic nanojets from single spheres require strictly plane-wave or conical illumination which is not readily available in devices using flexible optical delivery systems.

More recently, periodic focusing of light has been observed in chains of polystyrene microspheres assembled on substrates [14–17]. In these chains, the photonic nanojets were quasi-periodically reproduced along the chain giving rise to “nanojet-induced modes” (NIMs). The coupled nanojets decreased in size along the chain, reaching wavelength-scale dimensions, even for non-collimated input beams. The periodicity, spectral transmission properties, and losses of NIMs were studied [14, 15] for such chains.

In this work, we study focusing properties of chains of microspheres assembled inside the cores of hollow waveguides or microcapillary tubing. Using ray tracing ZEMAX-EE software [18] we show that chains of microspheres have significant advantages over single lenses in such systems. They filter the nanojet-induced modes with the best focusing properties in such structures. This allows reduction in the sizes of the focused beams to wavelength-scale dimensions while maintaining high optical transmission. Using high index spheres, we demonstrate that these structures are capable of focusing light into tissue or a sample in close proximity to the end sphere. Light propagation effects observed in such chains are found to be in a good agreement with numerical modeling results.

2. NUMERICAL MODELING

An example of a delivery system based on a hollow waveguide is illustrated in Fig. 1(a). Multiple reflections by the sidewalls of the waveguide lead to formation of a number of modes incident on a focusing element at different angles. A single sphere with size matching the diameter of the bore can be integrated with the hollow waveguide. Each waveguide mode is focused at the focal plane of a spherical lens, as illustrated in Fig. 1 by numerical ray tracing performed using ZEMAX-EE software [18]. In our modeling we used spheres with radius $a = 150 \mu\text{m}$ and $\lambda = 2.96 \mu\text{m}$. It is well known that in the limit $a \gg \lambda$ the index of refraction of the sphere must be close to 2 to provide maximum intensity of focused light at the “shadow” surface of the sphere [1–3], as illustrated in Fig. 1(b). In the limit of geometrical optics, each spot size is determined by the

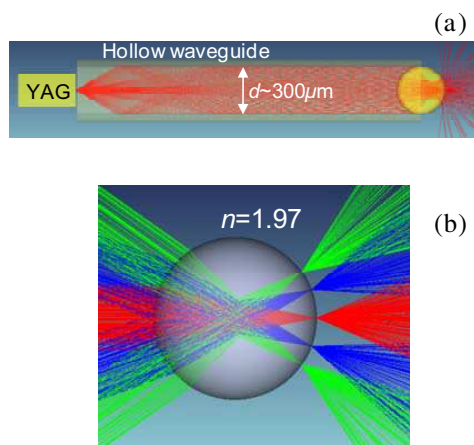


Figure 1: (a) Single sphere with $a = 150 \mu\text{m}$ integrated with a hollow waveguide coupled to a laser at $\lambda = 2.96 \mu\text{m}$. (b) Ray tracing of several beams in a single high index (1.97) sphere showing multiple focused spots.

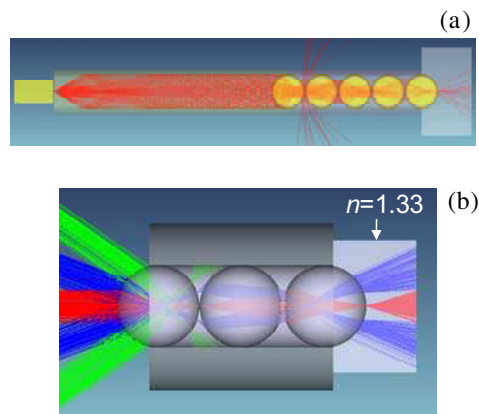


Figure 2: (a) Chain of spheres with $a = 150 \mu\text{m}$ integrated with a hollow waveguide coupled to a laser at $\lambda = 2.96 \mu\text{m}$. (b) Ray tracing of several beams demonstrating the mode filtering properties leading to sharp focusing by the end sphere.

spherical aberrations. According to a more rigorous physical optics approach, each focused spot in Fig. 1(b) should have at least diffraction-limited dimensions [8]. If the incident beams have a continuous angular distribution, all the focused spots originating from the individual modes are overlapped near the back surface of the sphere forming a broad intensity distribution with characteristic sizes well in excess of the diffraction limit. Thus, the spatial resolution of optical microprobes based on single spheres is expected to be significantly below the diffraction limit due to multimode illumination.

Focusing effects in a chain of microspheres are illustrated by numerical ray tracing in Fig. 2 for high (1.97) index spheres. Only illumination along the axis leads to efficient coupling of light to optical modes propagating in such chains. Axial beams (red) are periodically focused inside the structure with the periodicity depending on the index of refraction. The meridional beams, however, are scattered away from such chains due to reflections of light beams provided at the spherical interfaces. Propagation effects inside the chain are modeled by taking into account multiple refractions and reflections at the spherical interfaces. Only refracted beams are shown in Fig. 2 to simplify the images.

In some applications (e.g., ultra-precise laser surgery) a short focusing depth is required in a fluid or tissue. It is well known, however, that the focusing properties of microprobes based on single lenses are limited in a fluid due to its high index of refraction [19]. In contrast, the chains of microprobes can be enclosed in a tube, so that all the beads except the last sphere are completely isolated from the fluid. Only the last sphere is exposed to fluid (or tissue) with index 1.33, as illustrated in Fig. 2. The focusing effects are observed to be preserved in a fluid despite its index of refraction. This opens up the possibility of using similar focusing structures in a liquid or in direct contact with tissue. Detailed study of the focused beams' sizes involves taking into account the diffraction effects. This task requires a rigorous solution of Maxwell's equations without assumptions used in geometrical optics, which goes beyond the scope of the present work. It should be noted, however, that spot sizes comparable to the wavelength of light were observed [14] in chains of $3 \mu\text{m}$ polystyrene microspheres coupled to multimodal light sources (dye-doped spheres).

3. EXPERIMENTAL RESULTS

Chains of microspheres made from borosilicate glass ($n = 1.47$), soda-lime glass ($n = 1.50$), polystyrene ($n = 1.59$), and barium titanate glass ($n = 1.9$) were assembled inside plastic and glass microcapillaries as well as inside hollow waveguides. Infiltration was performed using micro-manipulation and micro-pneumatic propelling of spheres with diameters from 10 to $300 \mu\text{m}$. In order to provide tight packing of microspheres, while keeping the chains straight and symmetric along the long central axis of the cylindrical structure, the size of microspheres should match the hole size in the microcapillary tube, as shown in Figs. 3(a) and 4(a).

The light attenuation properties of chains of microspheres inside capillary tubing were investi-

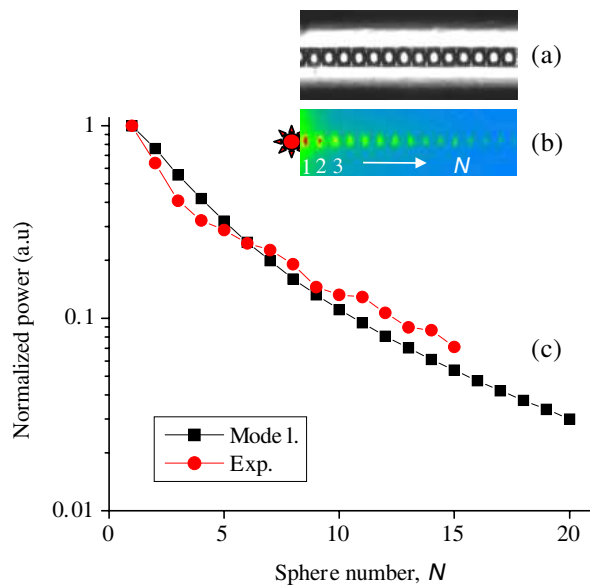


Figure 3: (a) Packing of $50\ \mu\text{m}$ polystyrene spheres inside a microcapillary. (b) Scattering image illustrating optical transport. (c) Measured (circles) and calculated (squares) attenuation of light.

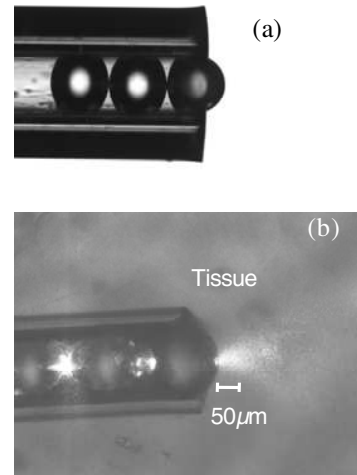


Figure 4: (a) Assembly of $125\ \mu\text{m}$ barium titanate microspheres inside microcapillary. (b) Focusing at $\lambda = 0.63\ \mu\text{m}$ in contact with tissue-mimicking gel with an index of 1.4.

gated by imaging through the sidewall using scattered light, as illustrated for $50\ \mu\text{m}$ polystyrene beads in Fig. 3(b). The studies were performed using dye-doped fluorescent (FL) polystyrene spheres with the same $50\ \mu\text{m}$ size as local light sources. The FL excitation was provided at 460–500 nm by a mercury lamp. The FL emission was provided in a 500–570 nm spectral range. A fraction of this power was coupled to modes propagating in the chain formed by undoped spheres away from the source. These propagation effects were visualized with an inverted IX-71 Olympus microscope due to scattered light, as shown in Fig. 3(b).

The positions of bright spots observed in Fig. 3(b) correspond to areas at the spherical surfaces near the touching points of the neighboring spheres. Since the conditions of collection of scattered light were fixed along the chain, one can assume that the power contained in the bright spots should be proportional to the power of modes propagating inside the chain. In order to estimate the total power contained in the bright spots, the intensity distribution was integrated within each spot and represented by red dots in Fig. 3(c). This experimental power distribution along the chain was observed to be in reasonable agreement with the results obtained by numerical ray tracing using ZEMAX-EE software [18], also shown in Fig. 3(c). It should be noted that smaller losses $\sim 0.1\ \text{dB/sphere}$ were reported [15] for very long chains (up to 100 beads) formed by much smaller ($5\ \mu\text{m}$) polystyrene spheres. Similar results were obtained for chains formed by the borosilicate ($n = 1.47$) and soda-lime glasses ($n = 1.50$). For chains formed by high index ($n = 1.9$) barium titanate glass spheres the experimentally measured transmission was less than the theoretical values due to absorption of light by the microsphere material at 510–570 nm.

In order to test the focusing properties of the microprobe in the presence of a tissue-like medium, the structure formed by barium titanate glass microspheres with $a = 125\ \mu\text{m}$ was completely embedded in a gel, so that the surface of the end sphere was in contact with the medium with index around 1.4, similar to the case considered earlier by theoretical modeling in Fig. 2. Illumination was provided at $\lambda = 630\ \text{nm}$ by the single mode fiber inserted in a capillary tube holding the chain of microspheres. The gel makes visible the beam inside such a “tissue”, due to light scattering properties, as shown in Fig. 4(b). The beam is focused in the vicinity of the surface of the end sphere with the beam waist measuring about $5\ \mu\text{m}$. Due to significant beam divergence the intensity distribution has a small depth of $\sim 10\text{--}20\ \mu\text{m}$. Thus, such structures are capable of focusing light into tissue in contact mode and may provide laser interaction with the tissue in close proximity to the end sphere.

4. CONCLUSIONS

Conventional single lens-based microprobes based on multimodal delivery systems can focus light to spot sizes which are *a priori* significantly larger than the diffraction limited dimensions. In this study we demonstrate that a trade-off between focused spot sizes and transmitted power can be conveniently controlled in microprobes by using chains of microspheres. Increasing the number of spheres in such chains generally provides smaller focused spot sizes at the expense of transmitted power. Simple integration of microsphere arrays with flexible fibers and hollow waveguides permit sharp focusing of a light beam and operation in contact mode with tissue. Thus, microsphere arrays can be used in a variety of biomedical and photonics applications as a compact focusing tool. We show that such structures allow one to obtain focused beams with spot sizes of several wavelengths and with a treatment depth of approximately 10–20 μm in tissue. Potential applications include ultra-precise laser procedures on the eye and brain or piercing a cell, and the coupling of light into photonic nanostructures.

ACKNOWLEDGMENT

The authors gratefully acknowledge support for our work from the U.S. Army Research Office (ARO) under Contract No. W911NF-09-1-0450 (J. T. Prater) and from the National Science Foundation (NSF) under grant ECCS-0824067. This work was also supported by Award Number R41EY019598 from the National Eye Institute. The content is solely the responsibility of the authors and does not necessarily represent the official views of the National Eye Institute or the National Institutes of Health. This work was also partially supported by funds provided by The University of North Carolina at Charlotte. The authors also wish to thank Mo-Sci and Thermo Fisher Scientific Corporations for donating microspheres for this research.

REFERENCES

1. Chen, Z., A. Taflove, and V. Backman, "Photonic nanojet enhancement of backscattering of light by nanoparticles: A potential novel visible-light ultramicroscopy technique," *Opt. Express*, Vol. 12, No. 7, 1214–1220, 2004.
2. Lecler, S., Y. Takakura, and P. Meyrueis, "Properties of a three-dimensional photonic jet," *Opt. Lett.*, Vol. 30, No. 19, 2641–2643, 2005.
3. Itagi, A. V. and W. A. Challener, "Optics of photonic nanojets," *J. Opt. Soc. Am. A*, Vol. 22, No. 12, 2847–2858, 2005.
4. Chen, Z., A. Taflove, and V. Backman, "Highly efficient optical coupling and transport phenomena in chains of dielectric microspheres," *Opt. Lett.*, Vol. 31, No. 3, 389–391, 2006.
5. Gerlach, M., Y. P. Rakovich, and J. F. Donegan, "Nanojets and directional emission in symmetric photonic molecules," *Opt. Express*, Vol. 15, No. 25, 17343–17350, 2007.
6. Ferrand, P., J. Wenger, A. Devilez, M. Pianta, B. Stout, N. Bonod, E. Popov, and H. Rigneault, "Direct imaging of photonic nanojets," *Opt. Express*, Vol. 16, No. 10, 6930–6940, 2008.
7. Devilez A., N. Bonod, J. Wenger, D. Gérard, B. Stout, H. Rigneault, and E. Popov, "Three-dimensional subwavelength confinement of light with dielectric microspheres," *Opt. Express*, Vol. 17, No. 4, 2089–2094, 2009.
8. Born, M. and E. Wolf, *Principles of Optics*, Cambridge University Press, 1997.
9. Luk'yanchuk, B. S., N. Arnold, S. M. Huang, Z. B. Wang, and M. H. Hong, "Three-dimensional effects in dry laser cleaning," *Appl. Phys. A: Mater. Sci. Process.*, Vol. 77, 209–215, 2003.
10. Yakovlev, V. V. and B. Luk'yanchuk, "Multiplexed nanoscopic imaging," *Laser Physics*, Vol. 14, No. 8, 1065–1071, 2004.
11. McLeod, E. and C. B. Arnold, "Subwavelength direct-write nanopatterning using optically trapped microspheres," *Nature Nanotechnology*, Vol. 3, No. 7, 413–417, 2008.
12. Yi, K. J., H. Wang, Y. F. Lu, and Z. Y. Yang, "Enhanced Raman scattering by self-assembled silica spherical microparticles," *J. Appl. Phys.*, Vol. 101, 063528, 2007.
13. Kong, S.-C., A. Sahakian, A. Taflove, and V. Backman, "Photonic nanojet-enabled optical data storage," *Opt. Express*, Vol. 16, 13713–13719, 2008.
14. Kapitonov, A. M. and V. N. Astratov, "Observation of nanojet-induced modes with small propagation losses in chains of coupled spherical cavities," *Opt. Lett.*, Vol. 32, No. 4, 409–411, 2007.

15. Yang, S. and V. N. Astratov, “Photonic nanojet-induced modes in chains of size-disordered microspheres with an attenuation of only 0.08 dB per sphere,” *Appl. Phys. Lett.*, Vol. 93, 261111, 2008.
16. Mitsui, T., Y. Wakayama, T. Onodera, Y. Takaya, and H. Oikawa, “Light propagation within colloidal crystal wire fabricated by a dewetting process,” *Nano Lett.*, Vol. 8, No. 3, 853–858, 2008.
17. Mitsui, T., Y. Wakayama, T. Onodera, Y. Takaya, and H. Oikawa, “Observation of light propagation across a 90° corner in chains of microspheres on a patterned substrate,” *Opt. Lett.*, Vol. 33, No. 11, 1189–1191, 2008.
18. <http://www.zemax.com/>, “The ZEMAX is software for optical system design,” Accessed 7 February 2010.
19. Utzinger, U. and R. R. Richards-Kortum, “Fiber optic probes for biomedical optical spectroscopy,” *J. Biomed. Opt.*, Vol. 8, No. 1, 121–147, 2003.

Sensorless Control of Permanent Magnet Synchronous Motor Using Luenberger Observer

P. Brandstetter, P. Rech, and P. Simonik

Department of Electronics, VSB-Technical University of Ostrava, Czech Republic

Abstract— The paper describes sensorless control of the permanent magnet synchronous motor (SMPM). The control method uses a Luenberger state reduced observer for estimation the back electromagnetic force. The speed, direction and position of rotor are calculated from this estimated quantity. The SMPM is controlled by the vector control with estimated signals in the feedback. The block scheme, mathematical description and simulation results are contained in the paper.

1. INTRODUCTION

The electric drives are a source of mechanic energy at various systems. They have a lot of advantages in comparison with the others sources mechanic energy. Especially it is high efficiency, great power density, excellent behavior at dynamic states and wide speed and torque ranges. The synchronous machine with permanent magnets (SMPM) can be considered as the most modern of them. The development of these machines is given by the evolvement of permanent magnets. Don't forget, that the electric drives consume considerable amount electric energy, which was made. For this reason, it is very important to improve their properties.

Present trends at this domain are the sensorless control. This control without speed sensor can be base on a many principles. Some of them are systems working with math model of the motor. The estimators and observers are two essential facilities for processing of them [1].

2. LUENBERGER STATE REDUCED OBSERVER

The behavior SMPM at dynamic or steady states is based on the equations which describe electric and mechanic dependencies of AC motor quantities. The state reduced order uses similar principle. The Luenberger reduced observer reconstructs the state variables based on the knowledge of inputs and outputs of the system. The outputs of the observer are induced voltages of the motor.

Mathematical model of the SMPM in the coordinates α , β and in the matrix form is given by Equation (1). This is a better option for mathematical expression of the Luenberger reduced observer [1].

$$\begin{bmatrix} u_{\alpha}^S \\ u_{\beta}^S \end{bmatrix} = \begin{bmatrix} R_S + L_S \frac{d}{dt} & 0 \\ 0 & R_S + L_S \frac{d}{dt} \end{bmatrix} \cdot \begin{bmatrix} i_{\alpha}^S \\ i_{\beta}^S \end{bmatrix} + K_E \cdot \omega_e \cdot \begin{bmatrix} \cos \theta_e \\ \sin \theta_e \end{bmatrix} \quad \frac{d}{dt} \begin{bmatrix} u_{i\alpha}^S \\ u_{i\beta}^S \end{bmatrix} = \begin{bmatrix} 0 & -\omega_e \\ \omega_e & 0 \end{bmatrix} \cdot \begin{bmatrix} u_{i\alpha}^S \\ u_{i\beta}^S \end{bmatrix} \quad (1)$$

Combining these equations and by modifications we complete SMPM matrix model designed for the observer:

$$\frac{d}{dt} \begin{bmatrix} i_{\alpha}^S \\ i_{\beta}^S \\ u_{i\alpha}^S \\ u_{i\beta}^S \end{bmatrix} = \begin{bmatrix} -\frac{R_S}{L_S} & 0 & -\frac{1}{L_S} & 0 \\ 0 & -\frac{R_S}{L_S} & 0 & -\frac{1}{L_S} \\ 0 & 0 & 0 & -\omega_e \\ 0 & 0 & \omega_e & 0 \end{bmatrix} \begin{bmatrix} i_{\alpha}^S \\ i_{\beta}^S \\ u_{i\alpha}^S \\ u_{i\beta}^S \end{bmatrix} + \begin{bmatrix} \frac{1}{L_S} & 0 \\ 0 & \frac{1}{L_S} \\ 0 & 0 \\ 0 & 0 \end{bmatrix} \begin{bmatrix} u_{\alpha}^S \\ u_{\beta}^S \end{bmatrix} \quad (2)$$

where

$u_{\alpha}^S, u_{\beta}^S, i_{\alpha}^S, i_{\beta}^S$ stator voltages and currents in α, β , coordinates

$u_{i\alpha}^S, u_{i\beta}^S$ electrical induced voltages in α, β coordinates

R_S, L_S stator resistance and inductance

ω_e, θ_e electric angular speed and rotor angle

K_E voltage constant of SMPM

The relations among stator voltages, stator currents and back electromagnetic force are the first two voltage equations. It is possible to derive previous equations from the electric circuit with resistance, inductance and source of induced voltage. The generated voltage is proportional to the angular speed. It describes the second matrix difference equations. There is a precondition of

constant angular speed during computing cycle. Short time interval and high mechanical constant are the parameters, which help realize it.

A simple reduced order observer named Luenberger observer can be applied for the stable estimation of the back electromagnetic force instead of a complex full order observer. The observer can be constructed according to following relations.

We can define the state space and state vector [2]:

$$\begin{aligned} \dot{\mathbf{x}} &= \mathbf{Ax} + \mathbf{Bu} \quad \text{where } \mathbf{x} = [i_{\alpha}^S \quad i_{\beta}^S \quad u_{i_{\alpha}}^S \quad u_{i_{\beta}}^S]^T \\ \mathbf{y} &= \mathbf{Cx} + \mathbf{Du} \end{aligned} \tag{3}$$

For the case where the state vector contains only two measured variables, reduced form of the Luenberger observer can be used. Therefore, we modify Equation (2) to the following form:

$$\begin{aligned} \frac{d}{dt} \begin{bmatrix} \mathbf{x}_n^S \\ \mathbf{x}_u^S \end{bmatrix} &= \begin{bmatrix} A_{11} & A_{12} \\ A_{21} & A_{22} \end{bmatrix} \cdot \begin{bmatrix} \mathbf{x}_n^S \\ \mathbf{x}_u^S \end{bmatrix} + \begin{bmatrix} B_1 \\ B_2 \end{bmatrix} \mathbf{u} \\ \mathbf{y} &= [\mathbf{I} \quad 0] \cdot \begin{bmatrix} x_n^S \\ x_u^S \end{bmatrix} \end{aligned} \quad \text{where } \begin{aligned} \mathbf{x}_n^S &= [i_{\alpha}^S \quad i_{\beta}^S]^T \\ \mathbf{x}_u^S &= [u_{i_{\alpha}}^S \quad u_{i_{\beta}}^S]^T \end{aligned} \tag{4}$$

The Luenberger reduced observer can be made from the classical theory of state observers [2]. State description and meaning of the matrix will be as follows:

$$\begin{aligned} \dot{\mathbf{z}} &= \mathbf{Dz} + \mathbf{Fi} + \mathbf{Gu}_i \quad \text{where } \mathbf{z} = \begin{bmatrix} z_1^S \\ z_2^S \end{bmatrix} \quad \mathbf{u}_i = \begin{bmatrix} u_{i_{\alpha}}^S \\ u_{i_{\beta}}^S \end{bmatrix} \quad \mathbf{i} = \begin{bmatrix} i_{\alpha}^S \\ i_{\beta}^S \end{bmatrix} \\ \widehat{\mathbf{x}}_u &= \mathbf{z} + \mathbf{Li} \end{aligned} \tag{5}$$

$$D = d[\mathbf{I}] = \begin{bmatrix} d & 0 \\ 0 & d \end{bmatrix} \quad \mathbf{F} = [-\mathbf{L}A_{11} + A_{22} + \mathbf{D}\mathbf{L}] = (R_S + dL_S) \begin{bmatrix} d & \omega_e \\ -\omega_e & d \end{bmatrix}$$

$$\mathbf{G} = [-\mathbf{L}B_1 + B_2] = - \begin{bmatrix} d & \omega_e \\ -\omega_e & d \end{bmatrix} \quad \mathbf{L} = [-\mathbf{D} + A_{22}] A_{22}^{-1} = L_S \begin{bmatrix} d & \omega_e \\ -\omega_e & d \end{bmatrix}$$

Last mathematical adjustment is necessary due to the implementation of the observer in Matlab-Simulink software. It requires state matrices only in traditional form.

$$\begin{aligned} \dot{\mathbf{x}} &= \mathbf{Ax} + \mathbf{Bu} \\ \mathbf{y} &= \mathbf{Cx} + \mathbf{Du} \end{aligned} \quad \text{where } \begin{aligned} \mathbf{u} &= \begin{bmatrix} i_{\alpha}^S \\ i_{\beta}^S \\ u_{i_{\alpha}}^S \\ u_{i_{\beta}}^S \end{bmatrix} \quad \mathbf{x} = \begin{bmatrix} x_{\alpha}^S \\ x_{\beta}^S \\ u_{i_{\alpha}}^S \\ u_{i_{\beta}}^S \end{bmatrix} \\ \mathbf{y} &= \begin{bmatrix} u_{i_{\alpha}}^S \\ u_{i_{\beta}}^S \end{bmatrix} \end{aligned} \tag{6}$$

$$\mathbf{A} = \begin{bmatrix} d & 0 \\ 0 & d \end{bmatrix} \quad \mathbf{B} = \begin{bmatrix} d(R_S + dL_S) & -\omega_e \cdot (R_S + dL_S) & d & -\omega_e \\ -\omega_e \cdot (R_S + dL_S) & d(R_S + dL_S) & \omega_e & d \end{bmatrix}$$

$$\mathbf{C} = \begin{bmatrix} 1 & 0 \\ 0 & 1 \end{bmatrix} \quad \mathbf{D} = L_S \begin{bmatrix} d & \omega_e & 0 & 0 \\ -\omega_e & d & 0 & 0 \end{bmatrix}$$

Now we have the final equations that were used in the simulation. The parameter d is used to set the observer, respectively, gives a compromise between speed and accuracy.

3. OBSERVER APPLICATION IN VECTOR CONTROL STRUCTURE

From the previous explanation we know the observer mathematic principle. After connection stator currents and voltages at stator frame reference we obtain an induced voltage waveform. But there can be the offset in this signal. Common derivation is one of the easy ways how to diminish it. The math model uses this possibility because the implementation into DSC is easy. Then it is possible to apply the function arctan 2 for calculation the rotor position. The difference with function arctan can be found only in changing the field of values from the interval $[-0.5\pi, 0.5\pi]$ to range $[-\pi, \pi]$. It is necessary to add angle 0 or π to actual rotor position according to direction of angular speed.

The movement direction is obtained from required speed at the first starting. Then the change of speed is evaluated from moment when the both components pass through the zero. This way

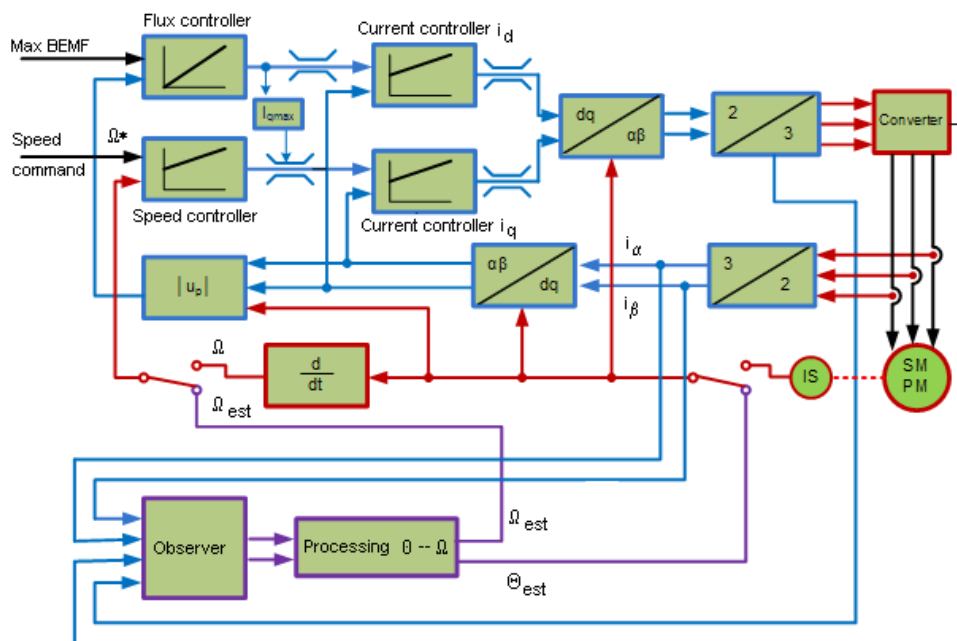


Figure 1: Control structure of PMSM with vector control and observer.

of processing appears as more accuracy in comparison to the speed direction calculated from angle increment.

Angular velocity can be obtained by derivative of rotor position angle. A better option is to calculate the speed from actual values of the two components of induced voltage. However, it should be noted that this method can calculate only the size of speed. Its direction is necessary to find another way. As can be seen the direction of the signal speed is very important because it is necessary for the estimation speed and angular position. The first option to get the signal to identify it is from the derivative sign. Another option for obtaining the direction of rotation is that at direction change or stop the components of the induced voltage have to pass zero.

The speed calculation is based on similar principle. The speed direction uses same signal as angle estimation. The benefit of this method is that the speed and angle calculation are independent. So the error in position estimation doesn't affect the magnitude of speed estimation if compare it with calculation from the change of position.

The speed is obtained from magnitudes of electrical induced voltages according to following equation:

$$\omega_{e_est} = \frac{1}{K_E} \sqrt{(u_{i\alpha}^S)^2 + (u_{i\beta}^S)^2} \operatorname{sign} \left(\frac{d\theta_{e_est}}{dt} \right) \quad (7)$$

The permanent magnet synchronous motor is controlled by typical vector control structure (see Figure 1). There is a possibility for change feedback signals by signal switch. The first switch position connects real rotor angle and speed information to feedback. The second switch position connects signals calculated by observer.

4. SIMULATION RESULTS

The simulation results are shown on the Figures 2 and 3. The curves of required speed and load torque were chosen so that they covered all operating states.

Figure 2 shows waveforms of important quantities of SMPM with control values of incremental sensor in feedback. It is suitable for comparison the estimation precision. We can see from them, that the described method provides high-quality results. Only around zero speed there is an inaccuracy on load. Really it is not possible to obtain the true information from estimation process around zero crossing. Because the input measure voltage values are low and then back electromagnetic force is also near zero. Figure 3 contains all curves as previous figure, but there are the calculated speed and angle values in feedback. As we are allowed to see from them, all curves are almost identical. It means that this estimation structure works and provides good results.

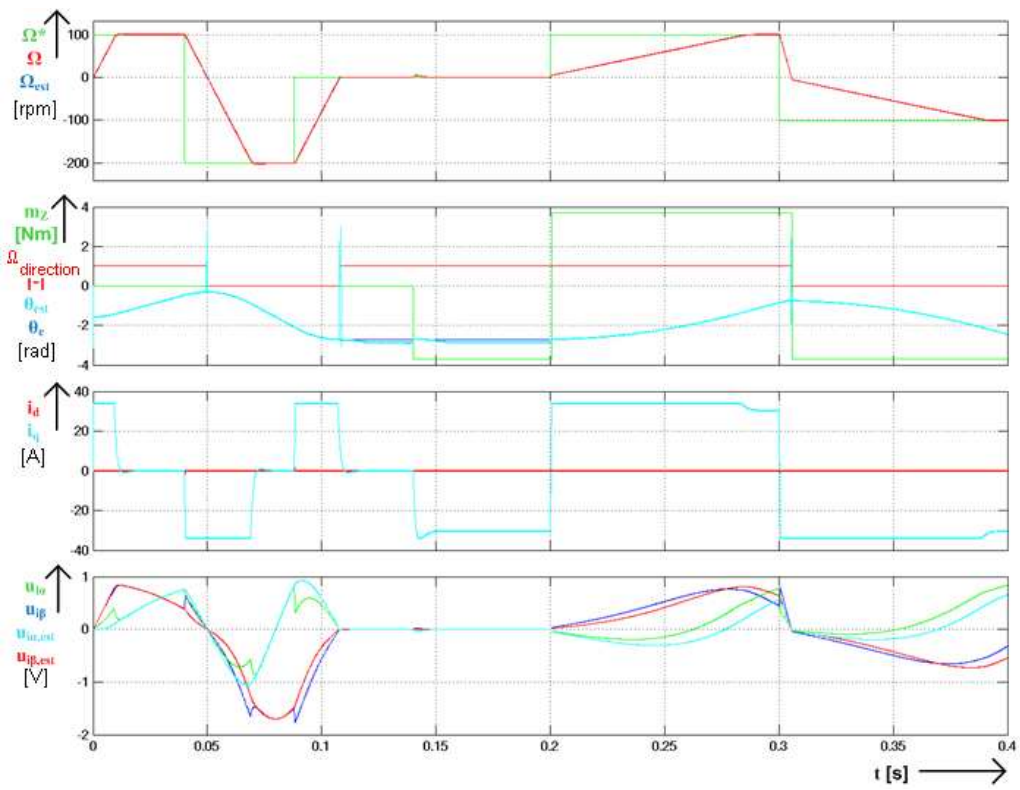


Figure 2: Vector control of PMSM with incremental sensor in feedback.

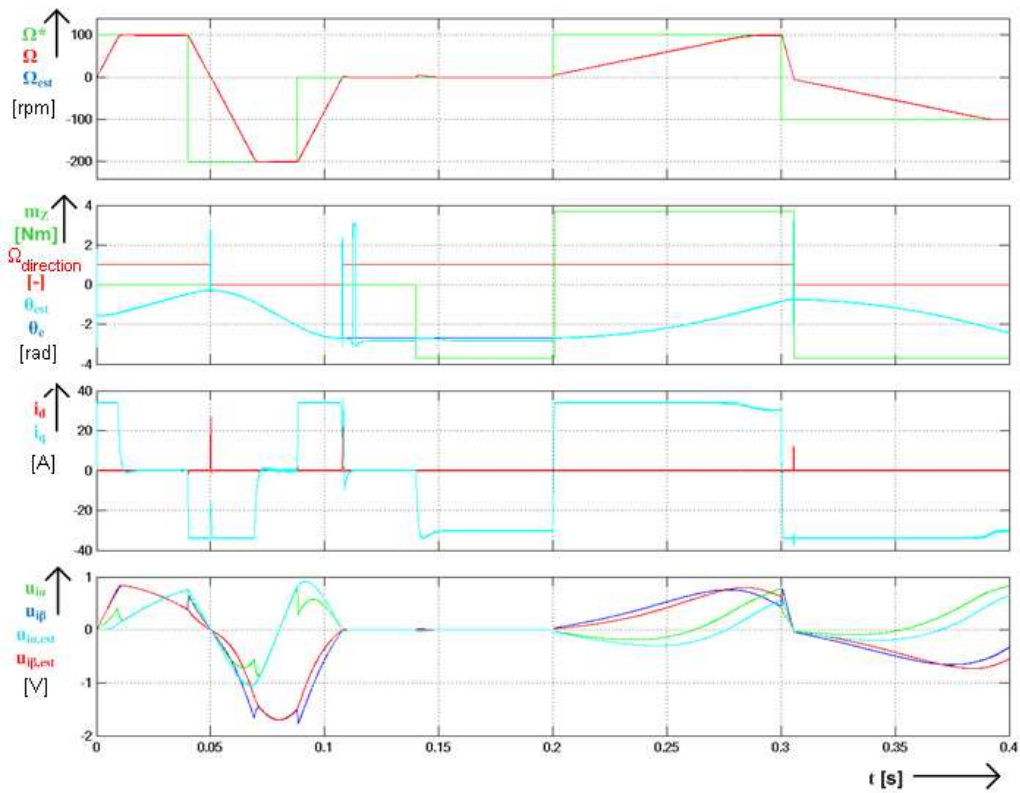


Figure 3: Sensorless vector control of PMSM without incremental sensor in feedback.

5. CONCLUSIONS

There are many problems at sensorless control of AC motor particularly at the low speed range. Because at this domain there are sluggish changes of signals and offsets, and inaccuracies of sensors are more evidently. The main advantages of sensorless vector control are following. Sensorless vector control brings the cost saving. If the drive doesn't have the speed sensor there are smaller dimensions and weight. Next they achieve more reliability and noise immunity by elimination the number of sensors. The computing power of digital signal controller (DSC) allows application with complicated math models and their processing in real-time. The paper is one of the possibilities of PMSM sensorless control and shows the basic advantages and disadvantages of the used method.

ACKNOWLEDGMENT

Research described in the paper was financially supported by the Czech Grant Agency (grant No. 102/08/0775).

REFERENCES

1. Brandstetter, P. A. C., *Control Drives — Modern Control Methods*, VSB-Technical University of Ostrava, 1999.
2. Kim, J. K. and S. K. Sul, "High performance PMSM drives without rotational position sensors using reduced order observer," *Proceedings of Industry Applications Conference*, 75–82, Orlando, USA, 1995.
3. Chlebis, P., P. Moravcik, and P. Simonik, "New method of direct torque control for three-level voltage inverter," *Proceedings of 13th European Conference on Power Electronics and Applications*, Barcelona, Spain, 2009.
4. Osmancik, L., M. Polak, P. Simonik, L. Hrdina, P. Skotnica, and P. Palacky, "Digital signal processor TMS320F2812 and its application in electric drives," *Proceedings of International Conference on Applied Electronics*, 129–132, Pilsen, Czech Republic, 2006.
5. Lettl, J., "Matrix converter induction motor drive," *Proceedings of 12th International Power Electronics and Motion Control Conference*, 787–792, Maribor, 2006.
6. Perdukova, D. and P. Fedor, "Fuzzy model based control of dynamic system," *Journal of Electrical Engineering*, Vol. 7, No. 3, University Polytechnics Romania, 2007.

Control Algorithms of Active Power Filters

P. Brandstetter, P. Chlebis, and P. Simonik

Department of Electronics, VSB-Technical University of Ostrava, Czech Republic

Abstract— The paper deals with the control methods of the active power filter with voltage source which can be used for reduction of high harmonics in the supply current. For the correct function of the filter, it is necessary to determine magnitude of the currents, which have to be added to load current so as to eliminate high harmonics in the supply current. Several methods of the filter current control are described. Theoretical assumptions are confirmed by practical test on laboratory model of the active power filter which is controlled by modern digital signal processor.

1. INTRODUCTION

The power semiconductor converters are becoming to typical load in the distribution mains. Input circuits of these converters are often designed as a non-controlled rectifier, which consists of power semiconductor devices. Converter is non-linear load in the mains and its current consumption it is not only sinusoidal, but there are higher current harmonics, which unfortunately influence feed system. For reduction of the higher harmonics influence the filters compounded by inductors and capacitors are used. However these devices have many basic disadvantages, for example they and inner line impedance are making resonance circuit with sharp tuned resonances. All these undesirable properties it is possible to remove by using active power filters. For this purpose a semiconductor converter with current or voltage source shows as suitable. That converter is able to add or to take the theoretically any course of current in mains. The active filters with current source have more complicated structure and their purchase price is higher than price of the filters with voltage source. That is why the active power filters with voltage source are often used and we are interesting in them in our research [1, 2].

2. ACTIVE POWER FILTER WITH VOLTAGE SOURCE

The active power filter (APF) consists of six a semiconductor switches (IGBT transistors), *dc* link capacitor as a voltage source and reactors for limitation of the current rate of rise (see Fig. 1). A fast microcomputer control system is needed of course. Principle of the filter is such, that a filter current is injected to mains by generation of output voltage out of converter. It can be achieved desired course of the current by suitable switching of converter's switches. A voltage of the *dc* link capacitor (voltage source) has to be kept with desired value. It is achieved by means of an active power flow through the converter. For correct work of the filter it is necessary exactly and fast to determine a magnitude of the filter currents, which have to be added to load currents so as to be removed higher harmonics.

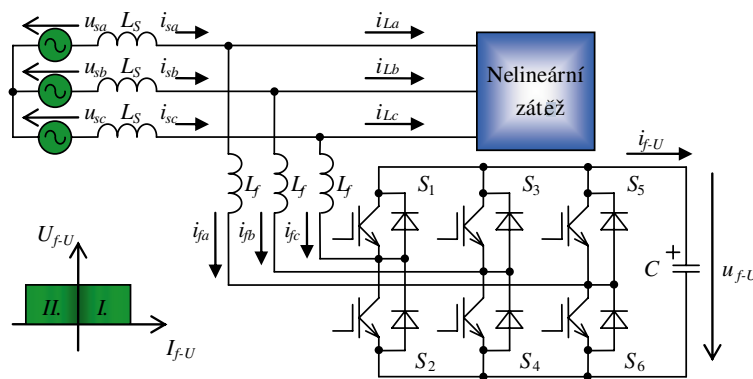


Figure 1: Active power filter with voltage source.

It is effort to achieve as high rate of current rise as possible, because in this way the highest harmonics are filtered. At the same time the ripple of current increases if converter switching frequency is not high enough.

The real effect of the filtration depends on the performance of the filter and on the properties of the loads to be compensated as well. In the case of supply system with finally short circuit power the inner line impedance have to be taken into consideration.

The filter currents are calculated from the measured load currents. There exist several ways how to solve the problem of determination of the filter currents. The next chapter will describe the control methods which were examined at the Department of Electronics.

3. CONTROL METHODS

For the correct function of the filter, it is necessary to determine magnitude of the currents, which have to be added to load current so as to eliminate high harmonics.

This problem will be made easy very much by establishing a rotation axis system and by transformation load currents into this system. Rotation system forms two axes d , q , d -axis is in direction of supply voltage space vector. By the vector rotation with an angle θ , where θ is an angle between α -axis and d -axis, the two current components i_{Ld} and i_{Lq} are obtained. The component i_{Ld} is proportional to active power and the component i_{Lq} is proportional to reactive power.

Vector rotation and inverse rotation are calculated by following equations:

$$\begin{bmatrix} i_{Ld} \\ i_{Lq} \end{bmatrix} = \begin{bmatrix} \cos \theta & \sin \theta \\ -\sin \theta & \cos \theta \end{bmatrix} \cdot \begin{bmatrix} i_{L\alpha} \\ i_{L\beta} \end{bmatrix} \quad \begin{bmatrix} i_{L\alpha} \\ i_{L\beta} \end{bmatrix} = \begin{bmatrix} \cos \theta & -\sin \theta \\ \sin \theta & \cos \theta \end{bmatrix} \cdot \begin{bmatrix} i_{Ld} \\ i_{Lq} \end{bmatrix} \quad (1)$$

We can express the current components i_{Ld} and i_{Lq} as a sum of direct component and alternating component:

$$\begin{bmatrix} i_{Ld} \\ i_{Lq} \end{bmatrix} = \begin{bmatrix} i_{Ld_DC} & i_{Ld_AC} \\ i_{Lq_DC} & i_{Lq_AC} \end{bmatrix} \cdot \begin{bmatrix} 1 \\ l \end{bmatrix} \quad (2)$$

The DC component i_{Ld_DC} determines magnitude of fundamental harmonic of the active power and the AC component i_{Lq_AC} is consisted of harmonics. The same is valid for reactive power in the q -axis.

The purpose of the active power filtration is an elimination of alternating component in both axis, or direct component in q -axis for compensation of reactive power. For a calculation of reference filter currents there are several methods. We are intended on three of them — determination of reference currents by means of high band pass filter, mean value method and PI-controller method. Control structure of the active filter is shown in Fig. 2.

For the correct function of the filter, it is necessary to determine magnitude of the currents, which have to be added to load current so as to eliminate high harmonics.

3.1. Method with High Band Pass Filter

A principle of the method is removing of the DC component i_{Ld_DC} by a high band pass filter (HBPF). The load currents are transformed to two axis system $[\alpha, \beta]$ and then they are rotated to orientated system $[d, q]$ by means of angle θ . The current component i_{Ld} is filtered by HBPF so as to obtain only alternating current component. The current, which is necessary to keep up the voltage of the capacitor, is taken from it. Then follows inverse vector rotation and after changing of sign of the reference filter currents are obtained. By that way it is compensated all reactive current and power factor $\cos \varphi$ is 1. If current component i_{Ld} is filtered then high harmonics of reactive current are only compensated and power factor $\cos \varphi$ is unchanged. We chose the 4th order Butterworth low pass filter as the HBPF with cut off frequency $f_c = 150$ Hz.

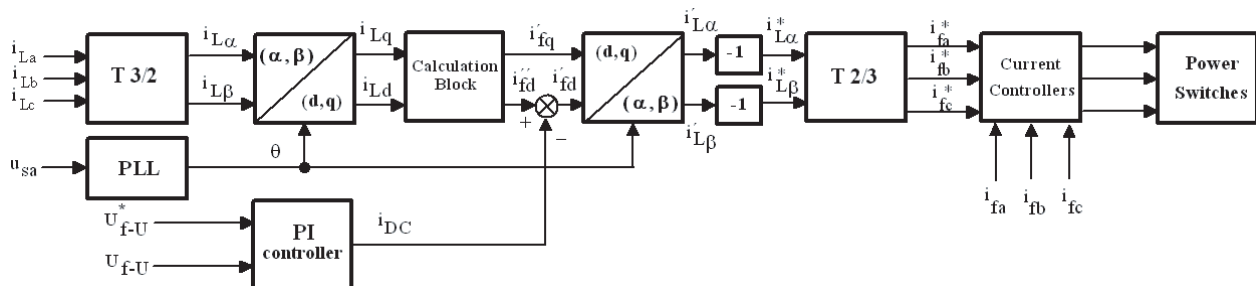


Figure 2: Control structure of active power filter.

3.2. Mean Value Method

For right compensation dynamic, it is necessary to determinate magnitude of the *DC* component i_{Ld_DC} . The equation, that is suitable for calculating of mean value, is:

$$i_{Ld_DC}(t) = \frac{1}{T} \int_{t-T}^t i_{Ld}(t) dt \quad i''_{fd} = i_{Ld} - i_{Ld_DC} \quad i'_{fd} = i_{Ld} \quad (3)$$

$T = T_0$ is fundamental period.

In digital form:

$$i_{Ld_DC}(k) = \frac{1}{N} \sum_{k-N}^k i_{Ld}(kT_S) \quad \text{or} \quad i_{Ld_DC}(k) = \frac{1}{N} \left[\sum_{k-N}^k i_{Ld}(k) - i_{Ld}(k-N) \right] \quad (4)$$

$N = T/T_S$, T_S is sampling period. N is a element number of a circular buffer.

We can calculate in one period of fundamental harmonic this way. Power difference between actual and calculated direct component is compensated from storage energy of the condenser. So the speed of active power determination influences voltage magnitude of the voltage source and with faster determination of mean value, the condenser capacity may be smaller. The mean value determination inserted in control structure is shown in Fig. 3.

3.3. PI-controller Method

The method uses the PI-controller of *dc* link capacitor voltage (see Fig. 4). It presents very simple way of control active filter being sufficient for non-linear loads with slower current changes. Direct current component in *d*-axis is removed by PI-controller which lets only active current flow needed for keeping condenser voltage through filter converter.

The current components are described by following equations:

$$i'_{fd} = i_{Ld} - i_{DC} \quad i'_{fd} = i_{Lq} \quad (5)$$

4. CURRENT CONTROL OF THE ACTIVE POWER FILTER

The current control can be performed by two-level hysteresis controllers or PI-controllers with vector pulse-width modulation (PWM) [3, 5].

The two-level hysteresis controller is classical controller which is very simple and fast, but requires fast sampling frequency in the case of digital signal processor (DSP) implementation (see Fig. 5).

The filter currents in axes *d*, *q* can be controlled by PI-controllers (see Fig. 6). The outputs of the controllers are reference voltages u_{fdh}^* and u_{fqh}^* . However the current in *d*-axis is not only affected by voltage in this axis, but also by voltage in *q*-axis. That means, there is mutual coupling between *d*-axis and *q*-axis and must be cancelled in block of decoupling. The voltages u_{fdh}^* and u_{fqh}^* are afterwards transformed to α , β -components and enter to PWM modulator of the converter. There is used vector PWM technique.

5. EXPERIMENTAL RESULTS

The active power filter was practically performed according to Fig. 1. The IGBT switches of converter are for frequency up to 20 kHz, maximum current is 78 A and maximum collector-emitter voltage is 1200 V. The filter is controlled by control system based on the Texas Instruments

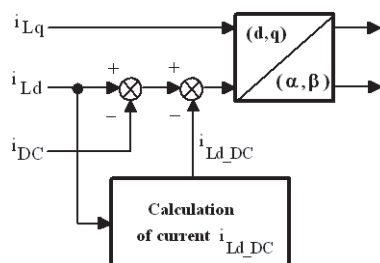


Figure 3: Mean value method.

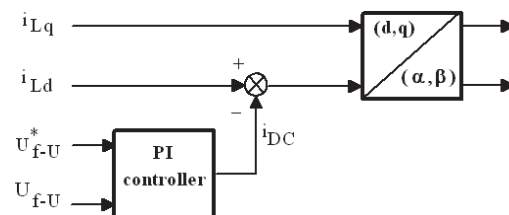


Figure 4: PI-controller method.

TMS320F2812 Digital Signal Processor (see Fig. 7). Generation of TMS320C28x™. digital signal controllers are the industry’s first 32-bit DSP-based controllers with on-board Flash memory and performance up to 150 MIPS [4].

Figures 8 and 9 show time courses of important quantities of the APF. Fig. 8 shows current waveforms in steady state. Fig. 9 shows current waveforms in case of load change from 0% to 100%. There we can see the right and quick filtration.

The first trace in both figures is the input current of the non-linear load (three phase non-controlled rectifier loaded by resistor $R = 20\Omega$ and inductor $L = 60\text{mH}$). The second trace is output current of the proposed APF which is injected to the power supply line by the APF. The third trace is line current compensated by proposed APF. The current scale is 10 A per division. The current control of the APF was performed by two-level hysteresis controllers.

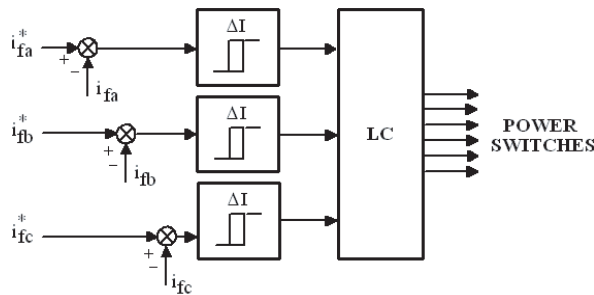


Figure 5: Two-level hysteresis current controllers.

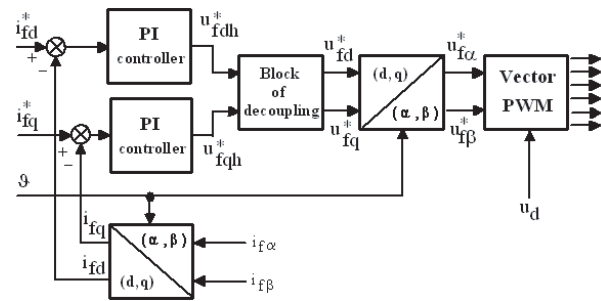


Figure 6: PI-controllers with vector PWM.

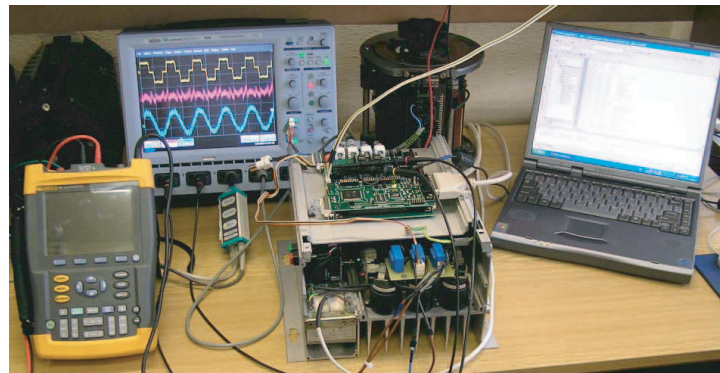


Figure 7: Laboratory workplace with active power filter.

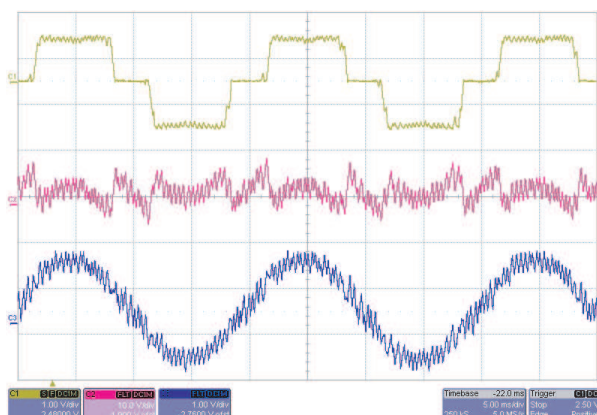


Figure 8: Time courses of important quantities of the APF in steady state.

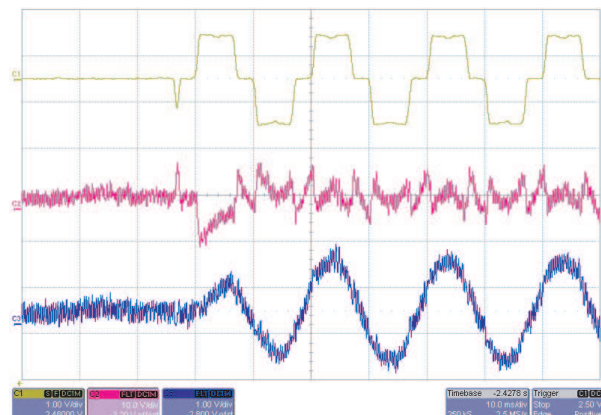


Figure 9: Time courses of important quantities of the APF at load change from 0% to 100%.

6. CONCLUSION

Power quality problems are important in most commercial, industrial and utility networks. In the paper there is described active power filter which uses the rotating axis system enabling simple separate active and reactive current components. Some control algorithms for removing of high harmonics and current control of active power filter are described here. The practical results, which show the dynamic state system performances, are presented.

ACKNOWLEDGMENT

Research described in the paper was financially supported by the Czech Grant Agency (grant 102/09/P665).

REFERENCES

1. Brandstetter, P., "Research of active power filters," Research Report of Project GA CR 102/99/0193, VSB, Technical University of Ostrava, 2001.
2. Brandstetter, P., P. Chlebis, P. Palacky, and P. Simonik, "Unconventional soft switched parallel active power filter," *Proceedings of 10th International Scientific Conference Electric Power Engineering*, 347–351, ISBN 978-80-248-1947-1, Kouty nad Desnou, Czech Republic, 2009.
3. Chlebis, P., P. Moravcik, and P. Simonik, "New method of direct torque control for three-level voltage inverter," *Proceedings of 13th European Conference on Power Electronics and Applications*, ISBN 978-1-4244-4432-8, Barcelona, Spain, 2009.
4. Osmancik, L., M. Polak, P. Simonik, L. Hrdina, P. Skotnica, and P. Palacky, "Digital signal processor TMS320F2812 and its application in electric drives," *Proceedings of International Conference on Applied Electronics*, 129–132, ISBN 978-80-7043-442-0, Pilsen, Czech Republic, 2006.
5. Lettl, J., "Matrix converter induction motor drive," *Proceedings of 12th International Power Electronics and Motion Control Conference*, 787–792, ISBN 1-4244-0121-6, Maribor, 2006.

Compatibility of Different Types of Frequency Converters with Supply Network

J. Lettl and J. Bauer

Faculty of Electrical Engineering, Czech Technical University in Prague, Czech Republic

Abstract— The presented paper compares in light of the electromagnetic compatibility (EMC) with the supply network three frequency converter topologies that are being used for supplying of induction machines. The topic of the EMC of the converters becomes very important in these days, because some of the semiconductor converters can be ranked as the worse supply network polluters. These negative side effects of the converters were previously overlooked, but with the widespread of power electronics they can not be ignored more. That is why the test beds of these three frequency converter input parts were realized and experimental results obtained by the measurement were analyzed and discussed.

1. INTRODUCTION

Nowadays the indirect frequency converter is typically used for the induction motor feeding. This converter consists of the input rectifier, DC-link capacitor, and output inverter. The control algorithm of the output inverter has substantial influence on the induction machine behaviour. The weakness of the indirect frequency converter consists in its input part. As the input rectifier usually acts a three phase diode rectifier or sometimes a controlled thyristor rectifier that allows the DC-link voltage control. In case of the diode rectifier energy can flow through in one direction only, therefore energy recuperation is not possible. The rectifier also does not allow the power factor control and it consumes the non sinusoidal current. As a result the supply network is loaded by higher harmonics and reactive power.

In recent years especially the traction vehicles are equipped by rectifiers that allow bidirectional power flow, so called “Compatible Rectifiers” or “Active Front End”. The rectifier has an inductor on the input and it is controlled mostly by PWM strategy. The rectifier controlled in this way consumes current of required waveform, which is mostly sinusoidal. It works with a given phase displacement between the consumed current and supply voltage, i.e., the power factor can be controlled. The energy recuperation is also possible and the converter has in such case minimal influence on the supply network.

The direct frequency converters are not so widespread because their control requires more complex control algorithms that were not realizable till now without powerful microprocessors. “Matrix Converter” belongs to the direct frequency converters category. The name “Direct Frequency Converter” comes out of the fact that they do not need the DC-link. The output voltage is produced by direct switching of the input phases to the output phases. In consequence the maximal output voltage value is limited to 86% of the input voltage amplitude. To the main advantages of matrix converter belongs operation in all four quadrants, therefore the recuperation is possible. The converter has high dynamics, enables power factor control, and consumes nearly sinusoidal current from the supply network. It means that the matrix converter does not load supply network with higher harmonics and it can work with given power factor. As mentioned above, the converter has no DC-link, which is the great advantage of the converter, because the accumulation element in the DC-link is mostly very large, takes large room, and usually is very heavy.

2. INDIRECT FREQUENCY CONVERTER

Block diagram of the common indirect frequency converter is in Fig. 1. The converter consists of input rectifier, DC link, and output inverter. When the recuperation is not possible, the DC link must be also equipped with the braking chopper that converts excessive energy into the heat.

2.1. Diode or Thyristor Rectifier

Indirect frequency converter with 6 pulse diode rectifier on its input is the most used variant. Rectifier made of diodes is robust and failure-free. But it does not allow recuperation and due to non-linear characteristic the turning-on delays causes the phase shift between the supply voltage first harmonic and the consumed current first harmonic. This shift leads to power factor degradation and the reactive power is consumed. Another problem lies in the shape of the consumed current

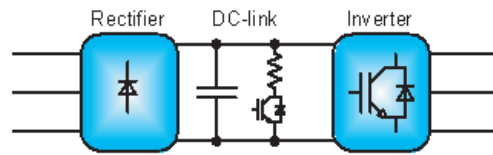


Figure 1: Block diagram of the indirect frequency converter.

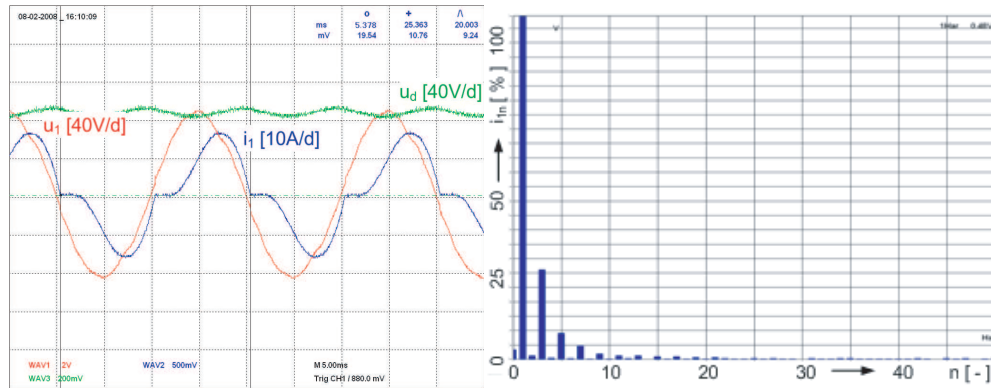


Figure 2: Diode rectifier waveforms and input current harmonic analysis.

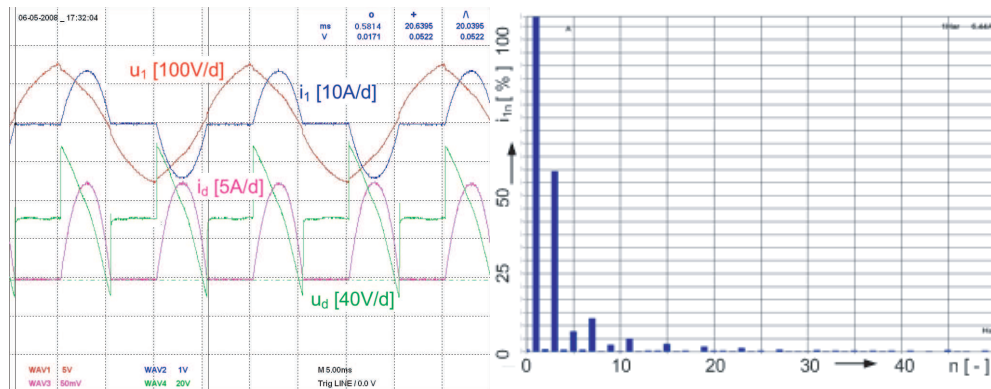


Figure 3: Thyristor rectifier waveforms and input current harmonic analysis.

waveform. The non-linearity of semiconductor switches and commutation leads to high content of higher harmonics. Fig. 2 shows the voltage and current waveforms of one phase of the diode rectifier. The harmonic analysis of the input current proves high content of the higher harmonics.

These harmonics cause the voltage drop on the supply network's inductances and degradation of the network voltage waveform. It can lead to failures of other devices supplied from the network. The situation in case of the thyristor rectifier is less convenient because of the thyristors' phase control, which is used for regulating mean value of output voltage. It causes phase shift between input current first harmonic and input voltage. The phase shift depends on the rectifier control angle. The waveforms taken from the thyristor rectifier are shown in Fig. 3.

2.2. PWM Rectifier

To eliminate the side effects of the diode rectifier the idea of pulse width modulation was implemented to rectifier control algorithm. To use the PWM control, it is necessary to equip the converter with switches that can be both turned-on and moreover turned-off, and can transfer high electric power. This condition was fulfilled with development of IGBT's. The rectifier can be then controlled to consume nearly sinusoidal current and to operate with chosen power factor, or the PWM rectifier can be controlled in such a way to be able partly compensate the non-harmonic consumption of the other devices connected to the supply network.

The rectifier is made of input inductance and IGBT switches. Fig. 4 shows one phase PWM rectifier. The inductance on the input creates two separated sinusoidal voltage phasors. Therefore

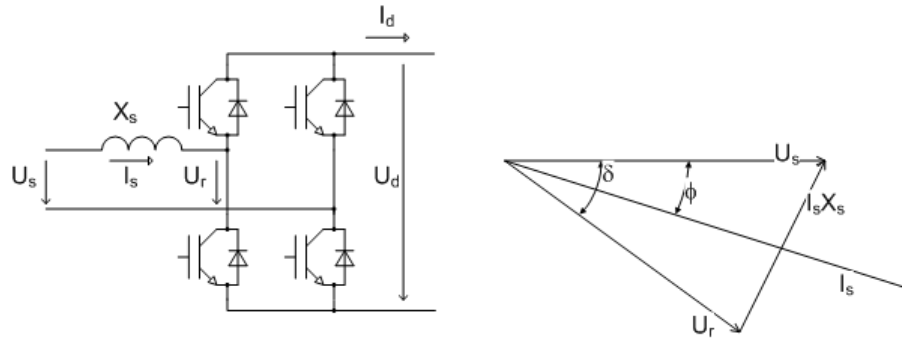


Figure 4: PWM rectifier schematic diagram and phasor diagram.

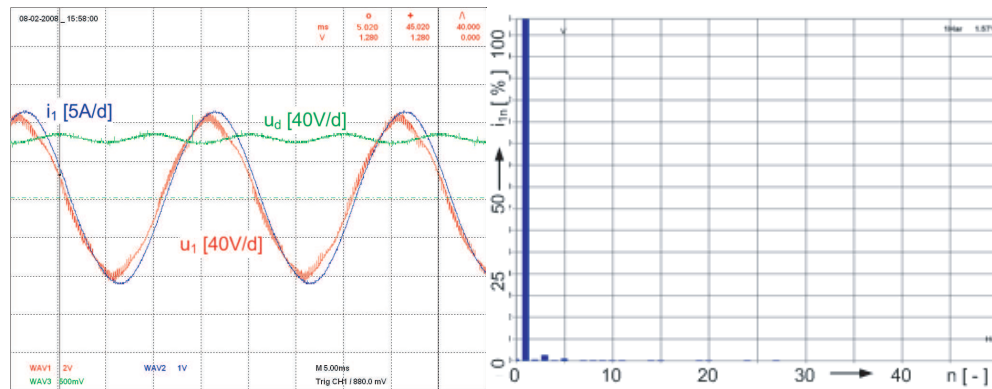


Figure 5: PWM rectifier waveforms and input current harmonic analysis.

the direction of the power flow depends on the phase angle between these two phasors (see Fig. 4).

Usually the rectifier is controlled to consume sinusoidal current and to work with power factor equal to unity. The input current and voltage waveforms of the rectifier with PWM control are shown in Fig. 5.

The simple control algorithm can be derived from transferred power. In order to maintain the output rectified voltage constant the powers on the both sides of the inductor must be equal (1).

$$P_{SR} = (U_s U_r / X_s) \sin \delta = U_s I_s \cos \phi \quad (1)$$

After several adaptations of Equation (1) and with help of phasor diagram in Fig. 4, we obtain the two final Equation (2) for the simple control of the PWM rectifier.

$$\delta = \arctg \frac{\omega L I_s (1)m}{U_{sm}} \quad \text{and} \quad z = \frac{U_r (1)m}{U_{dAV}} \quad (2)$$

3. MATRIX CONVERTER

The converter belongs to the direct frequency converters category. The output voltage is produced by direct switching of the input phases to the output phases. This means that the converter has no DC-link. The absence of the DC-link means that the output voltage amplitude is limited to 86.6% of the input voltage amplitude at consideration of the sinusoidal input currents. Higher voltages can be achieved by overmodulation that causes input current distortion.

The matrix converter is controlled by indirect space vector modulation method. The method is based on the virtual DC-link idea. The converter is virtually divided into two parts: a rectifier part and an inverter part (see Fig. 6). This method generates a desired output voltage vector and at the same time it consumes from the supply network a current space vector that keeps constant input displacement factor $\cos \varphi_{in}$ (see Fig. 7).

Because of the absence of the accumulation elements in the DC-link the rectifier and the inverter parts are not completely independent. The converter transfer function can be expressed as (3).

$$\underline{u}_{out} = M_{u-\alpha\beta} \cdot M_{i-\gamma\delta} \cdot \underline{u}_{in} \quad (3)$$

Figure 8 shows the input current, input and output voltage waveforms of the matrix converter.

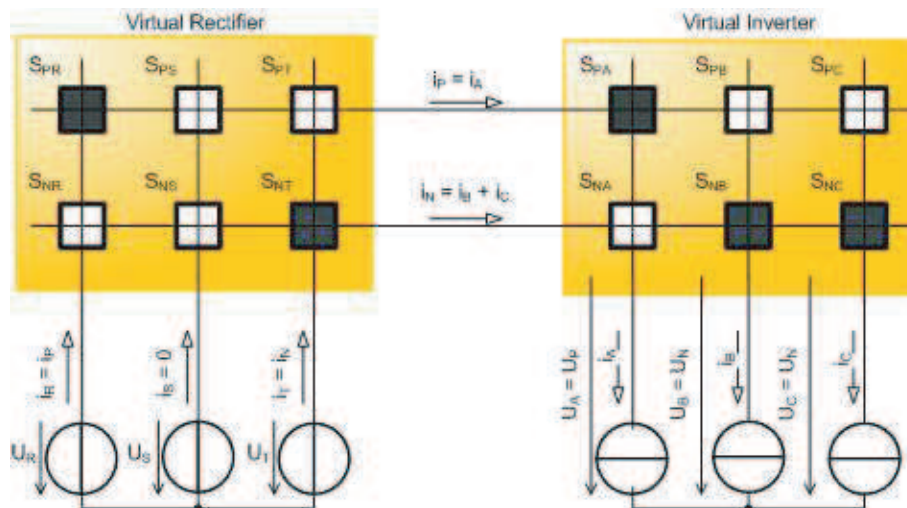


Figure 6: Virtual DC-link concept applied on the matrix converter topology.

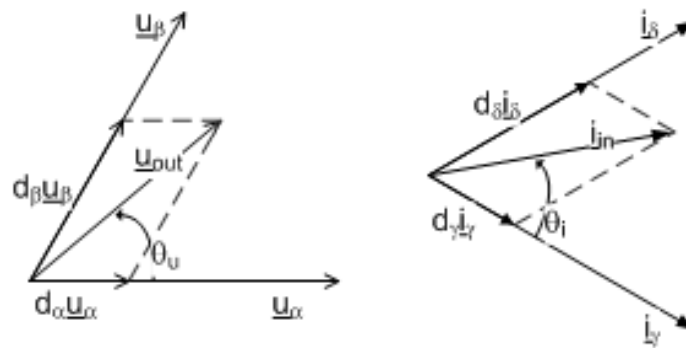


Figure 7: Virtual rectifier and inverter phasor diagrams.

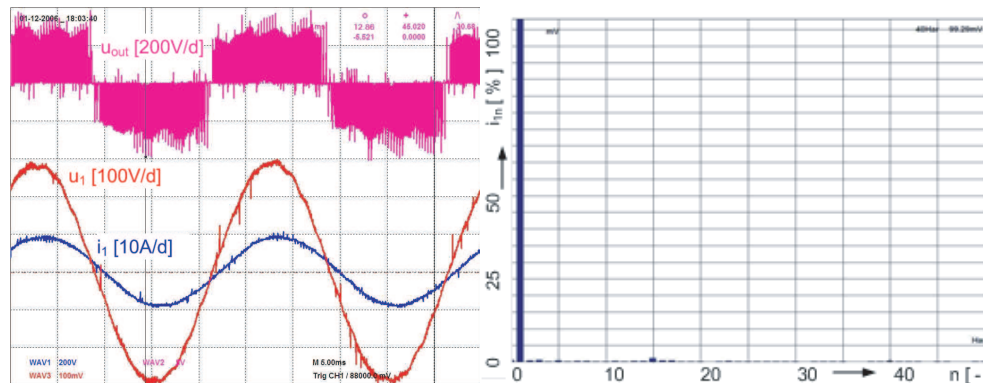


Figure 8: Matrix converter waveforms and input current harmonic analysis.

4. RESULTS COMPARISON

The different waveforms currents consumed by the converters can be seen from the oscillograms. Mathematically can be the non-sinusoidal shape of the input current waveforms expressed by the harmonic coefficients (4). These coefficients show amount of the harmonics content in the consumed current.

$$\nu = \frac{I_{(1)}}{I}, \quad THD = \frac{\sqrt{\sum_{n=2}^{\infty} I_{(n)}^2}}{I_{(1)}}, \quad k_z = \frac{\sqrt{\sum_{n=2}^{\infty} I_{(n)}^2}}{I} \quad (4)$$

Calculated coefficients for all three converter types are summarized in Table 1.

Table 1: Harmonic coefficients.

Coefficient	Diode rectifier	Thyristor rectifier	PWM rectifier	Matrix converter
ν	92,83%	87,45%	99,78%	99,98%
THD	40,16%	55,36%	2,12%	1,70%
k_z	37.16%	48,43%	2,12%	1,70%

5. CONCLUSION

The harmonic coefficients that are summarized in Table 1 and taken oscillograms show the differences between these four converter topologies. The worse supply network polluter is thyristor rectifier. This is caused by phase control of the rectifier. Little bit better are the waveforms obtained from diode rectifier. But the greatest disadvantage of these two topologies is the fact that they do not support recuperation. The next two topologies, the rectifier with PWM control and the matrix converter look more promising. Both of them do not load supply network with reactive power, they consume sinusoidal current and are capable of recuperation. This was also proved by the performed harmonic analysis. From these two topologies, the topology of the matrix converter looks more promising. Compared to indirect frequency converter it does not need the DC-link.

REFERENCES

1. Lettl, J. and R. Dolecek, "EMC increasing of PWM rectifier in comparison with classical rectifier," *Radioengineering*, Vol. 17, No. 4, 93–100, 2008.

Leakage Inductance Determination for Transformers with Interleaving of Windings

R. Doebbelin and A. Lindemann

Institute of Electric Power Systems, Otto-von-Guericke-University Magdeburg, Germany

Abstract— A diversity of formulas is given in literature for leakage inductance calculation of transformers with interleaving of windings. In the paper, the meaning of included terms and details of the application for concentric and pie windings transformers shall be discussed. Considering the limitation of common formulas to magnetically symmetric transformers an alternative approach shall be demonstrated, which enables leakage inductance prediction also in the case of transformers with magnetically asymmetric arrangements of windings.

1. INTRODUCTION

Several aspects of the operation of power-electronic circuits with transformers are significantly influenced by the leakage inductance of the respective transformer. For instance, it concerns power transfer capability of the circuit and power semiconductor stress parameters. The tendency to higher switching frequencies of power-electronic apparatuses results in an increasing relevance of low transformer leakage inductance values. Mostly, the so-called interleaving of windings (i.e., the fragmentation of the primary and the secondary windings into a certain number of sub-windings and alternate interleaving of primary and secondary sub-windings) is used to meet this requirement.

Using an appropriate approximation method it is possible to determine the leakage inductance of a transformer already in the design phase on the basis of predicted geometry parameters. Thus, circuit simulation can be used to shorten the development process of power-electronic apparatuses. Formulas which are given in literature generally rely on an approximation method for leakage inductance determination which has been established by Rogowski [1]. It is based on the consideration of the energy of the leakage magnetic field and applies to a transformer design with windings arranged on the same leg. The basic formula of this method is

$$L_L = \mu_0 \cdot N^2 \cdot l_m \cdot \lambda \cdot k_\sigma \quad (1)$$

with L_L — leakage inductance, μ_0 — absolute permeability, N — number of turns of the winding to which the leakage inductance refers, l_m — mean length per turn for whole arrangement of windings, λ — relative leakage conductance (depending on geometry parameters and on the degree of interleaving of windings), k_σ — Rogowski factor (also depending on geometry parameters).

The formulas which can be found in contemporary technical literature mostly represent simplified variants of the mentioned basic formula. Usually the Rogowski factor (whose value is nearly 1 in most arrangements) is omitted and the formula describing the relative leakage conductance is included in the main formula. Often, constant factors like absolute permeability and numerical values are merged into one coefficient, so that the physical background of the formula is not recognizable anymore, e.g., in [2]. In some cases different formulas are given for a transformer design without interleaving of windings and for transformer arrangements with interleaving of windings, e.g., in [3]. The degree of interleaving is considered in literature by the number of the couples of sub-windings [4, 5] or by the number of interfaces (insulating interspaces) between the single sub-windings of an arrangement of windings [6, 7]. Furthermore, the aim to present a universal formula which is valid for transformer versions with concentric and also with pie windings arrangements often causes some confusion. It also results from the diversity of terms which are used for the dimensions of windings (e.g., breadth, width, traverse, build, height, length) comparing the formulas and their descriptions which are given in different books and papers.

2. LEAKAGE INDUCTANCE CALCULATION FOR MAGNETICALLY SYMMETRIC ARRANGEMENTS

To enable a correct application of a formula for leakage inductance calculation both for transformers with concentric and transformers with pie windings, the attribution of the chosen symbols for geometry parameters to the respective dimensions of the arrangement of windings has to be made

quite clear. Therefore, based on variants which are valid for transformer versions without and with interleaving of windings, the following representation of the formula is proposed:

$$L_L = \mu_0 \cdot N^2 \cdot \frac{l_m}{n_{if}^2 \cdot X_{par-lf}} \cdot \left(\frac{\Sigma X_{perp-lf}}{3} + \Sigma \delta \right) \quad (2)$$

with $\Sigma X_{perp-lf}$ — sum of the dimensions of all sub-windings which are orientated perpendicular to the leakage flux, X_{par-lf} — dimension of the sub-windings which is orientated parallel to the leakage flux, $\Sigma \delta$ — sum of the thicknesses of all insulating interspaces between the sub-windings, n_{if} — number of insulating interspaces between the sub-windings (no consideration of Rogowski factor).

Thus, in this formula the respective dimensions of the sub-windings are identified based on a comparison between their orientation and the orientation of leakage flux within the core window. The meaning of the geometry parameter symbols and the path of leakage flux Φ_l within the core window are illustrated in principle in Fig. 1 assuming the leakage flux to be concentrated in the insulating interspaces between the windings or sub-windings.

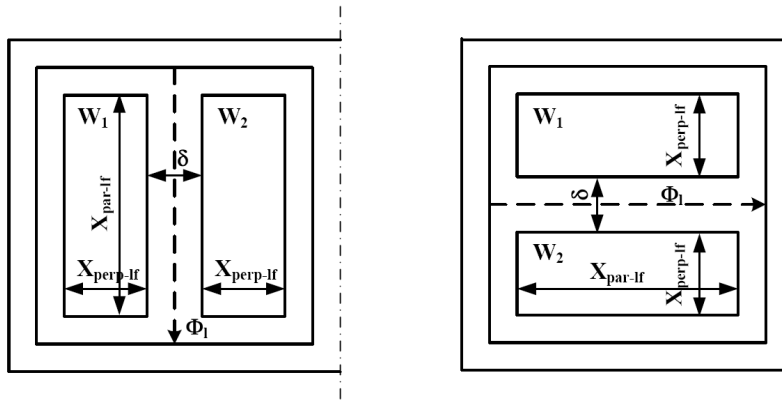


Figure 1: Illustration of attribution of the dimensions of windings or sub-windings used in formula (2) and their orientation compared to the orientation of leakage flux Φ_l within the core window (left: concentric windings, right: pie windings, only left hemisphere of arrangement displayed).

The proposed representation and also the variants of the formula which are given in literature enable a relatively uncomplicated approximate calculation of the leakage inductance of a transformer even in the case of interleaving of windings. However, it has to be stated that the scope is limited to magnetically symmetric arrangements of windings. These transformer versions are characterized by an odd number of primary sub-windings and an even number of secondary sub-windings or vice versa. Furthermore, the number of turns of outer sub-windings is half of the number of turns of the inner sub-windings which belong to the same group of sub-windings (inner primary sub-windings if the outer sub-windings belong to the primary winding; inner secondary sub-windings if the outer sub-windings belong to the secondary winding). In connection with this, it can be assumed that the outer sub-windings show a dimension perpendicular to the leakage flux which is half of the same dimension of an inner sub-winding which belongs to the same group of sub-windings.

3. UNIVERSAL LEAKAGE INDUCTANCE CALCULATION

In the majority of applications magnetically symmetric transformer versions are used because they show the lowest leakage inductance values considering a certain degree of interleaving of windings. However, also magnetically asymmetric designs of windings are used in praxis. For instance in transformers for capacitor discharge welding machines a magnetically asymmetric design of windings is often applied to enable a variation of the turns ratio by means of alteration between series and parallel connection of the primary sub-windings. Also transformer versions, whose primary sub-windings have identical numbers of turns independent of the location of the respective sub-windings in inner or outer position, represent a typical example of magnetically asymmetric transformers.

In formula (2) and its variants which are given in literature it is not possible to consider the real design and arrangement of sub-windings of a magnetically asymmetric transformer because only the sum value of the relevant dimension of the single sub-windings and the sum of thicknesses of

all insulating interspaces between the sub-windings can be taken into account. Therefore, in this case the mentioned formulas will deliver a result less than the real leakage inductance value which can only represent a rough approximation.

Prediction of leakage inductance with a higher degree of accuracy even in the case of magnetically asymmetric transformers is possible based on the calculation of the individual leakage inductance values of all existing couples of sub-windings of the transformer arrangement which have finally to be merged together to the total leakage inductance of the transformer. In [8], Petrov described an abstract method to establish the required combination formulas.

This approach shall be illustrated by means of leakage inductance determination for different arrangements of windings of an experimental transformer. The basic elements of the windings of the transformer are single pie-shaped coils (number of turns: 11). Furthermore the transformer (displayed in Fig. 2 (left)) is characterized by the following features:

Core: PM 114/93 [9], material N_{27}

Primary winding:

Consisting of 3 sub-windings (W_{11} , W_{12} , W_{13}) realized using 8 coils

Total number of turns: $N_1 = 88$

Different arrangements of sub-windings and distribution of turns considered

Series connection of the sub-windings and the coils forming the sub-windings

Secondary winding:

Consisting of 2 sub-windings (W_{21} , W_{22}), realized using 8 coils

Each sub-winding consisting of 4 coils connected in parallel

Sub-windings connected in series

Total number of turns: $N_2 = 22$ ($W_{21} : N_{21} = 11$; $W_{22} : N_{22} = 11$)

Thickness of insulating interspaces between the sub-windings: 0.1 mm

In Fig. 2 (right), the location of the sub-windings is illustrated. Due to the height of the outer primary sub-windings (W_{11} and W_{13}) which is half of the height of the inner primary sub-winding (W_{12}) the displayed version represents a magnetically symmetric arrangement. This classification is founded by the curve of the magnetomotive force (mmf) between the center leg and the outer leg of the core which shows the same maximum values in positive and negative range.

According to the existence of 3 primary sub-windings and 2 secondary sub-windings in the considered transformer we call it a 3-2 version. Applying the method described in [8] we derived the following formula which enables the calculation of the total leakage inductance of a transformer with a 3-2 arrangement of its windings whose sub-windings are connected in series at the primary side and at the secondary side as well:

$$L_{Ltotal} = \frac{N_1^2}{N_{ref}^2} \cdot \left(\begin{aligned} & \frac{N_{11} \cdot N_{21}}{N_1 \cdot N_2} \cdot L_{L11/21} + \frac{N_{12} \cdot N_{21}}{N_1 \cdot N_2} \cdot L_{L12/21} + \frac{N_{13} \cdot N_{21}}{N_1 \cdot N_2} \cdot L_{L13/21} \\ & + \frac{N_{11} \cdot N_{22}}{N_1 \cdot N_2} \cdot L_{L11/22} + \frac{N_{12} \cdot N_{22}}{N_1 \cdot N_2} \cdot L_{L12/22} + \frac{N_{13} \cdot N_{22}}{N_1 \cdot N_2} \cdot L_{L13/22} \\ & - \frac{N_{11} \cdot N_{12}}{N_1^2} \cdot L_{L11/12} - \frac{N_{11} \cdot N_{13}}{N_1^2} \cdot L_{L11/13} - \frac{N_{12} \cdot N_{13}}{N_1^2} \cdot L_{L12/13} - \frac{N_{21} \cdot N_{22}}{N_2^2} \cdot L_{L21/22} \end{aligned} \right) \quad (3)$$

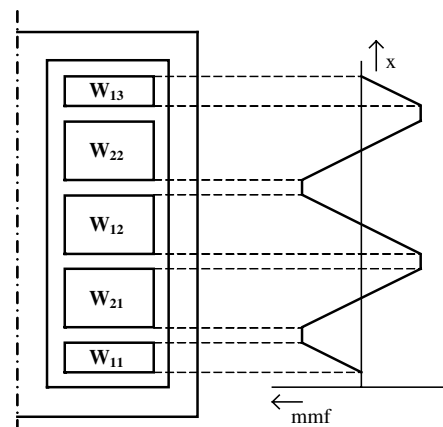
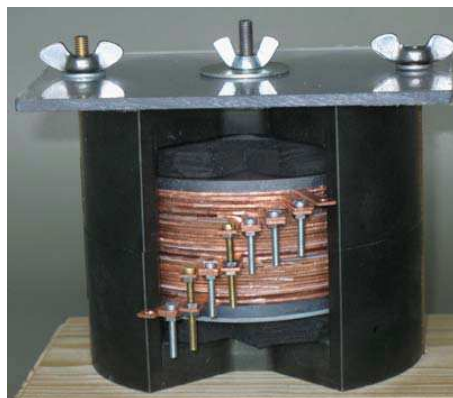


Figure 2: Left: Experimental transformer. Right: Illustration of the location of sub-windings within the core window (only right hemisphere of the transformer displayed) and curve of the magnetomotive force (mmf) across the core window.

N_{ref} is the number of turns to which the leakage inductance values of the couples of sub-windings refer (advantageously $N_{ref} = 1$ should be chosen). The single leakage inductance values of the couples of sub-windings have been calculated using the basic formula of the method of Rogowski (1) omitting the Rogowski factor. Due to the number of primary turns in the coefficient preceding the term in parentheses, the resulting total leakage inductance refers to the primary side of the transformer. As it can be seen comparing the formulas (2) and (3), in contrast to leakage inductance calculation for magnetically symmetric transformers it is a more complex procedure in the case of magnetically asymmetric versions. However, today the calculation of the single leakage inductance values of the existing couples of sub-windings of the transformer arrangement and merging them together using the respective combination formula can be realized conveniently implementing the algorithms into a PC [10]. The values of total leakage inductance have been calculated using formula (3) for the magnetically symmetric version and for different magnetically asymmetric arrangements of the windings of the experimental transformer. To enable an evaluation of the accuracy of leakage inductance prediction, also measurements have been carried out. So, concerning the realized transformer versions the respective short-circuit inductance values have been determined using an RLC meter (inductance measurement at the primary side during short-circuiting the output terminals of the secondary side, measuring frequency 50 Hz). Due to the given transformer design showing a closed core (no air gap intended) and hence a very high magnetizing inductance, the measured short-circuit inductance values will nearly coincide with the respective leakage inductance values. Therefore, the measured values are considered to be the sought leakage inductance values. The results are presented in Table 1.

Table 1: Comparison of calculated and measured leakage inductance values.

	Arrangement of the primary sub-windings $W_{11}, W_{12}, W_{13} (N_{11}-N_{12}-N_{13})$			
	22-44-22	33-22-33	11-66-11	22-22-44
Calculation	67,88 μH	117,69 μH	117,69 μH	167,5 μH
Measurement	74,2 μH	116,0 μH	121,4 μH	159,4 μH

In the case of the magnetically symmetric arrangement of the primary sub-windings with the numbers of turns 22–44–22 the calculated result is identical to the value which is delivered by formula (2). The leakage inductance values calculated by means of formula (3) show an average deviation from the measured values of about 4.5%. In the case of thicker insulating interspaces between the sub-windings (0.4 mm) the deviation is even slightly lower.

4. CONCLUSIONS

The calculation of leakage inductance of transformers with interleaving of windings has been discussed. The origin of certain terms in approximation formulas for magnetically symmetric transformers and the attribution of these terms to the geometry of concentric and pie windings arrangements has been clarified. An approach which enables leakage inductance prediction also in the case of magnetically asymmetric arrangements of windings has been demonstrated yielding good coincidence with results of measurement in the considered example.

REFERENCES

1. Rogowski, W., "Ueber das Streufeld und den Streuinduktionskoeffizienten eines Transformators mit Scheibenwicklung und geteilten Endspulen," Dissertation, Mitteilung ueber Forschungsarbeiten auf dem Gebiet des Ingenieurwesens, VdI, 1909.
2. McLyman, W. T., *Transformer and Inductor Design Handbook*, Marcel Dekker Inc., New York, 1988.
3. Flanagan, W. M., *Handbook of Transformer Design and Applications*, McGraw-Hill, 1992.
4. Mecke, H., "Transformatoren für das Lichtbogenschweissen," Dissertation B, TH Magdeburg, 1978.
5. Schuelting, L., "Optimierte Auslegung induktiver Bauelemente für den Mittelfrequenzbereich," Dissertation, RWTH Aachen, 1993.
6. Snelling, E. C., *Soft Ferrites*, Butterworth & Co., 1988.
7. Tarter, R. E., *Solid-state Power Conversion Handbook*, Wiley-Interscience, 1993.

8. Petrov, G. N., “Allgemeine Methode der Berechnung der Streuung von Transformatoren,” *Elektrotechnik und Maschinenbau*, Vol. 51, No. 25, 345–350, 1933.
9. Data Sheet, “PM 114/93 Core and accessories,” EPCOS, 2006.
10. Doebbelin, R., C. Teichert, M. Benecke, and A. Lindemann, “Computerized calculation of leakage inductance values of transformers,” *PIERS Online*, Vol. 5, No. 8, 721–726, 2009.

Controlled Battery Charger for Electric Vehicles

M. Geske¹, T. Winkler², P. Komarnicki², and G. Heideck¹

¹Otto-von-Guericke-University Magdeburg, Magdeburg, Germany

²Fraunhofer Institute of Factory Operation and Automation IFF, Magdeburg, Germany

Abstract— Due to rising fuel consumption, price of CO₂ emissions and growing urban air pollution, the global interest of the automobile industry, politics and scientists in electric mobility is increasing in the recent years worldwide. Thus, future challenges will be the integration of electric vehicles in distribution networks under the scope of balancing multiple charging processes while, at the same time, increasing dispersed generation. The development of a controlled battery charger for traction batteries aims to reduce the peak load and to shift energy demand.

1. INTRODUCTION

During charging, electrical energy is converted and stored in form of chemical energy. A conventional battery charger is supplied by mains voltage and feeds the battery with DC voltage and current. Therefore, a battery charger adapts the voltage and the charging current from the mains voltage to the specified battery parameters. For electric mobility, battery chargers of electric vehicles (EV) should fulfill additional future task. At one hand, exceeding of the maximum power of the grid and possible overloads in distribution networks by simultaneous charging of a fleet of EVs with large batteries must be avoided by means of controlled battery charging. At the other hand, batteries of EVs can be a possibility for better use of variable power sources like wind power [1] or photovoltaic [2, 3]. The more flexible use of traction batteries is a challenge for the future of electric mobility. The application of traction batteries as an energy storage for power grids is also moving into focus of research [4–7]. Hence, a charging process can be adapted to the total power consumption of a household to reduce or shift power consumption. Controlling the charging current makes it possible to keep load profiles inside defined ranges. A charger for the batteries of a small-sized experimental vehicle was developed and tested. The results of the operation of the charger will be presented and discussed.

2. CONCEPT OF THE BATTERY CHARGER

Requirements to electric vehicles and their charging environment, resulting from the grid parameters, should be considered in the charging concepts carefully [8]. The most comfortable option would be contact-less charging, it offers the possibility to charge batteries during stops along the route [9], but it demands adequate and cost-intensive charging spots. However, single-phase sockets will be the most available and public accessible connection points for electric vehicles. Due to a simple access to the electric grid and the lower complexity of the system components a concept for conductive battery charging was chosen for experimental setup.

The battery charger was developed for a lithium iron phosphate battery with 48 V and a capacity of 15 Ah. The charging device (Figure 1) consists of an input rectifier and a d.c. link, an inverter bridge on basis of a commercial IGBT module, a medium frequency transformer for adapting the voltage level to the battery voltage and for insulation from the mains, an output rectifier and a control unit.

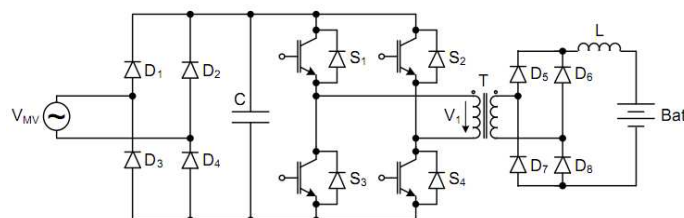


Figure 1: Topology of the developed battery charger.

3. DESIGN OF THE TRANSFORMER

The frequency is set to 10 kHz because of the maximum frequency of the IGBT. The transformer is designed for a minimum frequency of 5 kHz and allows even higher frequencies. Therefore, the core of the transformer requires material with special frequency characteristics. The chosen core material is characterized by lower hysteresis losses and a steep hysteresis curve due to a ferrite material. The dimensioning was made for an U93 core. Material properties and magnetic parameters used for calculation of the windings are shown in Table 1.

Table 1: Material properties and magnetic parameters of the core.

Parameter	Symbol	Value
Maximum flux density	B_{\max}	≥ 455 mT
Length of magnetic path	L_{Fe}	355 mm
Magnetic cross-section	A_{Fe}	840 mm ²

The voltage that is induced in a number of windings N by a magnetic flux Φ can be calculated by Eq. (1)

$$V = N \frac{d\Phi}{dt} \quad (1)$$

Assuming a triangular current, resulting from the primary voltage V_1 , which is approximately rectangular, the voltage induced by the current can be calculated by Eq. (2).

$$V_1 = N_1 \frac{\Delta\Phi}{\Delta t} = N_1 \frac{4 \cdot \hat{\Phi}}{T} = 4 \cdot f \cdot \hat{\Phi} \quad (2)$$

$$\Phi = \int B \cdot dA \quad (3)$$

$$\hat{\Phi} = \hat{B} \cdot A_{Fe} \quad (4)$$

The number of turns N_1 (Eq. (5)) can be obtained by substituting the magnetic flux $\hat{\Phi}$ using Eq. (4).

$$N_1 = \frac{V_1}{4 \cdot f \cdot \hat{B} \cdot A_{Fe}} \quad (5)$$

The transformer is dimensioned for the maximum of primary voltage V_1 resulting from the rectified mains voltage V_{MV} , Eq. (6).

$$V_1 = \frac{2 \cdot \sqrt{2}}{\pi} \hat{V}_{MV} \quad (6)$$

At the maximum mains voltage (nominal voltage of 230 V + 10% overvoltage), V_1 equals 227.2 V. The number of turns of the primary winding N_1 is set to 30. The number of turns of the secondary winding must enable a secondary voltage of 75 V also in case of 10% undervoltage. Therefore the secondary number of turns N_2 is set to 11. The windings of the transformer consist of copper foil with thickness of 0.125 mm and width of 83 mm. The windings are electrically isolated by insulating foil with a thickness of 40 μ m. For the selected material and a given current density of 3 A/mm² the maximum current is 31.2 A for each winding.

The transformer consists of two primary and two secondary windings. Using these windings in parallel allows higher currents and halves the value of leakage inductance, approximately.

4. IMPLEMENTATION OF CHARGING CHARACTERISTICS

Chargers for traction batteries can be subdivided into chargers with taper characteristic and chargers with regulated characteristic [10]. The taper characteristic charges in relation to the resistance but has the disadvantage that the charge time varies corresponding to the variation of the mains voltage. Regulated charging controls the current and voltage, achieves shorter charging times and enables the control of charging current for controlled charging. To investigate the developed controller a lithium iron phosphate battery with 15 Ah capacity was charged. This type of battery

requires the constant current constant voltage (CCCV) charging characteristic. The first step of charging is characterized by constant charging current. When the battery voltage exceeds the charge termination voltage the charge control switches to constant voltage charging. The controller for charging can be made by integrated circuits [11] or by programming a microcontroller that enables quick adaptation of the reference variables. Thus, a simplified PI control algorithm has been implemented, that changes the reference variable from charging current to charging voltage in the event that the charge termination voltage is exceeded. The charge termination of the whole charging process is initiated through by fall below a minimum charging current of 50 mA. The current and the voltage transducer provide accuracies of 0.8 and 0.9%. The sensors of the battery charger were calibrated using a high precised measurement device.

The battery voltage in Figure 2 increase weakly up to the charge termination voltage of 58.4 V and indicates the typical charging behavior of lithium iron phosphate batteries due to a strong reversible two phased reaction [12]. The further constant voltage charging is terminated after half an hour through the mentioned current criteria.

5. INVESTIGATION OF CONTROLLED CHARGING

The controlled charging modifies the reference variable of the PI control algorithm during the charging process. A scenario for a useful investigation of controlled charging is given by means of a shifted charging process adapted to a household. The investigations use the German standard load profile H_0 [13]. This profile, shown in Figure 4(a), reflects an averaged energy consumption of households on working days in winter, normalized to 1000 kWh per year. The approach of controlled charging aims to keep the sum of energy consumption below a defined value, in the test below 150 W after 10 p.m. The measurement is carried out using the normalized value, the test results will be scalable. The experimental setup in Figure 3 uses simulation software to compare the normalized load profile and the current power consumption of battery charging with the limiting value of 150 W. Every five minutes the software calculates a new value for the reference variable and sends it via serial interface to the battery charger. The resolution of the reference variable was set to 0.1 A. To achieve comparable results the battery capacity was discharged to 10.2 Ah before the charging process starts.

The charging processes have been initiated at 10 p.m. (Figure 4(a)). The uncontrolled charging

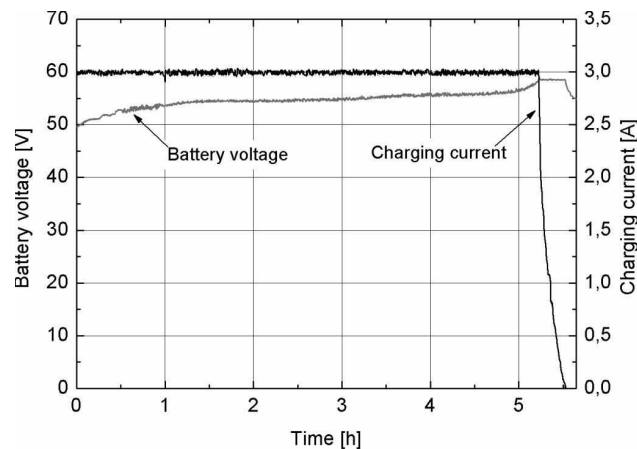


Figure 2: Measured charging characteristic of the developed battery charger.

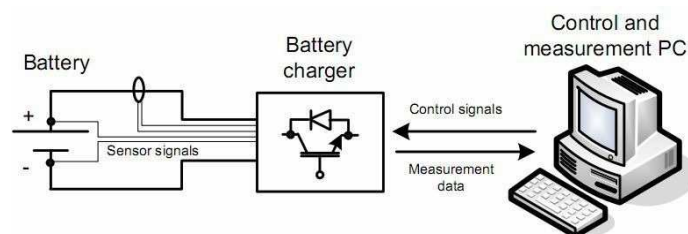


Figure 3: Experimental setup.

process in Figure 4(a) is similar to the characteristic in Figure 2 and causes a high peak of 288 W during the charging process. The load profile relating to the controlled charging shows maximal total power consumption that does not exceed the defined limit of 150 W during battery charging. The graph of charging current in Figure 4(b) points out the implemented resolution of the reference variable and time steps. The controlled charging extends the charging time up to 4 hours, while the corresponding uncontrolled charging time is 1 hour and 48 minutes.

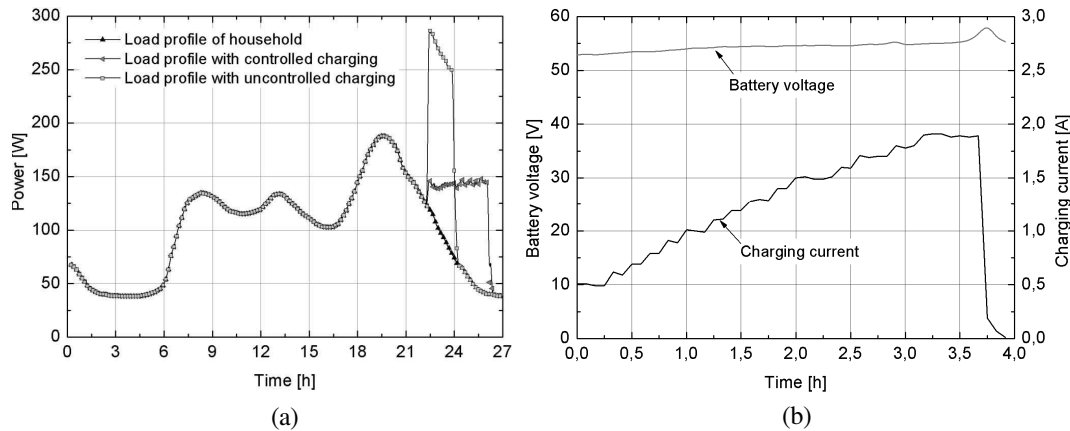


Figure 4: (a) Comparison of different charging concepts based on normalized load profile H_0 and (b) resulting charging characteristic for controlled battery charging.

6. CONCLUSIONS

The functionality of the developed battery charger for an experimental electric vehicle has been proved by charging a lithium iron phosphate battery with a nominal capacity of 15 Ah. A proposal for controlled battery charging of electric vehicles has been successfully implemented. Reducing the peak load of households within controlling the charging current has been demonstrated. The total power consumption has been kept below a defined limit by temporally modifying the internal reference variable of the battery charger. The calculation of the reference variable was made by means of simulation software that processes present measurement data and a standard load profile for households. Batteries of real EVs are some times bigger than the one of the experimental setup. The control of battery charging on the basis of a given constant or varying maximum load can be an effective instrument to reduce peak loads in the electric power grid as compared to uncontrolled charging. Further investigations are necessary to generate the peak load signals depending from the load status of the distribution networks and to transfer these signals to real households and to the chargers of the EVs.

REFERENCES

1. Kiviluoma, J. and P. Meilborn, "Influence of wind power, plug-in electric vehicles, and heat storages on power system investments," *Energy*, 2009.
2. Dunbar III, P. B., "Solar-to-vehicle (S2V) systems for powering commuters of the future," *Journal of Power Sources*, Vol. 186, No. 2, 2009.
3. Broderick, R. J. and J. J. Bzura, "Investigation of Plug-in Hybrid EVs (PHEVs) and their effects on power distribution systems in the NE and SW united states: Summary of a panel session presentation," *IEEE*, 2009.
4. Kempton, W. and J. Tomic, "Vehicle-to-grid power fundamentals: Calculating capacity and net revenue," *Journal of Power Sources*, Vol. 144, No. 1, 268–279, 2005.
5. Turton, H. and F. Moura, "Vehicle-to-grid systems for sustainable development: An integrated energy analysis," *Technological Forecasting and Social Change*, Vol. 75, No. 8, 1091–1108, 2008.
6. Sauer, D. U., M. Kleimaier, and W. Glaunsinger, "Relevance of energy storage in future distribution networks with high penetration of renewable energy sources," *Proceedings of 20th International Conference on Electricity Distribution (CIRED)*, Prague, Czech Republic, 2009.
7. Heuer, M., G. Heideck, Z. A. Styczynski, T. Winkler, P. Komarnicki, and G. Miller, "Electric vehicle charging stations in Magdeburg," *Proceedings of 5th International IEEE Vehicle Power and Propulsion Conference*, 60–67, Dearborn, USA, September 2009.

8. Kroitzsch, J. and T. Winkler, “Intelligentes batteriemanagementsystem für elektrofahrzeuge,” *Proceedings of 6th IFF-Kolloquium*, 72–76, Magdeburg, Germany, November 2008.
9. Villa, J. L., J. Sallán, A. Llombart, and J. F. Sanz, “Design of a high frequency inductively coupled power transfer system for electric vehicle battery charge,” *Applied Energy*, Vol. 86, No. 3, 355–363, 2009.
10. Kiehne, H. A., *Battery Technology Handbook*, Second Edition, Marcel Dekker Inc., Basel, New York, 2003.
11. Tsang, K. M. and W. L. Chan, “A simple and low-cost charger for lithiumion batteries,” *Journal of Power Sources*, Vol. 191, No. 2, 633–635, 2009.
12. Jossen, A. and W. Weydanz, *Moderne Akkumulatoren Richtig Einsetzen*, Reichardt Verlag, Untermeitingen, 2006.
13. Schieferdecker, B., C. Fünfgeld, H. Meier, and T. Adam, “Repräsentative VDEW-Lastprofile,” VDEW-Materialien M-28/99, 2009.

Modeling the Electromagnetic Behavior of Power Converters

S. Schulze, M. Al-Hamid, R. Vick, and R. Doebbelin
Otto-von-Guericke University of Magdeburg, Germany

Abstract— The compliance with the limit values for emission and immunity which are defined for variable-speed drives in the product norm EN 61800 has to be guaranteed by evaluations, measurements or simulations. It becomes challenging to analyze a complex system, such as a power converter with cables and a motor as a load. The development of tools and methods to achieve electromagnetic compatibility (EMC) for variable-speed drive systems was the aim of the described investigations. By using these tools manufacturers of power drive systems will be able to qualify the EMC of their systems during development process. The following paper focuses on the prediction of the electromagnetic radiated emission of a drive system consisting of a converter, a permanent magnet synchronous motor (PMSM), a mains choke and a mains filter.

1. INTRODUCTION

Undesirable stray currents are caused by high-frequency switching power semiconductors in modern inverters. The circuit for the common-mode (CM) currents is closed via stray capacitances inside the components. A high-frequency model of such a system has to include all parasitic elements to predict the conducted and the radiated emissions. Many papers focus on the prediction of conducted common-mode emissions which can be measured by a line impedance stabilizing network (LISN), e.g., [1–4]. This paper mainly deals with the prediction of radiated emissions from the power cable between the converter and the motor. Norm-compliant measurements of the radiated field strength were performed in the frequency range from 30 MHz to 1 GHz for later comparison with the simulation results. After that we built a simplified 3D model of the complete arrangement in CONCEPT II [5]. This software uses the methods of moments (MoM) algorithm for calculations in frequency domain. The parameters of the feeding source inside the model can be obtained by either measuring the common-mode currents on the cable shield or from a high-frequency equivalent network simulation in SPICE [6], that includes all high-frequency elements. Both procedures are explained in the paper.

2. CURRENT MEASUREMENTS

The circuit for the common-mode current on the cable shield which causes radiation in the observed frequency range closes via the grounding straps or via the stray capacitance between the arrangement and ground. The best way to determine the current is to measure it with a broadband current clamp. So it is not required to construct an adaptor for the cable to measure the common-mode voltage. The current clamp was connected to a low noise amplifier and a spectrum analyzer and placed at different positions along the cables. Our drive system uses an additional cable for sensor signals and closed-loop control (length: 2.73 m). The frequency interval ranged from 30 MHz up to 500 MHz with a resolution bandwidth of 120 kHz. The measurement setup is shown in Fig. 1. The inverter housing is attached to a second small groundplane. This plate as well as the motor are fixed at a height of 80 cm above the ground.

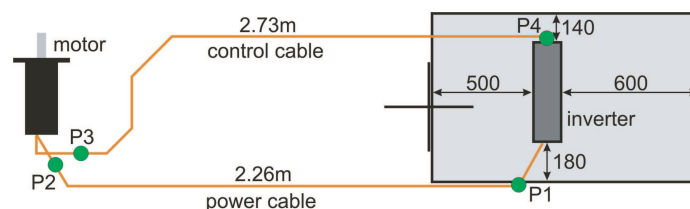


Figure 1: Arrangement (top view) for current and field strength measurement (points P1 . . . P4).

3. HIGH-FREQUENCY CIRCUIT MODEL

3.1. Inverter

The inverter is the main source of the common-mode disturbances. In order to predict these unwanted emissions we can try to create a SPICE equivalent circuit diagram of the inverter with

high-frequency equivalent elements. To keep the complexity of the circuit as low as possible, no specific IGBT model was used for the switching devices, but a simple voltage controlled switch with hysteresis. In the switch state “on” it has a resistance of $100\text{ m}\Omega$, in the state “off” it is high-resistance with $10\text{ k}\Omega$. The transition levels are $U_{\text{on}} = 950\text{ mV}$ and $U_{\text{off}} = 5\text{ mV}$. Each switching element in the three phase legs has an antiparallel diode (MUR460, $I_{\text{avg}} = 4\text{ A}$). The control function for each switch was assumed to have a trapezoidal shape with an amplitude of 1 V and equal rise and fall times of 300 ns . The magnitude of the parasitic current is mainly dependent on the rate of rise of the voltage du/dt . The maximum used switching frequency for our system is 16 kHz which gives a switching period of $T = 62.5\text{ }\mu\text{s}$. The conduction interval is then $t = 30.65\text{ }\mu\text{s}$. The real commutation is taken into account by time delays between the phase legs, which results in a simplified pulse width modulation (PWM). Of course the output current will not be sinusoidal when using this shape of function, but this is not of interest here. The dc bus capacitance has a value of $540\text{ }\mu\text{F}$, taken from the data sheet. One path for the common-mode current closes across the parasitic heatsink capacitances of each leg connected in series with the capacitance between the heatsink and ground ($\approx 1\text{ nF}$).

3.2. Cables

The two connected cables have a shielded assembly whereas the shield is a part of the common-mode circuit and is able to act as an antenna for the high-frequency currents. The cable length between inverter and motor is crucial for damping losses and transmission line resonances. Knowledge of the cable interior setup is essential to provide an equivalent circuit diagram. A complete model would include the frequency dependence of the cable parameters (skin effect and dielectric losses). An impedance analyzer can be used to measure the common-mode impedance. Special software [9] helps creating equivalent ladder networks from the measured curves [1, 8].

As a rule three-phase drives are connected without neutral conductor. The power cable in our examined variable-speed drive has four conductors whereas one conductor is protective earth (PE). The arrangement is symmetrical. If we consider all serial and parallel impedances of a shielded four-wire cable, it accumulates to 40 parameters. With these an equivalent basic cell for the cable can be built [1, 7]. By connecting some of these basic cells in series higher resonances up to $\approx 100\text{ MHz}$ will be included. For the cables observed here only one cell was generated which consists of 11 parameters. This is acceptable, because the cable length is short and hence no significant reflections occur at the wire ends for the given frequency range. The parameters were calculated analytically with formulas taken from [7]. For the power cable (subscript “pc”) the first resonance frequency is 104.2 MHz . For the control cable (subscript “cc”) only its shield serial impedance was calculated. The skin effect is taken into account. Fig. 2 summarizes all equivalent high-frequency elements and their values can be read from Table 1. For the ground path the impedance was taken from a measurement with Fluke PM6306 ($f_{\text{meas}} = 1\text{ MHz}$).

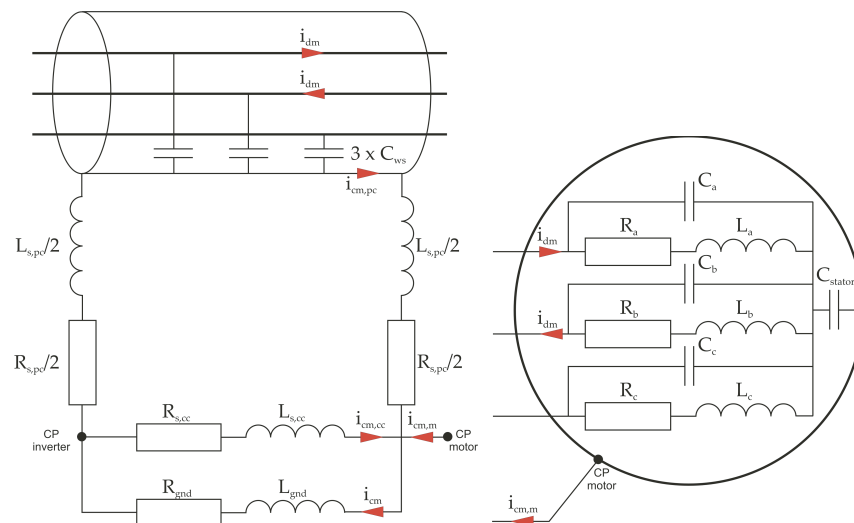


Figure 2: Equivalent circuit for the cable assembly (left) and the three-phase PMSM (right). The wire impedance $R_w + j\omega L_w$ is not drawn.

Table 1: Equivalent electrical parameters of the cables.

Part	R_w in $m\Omega$	R_s in Ω	L_w in nH	L_s in nH	C_{ws} in pF	R_{gnd} in Ω	L_{gnd} in nH
Power cable	40	2.33	597	87.73	154.3	–	–
Control cable	–	4.77	–	203.7	–	–	–
Ground path	–	–	–	–	–	1.91	130

3.3. Motor

To find equivalent elements for the motor (PMSM, type: Indramat MKD071B-061-GG0-KN), the electrical parameters for the stator wiring as well as for the stray components have to be determined. They can be decomposed into common-mode and differential-mode impedances. The common-mode impedance can be determined with the help of an impedance analyzer in a configuration where three phases are connected together and the other port is connected to the motor case. We were not able to measure the impedances because an impedance analyzer was not available. Instead we took experimental results from [3], where a similar PMS motor (type: Indramat MMD082A) was investigated. The wiring parameters are related to the common-mode impedance as

$$R_a = R_b = R_c = 3 \cdot R_{cm} = 3 \cdot 2.4 \Omega \tag{1}$$

$$L_a = L_b = L_c = 3 \cdot L_{cm} = 3 \cdot 950 \text{ nH} \tag{2}$$

$$C_a = C_b = C_c = 1.1 \text{ nF}. \tag{3}$$

The capacitance between the center of all stator wirings and the motor case C_{stator} has a value of 7.3 nF. Fig. 2 shows the connections between these discrete elements. Due to symmetry no common-mode to differential-mode conversion and vice versa should occur.

3.4. Simulation Results

For the creation of the complete SPICE network we used LTspice [6] as a frontend. It has a graphical user interface. After a transient analysis all currents and voltages can be observed dependent on time. The currents through the cable shield elements of the power cable, i.e., $R_{s,pc}$, and the control cable, i.e., $R_{s,cc}$, are of interest here. The simulation time was adjusted to 100 μ s. So several of the switching events will be covered. We saw oscillations which occur after each switching process. They have a frequency of ≈ 6 MHz. However, the attention should lie on the spectral content of the two currents. This is done easily using Fourier transform. The full spectrum shows a first peak at 48 kHz, which is the third harmonic of the switching frequency. The second peak is at 6 MHz, as expected because of the oscillations observed in time domain. In Fig. 3, the displayed frequency range is from 30 MHz to 500 MHz. The comparison between the simulated (left side) and measured (right side) CM currents shows good conformity. Single resonances above 100 MHz origin from various other processes in the real drive system and are not captured by our model.

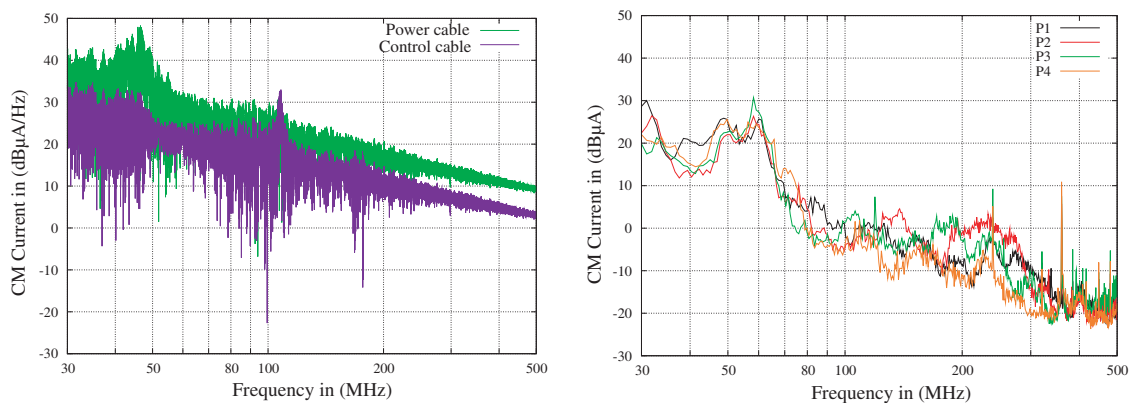


Figure 3: Comparison between the simulated (left) and measured (right) CM cable shield currents.

4. NUMERICAL FIELD SIMULATION

4.1. CONCEPT Model

The cable routing and the position of the inverter housing on its small groundplane, including earth straps, were constructed to scale in a model for the software package CONCEPT II [5]. All metallic surfaces were assumed to be perfectly conducting and all parts were discretized according to the shortest wavelength ($f = 500$ MHz) in the simulation. The arrangement is shown in Fig. 4. The inverter housing is a simple block and the motor is composed of two closed cylinders and a flange. The point of origin of the arrangement is shown. This was the center of rotation for the measurement (see also the cross in Fig. 1). The easiest feeding in CONCEPT is a voltage source with constant amplitude and variable internal resistance. But we wanted to use the measured or simulated CM current amplitudes i_{meas} as a source which is placed on one wire segment. So we calculated an equivalent internal resistance R_{eq} for each frequency step and held the voltage fixed at 1 V. The equivalent series resistance may be expressed as

$$R_{\text{eq}}(f) = \frac{1 \text{ V} - i_{\text{meas}}(f) \cdot |\underline{Z}_{\text{in}}(f)|}{i_{\text{meas}}(f)}, \quad (4)$$

where $\underline{Z}_{\text{in}}$ is the complex valued input impedance of the arrangement that needs to be calculated in a first simulation run. After the simulation run the electrical field strength at 36 equally spaced field points around the structure (distance: 10 m, height: 1 m) was calculated. The field amplitudes from all observation points and from two simulation runs (source at P1 and P4 respectively, see Fig. 1) were combined by taking the overall maximum. This reflects the procedure of the normative emission measurement. Fig. 5 depicts the comparison between the measured and the simulated field strength. The conformity is satisfying. The frequency range below 100 MHz of the displayed simulated spectra results from feeding at point P1, and above 100 MHz it results from feeding at point P4. The sharp resonances in the current spectrum appear also in the field spectrum.

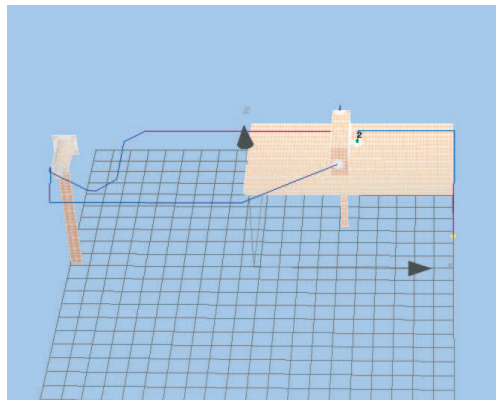


Figure 4: View of the 3D model with surfaces and wire segments.

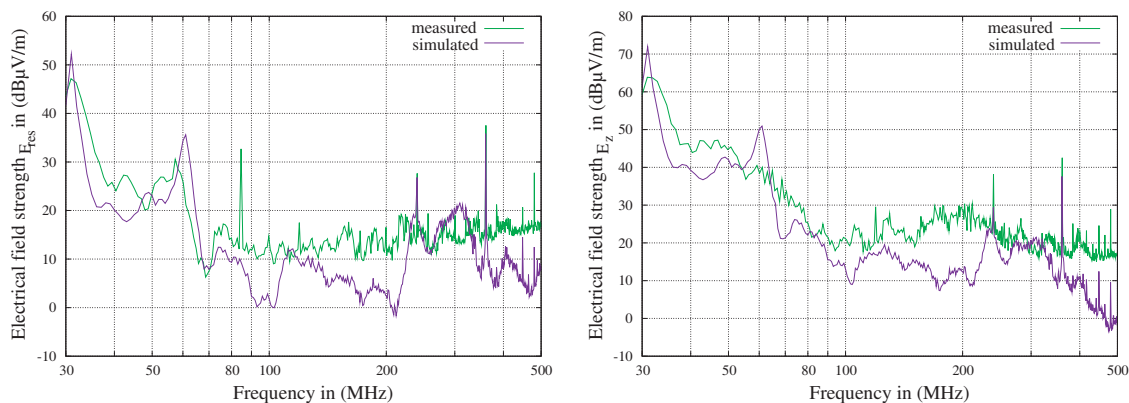


Figure 5: Overall comparison between measurement and simulation for the horizontal (left) and vertical (right) field strength component.

5. CONCLUSION

In this paper, a high-frequency model for a variable-speed drive system was proposed. We focused only on the prediction of radiated emissions from the system. Therefore a SPICE network with high-frequency equivalent elements was created and the common-mode currents on the cable shields were simulated. Their spectral content shows satisfying match compared with measurements. The measured values were then taken as a source inside a simplified 3D model in CONCEPT II to compute the radiated emissions. The correspondence of the results with normative emission tests performed in our semi-anechoic chamber is very good (deviation ± 10 dB).

ACKNOWLEDGMENT

The project is supported by Forschungsvereinigung Antriebstechnik e.V. (FVA), Frankfurt, Germany.

REFERENCES

1. Moreau, M. and N. Idir, "Modeling of conducted EMI in adjustable speed drives," *IEEE Trans. on EMC*, Vol. 51, No. 3, 665–672, August 2009.
2. Costa, F., C. Vollaire, and R. Meuret, "Modeling of conducted common-mode perturbations in variable-speed drive systems," *IEEE Trans. on EMC*, Vol. 47, No. 4, 1012–1021, November 2005.
3. Gulez, K. and A. A. Adam, "High-frequency common-mode modeling of permanent magnet synchronous motors," *IEEE Trans. on EMC*, Vol. 50, No. 2, 423–426, May 2008.
4. Gubia, E., P. Sanchis, A. Ursúa, J. López, and L. Marroyo, "Frequency domain model of conducted EMI in electrical drives," *IEEE Power Electronics Letters*, Vol. 3, No. 2, 45–49, June 2005.
5. Brüns, H.-D., A. Freiberg, and H. Singer, "CONCEPT II User's Manual," <http://www.tet.tu-harburg.de/concept>.
6. Linear Technology LTspice IV, <http://www.linear.com>.
7. Weber, S.-P., A. Linde, E. Höne, S. Guttowski, J. Werner, and H. Reichel, "Modellierung geschirmter Leistungskabel im frequenzbereich der EMV," *Proceedings of the EMC Conference 2006*, Düsseldorf, Germany, 655–663, March 2006.
8. Idir, N., Y. Weens, and J.-J. Franchaud, "Skin effect and dielectric loss models of power cables," *IEEE Trans. on Dielectrics and Electrical Insulation*, Vol. 16, No. 1, 147–154, February 2009.
9. "APLAC User's manual," *Circuit Simulation and Design Tool*, 2007.

Frequency-adjustable Circularly-polarized Ceramic Dielectric Resonator Antenna

S.-S. Zhong¹, L.-X. Li¹, S.-Q. Xu^{1,2}, and M.-H. Chen¹

¹School of Communication and Information Engineering, Shanghai University, Shanghai 200072, China

²Zhejiang Zhengyuan Electric Co. Ltd., Jiaxing, Zhejiang 314003, China

Abstract— A ceramic dielectric resonator antenna excited by a corner-cut square patch is introduced for the circular polarization (CP) operation. The effect of patch size and cut size are investigated, showing that the resonant frequency of the antenna can be adjusted by simply changing the patch size. Its return loss, axial ratio, and radiation characteristics are found. Measurements were carried out to verify the design. This CP ceramic dielectric resonator antenna is compact in structure, which is attracted for the application as the satellite communication terminal.

1. INTRODUCTION

More and more dielectric resonator antennas (DRAs) have been used due to its advantages such as small size for lower microwave frequency applications, high radiation efficiency even at higher frequencies, and ease of excitation, etc. Normally the resonant frequency of DRA is determined as long as the dielectric resonator is chosen, but the measured and calculated resonant frequencies are usually different from each other due to the fabrication tolerance. Therefore, except the studies on one or dual linear-polarization [1, 2] and circular-polarization (CP) [3] operation of DRAs, more attention has been paid to the frequency-adjustable DRAs, such as using a loading cap [4], using multiple parasitic strips [5], etc.

In this letter, an easy way of tuning the resonant frequency of circularly-polarized (CP) DRA using different sizes of square patches is presented. This method can tune a DRA to operate in the frequency range from 5.17 GHz to 5.31 GHz without a big change of antenna performance. Moreover, the square patch can make antenna realize the CP operation by cutting corners. Its detailed design considerations are described, and then simulated and measured results are presented and discussed.

2. ANTENNA DESIGN

The antenna configuration is shown in Figure 1 with the cylindrical DR of radius D , height H , and relative permittivity $\epsilon_{r1} = 38$. Using high dielectric constant makes the antenna miniaturize at the cost of narrow bandwidth. To broaden the operation bandwidth, the DR is excited by a square patch with a $50\ \Omega$ T-shaped microstrip feed line, which has a stub of $L_S = 17\ \text{mm}$, $W_S = 0.5\ \text{mm}$. The cylindrical DR is etched on a substrate of thickness $h_2 = 0.5\ \text{mm}$ and relative permittivity $\epsilon_{r2} = 4.2$. The T-shaped microstrip feed line is fabricated on a substrate of thickness $h_1 = 2\ \text{mm}$ and relative permittivity $\epsilon_{r2} = 4.2$. The square patch of side length α is perturbed by cutting two equilateral triangles of length δ in its diagonal corner.

Figure 2 plots the simulated and measured return loss curves of the test antenna with parameters $D = 9\ \text{mm}$, $H = 4.1\ \text{mm}$, $\alpha = 2.5\ \text{mm}$, $\delta = 1.2\ \text{mm}$, which are optimized by using the simulation software HFSS¹⁰. It is noted that the simulated impedance bandwidth of the antenna is 5.2% for S_{11} less than $-10\ \text{dB}$, covering the frequency range from 5.08 to 5.35 GHz. The measured impedance bandwidth is 5.8%, from 5.15 to 5.44 GHz, covering the required bandwidth for WLAN application in the 5.2 GHz band. The difference between simulated and measured frequency range is probably due to the air gaps between the DR and the substrate, which slightly lowers the equivalent permittivity of the DRA, thus leading to the increasing in the resonant frequency and the expanding of the bandwidth [6].

The simulated and measured axial ratio curves of the antenna are shown in Figure 3. The simulated bandwidth ($\text{AR} \leq 3\ \text{dB}$) is 70 MHz, covering the frequency range from 5.195 to 5.265 GHz with the minimum AR of 0.4 dB at 5.23 GHz, while the measured axial-ratio curve shows a little shift, which covers the frequency range from 5.245 to 5.315 GHz (1.33%) with the minimum AR of 1 dB at the 5.285 GHz.

Figure 4 displays the return loss and axial ratio vs. frequency for patch size $\alpha = 2.3, 2.4, 2.5\ \text{mm}$. As predicted, the resonant frequency changes with length α significantly. When α increases, the

resonant frequency of DRA decreases. Nevertheless, the bandwidth and minimum axial ratio are only slightly changed with α . This is a very favorable result, which means that one can tune

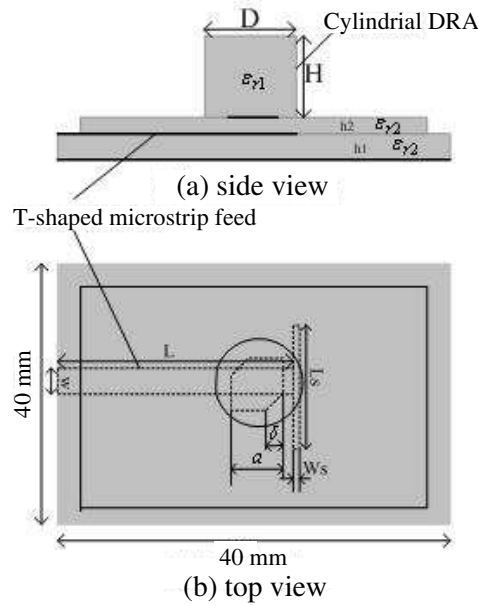


Figure 1: Configuration of proposed antenna.

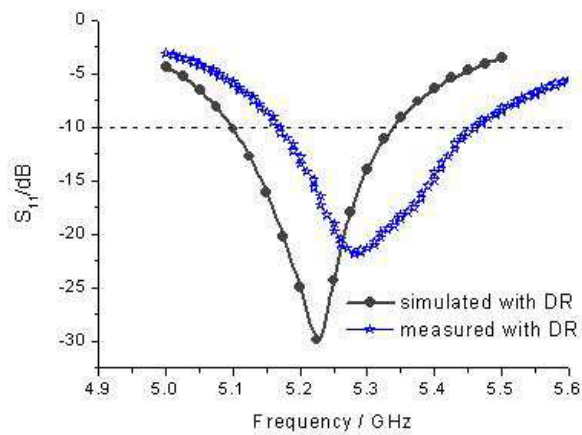


Figure 2: Simulated and measured return loss curves.

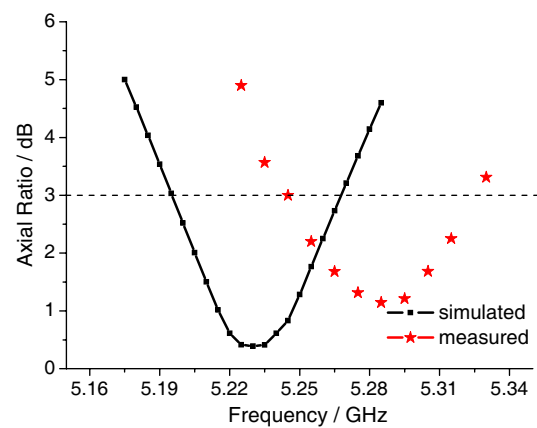


Figure 3: Simulated and measured axial ratio of the antenna.

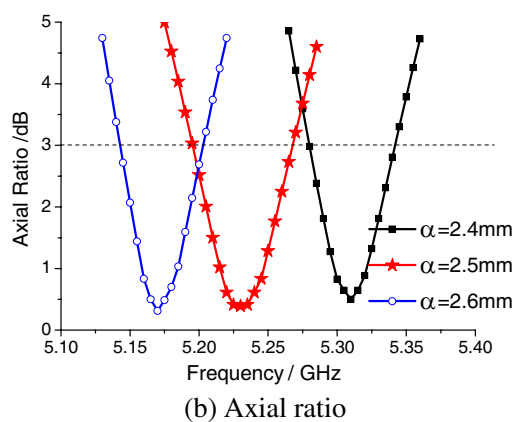
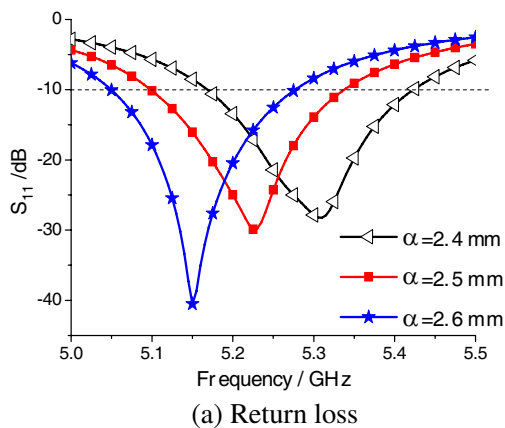


Figure 4: Return loss and axial ratio against frequency for different value of α .

the resonant frequency by simply changing α without affecting the bandwidth and axial ratio characteristic too much.

Figure 5 shows the return loss and axial ratio as a function of frequency for different cut size $\delta = 1.1$ mm, 1.2 mm, 1.3 mm. It is seen that the effect of δ on the antenna is weaker than that of α . The good impedance match and axial ratio are achieved for $\delta = 1.2$ mm, and 1.3 mm both. Therefore the cut size δ is not critical, and thus it is not difficult to design this CP DRA.

The simulated and measured xz and xy plane radiation patterns are shown in Figure 6 for $\alpha = 2.5$ mm, $\delta = 1.2$ mm, showing the broadside radiation, as expected. Also very good left-hand CP (LHCP) fields are observed, which are about 20 dB stronger than the right-hand CP (RHCP) fields in the broadside direction ($\theta = 0^\circ$). The gain of the antenna with $\alpha = 2.5$ mm, and $\delta = 1.2$ mm is also measured, which is 6.2 dBi at 5.285 GHz.

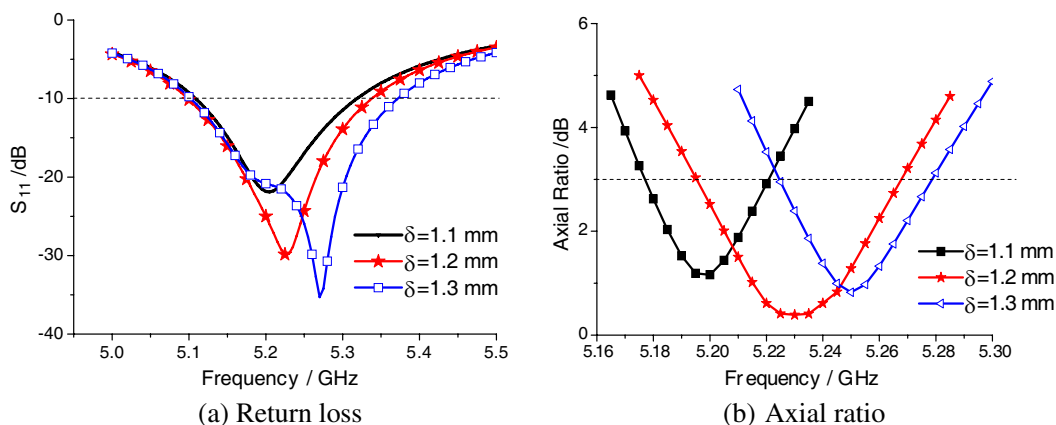


Figure 5: Return loss and axial ratio for different values of δ .

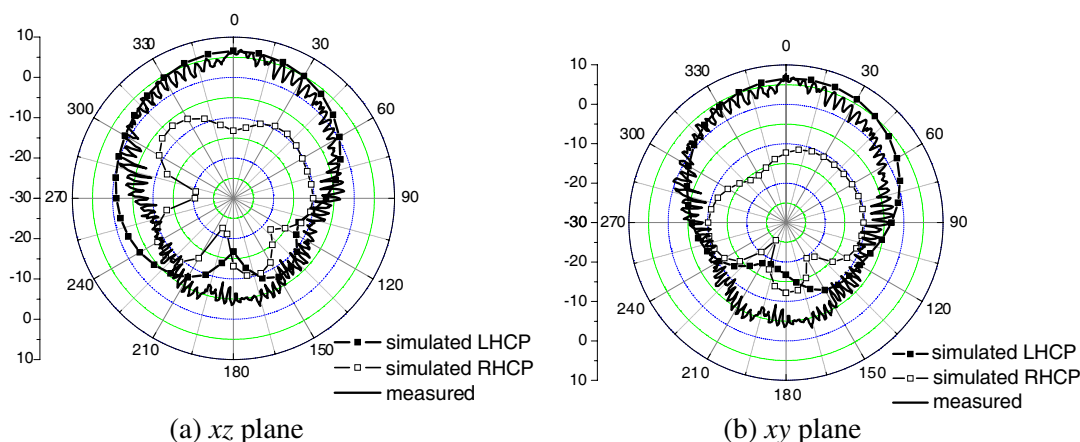


Figure 6: Simulated and measured radiation patterns at 5.285 GHz.

3. CONCLUSION

A novel frequency-adjustable circularly-polarized DRA has been introduced. The resonant frequency of the proposed antenna can be controlled by simply changing the square patch size which is located between the DR and the substrate, and its CP radiation can be easily achieved by cutting corners of the square patch. The antenna is compact in structure, as it consists of only a cylindrical DR with radius of 4.5 mm and a substrate of 40 mm \times 40 mm. The measured impedance bandwidth reaches 309 MHz with good broadside radiation characteristics. And the measured axial-ratio bandwidth is 70 MHz, with a minimum axial ratio of 1 dB. The compact CP DRA is attractive for the application as the terminal of satellite communication systems.

ACKNOWLEDGMENT

This work was supported by the National High-Technology Research and Development (863) Project of China, under Grant No. 2007AA12Z125, and the Shanghai University Innovation Fund Project, No. SHUCX092130.

REFERENCES

1. Zhang, L. N., S. S. Zhong, and S. Q. Xu, "Broadband U-shaped dielectric resonator antenna with elliptical patch feed," *Electronics Letters*, Vol. 44, No. 16, 947–949, 2008.
2. Tang, X. R., S. S. Zhong, L. B. Kuang, and Z. Sun, "Dual-polarized dielectric resonator antenna with high isolation and low cross-polarization," *Electronics Letters*, Vol. 45, No. 14, 719–720, 2009.
3. Li, L. X., S. S. Zhong, S. Q. Xu, and M. H. Chen, "Circularly polarized ceramics dielectric resonator antenna excited by Y-shaped microstrip," *Microwave and Optical Technology Letters*, Vol. 51, No. 10, 2416–2418, 2009.
4. Ng, H. K. and K. W. Leung, "Frequency tuning of the dielectric resonator antenna using a loading cap," *IEEE Transaction and Antennas Propagation*, Vol. 53, No. 3, 1229–1232, 2005.
5. Ng, H. K. and K. W. Leung, "Frequency tuning of the linearly and circularly polarized dielectric resonator antennas using multiple parasitic strips," *IEEE Transaction and Antennas Propagation*, Vol. 54, No. 1, 225–230, 2006.
6. Drossos, G., Z. P. Wu, and L. E. Davis, "The air gap effect on a microstrip-coupled cylindrical dielectric resonator antenna," *Microwave and Optical Technology Letters*, Vol. 21, No. 1, 36–40, 1995.

Effects of Metallic Strips on the Radiation Characteristics of Dish Reflector Antennas

Ali H. Harmouch², Walid A. Kamali¹, Ghaleb A. Sanjakdar¹, and Ahmad Y. El-Abed¹

¹Al-Manar University of Tripoli, Lebanon

²American University of Science and Technology, Lebanon

Abstract— Sidelobes in dish reflector antennas are wasted energy in unwanted directions making the antenna more susceptible to noise. They represent security vulnerability since an unintended receiver may pick up the classified communication and most importantly yield to interference. Therefore reducing the near-in sidelobes which is desirable in parabolic reflectors and can be achieved by adding metallic stripes to scatter and diffract the unwanted radiation. The amount of reduction that can be attained ranges from 15 to 20 dB.

1. INTRODUCTION

Wireless telecommunication has become an emerging need in today's evolved networks. The urge for higher data rates, high quality service and the growth in traffic necessitated that wireless systems be more efficient. One way to improve the efficiency of a wireless communication system is to improve the antenna which is considered as a key factor in the systems. A common way to improve the antenna is reducing the near-in sidelobes which are the largest sidelobes. These are considered as wasted energy in unwanted direction and the communication system cannot make use of this lost energy. Near-in sidelobes, which are the largest sidelobes, make the antenna more vulnerable to noise and can be considered as security vulnerability for the transmitting antenna since an unintended receiver can receive the classified communication. Additionally, since these sidelobes are large they may lead to interference. However, the reduction must not affect the directional characteristics of the antenna that is the beamwidth of the main beam of the radiation pattern.

Many designs and methods were proposed to reduce the sidelobes such as adding auxiliary subreflectors; either internally or externally, where the mainlobe is in direction of the sidelobe of the main reflector [1]. Another method consists of employing shrouds bottled on the reflector's surface to collect the spillover energy that misses the reflector [2] or using circular waveguide feed which employs a non-planar corrugated subreflector, to concentrate the energy from the waveguide onto the main reflector, without allowing it to pass directly to the far field of the antenna [3]. Although all these methods brought reduction in the sidelobes but this was on the expense of the significant reduction in the gain of the antenna. Also some of the designs suffer from low wind resistance, or increase in the weight and size of the reflector, or a modification in its shape.

The method proposed in this paper does not lead to a change in the shape of the reflector itself and thus existing antennas in the market can benefit from such a method. It consists simply of attaching metallic stripes to the reflector in order to diffract and scatter the unwanted radiations that are responsible for creating the sidelobes. This study will be conducted on center-fed dish reflector antennas although it is supposed to be functional on other parabolic reflector configurations. The paper is organized in the following order: In Section 2, the proposed method is presented. In Section 3, simulations using method of moments are shown and in Section 4 the experimented results are presented. And last but not least, in Section 5 a comparison between both results is performed and later the conclusion is given.

2. THEORETICAL METHOD

It is well known that when an incident wave hits the sharp edge of an object, a portion of this wave will continue in its direction, while the other portion will be diffracted and scattered in another direction. Thus, based on the knife edge diffraction effect, if it is possible to find the rays responsible for the creation of sidelobes and put an object that is able to diffract and scatter these unwanted rays, the sidelobes would be reduced. The loss due to edge knife edge diffraction effect in decibels is given by the ratio of the diffracted to the incident magnetic field:

$$L_{ke} = 10 \log(E_d/E_i) \quad (1)$$

The first step is to choose the type of the obstacle or in other words the object to use. Metallic stripes are chosen, mainly because of three factors. The first advantage of using metallic stripes, from the electrical point of view, is that the theory of knife edge diffraction applies when using them and therefore they can diffract and scatter waveforms. From the Mechanical standpoint, they are thin and light and accordingly do not affect the size and weight of the reflector. Moreover, it is easy to utilize them since they can be modeled into different shapes as needed. Furthermore, these stripes are widely available and very cheap.

The position where the stripes must be placed is very crucial. First of all, the stripes must be placed in a way to reduce the near-in sidelobes but without being on the expense of the main lobe, In other words, the stripes should not alter the directivity characteristics of the main beam especially its beamwidth.

The theoretical method consists of simulating the radiation pattern of the dish reflector and then calculating the radial distance range from the sidelobe region which is of the region of the significant sidelobes, using the following formula:

$$\rho = 2F \tan \frac{\theta}{2} \tag{2}$$

where ρ is the radial distance, F is the focal depth and θ is the appropriate angle. Then, two symmetrical stripes are disposed on various positions in this range and on every position the radiation pattern is simulated and compared with the main simulation of the reflector without the stripes. During the experiments and simulations performed the stripes showed a reduction between 15 to 20 dB depending on the antenna, the operating frequency, the shape of the stripes and their metal type and the reduction was significant between $5\lambda/2$ and $7\lambda/2$. As said, several shapes can lead to several diffraction and scattering properties and thus diverse amounts of reductions, thus rectangular, cylindrical and blades shaped stripes, which are composed of four rectangular stripes crossed together with an angle of 45° , are taken into consideration. Fig. 3 shows blades shaped stripes placed on a dish parabolic reflector.

3. SIMULATIONS

The simulation in this paper is done using the method of moments. A center-fed dish reflector antenna employing a horn waveguide and having the following parameters is considered: The antenna is operating at a frequency of 2.4 GHz, having a diameter of 1.49 meters, a focal length of 8.9 centimeters and a focal depth of 1.17 meters. The horn waveguide is of 49 cm in height, 12 cm in length and 9.8 cm in width. The far field of an antenna is the Fourier transform of the aperture

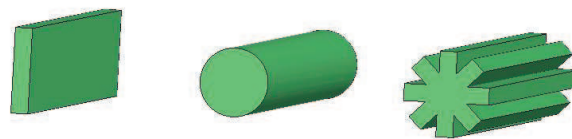


Figure 1: Different metallic shapes: rectangular, cylindrical and blades shaped stripes.

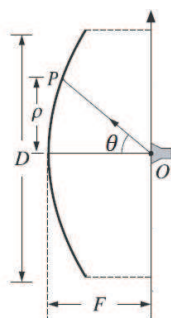


Figure 2: Center-fed reflector parameters.

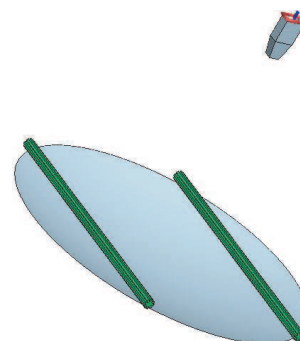


Figure 3: Blades shaped metallic stripes positioned at a distance of $7\lambda/2$ on a center-fed dish parabolic reflector.

distribution. The gain of the radiation pattern of this dish reflector is shown in Fig. 4. as well as the region of the near-in sidelobe or the region of intended reduction. The largest sidelobe peaks at 7.8 dB.

First, a study on the position of the metallic scatters is conducted in which random shaped stripes are considered and as such the rectangular scatters of 0.1 cm in width, 0.5 cm in depth and 12.6 cm in height are placed at $5\lambda/2$ and $7\lambda/2$ and the results in comparison with that of the main radiation pattern are shown in Fig. 5. At $5\lambda/2$ a reduction of 5.19 dB occurred while at $7\lambda/2$ the reduction was of 8.31 dB. It is obvious that the beamwidth was not affected.

Since different shapes exhibit different diffraction and scattering properties, cylindrical and blades shaped stripes were placed at the position of $7\lambda/2$ in order to measure the near-in sidelobes reduction. The cylindrical stripes are of 2 cm in radius and 63 cm in length. The blades are four of the same rectangular scatters used before but with 45° between them. The results are shown in Fig. 6, a reduction of 16.7 dB occurred when the blade shaped stripes were used while a reduction of 17 dB occurred when cylindrical stripes were attached to the reflector.

4. EXPERIMENTAL RESULTS

To conduct the experiment two antennas are needed, one as the receiver and the other as the transmit antenna. The electric field will be measured before and after attaching the stripes to one of the antennas. The experiments were done in an open air environment using Andrew P2F-23-NXA antenna which is connected to a rotor.

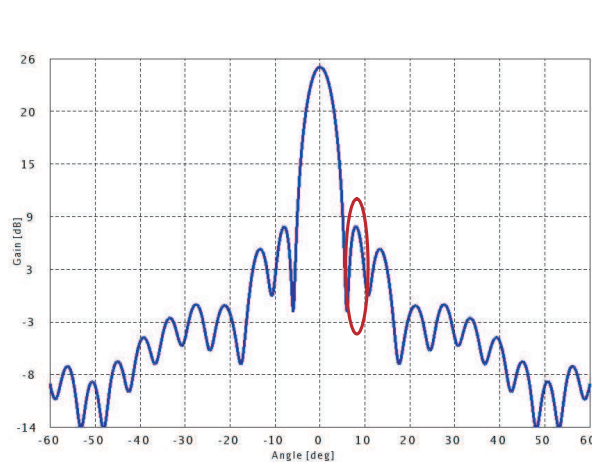


Figure 4: Gain of center-fed dish reflector with the intended reduction region.

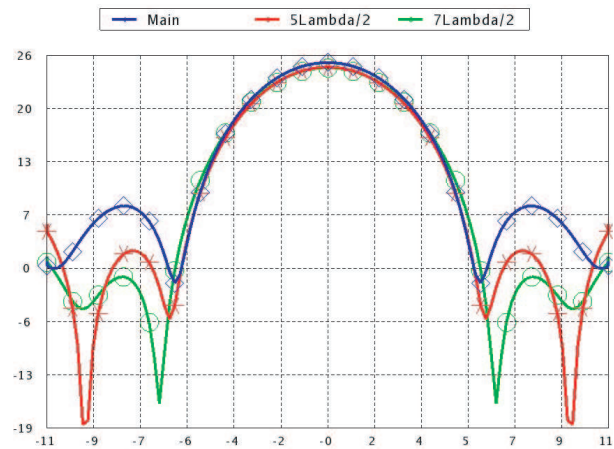


Figure 5: Simulations of rectangular stripes at $5\lambda/2$ and $7\lambda/2$.

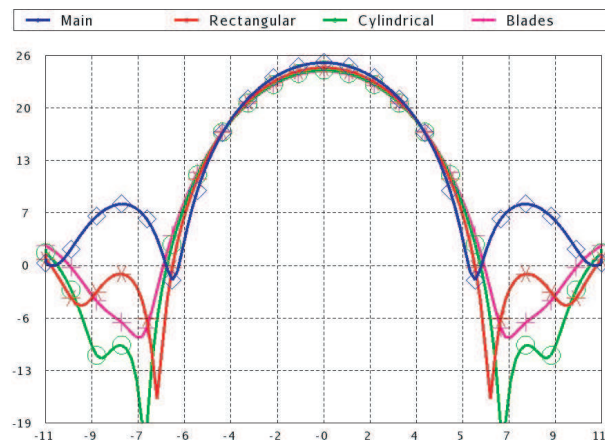


Figure 6: Different stripes shapes at a distance of $7\lambda/2$.

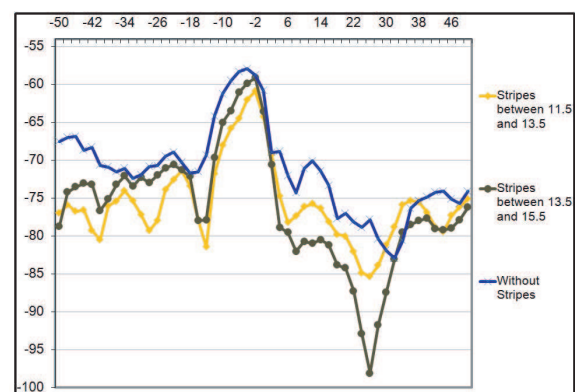


Figure 7: Experimental results on Andrew P2F-23-NXA antenna.

The electric field pattern is obtained by rotating the test antenna while receiving the data of

the transmitting antenna and measuring it using a spectrum analyzer. The stripes were placed first between 11.5 and 13.5 cm and later that they were placed between 13.5 and 15.5 cm, the results are plotted in Fig. 7.

It is clear that there is a 20 dB reduction between the main simulation and the one where the stripes were placed between 13.5 cm and 15.5 cm. This experiment showed that the stripes that used were simple flat rectangular stripes.

Table 1: Summary of results.

Stripes Type	Sidelobes Reduction [dB]
	<i>Simulation — MoM</i>
Rectangular Stripes	8.31 dB
Blades Stripes	16.7 dB
Cylindrical Stripes	17 dB
	<i>Experimental Results</i>
Rectangular Stripes	20 dB

5. CONCLUSION

The experimental results showed a 23 dB reduction in the largest sidelobes or near-in sidelobes after attaching the stripes to the best position. With the help of the simulations the best distance range to have the maximum reduction was detected to be between $5\lambda/2$ and $7\lambda/2$ where the reduction is normally maximum at the latest distance and is normally between 15 and 23 dB. All the shapes showed reduction where the cylindrical and blade shaped had the most influence on the reduction. The results showed approximately no effect on the beamwidth or the half power beamwidth and thus this approach does not alter the directional characteristics of the dish reflector antenna. The importance of this method lies in the fact that it is cheap, feasible and does not change the original shape of the antenna.

ACKNOWLEDGMENT

The authors wish to acknowledge the assistance and support of the technicians and the management at *GlobalCom Data Service "GDS"*.

REFERENCES

1. Lam, P. T., et al., "Sidelobe reduction of a parabolic reflector with auxiliary reflectors," *IEEE AP-S Trans.*, Vol. 35, No. 12, 1367–1374, Dec. 1987.
2. Singer, A., "Broadband high performance antenna design," *Mobile Radio Technology Magazine*, May 2003.
3. Sanford, J. R., et al., "Low sidelobe reflector antenna system employing a corrugated subreflector," US Patent 5959590, 1999.
4. Saunders, S. R. and A.-Z. Alejandro, *Antennas and Propagation for Wireless Communication Systems*, 2007.
5. Ofranidis, S. J., *Electromagnetics Waves and Antennas*, Rutgers University, 2008.
6. Harmouch, A., E. Nassar, D. Akiki, W. Beaineh, and N. Chamy, "Reduction of side lobe level using metallic strip positioning method," *IEEE Trans. on MMS 08, International Conference*, Damascus, Syria, 2008.

The Gain Effects of Air Gap Quadratic Aperture-coupled Microstrip Antenna Array

M. F. Jamlos¹, T. A. Rahman², M. R. Kamarudin², M. T. Ali²,
M. N. Md Tan², and P. Saad³

¹Faculty of Computer and Communication Engineering, University of Malaysia Perlis (Unimap), Malaysia

²Wireless Communication Center (WCC), University of Technology Malaysia (UTM), Malaysia

³Faculty of Computer Science and Information System (FSKSM)

University of Technology Malaysia (UTM), Malaysia

Abstract— This paper describes the concept of air gap structure to enhance the antenna's gain. The structure of the planar antenna array consisting rectangular 16 elements is comprised based on corporate feed network. The advanced of this antenna design is the antenna's feeding network is etched on a different layer from the elements by certain of air gap distances. The air gap antenna was separated and measured from 0 mm to 20 mm, in 0.5 mm increments respectively. Quadratic slots enabled most of the induced current and power from source to the radiating patches. The magnetic characteristics of quadratic allowed absorbing the reflected electrical fields around the slots. The configuration of air gap is competent influencing a stronger fringing field at the edge of the patches. The fringing fields become stronger as the distance is getting increased. A strong fringing fields leads for the patches to radiate even further. The air gap increased the radiated power and reduced conductor loss. The gap coupling is more feasible to reduce surface wave excitation between elements which are separated by a ground plane. The combination of air gap structure with quadratic slots the gain grooming 400% times larger than a quadratic aperture coupled microstrip array antenna without an air gap. The proposed antenna also has significant 50% of gain compared to the conventional transmission line antenna array. The air gap has successfully increased the level of isolation up to 1.5 times bigger than without air gap. The effects of the gap on parameters such as radiation patterns and gain are observed. Good agreement between simulations and measurements is also obtained. These results extend the validity of the analysis and will be useful for higher gain applications.

1. INTRODUCTION

Aperture coupled is one of the methods that are using multilayered dielectric substrates. This type of antenna has the ability to reduce surface wave excitation between elements which are separated by a ground plane. However, at 2.3 GHz of the resonant frequency, FR4 stated a 30% of loss percentage and 4.7 of permittivity, ϵ_r which is considered as a high dielectric constant and unstable [3, 4]. Conventional aperture-coupled antenna only stated a 35% of efficiency due to the limitation of FR4 [9, 10]. As a result, gain and directivity of the antenna are declining.

However, by introducing the air gap, the impedance is starting to decrease. The antenna impedance approaching zero as the antenna approaches the lower substrate. The impedance usually represents as a function of frequency. The changes of impedance had affected on resonant frequency indirectly. In this paper, the air gap of quadratic aperture coupled microstrip antenna array (Q-ACMAA) has an ability to take the efficiency up to 70% simultaneously maintained the impedance and decreasing the power being radiated. The effects of the various parameters of the structure, such as the gap and aperture's slots dimension on parameters such as gain and efficiency are observed.

2. ANTENNA STRUCTURE

To form a uniform monolithic structure, both the upper and lower substrates are composed of FR4 (relative permittivity = 4.7, loss tangent = 0.019) dielectric layer. The detail of sub-array of Q-ACMAA antenna measured in this experiment is shown in Figure 1. Given in Figure 2, the antenna is designed with a variety of air gap separation distances, d , therefore, these experiments not only measure the effect of the air gap structure, but they also measure the effect of overall antenna design. Figure 3 shows the antenna structure and printed circuit board, PCB stands with certain height are used as to varying the gap of separations.

Figure 2 shows the different separations from 0 mm to 20 mm. The air gap is used as spacers between the antenna and the ground plane. The Q-ACMAA is brought back to back with the ground plane initially 0 mm or 0λ . The antenna was then moved from 0 mm to 20 mm, 0.33λ in

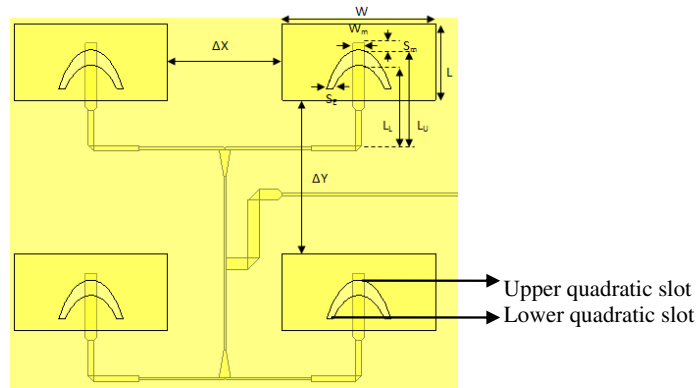


Figure 1: Single sector of Q-ACMAA $S_m = 1.5$, $S_E = 2.3$, $W = 40$, $W_m = 3$, $L = 22$, $L_u = 29.6$, $L_L = 20.2$, $\Delta X = 30$, $\Delta Y = 38$ all in mm.

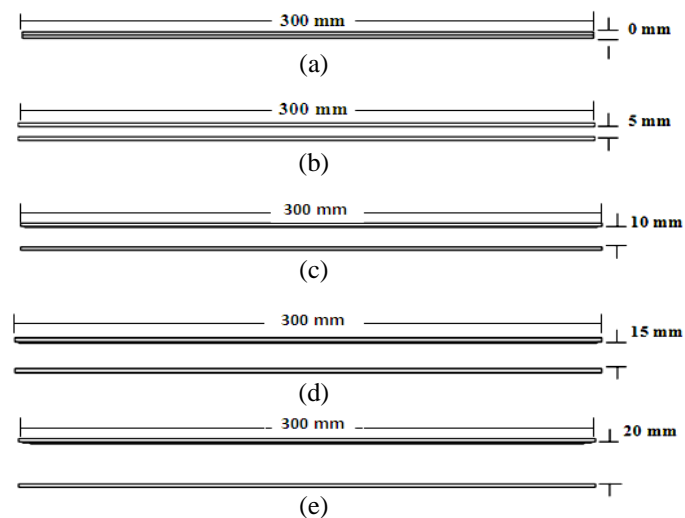


Figure 2: Gap-coupling structure of Q-ACMAA. (a) $d = 0$ mm, (b) $d = 5$ mm, (c) $d = 10$ mm, (d) $d = 15$ mm, (e) $d = 20$ mm.

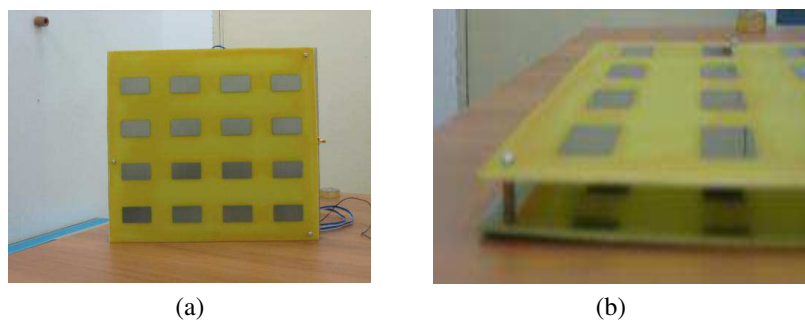


Figure 3: (a) 16 elements of Q-ACMAA, (b) layout view of Q-ACMAA with gap-coupling.

0.5 mm, 0.008λ increments. At each step, the gain was measured using the network analyzer in anechoic chamber. To determine the exact dimensions of the slot, the modified formulas as follows can be used.

$$Y_1 = -ax^2 + bx + c \tag{1}$$

$$Y_2 = -ax^2 + bx + (c - 5) \tag{2}$$

where Y_1 = upper of quadratic slot, Y_2 = lower of quadratic slot.

The effects of the various parameters of the structure, such as the gap and aperture's slots

dimension on related parameters such as Q factor, gain and efficiency are observed. It can also be expressed in a formula as follows:

$$\eta = \frac{Q_T}{Q_{rad}} \quad (3)$$

$$Q_T = \frac{1}{\tan \delta} = \frac{\varepsilon_r}{d} \quad (4)$$

where: η = Antenna efficiency, ε_r = Dielectric constant, d = Air gap distance, Q_T = Total quality, Q_R = Radiation loss, $\tan \delta$ = Dielectric loss tangent.

3. RESULT AND DISCUSSION

The agreement between experimental and theoretical results is good as shown in Tables 1 and 2. The simulation takes the air gap distance, d from 0 to 20 mm with an increment of 1 mm each respectively. Only 5 measurements are taken into account because the height limitation of the PCB stands which increment of 5 mm from 0 mm to 20 mm. By introducing an air gap, the effective relative permittivity of the structure is forced to decreased, though the electrical thickness of the antenna is increased. A low value of ε_r will increase the fringing field at the patch periphery and

Table 1: Simulations efficiency of Q-ACMAA air gap microstrip antenna.

Thickness of air gap, d (mm)	Directivity (dBi)	Gain (dB)	Efficiency, η
0	16.11	3.12	0.1936
5	17.31	8.04	0.4644
10	17.42	12.53	0.719
15	17.47	10.12	0.5792
20	17.46	6.75	0.3865

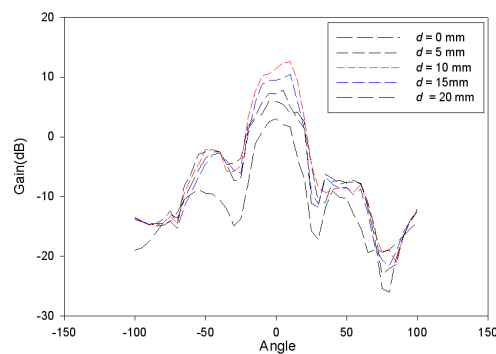


Figure 4: Measurements of radiation pattern at different distance of air gap, d .

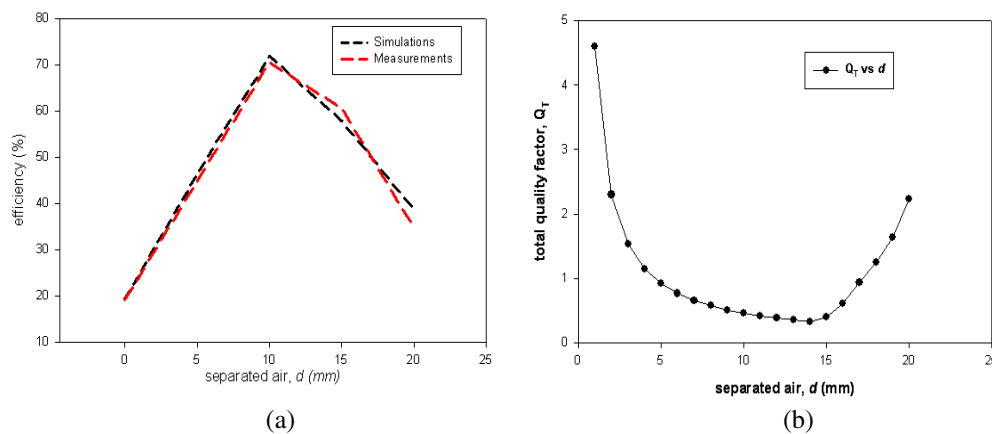


Figure 5: Effects of the air gap configuration on (a) efficiency, (b) quality Factor.

thus radiates power. The antenna efficiency increases up to 46.44% with an increase in d equal to 5 mm. A maximum of almost 72% of efficiency is stated when d equal to 10 mm initially due to the increase in radiated power as shown in Table 1.

The fringing fields from the edges increase with the increase in d simultaneously increase the amount of radiating power. Consequently, efficiency of the antenna had increased up to 70.52% as shown in Table 2. Generally, both of simulations and measurements antenna efficiency are increases with an increase in d , but thereafter it starts decreasing more than 40% beginning d equal to 11 mm because of the higher cross-polar level and excitation of the surface waves as stated in Equation (4) and Figure 5(a). Figure 4 shows five radiation patterns measured for d from 0 to 20 mm.

4. CONCLUSION

A novel of air gap quadratic aperture coupled microstrip array antenna is introduced in this paper. This antenna is designed on FR4 substrates. The proposed antenna makes the efficiency range 25% times larger than a quadratic aperture coupled microstrip array antenna without air gap and compared with the traditional rectangular microstrip antenna etched on the same substrate which only take 30% of efficiency. With etched on lossy substrates, this structure would be greatly suitable to overcome the 30% loss percentage of the FR4 at 2.3 GHz. The novel air gap of Q-ACMAA has successfully maintained the frequency resonant and impedance at 2.3 GHz simultaneously increased radiating power as well as efficiency increase.

ACKNOWLEDGMENT

The authors would like to thank to everyone for their helps and supports in completing this project especially to Wireless Communication Center (WCC), University of Technology Malaysia (UTM) and University of Malaysia Perlis (Unimap).

REFERENCES

1. Ghassemi, N., J. Rashed-Mohassel, and M. H. Neshati, "Microstrip antenna design for ultra wideband application by using two slots," *PIERS Proceedings*, 159–161, Hangzhou, China, March 24–28, 2008.
2. Spasos, M., N. Charalampidis, N. Mallios, D. Kampitaki, K. Tsiakmakis, P. Tsivos Soel, and R. Nilavalan, "On the design of an Ohmic RF MEMS switch for reconfigurable microstrip antenna applications," *WSEAS Transactions on Communications*, Vol. 8, No. 1, January 2009.
3. Li, L., Y. Yang, and R. Li, "Input impedance of microstrip antenna with thick multilayer substrate," Vol. 7, No. 3, *Journal of Electronics*, July 1990.
4. Ramesh, M. and K. B. Yip, "Design formula for inset fed microstrip patch antenna," *Journal of Microwaves and Optoelectronics*, Vol. 3, No. 3, December 2003.
5. Kanamaluru, S., M.-Y. Li, and K. Chang, "Analysis and design of aperture-coupled microstrip patch antennas and arrays fed by dielectric image line," *IEEE Transactions on Antennas and Propagation*, Vol. 44, No. 1, July 1996.
6. Sievenpiper, D., J. Schaffner, R. Loo, G. Tangonan, S. Ontiveros, and R. Harold, "A tunable impedance surface performing as a reconfigurable beam steering reflector," *IEEE Transactions on Antennas and Propagation*, Vol. 50, No. 3, March 2002.
7. Kim, B., B. Pan, S. Nikolaou, Y.-S. Kim, J. Papapolymerou, and M. M. Tentzeris, "A novel single-feed circular microstrip antenna with reconfigurable polarization capability," *IEEE Transactions on Antennas and Propagation*, Vol. 56, No. 3, March 2008.
8. Pozar, D. M., "Analysis of an infinite phased array of aperture coupled microstrip patches," *IEEE Transactions on Antennas and Propagation*, Vol. 37, No. 4, April 1989.
9. Colotti, J., "Analog, RF and EMC derivations in printed wiring board (PWB) design," IEEE Long Island (LI) Section.
10. Barnes, H., J. Moreira, T. McCarthy, C. Gutierrez, and M. Resso, "ATE interconnect performance to 43 Gbps using advanced PCB materials," DesignCon 2008.

Polarization Diversity Monopole Antenna

N. S. Awang Da, M. R. Dzulkifli, and M. R. Kamarudin

Wireless Communication Centre (WCC), Faculty of Electrical Engineering
Universiti Teknologi Malaysia, Malaysia

Abstract— The increasing number of user in ISM 2.4 GHz band has caused the spectrum to be crowded. The emerging technology of cognitive radio has paved the way of improving the spectrum utilization. Apart from that, antenna diversity is a well-known technique to enhance the performance of wireless communication systems by reducing the fading effects. In order to create an antenna diversity system on a wireless device, two or more antenna elements could be placed in positions that provide uncorrelated signals of the same power level. A printed polarization diversity monopole antenna for Cognitive Radio system application to improve the spectrum utilization in the 2.4 GHz ISM band is proposed in this paper. The proposed antenna is composed of two monopoles which are orthogonal to each other. CST Microwave Studio software was used to evaluate the antenna design. This antenna was fabricated on 50 mm × 50 mm FR4 board with thickness of 1.6 mm and dielectric permittivity 4.7. The front and back view of the proposed antenna were showed in Figs. 2 and 3 respectively. The simulated and measured return losses of the antenna are shown in Figs. 3 and 4. Even though the return loss at the two ports are different but the antennas have -15 dB and -12 dB return loss which were lower than -10 dB at 2.4 GHz. The radiation pattern for the antenna was different with single monopole antenna since the ground plane from antenna #2 reflected the signal radiated by antenna #1. This diversity antenna also offers wide bandwidth ($\sim 17\%$) and low correlation since the antenna orthogonal to each other.

1. INTRODUCTION

The evolution of wireless communication is rapidly evolving for the past two decades. The introduction of wireless local area network (WLAN) increases the awareness of consumers towards the potential of being wireless, hence the rise of the number of wireless user especially WLAN's user. The concept of mobility is one of the main reasons of attraction of the wireless technology. Moreover, WLAN is designed to work on the ISM band, such as the 2.4 GHz band, which is free for access to anyone. However, as time goes by, the high number of users causes the free spectrum to be crowded. The crowded spectrum [1] is an experiment done to investigate the usage of the 2.4 GHz ISM Band. The results reveal that the band is full of applications ranging from 802.11b, 802.15.1, 802.15.4 and the strong interferences generated from the microwave devices. This indicates the spectrum crisis.

Cognitive radio (CR) is considered as one of the solution to solve the crowded spectrum in the 2.4 GHz ISM band. CR is a set of transceiver that is able to sense and learn about the environment it operates thus adapting itself to the desired operation of the user. It was first introduce as an idea to improve the flexibility of personal services [2]. Moreover, CR is considered as the emerging technology to improve the spectrum utilization with its ability to be able to use the licensed band by unlicensed devices through the means of secondary usage [3]. This is achieved through continuously monitoring the spectrum usage in the process which runs in parallel with the communication link or use of a single channel for both spectrum sensing and communication [4]. A novel antenna for CR and its challenges is also presented in [4]. Therefore, the antenna factor is important, such as using a very wide band antenna for sensing and a narrowband antenna for communication or using a wideband antenna or a narrowband antenna for both sensing and communication in a single channel. In this paper, the focus is on the latter approach.

Antenna diversity is a well-known technique to enhance the performance of wireless communication systems. In order to create an antenna diversity system on a wireless device, two or more antenna elements could be placed in positions [5]. Diversity reception techniques are one of the best known methods to mitigate and reduce the effects of fading and are used widely in wireless communication. The method can be applied either at the transmitter or receiver. The principle behind diversity is the use of more than one independent and hence uncorrelated received signal which will fade independently of each other. Diversity can be achieved in various ways such as frequency diversity, time diversity and antenna diversity. Antenna diversity involves the use of multiple antenna, different radiation pattern, and/or polarizations. There are several forms of diversity methods such as space, frequency, polarization, and field and pattern diversity.

In general, the signals from the branches are combined using linear combines such as selection, equal gain, maximal ratio or switched combining. Some preliminary diversity measurements have shown that antenna diversity can offer significant improvement for the on body channels. Space diversity is by far the most popular technique. Space diversity is achieved by using more than one antenna at the transmitter or receiver side. This technique does not consume extra spectrum and the basic issue is that of antenna spacing. When two antennas are placed close to each other, mutual coupling between the antennas must be low to prevent the effect of one antenna on the other. Measurements in the past [6, 7] show that closely spaced dipole antennas (0.05 wavelengths apart) can still give a low signals correlation, in contrast to previous work on uncoupled dipoles showing that 0.5 wavelengths spacing is needed. To date, there have been considerable researched compacted antennas for handheld terminals [8, 9]. Many of these configurations are not suitable for handheld devices due to space limitation so suitable diversity method should be considered in designing diversity antenna.

2. ANTENNA DESIGN

This antenna consists of two monopole antennas that orthogonal to each other. The antenna is designed on FR4 substrate with thickness of 1.6 mm. The specifications of the substrate for dielectric permittivity, is 4.7 and tangent loss is 0.019. All the simulations are carried out using CST software. The simulation results will be compared to measurement result for fabrication stage. The width of the monopole trace is $W = 1.5$ mm and the length of the monopole $L = 23$ mm. The polarization monopole is designed to be operating at 2.4 GHz. The waveguide port feeding technique is use in the simulation where the dimension of feeding is 2.4×16 mm² in order to match to the patch for 50 Ω.

3. RESULT

Figures 1 and 2 shows the photograph of the polarization diversity monopole antenna. The simulated and measured return loss for polarization monopole antenna 1 and antenna 2

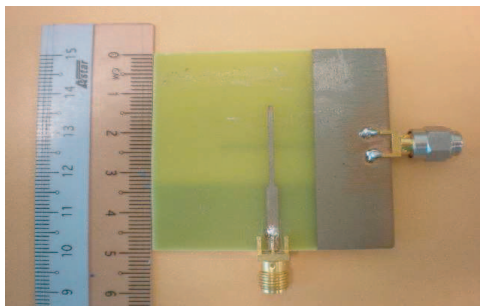


Figure 1: Front view of the proposed antenna.

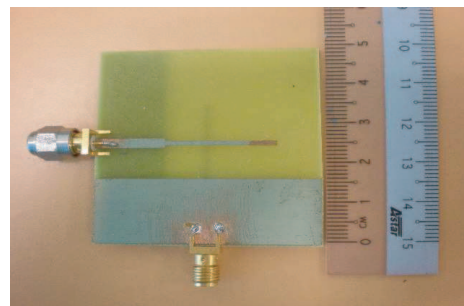


Figure 2: Back view of the proposed antenna.

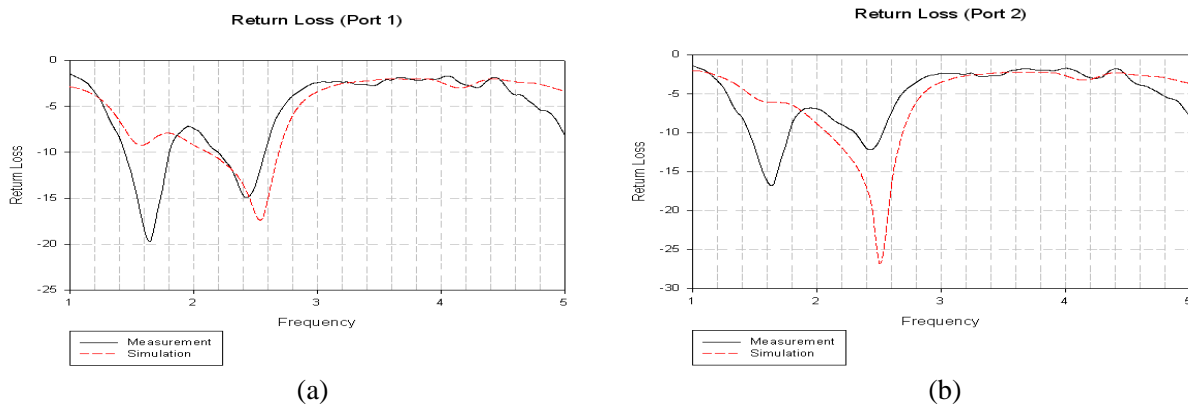


Figure 3: The simulated and measured return loss. (a) Polarization monopole antenna 1, (b) polarization monopole antenna 2.

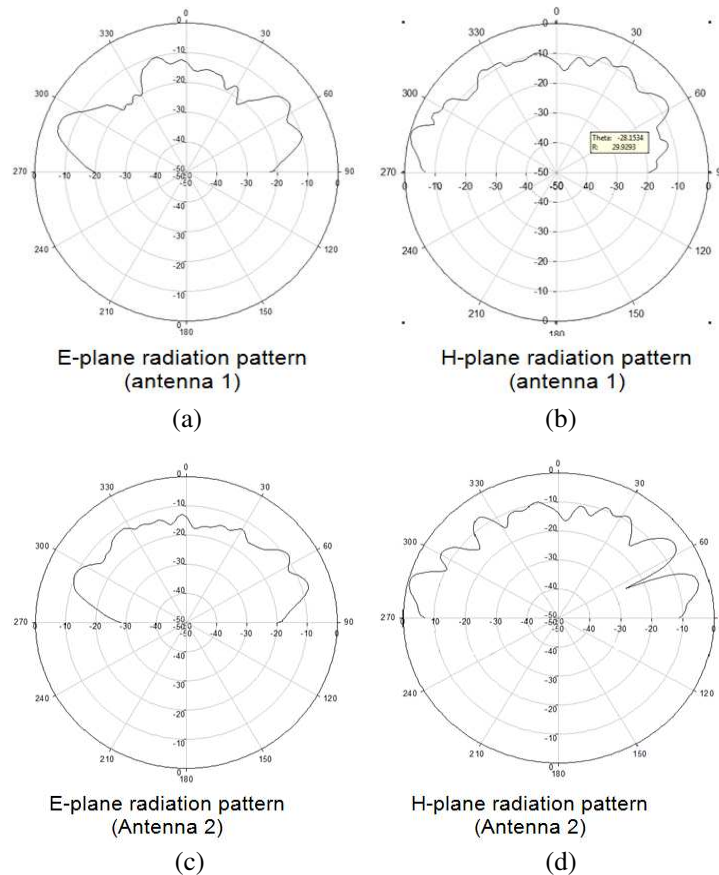


Figure 4: Measured radiation patterns of the polarization diversity monopole antenna at 2.4 GHz.

are shown in Figs. 3 and 4. Good agreement between the simulated and the measured results has been achieved. From the figures, the fractional bandwidth for reflection coefficient below -10 dB is about 17%

Figure 4 demonstrates the measured radiation patterns of the antennas for measurement. Figs. 4(a) and 4(b) show the radiation patterns of the antenna 1 whilst Figs. 4(c) and 4(d) show the radiation patterns of the antenna 2. The far-field is measured in range of -90° to 90° .

4. CONCLUSION

A compact polarization diversity monopole antenna is designed. Two diversity antennas operating at 2.40 GHz are designed. The return loss is found to be better than -10 dB and the usable bandwidth is about 17% in measurement. The measured results also show that such antenna design could be use in a CR system to improve the spectrum utilization. The antenna has good agreement between the simulated and measured results.

ACKNOWLEDGMENT

The authors wish to acknowledge the Government of Malaysia, Ministry of Science, Technology and Innovations (MOSTI) and Malaysia Communications and Multimedia Commission (MCMC) for the funding that enables this work to be accomplished and also special thanks to the members of Wireless Communication Centre (WCC), Faculty of Electrical Engineering, Universiti Teknologi Malaysia for their helps and kindness.

REFERENCES

1. Zhou, G., J. A. Stankovic, and S. Son, "Crowded Spectrum in wireless sensor networks," *IEEE EmNets*, 2006.
2. Mitola, J. and G. Q. Maguire, Jr., "Cognitive radio: Making software radios more personal," *IEEE Personal Communications*, Aug. 1999.

3. Haykin, S., “Cognitive radio: Brain-empowered wireless communications,” *IEEE Journal on Selected Areas in Communications*, Vol. 23, No. 2, Feb. 2005.
4. Hall, P. S., P. Gardner, J. Kelly, E. Ebrahimi, M. R. Hamid, and F. Ghanem, “Antenna challenges in cognitive radio,” *Proc. ISAP 08*, Taiwan, Oct. 2008.
5. Khaleghi, A., “Diversity techniques with parallel dipole antennas: Radiation pattern analysis,” *Progress In Electromagnetics Research*, PIER 64, 23–42, 2006.
6. Parson, J. D., *The Mobile Radio Propagation Channel*, 2nd Edition, Wiley, 2000.
7. Khaleghi, A., A. Azoulay, and J. C. Bolomey, “Diversity techniques with dipole antennas in indoor multipath propagation,” *16th Annual IEEE International Symposium on Personal Indoor and Mobile Radio Communication (PIMRC)*, Berlin, Germany, Sep. 2005.
8. Yeap, S. B., X. Chen, J. A. Dupuy, C. C. Chiau, and C. G. Parini, “Low profile diversity antenna for MIMO applications,” *Electronics Letters*, Vol. 42, No. 2, 69–71, 2006.
9. Douglas, M. G., M. Okoniewski, and M. A. Stuchly, “A planar diversity antenna for handheld PCS devices,” *IEEE Transactions on Vehicular Technology*, Vol. 47, No. 3, 747–754, 1998.

Effective Parameters of Artificial Material Composed of Dielectric Particles

Arun Kumar Saha and Matthew Hawthorn
Albany State University, USA

Abstract— In this research, a theory has been developed to estimate the effective parameters of artificial material composed of dielectric bars placed in a periodic fashion in dielectric host medium (air) from equivalent circuit point of view and verified with HFSS simulation. The theory provides a relationship between effective permittivity and the filling factor of the constituent particle and explains the anisotropic property of the artificial material macroscopically.

1. INTRODUCTION

In previous research it has been shown theoretically that effective material parameter (permittivity ϵ_r , and permeability μ_r) of artificial material, composed of spherical metal or dielectric balls embedded in host dielectric medium in a regular three dimensional fashion, depend on the *filling factor* [1]. This theoretical concept has been verified by simulation [2–4] too. In this research, a theory is developed to predict effective material parameters macroscopically from lumped element circuit parameters, inductance and capacitance, resulted from constituent particle. As inductance and capacitance are geometry-dependent parameters, so effective parameters, sensitivity of effective permittivity to particle permittivity and anisotropic behavior, which are discussed in this research, can be explained from particle geometry and particle permittivity.

2. THEORY

When rectangular dielectric bars are arranged in space to form an artificial material, a unit cell of that material is shown in Fig. 1. The dimensions of the bar is $x \times y \times h$ and cell is $\Delta x \times \Delta y \times H$ as shown in Fig. 1. The total capacitance of the cell C_{cell} is the parallel combination of two of capacitances; one is the contribution from the shaded area C_s and other is from the unshaded area C_{us} as shown in Fig. 1(b). Again C_s is the series combination of three capacitances C_a , C_d and C_a as shown in Fig. 1(c).

Now,

$$\begin{aligned} C_{us} &= \epsilon_0(\Delta x \Delta y - xy)/H \\ C_a &= 2\epsilon_0 xy/(H - h) \\ C_d &= \epsilon_r \epsilon_0 xy/h \end{aligned} \quad (1)$$

Therefore,

$$C_s = \frac{1}{1/C_a + 1/C_d + 1/C_a} = \frac{\epsilon_0 \epsilon_r xy}{(H - h)\epsilon_r + h} \quad (2)$$

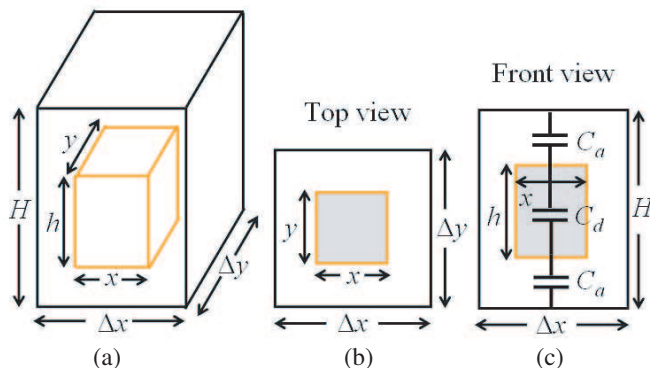


Figure 1: (a) Unit cell with dielectric bar as constituent particle, (b) top view, (c) front view.

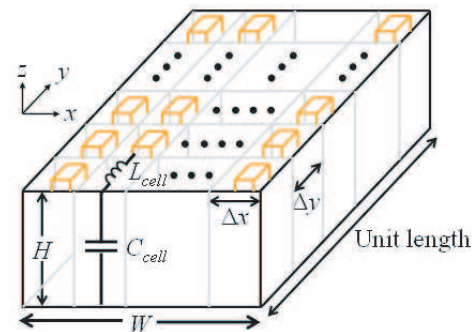


Figure 2: A parallel plate waveguide of unit length with width W and height H , filled with unit cells showing total cell capacitance C_{cell} and cell inductance L_{cell} .

Therefore total cell-capacitance

$$C_{cell} = C_{us} || C_s = \frac{\varepsilon_0(\Delta x \Delta y - xy)}{H} + \frac{\varepsilon_0 \varepsilon_r xy}{(H - h)\varepsilon_r + h} \quad (3)$$

As there is no magnetic material in the cell, total cell-inductance

$$L_{cell} = \mu_0 H \Delta y / \Delta x \quad (4)$$

Now, to calculate the effective parameter, it is sufficed to consider that a Parallel Plate Waveguide (PPWG) with width W and height H as shown in Fig. 2 is loaded with the unit cells as described in Fig. 1, where electric field is polarized in z -direction, magnetic field is polarized in x -direction and direction of wave propagation is in y -direction. Total capacitance per unit length of PPWG is

$$C_0 = C_{cell} \times (W / \Delta x \Delta y) \quad (5)$$

and total shunt admittance per unit length is

$$Y_0 = j\omega C_0 \quad (6)$$

Total inductance per unit length of PPWG is

$$L_0 = (L_{cell} / \Delta y) / (W / \Delta x) \quad (7)$$

and total series impedance

$$Z_0 = j\omega L_0 \quad (8)$$

Therefore, propagation constant

$$\gamma = \alpha + j\beta = \sqrt{Z_0 Y_0} = j\omega \sqrt{L_0 C_0} \quad (9)$$

Considering the lossless case

$$\beta^2 = \omega^2 \varepsilon_0 \varepsilon_r^{eff} \mu_0 \mu_r^{eff} = \omega^2 L_0 C_0 \quad (10)$$

Using Eqs. (3), (4), (5) and (7) in Eq. (10) yields

$$\varepsilon_r^{eff} \mu_r^{eff} = \left[\frac{(\Delta x \Delta y - xy)}{H} + \frac{\varepsilon_r xy}{(H - h)\varepsilon_r + h} \right] \times \frac{H}{\Delta x \Delta y} \quad (11)$$

Now characteristic impedance of PPWG, filled with particles, is

$$Z_c = \frac{H}{W} \sqrt{\frac{\mu_r^{eff}}{\varepsilon_r^{eff}}} = \sqrt{\frac{Z_0}{Y_0}} \quad (12)$$

Using Eqs. (3), (4), (5) and (7) in Eq. (12) yields

$$\frac{\varepsilon_r^{eff}}{\mu_r^{eff}} = \left[\frac{(\Delta x \Delta y - xy)}{H} + \frac{\varepsilon_r xy}{(H - h)\varepsilon_r + h} \right] \times \frac{H}{\Delta x \Delta y} \quad (13)$$

Introducing the filling factor term $f = xyh / (\Delta x \Delta y H)$ and ratio of particle-height (h) to cell-height (H) in the direction of electric field $a = h / H$ in Eqs. (11) and (13) yields

$$\mu_r^{eff} = 1 \quad (14)$$

$$\varepsilon_r^{eff} = 1 + \frac{f}{a} \left(\frac{\varepsilon_r}{a + \varepsilon_r(1 - a)} - 1 \right) \quad (15)$$

This is a very general equation for effective permittivity in terms of filling factor f and a ($= h / H$).

3. SIMULATION

3-D electromagnetic simulation software HFSS are used for simulation work. In simulation, the particle is put inside an air-cell as shown in Fig. 3. The side walls of air-cell are assumed perfect magnetic conductors, whereas the upper and bottom walls are perfect electric conductors. The dimension of the air-cell is 2.1 mm in each side. The electric and magnetic field of the incident electromagnetic plane wave is polarized in the direction of the z -axis and x -axis respectively. When incident plane wave falls on the unit cell, a part of the wave power is reflected back and the rest are transmitted. Numerically calculated scattering matrix parameter, S_{11} and S_{21} are used to calculate characteristic impedance Z_c and refractive index n from the following equations [5]:

$$Z_c = \sqrt{\frac{(1 + S_{11})^2 - S_{21}^2}{(1 - S_{11})^2 - S_{21}^2}} \quad (16)$$

$$n = \frac{1}{kl} \cos^{-1} \left[\frac{1}{2S_{21}} (1 - S_{11}^2 + S_{21}^2) \right] \quad (17)$$

$$\epsilon_r = n/Z_c \quad (18)$$

$$\mu_r = nZ_c \quad (19)$$

here l is the cell length and k is wave vector. Fig. 4 shows the calculated and simulated values of ϵ_r^{eff} with respect to filling factor (f) for $a = 0.976$, $\epsilon_r = 10$ and exhibits a very good agreement between those. In fact, total cell capacitance C_{cell} increases when filling factor is increased and for this reason ϵ_r^{eff} increases as predicted from Eq. (10). This equation of effective permittivity of artificial material in terms of filling factor (f) and ratio of particle-height to cell-height (a) in the direction of electric field is very meaningful from macroscopic point of view to understand the following cases: (1) Justification of special condition, (2) sensitivity of ϵ_r^{eff} to ϵ_r , (3) anisotropic behavior and (4) dependence of ϵ_r^{eff} on particle shape.

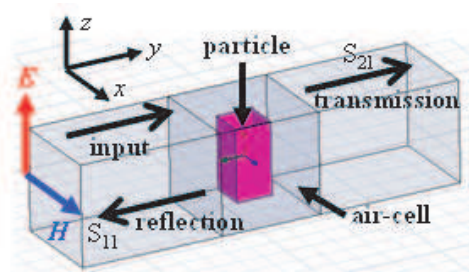


Figure 3: Dielectric particle in an air-cell, polarization of input fields and reflection and transmission of wave.

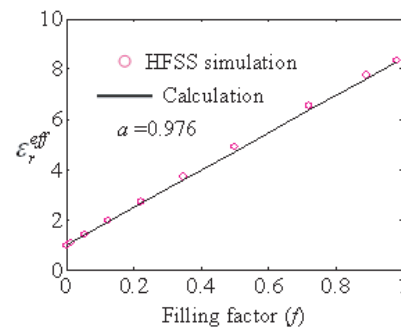


Figure 4: Dependence of relative effective permittivity of artificial material on filling factor for $a = 0.976$.

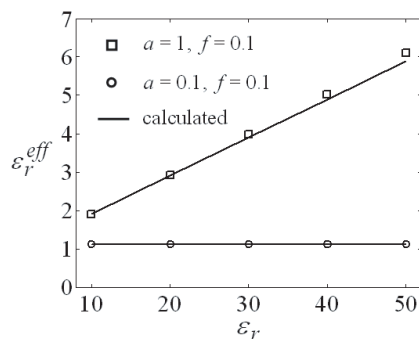


Figure 5: Sensitivity of effective permittivity of material to particle permittivity.

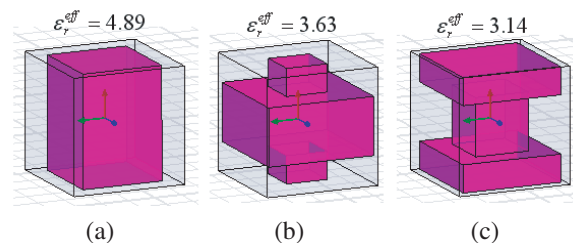
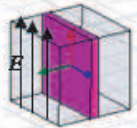
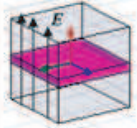


Figure 6: Variation effective permittivity with particle shape with same values of filling factor f , a and particle's relative permittivity ($= 10$).

Table 1: Anisotropy in artificial material.

Electric field orientation with respect to particle with $\epsilon_r = 50$	$a=h/H$	f	ϵ_r^{eff} (simulation)	ϵ_r^{eff} (calculation)
	1.0	0.1	5.97	5.90
	0.10	0.1	1.13	1.11

(1) Justification of special condition: When there is no particle in the cell, then $f = 0$, $\epsilon_r^{eff} = 1$ and when unit cell is filled with material of particle, then $f = 1$, and $\epsilon_r^{eff} = \epsilon_r$. Thus proves the validity of the derived Eq. (15) for effective permittivity.

(2) Sensitivity of ϵ_r^{eff} to ϵ_r : Effective permittivity Equation (15) predicts that for small value of a , relative effective permittivity ϵ_r^{eff} is insensitive to ϵ_r . Fig. 5 demonstrates both the simulation and calculated values of ϵ_r^{eff} to show this insensitiveness. Again, when $a = 1$, Eq. (15) reduces to $\epsilon_r^{eff} = 1 + f(\epsilon_r - 1)$ and predicts that ϵ_r^{eff} is very much sensitive to ϵ_r . Fig. 5 shows this sensitiveness by simulation and calculation both.

(3) Anisotropic behavior: The term a , which is the ratio of particle-height to cell-height in the direction of electric field, in Eq. (15) explains the anisotropy behavior of the artificial material. When the orientation of electric field is changed with respect to the particle, a is changed but filling factor f remains same in Eq. (15) and thus give rise to different values of ϵ_r^{eff} for different direction of electric field. Anisotropy is demonstrated by the configuration of electric field excitation with respect to the particle as shown in the Table 1.

(4) Dependence of ϵ_r^{eff} to particle shape: For given values of a and f , ϵ_r^{eff} is not supposed to change according to Eq. (15). But simulation result shows that shape of particle affects slightly. Fig. 6 displays various shapes of particles with given values of a ($= 0.975$) and f ($= 0.50$) and indicates the simulated ϵ_r^{eff} values which are slightly different from each other. This may be attributed to the fact that although f and a remain constant but due to change in particle shape, the total cell capacitance C_{cell} might be changed. Investigation is underway to find the cause of this.

4. CONCLUSION

A generalized equation for effective permittivity of artificial material composed of dielectric bar has been developed from lumped element circuit point of view. This generalized theory explains the dependence of effective permittivity on filling factor f and a , the ratio of particle-height to the cell-height in the direction of electric field. Macroscopically, it has been shown that total cell capacitance plays the vital role to determine the effective permittivity of dielectric-filled artificial material. The derived permittivity equation successfully estimates the effective permittivity of two special conditions (no particle in the cell and cell is filled with particle) and thus validates the proposed model. This study shows that effective permittivity is very sensitive to filling factor when $a = 1$ and thus macroscopically explains the anisotropic behavior of this artificial material.

ACKNOWLEDGMENT

The authors are grateful to the department of Natural Sciences of Albany State University, GA for the financial support and facility to conduct this research. The authors are also thankful to Dr. Kwai Chow Chan, Professor of Physics, Department of Natural Sciences, Albany State University for valuable discussions.

REFERENCES

1. Lewin, L., “Electrical constants of spherical conducting particles in a dielectric,” *J. IEE*, Vol. 94, Part 3, 65–68, London, 1947.
2. Saha, A. K., I. Awai, and O. Mizue, “Construction of dielectric resonator from artificial molecules,” *IEICE Technical Report*, 2007.
3. Awai, I., I. Mizue, and A. K. Saha, “Artificial dielectric resonator made of spherical metal particles,” *IEICE Transactions on Electronics*, Vol. E92-C, No. 1, 72–76, 2009.
4. Awai, I., “Artificial dielectric resonators for miniaturized filters,” *IEEE Microwave Magazine*, 55–64, Oct. 2008.
5. Smith, D. R., S. Schultz, P. Markos, and C. M. Soukoulis, “Determination of effective permittivity and permeability of metamaterial from reflection and transmission coefficients,” *Phys. Rev. B*, Vol. 65, No. 19, 1–5, 2002.

Franck-Hertz Experiment in Magnetic Field

Ying Weng¹ and Zi-Hua Weng²

¹College of Chemistry & Chemical Engineering, Xiamen University, Xiamen 361005, China

²School of Physics and Mechanical & Electrical Engineering, Xiamen University, Xiamen 361005, China

Abstract— The paper studies the impact of applied magnetic field on the inelastic collisions of electrons with argon atoms. In the electron-argon Franck-Hertz experiment, the influence of applied magnetic field emerges complicated features, and is equivalent to that of the temperature. In case the accelerating electric intensity becomes strong enough, enlarging magnetic flux density will be equivalent to the increasing of oven temperature. When the accelerating electric intensity is very weak and the applied magnetic field occupies a dominant position, enhancing magnetic flux density is identical with the decreasing of oven temperature. And the non-uniform distribution of applied magnetic field has an influence on the inelastic collision as well. The study claims that the influence of magnetic field variation is equivalent to that of temperature variety, and that it leads the electron energy to transfer obviously in the experiment.

1. INTRODUCTION

Franck-Hertz (F-H) experiment is vital to the modern physics, for it confirmed first the existence of discrete energy levels in atoms. In 1914, J. Franck and G. Hertz [1] reported an experiment on the collision of electrons with mercury vapor atoms. The authors observed a stepwise loss of electron energy in the experiment. N. Bohr in 1915 adverted to the F-H experiment and brought forward some related advisements. B. Davis and F. S. Goucher [2] in 1917 modified F-H tube to validate Bohr's predictions about the discrete energy level of gas atoms. In 1919, J. Franck and G. Hertz rechecked prototype F-H experiment, and claimed to support Bohr's viewpoint. Further, they improved their classic experimental devices the next year to study the high excitation level. Subsequently many research experiments [3, 4] have been carried out on the different features of F-H experiment with the mercury vapor, argon gas, and neon gas etc.

In a F-H tube filled with argon gas, the inelastic collisions of electrons with argon atoms will alter not only collided particles' velocity and direction, but also their energies and physics states. The result is the argon atoms acquire the energy while the electrons lose their energies. Decreasing the energy will cut down the number of electrons reaching the collector, consequently the collected current drops. Along with the increasing of electric voltage, the collected current will be oscillated periodically. And that this variation situation will be repeated again and again. The current variation is reported to be determined by the emitting voltage, accelerating voltage, retarding voltage, and temperature etc. Besides those main factors, the magnetic field is also an important and even more complicated factor.

By means of the air core solenoid and the permanent magnet, the paper studies the applied magnetic field's impact on the inelastic collisions of electrons with argon atoms. And the authors observed a few contrary influences of applied magnetic flux density on different accelerating electric intensity stages. The results obtained show that the influence of applied magnetic field on collected current emerges complicated features in the experiment.

2. INFLUENCE OF TEMPERATURE

In the electron-argon collision experiment, the increasing of oven temperature enlarges the electron kinetic energy and collecting current, but it does not vary the mean-free-path of electrons almost. Therefore the increasing of oven temperature leads testing curves to lift up, while the wave troughs of testing curves do not shift approximately.

2.1. F-H Tube Configuration

The tetrode F-H tube used in the experiment is a cylindrical tube filled with argon gas in Figure 1. The F-H tube configuration includes an indirectly heated cathode K, the heater F, grid G₁, grid G₂, and collector C. The grids G₁ and G₂ both are helix rounded by the nickel filaments. The G₁ coated with the gold is located in the tube center along the cylindrical axis. The distance between G₁ and K is near 0.3 mm. The grid G₂ is arranged outside G₁ and is 1 mm from the collector C. The distance between G₁ and G₂ is shorted to be comparable with the mean-free-path of electron

in the argon gas at operating temperature. The result shows an excellent characteristic curve in which as many as 6 wave crests can be seen.

The F-H tube is divided into three parts: The emitting region K-G₁, the accelerating and collision region G₁-G₂, and the retarding region G₂-C. Selecting a proper pressure of argon gas, the mean-free-path of electrons will be slightly larger than the distance between K and G₁. Consequently the electrons will be accelerated without collided in the emitting region. The electrons emitted from the cathode are accelerated by the voltage applied on the grids G₁ and G₂. The advantage of F-H tube configuration is that a large region between G₁ and G₂ will increase greatly the collision possibility among electrons and argon atoms. The most electrons collided inelastically with argon atoms loose a large part of their energies, they can not overcome the retarding electric field to reach the collector. Accordingly it drops the collected current. It is clear that when the critical level of argon atoms are reached, a series of successive wave crests and troughs on the voltage-current curves will be obtained in the experiment.

2.2. Temperature Effect

The F-H tube is located in an oven, which wrapped with an aluminum electrical shield. The oven temperature is raised to the operating value, and the heater supplies heat to the cathode. A lower cathode temperature will minimize the disturbance of velocities distribution of thermionic emitted electrons. During the experiment, the temperatures of oven and heater are kept constantly, since the collected current is sensitive to these temperatures.

For small accelerating voltages the collected current characteristics of the F-H tube are similar to that of a tetrode. At certain accelerating voltage, however, the collected current reaches a maximum. Increasing the accelerating voltage further decreases the collected current as the cross section for inelastic collision changes with the electron energy. When almost electrons have suffered the inelastic collision, the collected current traverses a minimum, and then it increases again.

It can easily be seen that there are a series of successive wave crests and troughs on the testing curve. In case emitting voltage and retarding voltage both are kept constantly, increasing the oven temperature lifts up the testing curve. When the oven temperature increases, the mean-free-path of electron varies slightly and the requested accelerating voltage keeps the same, according to the formula of mean-free-path of electron, $\lambda = K_b T / p \sigma$. Here K_b is the Boltzmann constant; T and p are the systematic temperature and pressure respectively; σ is the cross section for inelastic collision. Therefore the each wave trough of testing curves does not shift almost, due to the mean-free-path of electron keeps the same approximately. Moreover, the testing curves will lift up, because increasing the oven temperature enlarges the electron kinetic energy and the number of electron reaching the collector in Figure 2. Besides the temperature and electric intensity, the magnetic flux density has an influence on the electron-argon inelastic collision in F-H experiment also.

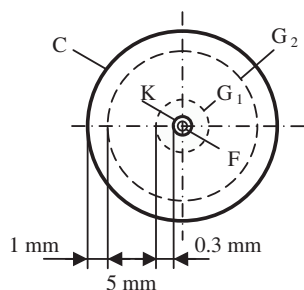


Figure 1: Cross-section sketch of a F-H tube with the cylindrical configuration. This tube filled with argon gas includes the heater F, cathode K, grid G₁, grid G₂, and collector C.

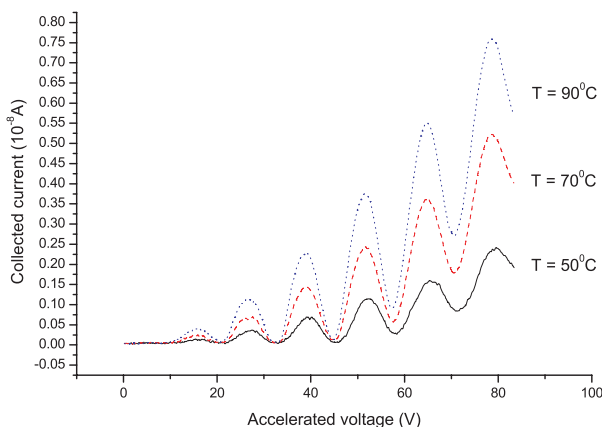


Figure 2: Increasing oven temperatures enlarge the electron kinetic energy and lead the voltage-current curves to lift up. $V_f = 3.75$ V, $V_{G_1K} = 0.7$ V, $V_{G_2C} = 7$ V. $T = 50^\circ\text{C}$, 70°C , and 90°C .

3. IMPACT OF MAGNETIC FIELD

In the F-H experiment a uniform magnetic field is applied properly in a direction perpendicular to the accelerating electric intensity. Wrapping the copper enameled wire on the surface of paper cylindrical canister to construct a solenoid, which inducing the uniform magnetic field by applied electric current I . Firstly, this solenoid is 9 cm and longer than the tube length. And it produces a uniform magnetic field to eliminate the disturbance of non-uniform distribution of magnetic field. The non-uniform distribution of applied magnetic field may cause the variation of magnetic potential energy to bother the measure precision. Secondly, the radius of solenoid is larger than that of tube. The F-H tube is located inside the solenoid, and has 5 mm air interval between them. This solenoid configuration and its paper material both dispel maximally the interference of temperatures. The final results verify the above advisement is effective in fact.

The F-H experiment in uniform magnetic fields is processing in the room temperature. And the influence of applied magnetic field emerges complicated features in the experiment.

3.1. Dominant Electric Intensity

In the test, the impact of magnetic field variation is equal to that of temperature variety. This indicates that the applied magnetic field results in electrons' energy transferring.

During the F-H experiment, the room temperature and the heating voltage V_f both are kept constantly, when the accelerating voltage V_{G_2K} is strong enough and is increasing continually further. There are a series of wave crests and wave troughs on the voltage-current curve, when the emitting voltage V_{G_1K} and retarding voltage V_{G_2C} both be kept constantly.

When the magnetic flux density \mathbf{B} increases, the mean-free-path of electron and the requested accelerating voltage both keep the same. In the experiment, we find that increasing the magnetic flux density lifts up the testing curve, while each wave trough of testing curves does not shift almost in Figure 3. This means that increasing magnetic flux density in short time enlarges the electron kinetic energy in spite of cyclotron emission, consequently the collected current increases. Therefore enlarging magnetic flux density is equivalent to the increasing of oven temperature, when the accelerating electric intensity is strong enough and occupies a dominant position.

3.2. Dominant Magnetic Flux Density

However, enlarging the magnetic flux density in the F-H experiment does not always imply the increasing of collected current, especially in weak accelerated voltages. Introducing a few necessary processing in the test to eliminate the interference coming from oven temperature and non-uniform magnetic field distribution, and protrude directly the effect of uniform magnetic field.

The room temperature, heater temperature, emitting voltage, and retarding voltage are kept constantly in the test. The emitting voltage and accelerating voltage both are weak enough and invariable, meanwhile the magnetic flux density occupies a dominant position. There are a series of

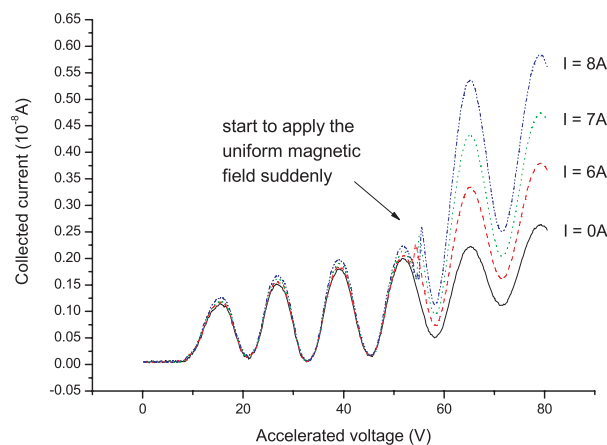


Figure 3: When the electric intensity is in a prominent place, increasing the magnetic flux density causes the voltage-current curve to jump up. $V_f = 3.78\text{ V}$, $V_{G_1K} = 2.3\text{ V}$, $V_{G_2C} = 7\text{ V}$. $I = 6\text{ A}$, 7 A , and 8 A , and their $\mathbf{B} = 19.5\text{ mT}$, 23.7 mT , and 26.3 mT correspondingly.

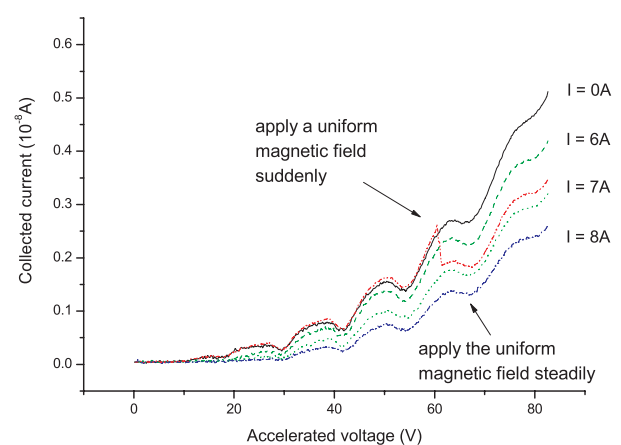


Figure 4: When the magnetic flux density occupies a dominant position, enhancing the magnetic flux density lowers the voltage-current curve suddenly or steadily. $V_f = 3.9\text{ V}$, $V_{G_1K} = 0.7\text{ V}$, $V_{G_2C} = 1\text{ V}$. $I = 6\text{ A}$, 7 A , and 8 A , and their $\mathbf{B} = 19.5\text{ mT}$, 23.7 mT , and 26.3 mT respectively.

wave crests and wave troughs on the testing curve too, when the magnetic flux density is increasing continually further.

When the accelerating electric intensity is very weak and the applied magnetic flux density occupies a dominant position, enhancing magnetic flux density over a short period of time should be identical with the oven temperature decreasing. In the test, we are surprised to find that increasing the magnetic flux density drops down the testing curve in Figure 4. This means that increasing magnetic flux density reduces the number of electron reaching the collector. Analyzing results recovers that the increasing magnetic flux density will enhance the electron kinetic energy and escaping velocity. And then increasing the number of electrons escaping from the tube leads the collected current to decrease. As a result, when the accelerating electric intensity is weak enough and the applied magnetic flux density occupies a dominant position, enlarging magnetic flux density is equivalent to the decreasing of oven temperature. This phenomenon can be explained partly by the secondary electron emission, and partly by the quaternion electromagnetic theory.

4. QUATERNION ELECTROMAGNETISM

According to classic electromagnetic theory, the uniform magnetic field has not an influence on the inelastic collisions of electrons with argon atoms, and on the electrons' energy transferring either. However the experiment results contradict this usual assumption. No matter how to apply the uniform magnetic field, either steadily or instantaneously, the collected current will appear to be fluctuated observably.

This means that applying uniform magnetic field leads to electrons' energy fluctuating. But the classic electromagnetic theory does not explain effectively why the phenomena will happen. The research assumes that there may be one new kind of electromagnetic force component, which results in the electrons to be accelerated continually, and then be transferred their energies.

4.1. Electromagnetic Force

The quaternion was invented by W. R. Hamilton [5] in 1843, and was first used by J. C. Maxwell in 1861 to represent electromagnetic theory [6]. At present, the algebra of quaternions can be used to describe either electromagnetic field or gravitational field.

The electromagnetic theory [7] described by quaternions predicts that there exists one new kind of electromagnetic force component, $qv_0\mathbf{B}$, along the direction of magnetic field line, besides the Lorentz force etc. Here q is the electric charge, and v_0 is the speed of light. This assumed force component will accelerate the electric charge along the direction of magnetic field line, and then vary the electric charge's energy. While Lorentz force causes electrons to turn near the cathode but does not change the electron energy in F-H experiment.

4.2. Electron Escaping

The influence of applied magnetic field in F-H experiment emerges complicated features. In the test, the impact of magnetic field variation is equal to that of temperature variety. This indicates that the applied magnetic field results in electrons' energy transferring. And it also states that

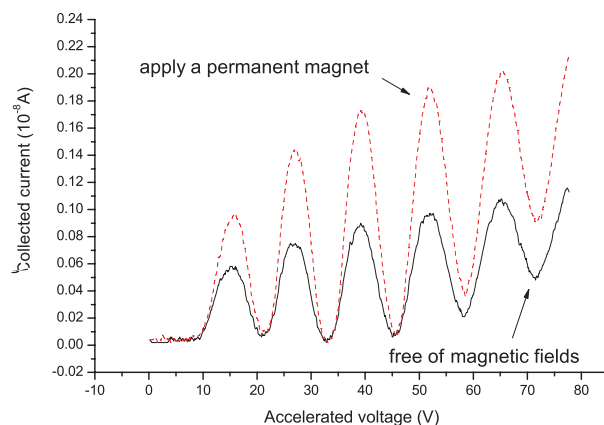


Figure 5: Influence of a permanent magnet on the collected current, when the accelerating electric intensity is in a prominent place. $\mathbf{B} = 43 \text{ mT}$. $V_f = 3.42 \text{ V}$, $V_{G_1K} = 2.3 \text{ V}$, $V_{G_2C} = 7.5 \text{ V}$.

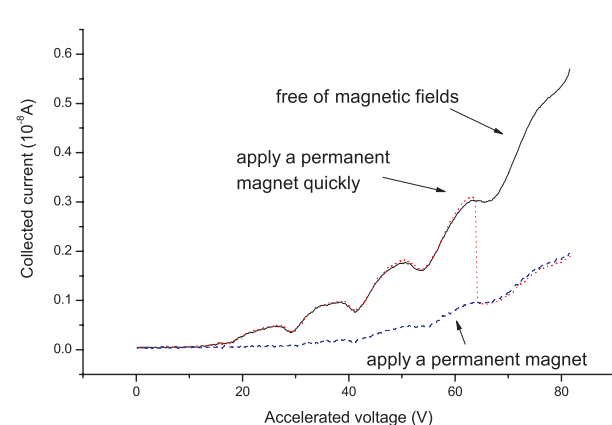


Figure 6: Impact of the permanent magnet on the collected current, when the magnetic flux density occupies a dominant position. $\mathbf{B} = 43 \text{ mT}$. $V_f = 3.95 \text{ V}$, $V_{G_1K} = 0.6 \text{ V}$, $V_{G_2C} = 1 \text{ V}$.

enlarging magnetic flux density leads electrons' energy to increase, when the accelerating electric intensity is strong enough and occupies a dominant position.

In case the accelerating electric intensity occupies a dominant position, the medial electric force is much bigger than the assumed force. The assumed force will accelerate electrons along the magnetic field line, and lift up the electrons' energy by the interparticle collision. Accordingly, it increases electrons' number reaching the collector, and enlarges the collected current in Figure 5. In the same time, the assumed force will cause tiny part of electrons escaping from the F-H tube along the magnetic field lines. Due to the electrons speed from cathode to collector are high enough, the accelerating time is quite short, and then the number of escaping electrons is very small.

Further we lower the accelerated electric intensity while increase the magnetic flux density, it will drop the radius component of electron's speed and increase number of escaping electrons. When the accelerating electric intensity is low enough, the uniform magnetic field will be in a prominent place, the assumed force is much bigger than the medial electric force. It will accelerate electrons and have enough time to thrust them escaping along the magnetic field line, and then decrease electrons' number reaching the collector and cut down the collected current in Figure 6. Although it will also increase the electrons' energy to reach the collector by the interparticle collision.

The results obtained indicate that the impact of magnetic field on the collected current in the F-H experiment is different even contrary distinctly, when the accelerate electric field and applied magnetic field are situated on different intensity stages.

5. CONCLUSION

In the F-H experiment, some complicated impacts of applied magnetic field on the collected current have been observed. Increasing the applied magnetic field will lift up the electron kinetic energy, and enlarge the number of escaping electrons. Consequently increasing the applied magnetic field has a quite strange and complex influence on the collected current.

The impact of magnetic field variation on the collected current in the F-H test is equal to that of temperature variety. On the one hand, in case the accelerating electric intensity occupies a dominant position, enlarging magnetic flux density is equivalent to increasing of temperature. On the other hand, when the accelerating electric intensity becomes weak enough and applied magnetic flux density is in a prominent place, enhancing magnetic flux density should be identical with temperature decreasing.

It should be noted that the study for impacts of applied magnetic field on F-H test examined only some simple cases in the room temperature. Despite its preliminary characteristics, this study can clearly indicate that the applied magnetic flux density has an influence on the inelastic collisions of electrons with argon atoms. For the future studies, the research will concentrate on only more inferences about the impact of applied magnetic field on collected currents.

ACKNOWLEDGMENT

This project was supported partially by the National Natural Science Foundation of China under grant number 60677039.

REFERENCES

1. Franck, J. and G. Hertz, "Über Zusammenstöße zwischen Elektronen und Molekülen des Quecksilberdampfes und die Ionisierungsspannung desselben," *Verh. Dtsch. Phys. Ges.*, Vol. 16, 456–457, 1914; English translation: *World of the Atom*, edited by H. A. Boorse and L. Motz, Vol. I, 770–778, Basic Books, New York, 1966.
2. Davis, B. and F. S. Goucher, "Ionization and excitation of radiation by electron impact in mercury vapor and hydrogen," *Physical Review*, Vol. 10, No. 2, 101–115, 1917.
3. Liu, F.-H., "Franck-Hertz experiment with higher excitatin level measurements," *American Journal of Physics*, Vol. 55, No. 4, 366–369, 1987.
4. Robson, R. E., B. Li, and R. D. White, "Spatially periodic structures in electron swarms and the Franck-Hertz experiment," *Journal of Physics B: Atomic, Molecular and Optical Physics*, Vol. 33, No. 3, 507–520, 2000.
5. Hamilton, W. R., *Elements of Quaternions*, Longmans, Green & Co., London, 1866.
6. Maxwell, J. C., *A Treatise on Electricity and Magnetism*, Dover Publications Inc., New York, 1954.
7. Weng, Z.-H., "Electromagnetic forces on charged particles," *PIERS Proceedings*, 361–363, Moscow, Russia, August 18–21, 2009.

Coordinate Transformations with Variable Speed of Light

Zi-Hua Weng

School of Physics and Mechanical & Electrical Engineering, Xiamen University, Xiamen 361005, China

Abstract— The coordinate transformation with variable speed of light is proposed by means of the algebra of quaternions. The quaternions can be used to describe the property of electromagnetic field and gravitational field. In the quaternion space, some coordinate transformations can be deduced from the feature of quaternions, including Lorentz transformation and Galilean transformation. And that some coordinate transformations with variable speed of light can be obtained as well. The paper claims that the speed of light will be varied with the movements in the electromagnetic field and gravitational field.

1. INTRODUCTION

The variable speed of light concept states that the speed of light in a vacuum may not be constant in some particular cases. In 1937, P. Dirac and others began to investigate the consequences of natural constants changing with time, including the varying speed of light in time. In the quantum theory, R. Feynman believed that there is an amplitude for light to go faster or slower than the conventional speed of light. The light doesn't go only in straight lines, and it doesn't go only at the speed of light either. In the cosmology, the first variable speed of light model has been proposed by J.-P. Petit [1] from 1988. Later, the second model by J. W. Moffat [2] in 1992, and A. Albrecht and J. Magueijo in 1998 respectively. Some alternative models have also been proposed.

Making use of the property of quaternions [3], we can obtain Galilean transformation and Lorentz transformation [4], when the speed of light is invariable. However the viewpoint about invariable speed of light is being doubted and challenged for a long time. Consequently the people question the validity of these coordinate transformations with invariable speed of light. Up to now, this suspicion remains as puzzling as ever. The paper attempts to explain why the above coordinate transformations remain unchanged in most cases.

The quaternion was invented in 1843 by W. R. Hamilton. He made a great effort for theoretical analysis of quaternions, and tried to apply quaternions to describe several physical phenomena. In 1861, J. C. Maxwell applied the algebra of quaternions to depict the properties of electromagnetic field [5]. With the feature of quaternions, we deduce some coordinate transformations, including Galilean transformation, Lorentz transformation, and the coordinate transformations with variable speed of light. In the quaternion spaces, the speed of light will be varied with the movements in either electromagnetic field or gravitational field.

2. TRANSFORMATIONS IN THE QUATERNION SPACE

The electromagnetic theory can be described with the algebra of quaternions. In the treatise on electromagnetic theory, the algebra of quaternion was first used by J. C. Maxwell to represent the various properties of the electromagnetic field [6]. At present, the gravitational field can be described by the algebra of quaternions as well.

2.1. Coordinate Transformation

In the quaternion space, the basis vector is $\mathbb{E} = (1, i_1, i_2, i_3)$, and the radius vector $\mathbb{R}(r_0, r_1, r_2, r_3)$ is defined as,

$$\mathbb{R} = r_0 + i_1 r_1 + i_2 r_2 + i_3 r_3, \quad (1)$$

where $r_0 = v_0 t$; t denotes the time; v_0 is the speed of gravitational intermediate boson.

The physical quantity $\mathbb{D}(d_0, d_1, d_2, d_3)$ in quaternion space is defined as,

$$\mathbb{D} = d_0 + i_1 d_1 + i_2 d_2 + i_3 d_3. \quad (2)$$

When we transform the quaternion coordinate system from one into the other, the physical quantity \mathbb{D} is transformed into $\mathbb{D}'(d'_0, d'_1, d'_2, d'_3)$,

$$\mathbb{D}' = \mathbb{K}^* \circ \mathbb{D} \circ \mathbb{K}, \quad (3)$$

where \mathbb{K} is the quaternion, and $\mathbb{K}^* \circ \mathbb{K} = 1$; $*$ denotes the conjugate of quaternion.

On the one hand, in case the coordinate system is transforming, the quaternions in the above satisfy the relation as follows,

$$\mathbb{D}^* \circ \mathbb{D} = (\mathbb{D}')^* \circ \mathbb{D}'. \quad (4)$$

On the other hand, when the scalar part of quaternion physical quantity \mathbb{D} does not take part in the coordinate transformations, the scalar part d_0 remains the same,

$$d_0 = d'_0. \quad (5)$$

From Eqs. (4) and (5), we can obtain some coordinate transformations in the quaternion space.

2.2. Galilean Transformation

In the quaternion space, the velocity $\mathbb{V}(v_0, v_1, v_2, v_3)$ is

$$\mathbb{V} = v_0 + i_1 v_1 + i_2 v_2 + i_3 v_3. \quad (6)$$

As the coordinate system is transformed into other one, we have a radius vector $\mathbb{R}'(r'_0, r'_1, r'_2, r'_3)$ and velocity $\mathbb{V}'(v'_0, v'_1, v'_2, v'_3)$ respectively from Eq. (3).

From Eqs. (1), (3), (5), and (6), we have

$$r_0 = r'_0, \quad v_0 = v'_0, \quad (7)$$

and then from Eqs. (1) and (4) and the above ($j = 1, 2, 3$)

$$t_0 = t'_0, \quad \Sigma(r_j)^2 = \Sigma(r'_j)^2. \quad (8)$$

The above means that emphasizing especially the important of radius vector Eq. (1) and velocity Eq. (6) will deduce Galilean transformation of coordinate system from Eqs. (1), (5), and (6).

2.3. Lorentz Transformation

In some special cases, we have to emphasize the importance of the power function of radius vector rather than the influence of radius vector. The physical quantity $\mathbb{D}(d_0, d_1, d_2, d_3)$ is defined as

$$\mathbb{D} = \mathbb{R} \circ \mathbb{R} = d_0 + i_1 d_1 + i_2 d_2 + i_3 d_3. \quad (9)$$

In the above equation, the scalar part remains the same during the quaternion coordinate system is transforming. From Eq. (5) and the above, we have

$$(r_0)^2 - \Sigma(r_j)^2 = (r'_0)^2 - \Sigma(r'_j)^2. \quad (10)$$

The above means the spacetime interval d_0 remains unchanged, when the coordinate system rotates. From Eqs. (5), (6), and (9), we obtain the Lorentz transformation,

$$(r_0)^2 - \Sigma(r_j)^2 = (r'_0)^2 - \Sigma(r'_j)^2, \quad v_0 = v'_0. \quad (11)$$

The above means that it will deduce Lorentz transformation of coordinate system, when we emphasize the velocity Eq. (6) and physical quantity Eq. (9) rather than the radius vector Eq. (1). It recovers that Galilean transformation and Lorentz transformation depend on the choosing from different combinations of the basic physical quantities. When $r_0^2 \gg \Sigma(r_j)^2$ and $(r'_0)^2 \gg \Sigma(r'_j)^2$, we have $r_0^2 \approx (r'_0)^2$. And then Eq. (11) is reduced to Eq. (7).

2.4. Variable Speed of Light

In some particular cases, we need to emphasize the importance of the power function of velocity rather than the influence of velocity. The physical quantity $\mathbb{Q}(q_0, q_1, q_2, q_3)$ is defined as,

$$\mathbb{Q} = \mathbb{V} \circ \mathbb{V} = q_0 + i_1 q_1 + i_2 q_2 + i_3 q_3. \quad (12)$$

When the coordinate system is transformed into other one, we have one physical quantity $\mathbb{Q}'(q'_0, q'_1, q'_2, q'_3)$ from Eq. (3). In the above equation, the scalar part remains the same during the coordinate system is transforming. From Eq. (5) and the above, we have,

$$(v_0)^2 - \Sigma(v_j)^2 = (v'_0)^2 - \Sigma(v'_j)^2. \quad (13)$$

The above states that the speed of light v_0 will be changed, when the coordinate system rotates in the quaternion spaces.

From Eqs. (1), (5), and (12), we obtain the transformation A with variable speed of light,

$$r_0 = r'_0, \quad (v_0)^2 - \Sigma(v_j)^2 = (v'_0)^2 - \Sigma(v'_j)^2. \tag{14}$$

From Eqs. (5), (9), and (12), we acquire the transformation B with variable speed of light,

$$(r_0)^2 - \Sigma(r_j)^2 = (r'_0)^2 - \Sigma(r'_j)^2, \quad (v_0)^2 - \Sigma(v_j)^2 = (v'_0)^2 - \Sigma(v'_j)^2. \tag{15}$$

When $v_0^2 \gg \Sigma(v_j)^2$ and $(v'_0)^2 \gg \Sigma(v'_j)^2$, we obtain $v_0^2 \approx (v'_0)^2$. Therefore Eq. (14) is reduced to Eq. (7), while Eq. (15) to Eq. (11).

In a similar way, the quantity \mathbb{D} and \mathbb{Q} can be defined as other kinds of power functions of radius vector \mathbb{R} or velocity \mathbb{V} , such as $\mathbb{D} = \mathbb{R} \circ \mathbb{R} \circ \mathbb{R} \circ \mathbb{R}$ or $\mathbb{Q} = \mathbb{V} \circ \mathbb{V} \circ \mathbb{V}$, etc. Consequently we may have some more complicated coordinate transformations in the quaternion spaces.

Table 1: Some coordinate transformations in the quaternion space.

transformations	radius vector	velocity
<i>Galilean</i>	$r_0 = r'_0$	$v_0 = v'_0$
<i>Lorentz</i>	$(r_0)^2 - \Sigma(r_j)^2 = (r'_0)^2 - \Sigma(r'_j)^2$	$v_0 = v'_0$
<i>A</i>	$r_0 = r'_0$	$(v_0)^2 - \Sigma(v_j)^2 = (v'_0)^2 - \Sigma(v'_j)^2$
<i>B</i>	$(r_0)^2 - \Sigma(r_j)^2 = (r'_0)^2 - \Sigma(r'_j)^2$	$(v_0)^2 - \Sigma(v_j)^2 = (v'_0)^2 - \Sigma(v'_j)^2$
<i>others</i>	$\mathbb{D} = \mathbb{R} \circ \mathbb{R} \circ \mathbb{R} \circ \mathbb{R} \text{ etc}$	$\mathbb{Q} = \mathbb{V} \circ \mathbb{V} \circ \mathbb{V} \text{ etc}$

3. TRANSFORMATIONS IN THE OCTONION SPACE

The gravitational field and electromagnetic field both can be demonstrated by quaternions, but they are quite different from each other indeed. We add another quaternion space to the ordinary quaternion space to encompass the feature of the gravitational and electromagnetic fields [7].

3.1. Coordinate Transformation

The basis vector of quaternion space for the gravitational field is $\mathbb{E}_g = (1, i_1, i_2, i_3)$, and that for the electromagnetic field is $\mathbb{E}_e = (I_0, I_1, I_2, I_3)$. While the \mathbb{E}_e is independent of the \mathbb{E}_g , with $\mathbb{E}_e = (1, i_1, i_2, i_3) \circ I_0$. The basis vectors \mathbb{E}_g and \mathbb{E}_e can be combined together to become the basis vector \mathbb{E} of octonion space, that is, $\mathbb{E} = \mathbb{E}_g + \mathbb{E}_e = (1, i_1, i_2, i_3, I_0, I_1, I_2, I_3)$.

The radius vector $\mathbb{R}(r_0, r_1, r_2, r_3, R_0, R_1, R_2, R_3)$ in the octonion space is,

$$\mathbb{R} = \Sigma(i_i r_i) + \Sigma(I_i R_i), \tag{16}$$

and the velocity $\mathbb{V}(v_0, v_1, v_2, v_3, V_0, V_1, V_2, V_3)$ is

$$\mathbb{V} = \Sigma(i_i v_i) + \Sigma(I_i V_i), \tag{17}$$

where $R_0 = V_0 T$; T is one time-like quantity; V_0 is the speed of electromagnetic intermediate boson. $i_0 = 1, i = 0, 1, 2, 3$.

When the coordinate system is transformed into other one, the octonion physical quantity \mathbb{D} will be transformed into $\mathbb{D}'(d'_0, d'_1, d'_2, d'_3, D'_0, D'_1, D'_2, D'_3)$,

$$\mathbb{D}' = \mathbb{K}^* \circ \mathbb{D} \circ \mathbb{K}, \tag{18}$$

where \mathbb{K} is the octonion, and $\mathbb{K}^* \circ \mathbb{K} = 1$; $*$ denotes the conjugate of octonion.

On the one hand, in case the coordinate system is transforming, the octonions in the above satisfy the relation as follows

$$\mathbb{D}^* \circ \mathbb{D} = (\mathbb{D}')^* \circ \mathbb{D}'. \tag{19}$$

On the other hand, when the scalar part of octonion does not take part in the coordinate transformation, the d_0 remains the same,

$$d_0 = d'_0. \tag{20}$$

From the above, we can obtain some coordinate transformations in the octonion space.

Table 2: The octonion multiplication table.

	1	i_1	i_2	i_3	I_0	I_1	I_2	I_3
1	1	i_1	i_2	i_3	I_0	I_1	I_2	I_3
i_1	i_1	-1	i_3	$-i_2$	I_1	$-I_0$	$-I_3$	I_2
i_2	i_2	$-i_3$	-1	i_1	I_2	I_3	$-I_0$	$-I_1$
i_3	i_3	i_2	$-i_1$	-1	I_3	$-I_2$	I_1	$-I_0$
I_0	I_0	$-I_1$	$-I_2$	$-I_3$	-1	i_1	i_2	i_3
I_1	I_1	I_0	$-I_3$	I_2	$-i_1$	-1	$-i_3$	i_2
I_2	I_2	I_3	I_0	$-I_1$	$-i_2$	i_3	-1	$-i_1$
I_3	I_3	$-I_2$	I_1	I_0	$-i_3$	$-i_2$	i_1	-1

3.2. Galilean Transformation

When the coordinate system is rotated, we have one radius vector $\mathbb{R}'(r'_0, r'_1, r'_2, r'_3, R'_0, R'_1, R'_2, R'_3)$ and velocity $\mathbb{V}'(v'_0, v'_1, v'_2, v'_3, V'_0, V'_1, V'_2, V'_3)$ respectively from Eq. (18).

From Eqs. (16), (17), (18), and (20), we have

$$r_0 = r'_0, \quad v_0 = v'_0, \quad (21)$$

and then from Eqs. (16) and (19) and the above

$$t_0 = t'_0, \quad \Sigma(r_j)^2 + \Sigma(R_i)^2 = \Sigma(r'_j)^2 + \Sigma(R'_i)^2. \quad (22)$$

The above means that emphasizing the important of radius vector Eq. (16) and velocity Eq. (17) will deduce Galilean transformation of coordinate system. The above implies that the r_0 remains unchanged when the quaternion coordinate system rotates, while the R_0 keeps changed as a vectorial component. When $R_i \approx R'_i$, Eq. (22) is reduced to Eq. (8).

3.3. Lorentz Transformation

In some special cases, we need to emphasize the power function of radius vector rather than the radius vector. The physical quantity $\mathbb{D}(d_0, d_1, d_2, d_3, D_0, D_1, D_2, D_3)$ is defined as

$$\mathbb{D} = \mathbb{R} \circ \mathbb{R} = \Sigma(i_i d_i) + \Sigma(I_i D_i). \quad (23)$$

By Eqs. (20) and (23), we have

$$(r_0)^2 - \Sigma(r_j)^2 - \Sigma(R_i)^2 = (r'_0)^2 - \Sigma(r'_j)^2 - \Sigma(R'_i)^2. \quad (24)$$

The above represents that the spacetime interval d_0 keeps unchanged when the coordinate system rotates in the octonion space. When the octonion space is reduced to the quaternion space, the above equation should be reduced to Eq. (10) in the quaternion space. By Eqs. (17), (20), and (23), we have Lorentz transformation,

$$(r_0)^2 - \Sigma(r_j)^2 - \Sigma(R_i)^2 = (r'_0)^2 - \Sigma(r'_j)^2 - \Sigma(R'_i)^2, \quad v_0 = v'_0. \quad (25)$$

The above means that emphasizing the important of velocity Eq. (17) and of physical quantity Eq. (23), we obtain Lorentz transformation of coordinate system. In the octonion space, when $R_i \approx R'_i$, Eq. (25) is reduced to Eq. (11) in the quaternion space.

3.4. Variable Speed of Light

In some particular cases, we have to emphasize the power function of velocity rather than the velocity. The physical quantity $\mathbb{Q}(q_0, q_1, q_2, q_3, Q_0, Q_1, Q_2, Q_3)$ in octonion space is defined as

$$\mathbb{Q} = \mathbb{V} \circ \mathbb{V} = \Sigma(i_i q_i) + \Sigma(I_i Q_i). \quad (26)$$

When the coordinate system is rotated, we have one quantity $\mathbb{Q}'(q'_0, q'_1, q'_2, q'_3, Q'_0, Q'_1, Q'_2, Q'_3)$ from Eq. (18). In the above, the scalar part remains the same during the octonion coordinate system is transforming. From Eqs. (18) and (20) and the above, we have

$$(v_0)^2 - \Sigma(v_j)^2 - \Sigma(V_i)^2 = (v'_0)^2 - \Sigma(v'_j)^2 - \Sigma(V'_i)^2. \quad (27)$$

The above equation represents the speed of light v_0 will be changed when the coordinate system rotates in the octonion spaces.

From Eqs. (16), (20), and (27), we obtain the transformation A with variable speed of light,

$$r_0 = r'_0, \quad (v_0)^2 - \Sigma(v_j)^2 - \Sigma(V_i)^2 = (v'_0)^2 - \Sigma(v'_j)^2 - \Sigma(V'_i)^2. \quad (28)$$

From Eqs. (24) and (27), we gain the transformation B with variable speed of light,

$$\begin{aligned} (r_0)^2 - \Sigma(r_j)^2 - \Sigma(R_i)^2 &= (r'_0)^2 - \Sigma(r'_j)^2 - \Sigma(R'_i)^2, \\ (v_0)^2 - \Sigma(v_j)^2 - \Sigma(V_i)^2 &= (v'_0)^2 - \Sigma(v'_j)^2 - \Sigma(V'_i)^2. \end{aligned}$$

In the octonion space, when $V_i \approx V'_i$, Eq. (28) is reduced to Eq. (14) in the quaternion space. It is easy to find that we may similarly have other kinds of coordinate transformations in the octonion space by defining different physical quantities.

4. CONCLUSIONS

In the quaternion and octonion spaces, Galilean transformation and Lorentz transformation etc can be deduced from the features of quaternions and octonions. This states that Lorentz transformation is only one of several coordinate transformations in electromagnetic and gravitational fields.

There exist coordinate transformations with variable speed of light in quaternion and octonion spaces. In the electromagnetic and gravitational fields, different coordinate transformations depend on different choosing from the combination of basic physical quantities. And the speed of light will be changed with the movements in electromagnetic field and gravitational field.

It should be noted that the study for the coordinate transformation has examined only some simple cases, including Galilean transformation and Lorentz transformation. Despite its preliminary character, this study can clearly indicate that there are several kinds of coordinate transformations with the variable speed of light. For the future studies, the research will concentrate on only some predictions about the complicated coordinate transformations with variable speed of light.

ACKNOWLEDGMENT

This project was supported partially by the National Natural Science Foundation of China under grant number 60677039.

REFERENCES

1. Petit, J.-P., "An interpretation of cosmological model with variable light velocity," *Modern Physics Letters A*, Vol. 3, No. 16, 1527–1532, 1988.
2. Moffat, J. W., "Superluminary universe: A possible solution to the initial value problem in cosmology," *International Journal of Modern Physics D*, Vol. 2, No. 3, 351–366, 1993.
3. Morita, K., "Quaternions, lorentz group and the dirac theory," *Progress of Theoretical Physics*, Vol. 117, No. 3, 501–532, 2007.
4. Teli, M. T., "Quaternionic form of unified lorentz transformations," *Physics Letters A*, Vol. 75, No. 6, 460–462, 1980.
5. Grusky, S. M., K. V. Khmelnytskaya, and V. V. Kravchenko, "On a quaternionic Maxwell equation for the time-dependent electromagnetic field in a chiral medium," *Journal of Physics A*, Vol. 37, No. 16, 4641–4647, 2004.
6. Schwartz, C., "Relativistic quaternionic wave equation," *Journal of Mathematical Physics*, Vol. 47, No. 12, 122301, 2006.
7. Weng, Z.-H., "Influence of field potential on the speed of light," *PIERS Proceedings*, 896–899, Moscow, Russia, August 18–21, 2009.

Radiometry, Wave Optics and Spatial Coherence

A. S. Marathay¹, J. F. McCalmont², and D. B. Pollock³

¹College of Optical Sciences, University of Arizona, Tucson, AZ, USA

²Air Force Research Laboratory, Sensors Directorate, WPAFB, OH, USA

³Center for Applied Optics, University of Alabama, Huntsville, AL, USA

Abstract— Conventional radiometry concepts are based on geometry or ray optics. However, radiation is an electromagnetic wave. In this paper, radiometry is generalized to include the framework of wave theory. Key radiometric quantities and sources of conventional radiometry are redefined in the context of wave optics. The mutual coherence function and other statistical quantities are incorporated and play a central role in connecting the radiometric quantities of conventional radiometry to those of generalized radiometry. Stationary phase concepts are employed to determine the radiometry of diffracting systems. Specific examples of generalized radiometry are examined such as black body radiation, partially coherent sources, and coherent sources.

1. INTRODUCTION

Radiometry is the science of detection and measurement of radiation. The ideas and concepts of this science are based on geometrical or ray optics. However, radiation is an electromagnetic wave. Waves diffract and have states of partial coherence and polarization. Therefore, it is important to include the wave nature of radiation and formulate radiometry in the framework of wave theory. Radiometry based on ray theory is conventional radiometry and that based on wave theory is generalized radiometry.

2. CONVENTIONAL RADIOMETRY

The inter-relationships among the spectral functions of conventional radiometry are displayed in Table 1. The symbol A under the integral stands for the integration over the area of the source and the $1/2$ under the integral implies the angle integration is limited to the right-half space, $0 \leq \theta \leq \pi/2$ and $0 \leq \phi \leq 2\pi$. The product $\cos\theta d\Omega$ is called the projected solid angle differential element.

Table 1: Inter-relationships among the spectral functions of conventional radiometry.

$\hat{L}(\vec{r}, \hat{n}, \nu)$, Spectral Radiance [W/cm ² /sr/Hz]	
$\hat{\Phi}(z, \nu) = \int_{A/2} \int \hat{L}(\vec{r}, \hat{n}, \nu) \cos\theta d\Omega dA$ Spectral Radiant Power [W/Hz]	
Spectral Radiant Exitance [W/cm ² /Hz] $\hat{M}(\vec{r}, \nu) = \int_{1/2} \hat{L}(\vec{r}, \hat{n}, \nu) \cos\theta d\Omega$	Spectral Radiant Intensity [W/sr/Hz]. $\hat{I}(z, \hat{n}, \nu) = \cos\theta \int_A \hat{L}(\vec{r}, \hat{n}, \nu) dA$
Spectral Radiant Power [W/Hz] $\hat{\Phi}(z, \nu) = \int_A \hat{M}(\vec{r}, \nu) dA$	Spectral Radiant Power [W/Hz] $\hat{\Phi}(z, \nu) = \int_{1/2} \hat{I}(z, \hat{n}, \nu) d\Omega$

3. LAMBERTIAN SOURCES

Consider a source whose spectral radiance is independent of position \vec{r} on the source and the direction of observation \hat{n} , that is, $\hat{L}(\vec{r}, \hat{n}, \nu) = \hat{L}_0(\nu)$. Such a source is called a *Lambertian* source. For a planar Lambertian source radiating in the right-half space, it follows from Table 1 that, $\hat{\Phi} = \pi A \hat{L}_o$, $\hat{M} = \pi \hat{L}_o$, $\hat{I} = \cos\theta A \hat{L}_o$

4. MUTUAL COHERENCE FUNCTION

Radiometry and Wave Optics are brought together by use of the Mutual Coherence Function (MCF). Details of the theory may be found in Born and Wolf [1], and Marathay [2]. The MCF is defined as a cross-correlation in the time domain. We use the spectral version of the MCF as given by,

$$\Gamma(\vec{r}_1, \vec{r}_2, \nu) = \langle \psi(\vec{r}_1, \nu) \psi^*(\vec{r}_2, \nu) \rangle, \quad \gamma_{12}(\nu) = \frac{\Gamma(\vec{r}_1, \vec{r}_2, \nu)}{\sqrt{\Gamma(\vec{r}_1, \vec{r}_1, \nu) \Gamma(\vec{r}_2, \vec{r}_2, \nu)}}$$

5. STATIONALRY PHASE APPROXIMATION

It can be shown, the diffracted field can be represented by the following expression [1, 3]

$$\psi(\vec{r}, \nu) = \psi(r, p, q, \nu) = \frac{-i}{\lambda} m \frac{\exp(ikr)}{r} \iint_A \psi(x_s, y_s, 0) \exp\left[-i\frac{2\pi}{\lambda}(px_s + qy_s)\right] dx_s dy_s$$

Here, we have used the direction cosines $p = x/r$, $q = y/r$, and $m = z/r$. The diffracted field on a hemisphere of radius r is simply the spatial Fourier transform of the field distribution in the aperture as long as the distance r to the observation point satisfies the far-field condition, $r \gg 2m^2a^2/\lambda$; $m = z/r = \cos\theta$, a is the radius of the aperture. The z -axis is perpendicular to the aperture plane and θ is measured from the z -axis.

6. RADIOMETRY AND WAVE OPTICS

Radiation incident from the left on an aperture in a plane at $z = 0$ diffracts radiation into the right-half space. The diffracted field resides on a hemisphere of radius r . The origin of the coordinate system is in the open aperture. Let $d\Omega$ denote a differential element of solid angle. The differential element of area on the hemisphere is $r^2 d\Omega$. A radiation detector responds to the ensemble average of the squared modulus of the optical field; the output is in watts [W]. To find the total power radiated into the right half space, we integrate over the hemisphere. The *Spectral Radiant Power* in the right-half space is given by, $\Phi(\nu) = \iint_{1/2} \langle |\psi(\vec{r}, \nu)|^2 \rangle r^2 \sin\theta d\theta d\phi = \iint_{1/2} \langle |\psi(\vec{r}, \nu)|^2 \rangle r^2 d\Omega$. In this

expression, the angular brackets denote the ensemble average. The integrand contains the diffracted field $\psi(\vec{r}, \nu)$. It is clear that the *ensemble average of the squared modulus of the diffracted field* $\langle |\psi(\vec{r}, \nu)|^2 \rangle$ plays the role of *spectral radiance with units* [W/cm²/sr/Hz] for radiation detection on the surface of the hemisphere. With a change of variable, \vec{r}_s (average vector) and \vec{r}_{s12} (difference vector) this expression is re-grouped as,

$$\Phi(\nu) = \iint_A d^2\vec{r}_s \iint_{1/2} m d\Omega \left\{ \frac{m}{\lambda^2} \iint_A \Gamma(\vec{r}_s + \frac{1}{2}\vec{r}_{s12}, \vec{r}_s - \frac{1}{2}\vec{r}_{s12}, 0, \nu) \exp[-ik\hat{n} \cdot \vec{r}_{s12}] d^2\vec{r}_{s12} \right\}$$

Now following Walther [4], we identify the expression in the braces as the *Spectral Radiance* [W/cm²/sr/Hz] function and denote it as,

$$\begin{aligned} B(\vec{r}_s, 0, \hat{n}, \nu) &= \frac{m}{\lambda^2} \iint_A \Gamma(\vec{r}_s + \frac{1}{2}\vec{r}_{s12}, \vec{r}_s - \frac{1}{2}\vec{r}_{s12}, 0, \nu) \exp[-ik\hat{n} \cdot \vec{r}_{s12}] d^2\vec{r}_{s12} \\ &= \frac{m}{\lambda^2} \iint_A \langle \psi(\vec{r}_s + \frac{1}{2}\vec{r}_{s12}, 0, \nu) \psi^*(\vec{r}_s - \frac{1}{2}\vec{r}_{s12}, 0, \nu) \rangle \exp[-ik\hat{n} \cdot \vec{r}_{s12}] d^2\vec{r}_{s12} \end{aligned}$$

with this definition, the total spectral radiant power is $\Phi(\nu) = \iint_A \left[\iint_{1/2} B(\vec{r}_s, 0, \hat{n}, \nu) m d\Omega \right] d^2\vec{r}_s$.

Following this first step, Marchand and Wolf [5] developed the following functions of radiometry of

wave optics:

$$M(\vec{r}_s, 0, \nu) = \iint_{1/2} B(\vec{r}_s, 0, \hat{n}, \nu) m d\Omega, \quad \Phi(\nu) = \iint_A M(\vec{r}_s, 0, \nu) d^2\vec{r}_s.$$

$$J(\hat{n}, \nu) = m \iint_A B(\vec{r}_s, 0, \hat{n}, \nu) d^2\vec{r}_s, \quad \Phi(\nu) = \iint_{1/2} J(\hat{n}, \nu) d\Omega.$$

These equations form the structure of wave-theoretic radiometry. The radiometry formulated in this way is free from any paraxial restrictions. Based on the definition of Φ in terms of J we observe that $J(\hat{n}, \nu) = r^2 \langle |\psi(r, p, q, \nu)|^2 \rangle$. We have just established that for radiation detection on a hemisphere the Spectral Radiant Intensity is directly related to the ensemble average of the squared modulus of the diffracted field multiplied by the square of the radius of the hemisphere. The *The spectral radiant intensity is a conserved quantity from one hemisphere to the next concentric hemisphere since $|\psi|^2$ depends on $1/r^2$.*

7. GENERALIZED RADIOMETRY EXAMPLES

7.1. Blackbody Radiation

Mehta and Wolf [6] have calculated the spatial coherence function of radiation in thermal equilibrium with the walls of a cavity. We can write it in the form, $\Gamma(\vec{r}_s + \frac{1}{2}\vec{r}_{s12}, \vec{r}_s - \frac{1}{2}\vec{r}_{s12}, 0, \nu) = 2\pi S \frac{\sin kr_{s12}}{kr_{s12}}$. In this expression $r_{s12} = \sqrt{(x_{s1} - x_{s2})^2 + (y_{s1} - y_{s2})^2}$ is the magnitude of the vector \vec{r}_{s12} . The function S is Planck's Radiation Law. The spectral density is

$$S_{BB} \equiv S_{BB}(\nu, T) = \frac{c}{4\pi} \frac{8\pi h\nu^3}{c^3} \left[\frac{1}{\exp(h\nu/k_B T) - 1} \right] = \frac{2h\nu^3}{c^2} \left[\frac{1}{\exp(h\nu/k_B T) - 1} \right].$$

The following expressions are developed:

$$B(\vec{r}_s, 0, \hat{n}, \nu) = \frac{m}{\lambda^2} 2\pi S_{BB} \cdot \frac{\lambda^2}{2\pi} \frac{1}{m} = S_{BB}(\nu, T), \quad \Phi = \pi A S_{BB}(\nu, T)$$

$M(\vec{r}_s, 0, \nu) = \pi S_{BB}(\nu, T)$, $J(\hat{n}, \nu) = \cos\theta A S_{BB}(\nu, T)$. A is the area of the hole in the cavity. Blackbody radiation is Lambertian.

7.2. Non-coherent Wave Fields

$\Gamma(\vec{r}_s + \frac{1}{2}\vec{r}_{s12}, \vec{r}_s - \frac{1}{2}\vec{r}_{s12}, 0, \nu) = \frac{\lambda^2}{\pi} \hat{I}_0(\nu) \delta(\vec{r}_{s12})$. In this expression, $\hat{I}_0(\nu)$ is the "squared modulus of the optical field" at frequency ν . The remaining relationships are:

$$B(\vec{r}_s, 0, \hat{n}, \nu) = \frac{m}{\lambda^2} \frac{\lambda^2}{\pi} \hat{I}_0(\nu) = \frac{m}{\pi} \hat{I}_0(\nu), \quad \Phi(\nu) = \frac{2}{3} A \cdot \hat{I}_0(\nu).$$

$$M(\vec{r}_s, 0, \nu) = \frac{2}{3} \hat{I}_0(\nu), \quad J(\hat{n}, \nu) = m^2 \frac{A}{\pi} \hat{I}_0(\nu).$$

Owing to the factor $m^2 = \cos^2\theta$, the non-coherent source will appear *darker* when viewed at large angles from the normal.

7.3. Coherent Wave Fields

$$\Gamma(\vec{r}_s + \frac{1}{2}\vec{r}_{s12}, \vec{r}_s - \frac{1}{2}\vec{r}_{s12}, 0, \nu) = U(\vec{r}_s + \frac{1}{2}\vec{r}_{s12}) U^*(\vec{r}_s - \frac{1}{2}\vec{r}_{s12}) \delta(\nu - \nu_0)$$

where U is any solution of the Helmholtz equation at frequency ν_0 .

$$B(\vec{r}_s, 0, \hat{n}, \nu_0) = \frac{m}{\lambda_0^2} \left| \tilde{U}\left(\frac{\hat{n}}{\lambda_0}\right) \right|^2, \quad \Phi(\nu) = A \iint_{1/2} \left| \frac{m}{\lambda_0} \tilde{U}\left(\frac{\hat{n}}{\lambda_0}\right) \right|^2 d\Omega$$

$$M(\vec{r}_s, 0, \nu_0) = \iint_{1/2} \left| \frac{m}{\lambda_0} \tilde{U}\left(\frac{\hat{n}}{\lambda_0}\right) \right|^2 d\Omega, \quad J(\hat{n}, \nu_0) = A \left| \frac{m}{\lambda_0} \tilde{U}\left(\frac{\hat{n}}{\lambda_0}\right) \right|^2$$

A is the area of the open aperture in the $z = 0$ plane containing the coherent field.

7.4. QUASI-homogeneous Wave Fields

$\Gamma_s(\vec{r}_{s1}, \vec{r}_{s2}, \nu) = I_s(\vec{r}_s, \nu) g_s(\vec{r}_{s12}, \nu)$ where I_s is the ensemble average of the squared modulus of the optical field and is assumed to be very broad and slowly varying compared to the coherence function $g_s(\vec{r}_{s12}, \nu)$. The widths σ_Q and σ_g are both frequency ν dependent and $\sigma_Q \gg \sigma_g$.

$$B(\vec{r}_s, \hat{n}, \nu) = \frac{1}{\pi} I_s(\vec{r}_s, \nu) \frac{m}{2} (k\sigma_g)^2 \text{Exp} \left[-\frac{1}{2} (k\sigma_g)^2 (p^2 + q^2) \right]$$

$$\Phi(\nu) = \int I_s(\vec{r}_s, \nu) d^2\vec{r}_s \quad \text{and} \quad M(\vec{r}_s, \nu) = I_s(\vec{r}_s, \nu)$$

$$J(\hat{n}, \nu) = \frac{1}{2\pi} (k\sigma_g)^2 \exp \left[-\frac{1}{2} (k\sigma_g)^2 \sin^2 \theta \right] \int I_s(\vec{r}_s, \nu) d^2\vec{r}_s \quad \theta \text{ and varies from } 0 \text{ to } \pi/2.$$

REFERENCES

1. Born, M. and E. Wolf, *Principles of Optics*, Pergamon Press, 1959.
2. Marathay, A. S., *Elements of Optical Coherence Theory*, Chapter 3, 29–32, John Wiley & Sons, 1982.
3. Marathay, A. S., J. F. McCalmont, and J. Shiefman, “Diffraction,” *Optical Engineer’s Desk Reference*, Edited by William L. Wolfe, Chapter 6, Optical Society of America and The International Society for Optical Engineering, 2003.
4. Walther, A., “Radiometry and coherence,” *J. Opt. Soc. Am.*, Vol. 58, No. 9, 1256–1259, 1968.
5. Marchand, E. W. and E. Wolf, “Radiometry with sources of any state of coherence,” *J. Opt. Soc. Am.*, Vol. 64, No. 9, 1219–1226, 1974.
6. Mehta, C. L. and E. Wolf, “Coherence properties of blackbody radiation, I. Correlation tensors of the classical field,” *Phys. Rev. A*, Vol. 134, No. 5, 1143–1149, 1964.

Homogeneous Bianisotropic Medium, Dissipation and the Non-constancy of Speed of Light in Vacuum for Different Galilean Reference Systems

Namik Yener

Technology Faculty, Umuttepe Campus, Kocaeli University, Izmit, Kocaeli 41380, Turkey

Abstract— A procedure is developed which leads to a relation that can be used to argue the negation of the Special Relativity Theory when there exists a general homogeneous bianisotropic medium with dissipation. The unbounded general bianisotropic medium is interfaced with a perfectly conducting medium filling a half space so that the interface is an infinite plane. The perfectly conducting half space (medium (II)) is assumed to move uniformly and along the $O'z'$ axis of the Galilean reference system K' which is attached to medium (II), and the interface plane with medium (I), the bianisotropic medium which is at rest and to which is attached the Galilean reference system K , is assumed to be perpendicular to the $O'z'$ axis. The relation found is between constitutive parameters, the direction cosines with respect to $Oxyz$ axes of the incident plane wave impingent on the infinite plane interface, the incident wave parameters, v_1 the relative speed of K' with respect to K and c the speed of light in vacuum. This relation is shown to be interpretable to falsify the Special Relativity Theory. On the other hand it is demonstrated also that when the same homogeneous bianisotropic medium without loss is considered no such relation can be obtained and the Special Relativity Theory cannot be contradicted.

Three examples are presented. One for a lossless electrically uniaxially anisotropic medium, one for a dissipative simple medium and another for a dissipative electrically uniaxially anisotropic medium. While the first one does not lead to any contradiction of Maxwell's equations with Special relativity Theory, the other two are shown to lead to such relations.

1. INTRODUCTION

A coordinate system called the kDB system will be adopted to ease discussions on solutions of field vectors inside a general homogeneous medium. The kDB system devised originally by J. A. Kong, consists of the \vec{k} vector and the DB plane [1]. The kDB system has unit vectors \vec{e}_1, \vec{e}_2 and \vec{e}_3 . \vec{e}_3 is taken in direction of \vec{k} so that $\vec{k} = k\vec{e}_3$. The unit vector is in the radial direction in the spherical coordinate system. In terms of the xyz coordinate system we find $\vec{e}_3 = \vec{e}_r = \sin \theta \cos \phi \vec{a}_x + \sin \theta \sin \phi \vec{a}_y + \cos \theta \vec{a}_z$. The unit vector \vec{e}_2 is in the \vec{e}_θ direction again in the spherical coordinate system. We thus have $\vec{e}_2 = \vec{e}_\theta = \cos \theta \cos \phi \vec{a}_x + \cos \theta \sin \phi \vec{a}_y$. The unit vectors \vec{e}_1, \vec{e}_2 and \vec{e}_3 form a right hand orthogonal coordinate system so that $\vec{e}_1 = \vec{e}_2 \times \vec{e}_3 = \sin \phi \vec{a}_x - \cos \phi \vec{a}_y$. In the above $\vec{a}_x, \vec{a}_y, \vec{a}_z$ are the unit orthogonal vectors of the Cartesian coordinate system.

We assume that the uniform velocity of frame K' attached to a perfectly conducting half space, with respect to K attached to a homogeneous bianisotropic medium at rest, is in the \vec{a}_z direction. This assumption for an unbounded medium does not impose a restriction on the validity of the results that are obtained because we can always rotate our coordinate system so that the z axis points in the direction of motion. Even though this coordinate rotation certainly affects the element values of the constitutive matrix, the form of the matrix will remain intact after the transformation. This is because the projections of the vectors on the new coordinate system axes will change numerically while the vectors are preserved in form [1].

We shall use two constitutive matrix formalisms in this paper. The first is the Lorentz covariant form given by Equation (5) [2]. The second is the one which is the result of the kDB approach and from which the linear algebraic equation system of (6) can be derived. The two formalisms are equivalent in the sense they can be obtained from each other using simple matrix operations.

Now we assume the interface of the perfectly conducting half space (medium (II)) and the bianisotropic medium (medium (I)) is an infinite plane perpendicular to the velocity of K' with respect to K or the z axis. Then the wave vector components and frequencies of incident and reflected plane waves will be as follows due to enforcement of the phase invariance principle and the boundary condition on the interface plane after the Lorentz transformation has been applied.

Here subscript i indicates incident, while r indicates reflected.

$$k_{iz} = \alpha(k'_z - \omega' r/c) \quad (1a)$$

$$k_{ix} = k'_x \quad (1b)$$

$$k_{iy} = k'_y \quad (1c)$$

$$\omega_i = \alpha(\omega' - rck'_z) \quad (1d)$$

$$k_{rz} = \alpha(k'_z + \omega' r/c) \quad (2a)$$

$$k_{rx} = k'_x \quad (2b)$$

$$k_{ry} = k'_y \quad (2c)$$

$$\omega_r = \alpha(\omega' + rck'_z) \quad (2d)$$

Primed quantities denote those measured from K' while unprimed ones denote those measured from K . ω represents angular frequency while k represents wave numbers. α , r are defined in [3] and c is the speed of light in vacuum. In the kDB system, the incident wave vector will have the following components.

$$k_{i1} = 0, \quad k_{i2} = 0, \quad k_{i3} = k_i \quad (3)$$

In Cartesian coordinates these will transform into:

$$k_{ix} = k_i \sin \theta \cos \phi = k'_x = k_{rx} \quad (4a)$$

$$k_{iy} = k_i \sin \theta \sin \phi = k'_y = k_{ry} \quad (4b)$$

$$k_{iz} = k_i \cos \theta = \alpha(k'_z - \omega' r/c) \quad (4c)$$

On the surface of the perfect electric conductor (at $z' = 0$) tangential electric field component must vanish. This implies that the equalities (1b), (2b) and (1c), (2c) must have the same right hand sides. On the other hand the incident electric field vector observed from K' will read:

$$\vec{E}'_i = [E'_{ix}\vec{a}_x + E'_{iy}\vec{a}_y + E'_{iz}\vec{a}_z] \exp\{j(k'_x x' + k'_y y' + k'_z z' - \omega' t')\},$$

with $\vec{k}'_i = k'_x \vec{a}_x + k'_y \vec{a}_y + k'_z \vec{a}_z$ while the reflected electric field observed from K' will read:

$$\vec{E}'_r = [E'_{rx}\vec{a}_x + E'_{ry}\vec{a}_y + E'_{rz}\vec{a}_z] \exp\{j(k'_x x' + k'_y y' - k'_z z' - \omega' t')\}.$$

Since our interface plane is smooth, the result of specular reflection will yield the following wave vector for the reflected wave if \vec{k}'_i is as given above: $\vec{k}'_r = k'_x \vec{a}_x + k'_y \vec{a}_y - k'_z \vec{a}_z$. Notice components of \vec{k}'_i and \vec{k}'_r tangential to the interface surface are equal. Note that all these properties are implicit in (1) and (2).

Then the relation $\vec{k}'_r \times \vec{E}'_r = j\omega' \vec{B}'_r$ must hold, and we conclude that $\vec{B}'_r = \frac{1}{j\omega'} [\vec{a}_x(k'_y E'_{rz} + k'_z E'_{ry}) - \vec{a}_y(k'_x E'_{rz} + k'_z E'_{rx}) + \vec{a}_z(-k'_y E'_{rx} + k'_x E'_{ry})]$. Furthermore according to [1] we have

$$\begin{bmatrix} c\vec{D}' \\ \vec{H}' \end{bmatrix} = \begin{bmatrix} \bar{P}' & \bar{L}' \\ \bar{M}' & \bar{Q}' \end{bmatrix} \begin{bmatrix} \vec{E}' \\ c\vec{B}' \end{bmatrix}, \quad (5)$$

where the coefficients matrix on the right hand side is the constitutive matrix of the bianisotropic medium observed from K' . Entries of this matrix are given in [1]. In other words $\vec{D}'_r = \bar{P}' \vec{E}'_r/c + \bar{L}' \vec{B}'_r$ and $\vec{H}'_r = \bar{M}' \vec{E}'_r + c\bar{Q}' \vec{B}'_r$ are true. On the other hand inserting this \vec{H}'_r into the Maxwell's equation $\vec{k}'_r \times \vec{H}'_r = -j\omega' \vec{D}'_r$, we shall obtain another expression for \vec{D}'_r . Equating these two vectors will yield three linear algebraic homogeneous equations for E'_{rx} , E'_{ry} , E'_{rz} with coefficients as functions of k'_x , k'_y and k'_z . For a non-zero solution for the set E'_{rx} , E'_{ry} , E'_{rz} , the coefficient matrix must have a vanishing determinant. This vanishing determinant will yield the dispersion equation for the reflected wave observed from K' . All field components will thus have been expressed in terms of one scalar function assuming the coefficients matrix has rank 2. Otherwise the field components will have been expressed in terms of two scalar functions. These scalar functions are elements of the set of E'_{rx} , E'_{ry} , E'_{rz} field components and they will be constrained by the initial conditions.

The exact same procedure will yield the solution for the incident wave. The boundary condition on the infinite perfectly conducting interface plane will require $E'_{iy} = -E'_{ry}$, $E'_{ix} = -E'_{rx}$. Since all the field components will again be determined by one or two scalar functions, choosing these functions as $-E'_{ry}$ and/or $-E'_{rx}$ will yield the solution for the other field components. Also the determinant of the pertinent linear algebraic equation system will yield the dispersion relation for the incident wave observed from K' . This completes determination of the field vectors that also satisfy the boundary conditions on interface of the two media.

2. DISPERSION RELATIONS FOR INCIDENT AND REFLECTED WAVES AND THE RELATION TO NEGATE SPECIAL RELATIVITY THEORY

The dispersion relation of medium (I) as observed from K can be obtained from the determinant of following coefficient matrix for D_1 and D_2 , the first two components of the displacement flux density vector in the kDB system.

$$\left\{ \begin{bmatrix} \chi_{11} & \chi_{12} - u \\ \chi_{21} + u & \chi_{22} \end{bmatrix} \begin{bmatrix} \nu_{22} & -\nu_{12} \\ -\nu_{21} & \nu_{11} \end{bmatrix} \begin{bmatrix} \gamma_{11} & \gamma_{12} + u \\ \gamma_{21} - u & \gamma_{22} \end{bmatrix} - \begin{bmatrix} \kappa_{11} & \kappa_{12} \\ \kappa_{21} & \kappa_{22} \end{bmatrix} \cdot N \right\} \begin{bmatrix} D_1 \\ D_2 \end{bmatrix} = 0 \quad (6)$$

where $N = \nu_{11}\nu_{22} - \nu_{12}\nu_{21}$. The meanings of particular symbols used in (6) can be found in [1]. Except for u which is equal to $\frac{\omega}{k}$, all others are functions involving the angles ϕ , θ which appear in the direction cosines of the wave vector with respect to the xyz coordinate system, and the constitutive parameters in the xyz coordinate system, which may include frequency dependence as well. This determinant will yield a quartic in $\frac{\omega_i}{k_i}$ as follows when the dependence on the constitutive parameters are suppressed in the coefficients, while frequency dependence is exposed.

$$A(\phi, \theta, \omega) \left(\frac{\omega_i}{k_i}\right)^4 + B(\phi, \theta, \omega) \left(\frac{\omega_i}{k_i}\right)^3 + C(\phi, \theta, \omega) \left(\frac{\omega_i}{k_i}\right)^2 + D(\phi, \theta, \omega) \left(\frac{\omega_i}{k_i}\right) + E(\phi, \theta, \omega) = 0 \quad (7)$$

Here $\phi = \arctan(k_{iy}/k_{ix})$, $\theta = \arctan\left(\frac{\sqrt{k_{ix}^2 + k_{iy}^2}}{k_{iz}}\right)$. ϕ will be common for both incident and reflected waves whereas θ will be a function of ω' for reflected wave and will be the same function of $-\omega'$ for the incident wave when (1a) and (2a) are noted. So we can write

$$\tilde{A}(\phi, \mp\omega', \omega) \left(\frac{\omega}{k}\right)^4 + \tilde{B}(\phi, \mp\omega', \omega) \left(\frac{\omega}{k}\right)^3 + \tilde{C}(\phi, \mp\omega', \omega) \left(\frac{\omega}{k}\right)^2 + \tilde{D}(\phi, \mp\omega', \omega) \left(\frac{\omega}{k}\right) + \tilde{E}(\phi, \mp\omega', \omega) = 0 \quad (8)$$

Upper signs refer to incident wave when ω , k possess subscript i and lower signs refer to reflected wave when ω , k possess subscript r . The tildes are used to indicate the different coefficient functions that appear when θ is replaced by $\mp\omega'$ as the independent variable.

2.1. Non-dissipative Case

The question rises how the ω dependences of the coefficients \tilde{A} through \tilde{E} will affect (8). Because of (1d) and (2d) $\omega_i = \alpha(\omega' - rck'_z)$, $\omega_r = \alpha(\omega' + rck'_z)$ hold, and replacing ω' by $-\omega'$ in either one gives the quantity for the other one except for a minus sign. However noting that a minus sign for frequency in the entries of constitutive matrices is tantamount to a complex conjugation of the corresponding entries for the same frequency with the plus sign [1, p308], we conclude that replacing ω' by $-\omega'$ in the coefficients \tilde{A} through \tilde{E} will switch us from ω_i to ω_r but at the same time also give the complex conjugates of the true coefficients \tilde{A} through \tilde{E} for the relevant wave — incident or reflected. Here one needs also to note that θ is real in the lossless case so that it does not take part in the complex conjugation operation.

Therefore

$$\frac{\omega_r(-\omega')}{k_r(-\omega')} = \frac{\omega_i^*(\omega')}{k_i^*(\omega')} \quad (9)$$

holds where (*) indicates complex conjugation. On the other hand by the definitions of ω_i , ω_r , k_i , k_r we can easily see that

$$\frac{\omega_i(-\omega')}{k_i(-\omega')} = -\frac{\omega_r(\omega')}{k_r(\omega')} \quad (10)$$

Equation (10) when considered with (9) yields $\text{Re}\left\{\frac{\omega_i(\omega')}{k_i(\omega')}\right\} = 0$ for simultaneous satisfaction of (8) for incident and reflected waves. Here $\text{Re}\{\}$ indicates the real part of the complex number

within braces. Now if we notice that k_i has to be real for a lossless medium, this last condition requires $\text{Re}\{\omega_i\} = 0$. The medium is non-dissipative and exponential decay in time can not be expected. Because frequency cannot be complex when there are no damping terms in the differential equations [4]. Hence this implies $\text{Im}\{\omega_i\} = 0$ also. Here $\text{Im}\{\}$ indicates the imaginary part of the complex number within braces. Then since $\omega_i = 0$ holds, due to (10) $\omega_r = 0$ must hold also. But $\omega_r = \omega_i = 0$ together with (1d) and (2d) implies $\omega' = k' = 0$ for a common solution of (8) for incident and reflected waves. I.e., there exists no relation to base an argument on to negate the Special Relativity Theory because then due to (1) and (2) the fields become static and we no longer have incident and reflected waves that simultaneously satisfy (8).

As an example we take as medium (I), a lossless uniaxially anisotropic medium. We have for the extra ordinary wave $\frac{\omega^2}{k^2} = \frac{1}{\mu}[\frac{1}{\varepsilon_1} \cos^2 \theta + \frac{1}{\varepsilon_3} \sin^2 \theta]$ as the dispersion relation. Here the permittivity matrix has ε_1 as the first two diagonal entries and ε_3 as the third [5]. Medium has scalar constant magnetic permeability μ . Since all quantities on the right are positive and real, in this dispersion relation, $\text{Re}\{\frac{\omega_i(\omega')}{k_i(\omega')}\} = 0$ can simply not hold and by the arguments above there exists no relation to argue against the Special Relativity Theory.

We neglect the ordinary wave case for conciseness, but it will also yield $\omega' = k' = 0$, i.e., no relationship to argue against the Special Relativity Theory.

2.2. Dissipative Case

In this case k_i will be complex, and to satisfy $\text{Re}\{\frac{\omega_i}{k_i}\} = 0$, ω_i will have to be complex as well, but then we cannot write down (9).

We rewrite (7) in the following form

$$A(\phi, \theta, \omega)\omega^4 + B(\phi, \theta, \omega)\omega^3 k + C(\phi, \theta, \omega)\omega^2 k^2 + D(\phi, \theta, \omega)\omega k^3 + E(\phi, \theta, \omega)k^4 = 0 \quad (11)$$

Now, $\omega = 0$, $k = 0$ is a solution of this equation. (11) is valid for both the ω_i, k_i and ω_r, k_r pairs with the coefficients depending on the respective frequency (ω_i or ω_r). Therefore $\omega_i = k_i = 0$ or $\omega_r = k_r = 0$ choices are possible for a solution of the equation. We pick the second solution since $\omega_i = k_i = 0$ would mean a static field is incident on the interface. Now setting $\omega_r = k_r = 0$ in (11) when it is written for ω_i, k_i pair, observing that

$$k'_z = -\omega'/(rc), \quad k'^2_{ix} + k'^2_{iy} = -\left(\frac{\omega'}{\alpha rc}\right)^2 \quad (12)$$

will hold now because $\omega_r = k_r = 0$, one has also

$$A(\phi, \theta, 2\alpha\omega')c^4 + B(\phi, \theta, 2\alpha\omega')c^3 + C(\phi, \theta, 2\alpha\omega')c^2 + D(\phi, \theta, 2\alpha\omega')c + E(\phi, \theta, 2\alpha\omega') = 0 \quad (13)$$

This gives a quartic relating c, ω', ϕ, θ and frequency independent part of constitutive parameters. This relation can always be used to justify that c depends on ω' and by writing ω' as $\omega' = \alpha(\omega_i - v_1 k_{iz})$ to justify that c depends on v_1 as well.

To see the latter part of this statement, import from (12), (1a) and (1d) into $\omega' = \alpha(\omega_i - v_1 k_{iz})$ and one will obtain an identity independent of ω' . This indicates that ω' is arbitrary and can be chosen at will with a corresponding k_{iz} and ω_i established from (12), (1a) and (1d). Because $\omega_i = 2\alpha\omega'$, fixing ω' will result in a change of $2\alpha\omega'$ with v_1 . When considered with (13), this will mean a change in the value of c in order to keep (13) satisfied while coefficients \tilde{A} through \tilde{E} vary with v_1 through $2\alpha\omega'$. Notice that the solution that is the subject of this sub-section is a solution that satisfies (7) simultaneously when it is written for incident and reflected waves.

Two examples we shall cite for this subsection are 1) a dissipative simple medium 2) dissipative uniaxially anisotropic medium.

1) We take as medium (I) of above development, a dissipative simple medium. We have $\frac{\omega^2}{k^2} = \frac{\omega}{\mu_1 \varepsilon_1 \omega + j \mu_1 \sigma_1}$ for the dispersion relation [6]. Here imposing $\omega_r = k_r = 0$ will cause $\omega_i = 2\alpha\omega'$ and $k_i = 2\alpha\omega'/c$ to hold so that $c^2 = \frac{2\alpha\omega'}{\mu_1 \varepsilon_1 2\alpha\omega' + j \mu_1 \sigma_1}$ will be found from the dispersion relation for the incident wave. When rearranged this reads $\frac{2\alpha\omega'}{c^2}(1 - \mu_1 \varepsilon_1 c^2) = j \mu_1 \sigma_1$ which is the basic equation obtained in [3] and used to negate the Special Relativity Theory.

2) We now take as medium (I), a dissipative uniaxially anisotropic medium. We have for the extra ordinary wave $\frac{\omega^2}{k^2} = \frac{1}{\mu}[\frac{1}{\varepsilon_1} \cos^2 \theta + \frac{1}{\varepsilon_3} \sin^2 \theta]$ as the dispersion relation [1]. Here the permittivity

matrix has ε_1 as the first two diagonal entries and ε_3 as the third. Medium has scalar constant magnetic permeability μ . Also $\varepsilon_1 = \varepsilon_{11} + j\sigma_{11}/\omega$ and $\varepsilon_3 = \varepsilon_{33} + j\sigma_{33}/\omega$ hold. When these and relations (12) are substituted in the dispersion relation for the incident wave we obtain the following quadratic for ω_i .

$$\begin{aligned} & c^2\mu [-\omega_i^2\varepsilon_{11}\varepsilon_{33} + \sigma_{11}\sigma_{33} - j\omega_i(\sigma_{11}\varepsilon_{33} + \sigma_{33}\varepsilon_{11})] \\ & = -\omega_i^2(\varepsilon_{33}\cos^2\theta + \varepsilon_{11}\sin^2\theta) - j\omega_i(\sigma_{33}\cos^2\theta + \sigma_{11}\sin^2\theta) \end{aligned} \quad (14)$$

(14) can always be explicitly solved for $\omega_i = 2\alpha\omega'$. Because $\omega_i = 2\alpha\omega'$, when ω' is fixed and v_1 varies, c has to change to keep up with the variation of ω_i with v_1 . This relation therefore can be used to argue against the Special Relativity Theory and to prove it cannot account for the loss in medium (I). The ordinary wave case is omitted because it reduces to Example 1 of this subsection.

REFERENCES

1. Kong, J. A., *Electromagnetic Wave Theory*, EMW Publishing, Cambridge, USA, 2005.
2. Kong, J. A., "Theorems of bianisotropic media," *Proc. of IEEE*, Vol. 60, No. 9, 1036–1046, 1972.
3. Yener, N., "On the non-constancy of speed of light in vacuum for different Galilean reference systems," *Journal of Electromagnetic Waves and Applications*, Vol. 21, No. 15, 2241–2255, 2007.
4. Courant, R. and D. Hilbert, *Methods of Mathematical Physics*, Vol. 2, 187–193, Interscience Publishers, New York, USA, 1962.
5. Ramo, S., J. R. Whinnery, and T. Van Duzer, *Fields and Waves in Communication Electronics*, John Wiley, New York, 1965.
6. Balanis, C. A., *Advanced Engineering Electromagnetics*, John Wiley, USA, 1989.

Enhanced Gain Planar Inverted-F Antenna with Metamaterial Superstrate for UMTS Applications

Hussein Attia, Mohammed M. Bait-Suwailam, and O. M. Ramahi
University of Waterloo, Waterloo, Canada

Abstract— Planar inverted-F antennas (PIFA) are widely used in wireless hand-held devices due to their small-size, moderate bandwidth and radiation patterns. However, the radiation patterns of such antennas degrade when placed very close to a conductive finite ground plane. In this paper, an engineered magnetic superstrate is introduced to enhance the gain of PIFA antennas. The engineered magnetic superstrate is based on the broad-side coupled split ring resonator (SRR) inclusions which have high real permeability value at the resonance frequency of the antenna. Numerical full-wave simulations are performed to analyze the entire radiating system (antenna with superstrate). By using the magnetic superstrate, a 3.2 dB improvement in the gain of the PIFA antenna working in the UMTS band was achieved. The total height of the proposed superstrate over the antenna is only $\lambda_0/14$ where λ_0 is the free-space wavelength at antenna's resonance frequency. Thus, the antenna structure remains low profile, and is advantageous in cell-phone applications.

1. INTRODUCTION

One of the design constraints on the new mobile handset generation is antenna-size miniaturization, as more antennas need to be integrated in the same handset to support multiple standards. Furthermore, antennas need to maintain good performance in terms of bandwidth, gain, and radiation pattern. PIFA antennas are widely used in mobile phones due to their small-size and moderate performance. Size reduction of PIFA antennas can be achieved using several techniques [1–4]. In [1], a small-size PIFA antenna operated at its one-eighth wavelength ($\lambda/8$) mode was proposed, the proposed PIFA constituted by two radiating strips of length about ($\lambda/8$) was fed using a coupling feed. Du et al. [2] used the idea of high-impedance surface to construct a photonic bandgap type (PBG-type) ground plan for a PIFA antenna in order to reduce the planar size of the antenna, the (PBG-type) ground plan was composed of a dielectric substrate on a metallic plate and an upper plate with periodically metallic patch overlays on the substrate. In [3], the impedance bandwidth of a miniature PIFA antenna was enhanced using very high permittivity superstrate ($\epsilon_r > 35$) without considering physical realization of the proposed superstrate. Another mechanism to miniaturize PIFA antenna is to have slots in the ground plane [4] to make the ground plane appear electrically longer. Although the slotted ground plane reduced the height of the antenna, this will add complexity in the design and housing of the mobile handset. Further, bandwidth becomes extremely narrow as antenna height is reduced. In [5], it was shown that the emitted power from current handset phones results in significant power loss absorbed by user's human head; thus decreasing the efficiency and possibly the gain of the antennas.

While reducing the size of PIFA antennas is important, what is typically neglected is the consequential effect on the antenna gain and radiation patterns. In this work, an engineered magnetic superstrate constituted by split ring resonators SRR printed on both sides of a dielectric slab is designed for gain enhancement of PIFA antennas. The SRR unit cell is designed to have positive values for the effective permeability and permittivity at the resonance frequency of the antenna [6, 7]. The reason behind using magneto-dielectric superstrate instead of dielectrics with high permittivity is that magneto-dielectrics decrease the wavelength in the media leading to significant reduction in antenna profile without sacrificing the antenna radiation efficiency. The SRR unit cell is analytically characterized to obtain its effective permeability and permittivity. The designed artificial magnetic superstrate along with the PIFA antenna is numerically simulated, and the effect of the superstrate on gain, impedance bandwidth, and radiation patterns of the antenna is investigated.

2. ARTIFICIAL MAGNETIC SUPERSTRATE WITH SRR INCLUSIONS

The SRR unit cell acting as building block of the artificial magnetic superstrate is shown in Fig. 1(a). The SRR inclusion consists of two parallel broken square loops. The host dielectric is made of Rogers RO4350 with a thickness of 0.762 mm, relative permittivity of $\epsilon_r = 3.48$, and loss tangent of $\tan \delta = 0.004$. A planar 12×12 array of SRRs was printed on the host dielectric layer to provide the

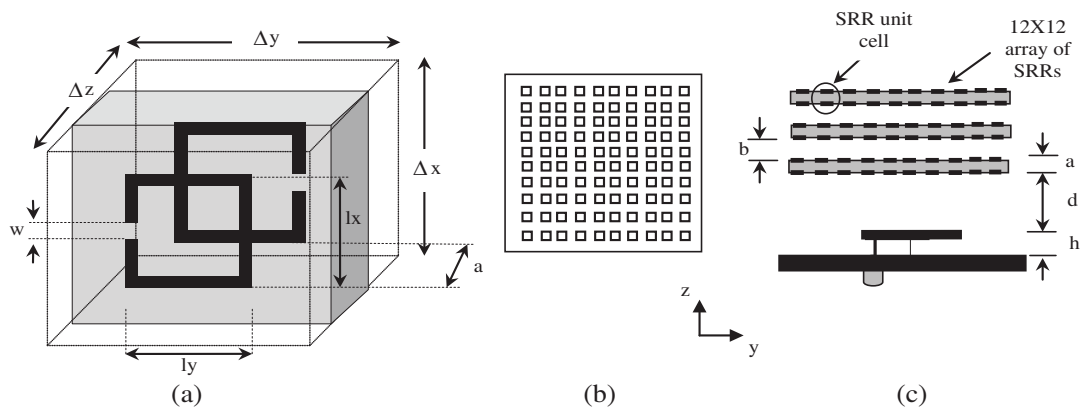


Figure 1: The proposed PIFA antenna covered with an engineered magnetic superstrate. (a) Unit cell. (b) Top-view. (c) Side-view. ($a = 0.762$ mm, $b = 2$ mm, $d = 4$ mm, and $h = 8.5$ mm)

engineered magnetic material. The superstrate used here consists of 3 layers of printed magnetic inclusions. The layers are separated by 2 mm of air layers as shown in Fig. 1(c).

The SRR unit cell is analytically modeled by obtaining its effective relative permeability as [6]

$$\mu_{r_{eff}} = 1 - \frac{j \omega L_{eff} S}{\Delta x \Delta z (R_{eff} - \frac{j}{\omega C_{eff}} + j \omega L_{eff})} \tag{1}$$

where S is the surface area of the inclusion ($l_x \times l_y$), Δx and Δz are the unit cell sizes in x and z directions as shown in Fig. 1(a). The dimensions of the designed SRR unit cell are $\Delta x = \Delta y = 8.5$ mm, $\Delta z = 2.762$ mm, $l_x = l_y = 6.5$ mm, $w = 0.3$ mm. The width of metallic strips (s) is equal to 0.3 mm, and the metallic strips are assumed to be made of copper. Formulas for R_{eff} , C_{eff} and L_{eff} can be found in [6].

Since the SRRs are aligned in the x - y plane, the resultant effective enhanced permeability as given by (1) is provided only in the z direction. Any incident magnetic field in the x or y direction will not couple to the SRR inclusion resulting in a permeability equal to that of free-space in those directions. Hence, the engineered material composed of the SRR inclusions will experience the anisotropic permeability tensor of

$$\mu = \mu_0 \begin{pmatrix} 1 & 0 & 0 \\ 0 & 1 & 0 \\ 0 & 0 & \mu_{r_{eff}} \end{pmatrix} \tag{2}$$

The analytically calculated effective relative permeability is shown in Fig. 2.

Inter-cell capacitors are formed in the gap regions between the metallic inclusions (unit cells) due to the incident x -directed electric field. The same phenomenon is observed for a y -directed incident electric field. However, in case of a z -directed electric field, the metamaterials superstrate will experience an effective permittivity equal to that of its host dielectric as the electric field would be perpendicular to the plane of the unit cell. Therefore, the artificial magnetic material composed of the SRRs inclusions will experience anisotropic electric permittivity of [8]

$$\epsilon = \epsilon_0 \begin{pmatrix} \epsilon_{r_{eff}} & 0 & 0 \\ 0 & \epsilon_{r_{eff}} & 0 \\ 0 & 0 & \epsilon_{r_{diel}} \end{pmatrix} \tag{3}$$

where,

$$\epsilon_{r_{eff}} = \epsilon_{r_{diel}} \left[1 + \frac{\Delta z l_x}{\Delta x \Delta y} \frac{K(\sqrt{1-g^2})}{K(g)} \right] \quad g = \frac{s/2}{s/2 + w}, \quad K(g) = \int_0^{\pi/2} \frac{d\theta}{\sqrt{1-g^2 \sin^2 \theta}}$$

According to the above formulas, the effective relative permittivity of the designed structure in the x , and y directions would be equal to 5.62.

3. ARTIFICIAL MAGNETIC STRUCTURE AS A SUPERSTRATE FOR PLANAR PIFA ANTENNAS

The analytically characterized SRR unit cell discussed in previous section acts as a building block for an artificial magnetic superstrate placed over a PIFA antenna as shown in Fig. 1(c). The PIFA antenna considered here (see Fig. 3) consists of a rectangular planar element located above a ground plane, a short-circuiting plate or pin, and a feeding mechanism for the planar element. The planar radiating element used here has dimensions of $24 \text{ mm} \times 8 \text{ mm}$, and is suspended on air substrate with a thickness of 8.5 mm . The antenna is fed using a coaxial probe feed and is shorted to the ground plane using a short-circuiting metallic pin of radius 0.35 mm . This metallic pin introduces inductance to antenna's equivalent circuit and hence reduces the planar size of the PIFA antenna to be used in cell-phones applications. The antenna is designed to operate at the frequency band of $2190\text{--}2210 \text{ MHz}$ (UMTS) at which the magnetic superstrate has an effective permeability of about 15 (real part) and a magnetic loss tangent of 0.11 (see Fig. 2).

The full-wave EM solver CST Microwave Studio was used to simulate the proposed antenna with and without superstrate. The distance between the PIFA antenna and superstrate was optimized numerically using CST to achieve the highest possible gain. Fig. 4(a) shows the reflection coefficient of the PIFA antenna before and after using the artificial magnetic superstrate at the optimized distance of 4 mm from the substrate. The overall height of the superstrate above the antenna is only $\lambda_0/14$ where λ_0 is the free-space wavelength at the resonance frequency. As shown in Fig. 4(a), the antenna impedance bandwidth ($S_{11} < -10 \text{ dB}$) and the resonance frequency of 2.2 GHz are slightly changed after using the metamaterial superstrate in comparison to the case without superstrate.

Figure 4(b) shows the gain of the PIFA antenna in the maximum radiation direction before and after using the artificial magnetic superstrate for different distances between the antenna and superstrate. It is observed that the gain is improved by 3.2 dB at the resonance frequency of 2.1 GHz after using the engineered superstrate at $d = 4 \text{ mm}$.

Figure 5 shows the radiation patterns (E -plane and H -plane) at the resonance frequency (2.10 GHz) of the PIFA antenna before and after using the engineered magnetic superstrate at $d = 4 \text{ mm}$, it is observed that the gain of the PIFA antenna is enhanced by about 3.2 dB in the maximum radiation direction after using the artificial magnetic superstrate.

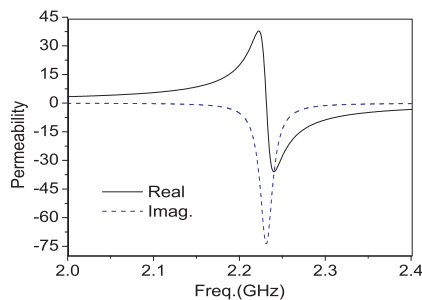


Figure 2: Analytically calculated relative permeability of the SRR inclusions.

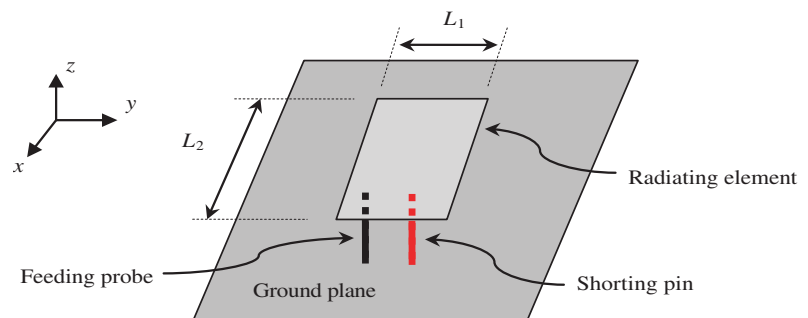


Figure 3: Geometry of the planar PIFA antenna. ($L_1 = 8 \text{ mm}$ and $L_2 = 24 \text{ mm}$).

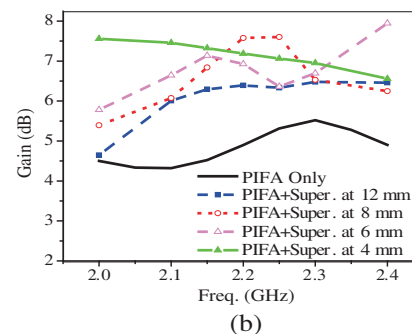
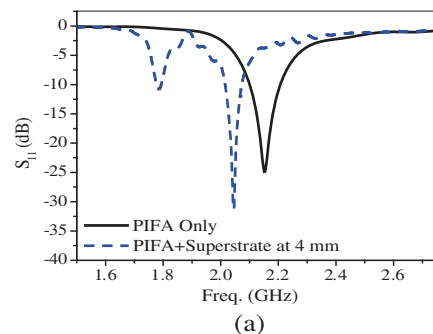


Figure 4: (a) The return loss and (b) the gain of the PIFA antenna before and after using the artificial magnetic superstrate for different distances between the antenna and superstrate.

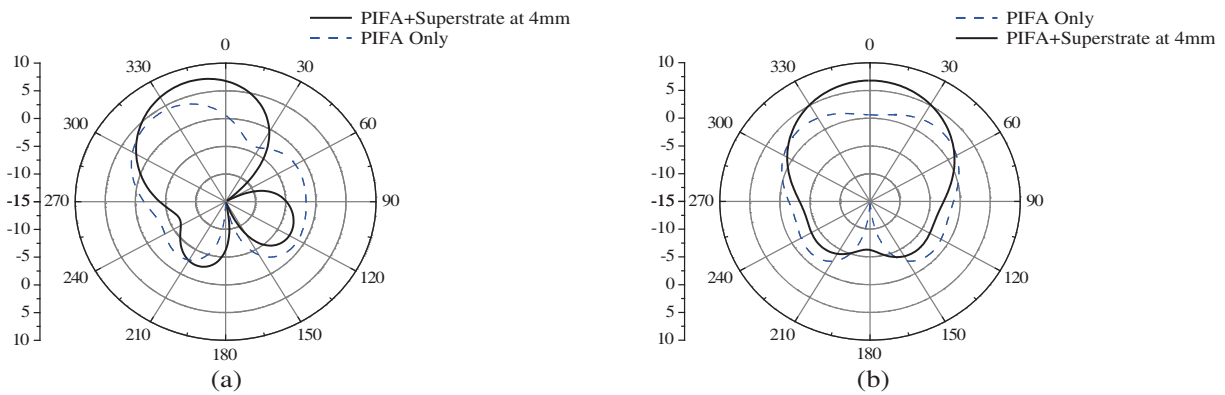


Figure 5: The gain radiation pattern at 2.10 GHz of the PIFA antenna covered with the artificial magnetic superstrate at $d = 4$ mm. (a) E -plan ($\phi = 0^\circ$), and (b) H -plan ($\phi = 90^\circ$).

4. CONCLUSION

An engineered superstrate was introduced for gain enhancement of planar PIFA antenna. The engineered superstrate based on the broad-side split ring resonator SRR was analytically designed and characterized. The PIFA antenna covered with the artificial superstrate was numerically investigated. It was shown that using the engineered magnetic superstrate, gain enhancement of 3.2 dB is attainable, while maintaining a superstrate profile of $\lambda_0/14$ where λ_0 is the free-space wavelength at the PIFA's resonance frequency.

REFERENCES

1. Chang, C.-H. and K.-L. Wong, "Printed $\lambda/8$ -PIFA for penta-band WWAN operation in the mobile phone," *IEEE Trans. Antennas Propagat.*, Vol. 57, No. 5, 1373–1381, May 2009.
2. Du, Z., K. Gong, J. S. Fu, B. Gao, and Z. Feng, "A compact planar inverted-F antenna with a PBG-type ground plane for mobile communications," *IEEE Trans. Vehicular Technology*, Vol. 52, No. 3, 483–489, May 2003.
3. Lo, T. K.-C. and Y. Hwang, "Bandwidth enhancement of PIFA loaded with very high permittivity material using FDTD," *Proceedings of IEEE Antennas and Propagation Society International Symposium*, Vol. 2, 798–801, Jun. 1998.
4. Abedin, M. F. and M. Ali, "Modifying the ground plane and its effect on planar inverted-F antennas (PIFAs) for mobile phone handsets," *IEEE Antenna Wireless Propagat. Lett.*, Vol. 2, 226–229, 2003.
5. Jensen, M. A. and Y. Rahmat-Samii, "EM interaction of handset antennas and a human in personal communications," *Proc. IEEE*, Vol. 83, No. 1, 7–17, Jan. 1995.
6. Maslovski, S., P. Ikonen, I. Kolmakov, and S. Tretyakov, "Artificial magnetic materials based on the new magnetic particle: Metasolenoid," *Progress In Electromagnetics Research*, PIER 54, 61–81, Sep. 2005.
7. Attia, H., L. Yousefi, M. M. Bait-Suwailam, M. S. Boybay, and O. M. Ramahi, "Enhanced-gain microstrip antenna using engineered magnetic superstrates," *IEEE Antenna Wireless Propagat. Lett.*, Vol. 8, 1198–1201, 2009.
8. Buell, K., H. Mosallaei, and K. Sarabandi, "A substrate for small patch antennas providing tunable miniaturization factors," *IEEE Trans. Antennas Propagat.*, Vol. 54, No. 1, 135–146, Jan. 2006.

Temporal Filtering in Phase-space

Cristina M. Gómez-Sarabia¹, Pedro Andrés², and Jorge Ojeda-Castañeda¹

¹University of Guanajuato, Salamanca, Guanajuato 36885, México

²Optics Department, Universitat de València, E46100 Burjassot, Valencia, Spain

Abstract— We use the ambiguity function, of the slowly varying complex-amplitude envelope, for visualizing the intensity-spectrum evolution through propagation in a first-order dispersive medium. We comment on the use of this formalism for temporal filtering.

1. INTRODUCTION

In several recent publications the authors discuss and apply the duality between the equations that describe paraxial, scalar diffraction and first-order temporal dispersion of optical short pulses [1–5].

In a nutshell, the temporal frequency corresponds to the lateral spatial frequency, and the time variation corresponds to the z coordinate along the optical axis. And consequently, there is also a correspondence between the temporal spectra and spatial frequency spectrum.

Based on the above analogy, the temporal Talbot effect finds practical applications for suppressing dispersion effects in pulsed fiber lasers [6], and for tailoring the reception rates and duty cycle of linearly chirped signals [7].

Furthermore, based on this analogy, one can define a temporal Lau effect [5, 8]. And since the spectral density function of the carrier acts as a lowpass filter, one can filter nonlinear chirp components just by using a broadband optical carrier source [9]. Moreover, the degree of temporal coherence of the optical source plays the role of a low-pass filter. Hence, the temporal Lau effect is useful for increasing the repetition rate of a pulse train, which is initially obtained from a sinusoidal phase modulation [10].

Here our aim is the following. We use phase-space formalism for visualizing the intensity-spectrum evolution through propagation in a first-order dispersive medium. We comment on the use of this formalism for applications of the temporal Talbot effect, and the temporal Lau effect.

To our end, in Section 2, we discuss the basic theory. In Section 3, we comment on the use of this formalism in the temporal Talbot effect, and in the temporal Lau effect. In Section 4, we summarize our presentation.

2. THE AMBIGUITY FUNCTION OF THE SLOWLY VARYING COMPLEX-AMPLITUDE ENVELOPE

We assume that optical fiber (GDD circuit) is represented by the following Taylor series expansion of dispersion relationship

$$\beta(\omega) = \beta_0 + \beta_1(\omega - \omega_0) + \beta_2(\omega - \omega_0)^2. \quad (1)$$

In Eq. (1), we use the customary notation where $\beta_n = (d/d\omega)^n \beta(\omega)$, at $\omega = \omega_0$. For a typical optical fiber operating at the third telecommunications window ($\lambda_0 = 1.55 \mu\text{m}$), $\beta_2 = -21.6 \text{ ps}^2/\text{km}$. We consider that at the input of the optical fiber (GDD circuit), the slowly varying complex-amplitude envelope is represented by the Fourier series

$$g(t) = \sum_{m=-\infty}^{\infty} a_m \exp\left(i2\pi t \frac{m}{T}\right). \quad (2)$$

In Eq. (2), we denote as $T = 2\pi/\Omega$ the period of the pulse train, hence Ω is the angular frequency. Next, we consider a monochromatic, CW, optical source. And as is common we use the proper time, $\tau = (t - \beta_1 z)t$. As is discussed in Reference [5], at the end of the optical fiber (GDD circuit), we can describe the temporal intensity as the ensemble average of the square modulus of the propagated slowly varying envelope. That is

$$I(\tau, z) = \left(\frac{1}{2\pi}\right) \sum_{m=-\infty}^{\infty} \sum_{n=-\infty}^{\infty} a_{m+n} a_n^* \exp(im\Omega\tau) \exp\left[im(m+2n) \left(\frac{\beta_2 \Omega^2 z}{2}\right)\right]. \quad (3)$$

Hence, the intensity-spectrum associated to Eq. (3) is

$$\tilde{I}(\omega, z) = \left(\frac{1}{2\pi}\right) \sum_{m=-\infty}^{\infty} \sum_{n=-\infty}^{\infty} a_{m+n} a_n^* \exp \left[im(m+2n) \left(\frac{\beta_2 \Omega^2 z}{2}\right) \right] \delta(\omega - m\Omega). \quad (4)$$

Now, according to References [11, 12], it is interesting to note that the ambiguity function of the slowly varying complex-amplitude envelope is

$$A(\omega, \tau) = \int_{t=-\infty}^{\infty} g\left(t + \frac{\tau}{2}\right) g^*\left(t - \frac{\tau}{2}\right) \exp(i\omega t) dt. \quad (5)$$

By substituting Eq. (2) in Eq. (5), it is straightforward to obtain that the ambiguity function of the slowly varying complex-amplitude envelope is

$$A(\omega, \tau) = \left(\frac{1}{2\pi}\right) \sum_{m=-\infty}^{\infty} \sum_{n=-\infty}^{\infty} a_{m+n} a_n^* \exp \left[i \left(\frac{m}{2} + n\right) \Omega \tau \right] \delta(\omega - m\Omega). \quad (6)$$

Therefore, the ambiguity function in Eq. (6) contains the mathematical expression of the intensity-spectrum, as in Eq. (4); provided that $\tau = m\beta_2 \Omega z$. And consequently, we claim that the values of the intensity spectrum (for variable z) are contained as the values of the ambiguity function of the slowly varying complex-amplitude envelope, along the lines $\tau = m\beta_2 \Omega z$. In other terms,

$$\tilde{I}(\omega, z) = A(\omega, m\beta_2 \Omega z). \quad (7)$$

Equivalently, at the output of the GDD circuit, the temporal intensity in Eq. (3) can be expressed as

$$I(\tau, z) = \sum_{m=-\infty}^{\infty} A(m\Omega, m\beta_2 \Omega) \exp(im\Omega\tau). \quad (8)$$

Equation (8) can be extended consider non monochromatic optical sources [10].

3. TEMPORAL TALBOT EFFECT AND TEMPORAL LAU EFFECT

In Reference [10], we indicate that if an electro-optic phase modulator shapes the slowly varying complex amplitude envelope, then the ambiguity function is a proportional to the Bessel function of the first kind, and integer order m . Hence, the present formalism leads to a closed formula that expresses temporal filtering effects, due either to the length of the dispersive media, or to the degree of temporal coherence of the optical source.

4. CONCLUSION

We have used the ambiguity function, of the slowly varying complex-amplitude envelope, for describing the evolution of the spectrum intensity as the periodic pulse propagates in GDD circuit. If an electro-optic phase modulator shapes the slowly varying complex amplitude envelope, then the present formalism leads an analytical expression for performing temporal filtering operations.

REFERENCES

1. Agrawal, G. P., *Nonlinear Fiber Optics*, 4th Edition, Academic, 2007.
2. Chantada, L., C. R. Fernandez-Pousa, M. T. Flores-Arias, and C. Gomez-Reino, "Focusing of a train of pulses in phase opposition through a linear dispersive medium," *J. Opt. A: Pure Appl. Opt.*, Vol. 7, No. 12, 767–773, 2005.
3. Torres-Company, V., J. Lancis, and P. Andrés, "Unified approach to describe optical pulse generation bypropagation of periodically phase-modulated CW laser light," *Opt. Express*, Vol. 14, 3171–3180, 2006.
4. Flores-Arias, M. T., L. Chantada, C. Bao, M. V. Pérez, and C. Gómez-Reino, "Temporal zone plate," *J. Opt. Soc. Am. A*, Vol. 25, 3077–3082, 2008.
5. Lancis, J., C. M. Gómez-Sarabia, J. Ojeda-Castaneda, C. Fernández-Pouza, and P. Andrés, "Temporal Lau effect: Noncoherent reconstruction of periodic pulse trains," *J. Eur. Opt. Soc.*, Vol. 1, 06018, Rapid Publications, 2006.
6. Fischer, B., B. Vodonos, S. Atkins, and A. Bekker, "Dispersion-mode pulsed laser," *Opt. Lett.*, Vol. 25, 728–730, 2000.

7. Lancis, J., J. Caraquitená, P. Andrés, and M. A. Muriel, “Temporal self-imaging effect for chirped laser pulse sequences: Repetition rate and duty cycle tunability,” *Opt. Comm.*, Vol. 253, 156–163, 2005.
8. Chantada, L., C. R. Fernandez-Pousa, and C. Gomez-Reino, “Theory of the partially coherent temporal Talbot effect,” *Opt. Comm.*, Vol. 266, 393–398, 2006.
9. Lancis, J., V. Torres-Company, P. Andres, and J. Ojeda-Castaneda, “Side-lobe suppression in electro-optic pulse generation,” *Electronics Letters*, Vol. 43, No. 7, Mar. 29th, 2007.
10. Ojeda-Castaneda, J., J. Lancis, C. M. Gómez-Sarabia, V. Torres-Company, and P. Andres, “Ambiguity function analysis of pulse train propagation: Applications to temporal Lau filtering,” *J. Opt. Soc. Am. A*, Vol. 24, No. 8, 2268–2273, 2007.
11. Dorrer, C. and I. Wamsley, “Phase space in ultra fast optics,” *Phase Space Optics: Fundamentals and Applications*, Chapter 11, 337–383, M. Testorf, B. Hennelly, and J. Ojeda-Castaneda, Eds., McGraw-Hill, 2010.
12. Guigay, J. P., “Ambiguity function in optical imaging,” *Phase Space Optics: Fundamentals and Applications*, Chapter 2, 45–62, M. Testorf, B. Hennelly, and J. Ojeda-Castaneda, Eds., McGraw-Hill, 2010.

Temporal Zone Plate by Linear Chirp Generator

Carlos Gomez-Reino, Ana I. Gómez-Varela, Carmen Bao Varela, and M. Teresa Flores-Arias
GRIN Optics Group, Optics and Optometry School and Faculty of Physics, Campus Sur,
Universidade de Santiago de Compostela, E15782 Santiago de Compostela, Spain

Abstract— The investigation on zone plates is extended to the temporal case. By exploiting the space-time duality between the paraxial diffraction of light in space and the linear dispersion of optical pulses, it presents the time-domain analog of multiple imaging formula at the replicas of the input pulse. The temporal system is created by using a linear chirp generator together with two dispersive delay lines. An example to illustrate the behavior of a temporal binary zone plate is considered.

1. INTRODUCTION

The main line of this paper is to show that, within the framework of the space-time duality, a linear chirp generator can be used to design temporal zone plates that reproduce in a multiple fashion optical pulses propagating in linear dispersive media. The duality permits to consider lenses that image by quadratic phase modulation of optical pulses in the time domain. This operation is analogous to the action of a conventional refractive lens on the light. The time lens has been widely analyzed and can be implemented in practice, for instance by using an electro-optic modulator [1–3], by mixing the original pulse with a chirped pulse in a nonlinear crystal [4] or by means of cross-phase modulation of the original pulse with an intense pump pulse in a nonlinear pulse [5]. In spatial optics, there is another quadratic phase transformer device based on diffraction. This device is the zone plate operating by blocking alternate zones or through introduction of a phase shift of “ π ” radians in alternate zones. The spatial zone plate is capable of focusing light at a set of points, thereby acting as a multiple imaging system. Although the spatial zone plate has been analyzed widely in optics [6], few studies of the temporal counterpart have been made [7, 8].

2. TEMPORAL ZONE PLATE

It is well known that a temporal imaging system is created by cascading one dispersive medium, a time lens and another dispersive medium. In other words, a temporal imaging system include input dispersion, phase modulation, and output dispersion of an optical pulse. We consider dispersion first. The impulse response of a linear dispersive medium is given by [9]

$$h_{\xi}(t) = (-i2\pi\xi)^{-1/2} \exp\left(-i\frac{t^2}{2\xi}\right) \quad (1)$$

where $\xi = \beta_2 z$ is the accumulated dispersion of the linear medium along a distance z , β_2 being the first-order coefficient.

The propagation of a narrowband optical envelope $O(t)$ carried by a monochromatic wave through a dispersive medium can be described as a convolution

$$E(t') = \int_{-\infty}^{\infty} O(t) h_{\xi}(t, t') dt \quad (2)$$

We consider phase modulation second. The effect of the temporal zone plate is to multiply the envelope time function $E(t')$ by a phase factor that is quadratic in time. In radar or sonar applications linear chirps are the most typically used signals to achieve pulse compression by quadratic phase modulation [10]. The phase of a linear FM chirp signal varies quadratically with time and it is characterized by the instantaneous frequency

$$f(t) = \alpha t \quad (3)$$

by ignoring the starting frequency at time $t = 0$ for the purpose of this paper. In Eq. (3), α denotes the chirp rate in Hz/s, which can be written as

$$\alpha = B/T \quad (4)$$

B being the bandwidth range in Hz and T the time duration of the pulse in seconds.

In accordance with the space time-duality, the temporal analogy of the zone plate is given by a signal arranged in time in the same way as the zones of a spatial zone plate bounded by dispersive media. This system leads to nearly distortionless multiple compression of the optical pulses. For the sake of brevity and without loss of generality we will focus on the temporal generalized zone plate whose profile is given by a binary ψ function which takes two levels 1 and 0, that is

$$\psi(t) = \begin{cases} 1 & \text{if } t_{2j}^2 \leq t^2 < t_{2j}^2 + \varepsilon \\ 0 & \text{if } t_{2j}^2 + \varepsilon \leq t^2 < t_{2j+2}^2 \end{cases} \quad \text{for } \varepsilon < \frac{2}{\alpha} \quad (5)$$

where ε is the width of the unit cell (see Figure 1), j is a natural number, and $t_j^2 = jt_1^2 = j/\alpha$, $2/\alpha$ being the period in t^2 for which a temporal zone of width ε is repeated. Eq. (5) represents the profile of a positive generalized binary zone plate; for a negative zone plate a complementary profile is defined.

Equation (5) can also be expressed by appropriate Fourier series, in complex form, as

$$\psi(t) = \frac{\alpha\varepsilon}{2} + \sum_{n=1}^{\infty} \left[a_n e^{-i\phi_n(t)} + a_n^* e^{i\phi_n(t)} \right] \quad (6)$$

where

$$a_n = \frac{i}{2n\pi} [1 - \exp(in\pi\alpha\varepsilon)] \quad (7)$$

$$\phi_n(t) = n\pi\alpha t^2 \quad (8)$$

Note that, for any n th harmonic of the zone plate, the phase factor ϕ_n is quadratic in time, the instantaneous frequency $\frac{1}{2\pi} \frac{\partial\phi_n}{\partial t}$ has a linear chirp and the chirp rate is given by $\frac{1}{2\pi} \frac{\partial^2\phi_n}{\partial t^2}$.

We now proceed to derive a time-domain analog to a space lens for any n th harmonic of the temporal zone plate. Since the action of a conventional refractive thin lens is to produce a phase shift in real space [11]

$$\phi(x, y) = \frac{k}{2f} (x^2 + y^2) \quad (9)$$

where k is the wavenumber in the lens material and f is the focal length, we can define a similar phase shift for the time-phase function corresponding to the n th harmonic of the zone plate such that

$$\phi_n(t) = \frac{n\omega_c}{2T} t^2 \quad (10)$$

where $\omega_c = 2\pi B$ is the bandwidth range of the chirp signal in rad/s. Comparing Eq. (10) to Eq. (9) we can find the time domain equivalent of the focal length for the n th harmonic. The n th focal time of the zone plate is given by

$$f_t^n = \frac{T}{n} = \frac{B}{n\alpha} \quad (11)$$

Eq. (11) contains the essence of the zone plate operation as a lens of a temporal multiple imaging system.

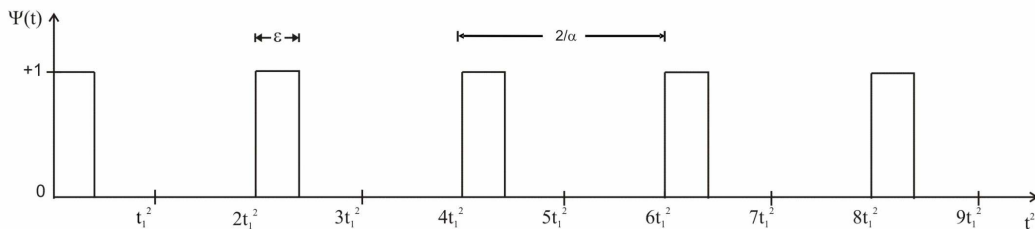


Figure 1: Positive temporal generalized binary zone plate.

3. TEMPORAL MULTIPLE IMAGING SYSTEM

Consider that an optical pulse $O(t)$ is launched into a temporal multiple imaging system based on temporal zone plate as shown in Figure 2. Combining the effects of input and output dispersion and zone plate modulation produced by a digital chirp signal generator, the output signal $E(t'')$ can be written as

$$E(t'') = \int_{-\infty}^{\infty} O(t) h_{\xi, \xi'}(t, t'') dt \quad (12)$$

where

$$h_{\xi, \xi'}(t, t'') = \int_{-\infty}^{\infty} h_{\xi}(t, t') \psi(t) h_{\xi'}(t', t'') dt' \quad (13)$$

is the impulse response of the whole system and h_{ξ} and $h_{\xi'}$ are the impulse responses of the input and output dispersive media, respectively. $\xi' = \beta_2' z'$ is the accumulated dispersion along a distance z' of the output dispersive medium of first-order coefficient β_2' .

By a straightforward calculation, Eq. (13) becomes

$$\begin{aligned} h_{\xi, \xi'}(t, t'') &= \frac{e^{-i\frac{t^2}{2\xi}} e^{-i\frac{t''^2}{2\xi'}}}{i2\pi(\xi\xi')^{1/2}} \left\{ \frac{\alpha\varepsilon}{2} \int_{-\infty}^{\infty} \exp\left\{-\frac{i}{2}\left(\frac{1}{\xi} + \frac{1}{\xi'}\right)t'^2\right\} \exp\left\{i\left(\frac{t}{\xi} + \frac{t''}{\xi'}\right)t'\right\} dt' \right. \\ &+ \sum_{n=1}^{\infty} a_n \int_{-\infty}^{\infty} \exp\left\{-\frac{i}{2}\left(\frac{1}{\xi} + \frac{1}{\xi'} + \frac{n\omega_c}{T}\right)t'^2\right\} \exp\left\{i\left(\frac{t}{\xi} + \frac{t''}{\xi'}\right)t'\right\} dt' \\ &+ \sum_{n=1}^{\infty} a_{*n} \int_{-\infty}^{\infty} \exp\left\{-\frac{i}{2}\left(\frac{1}{\xi} + \frac{1}{\xi'} - \frac{n\omega_c}{T}\right)t'^2\right\} \exp\left\{i\left(\frac{t}{\xi} + \frac{t''}{\xi'}\right)t'\right\} dt' \right\} \quad (14) \end{aligned}$$

If we require the quadratic phase factors of the integrands to go to unity, the integrals of Eq. (14) reduce to Dirac delta functions and the multiple temporal imaging formula is obtained. This formula can be written, in compact form, as

$$\frac{1}{\xi} + \frac{1}{\xi'} = \pm \frac{n\omega_c}{T} = \pm \frac{\omega_c}{f_t^n} \quad (15)$$

for any natural number n , where f_t^n is the focal time of n th order. The similarity between Eq. (15) and its spatial counterpart is striking for every n th order.

If the temporal lens law is satisfied, the output signal apart from constant phase factor is given by

$$E(t'') = \frac{i2\pi}{M_t^{1/2}} \left\{ \frac{\alpha\varepsilon}{2} O(t''/M_t) + \sum_{n=1}^{\infty} a_n O(t''/M_t) + \sum_{n=1}^{\infty} a_{*n} O(t''/M_t) \right\} \quad (16)$$

From Eq. (16) it follows that the output signal is composed of a superposition of replicas of the input signal rescaled by the magnification M_t given by the ratio of the output dispersion ξ' to the

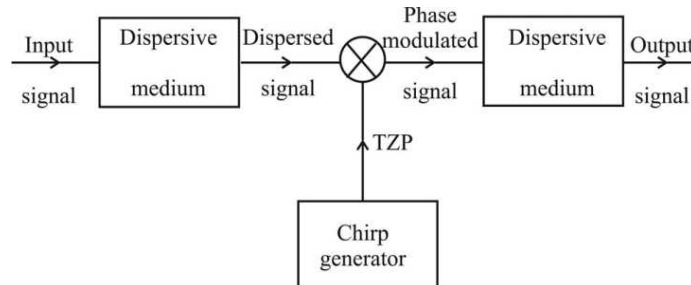


Figure 2: Block diagram of temporal imaging system based on temporal zone plate (TZP) produced by a digital chirp signal generator.

input dispersion ξ . These replicas of the original signal can be regarded as the pulses resulting from the dispersion orders of the temporal zone plate in analogy with the images resulting from the diffraction orders of the spatial zone plate. Stretched or compressed replicas are obtained as $M_t > 1$ or $M_t < 1$, respectively.

As an example to illustrate the behavior of a temporal multiple imaging system, we assume an optical pulse propagation through a standard single-mode fiber (SMF) of 10 km length in which $\beta_2 = -21 \text{ ps}^2/\text{km}\cdot\text{rad}$ at $\lambda = 1550 \text{ nm}$. A digital chirp generator produces a temporal generalized binary zone plate composed of a sequence of rectangular pulses in t^2 which takes two levels 1 and 0 with a repetition period of 200 ps^2 ($\alpha = 10 \text{ GHz/ps}$) and individual pulse width $\varepsilon = 60 \text{ ps}^2$. The phase modulated signal is launched into a dispersion-shifted fiber (DSF) in which $\beta_2' = -0.5 \text{ ps}^2/\text{km}\cdot\text{rad}$ at $\lambda = 1550 \text{ nm}$. Multiple imaging of the input signal at 30.46, 16.55, 10.89 and 8.12 km lengths is obtained in the DSF for the first four dispersion orders with 0.08, 0.04, 0.026 and 0.019 magnifications. Dispersive orders are compressed temporal images of the original pulse.

4. CONCLUSIONS

The investigation of zone plates has been extended to the temporal case. This paper proposes a temporal multiple imaging system combining two linear dispersive media and a temporal zone plate produced by a digital chirp signal generator. The temporal zone plate produces a quadratic phase modulation and acts as time multifocal lens. We have derived expressions for the focal times and the magnifications which they given at the output multiple time images of the input.

ACKNOWLEDGMENT

This work was supported by Ministerio de Ciencia e Innovación, Spain, under project MAT2010-18519 and by the Xunta de Galicia, Spain, under project INCITE08PXIB206013PR.

REFERENCES

1. Kolner, B. H. and M. Nazarathy, "Temporal imaging with a time lens," *Opt. Lett.*, Vol. 14, No. 12, 630–632, 1989.
2. Kolner, B. H., "Active pulse compression using an integrated electro-optic phase modulator," *Appl. Phys. Lett.*, Vol. 52, No. 14, 1122–1124, 1988.
3. Godil, A. A., B. A. Auld, and D. M. Bloom, "Time-lens producing 1.9 ps optical pulses," *Appl. Phys. Lett.*, Vol. 62, 047–1049, 1993.
4. Mouradian, L. K., F. Louradour, V. Messenger, A. Barthelemy, and C. Froehly, "Spectro-temporal imaging of femtosecond events," *IEEE J. Quantum Electron.*, Vol. 36, 795–801, 2000.
5. Bennet, C. V. and B. H. Kolner, "Upconversion time microscope demonstrating 103x magnification of femtosecond waveforms," *Opt. Lett.*, Vol. 24, No. 11, 783–785, 1999.
6. Ojeda-Castañeda, J. and C. Gomez-Reino, *Selected Papers on Zone Plates, SPIE Milestone Series*, Vol. MS128, SPIE Optical Engineering Press, 1996, and references therein.
7. Chantada, L., C. R. Fernandez-Pousa, M. T. Flores-Arias, and C. Gomez-Reino, "Focusing of a train of pulses in phase opposition through a linear dispersive medium," *J. Opt. A: Pure Appl. Opt.*, Vol. 7, No. 12, 767–773, 2005.
8. Flores-Arias, M. T., L. Chantada, C. Bao, M. V. Perez, and C. Gomez-Reino, "Temporal zone plate," *J. Opt. Soc. Am. A*, Vol. 25, No. 12, 3077–3082, 2008.
9. Saleh, B. E. A. and M. C. Teich, *Fundamentals of Photonics*, Wiley, New York, 1991.
10. Le Chevalier, F., *Principles of Radar and Sonar Signal Processing*, Artech House, Massachusetts, 2001.
11. Goodman, J. W., *Introduction to Fourier Optics*, 3rd Edition, Roberts & Company Publishers, Colorado, 2005.

Second Order Moments of Superpositions of Hermite-Laguerre-Gauss Modes

A. Cámara and T. Alieva

Facultad de Ciencias Físicas, Universidad Complutense de Madrid
Avda. Complutense, s/n, Madrid E-28040, Spain

Abstract— In this contribution, we derive an expression for the arbitrary-order moment of a signal expanded in Hermite-Gaussian modes. In addition the second-order moments for a signal presented as a series of Hermite-Laguerre-Gaussian modes are obtained. These results are useful for complete and partially coherent beam analysis and synthesis.

The moments of the Wigner distribution (WD) of a beam are widely used for coherent and partially coherent beam characterization [1, 2]. Parameters such as the size in phase space, the orbital angular momentum, and the quality factor of the beam can be obtained from the second order moments while the higher order moments describe more fine beam details as sharpness (kurtosis parameter), etc.

To find the moments for certain types of the beams such as Hermite-Gaussian (HG) and Laguerre-Gaussian (LG) beams is relatively easy. Note that the HG and LG modes are stable (they propagate through an isotropic optical system without changing the form of their intensity distribution). Taking into account that the families of HG and LG modes form the complete orthonormal sets other beams can be represented as their linear superpositions. This approach is suitable for beam analysis and synthesis. Thus for example a series of the HG modes with the same sum of the indices corresponds to another stable beam (Hermite-Laguerre-Gaussian beams (HLG)) [3, 4], while a certain combination of the LG modes compose the spiral beams, whose form of intensity distribution remains the same a part from rotation [4, 5].

The analytical expression of the second moments for a coherent beam expanded in series of Hermite-Gaussian (HG) modes was developed in [6]. Here we derive the expression for the higher order moments of coherent as well as for partially coherent beams presented as a linear superposition of the HG modes. It has been shown in Ref. [7] that from the analysis of the beam second order moments its principal axes in the phase-space can be found. They indicate a proper set of HLG modes for beam decomposition. In order to use this approach for signal characterization, we generalize the formula obtained for the second order moments to the case of beam decomposition on the HLG modes.

A beam in scalar monochromatic paraxial approximation is described in the coherent case by the complex field amplitude defined as $f(\mathbf{r}) = |f(\mathbf{r})| \exp[i\varphi(\mathbf{r})]$, where $\mathbf{r} = [x, y]^t$ is a two dimensional position vector at the plane transversal to the propagation direction. Similarly, the partially coherent beam is described by the mutual intensity, given by $\Gamma(\mathbf{r}_1, \mathbf{r}_2) = \langle f(\mathbf{r}_1) f^*(\mathbf{r}_2) \rangle$, where the brackets here and further indicate temporal averaging and * stands for complex conjugation. Both cases can be treated together applying the formalism of the Wigner distribution. Further, we will use the signal description in the form of mutual intensity since the coherent signal is a particular case of partially coherent ones.

The WD, $W_\Gamma(\mathbf{r}, \mathbf{p})$, is the spatial Fourier transform (FT) of the mutual intensity with respect to the coordinate difference, $\mathbf{r}' = \mathbf{r}_1 - \mathbf{r}_2$:

$$W_\Gamma(\mathbf{r}, \mathbf{p}) = \iint_{\mathbb{R}^2} d\mathbf{r}' \Gamma\left(\mathbf{r} + \frac{1}{2}\mathbf{r}', \mathbf{r} - \frac{1}{2}\mathbf{r}'\right) \exp(-i2\pi\mathbf{p} \cdot \mathbf{r}'), \quad (1)$$

where $\mathbf{p} = [p_x, p_y]^t$ denotes spacial frequencies.

The moments of order $z = r + s + k + l$ of a beam are expressed through its WD as

$$\mu_{r,s,k,l} = \iiint\iiint_{\mathbb{R}^4} d\mathbf{r}d\mathbf{p} x^r p_x^s y^k p_y^l W_\Gamma(\mathbf{r}, \mathbf{p}). \quad (2)$$

Note that the zero-order moment corresponds to the signal energy, while the first order moments indicate the centroid of the beam, which is used here are the origin of the coordinate system.

The signal mutual intensity can be expressed as the series of the HG modes [8]:

$$\Gamma(\mathbf{r}_1, \mathbf{r}_2) = \sum_{m,n} \sum_{m',n'} \langle a_{m,n} a_{m',n'}^* \rangle \mathcal{H}_{m,n}(\mathbf{r}_1; \mathbf{w}) \mathcal{H}_{m',n'}(\mathbf{r}_2; \mathbf{w}), \quad (3)$$

where $\langle a_{m,n} a_{m',n'}^* \rangle$ are the correlation coefficients, $\mathbf{w} = [w_x, w_y]^t$ is the vector containing the beam waist in the x and y directions, and the HG modes are defined as

$$\mathcal{H}_{m,n}(\mathbf{r}; \mathbf{w}) = \sqrt{2} \frac{H_m\left(\sqrt{2\pi} \frac{x}{w_x}\right) H_n\left(\sqrt{2\pi} \frac{y}{w_y}\right)}{\sqrt{2^m m! w_x} \sqrt{2^n n! w_y}} \exp\left[-\pi \left(\frac{x^2}{w_x^2} + \frac{y^2}{w_y^2}\right)\right], \quad (4)$$

being $H_m(\cdot)$ the Hermite polynomials of order n . For the coherent case $\langle a_{m,n} a_{m',n'}^* \rangle = a_{m,n} a_{m',n'}^*$. Then, the WD of a signal expanded as a series of HG modes is given by

$$W_\Gamma(\mathbf{r}, \mathbf{p}) = \sum_{m,n} \sum_{m',n'} \langle a_{m,n} a_{m',n'}^* \rangle \chi_{m,m'}(x, p_x) \chi_{n,n'}(y, p_y), \quad (5)$$

where

$$\begin{aligned} \chi_{m,m'}(q, p_q) &= (-1)^{m_{\min}} 2^{\frac{|m-m'|}{2}+1} \frac{m_{\min}!}{m_{\max}!} \left[\sqrt{2\pi} \left(\frac{q}{w_q} + \text{sgn}(m' - m) i w_q p_q \right) \right]^{|m-m'|} \\ &\times L_{m_{\min}}^{(|m-m'|)} \left[4\pi \left(\frac{q^2}{w_q^2} + w_q^2 p_q^2 \right) \right] \exp\left[-2\pi \left(\frac{q^2}{w_q^2} + w_q^2 p_q^2 \right)\right], \end{aligned} \quad (6)$$

$m_{\max} = \max(m, m')$, $m_{\min} = \min(m, m')$, and q is a placeholder for the x and y coordinates. Notice that $\chi_{m',m}(q, p_q) = \chi_{m,m'}^*(q, p_q)$. To obtain this result the expression 7.377 from Ref. [9],

$$\int_{-\infty}^{\infty} dx e^{-x^2} H_m(x+y) H_n(x+z) = 2^n \sqrt{\pi} m! z^{n-m} L_m^{(n-m)}(-2yz), \quad \text{if } m \leq n, \quad (7)$$

has been used. In the particular case of having only one mode, the WD is reduced to [10]

$$\begin{aligned} W_{\mathcal{H}_{m,n}}(\mathbf{r}, \mathbf{p}) &= 4(-1)^{m+n} L_m \left[4\pi \left(\frac{x^2}{w_x^2} + w_x^2 p_x^2 \right) \right] L_n \left[4\pi \left(\frac{y^2}{w_y^2} + w_y^2 p_y^2 \right) \right] \\ &\times \exp\left[-2\pi \left(\frac{x^2}{w_x^2} + \frac{y^2}{w_y^2} + w_x^2 p_x^2 + w_y^2 p_y^2 \right)\right]. \end{aligned} \quad (8)$$

Then, using Eqs. (2), (5), and (6), along with formula 7.414-7 from Ref. [9],

$$\int_0^\infty dt e^{-\gamma t} t^\beta L_n^{(\alpha)}(t) = \frac{\Gamma(\beta+1) \Gamma(\alpha+n+1)}{n! \Gamma(\alpha+1)} \gamma^{-\beta-1} {}_2F_1\left(-n, \beta+1; \alpha+1; \frac{1}{\gamma}\right), \quad (9)$$

being ${}_2F_1(\cdot, \cdot; \cdot; \cdot)$ the Gauss hypergeometric function, we obtain the following signal moments:

$$\mu_{r,s,k,l} = \sum_{m,n} \sum_{m',n'} \langle a_{m,n} a_{m',n'}^* \rangle \eta_{r,s}^{m,m'}(w_x) \eta_{k,l}^{n,n'}(w_y), \quad (10)$$

where

$$\begin{aligned} \eta_{r,s}^{m,m'}(w_x) &= \frac{(-1)^{m_{\min}} w_x^{r-s} 2^{\frac{|m-m'|}{2}}}{(\sqrt{2\pi})^{r+s} (|m-m'|)!} \sqrt{\frac{m_{\max}!}{m_{\min}!}} \Gamma\left(\frac{r+s+|m-m'|}{2} + 1\right) \\ &\times \Delta_{r,s,m-m'} {}_2F_1\left(-m_{\min}, \frac{r+s+|m-m'|}{2} + 1; |m-m'| + 1; 2\right), \end{aligned} \quad (11)$$

$\Gamma(\cdot)$ is the Euler gamma function, and $\Delta_{r,s,k}$ is an alias for the following integral

$$\Delta_{r,s,k} = \frac{1}{2\pi} \int_0^{2\pi} d\theta \cos^r \theta \sin^s \theta \exp(ik\theta). \quad (12)$$

Let us analyze the obtained expression. From the $\Delta_{r,s,k}$ term of Eq. (11), using the decomposition of the cosine and sine functions into the exponentials $e^{\pm i\theta}$, the binomial expansion, and the following integral value,

$$\frac{1}{2\pi} \int_0^{2\pi} d\theta \exp(ik\theta) = \begin{cases} 0, & \text{if } k \neq 0, \\ 1, & \text{if } k = 0, \end{cases} \quad (13)$$

we are able to demonstrate that some of the $\eta_{r,s}^{m,m'}$ terms are zero. For instance, the only non-vanishing terms are the ones for which the parity (even or odd) of $r + s$ is the same as the parity of $m - m'$, and correspondingly for $k + l$ and $n - n'$, and it is satisfied that $|m - m'| \leq r + s$ and $|n - n'| \leq k + l$. In particular it means that the beam with the mutual intensity expressed as a sum of uncorrelated HG modes ($\langle a_{m,n} a_{m',n'}^* \rangle = 0$ if $m \neq m'$ or $n \neq n'$) has zero moments for the same indexes r, s, k, l combination as any individual HG mode.

Taking into account the mode conversion under the gyrator transform [3] and the corresponding rotation of the WD the expressions for the moments of the signal with mutual intensity presenting as a series of the HLG modes,

$$\Gamma(\mathbf{r}_1, \mathbf{r}_2) = \sum_{m,n} \sum_{m',n'} \langle a_{m,n} a_{m',n'}^* \rangle \mathcal{H}_{m,n}^\alpha(\mathbf{r}_1) \mathcal{H}_{m',n'}^\alpha(\mathbf{r}_2), \quad (14)$$

can be obtained. Note that for $\alpha = 0$, $\mathcal{H}_{m,n}^\alpha$ corresponds to the HG modes and for $\alpha = \pi/4$ to the LG ones. Indeed, based on the second-order moment propagation equation for the ABCD system (here for simplicity we set $w_x = w_y = 1$) we derive the formulas for the corresponding moments:

$$\mu_{2000}^\alpha = \Re(K_x + L_x) \cos^2 \alpha + \Re(K_y - L_y) \sin^2 \alpha - \Im(N - M) \sin 2\alpha, \quad (15)$$

$$\mu_{0020}^\alpha = \Re(K_y + L_y) \cos^2 \alpha + \Re(K_x - L_x) \sin^2 \alpha - \Im(N + M) \sin 2\alpha, \quad (16)$$

$$\mu_{0200}^\alpha = \Re(K_x - L_x) \cos^2 \alpha + \Re(K_y + L_y) \sin^2 \alpha + \Im(N + M) \sin 2\alpha, \quad (17)$$

$$\mu_{0002}^\alpha = \Re(K_y - L_y) \cos^2 \alpha + \Re(K_x + L_x) \sin^2 \alpha + \Im(N - M) \sin 2\alpha, \quad (18)$$

$$\mu_{1100}^\alpha = -\Im(L_x) \cos^2 \alpha + \Im(L_y) \sin^2 \alpha - \Re(N) \sin 2\alpha, \quad (19)$$

$$\mu_{0011}^\alpha = -\Im(L_y) \cos^2 \alpha + \Im(L_x) \sin^2 \alpha - \Re(N) \sin 2\alpha, \quad (20)$$

$$\mu_{1010}^\alpha = \Re(M + N) \cos^2 \alpha + \Re(M - N) \sin^2 \alpha - \frac{1}{2} \Im(L_x + L_y) \sin 2\alpha, \quad (21)$$

$$\mu_{0101}^\alpha = \Re(M - N) \cos^2 \alpha + \Re(M + N) \sin^2 \alpha + \frac{1}{2} \Im(L_x + L_y) \sin 2\alpha \quad (22)$$

$$\mu_{0110}^\alpha = -\Im(M + N) \cos 2\alpha - \frac{1}{2} \Re(K_y - K_x + L_x + L_y) \sin 2\alpha, \quad (23)$$

$$\mu_{1001}^\alpha = \Im(M - N) \cos 2\alpha - \frac{1}{2} \Re(K_x - K_y + L_x + L_y) \sin 2\alpha. \quad (24)$$

where $\Re(\cdot)$ and $\Im(\cdot)$ represent the real and imaginary part operator respectively, and the same aliases as in Ref. [6] have been used,

$$K_x = \frac{1}{2} \sum_{m,n} |a_{m,n}|^2 (2m + 1), \quad (25)$$

$$K_y = \frac{1}{2} \sum_{m,n} |a_{m,n}|^2 (2n + 1), \quad (26)$$

$$L_x = \sum_{m,n} \langle a_{m,n} a_{m+2,n}^* \rangle \sqrt{(m+1)(m+2)}, \quad (27)$$

$$L_y = \sum_{m,n} \langle a_{m,n} a_{m,n+2}^* \rangle \sqrt{(n+1)(n+2)}, \quad (28)$$

$$M = \sum_{m,n} \langle a_{m,n+1} a_{m+1,n}^* \rangle \sqrt{(m+1)(n+1)}, \quad (29)$$

$$N = \sum_{m,n} \langle a_{m,n} a_{m+1,n+1}^* \rangle \sqrt{(m+1)(n+1)}. \quad (30)$$

Using the Eqs. (15)–(24) the important parameters widely applied for beam characterization can be obtained. Thus, for example, the signal width and its divergence along x and y coordinates are given by the Eqs. (15)–(24). The orbital angular momentum (OAM) of the beam expanded as a series of $\mathcal{H}_{m,n}^\alpha$ can also be calculated as

$$\text{OAM}^\alpha = \sin 2\alpha \sum_{m,n} |a_{m,n}|^2 (n - m) + 2 \cos 2\alpha \sum_{m,n} \Im \langle a_{m,n+1} a_{m+1,n}^* \rangle \sqrt{(m+1)(n+1)}. \quad (31)$$

Note that in the case of the signal decomposition as LG modes series ($\alpha = \pi/4$) the OAM is expressed as a weighted sum of the topological charges of all modes,

$$\text{OAM}^{\pi/4} = \sum_{m,n} |a_{m,n}|^2 (n - m). \quad (32)$$

We also observe that if the series contains only the modes with indices which differ at least by 3 units ($|m - m'|, |n - n'| \geq 3$) then, the second order momentum matrix has the same zero terms as the matrix corresponding to any non-fundamental mode $\mathcal{H}_{m,n}^\alpha$.

In this contribution, we have derived the expression for the arbitrary order moment of the signal represented as a series of the HG modes and have provided the rule for the moment analysis of a given mode combinations. We have generalized the formula for the second order moments developed in Ref. [6] to the case of partially coherent beams and to the field expanded in series of not only HG but also HLG modes. The obtained results are useful for optical signal synthesis and analysis.

ACKNOWLEDGMENT

The financial support of the Spanish Ministry of Science and Innovation under project TEC2008-04105 is acknowledged.

REFERENCES

1. Siegman, A. E., “New developments in laser resonators,” *Optical Resonators: Proc. SPIE*, Vol. 1224, No. 2, 1990.
2. Serna, J., R. Martínez-Herrero, and P. Mejías, “Parametric characterization of general partially coherent beams propagating through ABCD optical systems,” *J. Opt. Soc. Am. A*, Vol. 8, 1094–1098, 1991.
3. Rodrigo, J. A., T. Alieva, and M. L. Calvo, “Gyrator transform: Properties and applications,” *Opt. Express*, Vol. 15, 2190–2203, 2007.
4. Abramochkin, E. and V. Volostnikov, “Spiral light beams,” *Phys. Usp.*, Vol. 47, 1177–1203, 2004.
5. Alieva, T., E. Abramochkin, A. Asenjo-García, and E. Razueva, “Rotating beams in isotropic optical system,” *Opt. Exp.*, Vol. 18, 3568–3573, 2010.
6. Bekshaev, A. Y., “Intensity moments of a laser beam formed by superposition of Hermite-Gaussian modes,” *Fotoelektronika*, Vol. 8, 22–25, 1999.
7. Bastiaans, M. and T. Alieva, “Signal representation on the angular Poincaré sphere based on second-order moments,” *J. Opt. Soc. Am. A*, accepted for publication, 2010.
8. Borghi, R., G. Guattari, L. de la Torre, F. Gori, and M. Santarsiero, “Evaluation of the spatial coherence of a light beam through transverse intensity measurements,” *J. Opt. Soc. Am. A*, Vol. 20, 1763–1770, 2003.
9. Gradshteyn, I. S. and I. M. Ryzhik, *Table of Integrals, Series, and Products*, Academic Press, 1980.
10. Simon, R. and G. S. Agarwal, “Wigner representation of Laguerre-Gaussian beams,” *Opt. Lett.*, Vol. 25, 1313–1315, 2000.

The Phase-space Interpretation of Self-imaging and the Phase Retrieval Problem

Markus E. Testorf

Thayer School of Engineering at Dartmouth College, USA

Abstract— The problem of recovering the complex amplitude of optical signals from intensity measurements is studied in the context of phase-space optics. Special attention is given to periodic wavefronts subject to the self-imaging phenomenon. It is shown that for the case of bandlimited periodic signals perfect phase-retrieval can be achieved by recording the intensity in a finite set of fractional Talbot planes. This corresponds to a rigorous discrete formulation of phase-space tomography. Approximations inherent to the numerical implementation of phase-space tomography can be interpreted as a consequence of deviating from the ideal case of a periodic bandlimited signal, rather than as the byproduct of discretization.

1. INTRODUCTION

The phase problem is one of the most generic problems in optics. Interferometry and holography provide direct access to the phase information or the derivative of the phase of optical signals. For systems, where it is impossible to deduce the phase information from interference patterns iterative phase retrieval algorithms have proved effective and practical for recovering the phase information [1, 2]. An interesting alternative is offered by deterministic phase retrieval methods, which are based on analytical relations between the phase of the signal and the intensity distribution of the propagating wavefront [3, 4].

Phase-space tomography [5–8] is a deterministic phase retrieval concept with remarkable properties. It is based on the observation that projections of the phase space defined by the Wigner distribution function (WDF) of the propagating signal can be associated with the signal intensity in a particular diffraction plane. By taking multiple measurements of the signal in different diffraction planes the WDF can be tomographically reconstructed.

Phase-space tomography is a well-established method and has been studied in detail. It is nonetheless plagued with a number of inherent difficulties. In particular, phase-space distributions are not bounded. Any signal compact in one coordinate of phase-space has unlimited support in the orthogonal direction. This requires the truncation of the phase-space distribution and proper conditioning of the inverse problem to recover the phase information with acceptable accuracy. In addition, the WDF is a highly redundant signal representation, and as a consequence the data set required for recovering the WDF with projection tomography is considerably larger than needed to represent the actual signal.

Here, phase-space tomography is revisited in the rather narrow context of Fresnel diffraction of bandlimited periodic signals. For this class of signals it is possible to observe self-imaging and the fractional Talbot effect. The self-imaging phenomenon finds a particularly intuitive interpretation in phase-space optics [9], and it is this phase-space interpretation which can be used to establish a link between the fractional Talbot effect and phase-space tomography.

For the design of diffractive optical elements, and namely Talbot array illuminators, the fractional Talbot effect was previously associated with the phase retrieval problem [10, 11], and recovering the phase of a propagating wavefront is addressing the complementary problem. Phase-space tomography is an analytic phase retrieval method, where an excess amount of information is used to turn the inherently nonlinear signal recovery problem into a linear inverse problem.

Here, it is shown that it is possible to obtain a rigorous discrete formulation of phase-space tomography by considering sampled periodic signals, for which Fresnel diffraction is described as a discrete linear transformation. The successful recovery of the signal is possible by recording the intensity in a set of fractional Talbot planes defined by the number of samples necessary for representing the complex signal.

2. PHASE-SPACE TOMOGRAPHY AND FRESNEL DIFFRACTION

The principle of phase-space tomography can be summarized as follows. We consider the WDF of the complex amplitude $u(x)$, i.e.,

$$W[u](x, \nu) = \int_{-\infty}^{\infty} u(x + x'/2)u^*(x - x'/2) \exp(-i2\pi\nu x') dx' \quad (1)$$

The signal intensity can be recovered as the projection of the WDF

$$|u(x)|^2 = \int_{-\infty}^{\infty} W[u](x, \nu) d\nu \quad (2)$$

The signal can now be propagated through a paraxial optical system, which is specified by the $ABCD$ matrix of paraxial ray-tracing. The corresponding complex amplitude $u_{ABCD}(x)$ can be computed with the generalized Fresnel diffraction integral [12], and the corresponding WDF is the geometrical transformation of the WDF of the input signal,

$$W[u_{ABCD}](x, \nu) = W[u](Ax + B\nu, Cx + D\nu). \quad (3)$$

We can now choose the $ABCD$ parameters to define a rotation of the phase-space distribution, which is equivalent to a fractional Fourier transformation. The intensity at the output of the fractional Fourier transformer defines one projection of the WDF along a direction in phase-space corresponding to the rotation angle of the fractional Fourier transformation. The Fourier transformation of the recorded intensity then represents values of the ambiguity function, i.e., the double Fourier transformation of the WDF, along a line through the origin. This is the Fourier slice theorem of projection tomography and we obtain complete knowledge of the ambiguity function by recording a sufficiently large set of intensities at different rotation angles. The complex signal is obtained either by first recovering the WDF via Fourier transformation, which in turn allows one to recover the signal except for a constant phase factor, or by calculating the signal directly from the samples of the ambiguity function [8].

While rotations of the phase-space distribution correspond to the standard form of projection tomography [13] we can easily replace each rotation angle with alternative ray transfer parameters and obtain scaled versions of the same intensity distributions. For instance, Fresnel diffraction corresponds to a shear of the WDF

$$W[u_F](x, \nu) = W[u](x - \lambda z\nu, \nu) \quad (4)$$

and projections of the WDF at different angles can be obtained by recording the free space diffraction pattern at varying propagation distance z .

3. SIGNAL RECOVERY AND THE FRACTIONAL TALBOT EFFECT

We now consider a periodic signal $u_p(x + x_p) = u_p(x)$, which can be expressed by a Fourier series

$$u_p(x) = \sum_{n=-\infty}^{\infty} \tilde{u}_n \exp\left(i2\pi \frac{n}{x_p} x\right). \quad (5)$$

This can be used to compute the associated WDF,

$$W[u_p](x, \nu) = \sum_{n=-\infty}^{\infty} \sum_{n'=-\infty}^{\infty} \tilde{u}_n \tilde{u}_{n'}^* \delta\left(\nu - \frac{n+n'}{2x_p}\right) \exp\left(i2\pi \frac{n-n'}{x_p} x\right) \quad (6)$$

Figure 1 schematically illustrates the structure of the WDF. We recognize that the WDF not merely contains discrete frequency components at $\nu_m = m/x_p$, but also interlaced at intermediate frequencies $\nu_h = (h + 1/2)/x_p$. These additional components are a direct consequence of the bilinearity of the WDF and can be related to the mutual coherence properties of the plane wave components of the signal.

If we combine Eq. (6) with Eq. (4) the phase-space distribution in Fig. 1 is horizontally sheared. If the shear equals the displacement indicated by the dashed line T we recover an identical copy

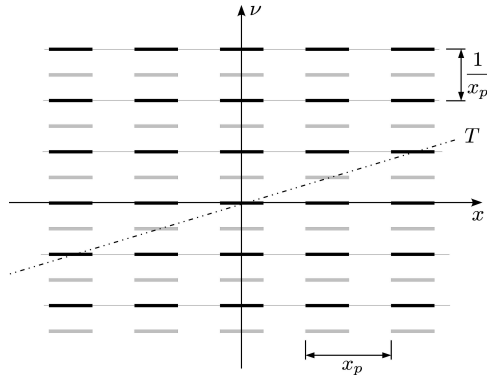


Figure 1: Phase-space diagram of a periodic signal. Line T indicates the shear necessary to observe Talbot self-imaging.

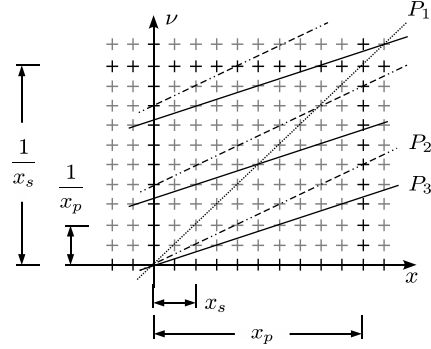


Figure 2: Phase-space diagram of a discrete periodic signal. Lines P_1 , P_2 , and P_3 represent three of the projections used for tomographic reconstruction.

of the initial WDF, which corresponds to the first self-image of the input signal. We easily deduce the self-imaging distance from the diagram as [9],

$$z_T = \frac{2x_p^2}{\lambda}. \quad (7)$$

We further assume that the periodic signal is bandlimited, i.e., it can be represented by a finite number of Fourier coefficients \tilde{u}_n , with $0 \leq n < N$. This means, we can use the sampling theorem to represent the signal. The periodic bandlimited signal is then expressed as

$$u_p(x) = u_s(x) * \text{comb}(x; x_s N) * h_{inp}(x) \quad (8)$$

with the interpolation function

$$h_{inp}(x) = \text{sinc}(x/x_s) \quad (9)$$

the delta-comb function

$$\text{comb}(x, x_s N) = \sum_{m=-\infty}^{\infty} \delta(x - mN x_s) \quad (10)$$

and the sampled signal of a single period

$$u_s(x) = \sum_{m=0}^{N-1} u_m \delta(x - m x_s) \quad (11)$$

assuming a sampling distance $x_s = x_p/N$. Substituting the sampled periodic signal in Eq. (1) we obtain a phase-space distribution which is discrete and periodic in both conjugate coordinates, having periods x_p and $1/x_s$ in x and ν , respectively. The bilinear interference terms occupy a grid with discrete samples separated $x_s/2$ in space and $1/(2N x_s)$ in frequency. Thus the WDF of the discrete signal has a structure which can be written as

$$W_{dis}(x, \nu) = W[u_s](x, \nu) *_{x, \nu} \sum_{n=-\infty}^{\infty} \sum_{n'=-\infty}^{\infty} \delta(x - n x_p) \delta(\nu - n' / x_s) \quad (12)$$

with $*_{x, \nu}$ denoting a double convolution with respect to x and ν , and

$$W[u_s](x, \nu) = \sum_{m=0}^{2N-1} \sum_{m'=0}^{2N-1} W_{m, m'} \delta(x - m x_s / 2) \delta(\nu - m' / (2N x_s)) \quad (13)$$

In Fig. 2, the effect of Fresnel diffraction on the the discrete phase-space distribution is illustrated. In particular, we can recognize shear parameters for which we recover the same grid of discrete samples as we found for $W_{dis}(x, \nu)$, in Eqs. (12) and (13), however with the samples having

changed lateral position. The diffraction planes associated with this condition correspond to a set of fractional Talbot planes, with propagation distance

$$z_k = \frac{k}{2N} z_T, \quad (14)$$

and $k = 1, \dots, 2N$. This set of fractional Talbot planes is remarkable because it can be used to formulate Fresnel diffraction rigorously in terms of the discrete samples u_m , which are related to the corresponding samples in the fractional Talbot plane by a discrete linear transformation [9, 14].

The perfect correspondence between the continuous and the discrete formulation of Fresnel diffraction can be understood with the help of Eq. (8) and the phase-space diagram in Fig. 2. In the signal domain Fresnel diffraction is equivalent to a convolution with a quadratic phase function (linear chirp). To compute the Fresnel diffraction amplitude of the signal in Eq. (8) merely amounts to an addition convolution. Since the convolution operation is commutative, Fresnel diffraction can be computed for the discrete signal before the interpolation of the continuous signal. However, as Fig. 2 illustrates, diffraction planes z_k are exactly those planes for which the structure of the discrete signal is preserved and only the discrete values have changed. In other words, Fresnel diffraction is completely described, if we find the linear transformation for computing the new sampling values from the samples u_m [9].

The price to pay for the strict correspondence between the continuous and the discrete formulation of Fresnel diffraction is the condition of a periodic signal which can be represented by the sampling expansion in Eq. (8), and the evaluation of the diffraction amplitude for a set of propagation distances which are strictly determined by the number of samples N .

Lines P_1 , P_2 , and P_3 indicate the shear corresponding to $k = 1, 2, 3$. If the intensity distribution is recorded in planes z_k the samples of the intensity are identical to projections of the discrete WDF along lines P_k . Due to the periodicity of the signal samples of the WDF belonging to the same projection are located along parallel lines within the basic cell of the WDF grid. The $2N$ intensity readings obtained in $2N$ diffraction planes then yield a set of data which ideally provide us with a unique reconstruction of all $4N^2$ samples $W_{m,m'}$ of the discrete samples of the WDF.

By identifying the fractional Talbot effect as a case for which discrete phase-space tomography can be formulated rigorously we have obtained a baseline for further inquiry. Most importantly, numerical implementations of phase-space tomography can be compared to the idealized scenario of processing periodic bandlimited signals.

In addition, the discrete formulation allows us to identify redundancies more explicitly. For instance, if we substitute a signal of finite support, samples $W_{m,m'}$ at the boundary of the support domain may be deduced from single intensity measurements. As a consequence overall fewer intensity measurements are required to deduce the remaining samples of the discrete representation of the WDF. Similar arguments may be used to reduce the required data set for other classes of signals for which we possess prior knowledge.

4. CONCLUSION

The fractional Talbot effect can be related to the recovery of complex signals and phase-space tomography. It was shown that a perfect correspondence exists between the continuous formulation of phase-space tomography and a discrete representation by considering periodic bandlimited signals. In this case the data set required for tomographic reconstruction of the phase-space representation is recorded in diffraction planes associated with the fractional Talbot effect. Similar to the discrete Fourier transformation, which is a rigorous representation of signals belonging to the class of periodic and bandlimited function, phase-space tomography based on the intensity in fraction Talbot planes can be regarded as a baseline for numerical computations. By characterizing signals in terms of their adherence to his class of signals, it is possible to select suitable signal processing methods for minimizing the impact of deviations from the ideal signal model.

REFERENCES

1. Gerchberg, R. W. and W. O. Saxton, "A practical algorithm for the determination of the phase from image and diffraction plane pictures," *Optik*, Vol. 35, 237–246, 1972.
2. Fienup, J. R., "Iterative method applied to image reconstruction and to computer generated holograms," *Opt. Eng.*, Vol. 19, 297–305, 1980.
3. Teague, M. R., "Deterministic phase retrieval: A Green's function approach," *J. Opt. Soc. Am.*, Vol. 73, 1434–1441, 1983.

4. Gureyev, T. E., A. Roberts, and K. A. Nugent, “Partially coherent fields, the transport-of-intensity equation, and phase uniqueness,” *J. Opt. Soc. Am. A*, Vol. 12, 1942–1946, 1995.
5. Raymer, M. G., M. Beck, and D. F. McAlister, “Complex wave-field reconstruction using phase-space tomography,” *Phys. Rev. Lett.*, Vol. 72, 1137–1140, 1994.
6. McAlister, D. F., M. Beck, L. Clarke, A. Mayer, and M. G. Raymer, “Optical phase retrieval by phase-space tomography and fractional-order Fourier transforms,” *Opt. Lett.*, Vol. 20, 1181–1183, 1995.
7. Semichaevsky, A. and M. Testorf, “Phase-space interpretation of deterministic phase retrieval,” *J. Opt. Soc. Am. A*, Vol. 21, 2173–2179, 2004.
8. Tu, J. and S. Tamura, “Wave field determination using tomography of the ambiguity function,” *Phys. Rev. E*, Vol. 55, 1946–1949, 1997.
9. Testorf, M., “Self-imaging in phase space,” *Phase-space Optics, Fundamentals and Applications*, M. Testorf, B. Hennelly, J. Ojeda-Castañeda, eds., Chapt. 9, 279–308, McGraw-Hill, 2009.
10. Testorf, M., V. Arrizón, and J. Ojeda-Castañeda, “Numerical optimization of phase-only elements based on the fractional Talbot effect,” *J. Opt. Soc. Am. A*, Vol. 16, 97–105, 1999.
11. Testorf, M., T. J. Suleski, and Y.-C. Chuang, “Design of Talbot array illuminators for three-dimensional intensity distributions,” *Opt. Express*, Vol. 14, 7623–7629, 2006.
12. Jr., Collins, S. A., “Lens-system diffraction integral written in terms of matrix optics,” *J. Opt. Soc. Am.*, Vol. 60, 1168–1177, 1970.
13. Kak, A. C. and M. Slaney, *Principles of Computerized Tomographic Imaging*, IEEE Press, 1988.
14. Arrizón, V., J. G. Ibarra, and J. Ojeda-Castañeda, “Matrix formulation of the Fresnel transform of complex transmittance gratings,” *J. Opt. Soc. Am. A*, Vol. 13, 2414–2422, 1996.

Digital Holography in the Light of Phase Space

B. M. Hennelly

Department of Computer Science, National University of Ireland, Maynooth, Co. Kildare, Ireland

Abstract— Digital holography is an imaging technique that has application in three dimensional imaging as well as phase contrast microscopy. In digital holography an interference pattern is recorded by a digital camera. The interference pattern is formed from a known reference eave and the light scattered from an object. The digital hologram is then input to a computer algorithm that simulates the back propagation of light from the camera plane to the image plane. In this paper we show how Phase Space Diagrams can be used to interpret and understand these systems.

1. INTRODUCTION

Holography is an imaging technique that was invented by Gabor in 1948 [1], for which he later received a Nobel prize. The technique was appended to remove the twin image by Leith and Upatnieks [2, 3]. Digital Holography is an optoelectronic version of this imaging technique [4–7]. The first half of digital holography is to record either one or multiple interferograms using a digital camera. These interferograms are recorded by intersecting a known reference beam with the light scattered by a reflecting or transmissive object. The second half of a digital holographic system is to numerically reconstruct the image using the recorded hologram as input to a numerical algorithm that simulates optical propagation of the wave field to the image plane. There are a host of different algorithms that can do this [8–12], each varying in accuracy and time taken and each providing a different point spread function for the overall record-reconstruction system.

Aside from applications in 3D imaging, one of the most important applications of digital holography is in the area of phase contrast microcopy [13, 14]. Microscopic digital holographic systems make use of a microscopic objective between the object and CCD and have become increasingly popular in recent years. This is firstly because because one can employ phase contrast techniques to the phase of the reconstructed image and secondly because it becomes possible to remove various types of aberrations digitally from these systems. In this paper we discuss both the recording and the reconstruction sides of digital holography from the phase space perspective. We show how phase space diagrams may be used to gain insight into the holographic process.

The Wigner Distribution function is a time frequency representation of signals which was introduced to the optics community My Bastians [15–17]. A simple graphical chart known as a ‘Wigner chart’ or ‘Phase Space Diagram’ (PSD) has often proved to be quite useful in understanding optical systems [18]. Indeed this approach has previously been employed to analyze holographic systems. In this paper we take the first steps to applying this approach to digital holographic systems by Lohmann and others [19–21]. The benefit here is that the digital camera can be classified as have a square like PSD — it has a physical width and a bandwidth defined by the inverse of the pixel pitch. By contrasting the PSD of the digital camera with that of the hologram to be recorded, we show how PSDs may be used to understand and interpret digital holography and to define optimum parameters.

2. WIGNER DISTRIBUTION FUNCTION BASICS

The Wigner Distribution function (WDF) is a bilinear transformation defined as follows.

$$W_u(x, f) = \int_{-\infty}^{\infty} u\left(x + \frac{x'}{2}\right) u^*\left(x - \frac{x'}{2}\right) \exp(-j2\pi f x') dx' \quad (1)$$

The WDF is a function of both the spatial coordinate x and the spatial frequency coordinate f . It has a number of useful properties that make it particularly useful for studying propagation through optical systems. Below we list the properties of the WDF that are of interest in this paper.

1. The first property that is of interest in this paper is the coordinate mapping of the WDF that occurs when the signal of interest undergoes a Fresnel propagation, i.e., free space propagations as described under the paraxial approximation. A fresnel transformation can be described as follows, $u(x) \rightarrow u(x) * \exp(j\frac{\pi}{\lambda z}x^2)$ where the $*$ denotes a convolution, λ is the wavelength

of the light and z is the propagation distance. In this case the coordinates of the WDF are mapped as follows $W_u(x, f) \rightarrow W_u(x - f\lambda z, f)$

2. The second property of interest is the WDF of the product of two signals. In this case the WDF of the product may be described by the convolution of the WDFs of the individual signals along the f axis, i.e., the WDF of $u(x)v(x)$ is given by $W_{uv}(x, f) = W_u(x, f) *^f W_v(x, f)$. This property is of interest in this paper when we describe the intensity of a signal as the product of the signal with its conjugate.
3. This leads us to our third property. The WDF of the conjugate of signal is equivalent to the WDF of the signal inverted along f , i.e., $W_{u^*}(x, f) = W_u(x, -f)$
4. The fourth property concerns the marginals of the WDF. It can be shown that $\int_{-\infty}^{\infty} W_u(x, f) df = |u(x)|^2$ and similarly $\int_{-\infty}^{\infty} W_u(x, f) dx = |U(f)|^2$ where $U(f)$ is the Fourier Transform of $u(x)$. If a signal has the vast majority of its energy distributed in x over a support (or width) W and it also has the vast majority of its energy distributed over a support (or bandwidth) B , then we can say that WDF has similar properties. The energy will be contained in a region in (x, f) defined by W and B . This property leads to the formation of the Phase Space Diagram (PSD) which is at the heart of this paper.
5. The fifth and final property of the WDF concerns sampling, a topic which is always of interest when dealing with digital cameras. The Nyquist criterion states that if a signal is sampled with a sampling interval T , this is sufficient to completely recover a signal that has a finite bandwidth B so long as the following condition is satisfied: $T \leq \frac{1}{B}$ [22]. However it has recently been shown that a signal can be completely recovered so long as $T \leq \frac{1}{L}$ where L is the local bandwidth of the signal. For a full description of this subject in terms of the WDF, the reader may consult chapter 10 in [23]. This property of the WDF is of particular interest when we consider the sampling (digital hologram recording) of a Fresnel propagated signal. As we shall see, such a signal often has a local bandwidth L that reduces linearly with the distance of propagation z , while the total bandwidth B remains constant under propagation.

3. DIGITAL HOLOGRAM RECORDING

In Fig. 1, we illustrate a typical optical setup that is used to record digital holograms. Having been spatially filtered using a pinhole the beam is expanded and it now passes through a beam splitter. One arm is aimed directly at an object, or in the case of transmissive objects it is aimed through the object. The light coming from the object is incident on a CCD via a second beam splitter. The second arm is the reference beam which takes an approximately equidistant path to the CCD via the same latter two elements. There are numerous elements that are not shown in the diagram. For example a final linear polarizer in the setup serves to force both the reference and object wave fields into the same state of polarization such that the diffraction efficiency of the systems is maximized. In addition we use neutral density filters, half wave plate, linear polarizer and the polarizing beam splitters, so that we can effectively change the ratio of powers in the two arms of system. We write the interference pattern recorded by the camera as

$$I(x) = |u_z(x)|^2 + |r(x)|^2 + u_z(x)r^*(x) + u_z^*(x)r(x) \quad (2)$$

where $u_z(x)$ represents the signal that has propagated a distance z from the object to the object to the CCD (we recall that this is given by $u(x) * \exp(j\frac{\pi}{\lambda z}x^2)$) and $r(x)$ denote the reference wave field at the plane of the CCD. In our setup a phase shifting mirror is moved and four captures enabling separation of $u_z(x)$ [24]. This signal is then numerically reconstructed by simulating a backwards Fresnel propagation, and thus we obtain an image of $u(x)$.

4. DIGITAL HOLOGRAPHY DESCRIBED USING PHASE SPACE DIAGRAMS

We now demonstrate that the PSD is a very useful tool for investigating a PSI Digital holography recording system. We begin by showing the PSD of the original signal before any propagation has taken place. For a 3D object, we can imagine this signal to lie in the plane immediately after the object. This is the leftmost figure in Fig. 2. We can see that the object signal $u(x)$ has a physical width W_O and a bandwidth B_O and thus we can describe the signal as having a square-like PSD. This follows from property 4 of the WDF discussed above. After the signal propagates a distance z (to the plane of the camera) the PSD now takes the form shown in the center part of Fig. 2. This is mathematically described by property 1 above. We can see that the signal spreads out in

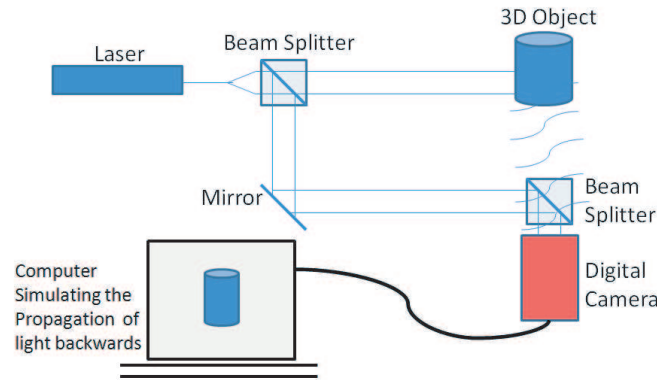


Figure 1: Digital holography in-line architecture. In our experimental set up we employ phase retarders (not shown) that allow us to make multiple captures with different constant phase shifts of the reference beam. We then implement the phase shifting interferometry algorithm to extract the complex wavefront.

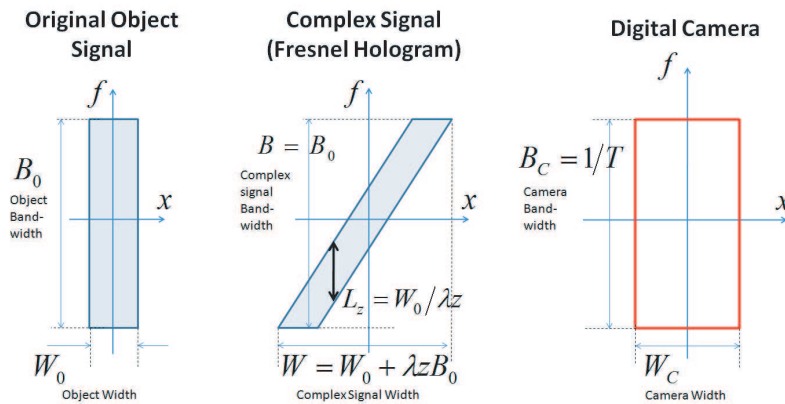


Figure 2: Phase space diagrams of original complex signal, the propagated complex signal in the plane of the camera and of the digital camera itself.

space and now occupies a larger support. We can deduce from simple geometry that the width of the signal will be given by $W_O + B_O\lambda z$ and the local bandwidth is given by $L = \frac{W_O}{\lambda z}$. We note that since the light diverges at all angles from the object, B_O will be infinite and thus the signal will theoretically be spread out over an infinite support after propagation. The propagated signal is now incident on a CCD where it is sampled over the width of the camera, W_C . The bandwidth of the camera B_C , or more accurately we can describe this as the maximum bandwidth of the signal that the CCD can record, is given by $1/T$. Thus the camera has a square like PSD as shown in the rightmost part of 2. Because PSI allows us to isolate $u_z(x)$ from Equation (2) we can consider only this signal as being recorded by the CCD. The PSDs of the recorded complex signal, and its intensity are shown in Fig. 3. From property 5 above we can deduce that the local bandwidth of $u_z(x)$ must be less than or equal to B_C . We can express this condition as follows, $\frac{W_O}{\lambda z} \leq \frac{1}{T}$. This gives us a minimum condition for z , $z \geq \frac{TW_O}{\lambda}$. In the literature the intensity of the signal is predicted to have a bandwidth that is equal to twice the bandwidth of $u_z(x)$ [22]. However from property 3 above we can predict that this bandwidth will be much less than this value and will be given by twice the local frequency of $u_z(x)$. We believe that this point is interesting in the context of off axis digital holography where we must take into account the recording of this intensity term. After the signal is reconstructed (numerical propagation a distance $-z$), we can again find its PSD by applying the coordinate mapping defined in property 1 to the PSD of the recorded signal. The PSD of the reconstructed signal is shown in Fig. 4. We can see that the local bandwidth of the reconstructed signal is defined by the camera width and is given by $\frac{W_C}{\lambda z}$ while the total bandwidth of the signal is much larger and is given by $\frac{W_C + W_O}{\lambda z}$. The PSD of the intensity is also shown in the Figure and from property 3 above we can conclude that it will be equal to $\frac{2W_C}{\lambda z}$.

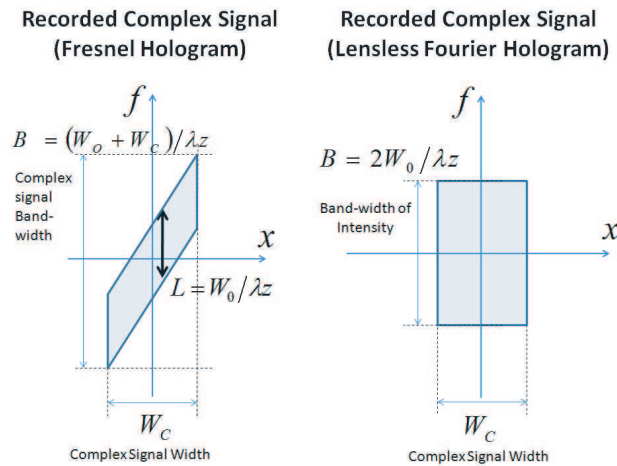


Figure 3: Phase space diagrams of the recorded complex signal and its intensity.

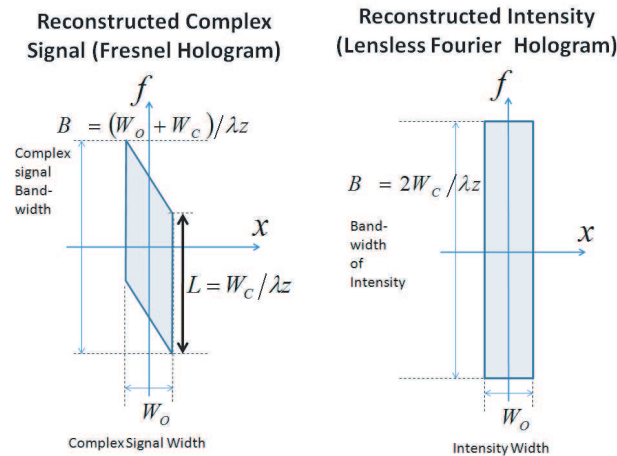


Figure 4: Phase space diagrams of the reconstructed complex signal and its intensity.

5. CONCLUSION

In this paper, we have analyzed digital holographic imaging using the properties of the Wigner Distribution function. Using Phase Space Diagrams we have found an expression for the minimum distance that we should place our object from the recording camera. We have also found expressions for the width, local bandwidth and overall bandwidth of the complex recorded and reconstructed signals, and their intensities. We have demonstrated that the WDF is useful for understanding and interpreting digital holographic imaging.

ACKNOWLEDGMENT

This research is funded from the European Community’s Seventh Framework Programme FP7/2007 2013 under grant agreement 216105 “Real 3D.”

REFERENCES

1. Gabor, D., “A new microscope principle,” *Nature*, Vol. 161, 777–778, 1948.
2. Leith, E. N. and J. Upatnieks, “Reconstructed wavefronts and communication theory,” *J. Opt. Soc. Am.*, Vol. 52, 1123, 1962.
3. Leith, E. N. and J. Upatnieks, “Wavefront reconstruction with continuous-tone objects,” *J. Opt. Soc. Am.*, Vol. 53, 1377, 1963.
4. Goodman, J. W. and R. Lawrence, “Digital image formation from electronically detected holograms,” *Appl. Phys. Lett.*, Vol. 11, 77–79, 1967.
5. Yaroslavskii, L. P. and N. S. Merzlyakov, *Methods of Digital Holography*, Consultants Bureau, 1980.

6. Kreis, T. M., M. Adams, and W. P. O. Juptner, "Methods of digital holography: A comparison," *Proc. SPIE*, Vol. 3098, 224–233, 1997.
7. Schnars, U. and W. P. O. Juptner, "Digital recording and numerical reconstruction of holograms," *Meas. Sci. Technol.*, Vol. 13, 85–101, 2002.
8. Kelly, D. P., B. M. Hennelly, W. T. Rhodes, and J. T. Sheridan, "Analytical and numerical analysis of linear optical systems," *Opt. Eng.*, Vol. 45, 008201, 2006.
9. Hennelly, B. M. and J. T. Sheridan, "Generalizing, optimizing, and inventing numerical algorithms for the fractional Fourier, fresnel, and linear canonical transforms," *J. Opt. Soc. Am. A*, Vol. 22, 917–927, 2005.
10. Hennelly, B. M. and J. T. Sheridan, "Fast algorithm for the linear canonical transform," *J. Opt. Soc. Am. A*, Vol. 22, 928–937, 2005.
11. Mendlovic, D., Z. Zalevsky, and N. Konforti, "Computation considerations and fast algorithms for calculating the diffraction integral," *J. Mod. Opt.*, Vol. 44, 407–414, 1997.
12. Mas, D., J. Garca, C. Ferreira, L. M. Bernardo, and F. Marinho, "Fast algorithms for free-space diffraction patterns calculation," *Opt. Commun.*, Vol. 164, 233–245, 1999.
13. Cucho, E., P. Marquet, and C. Depeursinge, "Simultaneous amplitude-contrast and quantitative phase-contrast microscopy by numerical reconstruction of Fresnel off-axis holograms," *Appl. Opt.*, Vol. 38, 6994–7001, 1999.
14. Marquet, P., B. Rappaz, P. J. Magistretti, E. Cucho, Y. Emery, T. Colomb, and C. Depeursinge, "Digital holographic microscopy: A noninvasive contrast imaging technique allowing quantitative visualization of living cells with subwavelength axial accuracy," *Opt. Lett.*, Vol. 30, 468–470, 2005.
15. Bastiaans, M. J., "The Wigner distribution function applied to optical signals and systems," *Opt. Commun.*, Vol. 25, 26–30, 1978.
16. Bastiaans, M. J., "Wigner distribution function and its application to first order optics," *J. Opt. Soc. Am.*, Vol. 69, 1710–1716, 1979.
17. Bastiaans, M. J., "Application of the Wigner distribution function in optics," *The Wigner Distribution Theory and Applications in Signal Processing*, 375–426, W. Mecklenbrucker and F. Hlawatsch, Eds., Elsevier, 1997.
18. Lohmann, A. W., "Image rotation, Wigner rotation, and the fractional Fourier transform," *J. Opt. Soc. Am. A*, Vol. 10, 2181–2186, 1993.
19. Lohmann, A. W., "The space-bandwidth product, applied to spatial filtering and to holography," *Selected Papers on Phase-Space Optics*, 11–32, M. E. Testorf, J. Ojeda-Castaeda, and A. W. Lohmann, Eds., SPIE Press, 2006.
20. Lohmann, A. W., M. E. Testorf, and J. Ojeda-Castaeda, "Holography and the Wigner function," *The Art and Science of Holography*, 129–144, H. J. Caulfield, Ed., SPIE Press, 2004.
21. Testorf, M. and A. W. Lohmann, "Holography in phase space," *Appl. Opt.*, Vol. 47, A70–A77, 2008.
22. Goodman, J., *Introduction to Fourier Optics*, 3rd Edition, Roberts and Company, Englewood, Colorado, 2005.
23. Testorf, M., B. Hennelly, and J. Ojeda-Castaneda, *Phase-Space Optics*, McGrawHill, 2009.
24. Yamaguchi, I. and T. Zhang, "Phase-shifting digital holography," *Opt. Lett.*, Vol. 22, 1268–1270, 1997.

Wigner Based Phase Space as a Tool to Analyze Super Resolved Imaging Configurations

Zeev Zalevsky

School of Engineering, Bar-Ilan University, Ramat-Gan 52900, Israel

Abstract— In this paper we provide a schematic description and an explanation for how the process of super resolved imaging may be understood by using Wigner based phase space. The advantage of using the Wigner space is related to the fact that it can mathematically be related to the spatial degrees of freedom of a signal and thus be used to understand the operation of super resolving imaging systems.

1. INTRODUCTION

Super resolution (SR) is a field integrating the sciences of optics together with the expertise of image processing and computer vision science [1, 2]. Basically any imaging system, digital as well as a human eye, has a limited capability to separate between spatially close features. This limitation can be related either to the diffraction or to the geometry of the imaging sensing array [1]. In the case of diffraction, given an imaging lens with limited aperture size, not all the rays that are reflected from the object, are collected by the lens. According to the Rayleigh criterion [3] this limitation is proportional to the product between the wavelength of the illumination and the F number of the optics (the ratio between the focal length and the diameter of the lens). Thus, the smaller the F number is, the better the spatial separation becomes. In the case of the geometry of the sensing array, the smaller the pixels are, i.e., the denser the spatial sampling of the space is, the better becomes the capability to reconstruct closer point sources originated from the imaged object [1].

In order to overcome the limitation of a given imaging system one may convert the spatial degrees of freedom, that before could not pass through the limited spatial-spectral bandwidth of the imaging system, into other domains which the imaging system can transmit and then after passing them through the system, to convert them back into their proper location in the space domain. The process of “converting to” and “back converting” of degrees of freedom is also called encoding and decoding or multiplexing and de-multiplexing. The improvement of resolution requires “payment”. The “payment”, that is needed in order to improve the resolution in the space domain, is the devotion of other domain or other sub spaces into which the required spatial degrees of freedom of the input signal can be converted to. The conversion of spatial degrees of freedom can be done to a single sub space or to a plurality of several such sub spaces.

In order to do this properly without losing the desired spatial information one needs to have a priori information on the signal. Having a priori knowledge that a certain domain is not used by the signal and thus it may allow us to designate it to the usage of spatial resolution improvement. For instance, knowing that the object does not vary in the time domain may assist in using the time domain for the process of converting to and converging back, the spatial degrees of freedom.

The pluralities of other domains that may be used for this temporary conversion of degrees of freedom are the time [4], wavelength [5], polarization [6], code [7], gray levels [8], field of view [9–11] and even light’s coherence [12] domain.

2. DESCRIPTION OF SR

We will assume a general imaging system as presented by Fig. 1. In this setup an encoding mask is positioned near the input object that is imaged by a finite imaging lens (which is schematically described as an aperture positioned at the optical Fourier plane), and later a decoding mask is positioned near the detector at which the output image is obtained. The detector performs time, wavelength or other types of averaging in order to decode the spatial information that was encrypted by the encoding input mask. The encoding mask can be a random spatial distribution, time varying spatial distribution or wavelength dependent filter etc. The dependency of this mask is related to the domain into which we aim to perform our conversion of the spatial degrees of freedom.

As mentioned before we assume that the spatial encoding mask, that has some polarization, wavelength, or temporal dependency, is positioned near the input object $u(x)$. We denote this mask as: $g(x, p(t, \lambda), \lambda, t)$. While the meaning of this notation is that at different spatial positions

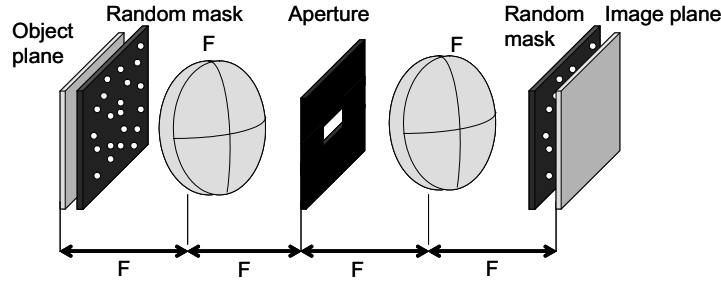


Figure 1: Schematic sketch of the imaging setup.

along the mask one may have wavelength dependencies (denoted by λ), time dependencies (denoted by t) or polarization dependency (denoted by p) while the polarization dependency for itself can have time and wavelength dependency as well: $p(t, \lambda)$.

We respectively denote the spatial spectrum of this mask and the spatial-spectrum of the object as:

$$G(\nu_x, p(\lambda, t), \lambda, t) = \int g(x, p(\lambda, t), \lambda, t) \exp(-2\pi i x \nu_x) dx \quad U(\nu_x) = \int u(x) \exp(-2\pi i x \nu_x) dx \quad (1)$$

Since the encoding mask is attached to the object (i.e., mathematically there is a multiplication operation between the two distributions in the space domain), in the spectrum we obtain a convolution operation between the spectrum of the input object and the Fourier of the mask. After passing through the finite aperture of the imaging lens we have a multiplication of this aperture (a rectangular one) by the overall spectral distribution: $rect(\nu_x/(\Delta\nu_x)) \int U(\nu'_x) G(\nu_x - \nu'_x, p(\lambda, t), \lambda, t) d\nu'_x$ while we denoted by $\Delta\nu_x$ the spatial width of the aperture. The decoding mask is attached to the output plane and thus its Fourier transform performs an additional convolution operation with the overall expression. If we denote by G_d the Fourier transform of the decoding mask g_d , this yields $\int G_d(\nu_x - \nu'_x, p(\lambda, t), \lambda, t) rect(\nu'_x/(\Delta\nu_x)) \int U(\nu''_x) G(\nu'_x - \nu''_x, p(\lambda, t), \lambda, t) d\nu''_x d\nu'_x$. Assuming that U_R is the spectrum of the reconstructed image u_R . and that the decoding mask is the complex conjugate of the encoding mask, the last expression becomes:

$$U_R(\nu_x) = \int G^*(-\nu_x + \nu'_x, p(\lambda, t), \lambda, t) rect(\nu'_x/(\Delta\nu_x)) \int U(\nu''_x) G(\nu'_x - \nu''_x, p(\lambda, t), \lambda, t) d\nu''_x d\nu'_x \quad (2)$$

2.1. Code Division Multiplexing

The expression of Eq. (2) can be reformulated as follows:

$$U_R(\nu_x) = \int U(\nu''_x) \left[\int rect(\nu'_x/(\Delta\nu_x)) G^*(\nu'_x - \nu_x) G(\nu'_x - \nu''_x) d\nu'_x \right] d\nu''_x \quad (3)$$

In the case of code division multiplexing there is no time, polarization or wavelength variations. For a random encoding mask having small spatial features, the internal integral may be approximated as follows:

$$\int rect(\nu'_x/(\Delta\nu_x)) G^*(\nu'_x - \nu_x) G(\nu'_x - \nu''_x) d\nu'_x \approx \delta(\nu''_x - \nu_x) \quad (4)$$

which leads to:

$$U_R(\nu_x) = \int U(\nu''_x) \delta(\nu''_x - \nu_x) d\nu''_x = U(\nu_x) \quad (5)$$

Note that the assumption of Eq. (4) is an approximation and in practice when $\Delta\nu_x$ is getting narrower the right wing can better be approximated with a spectral function which is wider than a delta function. In addition the right wing can contain another additive term that may be approximated by a constant. The widening of the delta will blur the spectral expression of U_R which means that the super resolved image will become field of view limited. The addition of the constant term will reduce the contrast or the SNR of the obtained reconstruction.

In Figs. 2(a) and 2(b), we numerically simulate the proposed approach for code division multiplexing SR. A resolution target was low pass filtered while being imaged through a band limited

lens aperture. The input object is a USAF (US Air Force) resolution target. Its spatial blurring is well seen in Fig. 2(a). However, after the addition of the random encoding and decoding code multiplexing mask one obtains the image of Fig. 2(b) where the high resolution features of the resolution target are almost completely reconstructed. The resolution improvement here is by more than a factor of 5. Obviously the image of Fig. 2(b) is obtained after image processing that includes some subtraction of background noises.

2.2. Time Multiplexing

In this case we will perform time averaging (that way we do not have to assume spatial randomness of the encoding and decoding masks as before), thus Eq. (2) becomes:

$$U_R(\nu_x) = \iint U(\nu_x'') \text{rect}(\nu_x' / (\Delta\nu_x)) \left[\int G(\nu_x' - \nu_x'', p(\lambda, t), \lambda, t) G^*(-\nu_x + \nu_x', p(\lambda, t), \lambda, t) dt \right] d\nu_x'' d\nu_x' \quad (6)$$

since we have a time varying mask we can approximate that by:

$$\int G(\nu_x' - \nu_x'', p(\lambda, t), \lambda, t) G^*(-\nu_x + \nu_x', p(\lambda, t), \lambda, t) dt \approx \delta(\nu_x - \nu_x'') \quad (7)$$

We obtain that the final expression for the reconstructed spectrum is:

$$U_R(\nu_x) = \left[\int \text{rect}(\nu_x' / (\Delta\nu_x)) d\nu_x' \right] \int U(\nu_x'') \delta(\nu_x - \nu_x'') d\nu_x'' = \Delta\nu_x \cdot U(\nu_x) \quad (8)$$

Numerical demonstration of the time averaging SR approach may be seen in Figs. 2(c) and 2(d) where in Fig. 2(c) we present the blurred (low passed) resolution target (USAF) and in Fig. 2(d) its reconstruction after the addition of the time varying encoding and decoding random mask and after performing of the averaging operation in the time domain. In the simulation we averaged 800 images. One can clearly see the resolution improvement that was demonstrated in this simulation. The obtained improvement is by a factor of about 3.

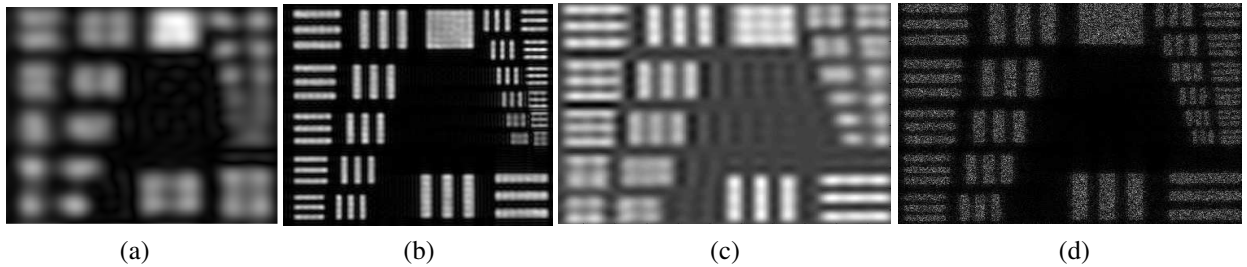


Figure 2: (a), (b) Code division multiplexing; (c), (d) Time division multiplexing. (a), (c) Low resolution USAF target. (b), (d) Super resolved reconstruction.

2.3. Polarization Multiplexing

In this case we will perform averaging over the time varying polarization state and thus Eq. (2) becomes:

$$U_R(\nu_x) = \iint U(\nu_x'') \text{rect}(\nu_x' / (\Delta\nu_x)) \left[\int G(\nu_x' - \nu_x'', p(\lambda, t), \lambda, t) G^*(-\nu_x + \nu_x', p(\lambda, t), \lambda, t) \left(\frac{dp}{dt} \right) dt \right] d\nu_x'' d\nu_x' \quad (9)$$

since

$$\int G(\nu_x' - \nu_x'', p(\lambda, t), \lambda, t) G^*(-\nu_x + \nu_x', p(\lambda, t), \lambda, t) \left(\frac{dp}{dt} \right) dt \approx \delta(\nu_x - \nu_x'') \quad (10)$$

we obtain once again that the final expression for the reconstructed spectrum is:

$$U_R(\nu_x) = \left[\int \text{rect} \left(\frac{dp}{dt} \right) d\nu_x' \right] \int U(\nu_x'') \delta(\nu_x - \nu_x'') d\nu_x'' = \Delta\nu_x \cdot U(\nu_x) \quad (11)$$

2.4. Wavelength Multiplexing

In this case we will perform wavelength averaging (that way we again do not have to assume the spatial randomness of the encoding and decoding masks), thus Eq. (2) becomes:

$$U_R(\nu_x) = \int \int U(\nu'_x) \text{rect}(\nu'_x / (\Delta\nu_x)) \left[\int G(\nu'_x - \nu''_x, p(\lambda, t), \lambda, t) G^*(-\nu_x + \nu'_x, p(\lambda, t), \lambda, t) d\lambda \right] d\nu''_x d\nu'_x \quad (12)$$

since

$$\int G(\nu'_x - \nu''_x, p(\lambda, t), \lambda, t) G^*(-\nu_x + \nu'_x, p(\lambda, t), \lambda, t) d\lambda \approx \delta(\nu_x - \nu''_x) \quad (13)$$

and we obtain that the final expression for the reconstructed spectrum equals to:

$$U_R(\nu_x) = \left[\int \text{rect}(\nu'_x / (\Delta\nu_x)) d\nu'_x \right] \int U(\nu''_x) \delta(\nu_x - \nu''_x) d\nu''_x = \Delta\nu_x \cdot U(\nu_x) \quad (14)$$

Note that in this case the meaning of the encoding mask is that every spatial pixel of the input object is “painted” with different color. The decoding mask is identical to the encoding one and it is picking out, from the blurred image, the right color in every high resolution spatial location.

2.5. Gray Level Multiplexing

Instead of using the previously discussed domains for the coding of the spatial degrees of freedom, one may use the gray level or the dynamic range domain as well. We assume that we have the a priori information that the dynamic range of the input object is limited. Once again we will attach a gray level coding mask to the input object. Thus, prior to the blurring due to the low resolution imaging, to each pixel of the input we attach a different transmission value while the ratio between every one of those values is 2^M where M is the a priori known and limited number of bits that are spanning the dynamic range of the imaged object. Obviously, the imager should have sufficient number of bits representing its dynamic range. It should be at least $M \times K^2$ where K is the SR factor in every spatial dimension.

To clarify this concept, the schematic description of the gray level coding mask appears in Fig. 3(a). In this figure the resolution improvement is by a factor of two in every axis thus the dynamic range of the detector should have four times more bits than the number of bits in the original object. Thus, if the sensor has a dynamic range of 12 bits, the imaged object should not have more than 3 bits of gray level ($= 12/4$). This coding causes a spatial blurring. However, since every high resolution spatial feature is attached to a different region in the dynamic range axis, it may later on be recovered. This is because we have the a priori knowledge of the encoding/decoding conversion map that converts between every high resolution spatial pixel and its corresponding region of bits along the dynamic range axis. Specifically referring again to the schematic sketch of Fig. 3(a), since the ratio between two adjacent pixels of the gray level coding mask is 2, the original object should have only one bit of dynamic range (i.e., a binary object).

In Figs. 3(b) and 3(c), we simulated this approach by taking an input LENA image containing 3 bits of gray level and coded it with gray level mask similar to the one presented by Fig. 3(a) (except that since the original object has 3 bits, the values of the coding mask should be 1, 8, 64, 512). We assumed that the dynamic range of the sensor has 12 bits (maximal value of 4096). In Fig. 3(b), we presented the low resolution and the dynamic range limited image. In Fig. 3(c), we

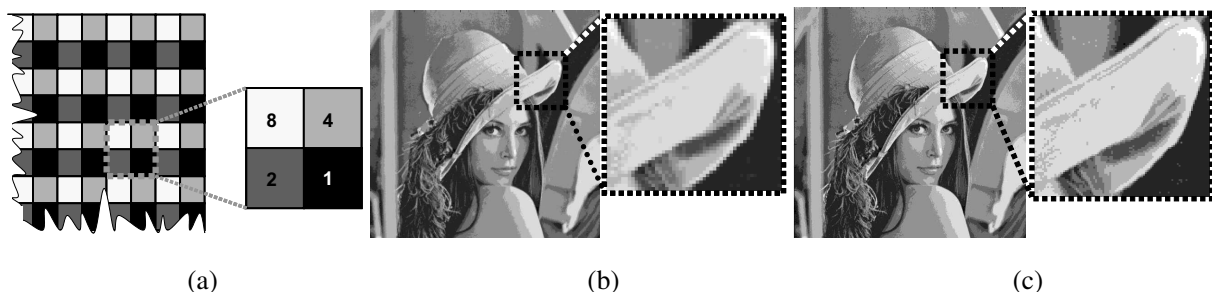


Figure 3: (a) Schematic sketch of gray level coding mask for binary objects. (b) Low resolution LENA image containing 3 bits of dynamic range. (c) Super resolved reconstruction using gray level multiplexing.

presented the reconstruction. One may see that indeed resolution improvement of close to a factor of two is obtained in every axis.

3. DESCRIPTION IN THE PHASE SPACE DOMAIN

Here we will try to describe the various SR principles that were previously discussed, while using the Wigner transformation which has the advantages of relating between its distribution and the spatial degrees of freedom.

In Fig. 4, we schematically present the various steps of the time and polarization (which is time varying) SR approaches where the spatial conversion of degrees of freedom is done to time or to polarization domains. In our schematic representations we deal with the case in which the spectral bandwidth of the signal is three times larger than the bandwidth that may be transmitted through the aperture of the imaging lens. The maximal bandwidth that may fit the aperture of the lens is denoted by $\Delta\nu$ where ν and x designate the spectral and the spatial domains/coordinates respectively. In Fig. 4(a), we present the phase space diagram of a randomly varied distribution having high spatial resolution. This chart presents the time varying random encoding mask that we will use. Every different spatial value is designated with different color. Since we are talking about time (or time varied polarization) multiplexing, this spatial distribution is varied with time. Thus, in Fig. 4(a), the order of the different colors is changed versus time. This designates that the spatial distribution of the encoding mask is time varying. The small spatial pixels of the chart occupy a size of $3\Delta\nu$ in the spectral axis because in the space domain the mask has pixels which are three times smaller than the imaging resolution. To simplify our explanation, if we denote by δx the spatial resolution that corresponds to spectral bandwidth of $\Delta\nu$ ($= 1/\delta x$), then in the case that we have three times finer resolution of $\delta x/3$ the spectral bandwidth will be three times larger, i.e., $3\Delta\nu$, because the product between the spatial resolution and the spectral bandwidth equals to one.

In Fig. 4(b), we present the phase space diagram of our signal which also has a bandwidth of $3\Delta\nu$ (three times larger than the bandwidth that may be transmitted through the aperture of the imaging lens). In Fig. 4(c), we present the schematic sketch of the phase space diagram of the product between the random coding mask and the signal. The phase space distribution of the signal does not vary with time but the encoding mask does. The bandwidth of the product equals to $6\Delta\nu$ since a well known Fourier relation dictates that the product in the space domain will be a convolution in the spectrum domain. A convolution between two spectral functions having spectral width of $3\Delta\nu$ yields a result with width of about $6\Delta\nu$.

In Fig. 4(d), we show what happens when the high resolution (and time varying) product distribution is passed through a size limited aperture. There is a spatial blurring which reduces the spatial resolution (the thin rectangles became three times wider in the spatial axis and three times narrower in the spectral axis) and thus the various colors that designated different gray levels of the spatial pixels are mixed together (which reduces their dimension in the spectral axis ν). Note that the area of each rectangle denotes a single degree of freedom and this area remains constant: increasing its length in the space domain reduces its width in the spectral axis.

The decoding process is described by Fig. 4(e) and it includes multiplication of the captured information by the same high resolution and time varying decoding spatial mask distribution and then performing time averaging. The time averaging that is performed after the multiplication will extract from every high resolution spatial degree of freedom (that occupies spatial size of $3\Delta\nu$) the original value while averaging to zero the non desired information that was added to it due to the spatial blurring. Note that the dashed line appearing in Fig. 4 represents a continuation of pixel values along the x axis of which we show three at the start and three at the end.

In Fig. 5, we present the schematic sketch of the phase space diagram in the case of wavelength or dynamic range encoding. In Fig. 5(a), we present the schematic sketch of the encoding process. There, once again the object contains small spatial features that occupy three times more than the bandwidth that the lens can transmit. Each of the spatial pixels is “painted” with a different wavelength or is associated with different regions along the dynamic range axis. In Fig. 5(b), we show how the spatial low pass filter affects the phase space diagram of Fig. 5(a). The spatial information is blurred and thus the spatial degrees of freedom become three times wider in the space axis x but also three times narrower in the spatial frequency domain ν_x . In Fig. 5(c), we present the schematic effect of the decoding. There, each one of the spatial degrees of freedom is multiplied by proper spatially high resolution distribution which corresponds to the spatial distribution that is used to encode the information as in Fig. 5(a). The decoding is designated by thin and long

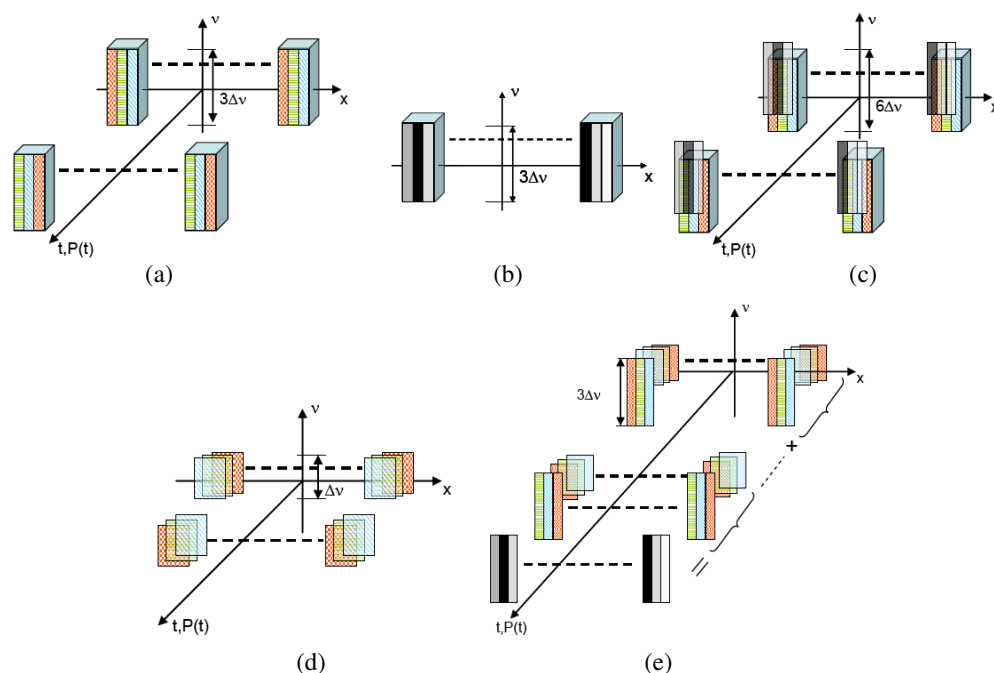


Figure 4: Schematic description of the adaptation of degrees of freedom in the phase space plane for time and polarization multiplexing. Distribution of: (a) The encoding mask. (b) The high resolution signal. (c) The product between the signal and the encoding mask. (d) Blurring due to reduced resolution of the imaging system. (e) Decoding procedure.

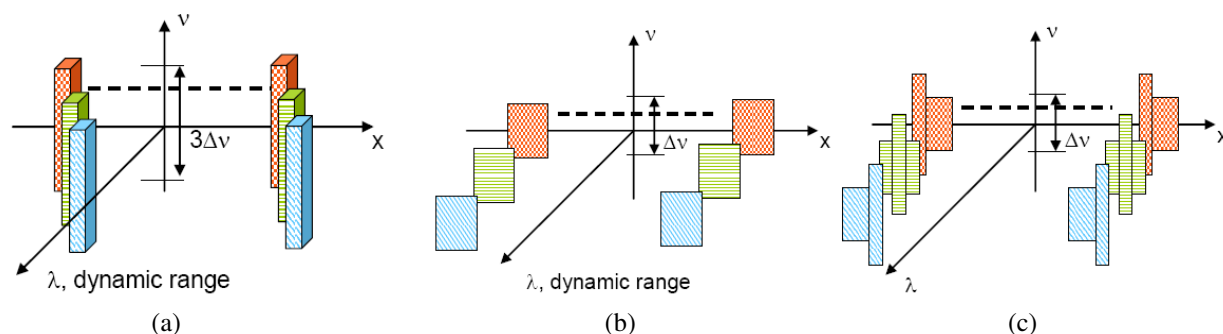


Figure 5: Schematic description of the adaptation of degrees of freedom in the phase space plane for wavelength and dynamic range multiplexing. (a) Encoding. (b) Blurring. (c) Decoding for wavelength multiplexing.

rectangles having spectral dimensions of $3\Delta\nu$ and which correspond to the highest spatial resolution that we aim to image. Those rectangles select out (or filter out) of the spatially blurred information (that is designated with short and wide rectangles having spectral width of $\Delta\nu$) the relevant gray level information of each high resolution pixel (having dimension of $\delta x/3$).

In Fig. 6, we present the schematic explanation for the case of field of view multiplexing SR and how it is seen in the phase space diagram space. In Figs. 6(a) and 6(b), one may see the phase space diagram of an object occupying the field of view of Δx and having spectral bandwidth of $3\Delta\nu$. If one divides the high spatial resolution over a three times larger field of view (i.e., reduces the spatial resolution by a factor of three by spreading it along the field of view), one obtains $3\Delta x$ for the spatial region and three times smaller spectral bandwidth of only $\Delta\nu$. In this figure every one out of the three spatial regions is reduced by three times in its resolution. A similar effect is obtained in the case of optical magnification or zooming.

Another type of field of view multiplexing approach can be the technique in which every one out of the three spectral slots (each one of the three slots has the bandwidth of $\Delta\nu$) is multiplexed by being shifted to different spatial positions, transmitted through the resolution limiting imager and later on demultiplexed back to compose the high resolution image. This multiplex-

ing/demultiplexing may be realized using proper gratings. The grating can redirect or reposition the different spectral slots (the modulation and the demodulation operations). This operation is described in Figs. 6(c) and 6(d). Here the various spectral slots are not changed in their shape as before (reduced in the spectral domain and expanded in the space domain) but rather only repositioned along the spatial axis. The optical realization of the relevant setup includes using gratings to perform the relocation of the spectral slots while sacrificing the field of view [9]. In many cases where the object is a 1D object, one may use the second spatial axis in order to improve the imaging resolution [11, 12]. Then, the schematic sketch of the phase space distribution is very similar to the one presented in Fig. 5 after renaming the axis which is denoted there as λ (e.g., in Fig. 5(a)) by the spectral axis ν corresponding to the second spatial dimension (y instead of x).

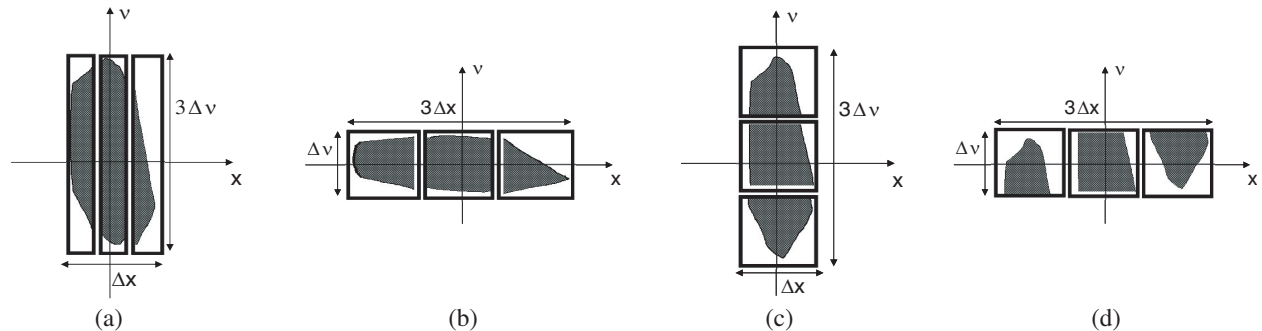


Figure 6: Schematic description of field of view multiplexing. (a), (b) Spatial separation of information by reducing its spectral resolution. (c), (d) Each spectral bandwidth is multiplexed to a different spatial position.

REFERENCES

1. Zalevsky, Z. and D. Mendlovic, *Optical Super Resolution*, Springer, 2002.
2. Freeman, W. T., T. R. Jones, and E. C. Pasztor, "Example-based super-resolution," *IEEE Computer Graphics and Applications*, Vol. 22, 56–65, 2002.
3. Abbe, E., "Beitrage zur theorie des mikroskops und der mikroskopischen wahrnehmung," *Arch. Mikrosk. Anat.*, Vol. 9, 413–468, 1873.
4. Lukosz, W., "Optical systems with resolving powers exceeding the classical limits." *J. Opt. Soc. Am.*, Vol. 56, 1463–1472, 1967.
5. Kartashev, A. I., "Optical systems with enhanced resolving power," *Opt. Spectrosc.*, Vol. 9, 204–206, 1960.
6. Lohmann A. W. and D. Paris, "Superresolution for nonbirefringent objects," *J. Opt. Soc. Am.*, Vol. 3, 1037–43, 1964.
7. Solomon, J., Z. Zalevsky, and D. Mendlovic, "Super resolution using code division multiplexing," *Appl. Opt.*, Vol. 42, 1451–1462, 2003.
8. Zalevsky, Z., P. García-Martínez, and J. García, "Superresolution using gray level coding," *Opt. Exp.*, Vol. 14, 5178–5182, 2006.
9. Zalevsky, Z., D. Mendlovic, and A. W. Lohmann, "Super resolution optical systems using fixed gratings," *Opt. Commun.*, Vol. 163, 79–85, 1999.
10. Zalevsky, Z., V. Eckhouse, N. Konforti, A. Shemer, D. Mendlovic, and J. Garcia, "Super resolving optical system based on spectral dilation," *Opt. Commun.*, Vol. 241, 43–50, 2004.
11. Grim, M. A. and A. W. Lohmann, "Super resolution image for 1-D objects," *J. Opt. Soc. Am.*, Vol. 56, 1151–1156, 1966.
12. Zlotnik, A., Z. Zalevsky, and E. Marom, "Optical Encryption using synthesized mutual intensity function," *Appl. Opt.*, Vol. 43, 3455–3465, 2004.

Tomographic Reconstruction of the Wigner Distribution of Non-separable Beams

A. Cámara¹, T. Alieva¹, J. A. Rodrigo², and M. L. Calvo¹

¹Facultad de Ciencias Físicas, Universidad Complutense de Madrid
Avda. Complutense, s/n, Madrid E-28040, Spain

²Instituto de Óptica (CSIC), Imaging and Vision Department
Serrano 121, Madrid E-28006, Spain

Abstract—The numerical demonstration of the phase-space tomographic reconstruction method of non-separable beams is presented in this contribution. The Wigner distribution of a Laguerre-Gaussian beam is recovered from numerically simulated intensity measurements. In order to compare the results with the theoretical Wigner distribution, a novel diagram for the representation of functions of four variables is introduced.

The determination of the phase of coherent beams or the mutual intensity of partially coherent beams is of great importance in many applications which require light characterization. Different interferometric and iterative methods have been developed to obtain this information, though they present difficulties that make them unsuitable for a fast and precise determination of the mutual intensity of optical beams.

In 1994, a new method for the reconstruction of the Wigner distribution (WD) of a coherent or partially coherent beam from its projections was established [1]. From the WD of a beam, the phase or the mutual intensity can be retrieved. The only measurements needed to reconstruct the WD are the intensity distributions at the output of a fractional Fourier transform (FRFT) system. These intensity distributions are often called fractional power spectra. The development of the method has been delayed due to the lack of suitable optical systems to perform the FRFT of variable order.

Recently we have demonstrated the tomographic reconstruction of the WD for the case of separable beams [2] using the setup performing the antisymmetric FRFT ($\gamma_x = -\gamma_y = \alpha$).

In this contribution we extend the former work to beams which cannot be factorized in both orthogonal transversal coordinates (non-separable beams). We consider the problem in the monochromatic paraxial approximation of the scalar diffraction theory. We demonstrate numerically the feasibility of the method in the case of a Laguerre-Gaussian (LG) mode.

For the experimental implementation of the method it is used the optical system suitable for the measurement of the fractional power spectra without additional scales for any pair of transformation angles (γ_x, γ_y) , where $\gamma_{x,y} \in [\pi/2, 3\pi/2]$, recently reported in Ref. [3]. This optical system is constructed by two generalized lenses implemented by spatial light modulators (SLMs) placed at a fixed distance. The application of the SLMs allow almost real-time performance in the fractional power spectra measurement.

Let us briefly introduce the principles of the phase-space tomography method. The WD of a signal described by its mutual intensity,

$$\Gamma(\mathbf{r}_1, \mathbf{r}_2) = \langle f(\mathbf{r}_1) f^*(\mathbf{r}_2) \rangle, \quad (1)$$

is defined as

$$W_\Gamma(\mathbf{r}, \mathbf{p}) = \iint_{\mathbb{R}^2} d\mathbf{r}' \Gamma\left(\mathbf{r} + \frac{1}{2}\mathbf{r}', \mathbf{r} - \frac{1}{2}\mathbf{r}'\right) \exp(-i2\pi\mathbf{p} \cdot \mathbf{r}'), \quad (2)$$

where $\mathbf{r} = [x, y]^t$ is the position vector, $\mathbf{p} = [p_x, p_y]^t$ is the momentum vector, and $f(\mathbf{r})$ the complex amplitude of the field. Besides, the transformation law for the FRFT applied to $\Gamma(\mathbf{r})$ is

$$\Gamma^{\gamma_x, \gamma_y}(\mathbf{r}_1, \mathbf{r}_2) = \iiint_{\mathbb{R}^4} d\hat{\mathbf{r}}_1 d\hat{\mathbf{r}}_2 \Gamma(\hat{\mathbf{r}}_1, \hat{\mathbf{r}}_2) K^{\gamma_x, \gamma_y}(\hat{\mathbf{r}}_1, \mathbf{r}_1) [K^{\gamma_x, \gamma_y}(\hat{\mathbf{r}}_2, \mathbf{r}_2)]^*, \quad (3)$$

being $K^{\gamma_x, \gamma_y}(\hat{\mathbf{r}}, \mathbf{r}) = K^{\gamma_x}(\hat{x}, x) K^{\gamma_y}(\hat{y}, y)$ the kernel of the transformation:

$$K^{\gamma_q}(\hat{q}, q) = (is \sin \gamma_q)^{-\frac{1}{2}} \exp\left\{ \frac{i\pi}{s \sin \gamma_q} [(\hat{q}^2 + q^2) \cos \gamma_q - 2\hat{q}q] \right\}, \quad (4)$$

q a placeholder for x and y , and s the experimental parameter of the optical system performing the FRFT.

The phase-space tomography method proposed in Ref. [1] is based on two facts. On the one hand, the application of a FRFT system to the signal rotates its WD, i.e., the WD of the signal at the output of a FRFT optical system is rotated respect to the WD of the original signal:

$$W_{\Gamma^{\gamma_x, \gamma_y}}(\mathbf{r}, \mathbf{p}) = W_{\Gamma}(\mathbf{r}', \mathbf{p}'), \tag{5}$$

where

$$\begin{bmatrix} q' \\ p'_q \end{bmatrix} = \begin{bmatrix} \cos \gamma_q & \sin \gamma_q \\ -\sin \gamma_q & \cos \gamma_q \end{bmatrix} \begin{bmatrix} q \\ p_q \end{bmatrix}. \tag{6}$$

On the other hand, each fractional power spectrum for angles (γ_x, γ_y) ,

$$S^{\gamma_x, \gamma_y}(\mathbf{r}) = \Gamma^{\gamma_x, \gamma_y}(\mathbf{r}, \mathbf{r}), \tag{7}$$

can be identified with the WD projection along a plane whose normal follow the direction

$$\mathbf{n} = (x_n, y_n, u_n, v_n) = (\sin \gamma_x, \sin \gamma_y, \cos \gamma_x, \cos \gamma_y) \tag{8}$$

in the phase-space. A 1D analogue is displayed in Fig. 1, where the WD is represented in a color contour plot in greyscale. The set of projections for different values of the FRFT angles is called Radon-Wigner transform of the WD.

The method to obtain the WD consists in two steps:

1. Registration of the intensity distribution at the output of a FRFT optical system for different angles
2. Application of the double inverse Radon transform to the previously recorded projections to obtain the WD directly.

Though the reconstruction is straightforward theoretically, some complications make it difficult in the practice. For instance, if we numerically discretize the WD in a $N \times N \times N \times N$ array and use 8 bytes to store its value in each point, then we would need around 32 GB just to store it when $N = 256$. This goes worse if we take into account that we need to operate with that data in order to obtain the mutual intensity or any other derived information. The result cannot be dumped into the random access memory (RAM) of a conventional computer when $N > 64$.

Another problem is the representation of the WD, as it is a real-valued function that depends on four variables. In the separable case, the WD inherited the separability, becoming a function of two variables. In such case it can be represented in a contour map. In the present situation however this solution is useless.

The storage problem can be addressed twofold. One solution can be the reconstruction of WD with small discretization ($N \leq 64$). This will allow the use of conventional computers to store the WD in the RAM and to operate with it. The drawback of this approach is that it will reconstruct low resolution WDs. Another course of action would be to use a different storing device such as

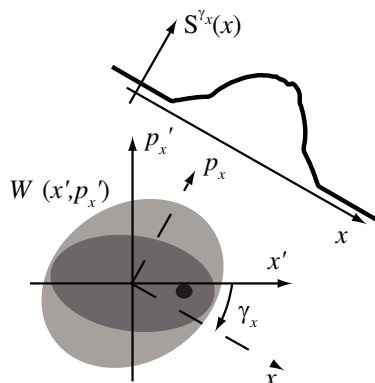


Figure 1: Illustration of the relation between the WD projections and the fractional power spectra for 1D signals. The WD is represented in the grayscale contour plot.

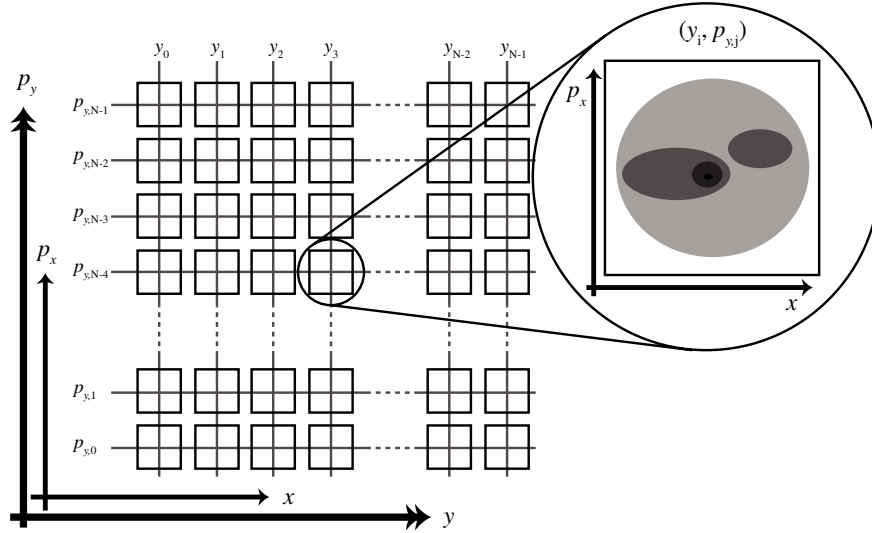


Figure 2: Illustration of the representation method for real-valued functions that depend on four variables. In the figure, the represented function is $W(x, y, p_x, p_y)$.

the hard drive. This will yield the reconstruction of the WD with potentially any number of points (N). In exchange for this capacity, the reconstruction algorithm become really slow, making the real-time reconstruction impracticable.

To engage the representation problem, we propose a novel diagram in which the WD in a region of interest of the phase-space can be displayed. The representation method is illustrated in Fig. 2. It consists on a 2D array of contour plots, each of them being the contour plot of the WD for a fixed value of two variables. For example, one can assign the pair (y, p_y) to the position of the contour in the array and the pair (x, p_x) to the contour plot variables.

The demonstration of the method consists in the numerical simulation of the fractional power spectra that would be registered by a CCD camera in an experimental situation. From the simultaed projections we obtain what we will refer as the simulated WD. The comparison of the simulated WD with the theoretical WD conforms the feasibility test for the method.

The selection of the LG modes is based in two reasons: they are non-separable beams and there exists a theoretical expression for its WD. In particular we have chosen the LG mode whose (p, l) indices are $(2, 3)$. The complex amplitude of a LG mode is

$$\text{LG}_p^{\pm l}(\mathbf{r}, w) = \frac{1}{w} \sqrt{\frac{p!}{(p+l)!}} \left[\sqrt{2\pi} \left(\frac{x}{w} \pm i \frac{y}{w} \right) \right]^l L_p^l \left(2\pi \frac{\mathbf{r}^2}{w} \right) \exp \left(-\pi \frac{\mathbf{r}^2}{w} \right), \quad (9)$$

where w is the beam waist and $L_p^l(t)$ is the Laguerre polynomial of radial index p and azimuthal index l . Furthermore, the expression for its WD is known [4]

$$\begin{aligned} W_{\text{LG}_p^{\pm l}}(\mathbf{r}, \mathbf{p}) &= (-1)^{2p+l} 4 \exp \left\{ -2\pi \left[\frac{x^2 + y^2}{w^2} + w^2 (p_x^2 + p_y^2) \right] \right\} \\ &\quad \times L_{p+l} \left[2\pi \left(\frac{x^2 + y^2}{w^2} + w^2 (p_x^2 + p_y^2) + 2xp_y - 2yp_x \right) \right] \\ &\quad \times L_{p-l} \left[2\pi \left(\frac{x^2 + y^2}{w^2} + w^2 (p_x^2 + p_y^2) - 2xp_y + 2yp_x \right) \right]. \end{aligned} \quad (10)$$

For the demonstration of the applicability of the reconstruction method, we numerically simulate the acquisition of the fractional power spectra process. Then, we apply the reconstruction algorithm and consider the result as our simulated WD. To check the validity of the method we compare the simulated WD with the one obtained using the theoretical expression [Eq. (10)] in a diagram similar to the one explained above [see Figs. 3(b) and 3(b)].

All the tests have been performed using the LG_2^3 mode with $w = \sqrt{s} = 0.73$ mm. In the first place, we simulated the registration of the fractional power spectra by a CCD camera with squared

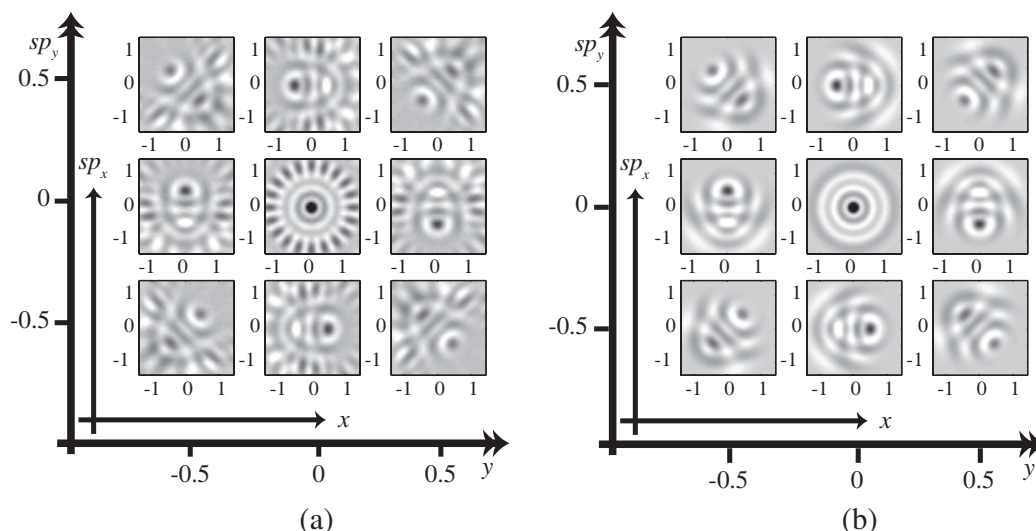


Figure 3: Simulated (a) and theoretical (b) WD for a LG_2^3 mode with $w = 0.73$ mm and $N = 64$ points of discretization. For the simulation we used 100 projections to reconstruct the WD.

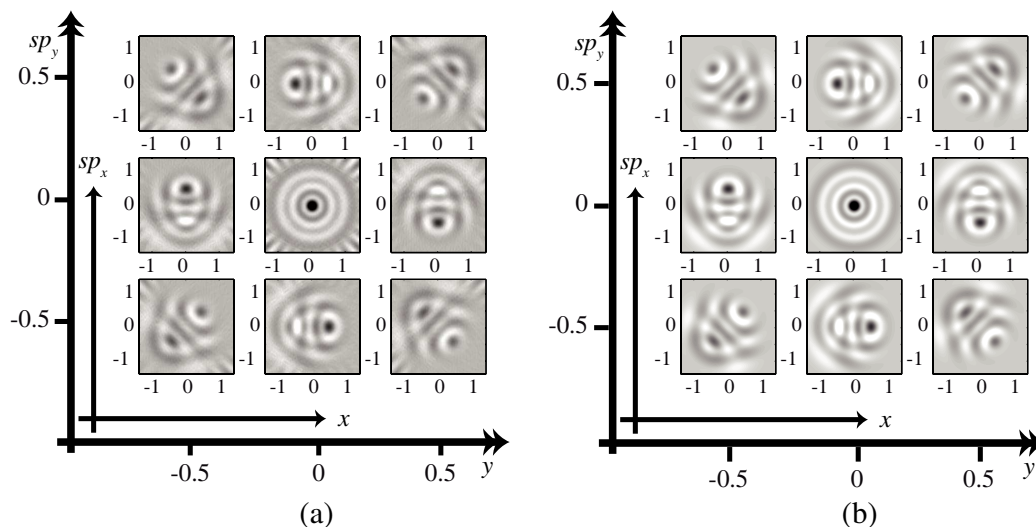


Figure 4: Simulated (a) and theoretical (b) WD for a LG_2^3 mode with $w = 0.73$ mm and $N = 256$ points of discretization. For the simulation we used 400 projections to reconstruct the WD.

chip, being $N = 64$ the number of pixels in each side. 100 projections sweeping both angles in the π -interval with 10 steps each have been used. The results are compared with the theoretical expressions in Fig. 3.

In spite the WD reconstruction from the reduced number of pixels demonstrates a good agreement with the theory, qualitatively better results are obtained increasing the number of points of the simulated fractional power spectra and the number of projections. The results obtained for $N = 256$ discretization points and 400 projections are displayed in Fig. 4.

The further research will be focused on the extraction of information about the beam mutual intensity around a certain point or along a line.

ACKNOWLEDGMENT

The financial support of the Spanish Ministry of Science and Innovation under project TEC2008-04105 is acknowledged.

REFERENCES

1. Raymer, M. G., M. Beck, and D. F. McAlister, "Complex wave-field reconstruction using phase-space tomography," *Phys. Rev. Lett.*, Vol. 72, 1137–1140, 1994.

2. Cámara, A., T. Alieva, J. A. Rodrigo, and M. L. Calvo, “Phase space tomography reconstruction of the Wigner distribution for optical beams separable in Cartesian coordinates,” *J. Opt. Soc. Am. A*, Vol. 26, 1301–1306, 2009.
3. Rodrigo, J. A., T. Alieva, and M. L. Calvo, “Programmable two-dimensional optical fractional Fourier processor,” *Opt. Express*, Vol. 17, 4976–4983, 2009.
4. Simon, S. and Argawal, G. S., “Wigner representation of Laguerre-Gaussian beams,” *Opt. Lett.*, Vol. 25, 1313–1315, 2000.

Tunable Phase Masks for Extended Depth of Field

Jorge Ojeda-Castañeda, Myrna M. Rodríguez, and Rafael Naranjo
 University of Guanajuato, Salamanca, Guanajuato 36885, México

Abstract— We apply the ambiguity function of the generalized pupil function for analyzing the impact of focus error on the Modulation Transfer Function. We show that by using a suitable pair of phase-only masks, it is possible to control the depth of field, without modifying either the resolution or the light gathering power of an optical system.

1. INTRODUCTION

The impact of focus errors on Modulation Transfer Function (MTF) limits the longitudinal range, in object space, for acquiring high quality pictures. The acceptable longitudinal range is denoted as the depth of field.

One can reduce the influence of focus error, and hence one can increase the depth of field, by reducing the pupil aperture of an optical system. However, by reducing the pupil aperture, one also reduces the resolution and the light gathering power of the optical system.

It is known that by using suitable masks, at the pupil aperture, one can reduce the influence of focus errors, and indeed of other wavefront aberrations [1–4].

In Reference [5], we emphasized on the use of pupil masks for reducing the influence of focus errors on the MTF. Since one simultaneously records the images of planar scenes located at different depths of the object field, with these masks we ensure that each recorded image will suffer from virtually the same amount of contrast reduction. Hence, later on, by digital processing, the image contrast can be simultaneously corrected for all the recorded images.

It has been shown that the ambiguity function, of the pupil mask, is a powerful tool for analyzing the MTF of an optical system suffering from focus errors [6, 7]. Furthermore, the ambiguity function formalism helps to link the use of a phase-conjugated pair of lenses [8, 9], with the use of a single phase mask [10–13], for extending the depth of field [14].

Here, our aim is the following. We show that by using a suitable pair of phase-only masks, it is possible to control the depth of field, without closing the pupil aperture. Hence, one can control the depth of field without reducing either the resolution or the light gathering power of an optical system.

In Section 2, we discuss the basic theory of our proposal. In Section 3, we unveil a phase-only mask that is useful for increasing or decreasing the depth of field, while preserving resolution and light gathering power.

2. BASIC THEORY

For the sake of clarity, our following discussion is 1-D. The optical system is represented by a generalized pupil function, whose complex amplitude transmittance is

$$P(\mu; W_{2,0}) = \exp \left[i2\pi \left(\frac{W_{2,0}}{\lambda} \right) \left(\frac{\mu}{\Omega} \right)^2 \right] Q(\mu) \text{rect} \left(\frac{\mu}{2\Omega} \right) \quad (1)$$

In Eq. (1) we denote as $W_{2,0}$ the wavefront focus error coefficient; λ is the wavelength of the radiation; $Q(\mu)$ is the complex amplitude transmittance of the phase mask; and the rectangular function represents the pupil aperture. The Optical Transfer Function, associated to Eq. (1), is

$$H(\mu; W_{2,0}) = N \int_{-\infty}^{\infty} P \left(\nu + \frac{\mu}{2}; W_{2,0} \right) P^* \left(\nu - \frac{\mu}{2}; W_{2,0} \right) d\nu. \quad (2)$$

In Eq. (2) we denote as N a suitable normalization factor. By substituting Eq. (1) in Eq. (2) we obtain

$$H(\mu; W_{2,0}) = N \int_{-(2\Omega-\mu)/2}^{(2\Omega-\mu)/2} Q \left(\nu + \frac{\mu}{2} \right) Q^* \left(\nu - \frac{\mu}{2} \right) \exp [i2\pi (2\mu W_{2,0}/\lambda\Omega^2) \nu] d\nu. \quad (3)$$

Now, it is convenient to note that the ambiguity function of the phase-only mask (inside the pupil aperture) is

$$A(\mu; y) = N \int_{-(2\Omega-\mu)/2}^{(2\Omega-\mu)/2} Q\left(\nu + \frac{\mu}{2}\right) Q^*\left(\nu - \frac{\mu}{2}\right) \exp[i2\pi y\nu] d\nu. \quad (4)$$

And consequently, from Eqs. (3) and (4) we have that along the line $y = (\frac{2W_{2,0}}{\lambda\Omega^2})u$, the ambiguity function of the phase-mask contains the OTF. Therefore, for reducing the impact of focus error (or if you will for extending the depth of field) it is convenient to identify ambiguity functions with rotational symmetry, which is also denoted as the “bow-tie” effect [15].

3. TUNABLE PHASE-MASKS

Here, we propose to use a pair of phase elements for implementing the following phase-only mask

$$Q(\mu; \sigma) = \exp\left\{-i2\pi a \cos\left(\frac{\pi(\mu + \frac{\sigma}{2})}{2\Omega}\right) + i2\pi a \cos\left(\frac{\pi(\mu - \frac{\sigma}{2})}{2\Omega}\right)\right\}. \quad (5)$$

In Eq. (5) we denote as a the maximum value of the optical path difference, which is generated by each element of the pair; and we denote as σ the lateral displacement (at the pupil aperture), which is introduced purposely between the elements of the pair. Of course, we can rewrite Eq. (5) as

$$Q(\mu; \sigma) = \exp\left\{i2\pi \left[2a \sin\left(\frac{\pi\sigma}{4\Omega}\right)\right] \sin\left(\frac{\pi\mu}{2\Omega}\right)\right\}. \quad (6)$$

It is apparent from Eq. (6) that by changing the lateral displacement σ , one can control the amount of optical path difference generated by the composed mask. At $\sigma = 0$, the two elements produce zero phase delay. And consequently, one has the lowest value of focal depth. However, for $\sigma \neq 0$, the two elements can increase the depth of field, as is discussed in References [15, 16]. Next, we include some numerical simulations.

In Figure 1, along the first line, we show the computer simulated images of a Siemens star, if the defocus coefficient $W_{2,0} = \lambda$. From left to right, the first image is noiseless; while the second image and the third image suffer from additive Gaussian noise, with zero average and with a variance equal to 0.001.

From left to right, along the first line, the first image and the second image were obtained with zero lateral displacement, $\sigma = 0$, between the elements of the pair. In the third image, the lateral displacement between the elements of the pair generates an optical phase difference of λ . It is apparent in the third image, along the first line, that the phase mask reduces the influence of focus error.

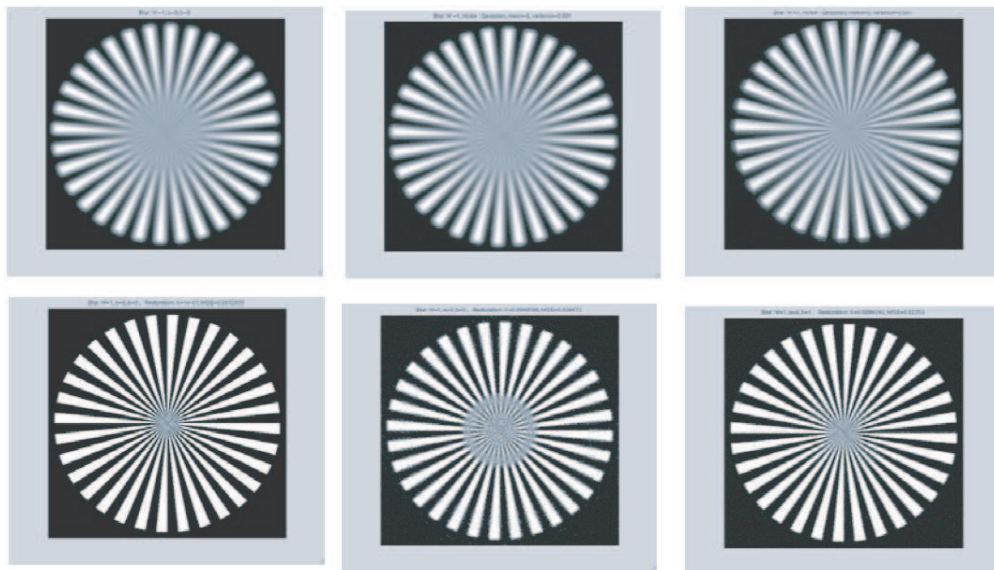


Figure 1: Computer simulated images of a Siemens star.

Furthermore, it is apparent from line two that after applying a digital restoration algorithm, the proposed phase mask is able to produce high quality images of the image suffering from both, focus error and the presence of additive Gaussian noise.

4. CONCLUSION

We use the ambiguity function of a phase-only mask for analyzing methods that reduce the influence of focus error in the MTF. We unveil the phase profile of a pair of elements that form a novel phase mask. By introducing a lateral displacement (between the elements of the pair) one can increase the optical path difference of the phase mask. And in this manner one can extend the depth of field, without reducing the pupil aperture.

REFERENCES

1. Welford, W. T., "Use of annular apertures to increase focal depth," *J. O. Opt. Soc. Am.*, Vol. 50, 749, 1960.
2. Mino, M. and Y. Okano, "Improvement in the OTF of a defocused optical system through the use of shade apertures," *Appl. Opt.*, Vol. 10, 2219, 1971.
3. Indebetouw, G. and H. X. Bai, "Imaging with fresnel zone pupil masks: Extended depth of field," *Appl. Opt.*, Vol. 23, 4299, 1984.
4. Ojeda-Castaneda, J., L. R. Berriel-Valdos, and E. Montes, "Spatial filter for increasing the depth of focus," *Opt. Lett.*, Vol. 10, 520–522, 1985.
5. Ojeda-Castaneda, J., R. Ramos, and A. Noyola-Isgleas, "High focal depth by apodization and digital restoration," *Appl. Opt.* Vol. 27, 2583–2586, 1988.
6. Brenner, K., A. Lohmann, and J. Ojeda-Castañeda, "The ambiguity function as a polar display of the OTF," *Opt. Commun.*, Vol. 44, 323–326, 1983.
7. Ojeda-Castañeda, J., L. R. Berriel-Valdos, and E. Montes, "Ambiguity function as a design tool for high focal depth," *Appl. Opt.*, Vol. 27, 790–795, 1988.
8. Alvarez, E. L. L. W., "Two-element variable-power spherical lens," U.S. patent 3305294, Dec. 3, 1964.
9. Lohmann, A. W., "Lente focale variabile," Italian patent 727848, Jun. 19, 1964.
10. Lohmann, A. W., "Improvements relating to lenses and to variable optical lens systems formed by such lenses," Patent Specification 998191, 1965.
11. Dowski, E. R. and T. W. Cathey, "Extended depth of field through wavefront coding," *Appl. Opt.*, Vol. 34, 1859–1865, 1995.
12. Castro, A. and J. Ojeda-Castañeda, "Asymmetric phase masks for extended depth of field," *Appl. Opt.*, Vol. 43, 3474–3479, 2004.
13. Saucedo, A. and J. Ojeda-Castaneda, "High focal depth with fractional power wavefronts," *Opt. Letters*, Vol. 29, 560–562, 2004.
14. Ojeda-Castañeda, J., J. E. A. Landgrave, and C. M. Gómez-Sarabia, "Conjugate phase-plate use in analysis of the frequency response of optical systems designed for extended depth of field," *Appl. Opt.*, Vol. 47, No. 22, E1–E7, 2008.
15. Castro, A., J. Ojeda-Castañeda, and A. W. Lohmann, "Bow-tie effect: Differential operator," *Appl. Opt.*, Vol. 45, No. 30, 7878–7884, 2006.
16. Ojeda-Castañeda, J., "Imaging devices: Phase space representations," *Phase Space Optics: Fundamentals and Applications*, Ch. 5, 165–191, M. Testorf, B. Hennelly, and J. Ojeda-Castaneda, Eds., McGraw-Hill, 2010.

Equivalent Circuit Models for Split-ring Resonator Arrays

P. Yasar-Orten^{1,2}, E. Ekmekci¹, and G. Turhan-Sayan¹

¹Department of Electrical and Electronics Engineering, Middle East Technical University, Ankara, Turkey

²ASELSAN Inc., Macunkoy, Ankara, Turkey

Abstract— In this study, a square-shaped single-ring SRR unit cell is modeled by using a suitable two-port resonant circuit representation that accounts for the conductor loss and dielectric loss effects as well. Capacitive and inductive coupling effects between adjacent SRR unit cells are also described by the two-port equivalent circuit approach. Finally, the resonance frequency of an infinitely long SRR array is estimated using its equivalent circuit model and compared to the value of the resonance frequency obtained by HFSS simulations for the same array topology.

1. INTRODUCTION

Split Ring Resonator (SRR) is a well known sub-wavelength metamaterial structure that exhibits negative values of permeability (μ) over a narrow frequency band around its resonance frequency. Theory and applications of single ring, double ring or multiple ring SRR cells with circular or square/rectangular geometry have been investigated in microwave and optical frequencies in a large number of publications [1–4]. Most of those studies have investigated the SRR behavior theoretically, experimentally or numerically by using full-wave electromagnetic solvers. Number of publications concentrated on the analysis of SRR structures using equivalent circuit models, however, has been relatively few [2, 5–8].

Describing SRR unit cells and SRR arrays by accurate circuit models offers an approximate yet practical alternative to the use of full-wave electromagnetic solvers based on numerical methods (such as the Ansoft's HFSS or CST Microwave Studio), which usually need very large computer memory space and quite long computer processing times. Sufficiently accurate equivalent lumped circuit models, on the other hand, can be effectively used to estimate the behavior of SRR structures in a simple, fast and computationally efficient manner. This approach would even make optimization approach feasible in the design of special SRR structures. Also, when an equivalent circuit model is available, it is much easier to establish explicit relationships between the physical properties (i.e., electrical parameters, dimensions, etc.) of the SRR structure and its frequency dependent transmission/reflection behavior.

2. DESIGN AND NUMERICAL SIMULATIONS FOR SRR ARRAYS

In this paper, transmission spectrum of the fully symmetrical four-split SRR unit cell shown in Figure 1(a) is simulated by HFSS over the frequency range from 30 GHz to 40 GHz by using PEC and PMC boundary conditions. Dimensions and electrical parameters of this SRR unit cell are as follows: Side length of SRR metal loop (L) is 2.8 mm, gap width (g) and metal strip width (w) are both 0.3 mm, substrate dimensions are $D_x = D_y = 4$ mm and the substrate thickness along z direction is $h = 0.5$ mm. Gold is assumed to be used for metal inclusions and a low loss dielectric material with relative permittivity $\epsilon_r = 4.6$ and dielectric loss tangent $\tan \alpha = 0.01$ is used as the substrate. The perfect electric conductor (PEC) type boundary conditions are applied at those surfaces of the computational volume which are perpendicular to the incident electric field vector. Similarly, perfect magnetic conductor (PMC) type boundary conditions are applied at those surfaces of the computational volume which are perpendicular to the incident magnetic field vector. The remaining surfaces are the input and output planes as shown in Figure 1(b). Due to the imaging effects of PEC and PMC boundaries, the computed transmission spectrum (i.e., magnitude of the S_{21} parameter computed as a function of frequency) represents a two dimensional infinite SRR array extending in the incident E -field and H -field directions with periodicities of $D_y = L + 2D_E$ and $D_z = h + 2D_H$, respectively. The periodicity parameters D_E and D_H are indicated in Figure 2.

Transmission spectrum of the SRR array is computed by HFSS for various periodicity parameters as shown in Figures 3 and 4. For the design parameters $D_E = 0.6$ mm and $D_H = 1.75$ mm, the SRR array resonates at $f_0 = 34$ GHz. As the array is chosen to be sparse in z -direction, coupling effects along this direction will be neglected and hence the resulting SRR array will be assumed to be a one dimensional infinite array extending in y -direction in the rest of the paper. This assumption

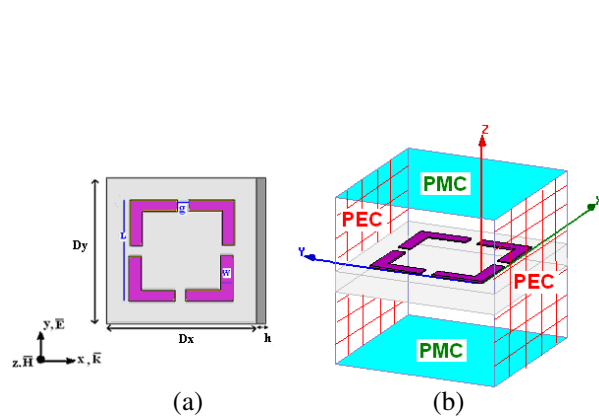


Figure 1: (a) Geometrical parameters of the SRR unit cell. (b) HFSS simulation setup and boundary conditions.

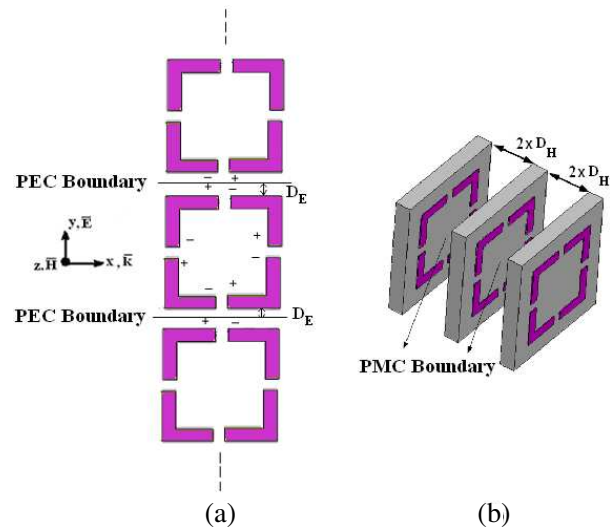


Figure 2: Two dimensional periodic SRR array implemented by the use of PEC and PMC boundary conditions in HFSS (a) Array in E field direction. (b) Array in H field direction.

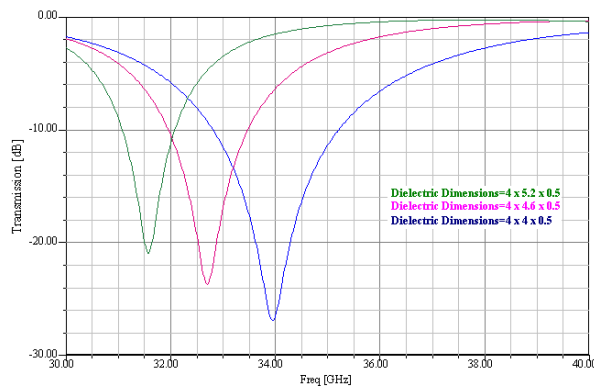


Figure 3: Variation of resonance frequency of the SRR array for the parameter of periodicity $D_E = 0.6$ mm (blue), 0.9 mm (red), 1.2 mm (green) in y -direction.

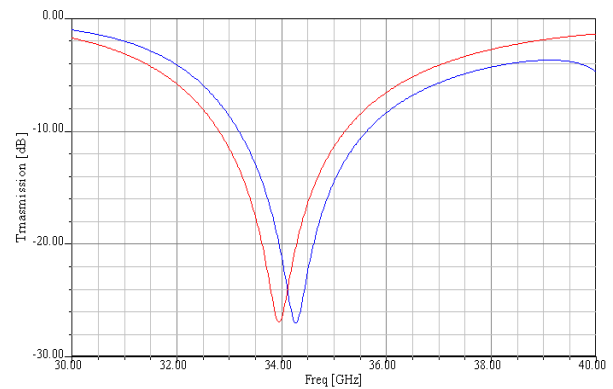


Figure 4: Variation of resonance frequency of the SRR array for the parameter of periodicity $D_H = 1.75$ mm (red), 3.5 mm (blue) in z -direction.

can be justified based on the results shown in Figure 4 where the resonance frequency changes by only 0.3 GHz (less than one percent) when D_H is doubled.

3. TWO-PORT EQUIVALENT CIRCUIT MODEL FOR SRR STRUCTURES

The two-port equivalent circuit representation suggested for this fully symmetrical SRR unit cell is shown in Figure 5 where L is the self-inductance of the metal loop, which can be computed by the expressions given in [9, 10]. The model parameter $C = C_{gap}/4$ is the equivalent capacitance computed for four individual gap capacitances connected in series. Each gap capacitance can be computed [6, 9] as $C_{gap} = C_{pp} + C_{cp}$ where C_{pp} and C_{cp} are parallel plate and coplanar capacitance contributions, respectively.

The equivalent loss resistances can be approximately computed using the expression $R = \frac{l}{\sigma S_{eff}}$ such that $l = 4(L - g)$ and $\sigma = \sigma_c$ will be used to compute R_c , while $l = 4g$ and $\sigma = \sigma_d$ are used in R_d computation. The effective current carrying cross-sectional area S_{eff} terms can be computed, in general, in terms of the geometrical parameters w , h , t and the skin depth δ .

Using the conversion formulas between Z -matrix and S -parameter matrix representations [11], the scattering parameter S_{21} of the two-port circuit representation shown in Figure 5 can be com-

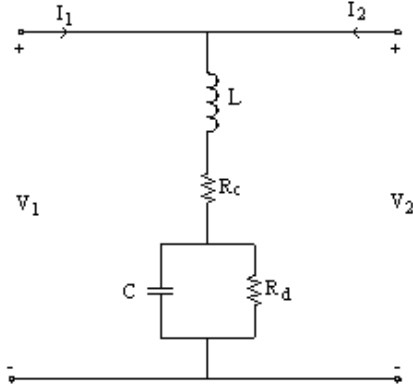


Figure 5: A feasible two-port equivalent circuit representation for the SRR unit cell including ohmic loss effects.

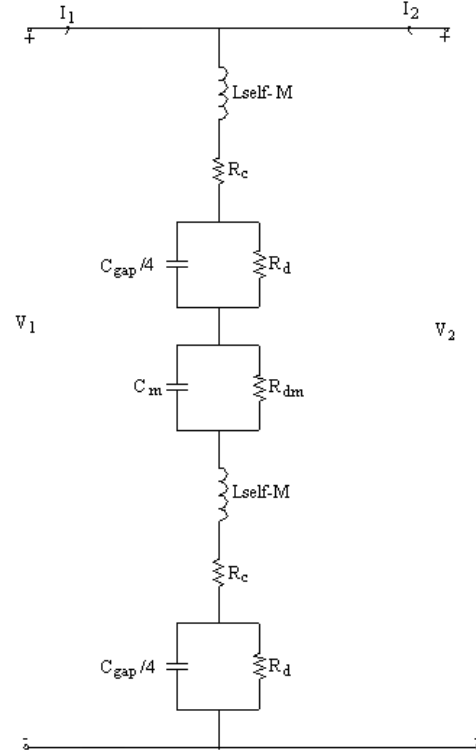


Figure 6: Equivalent two port circuit model for two SRR unit cells separated by $2D_E = 1.2 \text{ mm}$ along the y direction.

puted as

$$S_{21} = \frac{2Z}{2Z + Z_0} \quad (1)$$

where

$$Z = R_c + j2\omega L + \frac{R_d}{1 + j\omega C R_d} \quad (2)$$

is the impedance of the series RLC resonant circuit in the shunt branch of this two-port circuit and Z_0 is the terminal impedance which is given as an output by HFSS simulations.

The coupling effects between two SRR unit cells can also be described by a coupling two-port which consists of a parallel RC circuit in the shunt branch as shown in Figure 6. This coupling equivalent circuit is connected in series between two SRR blocks. The parameters C_m and R_{dm} can be computed by similar approaches used for the computation of the parameters C_{gap} and R_d mentioned above. The inductive coupling effect is taken into account by the effective inductance term $L = L_{self} - M$ for each SRR unit cell where M is the mutual inductance computed [9] between two SRR unit cells and it acts in a subtractive manner as the metal loops of both unit cells carry induced currents flowing in the same (clockwise or counterclockwise) direction. It should be noted that in an SRR array with n unit cells, each SRR unit cell (except those located at the ends) experiences subtractive inductive coupling stemming from both of its neighbors. Therefore, $L = L_{self} - 2M$ should be used in their equivalent circuit models.

When the equivalent impedances in the shunt branches of each SRR block and of each coupling circuit block are called Z and Z_m , respectively, the equivalent impedance in the shunt branch of the overall equivalent two-port circuit becomes

$$Z_{total} = nZ + (n - 1)Z_m \quad (3)$$

where

$$Z = \left(R_c + \frac{R_d}{1 + \omega^2 C^2 R_d^2} \right) + j \left(\omega(L_{self} - 2M) - \frac{\omega R_d^2 C}{1 + \omega^2 C^2 R_d^2} \right) \quad (4)$$

and

$$Z_m = \left(\frac{R_{dm}(1 - j\omega R_{dm}C_m)}{1 + \omega^2 C_m^2 R_{dm}^2} \right) \quad (5)$$

with n being the number of SRR unit cells in the array.

The resonance frequency of this array can be estimated by equating the imaginary part of Z_{total} to zero, namely by solving the following equation:

$$\text{Im}\{Z_{total}\} = 0 \quad (6)$$

Using the geometrical and physical parameters specified earlier, the resonance frequency of the infinite SRR array is estimated to be $f_0 = 35.6$ GHz from (6) by this equivalent circuit modeling approach. The resonance frequency obtained by HFSS simulations (see Figures 3 and 4) was 34 GHz. Namely, the suggested equivalent circuit model for the SRR array estimates the resonance frequency by less than 5 percent error.

4. CONCLUSIONS

In this study, an approximate equivalent two-port circuit modeling approach is suggested to describe the resonance behavior of SRR unit cells and SRR arrays. Results obtained by this approach are found in very good agreement with the results of HFSS simulations.

REFERENCES

1. Pendry, J. B., A. J. Holden, D. J. Robbins, and W. J. Stewart, "Magnetism from conductors and enhanced nonlinear phenomena," *IEEE Trans. Microwave Theory Tech.*, Vol. 47, No. 11, 2075–2084, 1999.
2. Marqués, R., F. Mesa, J. Martel, and F. Medina, "Comparative analysis of edge- and broadside-coupled split ring resonators for metamaterial design-theory and experiments," *IEEE Trans. Antennas Propag.*, Vol. 51, No. 10, 2572–2581, 2003.
3. Sauviac, B., C. R. Simovski, and S. A. Tretyakov, "Double split-ring resonators: Analytical modeling and numerical simulations," *Electromagnetics*, Vol. 24, 317–338, 2004.
4. Sydoruk, O., E. Tatartschuk, E. Shamonina, and L. Solymar, "Analytical formulation for the resonant frequency of split rings," *Journal of Applied Physics*, Vol. 105, 014903, 2009.
5. Bilotti, F., A. Toscano, L. Vegni, K. Aydin, K. B. Alici, and E. Ozbay, "Equivalent-circuit models for the design of metamaterials based on artificial magnetic inclusions," *IEEE Trans. Microwave Theory Tech.*, Vol. 55, No. 12, December 2007.
6. Chen, H., L. Ran, J. Huangfu, T. M. Grzegorzczuk, and J. Kong, "Equivalent circuit model for left-handed metamaterials," *Journal of Applied Physics*, Vol. 100, 024915, 2006.
7. Wu, M.-F., F.-Y. Meng, Q. Wu, J. Wu, and L.-W. Li, "SRRs' artificial magnetic metamaterials modeling using transmission line theory," *PIERS Online*, Vol. 1, No. 5, 630–633, 2005.
8. Ekmekci, E. and G. Turhan-Sayan, "Comparative investigation of resonance characteristics and electrical size of the double-sided SRR, BC-SRR and conventional SRR type metamaterials for varying substrate parameters," *Progress In Electromagnetics Research B*, Vol. 12, 35–62, 2009.
9. Johnson, N. P., A. Z. Khokhar, H. M. H. Chong, R. M. de La Rue, and S. McMeekin, "Characterisation at infrared wavelengths of metamaterials formed by thin-film metallic split-ring resonator arrays on silicon," *Electronics Letters*, Vol. 42, No. 19, September 14, 2006.
10. Thompson, M. T., *Inductance Calculation Techniques, Part II: Approximations and Handbook*, 1999.
11. Pozar, D. M., *Microwave Engineering*, 2005.

Effects of Substrate Parameters on the Resonance Frequency of Double-sided SRR Structures under Two Different Excitations

E. Ekmekci^{1,2,3}, R. D. Averitt³, and G. Turhan-Sayan¹

¹Department of Electrical and Electronics Engineering, Middle East Technical University, Ankara, Turkey

²Department of Electronics and Communication Engineering, Suleyman Demirel University
Isparta, Turkey

³Department of Physics, Boston University, Boston, MA, USA

Abstract— In this study, we numerically investigate the effects of substrate parameters (i.e., the thickness and the permittivity) on the resonance frequency of the double-sided SRR (DSRR) structure under two different excitation conditions. This includes either electric or magnetic excitations which are two common techniques to obtain a resonant effective permittivity or permeability, respectively. The numerical calculations are performed using CST Microwave Studio. The numerical results reveal a similar trend in the DSRR response as the substrate permittivity values are varied for either electric or magnetic excitation while an opposite behavior is observed for changes of the substrate thickness.

1. INTRODUCTION

The split-ring resonator (SRR) is a well-known metamaterial structure used to obtain negative values of the permeability or permittivity, depending on the type of electromagnetic excitation [1–5]. When a time-varying magnetic field is applied through the axis of this special structure, a magnetic resonance frequency together with a μ -negative (MNG) region can be obtained [2]. This property makes SRRs special, because existing materials in nature typically yield only positive values for the permeability. Besides having special magnetic properties, SRRs can also be utilized as an electrical resonator, when a time-varying electric field is applied perpendicular to the gaps of the structure thereby providing an ε -negative (ENG) region [3, 5]. At terahertz (THz) frequencies and above, electrical excitation is common since magnetic excitation is not practical due to the limitations of measurement systems and fabrication techniques.

Double-sided SRR (DSRR) structures take an important place in metamaterial applications. They are nothing but two identical SRR structures printed over both faces of the substrate, but in an inverted fashion [6, 7]. The special case with the single ring SRR on both faces is called the broadside coupled SRR (BS-SRR) structure [6]. The most recent applications reported in the literature on these structures are related to miniaturization [7] and structural tunability [8]. In this study, we investigate the effects of the substrate thickness and substrate permittivity on the resonance frequency of the DSRR structure under electrical and magnetic excitation.

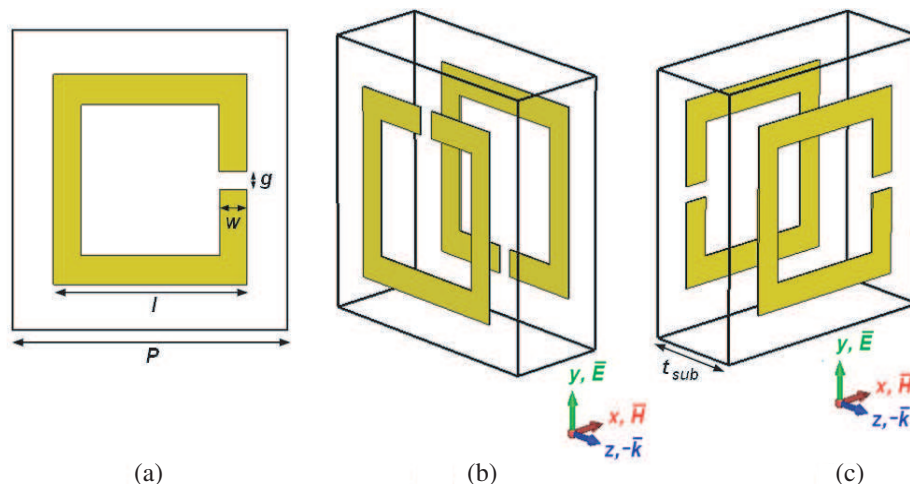


Figure 1: (a) Top view of the DSRR unit-cell with design parameters. (b) Perspective view of the unit-cell under magnetic excitation. (c) Perspective view of the unit-cell under electrical excitation.

2. DESIGN AND SIMULATIONS

Schematic views for the DSRR unit cell structure investigated in this study are given in Figure 1. Figure 1(a) shows the top view of the unit cell with design parameters. Figure 1(b) shows the perspective view for the unit-cell under magnetic excitation while Figure 1(c) shows the perspective view for the unit-cell under electrical excitation. Importantly, the DSRR structure consists of two identical SRRs on both faces, but in inverted fashion. For the square shaped unit-cell, the structure has a substrate side-length (P) of 5 mm, metallization side length (l) of 3.5 mm, gap width (g) of 0.3 mm, metal width (w) of 0.5 mm and metal thickness (t_m) of 0.03 mm (see Figure 1(a)). In this study substrate thickness (t_{sub}) (see Figure 1(c)) and substrate permittivity (ϵ_r) are chosen as variables, whereas the substrate dielectric loss-tangent ($\tan \delta_c$) is chosen to be 0.003. The metallization is made of copper lines with the conductivity (σ) of 58×10^6 S/m.

Numerical analysis of the DSRR arrays are performed using CST Microwave Studio using unit-cell boundary conditions (UC-BC) to provide periodicity along x and y directions. The structures are excited by an electromagnetic wave with the propagation vector (\mathbf{k}) along z direction, electric field vector (\mathbf{E}) along y direction, and magnetic field intensity vector (\mathbf{H}) along x direction.

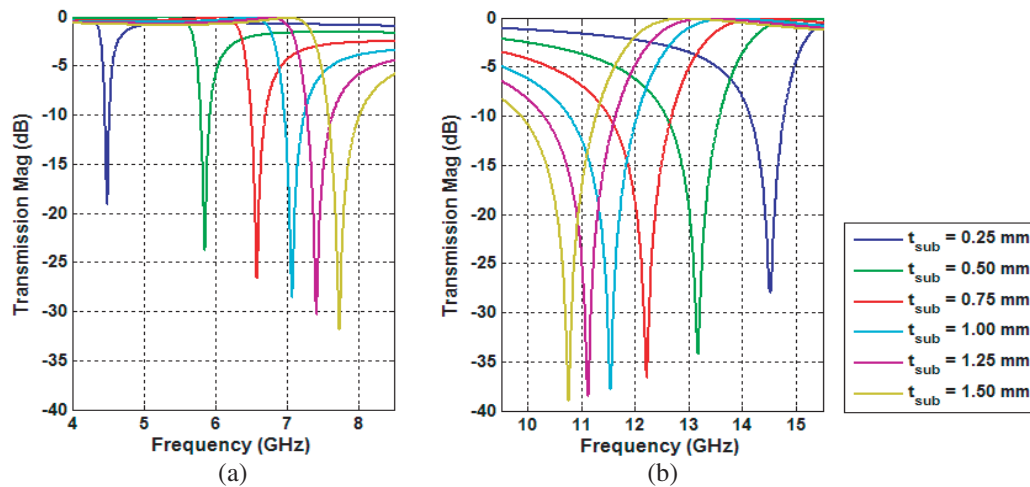


Figure 2: Effects of substrate thickness on resonance frequency of DSRR (i.e., BC-SRR) structure. (a) Magnetic excitation. (b) Electrical excitation.

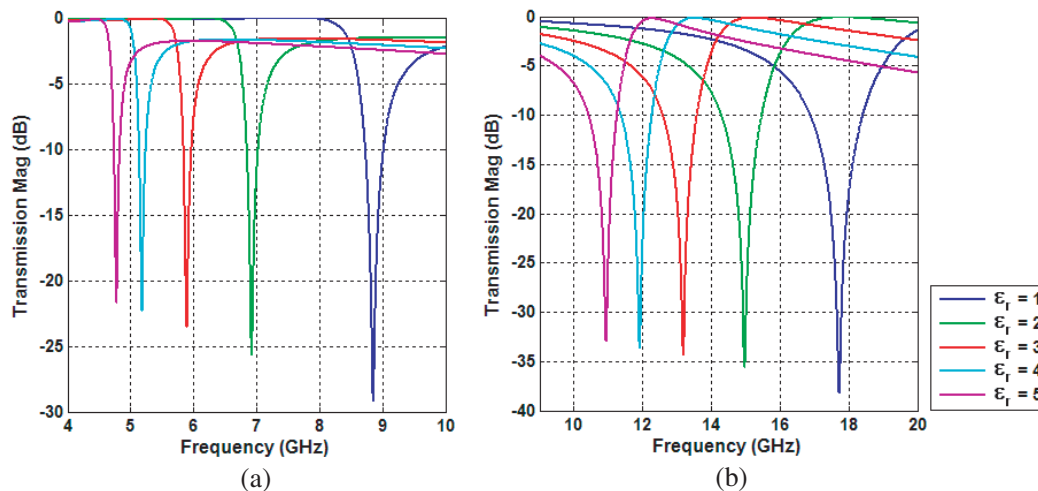


Figure 3: Effects of substrate permittivity on resonance frequency of DSRR (i.e., BC-SRR) structure. (a) Magnetic excitation. (b) Electrical excitation.

3. RESULTS

The simulation results obtained for different t_{sub} values, while keeping the substrate permittivity constant at $\varepsilon_r = 3$, under magnetic and electrical excitations are given in Figures 2(a) and 2(b), respectively. As we increase t_{sub} from 0.25 mm to 1.50 mm, the resonance frequency of the DSRR array increases from 4.49 GHz to 7.74 GHz for the magnetic excitation case, and it decreases from 14.52 GHz to 10.76 GHz for the electrical excitation case. For both cases, the frequency shifts are much larger for lower t_{sub} values. A second observation is that the resonance strength becomes stronger as the substrate thickness is increased for both types of excitation.

Next, we investigate the effects of substrate permittivity ε_r on the resonance frequency while keeping the value of the parameter t_{sub} constant at 0.5 mm. As seen in Figures 3(a) and 3(b), the resonance frequency decreases from 8.85 GHz to 4.77 GHz for the magnetic excitation case, and from 17.72 GHz to 10.94 GHz for the electrical excitation case as we increase ε_r value from 1 to 5. In this case, the structures resonate less strongly as the substrate permittivity becomes larger.

4. CONCLUSION

In this study, we investigated the effects of substrate parameters (i.e., substrate thickness and substrate permittivity) on the resonance frequencies of DSRR (i.e., BC-SRR) structure. We observed that the resonance frequency of DSRR structure increased from 4.49 GHz to 7.74 GHz for magnetic excitation, and decreased from 14.52 GHz to 10.76 GHz for electrical excitation as t_{sub} is increased from 0.25 mm to 1.50 mm. As we increased ε_r value from 1 to 5, the resonance frequency of DSRR structure decreased from 8.85 GHz to 4.77 GHz for the magnetic excitation and decreased from 17.72 GHz to 10.94 GHz for the electrical excitation.

In conclusion, resonance frequency of the DSRR array shows similar variations for either magnetic or electric excitations as the substrate permittivity is changed. However, completely opposite variation patterns are observed in response to changes in substrate thickness for these two different types of electromagnetic excitation. In a future study, the reason for these different behaviors will be investigated using equivalent circuit models describing the individual DSRR unit cells and cell-to-cell coupling mechanisms.

ACKNOWLEDGMENT

Evren Ekmekci acknowledges TUBITAK for supporting part of his Ph.D. studies through *Program 2214* while he is in Boston University.

REFERENCES

1. Pendry J. B., A. J. Holden, D. J. Robbins, and W. J. Stewart, "Magnetism from conductors and enhanced nonlinear phenomena," *IEEE Trans. Microwave Theory Tech.*, Vol. 47, No. 11, 2075–2084, 1999.
2. Smith D. R., W. J. Padilla, D. C. Vier, S. C. Nemat-Nasser, and S. Schultz, "Composite medium with simultaneously negative permeability and permittivity," *Phys. Rev. Lett.*, Vol. 84, No. 18, 4184–4187, 2000.
3. Tao, H., A. C. Strikwerda, K. Fan, C. M. Bingham, W. J. Padilla, X. Zhang, and R. D. Averitt, "Terahertz metamaterials on free-standing highly-flexible polyimide substrates," *J. Phys. D: Appl. Phys.*, Vol. 41, 232004, 2008.
4. Tao, H., A. C. Strikwerda, K. Fan, W. J. Padilla, X. Zhang, and R. D. Averitt, "Reconfigurable terahertz metamaterials," *Phys. Rev. Lett.*, Vol. 103, 147401, 2009.
5. Zhou J., T. Koschny, and C. M. Soukoulis, "Magnetic and electric excitations in split ring resonators," *Opt. Express*, Vol. 15, No. 26, 17881–17890, 2007.
6. Marqués, R., F. Mesa, J. Martel, and F. Medina, "Comparative analysis of edge- and broadside-coupled split ring resonators for metamaterial design-theory and experiments," *IEEE Trans. Antennas Propag.*, Vol. 51, No. 10, 2572–2581, 2003.
7. Ekmekci, E. and G. Turhan-Sayan, "Comparative investigation of resonance characteristics and electrical size of the double-sided SRR, BC-SRR and conventional SRR type metamaterials for varying substrate parameters," *Progress In Electromagnetics Research B*, Vol. 12, 35–62, 2009.
8. Lapine M., D. Powell, M. Gorkunov, I. Shadrivov, R. Marqués, and Y. Kivshar, "Structural tunability in metamaterials," *Appl. Phys. Lett.*, Vol. 95, 084105, 2009.

Transmission through Kerr Media Waveguide Barriers: Dispersive Properties

A. R. McGurn

Western Michigan University, USA

Abstract— The transmission properties of guided waves in photonic crystal waveguides containing barriers formed from Kerr nonlinear media are studied theoretically using a difference equations approach. The photonic crystal is a square lattice array of linear media dielectric cylinders, the waveguide is formed in the photonic crystal by cylinder replacement along the x -axis of the photonic crystal with linear media replacement cylinders, and the barrier is formed by replacing a finite number of waveguide cylinders with cylinders containing Kerr nonlinear optical media. The transmission properties of guided modes through the barrier are studied for barriers and barriers connected to an off-channel single site impurity. The effects of the dispersion of the waveguide modes are shown.

1. INTRODUCTION

Recently, there has been much interest in photonic crystal waveguides and the development from these of photonic crystal circuits for modulating the flow of electromagnetic energy [1–5]. Some of this work has focused on aspects of these systems which arise from the presence in them of optical nonlinear media [6–8]. This will be the focus of our presentation here. We will consider a waveguide formed along the x -axis of a square lattice photonic crystal of parallel axes linear media dielectric cylinders by cylinder replacement with linear media dielectric cylinders [9–11]. The dielectric properties of the replacement cylinders are chosen so that guided waves are bound to the waveguide channel and move parallel to the plane of the Bravais lattice of the photonic crystal, and we consider modes with electric fields parallel to the cylinder axes. A barrier of Kerr nonlinear media is introduced into the waveguide by replacing seven of the waveguide cylinders with barrier replacement cylinders formed from Kerr nonlinear media [12–14]. The barrier cylinders are placed so that between any two cylinders containing Kerr media there is an original cylinder of the waveguide [15]. A schematic figure of this is shown in Fig. 1. In addition, a barrier with an off-channel coupling to an impurity site formed by coupling the center barrier site to an adjacent impurity is considered. A schematic figure of the case of a barrier with an off-channel coupling is shown in Fig. 2.

The object of our discussions is to study the transmission properties of the guided modes through the barrier of nonlinear media. The transmission resonances of the system have been shown in previous studies on similar barrier systems [13–15] to be associated with various types of modes excited within the barrier media. These include Fabry-Perot, intrinsic localized, and dark-soliton-like modes. The focus here will be on intrinsic localized modes excited within the barriers.

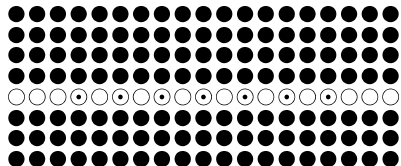


Figure 1: Photonic crystal and waveguide containing a simple barrier. Dark circles-bulk photonic crystal, open circles-waveguide, and open circles with center dot-barrier sites.

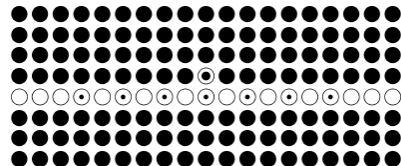


Figure 2: Photonic crystal and waveguide with barrier coupled to off-channel site. Dark circles-bulk photonic crystal, open circles-waveguide, open circles with center dot-barrier sites, open circle with large center dot-off-channel “Impurity”.

2. A REVIEW OF THE MODEL AND RESULTS

We consider a photonic crystal of infinite, parallel axes, dielectric cylinders of dielectric constant $\epsilon = 9.0$ and radii $R = 0.3779a_c$ that are arranged on a square Bravais lattice of lattice constant a_c [9–15]. The cylinders are surrounded by vacuum. Waveguides and barriers are formed by cylinder replacement along the x -axis by replacement cylinders that are formed from the cylinders of the photonic crystal by adding “impurity” dielectric media along the axes of the replacement cylinders. The “impurity” media makes a square cross section with sides of length $0.02a_c$ along the x - and y -axes in the plane of the Bravais lattice, and the replacement cylinders are translationally invariant in the direction perpendicular to the plane of the Bravais lattice. In Fig. 1, a schematic is presented in the plane of the Bravais lattice of a waveguide of linear “impurity” media containing a barrier of seven replacement cylinders containing Kerr nonlinear “impurity” media. Between each barrier cylinder containing Kerr media is a cylinder of linear “impurity” media of the type composing the waveguide. The alternating arrangement in the barrier simplifies the mathematics but does not qualitatively affect the physics presented below [15]. The models described in this paper have been used in many calculations of photonic crystal waveguides, and for brevity we refer the reader to our past papers, particularly Refs. [9, 10, 13], for further details of the geometry, dielectric properties, and the origin of the difference equation approach used in studying the waveguide and barrier systems of this paper.

For a guided mode of frequency $\frac{\omega a_c}{2\pi c} = 0.440$ in the second stop band of the photonic crystal, it is shown in Refs. [11, 15] that the guided mode propagation for the simple barrier system in Fig. 1 is described by the following set of difference equations: Taking the origin of the x - y coordinates in the Bravais lattice at the center site of the barrier so that the centers of the cylinders in Fig. 1 are located at (na_c, ma_c) for n and m integers, gives for the fields in the waveguide

$$E_{n,0} = g_l[E_{n,0} + b(E_{n+1,0} + E_{n-1,0})] \quad (1)$$

for $|n| > 7$. For the fields in the barrier

$$E_{2n,0} = g(1 + \lambda|E_{2n,0}|^2)E_{2n,0} + g_lb(E_{2n+1,0} + E_{2n-1,0}) \quad (2)$$

for $|n| \leq 3$ and

$$E_{2n+1,0} = g_lE_{2n+1,0} + gb[(1 + \lambda|E_{2n+2,0}|^2)E_{2n+2,0} + (1 + \lambda|E_{2n,0}|^2)E_{2n,0}] \quad (3)$$

for $-3 \leq n \leq 2$. At the connection between the barrier and the waveguide

$$E_{\pm 7,0} = g_l[E_{\pm 7,0} + bE_{\pm 8,0}] + gb(1 + \lambda|E_{\pm 6,0}|^2)E_{\pm 6,0}. \quad (4)$$

In these equations $E_{n,0}$ is the electric field intensity at the center of the replacement cylinder at the site $(na_c, 0)$, g_l is a function of the linear “impurity” dielectric constant of the waveguide replacement cylinders, and g and λ are functions of the nonlinear Kerr dielectric constant of the impurity media in the barrier replacement cylinders. The incident guided mode to the right of the barrier has the form $E_{n,0} = ue^{ikn} + ve^{-ikn}$ and the transmitted guide mode to the left of the barrier has the form $E_{n,0} = rxe^{ikn}$ so that the transmission amplitude of the incident wave is given by $T = |rx/u|^2$ [12, 13]. Substituting the guided mode forms into Eq. (1) gives $g_l = 1/[1 + 2b \cos(k)]$ so that for fixed frequency the dielectric properties of the waveguide change to support different k . We have also set $\lambda x^2 = 0.001$ so that varying r changes the intensity of the nonlinear part of the Kerr dielectric constant [13]. For the presentation given here we use the parameters $b = 0.0869$ and $\lambda x^2 = 0.001$ which are discussed in detail in our previous papers [11, 13]. We then find that, for fixed k , Eqs. (1) through (4) allow us to compute the transmission, T , as a function of r and g .

Briefly, the difference equations are obtained by using standard Green’s function methods to rewrite the Maxwell’s equations for the photonic crystal and waveguide system into the form of an integral equation. The kernel of the integral equation involves the Green’s function of the bulk photonic crystal in the absence of the waveguide and the difference in the dielectric constant between the waveguide cylinders and the cylinders of the bulk photonic crystal [9]. If the fields of the guided modes change slowly over the cross sectional area of the “impurity” material in the individual replacement cylinders of the waveguide, the integral equation formulation reduces to the difference equations, Eqs. (1) through (4). In this limit $g_l \propto \delta\epsilon_l$ where $\delta\epsilon_l$ is the difference in the dielectric constant of the linear media “impurity” material and the dielectric constant of the

bulk photonic crystal, and $g \propto \delta\epsilon$ where $\delta\epsilon$ is the difference in the dielectric constant of the Kerr “impurity” media in the $\lambda = 0$ limit and the dielectric constant of the bulk photonic crystal.

The object of the presentation is to present a plot of the resonant excitations (i.e., resonant transmission peaks) through the barrier, giving the location of the resonances in a two-dimensional (r, g) space [13–15]. Only resonances with $T > 0.6$ are presented. It was shown in our previous works on other systems that the lines and ridges in this plot are associated with a number of different types of barrier excitations. These include: bands of Fabry-Perot modes which start at $r = 0$ (i.e., in the linear limit of our system) and which can extend across the entire plot with increasing r (i.e., increasing nonlinearity) and intrinsic localized modes which only occur for $r > 0$. The interest is in how the resonant transmission changes with changes in the wavenumber of the incident guided modes. We shall see below that the general features of the (r, g) plot of the transmission resonances are maintained in a renormalized form with changing k . In previous discussions of (r, g) resonance plots, results for the wave functions along the different resonant lines were also given. Here, due to space limitations, only the wavefunctions of the intrinsic localized modes in some of our systems will be discussed. We point out that the intrinsic localized modes, that are of interest, have intensity profiles within the barriers which are small at the edges of the barriers and rise to large peak intensities at the center of the barriers. The Fabry-Perot mode intensities are more complex but retain their same general form along a given line of resonances but differ in general form along different lines of resonances in (r, g) space [13–15].

In Figs. (3) and (4), the resonant transmission peaks are shown for the simple barrier. Results are for $k = 2.9$ and $k = 2.2$ in the respective plots. An upper sequence of bands of Fabry-Perot modes is observed (i.e., for $1.0 < g < 1.3$) and a line of intrinsic localized modes (labeled ILM at the lower right of the line of these modes) are found. The intrinsic localized modes in Fig. 3 are in the region $0.2 < r < 0.7$ for $0.92 < g < 1.0$ and in Fig. 4 are in the region $0.2 < r < 1.5$ for $0.8 < g < 1.0$. The line of these modes are seen to rise to meet the lowest Fabry-Perot mode at $r \approx 0.7$ and $r \approx 1.5$, respectively.

In Table 1, the intrinsic localized mode field intensities, $\lambda|E_{n,0}|^2$, within the barrier are presented for a selection of (r, g) for $k = 2.9$ and $k = 2.2$. In general it is found that intrinsic localized modes with lower g values are more intensely peaked in the center of the barrier. Notice that the fields at the barrier edges can be small so that the intrinsic localized mode allows for an amplification of the intensity of the incident fields of the guided modes.

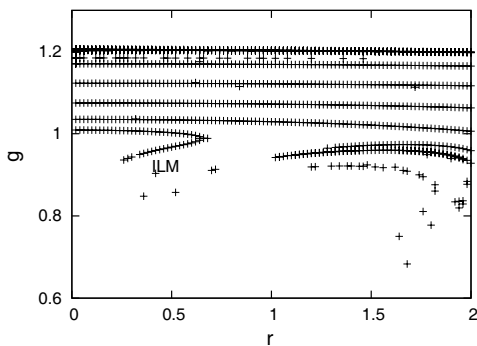


Figure 3: Plot of g versus r for the simple barrier with $k = 2.9$.

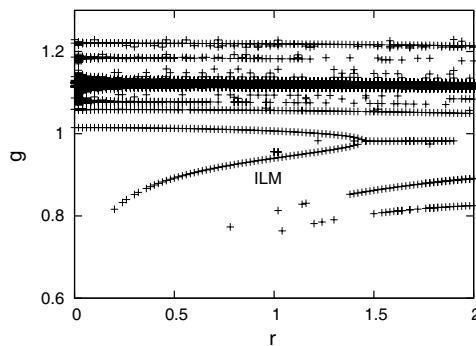


Figure 4: Plot of g versus r for the simple barrier with $k = 2.2$.

Table 1: Intrinsic localized mode field intensities, $\lambda|E_{n,0}|^2$, in the simple barrier sites for $n = 6, 4, 2, 0, -2, -4, -6$ for selected values of (r, g) and for $k = 2.9$ and $k = 2.2$.

(r, g)	k	$n = 6$	$n = 4$	$n = 2$	$n = 0$	$n = -2$	$n = -4$	$n = -6$
(0.3, 0.9433)	$k = 2.9$	0.0001	0.0026	0.0234	0.1197	0.0236	0.0027	0.0002
(0.4, 0.9570)	$k = 2.9$	0.0003	0.0038	0.0260	0.0948	0.0261	0.0039	0.0003
(0.3, 0.8519)	$k = 2.2$	0.0002	0.0026	0.0408	0.3121	0.0407	0.0025	0.0001
(0.5, 0.8922)	$k = 2.2$	0.0004	0.0046	0.0461	0.2347	0.0462	0.0047	0.0005

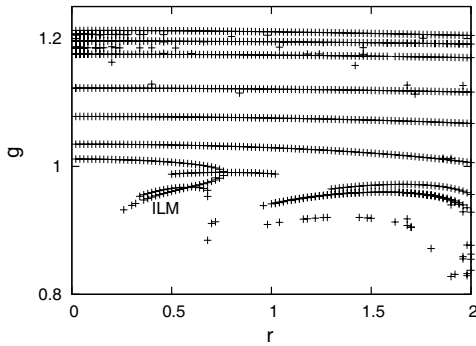


Figure 5: Plot of g versus r for the simple barrier with an off-channel coupling to a site with $g_i = 5.0$ for $k = 2.9$.

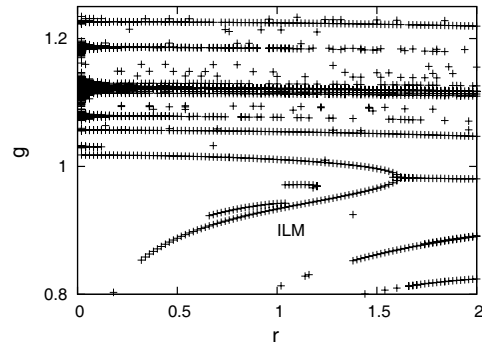


Figure 6: Plot of g versus r for the simple barrier with and off-channel coupling to a site with $g_i = 5.0$ for $k = 2.2$.

Table 2: The barrier field intensities, $\lambda|E_{n,0}|^2$, of $n = 6, 4, 2, 0, -2, -4, -6$ of the barrier with an off-channel “impurity” site with $g_i = 5.0$ for $k = 2.9$ and $k = 2.2$.

(r, g)	k	$n = 6$	$n = 4$	$n = 2$	$n = 0$	$n = -2$	$n = -4$	$n = -6$
(0.4, 0.9519)	2.9	0.0003	0.0041	0.0304	0.1126	0.0306	0.0042	0.0003
(0.4, 0.9593)	2.9	0.0003	0.0037	0.0242	0.0871	0.0582	0.0107	0.0007
(0.7, 0.9108)	2.2	0.0007	0.0072	0.0558	0.2065	0.0557	0.0071	0.0007
(0.7, 0.9263)	2.2	0.0007	0.0060	0.0398	0.1496	0.1118	0.0223	0.0025

In Figs. (5) and (6), the resonant transmission peaks are shown for the simple barrier with an adjacent neighbor off-channel Kerr “impurity” site (See Fig. 2.) for $k = 2.9$ and $k = 2.2$. Here Eqs. (1) through (4) are changed, with

$$E_{0,1} = g_i (1 + \lambda|E_{0,1}|^2) E_{0,1} + gb (1 + \lambda|E_{0,0}|^2) E_{0,0} \quad (5)$$

and a similar modification made to the equation for $E_{0,0} = etc.$ which now becomes

$$E_{0,0} = g (1 + \lambda|E_{0,0}|^2) E_{0,0} + g_l b (E_{1,0} + E_{-1,0}) + g_i b [1 + \lambda|E_{0,1}|^2] E_{0,1}. \quad (6)$$

Here g_i is for the off-channel Kerr impurity, and for simplicity we take λ the same for the barrier and off-channel impurities. To illustrate the results we have taken $g_i = 5.0$, and we note that for $g_i = 0$ the simple barrier in the absence of an off-channel impurity is obtained. Again the line of intrinsic localized modes are labeled at their lower right by “ILM” in the figure, i.e., for $g < 1.0$ and $0.2 < r < 0.8$ and $0.3 < r < 1.7$, respectively. An interest point is that now multiple bands of intrinsic localized modes are observed. The change from $k = 2.9$ to $k = 2.2$, however, is again a quantitative rather than a qualitative change.

In Table 2, the field intensities, $\lambda|E_{n,0}|^2$, of some intrinsic localized modes within the barrier for the barrier with off-channel impurity coupling are shown for $k = 2.9$ and $k = 2.2$. The intensities are presented to illustrate the nature of the modes in the multiple bands of intrinsic localized modes. The intensity peaks of the intrinsic localized modes are, again, greater for modes with smaller values of g .

It is interesting to note that, with an off-channel feature, there are multiple branches of intrinsic localized modes that cross in (r, g) . This provides for the opportunity of multiple switching devices which operate along paths that circulate about such crossing points in the (r, g) plane. In addition, the field intensities of the intrinsic localized modes are greatly peaked at the center of the barriers for the minimum intensities at the barrier edges. This opens possibilities for amplifications of amplitude modulated signals carried by the incident guided modes.

3. CONCLUSION

The effects of guided mode dispersion are shown on the resonant transmission peaks plotted within (r, g) space. The plots show only quantitative as opposed to qualitative changes with changes in k . This means that the classification scheme of resonances in the (r, g) space is robust, giving maps

of similar form for systems with different incident guided modes. The off-channel impurity cases show intrinsic localized mode band crossings which offers opportunities for device applications.

Recently, there has been much interest in photonic crystal defect and waveguide structures [1–4,16] which have potential for applications in electro-optical technologies. For more extensive applications, systems which display nonlinear behaviors are need. The study of the solutions of nonlinear systems is very complicated, and our discussions focus from specific applications onto how the solution space of nonlinear systems can be represented in a simple graphical manner. The types of graphical techniques suggested here are similar to methods of Poincare and Turning pattern representations that are standard in nonlinear studies [17].

ACKNOWLEDGMENT

The author wish to thank the hospitality of Prof. M. F. Thorpe and the Department of Physics, Arizona State University where this work was done.

REFERENCES

1. Joannopoulos, J. D., R. D. Meade, and J. N. Winn, *Photonic Crystals*, Princeton University Press, Princeton, 1995.
2. Londergan, J. T., J. P. Carini, and D. P. Murdock, *Binding and Scattering in Two-dimensional Systems: Applications to Quantum Wires, Waveguides, and Photonic Crystals*, Springer, Berlin, 1999.
3. Sakoda, K., *Optical Properties of Photonic Crystals*, Springer, 2004.
4. Zolla, F., G. Renversez, A. Nicolet, B. Kuhlmeiy, S. Guenneau, and D. Felbacq, *Foundations of Photonic Crystal Fibers*, World Scientific, New Jersey, 2005.
5. McGurn, A. R., *Survey of Semiconductor Physics*, K. W. Boer (ed.), Chp. 33, John Wiley and Sons, Inc., New York, 2002.
6. Soljacic, M and J. D. Joannopoulos, “Enhancement of nonlinear effects using photonic crystals,” *Nature Mater.*, Vol. 3, 211–219, 2004.
7. McGurn, A. R., “Nonlinear optical media in photonic crystal circuits: Intrinsic localized modes and device applications,” *Complexity*, Vol. 12, 18–40, 2007.
8. Kivshar, Y. S. and G. P. Agrawal, *Optical Solitons*, Academic Press, Amsterdam, 2003.
9. McGurn, A. R., “Green’s-function theory for row and periodic defect arrays in photonic band structures,” *Phys. Rev. B*, Vol. 53, 7059–7064, 1996.
10. McGurn, A. R., “Intrinsic localized modes in nonlinear photonic crystal waveguides,” *Physics Letters A*, Vol. 251, 322–335, 1999.
11. McGurn, A. R., “Photonic crystal circuits: A theory for 2D and 3D networks,” *Phys. Rev. B*, Vol. 61, 13235–13249, 2000.
12. McGurn, A. R. and G. Birkok, “Transmission anomalies in Kerr media photonic crystal circuits: Intrinsic localized modes,” *Phys. Rev. B*, Vol. 69, 235105, 2004.
13. McGurn, A. R., “Transmission through nonlinear barriers,” *Phys. Rev. B*, Vol. 77, 115105–1–115105-10, 2008.
14. McGurn, A. R., “Transmission through a Kerr barrier in photonic crystal waveguides: Dispersive effects,” *J. Phys.: Condens. Matter*, Vol. 21, 485302-1–485302-10, 2009.
15. McGurn, A. R., “Transmission through Kerr media barriers within waveguides and circuits,” *SPIE Proceedings*, E. S. Kawata, V. M. Shalev, and D. P. Tsai (ed.), Vol. 7395, 73951T-1–73951T-8, San Diego, USA, August 2009.
16. Noda, S, A. Chutinan, and T. Asano, “Trapping and emmission of photons by a single defect in a photonic bandgap structure,” *Nature*, Vol. 407, 608–610, 2000.
17. Lam, L., *Introduction to Nonlinear Physics*, Springer, New York, 1996.

Photonic Crystal Fiber Analysis Using Cylindrical FDTD with Bloch Boundary Conditions

Adam Mock and Paul Trader

School of Engineering and Technology, Central Michigan University, Mt. Pleasant, MI, USA

Abstract— A method for reducing the computational domain size in finite-difference time-domain analyses of structures with azimuthal periodicity is presented. Examples of such structures include two dimensional photonic crystals and microdisks with a periodic patterning. A form of Bloch’s theorem appropriate to periodicity in the azimuthal direction is derived and used to formulate boundary conditions used in the calculation. The method is applied to the modal analysis of a photonic crystal fiber.

1. INTRODUCTION

In general, analyzing the electromagnetics of dielectric structures with arbitrary geometry variation requires a numerical approach. Two dimensional photonic crystals represent one example of a dielectric structure that requires numerical analysis. Over the passed two decades, two dimensional photonic crystals have been of interest for both integrated photonics [1] and fiber optics [2]. Photonic crystal fibers are similar to ordinary optical fibers except with the addition of microstructured voids that run the length of the fiber. Microstructured optical fibers represent a complicated dielectric geometry, and numerical methods are required for accurate analysis of their dispersion characteristics and spatial field profiles. In this work, the finite-difference time-domain method is used to find the mode profiles and dispersion diagrams of microstructured fibers. Because fiber geometries are uniform along the longitudinal direction, the field behavior along this direction may be characterized by a propagation factor $\exp(j\beta z)$. Derivatives with respect to z can be evaluated analytically which reduces the computational domain from three to two dimensions while still maintaining a fully vectorial solution to Maxwell’s equations. In this paper, a method for further reduction in the computational domain size is presented for geometries that possess periodicity in the azimuthal direction. In these geometries only the unit sector is required for analysis, and spatially looped boundary conditions can be enforced. For photonic crystal fibers utilizing a triangular lattice, this results in a reduction by a factor of six in the domain size.

Several electromagnetic numerical methods exist that are capable of analyzing microstructured optical fibers with varying degrees of accuracy and computational effort [3]. Semianalytical approaches based on the effective index method [4] require little computational effort but come at the expense of inaccuracies in the vector properties of the fiber modes. The plane-wave expansion method [5] is a fully vectorial approach, but it assumes a periodic geometry. To analyze non-periodic geometries, a supercell must be defined and be large enough to limit cross talk with neighboring cells. Finite-difference methods [6] are fully vectorial mode solvers that solve an eigenvalue problem to obtain the propagating modes as a function of β . Computational domain size is limited in these methods due to the superlinear scaling in execution time for solving large matrix problems [7]. Localized function methods [8] seek to reduce the matrix size with judicious use of spatially local basis functions; however, calculating matrix elements can be computationally intensive, and scaling to three-dimensional problems may still result in large matrices. Furthermore, some prior knowledge of the field solutions must be known to select appropriate localized functions. The finite-element method [9] is popular due to its flexibility in handling arbitrary geometries and efficient discretization of fine geometrical details, but it involves eigenvalue solution, and scaling to three-dimensions can be problematic.

The finite-difference time-domain (FDTD) method [10] is attractive due to its generality, ease of implementation, linear scaling in execution time with problem size, and ability to handle dispersive and nonlinear materials. A “compact” version of FDTD applicable to waveguide geometries continuous along the propagation direction has been developed [11–13] and applied to optical fiber geometries [14, 15] and silicon-on-insulator ridge waveguides [16]. In what follows, compact FDTD in cylindrical coordinates is used to analyze photonic crystal fibers, and a method is presented for further reduction in the computational domain size based on azimuthal periodicity.

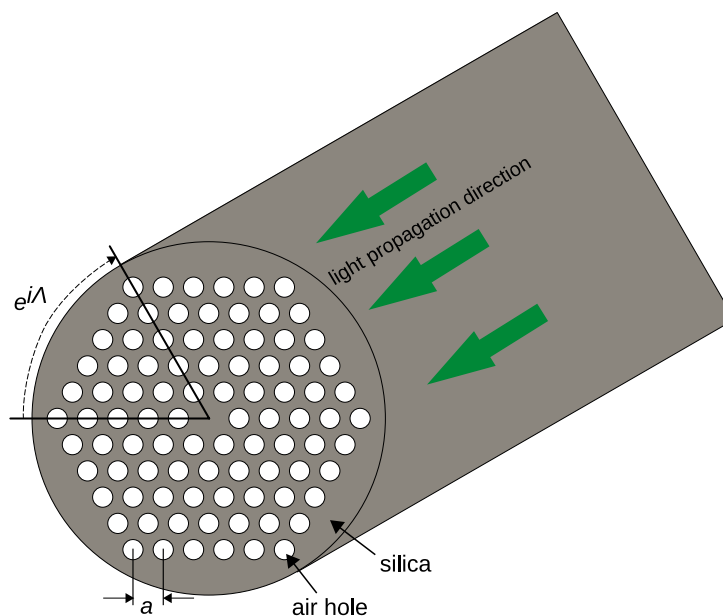


Figure 1: Schematic diagram of a photonic crystal fiber. A unit sector spanning an angle Λ is labeled. a denotes the lattice constant of the photonic crystal.

2. FORMULATION

FDTD in cylindrical coordinates is used, so that the computational domain has the same shape as the fiber, and the distance between the device and the computational boundary is uniform. Because domain sizes are set by the minimum distance between the device under analysis and the computational boundaries, using cylindrical coordinates avoids the unused space that would exist in the corners of an FDTD calculation using cartesian coordinates. Also, the cylindrical discretization scheme conforms more closely to the round shape of the fiber which reduces staircase approximation error associated with a cartesian discretization. In this work, we discuss another advantage of cylindrical coordinates which is the convenient use of spatially looped boundary conditions in the ϕ direction to further reduce computational burden.

Figure 1 displays a cross section of a microstructured optical fiber with a triangular lattice two dimensional photonic crystal pattern of air holes. The air holes run along the entire length of the fiber. Because of the photonic crystal geometry inscribed on the cross section, these microstructured fibers are often called photonic crystal fibers. In the center, a single hole is filled creating a spatial defect. These fibers guide via a combination of bandgap and index guiding. It should be noted that hollow core photonic crystal fibers have been demonstrated and guide light primarily based on bandgap guiding [17].

The spatially varying electric permittivity of the photonic crystal fiber is periodic in the ϕ direction with period $\Lambda = \pi/3$. That is, $\epsilon(r, \phi + \Lambda, z) = \epsilon(r, \phi, z)$. A unit sector is labeled in Figure 1. If the electric permittivity were *uniform* in the ϕ direction, then the azimuthal field behavior can be described by $\exp(im\phi)$ where m is an integer. This fact can be used to formulate a compact form of FDTD for structures uniform along ϕ [18]. In the case of a photonic crystal fiber, the material is nonuniform in the ϕ direction, but it is periodic. This work addresses the question of whether advantage can be taken of *periodicity* in the ϕ direction to reduce computational domain sizes.

The modes of a refractive index geometry uniform in the ϕ direction may be expressed as

$$F_m(r, \phi, z) = f_m(r, z)e^{im\phi} \quad (1)$$

where F refers to a component of the electric or magnetic field and m is an integer as required by the condition $F_m(r, \phi + 2\pi, z) = F_m(r, \phi, z)$. $f_m(r, z)$ represents the r and z dependence of the mode labeled by m . Let $\Phi(\phi')$ be an operator which rotates a function about the z axis by an angle ϕ' . For a dielectric function that contains discrete rotational invariance along ϕ with a period Λ , one has $\Phi(\Lambda)\epsilon(r, \phi, z) = \epsilon(r, \phi + \Lambda, z) = \epsilon(r, \phi, z)$. Therefore, solutions to Maxwell's equations

will be eigenfunctions of the operator $\Phi(\Lambda)$ [19]. Operating on Equation (1) with $\Phi(\Lambda)$ yields $\Phi(\Lambda)F_m(r, \phi, z) = f_m(r, z)e^{im(\phi+\Lambda)} = f_m(r, z)e^{im\Lambda}e^{im\phi} = e^{im\Lambda}F_m(r, \phi, z)$ which shows that $e^{im\Lambda}$ is an eigenvalue of $\Phi(\Lambda)$ acting on $F_m(r, \phi, z)$. Note, however, that m can be replaced by $m + n2\pi/\Lambda$ where n is an integer, and the eigenvalue $e^{im\Lambda}$ remains unchanged. This suggests that any linear superposition of $F_{m+n2\pi/\Lambda}(r, \phi, z)$ is also an eigenfunction of the operator $\Phi(\Lambda)$ with eigenvalue $e^{im\Lambda}$. This eigenfunction may be written as

$$F_m(r, \phi, z) = \sum_n f_{m,n}(r, z)e^{i(m+n\frac{2\pi}{\Lambda})\phi} = e^{im\phi} \sum_n f_{m,n}(r, z)e^{in\frac{2\pi}{\Lambda}\phi} \quad (2)$$

$$F_m(r, \phi, z) = e^{im\phi}u(r, \phi, z) \quad (3)$$

where $u(r, \phi + \Lambda, z) = u(r, \phi, z) = \sum_n f_{m,n}(r, z)e^{in\frac{2\pi}{\Lambda}\phi}$ has a Fourier series representation and is therefore periodic. Equation (3) has the same form as an electron wavefunction in a periodic potential or the electric or magnetic field in a photonic crystal. In these cases the integer m is usually written as a continuous valued wavenumber β , and the result is known as Bloch's theorem. Here we have shown that the same Bloch theorem wavefunction exists for structures that possess periodicity in the azimuthal direction. Because the fields must remain unchanged under rotation through a multiple of 2π , the phase factor which is analogous to the continuous valued propagation constant in structures with discrete translational invariance is restricted to integer values denoted by m above.

From Equation (3), one has $F_m(r, \phi + \Lambda, z) = e^{im\Lambda}F_m(r, \phi, z)$. Within an FDTD numerical calculation for a structure with periodicity in the azimuthal direction, one need only analyze a unit sector and spatially loop the boundaries. This is done by enforcing boundary conditions at $\phi = 0$ and $\phi = \Lambda$ so that the fields at the boundaries are related according to $F_m(r, \phi + \Lambda, z) = e^{im\Lambda}F_m(r, \phi, z)$. The user specifies the integer m and subsequent runs can be performed for different values of m .

Using group theory notation, discrete rotational invariance is described by the symbol C_{nv} where n is related to the period Λ via $n = 2\pi/\Lambda$. The photonic crystal fiber shown in Figure 1 possesses C_{6v} symmetry. In this example, the computational domain can be reduced by a factor of 6. In general, the computational domain for structures that possess C_{nv} symmetry can be reduced by a factor of n . This suggests that the relative performance improvement of the proposed method increases as the material variation in the ϕ direction becomes more rapid (as n increases).

To conclude this section, an alternative derivation of the boundary condition appropriate for spatially looping $F_m(r, \phi + \Lambda, z) = e^{im\Lambda}F_m(r, \phi, z)$ is presented. Consider a geometry possessing C_{nv} symmetry. Such a structure has a unit sector spanning an angle $\Lambda = 2\pi/n$. If the operator $\Phi(\Lambda)$ is applied n times to a representative field component $F(r, \phi, z)$, the field is returned to its original orientation since $n\Lambda = 2\pi$. This suggests $\Phi^n(\Lambda)F = F$. Earlier, we found that F is an eigenfunction of Φ . If we denote the corresponding eigenvalue by α , one has $\Phi(\Lambda)F = \alpha F$ and $\Phi^n(\Lambda)F = \alpha^n F = F$. This suggests that $\alpha^n = 1 = e^{im2\pi}$ and $\alpha = e^{im2\pi/n} = e^{im\Lambda}$. The eigenvalue equation can be written as $\Phi(\Lambda)F = F(r, \phi + \Lambda, z) = e^{im\Lambda}F(r, \phi, z)$ which is the same result given by Equation (3).

3. RESULTS

Figure 2 shows results of using the proposed FDTD method in the analysis of a photonic crystal fiber. Figure 2(a) shows the dispersion for four modes each with a different m value. The data points were obtained from individual FDTD runs with specified β and m values. Also illustrated in Figure 2(a) are the lightlines in free space and in the fiber material with a refractive index of $n_f = 1.45$. It is clear that the dispersion follows the usual trend of starting near the free space lightline at low frequencies and then moving closer to the fiber material lightline at higher frequencies.

Figure 2(b) shows the z component of the magnetic field for the four modes whose dispersion is shown in Figure 2(a). It is clear that the ϕ dependence of the field is related to the specified m value consistent with the analysis in the preceding section.

4. DISCUSSION

As discussed in Section 3, the method described here offers an n -fold reduction in computational domain size for structures possessing C_{nv} rotational symmetry. Such structures include photonic

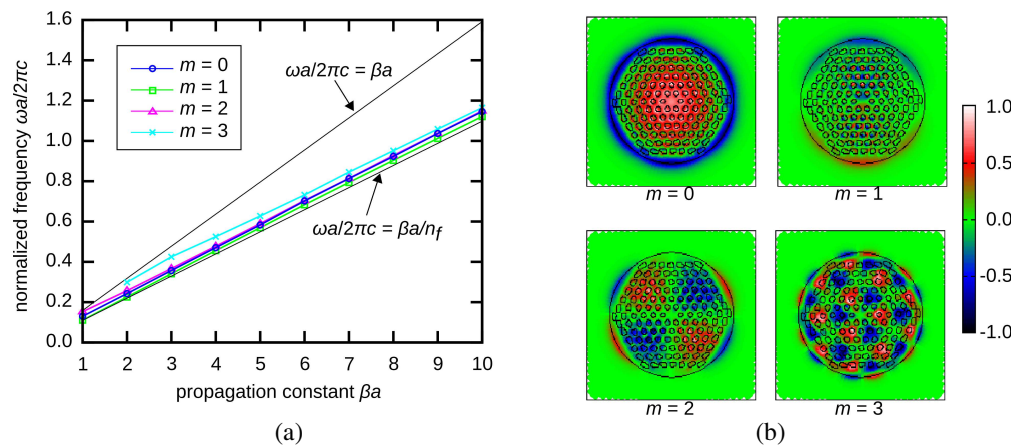


Figure 2: (a) Dispersion diagram for four different modes of a photonic crystal fiber calculated using the method described in the text. a is the lattice constant and is illustrated in Figure 1. Also shown are the light lines for free space and the optical fiber material ($n_f = 1.45$). (b) z component of the magnetic field ($H_z(r, \phi)$) for the four modes whose dispersion is shown in (a).

crystal fibers as well as microdisk geometries with a periodic patterning. One interesting feature of using FDTD in cylindrical coordinates is the use of a spatially nonuniform grid, which has both advantages and disadvantages. One disadvantage is shown in Figure 2(b), where it is clear that the geometry discretization becomes more coarse as the radius increases. Because the cell length along the ϕ direction is given by $r\Delta\phi$, the cell size can vary greatly between the origin and the domain boundary. Therefore, using a suitably small $\Delta\phi$ for resolution of fine features at large r may over-resolve the features at the origin and unnecessarily increase the computational burden. Furthermore, the FDTD time step is limited by the smallest grid spacing in the domain implying that parts of the domain are analyzed with both low resolution and an unnecessarily small time step duration limited by the grid size near the origin [20]. The authors are currently investigating whether subgridding approaches [21] can be used to make the discretization more uniform without undue burden on computational resources.

One advantage to the grid nonuniformity is that in many cases, the features requiring the most resolution are near the origin. As an example, microstructured fibers may have uniform cladding layers surrounding the microstructured core and these layers are then surrounded by air. These cladding layers are uniform in the ϕ direction and so do not require fine discretization to resolve their features. The resulting discretization uses more spatial grid points near the origin and fewer in the uniform cladding regions, resulting in a more computationally efficient distribution of grid points. As mentioned previously, this breaks down for fine geometrical features at intermediate radii as shown in Figure 2(b).

5. CONCLUSION

A method for reducing the computational domain size and thus computation time for FDTD analysis of geometries with periodicity in the azimuthal direction was presented and demonstrated. A derivation of Bloch's theorem applicable to geometries periodic in the azimuthal direction was derived and used to establish boundary conditions, so that only a unit sector of the domain is required for analysis. The method was demonstrated by obtaining the dispersion and mode profiles for photonic crystal fibers.

REFERENCES

1. Notomi, M., A. Shinya, S. Mitsugi, E. Kuramochi, and H.-Y. Ryu, "Waveguides, resonators and their coupled elements in photonic crystal slabs," *Optics Express*, Vol. 12, No. 8, 1551–1561, 2004.
2. Russell, P. S. J., "Photonic crystal fibers," *Science*, Vol. 299, 358–362, 2003.
3. Saitoh, K. and M. Koshiba, "Numerical modeling of photonic crystal fibers," *Journal of Light-wave Technology*, Vol. 23, No. 11, 3580–3590, 2005.
4. Birks, T. A., J. C. Knight, and P. S. J. Russell, "Endlessly single-mode photonic crystal fiber," *Optics Letters*, Vol. 22, No. 13, 961–963, 1997.

5. Ferrando, A., E. Silvestre, J. J. Miret, P. Andrés, and M. V. Andrés, “Vector description of higher-order modes in photonic crystal fibers,” *Journal of the Optical Society of America A*, Vol. 17, No. 7, 1333–1340, 2000.
6. Zhu, Z. and T. G. Brown, “Full vectorial finite-difference analysis of microstructured optical fibers,” *Optics Express*, Vol. 10, No. 17, 853–864, 2002.
7. Press, W. H., S. A. Teukolsky, W. T. Vetterling, and B. P. Flannery, *Numerical Recipes in C++*, Cambridge University Press, New York, 2003.
8. Monro, T. M., D. J. Richardson, N. G. R. Broderick, and P. J. Bennett, “Holey optical fibers: An efficient modal model”, *Journal of Lightwave Technology*, Vol. 17, No. 6, 1093–1102, 1999.
9. Brechet, F., J. Marcou, D. Pagnoux, and P. Roy, “Complete analysis of the characteristics of propagation into photonic crystal fibers by the finite element method,” *Optical Fiber Technology*, Vol. 6, 181–191, 2000.
10. Taflove, A. and S. C. Hagness, *Computational Electrodynamics*, Artech House, Massachusetts, 2000.
11. Asi, A. and L. Shafai, “Dispersion analysis of anisotropic inhomogeneous waveguides using compact 2D-FDTD,” *IEEE Electronics Letters*, Vol. 28, No. 15, 1451–1452, 1992.
12. Xiao, S., R. Vahldieck, and H. Jin, “Full-wave analysis of guided wave structures using a novel 2-D FDTD,” *IEEE Microwave and Guided Wave Letters*, Vol. 2, No. 5, 165–167, 1992.
13. Xiao, S. and R. Vahldieck, “An efficient 2-D FDTD algorithm using real variables [guided wavestructure analysis],” *IEEE Microwave and Guided Wave Letters*, Vol. 3, No. 5, 127–129, 1993.
14. Chen, Y. and R. Mittra, “A highly efficient finite-difference time domain algorithm for analyzing axisymmetric waveguides,” *Microwave and Optical Technology Letters*, Vol. 15, No. 4, 201–203, 1997.
15. Qiu, M., “Analysis of guided modes in photonic crystal fibers using the finite-difference time-domain method,” *Microwave and Optical Technology Letters*, Vol. 30, No. 5, 327–330, 2001.
16. Mock, A. and J. D. O’Brien, “Dependence of silicon-on-insulator waveguide loss on lower oxide cladding thickness,” *In Integrated Photonics and Nanophotonics Research and Applications Topical Meeting*, page IWG4, Boston, MA, USA, July 2008.
17. Ritari, T., J. Tuominen, H. Ludvigsen, J. C. Petersen, T. Sørensen, T. P. Hansen, and H. R. Simonsen, “Gas sensing using air-guiding photonic bandgap fibers,” *Optics Express*, Vol. 12, No. 17, 4080–4088, 2004.
18. Davidson, D. B. and R. W. Ziolkowski, “Body-of-revolution finite-difference time-domain modeling of space-time focusing by a three-dimensional lens,” *Journal of the Optical Society of America A*, Vol. 11, No. 4, 1471–1490, 1994.
19. Joannopoulos, J. D., R. D. Meade, and J. N. Winn, *Photonic Crystals*, Princeton University Press, Princeton, NJ, 1995.
20. Dib, N., T. Weller, M. Scardelletti, and M. Imparato, “Analysis of cylindrical transmission lines with the finite-difference time-domain method,” *IEEE Transactions on Microwave Theory and Transactions*, Vol. 47, No. 4, 509–512, 1999.
21. Yu, W. and R. Mittra, “A technique for improving the accuracy of the nonuniform finite-difference time-domain algorithm,” *IEEE Transactions on Magnetics*, Vol. 47, No. 3, 353–356, 1999.

Energy Band of Spin Waves in Ferromagnetic Bilayers with bcc Structures

Xiaoxia Wu^{1,2}, Guohong Yun^{2,3}, Xiaojuan Hou^{1,2}, and B. Narsu³

¹Department of Applied Physics, Inner Mongolia University of Science and Technology
Hohhot 014030, China

²College of Physical Science and Technology, Inner Mongolia University, Hohhot 010021, China

³Key Laboratory of Physics and Chemistry of Functional Materials
College of Physics and Electronic Information, Inner Mongolia Normal University, Hohhot 010022, China

Abstract— The eigen problem of the spin wave excitation in a bilayered ferromagnets with body centered crystal structures have been investigated by using the full quantum interface rescaling approach. The energy band of the spin waves in the ferromagnetic symmetric bilayers system has been calculated. And further the excitation and transmission properties of spin waves in exchange coupled bilayers with periodic boundary have been addressed.

1. INTRODUCTION

The mechanism of wave propagation in a ferromagnetic multilayered structure is one of the most interesting issues of recent research on electromagnetic materials [1]. Because of the interface constructed from different materials, many new phenomenon and effect had appeared in heterogeneous multilayer systems [2, 3]. Spin waves in such a system will be modulated by the interface and exhibits different modes, bulk mode, interface mode and confined mode etc [4], such properties can be applied for spin based logical devices and valves [5–7]. Many authors have studied the excitation and transmission properties of Spin waves in exchange coupled magnetic multilayered system [8–11]. Theoretically, the transfer matrix [10], green function [12] and first principle methods [13, 14] can resolve the coupled system, however, these theory show some deficiencies when they have been applied into the interface exchange coupled system. Puzskarski et al. [2] developed an interface rescaling approach and combined it with the Landau-Liftistz equation to depict the magnetically coupled system. The method is very effective in decoupling the equation set, and achieved many improvements [15–17]. The magnetic system is actually a full quantum system so that this interface rescaling approach was employed into a full quantum theory [4]. Based on the Heisenberg exchange model, the low energy excitation of the interface exchange coupled biferromagnetic system with simple cubic crystal structures was studied systematically [18–23]. As we know, however, most of the materials in cubic phase are not just simply with SC crystal structures. Therefore, the prevailing theories cannot present persuasive forecasting results for the practical systems. To be more realistic, the eigen value problem of the spin wave excitation in a bilayered ferromagnets with body centered crystal structures have been investigated by using the full quantum interface rescaling approach.

2. MODEL AND FORMULATION

Let us consider an interlayer exchange coupled biferromagnetic system consists of two sublayers with body centered crystal (bcc) structures. Generally, two ferromagnetic films have their periodicity in the film plane parallel to the interface, thus only the spin excitations in the direction perpendicular to the film plane should be addressed. For simplicity, we consider a symmetric bilayer system that the bulk exchange $J_A = J_B$, site spins $S_A = S_B$, and interlayer exchange is J_{AB} . And we assume that the bulk, surface and interface anisotropies are so small that can be neglected. Therefore, the exchange Hamiltonian can be given by,

$$\hat{H} = -\frac{1}{2} \sum_{m,n} \sum_{i,j} J(n,i;m,j) \mathbf{S}(n,i) \cdot \mathbf{S}(m,j) - \sum_{g^*(n,i)} \mu_0 \mathbf{B}_0 \cdot \mathbf{S}(n,i), \quad (1)$$

where the second term is the Zeeman energy of the spins. And $J(n,i;m,j)$ is the exchange constant, $S(n,i)$ is the site spin, n,m and i,j are the layer and site indices respectively. $g^*(n,i)$ and μ_0 are respectively the effective landé factor and the Bohr magnetron.

To be more realistic, we consider the ferromagnets with bcc structures and the lattice constant of two unit lengths. The nearest neighbor exchange interaction is taken into account in the following discussions. By applying the HP transformation [24] and the Fourier transformation, the Hamiltonian of the exchange coupled system can be diagonalized and the eigenequation can be obtained as follows [4, 18],

$$E_{p,k}f(n,p) = 4 \left\{ \left[J(n,n+1)S(n+1) + J(n,n-1)S(n-1) + \frac{1}{4}g^*(n)\mu_0B_0 \right] f(n,p) - \gamma \left[J(n+1,n)\sqrt{S(n)S(n+1)}f(n+1,p) + J(n-1,n)\sqrt{S(n)S(n-1)}f(n-1,p) \right] \right\} \quad (2)$$

Here the exchange constants satisfy $J(n,n\pm 1) = J(n,i,n\pm 1,i) = J(n\pm 1,n)$, and $\gamma = \cos k_x \cos k_y$ is the spin wave structure factor, it depicts the in-plane traveling spin waves. $f(n,p)$ is the wave function of the standing spin waves (SSWs) in the vertical direction. The interlayer exchange coupling constant, site spin take following constant,

$$J(n,n+1) = \begin{cases} J_A > 0 & 1 \leq n \leq 2N_A - 1 \\ J_B > 0 & 2N_A + 1 \leq n \leq 2N - 1 \\ J_{AB} > 0 & n = 0, 2N_A, 2N \end{cases} \quad (3)$$

$$\hat{S}(n) = \begin{cases} \hat{S}_A & 1 \leq n \leq 2N_A - 1 \\ \hat{S}_B & 2N_A \leq n \leq 2N \end{cases} \quad (4)$$

here N_A (or N_B) denotes the number of the atomic layers of sublayer A (or B). The indices p, k for energy E_{pk} and $f(n,p)$ is neglected for the sake of simplicity and the wave functions in the sublayers are set as,

$$f(n) = \begin{cases} f_A(n) & 1 \leq n \leq 2N_A - 1 \\ f_B(n) & 2N_A \leq n \leq 2N \end{cases} \quad (5)$$

Equation (2) gives a set of coupling equations, which is too difficult to be resolved at first hand. Therefore, the so-called interface rescaling approach [15, 16] will be adopted to resolve the equation set for the case of periodic boundary condition. Introducing a interface rescaling coefficient R [15, 16], and using the periodic boundary condition, one can obtain the energy restriction equation,

$$E = 8J_A S_A (1 - \gamma \cos k_A) + g_A^* \mu_0 B_0 = 8J_B S_B (1 - \gamma \cos k_B) + g_A^* \mu_0 B_0 \quad (6)$$

and

$$1 - \frac{J_{AB} S_B}{J_A S_A} (1 - \gamma R \alpha^{-1}) = \begin{cases} \gamma \cos(k_A N_A) / \cos(k_A (N_A - 1)), & P = 0 \\ \gamma \sin(k_A N_A) / \sin(k_A (N_A - 1)), & P = 1 \end{cases} \quad (7a)$$

$$1 - \frac{J_{AB} S_B}{J_B S_B} (1 - \gamma R \alpha^{-1}) = \begin{cases} \gamma \cos(k_B (N_B + 1)) / \cos(k_B N_B), & P = 0 \\ \gamma \sin(k_B (N_B + 1)) / \sin(k_B N_B), & P = 1 \end{cases} \quad (7b)$$

where $\alpha = \sqrt{S_B/S_A}$. Resolving Equations (6) and (7) numerically, one can obtain the quantized wave vector of the spin waves, and further, the excitation energy and wave functions.

3. RESULTS AND DISCUSSIONS

The band structure reveals the excitation and transmission properties of spin waves in the ferromagnetic bilayer films. Therefore, the energy band of the ferromagnetic bilayer film with interlayer ferromagnetic coupled is calculated by using following parameters, $J_A = J_B = 1$, $S_A = S_B = 1/2$, $N_A + N_B = 26$ and $J_{AB} = 0.6, 1.0, 1.2$, as shown in Figures 1–3.

In this system, the total number of the spin wave mode is 26 (equal to the number atomic layer, $N_A + N_B$), in which there are 14 even parity modes and 12 odd parity modes. For such a simple system, the inhomogeneity is due to the interface exchange coupling, which introduces an interface spin wave mode, namely, the spin wave modes consist of bulk mode and interface mode. As the interface exchange constant is greater than the bulk exchange, the energy of the interface mode is the larger than any other bulk modes. Conversely, if the interface exchange is weaker than the bulk exchange, the energy of the interface mode is smaller than the bulk mode.

In addition, the amount of the interface mode is determined by interface exchange constant, parity and the coordinate in the reduced Brillouin zone. At most, there are four interface modes

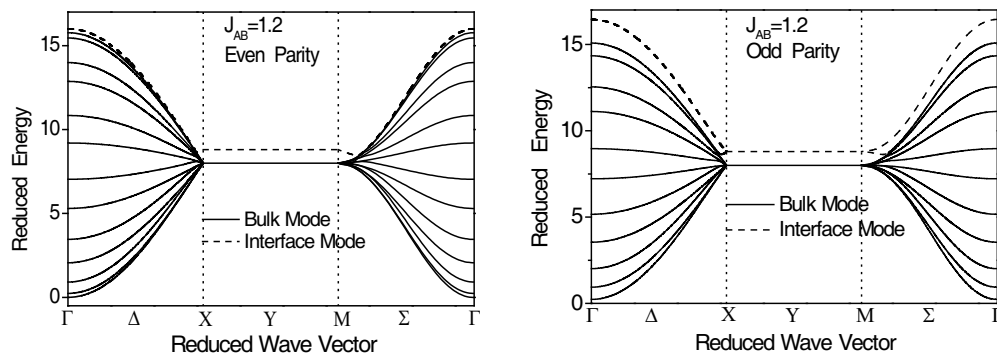


Figure 1: The spin wave energy bands of ferromagnetic bilayer system, the band with even parity is presented in left panel and the odd in right panel, the interlayer exchange coupling factor $J_{AB} = 1.2$.

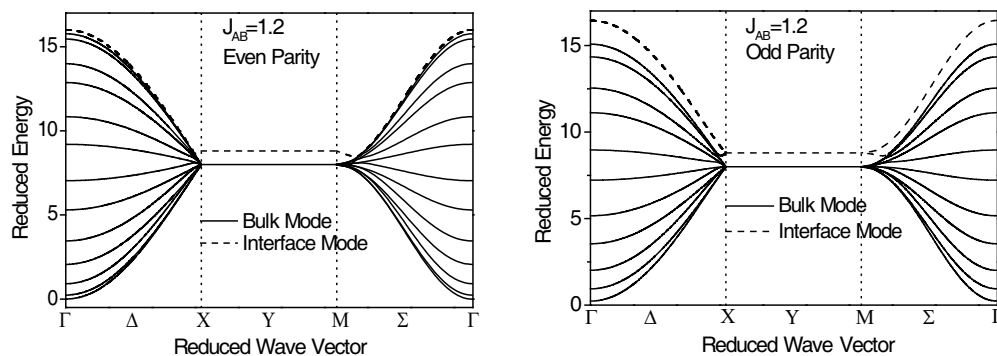


Figure 2: The same as Fig. 1, but the interlayer exchange coupling factor $J_{AB} = 0.6$.

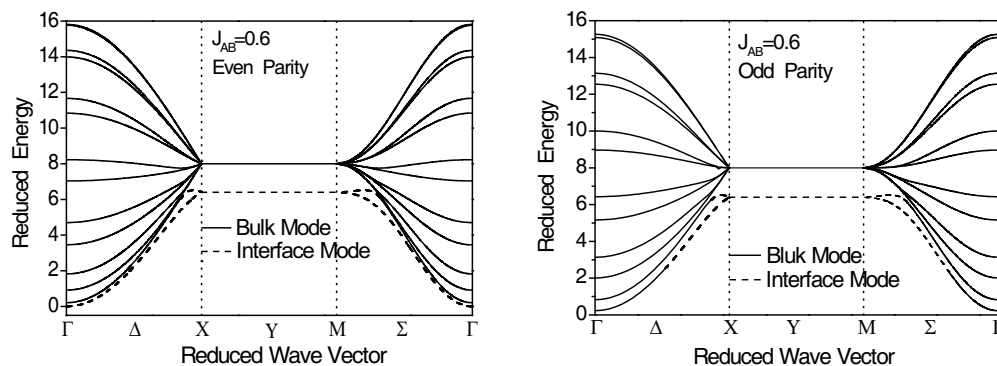


Figure 3: The same as Fig. 1, but the interlayer exchange coupling factor $J_{AB} = 0.6$.

in such a symmetric system with periodic boundary. At same extreme case, the interface mode will disappear, for instance, as the Figure 2 shows. When the interlayer exchange is equals to the bulk exchange, all the SSWs modes can transmit into the bilayer system, and the interface mode will disappear (See Figure 2), hence, property of the SSWs is identical to a ferromagnetic slab. There is only one interface mode with even parity, and it exists in the entire in-plane directions (k_x, k_y) . In comparison, the spin wave mode with odd parity may show two interface modes, in which, the one with greater (smaller) energy is always exist and the other is transferred from bulk mode. For instance, as the right panel of the Figure 1 and Figure 3 show, the bulk mode (solid line) with greatest energy will transferred into an interface mode when its momentum in x direction k_x is large enough. The phenomenon of mode transition suggests that some SSW can not transmit through the bilayer system thoroughly.

For all interface coupling cases, the energy of the SSW modes claps on the Y axis of the reduced Brillouin zone, i.e., all the SSW mode take the same energy. Moreover, the total value of the spin wave energy is kept constant on the boundary of the reduced Brillouin zone. The degeneracy of the spin wave energy on Y axis is much different from the simple cubic lattice [22] and it is due to the symmetry of the bcc structure.

4. CONCLUSION

The mechanism of spin wave excitation and propagation in a symmetrical ferromagnetic multilayered structure is studied. The eigen value problem of the spin wave excitation in a bilayered ferromagnets with body centered crystal structures have been investigated by using the full quantum interface rescaling approach. The energy band of the spin waves in the ferromagnetic symmetric bilayers have been presented. The energy bands show that, bulk and interface modes have been excited in the bilayer system. In addition, the evolution behavior of the interface modes is determined by the interlayer coupling, in plane transmission properties and the parity.

ACKNOWLEDGMENT

This work was supported by National Natural Science foundation under grant 10762001 & 50901039 and the Specialized Research Fund for the Doctoral Program of Higher Education of China (Grant No. 20080126003).

REFERENCES

1. Camley, R. E. and D. L. Mills, *J. Appl. Phys.*, Vol. 82, 3058, 1997.
2. Puzskarski, H., *Surf. Sci. Rep.*, Vol. 20, 45, 1994.
3. Krawczyk, M., H. Puzskarski, J.-C. S. Levy, and D. Mercier, *J. Phys.: Condens. Matter*, Vol. 15, 2449, 2003.
4. Yun, G. and J. Yan, "Spin-wave excitation in Ferromagnetic multilayers," *Theories of the Electron-phonon Interaction and Spin-waves in Layered Materials*, edited by X. X. Liang et al., Inner Mongolia University Press, 1994.
5. Livesey, K. L., D. C. Crew, and R. L. Stamps, *Phys. Rev. B*, Vol. 73, 184432, 2006.
6. Demokritov, S. O., *J. Phys.: Condens. Matter*, Vol. 15, S2575, 2003.
7. Gao, C. L., A. Ernst, G. Fischer, W. Hergert, P. Bruno, W. Wulfhekel, and J. Kirschner, *Phys. Rev. Lett.*, Vol. 101, 167201, 2008.
8. Au, Y., R. Sooryakumar, K. Bussmann, et al., *Phys. Rev. B*, Vol. 67, 214409, 2003.
9. Cochran, J. F., *J. Magn. Magn. Mater.*, Vol. 212, 40, 2000.
10. Hong, Q. and Q. Yang, *Phys. Rev. B*, Vol. 47, 7897, 1993.
11. Yaniv, A., *Phys. Rev. B*, Vol. 28, 402, 1983.
12. Fröbrich, P. and P. J. Kuntz, *Physics Reports*, Vol. 432, 223, 2006.
13. Udvardi, L., L. Szunyogh, K. Palota's, and P. Weinberger, *Phys. Rev. B*, Vol. 68, 104436, 2003.
14. Costa, A. T., R. B. Muniz, and D. L. Mills, *Phys. Rev. B*, Vol. 68, 224435, 2003.
15. Puzskarski, H. and L. Dobrzynski, *Phys. Rev. B*, Vol. 39, 1819, 1989.
16. Puzskarski, H. and L. Dobrzynski, *Phys. Rev. B*, Vol. 39, 1825, 1989.
17. Puzskarski, H., R. Jozefowicz, B. Kolodziejczak, et al., *Surf. Sci.*, Vol. 352–354, 914, 1996.
18. Yun, G. H., J. H. Yan, and S. L. Ban, *Phys. Rev. B*, Vol. 46, 12045, 1992.
19. Yun, G. H., J. H. Yan, S. L. Ban, and X. X. Liang, *Surf. Sci.*, Vol. 318, 177, 1994.
20. Yun, G. H. and X. X. Liang, *Eur. Phys. J. B*, Vol. 35, 261, 2003.
21. Zhou, W. P., G. H. Yun, and X. X. Liang, *Phys. Rev. B*, Vol. 77, 104403, 2008.
22. Zhou, W. P., G. H. Yun, and X. X. Liang, *Eur. Phys. J. B*, Vol. 55, 35, 2007.
23. Zhou, W. P., G. H. Yun, and X. X. Liang, *Chin. Phys. B*, Vol. 18, 5496, 2009.
24. Holstein, T. and H. Primakoff, *Phys. Rev.*, Vol. 58, 1098, 1940.

Analysis Propagation Characteristics of the Surface Plasmon Polariton Trench Waveguides by Method of Lines

T. T. Minh^{1,2}, K. Tanaka², and M. Tanaka²

¹Researching Department of Furuno Electric Co., LTD, Japan

²Department of Electronics and Computer Engineering, Gifu University, Japan

Abstract— A numerical study on the complex propagation constants of the surface plasmon polariton (SPP) trench waveguide constructed of gold by the method of lines (MoL) is performed. The dependences of propagation characteristics on the trench depth and the wavelength are investigated. The validity and limitations of the results are examined by comparing the present results with those calculated using the effective index method (EIM) and the finite-difference time-domain (FDTD). It is interesting that the counter-intuitive phenomenon of SPP trench waveguide is found by using MoL. The cut-off condition is significantly decreased and strong field confinement can be obtained by filling dielectric inside the trench depth.

1. INTRODUCTION

Construction of optical circuits on nanometric scales has attracted the attention of many researchers in the fields of nanophotonics and nanooptics [1, 2]. The diffraction limit of light makes it difficult to construct optical devices with dimensions that are much smaller than optical wavelengths and that have much higher integration densities than current optical integrated circuits. Recent theoretical and experimental studies have shown that optical circuits that use surface plasmon polaritons (SPPs) are promising candidates for future optical integrated circuits. Optical waveguides based on SPPs can be miniaturized much further than conventional diffraction-limited optical waveguides [3], opening up the possibility of developing nanometric integrated optical circuits. Although SPPs can travel no more than a few micrometers before extinguishing, such distances will be sufficiently long for future nanometric integrated optical circuits.

Recently, various geometries have been proposed to achieve confinement of the plasmon-polariton in the plane transverse to the propagation direction. Among these proposals, the plasmon-polariton guided by a rectangular grooves (trenches) and triangular (V-shaped) in metal is particular interesting [4–6]. The propagation characteristics of SPP trench have been investigated by the effective index method (EIM) [5] and 3D-FDTD [6]. However, the accuracy and the fundamental characteristics of SPP trench waveguide have been not been sufficiently revealed.

The method of lines (MoL) is a well-known and effective numerical technique and has been explored in a number of studies for calculating the propagation constants, including those of SPP waveguides [7, 8]. The authors have also successfully used the MoL to calculate the propagation constants of SPPs in a metallic hollow rectangular waveguide with high accuracy [7], and propagation characteristics of a SPP gap waveguide [8]. The MoL is expected to give more accurate results than the FDTD and EIM, because it partially employs analytical solutions, whereas FDTD is a purely numerical method, EIM is an approximate analytical method. However, to the best of our knowledge, the computation of the propagation constants of the SPP trench waveguide by the MoL has not been reported.

In this paper, we present a numerical investigation of the SPP trench waveguide by the method of lines (MoL). We calculate the dependences of the complex propagation constants on the waveguide sizes and on the optical wavelength. The fundamental, important, and interesting characteristics of the SPP waveguides have been investigated in detail. It is found that the possibility of decrease cut-off condition and strong field confinement inside trench depth can be obtained by filling dielectric.

2. GEOMETRY OF PROBLEM

The geometry of problem considered in the present study is shown in Fig. 1, this structure is described by three-layer structure, in which a rectangular gap is sandwiched by metallic layer and air layer. The rectangular hole has dimensions of $w \times d$ in the x - y plane with dielectric material filled shown in Fig. 1. We assume that the length of the waveguide in the z direction is infinite. In this paper, we calculate the complex propagation constant of SPP mode that propagates along the z -direction in Fig. 1 and consider the fundamental mode only. We employ the method of lines

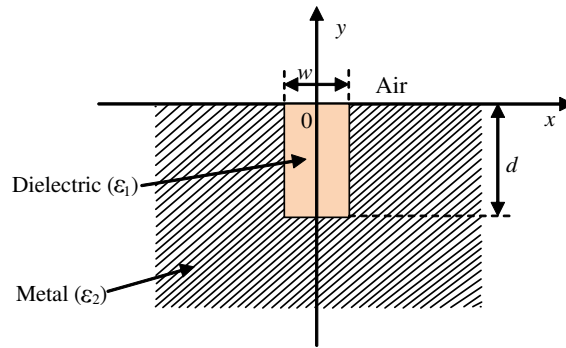


Figure 1: The geometry of the problem of the surface plasmon trench waveguide under consideration.

(MoL) to solve the complex and generalized eigenvalue problem in the two-dimensional cross section of the SPP waveguide shown in Fig. 1.

3. COMPARISON OF NUMERICAL RESULTS BY MOL WITH THOSE BY OTHER METHODS

In this section, we consider the first mode of a trench waveguide without filled dielectric, the metal that constitutes the surface plasmon trench waveguide is gold (Au) with a relative permittivity of $\epsilon_2/\epsilon_0 = -131.95 - j12.65$ at the wavelength $\lambda = 1550$ nm. The phase constant β and attenuation constant α normalized by the free space wavenumber defined as $jk_z/k_0 = \alpha + j\beta$, and propagation length L defined as $L = \lambda/2\alpha$.

The light transmission through the channel plasmon polariton trench waveguide (rectangular grooves), the field distributions of the trench are confined at two top corners and decreases nearly to zero at the trench bottom as shown in Figs. 2(a), (b), and (c). The field confinement decrease with the decreasing of trench depths d due to the mode penetrate larger into the depth in the air, these corresponds to normalized phase constant decrease and propagation length increase respectively. For the cases of the trench depth d decrease nearly to the cutoff size as Fig. 2(a), the field distribution being extended progressively outside of the trench, the propagation length is increased significantly since the mode near to free mode.

The dependences of normalized phase constant β and propagation length L on the trench depth d were presented in Figs. 3(a) and (b) respectively by comparison among our method (MoL) with the Effective index method (EIM) [5], and the numerical method (3D-FDTD) [6] for the case of $\lambda = 1550$ nm and trench widths $w = 500$ nm and 300 nm. The normalized phase constant β calculated by FDTD agrees with our results and the results obtained by EIM as shown in Fig. 3(a), however the results of propagation length obtained by FDTD [13] show that propagation length decrease with decreasing of trench depth d , this is unreasonable and contrary to results obtained by our method and EIM. It is interesting that the propagation length obtained by MoL is slightly decreasing before increasing significantly as trench depth decreasing while the authors of Ref. [5] have concluded that "this feature is not found for trench CPP (channel plasmon polariton) modes whose propagation length increases monotonously with the decrease of the trench depth" as shown in Fig. 3(b).

4. THE DEPENDENCE OF THE PROPAGATION CONSTANT ON WAVELENGTH

It is more intuitive to observe the characteristics of SPP trench waveguide by investigating dependences of the normalized phase constant β and attenuation constant α of the SPP trench waveguide made of gold on trench depth d with the various of wavelengths $\lambda = 1550$ nm, 1033 nm and 775 nm, the results are shown in Fig. 4. Attenuation constant α is first increases with the decrease of trench depth, starting to rapidly decrease only when the depth becomes close to the cutoff value, it is counterintuitive feature for SPP trench waveguide.

5. HIGH FIELD CONFINEMENT BY FILLING DIELECTRIC INTO CORE

The feature of the SPP trench waveguide is the field distribution mainly confine at the top of two corners, the field will be extended outside of the trench such as Fig. 5(a). From viewpoint confine the field distribution into core and tradeoff between normalized phase constant β and normalized

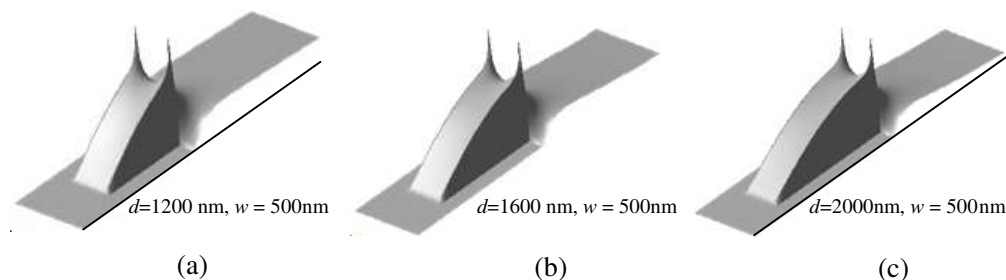


Figure 2: Typical distributions of the main electric field components $\Re[Ex(x, y)]$ of the SPP trench waveguide for the first mode. (a) $w \times d = 500 \text{ nm} \times 1200 \text{ nm}$, (b) $w \times d = 500 \text{ nm} \times 1600 \text{ nm}$, (c) $w \times d = 500 \text{ nm} \times 2000 \text{ nm}$.

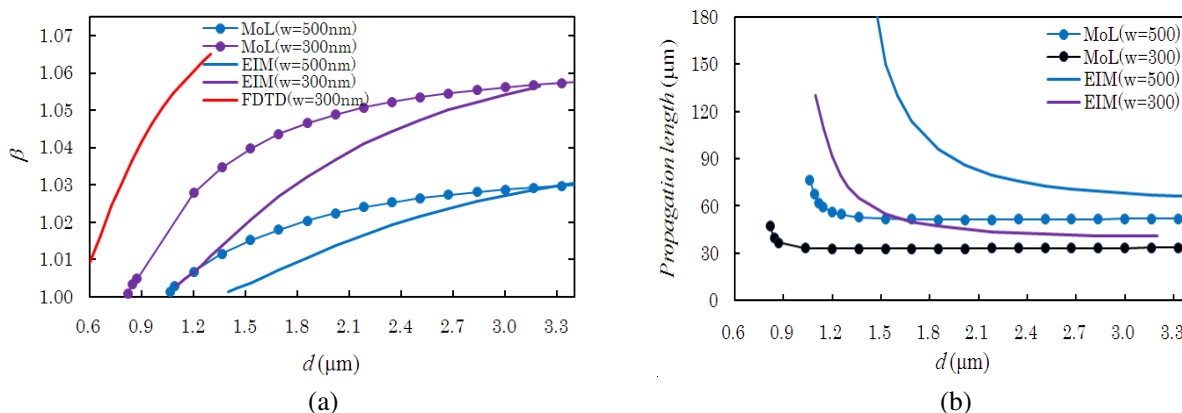


Figure 3: The dependences of the normalized propagation constant β and propagation length L on the trench depth d for the first mode with trench-widths $w = 500 \text{ nm}$, 300 nm at wavelength $\lambda = 1550 \text{ nm}$ (constructed of gold). Circle symbols denote the results for MoL, blue, violet curves denote the results for the EIM and red curve denote the results for the FDTD.

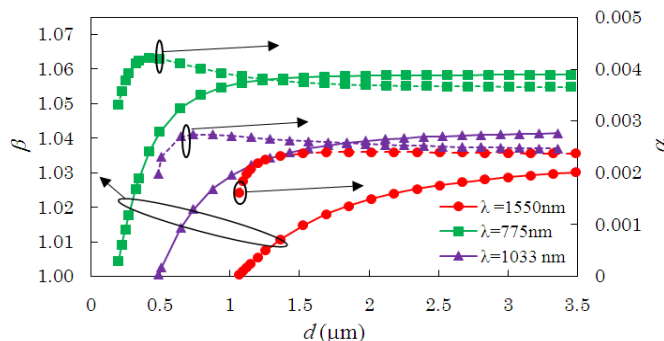


Figure 4: The dependences of normalized phase constant β and normalized attenuation constant on the wavelengths and the trench depth d with trench width $w = 500 \text{ nm}$ for the first mode (constructed of gold). Circle, triangle, square symbols denote the results for $\lambda = 1550 \text{ nm}$, 1033 nm and 775 nm in respectively.

attenuation constant α , we implement to fill the various values of dielectrics $n = 1.0, 1.44, 2.0, 3.0$ into trench slot, the main field distribution of the first mode E_x as shown in Figs. 5(a)–(c), and (d) in respectively. The results shown that the tendency of field distributions being confined strongly at the center of trench depth with the increase of the dielectric constant. These results show that normalized phase constants increase significantly together with strong confinement inside the trench depth in respectively. These interesting results will be very important for the applications of trench waveguide. In particularly, the cut-off condition for trench waveguide is decreased significantly with filled dielectric inside trench depth Figs. 6(a) and (b). However, the normalized phase constants are obtained simultaneously with increase of normalized attenuation constants. So these results are very important in order to find the optimum trade-off among the characteristics of strongly field

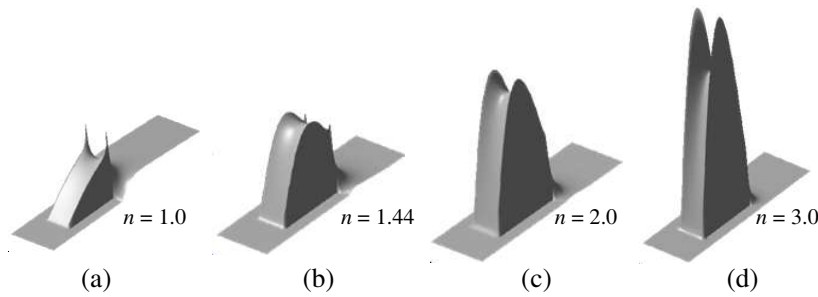


Figure 5: Typical distributions of the main electric field components $\Re[Ex(x, y)]$ of the trench waveguide $w \times d = 500 \text{ nm} \times 1200 \text{ nm}$, at wavelength $\lambda = 1550 \text{ nm}$ for the first mode where trench depth is filled by various dielectric. (a) $n = 1.0$, (b) $n = 1.44$, (c) $n = 2.0$, (d) $n = 3.0$.

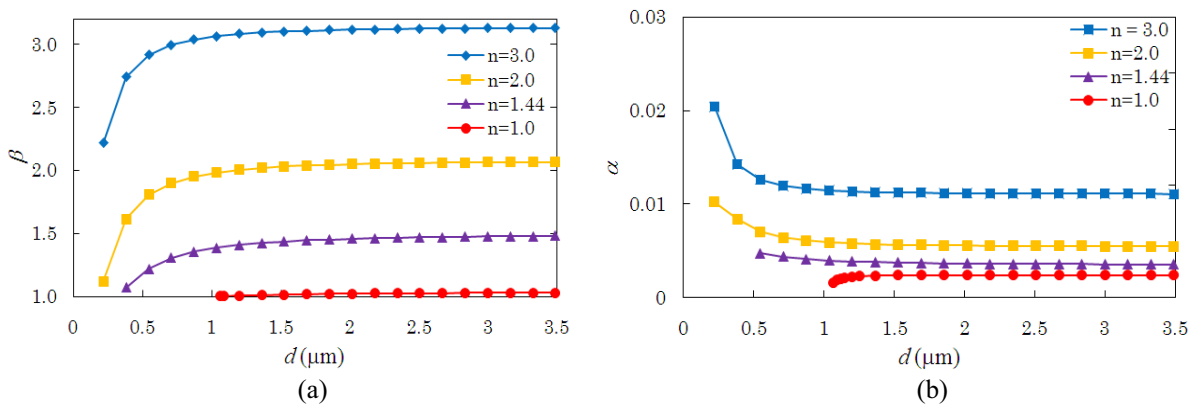


Figure 6: The dependence of normalized phase constant β and normalized attenuation constant α on the trench depth d for the first mode with trench-width $w = 500 \text{ nm}$, filled dielectric in at wavelength $\lambda = 1550 \text{ nm}$ (constructed of gold). Circle, triangle, rectangular and rhomb symbols denote the results for the dielectric inside trench depth $n = 1.0, 1.44, 2.0$ and 3.0 in respectively.

confinement, the waveguide size and propagation length.

6. CONCLUSIONS

A numerical study on the complex propagation constants of a surface plasmon polariton (SPP) trench waveguide made of the gold by the method of lines (MoL) has been performed. The dependences of complex propagation constants on the sizes and the wavelength of waveguide were investigated. The limitations of the previous results obtained by FDTD and EIM have been shown by comparing with ours. The counter-intuitive phenomenon of SPP trench waveguide has been found. Strong confinement can be achieved simultaneously with decrease of cut-off condition by filling various dielectric into trench depth. The results of the present study are important for additional theoretical and experimental research into SPP waveguide, nanometric optical circuits as well as applications.

REFERENCES

1. Ohtsu, M., K. Kobayashi, T. Kawazoe, T. Yatsui, and M. Naruse, *Principles of Nanophotonics*, Chapman & Hall, 2008.
2. Ohtsu, M. and H. Hori, *Near-field Nano-optics: From Basic Principles to Nano-fabrication and Nano-photonics*, Plenum Pub. Corp., 1999.
3. Takahara, J., S. Yamagishi, H. Taki, A. Morimoto, and T. Kobayashi, "Guiding of a one-dimensional optical beam with nanometer diameter," *Opt. Lett.*, Vol. 22, 475–477, 1997.
4. Tanaka, K. and M. Tanaka, "Simulations of nanometric optical circuits: Open-type surface plasmon polariton gap waveguide," *Jpn. J. Appl. Phys.*, Vol. 42, L585–L588, 2003.
5. Bozhevolnyi, S. I., "Effective-index modeling of channel plasmon polaritons," *Opt. Express*, Vol. 14, 9467–9476, 2006.

6. Chang, S. H. and T. C. Chiu, "Propagation characteristics of the supermode based on two coupled semi-infinite rib plasmonic waveguides," *Opt. Express*, Vol. 15, 1755–1761, 2007.
7. Minh, T. T., K. Tanaka, and M. Tanaka, "Complex propagation constants of surface plasmon polariton rectangular waveguide by method of lines," *Opt. Express*, Vol. 16, 9378–9390, 2008.
8. Tanaka, K., T. T. Minh, and M. Tanaka, "Analysis of propagation characteristics in the surface plasmon polariton gap waveguides by method of lines," *Opt. Express*, Vol. 17, 1078–1092, 2009.

General Study on Coherent Beam Combining of Interferometric Fiber Laser Arrays

J. Cao, Q. Lu, J. Hou, and X. Xu

College of Opto-electronic Science and Engineering, National University of Defense Technology
Changsha, Hunan, China

Abstract— In this paper, coherent beam combining of N -laser interferometric array fabricated with 2×2 couplers is theoretically studied. By investigating phase locking of the interferometric array, the conditions needed to get high-efficiency beam combining of this array are given. It is found that the gains of the array do not only provide the mechanism of longitudinal-mode competition, but also affect the phase-locked state of the array because of the detuning between the laser frequency and atomic frequency. In spite of that, it is also proved that the cold-cavity analysis is valid to predict the performance of the array. Furthermore, the results suggest that the interferometric array should be more suitable to combine no more than 10 lasers.

1. INTRODUCTION

Coherent beam combining of fiber laser arrays is a promising way to achieve high-power lasers with good beam-quality [1]. The interferometric fiber laser arrays (IFLA) is a sort of arrays for coherent beam combining [2–4]. The IFLA is fabricated by adding ion-doped fiber (as the gain medium) in each arm of fiber interferometer. It was experimentally demonstrated that this array could make a small quantity of fiber lasers coherently combined (i.e., phase-locked) without any active control. This phenomenon is considered as self-organization, and thus, the IFLA is one category of self-organized laser arrays. In experiments, 50 W and 200 W laser beams were obtained from two-laser IFLAs with all-fiber [3] and free-space [4] configurations, respectively. The self-organization of the IFLAs was revealed as the result of longitudinal-mode competition in the compound cavity of the array [2, 5–7]. However, presently, the theoretical understanding of this array is still limited: most of experimental results were interpreted with cold-cavity analysis which can not give a clear picture about the effect of gains [2, 7]; although the model presented in Refs. [5, 6] took gains into account, only two and four-laser IFLAs were studied in these references. In this paper, a general study will be given on the IFLAs, which will be of great help to understand the scaling of the interferometric arrays.

In this paper, we focus our discussion on phase locking of IFLA which plays an important role on coherent beam combining of the array. With help of the model given in Ref. [5], we deduce the phase-locked states of the N -laser IFLA. The phase-locking conditions needed to get high-efficiency beam combining of this array are given. The effect of gain on phase locking of the array is discussed. The valid of the cold-cavity analysis is studied. The effect of bandwidth on the coherent beam combining of the array is also briefly discussed.

2. DESCRIPTION OF THE N -LASER INTERFEROMETRIC ARRAY

The configuration of the N -laser IFLA is given in Fig. 1. The array is fabricated with 2×2 couplers and single-mode fibers. FBGs (fiber Bragg gratings) are used as the cavity mirrors with high (~ 1) reflectivity. The laser fields of the array which can be described by a set of differential equations with boundary conditions, i.e.,

$$\pm c \frac{dA_m^{(\pm)}(x)}{dx} = g_m(x) A_m^{(\pm)}(x) \quad (1)$$

$$\pm c \frac{d\varphi_m^{(\pm)}(x)}{dx} = -(\omega_{cm} - \omega) - \frac{(\varpi - \omega) g_m(x)}{\gamma_{\perp}} \quad (2)$$

$$\begin{aligned} & -\gamma_{//} [g_m(x) - g_{0m}] - g_m(x) \cdot \left\{ \left[A_m^{(+)}(x) \right]^2 + \left[A_m^{(-)}(x) \right]^2 \right\} \\ & - 2g_m(x) A_m^{(+)}(x) A_m^{(-)}(x) \cos \left[\varphi_m^{(+)}(x) - \varphi_m^{(-)}(x) + 2k_m x \right] = 0 \end{aligned} \quad (3)$$

where $A_m^{(\pm)}(x)$ and $\varphi_m^{(\pm)}(x)$ are the amplitude and phase of the complex slow-varying envelope of laser fields. The superscripts “+” and “-” represent right-going and left-going fields, respectively.

The subscript $m = 1, 2, \dots, N$ represents N elementary fiber lasers. $g_m(x)$ (g_{0m}) is the gain (pump) coefficient. ω is the laser frequency, ϖ is the atomic frequency. $\omega_{cm} = ck_m$ is the resonance frequency of the m th cavity; c is the velocity of light in vacuum; k_m is the wave vector. γ_{\perp} and $\gamma_{//}$ are transverse and longitudinal relaxation rates, respectively. Two boundary conditions are

$$\begin{pmatrix} \mathbf{A}_1^{(+)}(0, t) \\ \mathbf{A}_2^{(+)}(0, t) \\ \vdots \\ \mathbf{A}_m^{(+)}(0, t) \\ \vdots \\ \mathbf{A}_N^{(+)}(0, t) \end{pmatrix} = \mathcal{F} \begin{pmatrix} \mathbf{A}_1^{(-)}(0, t) \\ \mathbf{A}_2^{(-)}(0, t) \\ \vdots \\ \mathbf{A}_m^{(-)}(0, t) \\ \vdots \\ \mathbf{A}_N^{(-)}(0, t) \end{pmatrix}, \quad \begin{pmatrix} \mathbf{A}_1^{(-)}(L, t) \\ \mathbf{A}_2^{(-)}(L, t) \\ \vdots \\ \mathbf{A}_m^{(-)}(L, t) \\ \vdots \\ \mathbf{A}_N^{(-)}(L, t) \end{pmatrix} = \mathcal{F}' \begin{pmatrix} \mathbf{A}_1^{(+)}(L, t) \\ \mathbf{A}_2^{(+)}(L, t) \\ \vdots \\ \mathbf{A}_m^{(+)}(L, t) \\ \vdots \\ \mathbf{A}_N^{(+)}(L, t) \end{pmatrix} \quad (4)$$

where $\mathbf{A}_m^{(\pm)}(x) = A_m^{(\pm)}(x) \exp[i\varphi_m^{(\pm)}(x)] \exp(\pm ik_m x)$. \mathcal{F} and \mathcal{F}' represent transfer characteristics of Feedback and Coupling sections (see Fig. 1), respectively, which are determined by the configurations of these sections.

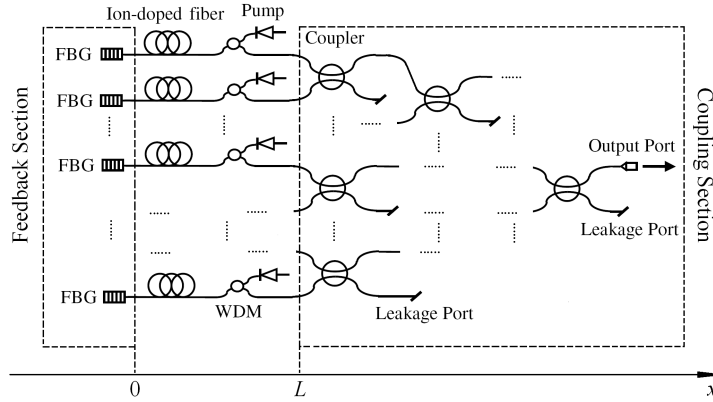


Figure 1: The configuration of N -laser interferometric fiber laser array.

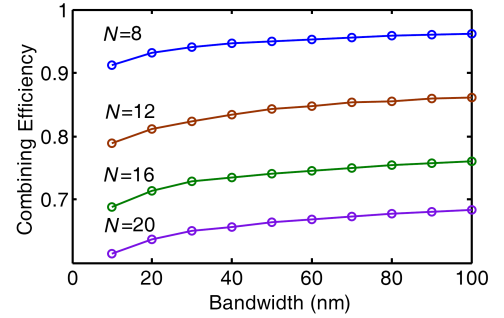


Figure 2: Plots of combining efficiency via the bandwidth of the compound cavity of array.

3. COHERENT BEAM COMBINING OF THE N -LASER INTERFEROMETRIC ARRAY

Note that the effect of coherent beam combining of IFLA is mainly determined by the phase-locked states of the array. Thus, we pay our attention on phase locking of IFLA in this paper. Because all the elementary lasers in IFLA share the same output port, all the laser fields $\mathbf{A}_m^{(-)}(L, t)$ come from the common laser field $\mathbf{A}^{(-)}(L_{out})$ ($x = L_{out}$ is the position of the output face). When these laser fields pass through each branch of the array and return to the output face, the laser field $\mathbf{A}^{(+)}(L_{out})$ can be expressed as (Eqs. (1), (2) and (4) are used here)

$$\mathbf{A}^{(+)}(L_{out}) = \sum_{m=1}^N \alpha_m \beta_m G_m \mathbf{A}^{(-)}(L_{out}) \exp \left\{ i \frac{2\omega}{c} l_m + i \delta \varphi_{R,m} + \frac{i(\varpi - \omega)}{\gamma_{\perp}} \ln \left[\frac{A_m^{(+)}(L) A_m^{(-)}(0)}{A_m^{(+)}(0) A_m^{(-)}(L)} \right] \right\} \quad (5)$$

where l_m is the optical path length of the m th elementary laser cavity which is defined by the FBG and the output face; $G_m = A_m^{(+)}(L) / A_m^{(-)}(L)$ represents the total gain of the m th elementary lasers of the array. Note that the transfer matrix of 2×2 coupler can be written as [8]

$$F_{cm} = \begin{pmatrix} \sqrt{1 - \varepsilon_m} & i\sqrt{\varepsilon_m} \\ i\sqrt{\varepsilon_m} & \sqrt{1 - \varepsilon_m} \end{pmatrix}, \quad (m = 1, 2, \dots) \quad (6)$$

where ε_m is the percentage of the input power coupled crossly into the other port, then

$$\alpha_m = \prod_{j=1}^{S_m} (-\varepsilon_j), \quad \beta_m = \prod_{j=1}^{(M_m - S_m)} (1 - \varepsilon_j) \quad (7)$$

Here, it is assumed that there are M_m couplers in the m th elementary lasers, and in S_m of M_m couplers, the laser field is coupled crossly into the other port. Eq. (5) indicates that the intensity of $\mathbf{A}^{(+)}(L_{out})$ is related to the laser frequency ω . As was discussed in Refs. [5, 6], because of mode competition, the frequency of the dominant longitudinal mode (i.e., the output laser frequency) should correspond to the maximum intensity of $\mathbf{A}^{(+)}(L_{out})$ and satisfy following conditions (see Eqs. (5) and (7)):

$$\begin{aligned} & \frac{2\omega}{c}(l_m - l_j) + (S_m - S_j)\pi + (\delta\varphi_{R,m} - \delta\varphi_{R,j}) \\ & + \frac{(\varpi - \omega)}{\gamma_{\perp}} \left\{ \ln \left[\frac{A_m^{(+)}(L) A_m^{(-)}(0)}{A_m^{(+)}(0) A_m^{(-)}(L)} \right] - \ln \left[\frac{A_j^{(+)}(L) A_j^{(-)}(0)}{A_j^{(+)}(0) A_j^{(-)}(L)} \right] \right\} = 2q\pi, \\ & (j, m = 1, 2, \dots, N; \quad j \neq m; \quad q = 0, \pm 1, \pm 2, \dots) \end{aligned} \quad (8)$$

Equation (8) indicates that the longitudinal mode(s) dominant in the mode competition can make(s) the elementary lasers phase-locked and exported with in-phase state, as long as the frequency of the dominant longitudinal mode(s) can satisfy all the equations given in Eq. (8). However, if there is no such a longitudinal mode to satisfy Eq. (8), the elementary lasers can not be phase-locked with in-phase state, which will reduce the combining efficiency of the array. Therefore, to realize high combining efficiency, there must be, at least, a longitudinal mode satisfying Eq. (9)

Equation (8) also implies that the frequency ω of the dominant longitudinal mode is not only affected by the length of elementary laser cavity, but also affected by the gain and FBG of elementary lasers. Then, there comes out a question whether the cold-cavity analysis (which appears to ignore the effect of gain [2, 7]) is suitable to analyze IFLA. After following discussion, it will be found that Eq. (8) is not contrary to the cold-cavity analysis. The reason can be given as follows. Consider the last two terms in left side of Eq. (8) as a source of length disturbance of elementary laser cavities, i.e., assume that

$$\delta l_m = \frac{c}{2\omega} \left\{ \delta\phi_{R,m} + \frac{(\varpi - \omega)}{\gamma_{\perp}} \ln \left[\frac{A_m^{(+)}(L) A_m^{(-)}(0)}{A_m^{(+)}(0) A_m^{(-)}(L)} \right] \right\} \quad (9)$$

Then, Eq. (11) can be reduced as

$$\frac{2\omega}{c} [(l_m + \delta l_m) - (l_j + \delta l_j)] + (S_m - S_j)\pi = 2q\pi \quad (10)$$

Equation (13) indicates that the frequency is only determined by the lengths $(l_m + \delta l_m)$ of elementary laser cavities. Actually, in the cold-cavity analysis, the effects of gain and FBG in Eq. (8) have been taken into account as a source of length disturbance of elementary laser cavities.

In experiment, IFLAs are often fabricated with symmetric configuration (i.e., all the elementary lasers are built with identical components), and the couplers are also properly chosen to make elementary lasers combined with the same intensity to obtain the most visible effect of beam combining [2–4]. In this case, we can know that the parameters in Eq. (8) have the following relationships, i.e.,

$$r_m = r_j, \quad \delta\varphi_{R,m} = \delta\varphi_{R,j}, \quad G_m = G_j \quad (11)$$

Then, Eq. (8) can be reduced as

$$\frac{2\omega}{c}(l_m - l_j) + (S_m - S_j)\pi = 2q\pi \quad (12)$$

which indicates that gain has no effect on the dominant longitudinal mode in the interferometric array with symmetric configuration.

Equation (11) gives C_N^2 conditions which need to be satisfied by the dominant longitudinal mode to realize in-phase state. Besides that, the dominant longitudinal mode should also satisfy the resonance conditions of N elementary lasers [5]. Thus, the dominant longitudinal mode should satisfy $(C_N^2 + N)$ conditions. Among these conditions, there are N independent ones. It means that the number of conditions of the dominant longitudinal mode increase with the number of elementary lasers. Therefore, it is more difficult to find a dominant longitudinal mode to satisfy all these N conditions with the number of elementary lasers, which will reduce combining efficiency and output stability of the array.

One way to improve the performance of the array is to make the bandwidth of the array as broad as possible (e.g., use broadband components) [2]. Here, with the help of the cold-cavity model of Ref. [7], we give the variation of the combining efficiency of the array with the bandwidth by numerical computation (see Fig. 2, the parameter values used here are the same as those used in Ref. [7], and the random length deviations of elementary laser cavities are in the range of $[-0.1\text{ m}, 0.1\text{ m}]$). From Fig. 2, it can be found that the improvement of the combining efficiency is limited with the increase of the bandwidth. Actually, Fig. 2 implies that the combining efficiency is determined by the number of elementary lasers. It is suggested that the interferometric array should be used to combine no more than 10 lasers to ensure high ($> 90\%$) combining efficiency.

4. CONCLUSION

In this paper, we make a general discussion on coherent beam combining of N -laser IFLA by studying phase locking of this array. It is found that the gains of the array do not only provide the mechanism of longitudinal-mode competition, but also affect the phase-locked state of the array. The results also reveal that the dominant longitudinal mode in the mode competition should satisfy N independent conditions to realize high-efficiency beam combining. It implies that the combining efficiency should be decrease with the increase of N (i.e., the number of elementary lasers of the array). The effect of bandwidth on the coherent beam combining of this array is also briefly discussed. It is suggested that the elementary lasers of the interferometric array should be no more than 10 lasers to ensure high ($> 90\%$) combining efficiency.

ACKNOWLEDGMENT

The authors would like to acknowledge the support from the Research Centre of Supercomputing Application, National University of Defense Technology.

REFERENCES

1. Fan, T. Y., "Laser beam combining for high-power, high-radiance sources," *IEEE J. Sel. Top. Quantum Electron.*, Vol. 11, No. 3, 567–577, 2005.
2. Shirakawa, A., K. Matsuo, and K. Ueda, "Fiber-laser coherent array for power scaling of single-mode fiber laser," *Proc. SPIE*, Vol. 5662, 482–487, 2004.
3. Mangir, M. S., "200 W self-organized coherent fiber arrays," *Conference on Lasers and Electro-Optics/Quantum Electronics and Laser Science and Photonics Applications Systems Technologies, Technical Digest (CD)*, paper CMDD4, Optical Society of America, 2005.
4. Wang, B., E. Mies, M. Minden, and A. Sanchez, "All-fiber 50 W coherently combined passive laser array," *Opt. Lett.*, Vol. 34, No. 7, 863–865, 2009.
5. Cao, J., Q. Lu, J. Hou, and X. Xu, "Dynamical model for self-organized fiber laser arrays," *Opt. Express*, Vol. 17, No. 7, 5402–5413, 2009.
6. Wu, T., W. Chang, A. Galvanauskas, and H. G. Winful, "Model for passive coherent beam combining in fiber laser arrays," *Opt. Express*, Vol. 17, No. 22, 19509–19518, 2009.
7. Cao, J., J. Hou, Q. Lu, and X. Xu, "Numerical research on self-organized coherent fiber laser arrays with circulating field theory," *J. Opt. Soc. Am. B*, Vol. 25, No. 7, 1187–1192, 2008.
8. Agrawal, G. P., *Applications of Nonlinear Fiber Optics*, Elsevier Science, USA, 2001.

The Effect of Temperature on the Soliton Propagation in Photorefractive SBN Crystal in One Dimension

Alireza Keshavarz¹, Farzin Emami², Mohsen Hatami³, and Parviz Elahi¹

¹Department of Physics, Faculty of Science, Shiraz University of Technology
P. O. Box 313-71555, Shiraz, Iran

²Optoelectronic Research Center, Shiraz University of Technology
P. O. Box 313-71555, Shiraz, Iran

³Department of Atomic and Molecular Physics, Faculty of Physics, Yazd University
P. O. Box 741-89195, Yazd, Iran

Abstract— The evolution of propagation of soliton is simulated in photorefractive SBN crystal in one dimension by numerical solution of the wave equation. Our simulation shows the strong stability of the soliton under propagation. Also we investigate the temperature effects on the evolution of the soliton by Crank-Nicholson method. As a result, the photorefractive soliton is stable although it is bending towards the biased external electric field. This bending effect can be controlled by the amount of the temperature and the external field. The outcome can be used in fabrication of all optical switching elements.

1. INTRODUCTION

Spatial solitons that do not spread owing to diffraction when they propagate have been investigated by many researchers because of their possible applications in photonic devices. Studying in this area shows that such solitons can be used to control the light by light. Today's solitons are known as self-guided localized beams propagating in nonlinear media that do not require waveguide. These optical fields satisfy in self-consistency principle.

In especial case, photorefractive (PR) screening solitons, have been shown to exhibit very interesting behavior in one and two dimensions. These solitons result from the nonlinear and nonlocal characteristics of the PR effect, which was first discovered in 1966 by Askin. PR solitons have three additional properties that make them considerable. The first is that in spite of the fact that many spatial solitons need a large initial operating power for their formation, PR medium support the soliton generation at low optical levels in order of micro-watts. The second is the wavelength dependence of material response. So, one can generate solitons with microwatts power and use the waveguides induced by these solitons to guide high power beams at other wavelengths that the material is less sensitive. The third property of PR solitons is that they are stable self-trapping optical beams in both transverse dimensions. In fact PR solitons were the first optical spatial solitons which were observed to be self-trapped in both transverse dimensions in a bulk material. Over the last decade several types of PR solitons have been discovered in biased PR crystals: quasi-steady state, screening and photovoltaic solitons. Recently, vector solitons and their interactions coupled soliton pairs and also two-photon solitons were predicted and observed. The theories of the soliton propagation predict that PR solitons propagate along a straight line with their shape reminds unchanged during the propagation. However, the effect of temperature on the evolution causes the self-deflection of the soliton during the propagation. This effect occurs when the diffusion process is taking into account. In this paper we consider diffusion term in dynamical evolution equation and the temperature dependence of the soliton propagation in biased PR Strontium-Barium-Niobate (SBN) crystal are investigated numerically.

2. THEORY

Let us assume that, the optical beam is linearly polarized along x and the external biased electric field is applied in the same direction. This field is necessary for the creation of solitons and modulates the refractive index of the medium via the Pockels linear electro-optic effect. In our study for SBN crystal the effective electro-optic tensor is r_{33} , so the perturbed refractive index is given by $\hat{n}^2 = n_0^2 - n_0^4 r_{33} E_{sc}$, where n_0 is unperturbed index of refraction, E_{sc} is the induced space-charge field, which is introduced in Kukhtarev et al. model as

$$E_{sc} = E_0 \frac{I_d}{1 + I_d} - \frac{K_B T}{e} \frac{\partial I / \partial x}{I + I_d}, \quad (1)$$

where $I = I(x, z) = I_d |U|^2$ is the power density of the normalized optical beam amplitude U under slow varying envelope condition. I_d is the so called dark intensity which is a material parameter proportional to the conductivity of the crystal that accounts for the rate of thermally generated electrons. E_0 is the space-charge field in the dark region of the crystal. The scalar propagation equation, with negligible absorption and by using the normalized coordinate can be written in dimensionless form as

$$i\partial_z U + \frac{1}{2}\partial_{xx} U - \beta \frac{U}{1 + |U|^2} + \gamma \frac{\partial_x |U|^2}{1 + |U|^2} U = 0. \tag{2}$$

The dimensionless quantities β and γ are associated with the processes of drift and diffusion respectively and are given by $\beta = (\frac{k_0}{x_0})^2 (\frac{1}{2} n_0^4 r_{33}) E_0$, $\gamma = (\frac{K_B T}{2e}) (k_0^2 x_0 n_0^4 r_{33})$. Here x_0 is an arbitrary spatial scale and $k_0 = \frac{2\pi}{\lambda_0}$ is the free space wavevector of the incident field. The common method for solving the wave Eq. (2) transforms this into the integral equation and then solves it numerically. But in the following, we will solve the wave equation directly by using the numerical Crank-Nicolson method for partial differential equations.

Studies of numerical simulation for formation of PR screening soliton is performed for the case of SBN crystal with $n_0 = 2.35$, $r_{33} = 180 \text{ pm/V}$, and the propagation distance is taken as the crystal length. We assume that the crystal is biased by a constant voltage of 6.1 kV between electrodes which are separated by 14 mm and the dark intensity chosen is $I_d = 10^{-3}$. The incident beam launched into the crystal may be chosen as a Gaussian beam with a 12 μm FWHM spot size, and a wavelength $\lambda = 488 \text{ nm}$ is chosen as used in the experiment. The result of the numerical calculation of the single beam soliton solution of Eq. (2) is shown in Figure 1(a). This bright PR screening soliton changes the refractive index of the medium and creates a graded index waveguide as shows in Figure 1(b). This graded index waveguide results from the negative nonlinear change in the refractive index, which depends on the direction of the space-charge field with respect to the

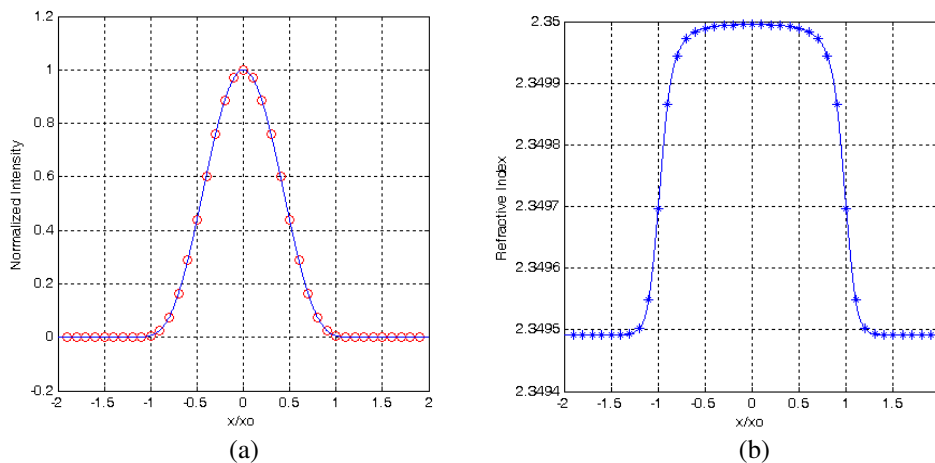


Figure 1: (a) Profile of the one-dimensional PR screening soliton intensity versus normalized axis. (b) The nonlinear refractive index profile induced by soliton intensity profile which is shown in Figure 1. This figure shows a negative nonlinear change in the refractive index and the creation of a graded index waveguide.

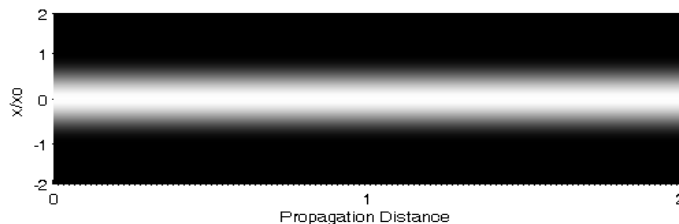


Figure 2: The stable propagation of one dimensional soliton in the length of the crystal without considering the diffusion term ($T = 0$).

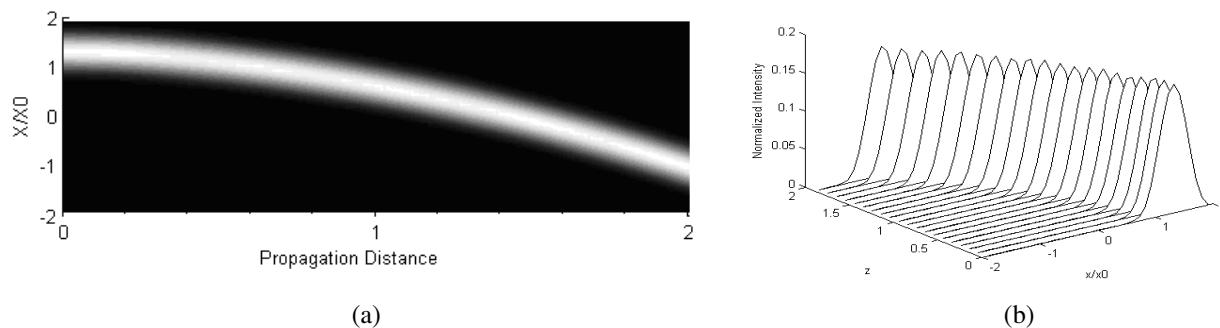


Figure 3: (a) The stable propagation of one dimensional soliton in the length of the crystal with considering the diffusion term ($T = 300K$). (b) Normalized intensity of soliton corresponding to Figure (a) when self-bending occurs.

principle axis of the crystal.

The soliton solution of Eq. (2) can be evaluated by using Crank-Nicholson numerical method. The Stable propagation of one dimensional soliton in the length of the crystal without considering the diffusion term ($T = 0$) are shown in Figure 2. This figure shows that the diffraction is compensated by the nonlinear response of the medium exactly. Thus, soliton propagates without any change along its diameter as well as intensity profile as expected. The effect of diffusion on the propagation of soliton is investigated at temperature $T = 300K$. As it can be seen in Figures 3(a) and (b), soliton propagates with constant shape and intensity, and just experiences self-deflection during propagation. The amount of bending can be controlled by the amount of temperature and the applied external field.

3. CONCLUSION

In conclusion, we have studied and simulated the effect of temperature on the soliton propagation in PR SBN crystal in one dimension. Crank-Nicholson numerical method has been used directly to solve wave equation. As results we have shown how the refractive index of the medium changes during propagation although it is bending toward the biased external electric field. This bending effect can be controlled by the amount of the temperature and the external field. The outcome can be used in fabrication of all optical switching elements.

REFERENCES

1. Kuroda, K., *Progress in Photorefractive Nonlinear Optics*, Taylor and Francis, 2002.
2. Stegeman, G., "Optical spatial solitons: Historical perspectives," *IEEE J. Select Top Quantum Electron.*, Vol. 6, 1419–1427, 2000.
3. Shi, T. and S. Chi, "Nonlinear photonic switching by using the spatial soliton collision," *Opt. Lett.*, Vol. 15, 1123–1125, 1990.
4. Evans, G., J. Blackledge, and P. Yardley, *Numerical Methods for Partial Differential Equations*, Springer Verlag, Berlin, 2000.
5. Zakery, A. and A. Keshavarz, "Simulation of the incoherent interaction between two bright spatial photorefractive screening solitons in one and two dimensions," *J. Phys. D: Appl. Phys.*, Vol. 37, 3409–3418, 2004.
6. Keshavarz, A. and Z. Khalifeh, "One-dimensional optical bright screening photovoltaic photorefractive solitons, soliton pairs and incoherent interaction between them in BaTiO₃ crystal," *Opt. Int. J. Light Electron. Opt.*, Vol. 120, 535–542, 2009.

Calculating Complex Propagation Constants of Finite-size Two Dimensional Photonic Crystal Waveguides

Y.-P. Chiou^{1,2}, K.-H. Chi³, and F.-C. Huang¹

¹Graduate Institute of Photonics and Optoelectronics
National Taiwan University, Taipei 10617, Taiwan

²Department of Electrical Engineering, National Taiwan University, Taipei 10617, Taiwan

³Department of Electrical Engineering and Computer Science
University of California, Irvine, CA 92697, USA

Abstract— Finite-difference method is adopted to calculate the complex propagation constants of leaky guided modes in finite-size photonic crystal waveguides. The formulation is modified to solve complex wavevectors for a given frequency, instead of solving resonant frequencies for a given real wavevector. Periodic boundary conditions are imposed along the propagation direction, and perfectly matched layers are imposed on the transverse domain boundaries. Square and hexagonal structures are investigated. Our results shows the logarithm of imaginary parts from the propagation constants are roughly proportional to the number of periods beside the waveguides, which is consistent to our semi-analytical derivation.

1. INTRODUCTION

Photonic crystals are periodic structures with different dielectric constants, which is similar to the crystal structures in semiconductors and has been drawn much attention due to their exotic behaviors [1–3]. One attractive property of photonic crystals is the photonic band gap, and wave propagation with frequencies in the band gap is prohibited. Adding line defects may result in guiding modes in the band gap, which is called band-gap guiding. It is very different from conventional index guiding based on total internal reflection. By applying this property, various photonic crystal waveguides and their applications have been proposed [4–6]. According to the theory, the photonic band gap exists in the infinitely periodic structure, and the guiding modes suffers no attenuation along the propagation if the dielectrics are lossless. However, in reality, devices are finite size. Light can still propagate in structures but with some leakage. In photonic crystal waveguides, guided waves suffer from attenuation due to the leakage caused by finite period “walls”, and their propagation constants become complex [7, 8].

In this paper, a modified finite-difference method [9, 10] derived from Maxwells equations is used to calculate wavevectors corresponding to a certain given frequency, while conventionally the resonant frequencies are found for a given wavevector. Such formulation has advantages that it can treat dispersive and lossy media, and leakage due to finite-size structures. Yee’s meshes are adopted. Periodic boundary conditions are imposed along the propagation direction, and perfectly matched layers are imposed on the transverse domain boundaries. The calculated wavevectors of leaky guided modes are complex numbers, and the imaginary parts of those wavevectors represent the attenuation due to leakage. The relationship between attenuation constants and the number of periods beside the wave guide is also shown in the following section.

2. FORMULATION

Time harmonic two dimensional Maxwell’s equations in transversely electric (TE) polarization are as follows.

$$\frac{\partial H_z}{\partial y} = j\omega\epsilon_0\epsilon_r E_x \quad (1)$$

$$-\frac{\partial H_z}{\partial x} = j\omega\epsilon_0\epsilon_r E_y \quad (2)$$

$$\frac{\partial E_x}{\partial y} - \frac{\partial E_y}{\partial x} = j\omega\mu_0 H_z \quad (3)$$

Equation (2) can be written as

$$E_y = -\frac{1}{j\omega\epsilon_0\epsilon_r} \frac{\partial H_z}{\partial x}. \quad (4)$$

Using (4) in (3), we have

$$\frac{\partial E_x}{\partial y} + \frac{\partial(\frac{1}{\epsilon_r} \frac{\partial H_z}{\partial x})}{j\omega\epsilon_0 \partial x} = j\omega\mu_0 H_z. \quad (5)$$

We assume the propagating direction is along y -direction, and express H_z and E_x by

$$E_x = e_x e^{-jk_y y}, \quad (6)$$

and

$$H_z = \frac{h_z}{\eta} e^{-jk_y y}, \quad (7)$$

where $\eta = \sqrt{\frac{\mu_0}{\epsilon_0}}$. Substituting (6) and (7) into (1) and (5), respectively, we have an eigen value equation

$$\begin{bmatrix} \frac{\partial}{\partial y} & (-jk_x + \frac{\partial}{\partial x})[\frac{1}{jk_0\epsilon_r}(-jk_x + \frac{\partial}{\partial x})] - jk_0 \\ -jk_0\epsilon_r & \frac{\partial}{\partial y} \end{bmatrix} \begin{bmatrix} e_x \\ h_z \end{bmatrix} = jk_y \begin{bmatrix} e_x \\ h_z \end{bmatrix}, \quad (8)$$

where $k_0 = \sqrt{\mu_0\epsilon_0}$ is the wavevector in free space. Equation (8) is discretized by Yee's meshes. Periodic boundary conditions are imposed along the propagation y direction, and perfectly matched layers are imposed on the transverse domain boundaries. The eigenvalue equation for TM polarization can also be derived similarly.

3. NUMERICAL RESULTS

First, we consider a square lattice with dielectric rods in air. The rod radius is $0.2a$, where a is the lattice constant. Relative dielectric constant of rods is 11.56, and that of air background is 1.00. A photonic crystal waveguide is made by removing one line of rods. To get better confinement and hence better fabrication tolerance, the normalized frequency is chosen at the middle of the frequency band gap, which is $0.35(c/a)$ in this case. Fig. 1 shows mode patterns of the waveguide with one and three rods beside the line defect. As expected, the more layers of rods beside the line defect, the less leakage, and hence less attenuation. Imaginary parts of the wavevectors for Figs. 1(a) and 1(b) are $(-0.016320j)(2\pi/a)$ and $(-0.000116j)(2\pi/a)$, respectively. Fig. 2 shows the attenuation constants for different number of periods beside guiding line defect. We can see that the relation is linear in semi-logarithmic plot, which means the attenuation decreases exponentially with increasing number of periods beside the line defect.

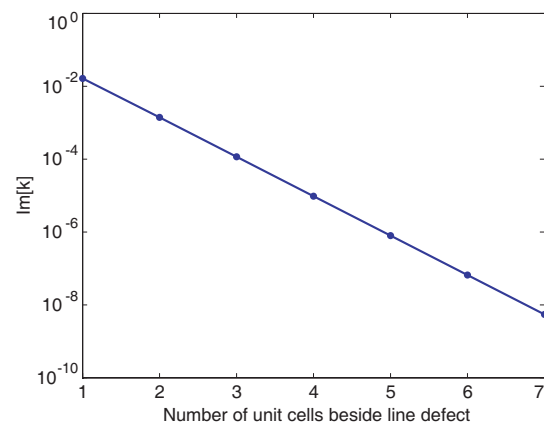
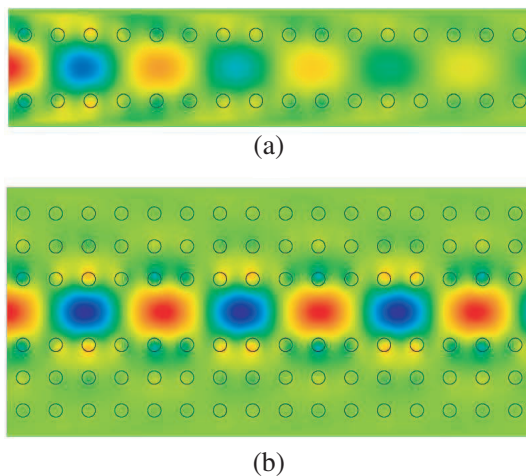


Figure 1: Mode patterns of photonic crystal waveguides with square lattice. (a) With only one period beside the guiding line defect. The corresponding wavevector is $k = (-0.216204 - 0.016320j)(\pi/a)$. (b) With three periods beside guiding line defect. The corresponding wavevector is $k = (-0.209902 - 0.000116j)(2\pi/a)$.

Figure 2: Attenuation constant for different number of periods beside the line defect in the square-lattice waveguides.

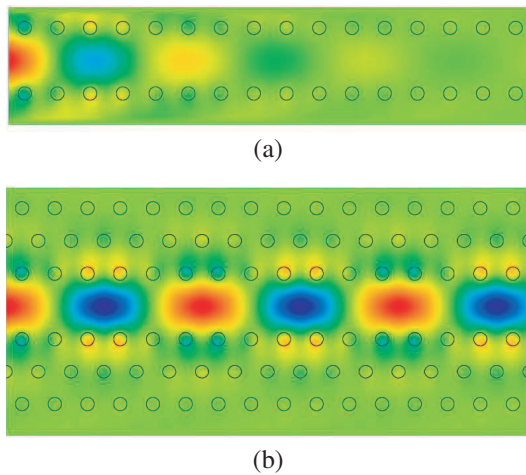


Figure 3: Mode patterns of photonic crystal waveguides with hexagonal lattice. (a) With only one period beside the guiding line defect. The corresponding wavevector is $k = (-0.180829 - 0.029670j)(2\pi/a)$. (b) With three periods beside guiding line defect. The corresponding wavevector is $k = (-0.166601 - 0.000195j)(2\pi/a)$.

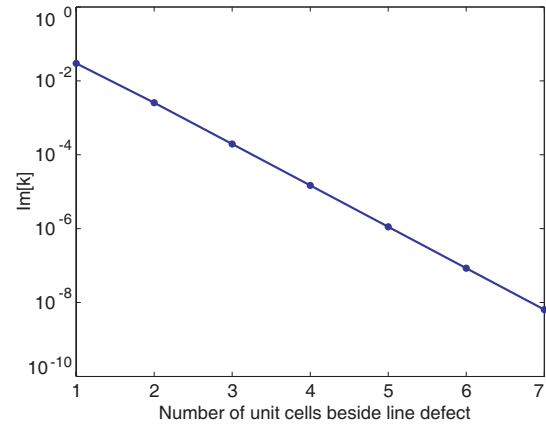


Figure 4: Attenuation constant for different number of periods beside the line defect in the hexagonal-lattice waveguides.

The behavior can be explained as follows. The attenuation is proportional to the leakage in the transverse direction due to finite periods beside the line defect. If the field decay in the transverse direction is large enough, the reflection from the outer boundary between the photonic crystal and the homogeneous region can be neglected. For example, the gap size is large and the operating frequency is chosen in the middle of the gap as in the case of Fig. 2. The leakage can be approximately proportional to the field at the outer boundary, which decays exponentially with the number of periods beside the line defect.

In addition to waveguides with square-lattice, we also analyze waveguides with hexagonal lattice. The radius of rods in the structures is also $0.2a$, and the dielectric constants are the same. The normalized frequency is $0.37(c/a)$. Mode patterns are shown in Fig. 3. The imaginary parts in Figs. 3(a) and (b) are $-0.029670j(2\pi/a)$ and $-0.000195j(2\pi/a)$, respectively. Fig. 4 shows the attenuation constants for different number of periods beside guiding line defect, which is approximately linear again.

4. CONCLUSION

We derived a modified finite-difference frequency domain method from Maxwells equations to solve the propagating characteristics of finite-size photonic crystal waveguides. Yee’s meshes are adopted, and periodic boundary condition and perfectly matched layers are imposed. Square and hexagonal lattices are investigated. The leakage is analyzed, and we find the attenuation for different number of periods beside the line defects are linear in the semi-logarithmic plots.

ACKNOWLEDGMENT

This work was supported in part by the National Science Council of Taiwan under grant NSC98-2221-E-002-170-MY3 and in part by the Excellent Research Projects of National Taiwan University under grant 98R0062-07.

REFERENCES

1. Yablonovitch, E., “Inhibited spontaneous emission in solid-state physics and electronic,” *Phys. Rev. Lett.*, Vol. 58, 2059–2062, 1987.
2. John, S., “Strong localization of photons in certain disordered dielectric superlattices,” *Phys. Rev. Lett.*, Vol. 58, 2486–2489, 1987.
3. Joannopoulos, J. D., R. D. Meade, and J. N. Winn, *Photonic Crystals: Molding the Flow of Light*, Princeton University Press, 1995.
4. Mekis, A., S. Fan, and J. D. Joannopoulos, “Bound state in photonic crystal waveguides and waveguide bends,” *Phys. Rev. B*, Vol. 58, 4809–4817, 1998.

5. Sharkawy, A., S. Shi, and D. W. Prather, “Electro-optical switching using coupled photonic crystal waveguides,” *Opt. Exp.*, Vol. 10, No. 20, 1048–1059, 2002.
6. Mekis, A., J. C. Chen, I. Kurland, S. Fan, P. R. Villeneuve, and J. D. Joannopoulos, “High transmission through sharp bends in photonic crystal waveguides,” *Phys. Rev. Lett.*, Vol. 77, 3787–3790, 1996.
7. Zhang, D. and H. Jia, “Numerical analysis of leaky modes in two-dimensional photonic crystal waveguides using Fourier series expansion method with perfectly matched layer,” *IEICE Trans. Electron.*, Vol. E90-C, No. 3, 613–622, 2007.
8. Li, S. and Y. Y. Lu, “Efficient Dirichlet-to-Neumann map method for leaky modes in photonic crystal waveguides,” *IEEE/LEOS 5th Workshop on Fibers and Optical Passive Components (WFOPC 2007)*, Th3A-5, Taipei, Taiwan, Dec. 2007.
9. Taflove, A. and S. C. Hagness, *Computational Electrodynamics: The Finite-difference Time-domain Method*, Artech House, Boston, 2000.
10. Berenger, J. P., “A perfect matched layer for the absorption of electromagnetic waves,” *J. Computat. Phys.*, Vol. 114, 185–200, 1994.

Level Set Method in EIT Image Reconstructions

J. Dědková, K. Ostanina, and Jan Mikulka

Department of Theoretical and Experimental Electrical Engineering, Brno University of Technology
 Kolejní 2906/4, Brno 612 00, Czech Republic

Abstract— In present there are a lot of different numerical methods, ways and approaches to obtain the stable and effective image reconstruction process, which can be used for efficient applications in physical and biological sciences. Electrical Impedance Tomography (EIT) belongs to methods which are very beneficial, especially in a medical imaging. This method is non-invasive technique and can be used very effectively for good detection of conductivity tissue changes. Unfortunately the back image reconstruction based on electrical impedance tomography is highly ill-posed inverse problem and it is necessary to find such techniques which offer stable, accurate and not too much time-consuming reconstruction process. This paper proposes new possibilities to improve the stability and the accuracy of today image reconstructions including the level set method.

1. INTRODUCTION

At the present time the image reconstruction problem is a widely investigated problem with many applications in physical and biological sciences. The Electrical Impedance Tomography can be used for reconstruction process. The theoretical background of EIT is given in [1]. The currents are applied through the electrodes attached to the surface of the object and the resulting voltages are measured using the same or additional electrodes. An arrangement of EIT system is shown in Fig. 1(left).

Finally the internal impedivity distribution is recalculated from the measured voltages and currents. The forward problem is well-posed, but the inverse problem is highly ill-posed. Various numerical techniques with different advantages have been developed to solve this problem. The common aim is to reconstruct the impedivity distribution in two or three dimensional models as accurately and fast as possible. Usually a set of voltage measurements is acquired from the boundaries of the determined volume, whilst it is subjected to a sequence of low-frequency current patterns, which are preferred to direct current ones to avoid polarization effects. Since the frequency of the injected current is sufficiently low, usually in the range of 10–100 kHz, EIT can be treated as a quasi-static problem. So we only consider the conductivity σ inside investigated object for simplicity. The scalar potential U can be therefore introduced, and so the resulting field is conservative and the continuity equation for the volume current density can be expressed by the potential U

$$\nabla \cdot (\sigma \nabla U) = 0 \tag{1}$$

Equation (1) together with the modified complete electrode model equations [2] are discretized by the finite element method (FEM) in the usual way. Using FEM we calculate approximate values of electrode voltages for the approximate element conductivity vector $\sigma(NE)$, NE is the number of finite elements. Furthermore, we assume the constant approximation of a conductivity

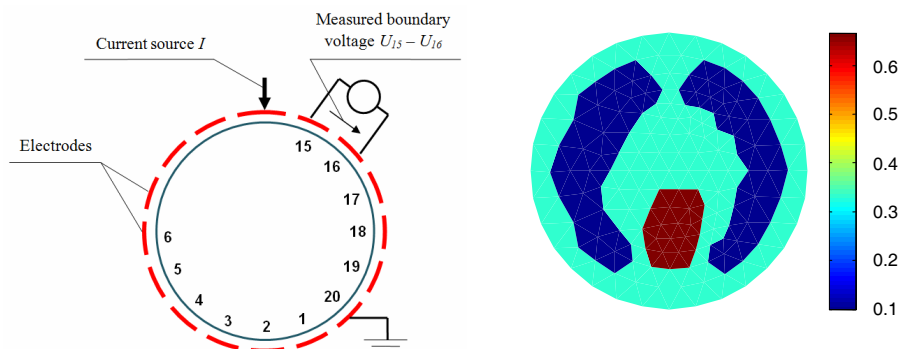


Figure 1: The arrangement of EIT system (left) and 2D model for simulation (right).

distribution σ on the finite element region. The forward EIT calculation yields an estimation of the electric potential field in the interior of the volume under certain Neumann and Dirichlet boundary conditions.

2. METHODS FOR SOLUTION OF INVERSE PROBLEM

The image reconstruction of EIT is an inverse problem, which is often presented as minimizing the suitable objective function $\Psi(\sigma)$ relative to σ . To minimize the objective function $\Psi(\sigma)$ we can use a deterministic approach based on the Least Squares method. Due to the ill-posed nature of the problem, regularization has to be used. First the standard Tikhonov Regularization method (TRM) described in [3] was used to solve this inverse EIT problem

$$\min_{\sigma} \Psi(\sigma) = \min_{\sigma} \left[\frac{1}{2} \sum \|U_M - U_{\text{FEM}}(\sigma)\|^2 + \alpha \|L\sigma\|^2 \right] \quad (2)$$

Here σ is the volume conductivity distribution vector in the object, U_M is the vector of measured voltages on the boundary, and $U_{\text{FEM}}(\sigma)$ is the vector of computed peripheral voltages relatively to σ , which can be obtained using FEM, α is a regularization parameter and L is a regularization matrix. For the solution of (2) we can apply the Newton-Raphson method and after the linearization we used the iteration procedure

$$\sigma_{i+1} = \sigma_i + (J_i^T J_i + \alpha L^T L)^{-1} (J_i^T (U_M - U_{\text{FEM}}(\sigma_i)) - \alpha L^T L \sigma_i) \quad (3)$$

Here i is the i -th iteration and J is the Jacobian for forward operator U_{FEM} . Unfortunately the iterative procedure is likely to be trapped in local minima and therefore a sophisticated algorithm must be taken into account to obtain the stable solution. It is necessary to mention that the stability of the TRM algorithm is also sensitive to the setting of correct starting values of unknown conductivity.

In recent years it is very common to identify regions with different image or material properties using the Level Set method (LSM) [4–7]. The level set idea is known to be a powerful tool to model evolution of interfaces and also has been used successfully to the inverse problem solution. Assuming known conductivity values the unknown conductivity interface can be solved by two methods. In the first method one can use values of Neumann data. The second method is used to obtain solution results in a thin layer along the boundary of an investigated region. The LSM has been also applied to solve elliptic inverse problem, where the unknown discontinuous coefficient has to be solved without the knowledge of both the values of the coefficient and interface between the regions having different coefficient values. By using results of solution or gradients of these results of the forward problem in the region, the coefficient can be accurately identified by utilizing LSM. In following we will consider the case where the conductivity is a piecewise constant function with possibility that conductivity values are unknown. The distribution of unknown conductivity σ can be described in terms of the level set function F depending on the position of the point r with respect to the boundary Γ between regions with different values of σ

$$\sigma(r) = \begin{cases} \sigma_{\text{int}} & \{r : F(r) < 0\} \\ \sigma_{\text{exp}} & \{r : F(r) > 0\} \end{cases}, \quad \Gamma = \{r : F(r) = 0\} \quad (4)$$

Then the final conductivity distribution $\sigma(r)$ is the steady state of the following time-dependent Hamilton-Jacobi equation

$$\frac{\partial \sigma}{\partial t} + F |\text{grad} \sigma| = 0, \quad t \rightarrow \infty \quad (5)$$

If the LSM is included smartly to the reconstruction algorithm we can obtain the very good tool for stable and accurate image reconstruction. To improve the stability and the accuracy of EIT image reconstructions new algorithm was created. This algorithm is based on both of mentioned methods TRM and LSM. During iteration process based on minimizing objective function $\Psi(\sigma)$ the boundary Γ is searched in accordance with request that the $\sigma(r)$ minimizes the $\Psi(\sigma)$, too. We suppose that the unknown conductivity distribution is given by a piecewise constant function $\sigma(NE)$.

3. EXAMPLES AND RESULTS

In this part we restrict a range of tasks to the objects with biological tissues only. The basic model of the simple 2D arrangement of the original conductivity distribution you can see in Fig. 1 (right). The conductivity of the homogenous region representing tissue is 0.333 S/m , the conductivity of the region representing heart (brown color) is 0.1 S/m and finally the conductivity of two regions representing lungs (dark blue color) is 0.667 S/m . The total number of FEM mesh elements is $NE = 300$. We assume that inside left region of lungs a subregion with different conductivity is located.

The aim is to find the location and correct values of conductivity inside this subregion. Two following examples demonstrate the results which we can obtain when we use suitable combination both of above mentioned methods. New algorithm for 2D model has been written in MATLAB 7.0.4.

During the reconstruction process the TRM was used to identify the locations and to specify exactly the conductivity values of non-homogenous regions. In the case of an unexpected finishing of iteration process caused by non-stability the LSM was applied to specify the locations of these regions. Finally, the TRM was applied again to specify the conductivity values, but only inside limited regions with non-homogeneity.

The results which can illustrate the reconstruction process are shown in Fig. 2 and Fig. 3. In Fig. 2, on the left you can see original conductivity distribution; subregion (with white line

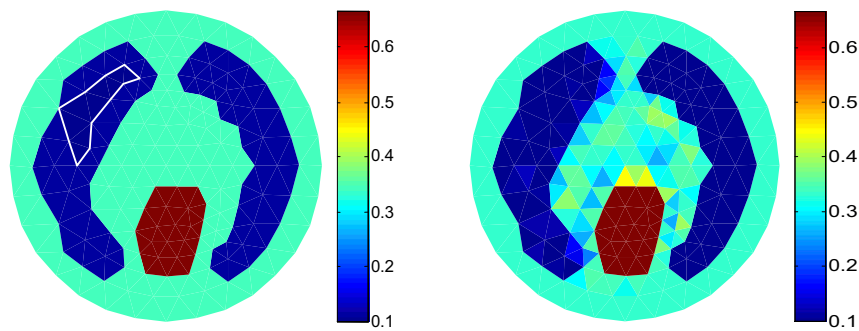


Figure 2: An original σ distribution (left), results after using TRM (right).

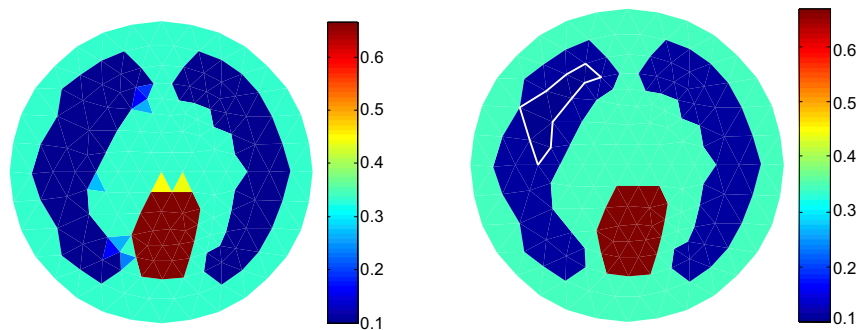


Figure 3: Reconstruction results after using LSM (left) and after the second using TRM.

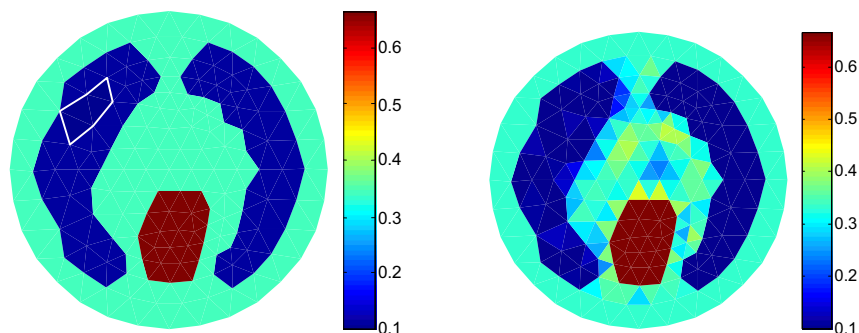


Figure 4: An original σ distribution (left), results after using TRM (right).

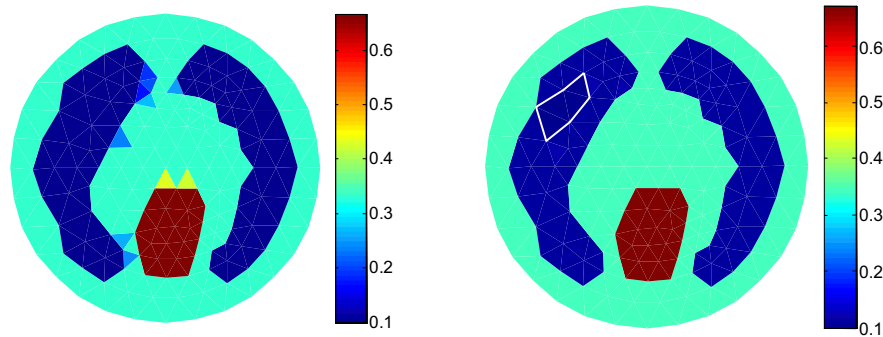


Figure 5: Reconstruction results after using LSM (left) and after the second using TRM (right).

boundary) has conductivity 80% of lungs conductivity. In the same figure on the right you can see result after first applying of TRM.

The results after using LSM are shown in Fig. 3 on the left. In Fig. 3, on the right you can see the final reconstruction result. The results of similar example are shown in Fig. 4 and Fig. 5. The unknown subregion is smaller in this case.

4. CONCLUSIONS

In this paper, a new practical approach to the reconstruction of non-homogeneities using EIT has been presented. Many numerical experiments performed during the above described research have resulted in the conclusion that the application of the TRM and LSM reconstruction algorithm has significant advantages over the TRM approach. We mostly obtain good accuracy using the TRM but there is often an unstable reconstruction process. We have introduced a level set approach for the elliptic inverse problem. In the paper the idea of new algorithm of the EIT image reconstruction is described, which combines advantages of the level set method and Tikhonov regularization method. This new way of an optimization process was used for the acquirement of more accurate reconstruction results in the specific cases. The new approach was tested on different shapes and sizes of non-homogenous subregions. Based on appreciable number of realized numerical tests we can summarize that the proposed algorithm ensures very good stability and very often the highest accuracy of reconstruction process in comparison with the algorithm which is based on the TRM only.

ACKNOWLEDGMENT

The research described in the paper was financially supported by the research program MSM 0021630503.

REFERENCES

1. Cheney, M., D. Isaacson, and J. C. Newell, "Electrical impedance tomography," *SIAM Rev.*, Vol. 41, No. 1, 85–101, 1999.
2. Somersalo, E., M. Cheney, and D. Isaacson, "Existence and uniqueness for electrode models for electric current computed tomography," *SIAM J. Appl. Math.*, Vol. 52, 1023–1040, 1992.
3. Vauhkonen, M., D. Vadász, P. A. Karjalainen, E. Somersalo, and J. P. Kaipio, "Tikhonov regularization and prior information in electrical impedance tomography," *IEEE Trans. Med. Eng.*, Vol. 17, 285–293, 1998.
4. Burger, M., "A level set method for inverse problems," *Inverse Problems*, Vol. 17, 1327–1356, 2001.
5. Sethiah, J., *A Level Set Methods and Fast Marching Methods*, Cambridge University Press, Cambridge, 1999.
6. Chan, T. and L. Vese, "Active contour without edges," *IEEE Trans. Imag. Proc.*, Vol. 10, 266–277, 2001.
7. Osher, S. and R. Fedkiw, *Level Set Methods and Dynamic Implicit Surfaces*, Springer-Verlag, New York, 2002.

An Effective Detection of Conductivity Changes in Biologic Tissue

T. Kríž, J. Dědková, and J. Mikulka

Department of Theoretical and Experimental Electrical Engineering, Brno University of Technology
Kolejní 2906/4, Brno 612 00, Czech Republic

Abstract— There are described positive and negative properties of weighty recent numerical techniques for a solution of electrical impedance tomography (EIT) inverse problem and their influences to the quality of image reconstruction. There are two different types of EIT image reconstructions, static and dynamic EIT. In static EIT, only the absolute conductivity in each element is computed and a picture of the internal organs of different conductivity is imaged. In dynamic EIT, temporal variations in conductivity are computed. Both types can be very useful especially in medical applications. The aim of this paper is to propose and realize a new algorithm for a successful detection of conductivity changes in biologic tissues. It is desirable to obtain high-quality reconstruction process because the medical imaging is a non-invasive and very helpful technique for a detection of pulmonary emboli, non-invasive monitoring of a heart function and a blood flow, or for the breast cancer detection. To obtain the stable reconstruction process for an effective detection of conductivity changes in biologic tissue we created a new algorithm based on Tikhonov regularization method (TMR) and level set method (LSM). An image reconstruction of EIT is an inverse problem. Solution is very dependent on initial parameters. There are tested two parameters in this article, parameter of regularization α and starting value of conductivity. The results are presented for tested parameters, their effect to reconstruction quality and speed of solution.

1. INTRODUCTION

The electrical impedance tomography (EIT) is a widely investigated problem with many applications in physical and biological sciences. Geophysical imaging is used for searching underground conducting fluid plumes near the surface and obtaining information about rock porosity or fracture formation. Another application of EIT is for example in non-destructive testing and identification of material defects like cracks or identification of corrosion in production materials. Medical imaging can be used primarily for the detection of pulmonary emboli, non-invasive monitoring of heart function and blood flow, and for breast cancer detection. The theoretical background of EIT is given in [1]. The principle of EIT is based on the back image reconstruction, which is highly ill-posed inverse problem. The aim is to reconstruct, as accurately and fast as possible, the internal conductivity or permittivity distributions in two or three dimensional models. The optimization necessitates algorithm that impose regularization and some prior information constraint.

2. BASIC PRINCIPLE OF USED METHODS

Let suppose an arrangement for EIT back reconstruction due to Fig. 1 (left). Further we will consider only the conductivity σ for simplicity. The scalar potential U can be therefore introduced, and so the resulting field is conservative and the continuity equation for the current density can be expressed by the potential U

$$\operatorname{div}(\sigma \operatorname{grad} U) = 0. \quad (1)$$

Equation (1) together with the modified complete electrode model equations are discretized by the finite element method (FEM) in the usual way. Using the FEM we calculate approximate values of electrode voltages for the approximate element conductivity vector σ ($NE \times 1$), NE is the number of finite elements, see Fig. 1 (right). Furthermore, we assume the constant approximation of the conductivity σ on each of all elements. The forward EIT calculation yields an estimation of the electric potential field in the interior of the volume under certain Neumann and Dirichlet boundary conditions. The FEM in two or three dimensions is exploited for the forward problem with current sources. Image reconstruction of EIT is an inverse problem, which is usually presented as minimizing the suitable objective function $\Psi(\sigma)$ relative to σ .

To minimize the objective function $\Psi(\sigma)$ we can use a deterministic approach based on the Least Squares method. Due to the ill-posed nature of the problem, regularization has to be used. It is possible to use the standard Tikhonov regularization method (TRM) described in [2] to solve

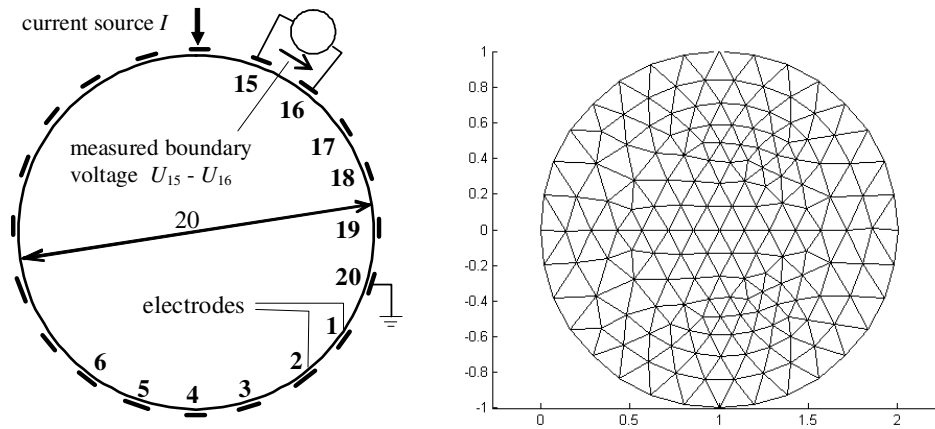


Figure 1: An arrangement for conductivity reconstruction, FEM grid with 300 elements and 167 nodes.

this inverse EIT problem. Then we have to minimize the objective function $\Psi(\sigma)$. Minimalize objective function $\Psi(\sigma)$ describe equation

$$\Psi(\sigma) = \frac{1}{2} \sum \|U_M - U_{FEM}(\sigma)\|^2 + \alpha \|L\sigma\|^2 \quad (2)$$

here σ is the unknown conductivity distribution vector in the object, U_M is the vector of measured voltages on the object boundary, $U_{FEM}(\sigma)$ is the vector of computed peripheral voltages in respect to σ which can be obtained using the FEM, α is a regularization parameter and L is a regularization matrix connecting adjacent elements of the different conductivities.

To obtain the solution of (2) we applied the Newton-Raphson method. This iterative procedure is commonly used in the EIT inverse problem for its fast convergence and good reconstruction quality. However, it is likely to be trapped in local minima and so additional regularization must be taken into account to obtain the stable solution. The stability of the TRM algorithm is a bit sensitive to the setting of the starting value of conductivity and to an optimal choice of the parameter α provides balance between the accuracy and the stability of the solution. The value of the parameter α can be adaptively changed during this iteration process. In this way we can obtain the stable solution with required higher accuracy of the reconstruction results. TRM is used to find regions with different conductivities and theirs near surroundings.

The level set method was applied to identifying of the location of the regions with different conductivities. Level set method is used to identify regions with different image or material properties [3–6]. The Level set method (LS) [3–5] is based on the deforming of a function ϕ . Then the border of object is given by the zero level of function ϕ . The evolution equation of the level set function ϕ in general form, described in [6] is

$$\frac{\partial \phi}{\partial t} + F |\text{grad} \phi| = 0 \quad (3)$$

here ϕ is level set function, F is speed function and t is time step.

The distribution of unknown conductivity can be described in terms of level set function F depending on the position of the point r with respect to the boundary D between regions with different values of conductivity. During the iteration process based on minimizing objective function $\Psi(\sigma)$ the boundary D is searched in accordance with the request that the $\sigma(r)$ minimize the $\Psi(\sigma)$

$$\sigma(r) = \begin{cases} \sigma_{int} \{r : F(r) < 0\} \\ \sigma_{ext} \{r : F(r) > 0\} \end{cases} \quad D = \{r : F(r) = 0\} \quad (4)$$

To improve the stability and the accuracy of EIT image reconstructions we created a new algorithm based on both of mentioned methods TRM and level set. During iteration process based on minimizing objective function $\Psi(\sigma)$ the boundary D is searched in accordance with request that the $\sigma(r)$ minimize the $\Psi(\sigma)$, too.

3. DESCRIPTION OF TASK

Model for the parameters testing (regularization parameter α and starting value of conductivity) is consist of homogenous region. There is defined an area with different conductivity (non-homogenous area) in this region. The parameters were tested on two models. There is one non-homogenous region in the first model Fig. 2 (left) and two non-homogenous regions in the second model Fig. 2 (right). Values of conductivity were defined in relation to usage in biomedicine. Value of homogenous region conductivity is 0.333 S/m (tissue) and value of non-homogenous region conductivity is 0.666 S/m (heart). There were found the final conductivity values identical as original ones Fig. 2. Objective function value and iterations count was monitored in testing process. These values were monitored before use of LSM when TRM found non-homogenous regions and theirs near surroundings (in tables marked *region*). There were also monitored the mentioned parameters after use of LSM when TRM was used for finding of final conductivity value (in tables marked *value*). The both models were tested with parameter α in the range 10^{-10} to 10^0 . Parameter α was changed during reconstruction process by 0.7. Starting conductivity value was set to 0.5 S/m (average value of the both tissue conductivities). The results of testing are in Table 1. When the parameter α is smaller then 10^{-10} the iterative solution is not stable. The both models were tested with starting conductivity and parameter alpha 10^{-7} . The models were tested for eight conductivities. Conductivity values were set to maximum of original conductivity 0.666 S/m, minimum of original conductivity 0.333 S/m, 150% of maximal original conductivity 1 S/m, 50% of minimal original conductivity 0.166 S/m, minimal value for stable solution 0.002 S/m, randomly set values to individual elements at interval $< 0.333; 0.666 >$ S/m and at interval $< 0.166; 1 >$ S/m. The results are in Table 2.

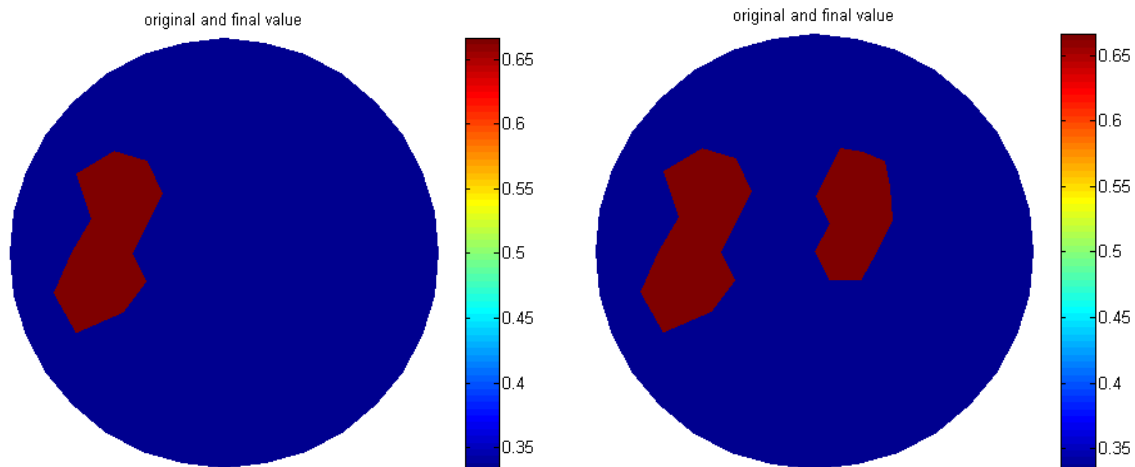


Figure 2: Original and found conductivity values.

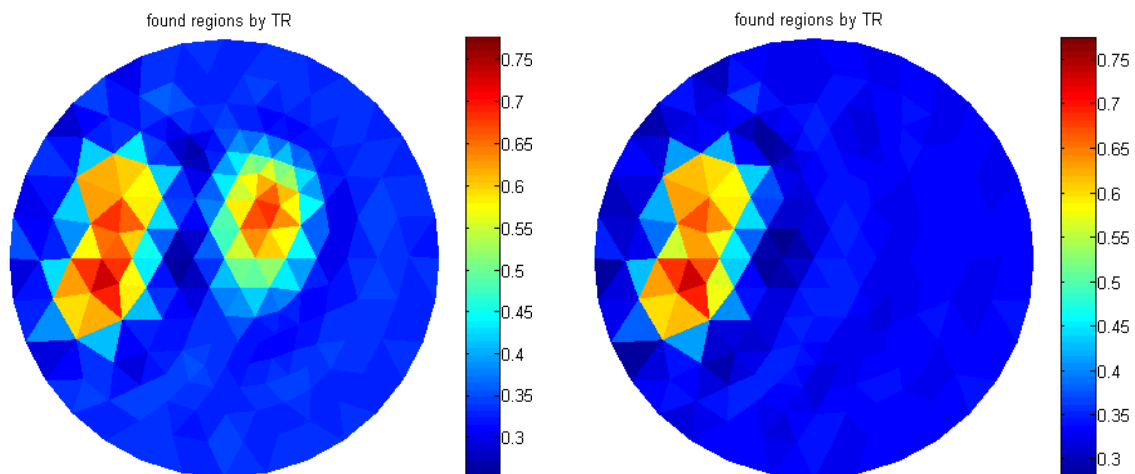


Figure 3: Found regions by TRM.

Table 1: Parameter α dependence.

α	one non-homogenous area					two non-homogenous areas				
	iterations			$\Psi(\sigma)$		iterations			$\Psi(\sigma)$	
	region	value	sum	region	value	region	value	sum	region	value
$1 \cdot 10^0$	284	71	355	$4.081 \cdot 10^{-8}$	$5.645 \cdot 10^{-23}$	475	186	661	$9.297 \cdot 10^{-8}$	$1.246 \cdot 10^{-22}$
10^{-1}	211	83	294	$4.698 \cdot 10^{-8}$	$1.259 \cdot 10^{-23}$	332	187	519	$8.919 \cdot 10^{-8}$	$4.824 \cdot 10^{-23}$
10^{-2}	139	82	221	$4.175 \cdot 10^{-8}$	$3.194 \cdot 10^{-23}$	172	196	368	$8.326 \cdot 10^{-8}$	$6.696 \cdot 10^{-23}$
10^{-3}	75	85	160	$4.808 \cdot 10^{-8}$	$1.637 \cdot 10^{-23}$	102	177	279	$9.043 \cdot 10^{-8}$	$1.944 \cdot 10^{-22}$
10^{-4}	46	83	129	$4.271 \cdot 10^{-8}$	$2.137 \cdot 10^{-23}$	79	64	143	$2.191 \cdot 10^{-9}$	$9.684 \cdot 10^{-23}$
10^{-5}	23	84	107	$4.921 \cdot 10^{-8}$	$7.479 \cdot 10^{-23}$	52	65	117	$2.507 \cdot 10^{-9}$	$9.385 \cdot 10^{-23}$
10^{-6}	7	79	86	$2.729 \cdot 10^{-8}$	$5.120 \cdot 10^{-24}$	36	70	106	$2.143 \cdot 10^{-9}$	$4.711 \cdot 10^{-23}$
10^{-7}	9	66	75	$1.102 \cdot 10^{-8}$	$4.341 \cdot 10^{-23}$	42	55	97	$4.730 \cdot 10^{-9}$	$6.809 \cdot 10^{-23}$
10^{-8}	8	52	60	$1.618 \cdot 10^{-10}$	$7.401 \cdot 10^{-23}$	19	70	89	$5.060 \cdot 10^{-9}$	$4.127 \cdot 10^{-23}$
10^{-9}	9	50	59	$4.838 \cdot 10^{-12}$	$2.934 \cdot 10^{-22}$	25	82	107	$4.161 \cdot 10^{-9}$	$2.049 \cdot 10^{-23}$
10^{-10}	8	62	70	$1.432 \cdot 10^{-10}$	$6.349 \cdot 10^{-23}$	18	84	102	$2.927 \cdot 10^{-12}$	$2.203 \cdot 10^{-22}$

Table 2: Starting conductivity value dependence.

σ [S/m]	one non-homogenous area					two non-homogenous areas				
	iterations			$\Psi(\sigma)$		iterations			$\Psi(\sigma)$	
	region	value	sum	region	value	region	value	sum	region	value
0.333	9	54	63	$1.196 \cdot 10^{-8}$	$9.546 \cdot 10^{-23}$	39	62	101	$2.436 \cdot 10^{-9}$	$3.775 \cdot 10^{-23}$
0.666	12	64	76	$1.425 \cdot 10^{-8}$	$5.971 \cdot 10^{-23}$	38	65	103	$2.436 \cdot 10^{-9}$	$6.511 \cdot 10^{-23}$
0.5	9	66	75	$1.102 \cdot 10^{-8}$	$4.341 \cdot 10^{-23}$	42	55	97	$4.730 \cdot 10^{-9}$	$6.809 \cdot 10^{-23}$
1.0	9	60	69	$1.102 \cdot 10^{-8}$	$3.627 \cdot 10^{-23}$	40	57	97	$2.463 \cdot 10^{-9}$	$1,280 \cdot 10^{-22}$
0.1666	8	59	67	$1.199 \cdot 10^{-8}$	$7.564 \cdot 10^{-23}$	40	57	97	$2.436 \cdot 10^{-9}$	$1.737 \cdot 10^{-22}$
0.002	13	63	76	$1.425 \cdot 10^{-8}$	$3.600 \cdot 10^{-23}$	43	57	100	$2.437 \cdot 10^{-9}$	$3.140 \cdot 10^{-23}$
Rand (0.33–0.66)	12	56	68	$1.425 \cdot 10^{-8}$	$8.087 \cdot 10^{-23}$	41	53	94	$2.436 \cdot 10^{-9}$	$3.317 \cdot 10^{-22}$
Rand (0.166–1)	13	61	74	$1.177 \cdot 10^{-8}$	$2.531 \cdot 10^{-23}$	43	61	104	$2.436 \cdot 10^{-9}$	$1.129 \cdot 10^{-22}$

4. CONCLUSIONS

The effects of parameter α to iterations count and $\Psi(\sigma)$ value are in Table 1 for both models. We can see that optimal parameter α values are at interval $< 10^{-8}; 10^{-4} >$. Solution could be unstable for smaller values. Solution is not stable for parameter α smaller than 10^{-10} for both models. Iterations count is increasing very fast for parameter α greater than 10^{-4} . Iterations count is dependent on non-homogenous regions location. Final size of objective function $\Psi(\sigma)$ isn't depend on parameter α . It depends on non-homogenous regions location.

The effects of starting conductivity to iterations count and $\Psi(\sigma)$ value are in Table 2 for both models. If starting conductivity value was used at interval $< 0.002; 1 >$ the solution is always stable. Iterations count was independent on starting conductivity value. Final size of objective function $\Psi(\sigma)$ isn't depend on starting conductivity value. The Non-homogenous regions were started to be recognizing by TRM after 5–15 iterations for randomly distribution of starting conductivity on elements. It's identical with constant conductivity. It's proper to use the starting conductivity near an original value.

ACKNOWLEDGMENT

This work was supported within the framework of the project of the Grant Agency of the Czech Republic GACR 102/09/0314, grant Ministry of Industry and Trade FR-TI1/001 and by research plan No. MSM 0021630513 ELCOM, No. MSM 0021630516.

REFERENCES

1. Cheney, M., D. Isaacson, and J. C. Newell, “Electrical impedance tomography,” *SIAM Rev.*, Vol. 41, No. 1, 85–101, 1999.
2. Borsic, A., “Regularization methods for imaging from electrical measurement,” PH.D. Thesis, Oxford Brookes University, 2002.
3. Burger, M., “A level set method for inverse problems,” *Inverse Problems*, Vol. 17, 1327–1356, 2001.
4. Sethiah, J. A., *Level Set Methods and Fast Marching Methods*, Cambridge University Press, Cambridge, 1999.
5. Osher, S. and R. Fedkiw, *Level Set Methods and Dynamic Implicit Surfaces*, Springer-Verlag, New York, 2002.

Monitoring of Diseases Progression by MR

J. Mikulka

Department of Theoretical and Experimental Electrical Engineering
Brno University of Technology, Kolejní 2906/4, 612 00 Brno, Czech Republic

Abstract— This paper deals with methods for monitoring of development of diseases with using the nuclear magnetic resonance. The paper compares the methods for monitoring the qualitative and quantitative parameters in the NMR images. The main goal is usually comparing the observed images of the human tissues in the time. There are the surfaces, volumes and their changes in the time most often monitored. The typical examples of these objects are several tumors, tubers, polypus or discs of temporomandibular joint. The goal of these methods comparison will be selection of suitable method for monitoring of development of treatment of diseases in the human stomach with using the modern nuclear magnetic resonance tomograph and other approaches. The paper is made as research material for the future work.

1. INTRODUCTION

The advantages of the nuclear magnetic resonance were described in many publications. It is approach to acquisition of spatial data of soft tissues, most often of human organs. The main advantage is absolutely the fact of unproved negative effects of the electromagnetic radiation to human organism subject to prescribed hygienic regulations. The observed images of sensed object can be used for three-dimensional model creation after the application of suitable preprocessing methods. The reconstructed object after that can be useful for example to the better diagnosis in medical sciences, for quantitative or qualitative description of tissues, tumors etc. We can find several evaluations of tissues volumes in many cases. It can be useful for monitoring of used treatment efficiency. The typical example can be a tumor volume reduction etc. This article describes recently published approaches and methods used in medical applications as initial research for forthcoming project witch deals with monitoring of treatment of human stomach efficiency.

2. THE RESEARCH OF RECENTLY PUBLISHED APPROACHES

The common of all published application is a segmentation of MR images. The accuracy of results of tissue volume evaluation is very dependent on the results of segmentation. There are used several approaches of segmentation from simple thresholding to region growing or active contours (snakes). According to publication research it's clear, that the combination of two-dimensional MR segmentation of tissue slices and following evaluation of volume by number and thickness of slices is the most popular. In many cases we can find a manual tracing of the searched area and following volume evaluation.

2.1. Bone Tumor Segmentation, Neural Networks Classification [1]

Monitoring viable tumor bone area over time is important in the ongoing assessment of the effect of preoperative chemotherapy [1]. In this application, the feed-forward neural network is proposed to classify pixels into viable, non-viable, and healthy tissue. The processing consists of two steps. First, a pharmacokinetic model is used to summarize the temporal information in the perfusion sequence into three main parameters. These parametric images are used to derive multi-scale features, they encode the spatial information not present in the original parametric images.



Figure 1: Segmentation results. Left, pre-contrast images; center, histological mask; right, neural network classification, [1].

2.2. Estimation of Tumor Volume with Fuzzy-connectedness Segmentation [2]

Reproducible measurements of brain tumor volume are helpful in evaluating the response to therapy and the need for changing treatment plans. In this paper [2] there is used an adaptation of the fuzzy-connectedness segmentation to measure tumor volume. Segmentation was performed on axial and coronal gadolinium-enhanced and axial fluid-attenuated inversion recovery (FLAIR) images by using a fuzzy-connectedness algorithm, and tumor volumes were generated. Operator interaction was limited to selecting representative seed points within the tumor and, if necessary, editing the segmented image to include or exclude improperly classified regions.

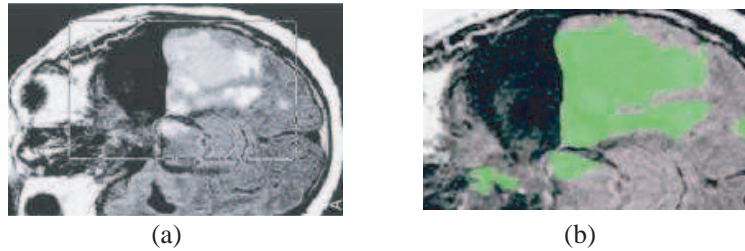


Figure 2: Images illustrate step 2: Segmentation of FLAIR images. (a), Placement of rectangular VOI around the area of presumed tumor and edema (FLAIR volume) on axial FLAIR images designated IF. (b), Delineated FLAIR volume displayed as a green overlay obtained after the deposition of seed points in the VOI [2].

2.3. Manual/Semiautomatic Tracing of Hippocampus [3]

There is some evidence that atrophy of certain medial temporal lobe structures may be present at early stages of cognitive decline, before dementia occurs [3]. There is a presentation of manual/semi-automated tracing method for segmentation of hippocampus of normal and demented subjects.

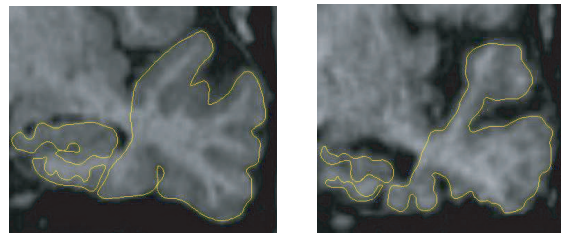


Figure 3: Hippocampus, entorhinal cortex, and temporal lobe were traced using strict anatomical boundaries. Left, normal; right demented [3].

2.4. Comparison of Tumor Volume Measurement in Subcutaneous Mouse XENOGRAFTS [4]

In animal studies tumor size is used to assess responses to anticancer therapy. Current standard for volumetric measurement of xenografted tumors is by external caliper, a method often affected by error. The aim of the present study [4] was to evaluate if microCT gives more accurate and reproducible measures of tumor size in mice compared with caliper measurements. Furthermore, they evaluated the accuracy of tumor volume determined from 18Ffluorodeoxyglucose (18F-FDG) PET. The tumor volume is there evaluated by the greatest longitudinal diameter (length) and the greatest transverse diameter (width), $Tumor\ volume = 1/2(length \times width^2)$.

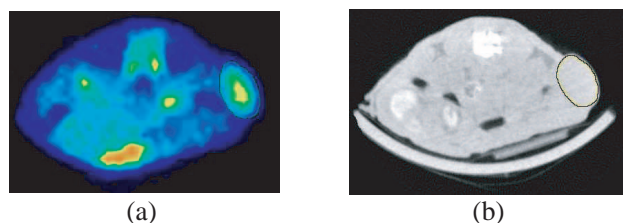


Figure 4: (a) PET and (b) microCT image of mouse with subcutaneous tumor [4].

2.5. MR Volumetry of Cortices [5]

The occurrence of damage in the entorhinal, perirhinal, and temporopolar cortices in unilateral drug-refractory temporal lobe epilepsy (TLE) was investigated with quantitative MR imaging. There was used an approach that consists of 4 steps. The images were magnified, interpolated, the outlines of each area were traced manually by a trackball-driven cursor and the volumes were evaluated by multiplying the areas by 2 mm thickness of slices [5].

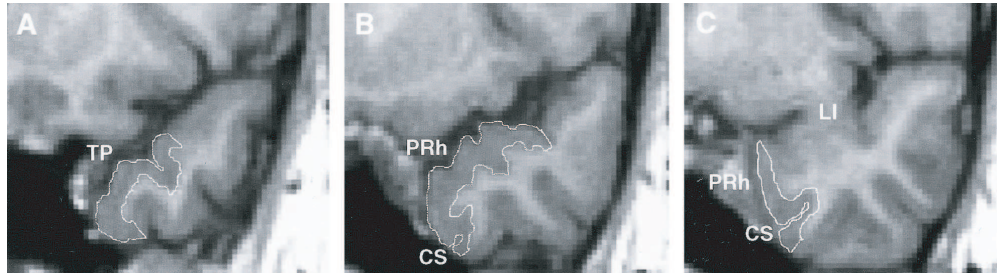


Figure 5: The example of manual tracing of coronal MR images [5].

3. CONCLUSION

This article shows possibilities of usage of image processing methods in quantitative parameters evaluation of scanned object by tomography methods. These methods are often used for assessment monitoring using volumetry – measuring of tumor volumes in the (human) tissues. This article is taken as initial study of methods and use of these image processing methods for the future work, which deals with an evaluation of treatment efficiency of the human stomach diseases.

ACKNOWLEDGMENT

This work was supported within the framework of the research plans MSM 0021630516, MSM 0021630513, grant Ministry of Industry and Trade FR-TI1/001 and project of the Grant Agency of the Czech Republic GA 102/09/0314.

REFERENCES

1. Frangi, A. F., et al., “Bone tumor segmentation from MR perfusion images with neural networks using multi-scale pharmacokinetic features. *Im and Vis Comp.* No. 19, 679–690, 2001. <http://citeseerx.ist.psu.edu/viewdoc/download;jsessionid=F04E632C74B7DEF2122D8F96BA779727?doi=10.1.1.19.6526&rep=rep1&type=pdf>.
2. Moonis, G., J. Liu, J. K. Udupa, and D. B. Hackney, “Estimation of tumor volume with fuzzy-connectedness segmentation of MR images,” *American Journal of Roentgenology*, No. 23, 1–8, 2002.
3. Eberling, J. L., “MR volumetry of hippocampus, entorhinal cortex, and temporal lobe at various stages of cognitive decline,” Center for Neuroscience, University of California, Davis, CA, http://idealab.ucdavis.edu/pubs/posters/wu_eberling_et_al_SF2000.pdf.
4. Jensen, M. M., “Tumor volume in subcutaneous mouse xenografts measured by microCT is more accurate and reproducible than determined by ¹⁸F-FDG-microPET or external caliper,” *BMC Medical Imaging*, Vol. 8, 1–9, 2008.
5. Jutila, L., “MR volumetry of the entorhinal, perirhinal and temporopolar cortices in drug-refractory temporal lobe epilepsy,” *American Journal of Neuroradiology*, Vol. 22, 1490–1501, Sep. 2001.

Photodynamic Therapy in the Dermatological Field and Enhanced Cutaneous Absorption of Photosensitizer

Makio Akimoto¹, Kazuhisa Maeda², Tokuya Omi³,
Tomonori Nishimura⁴, and Michio Miyakawa⁵

¹Kanto Gakuin University, 1-50-1, Mutsuurahigashi, Kanazawa-ku, Yokohama 236-8501, Japan

²Tokyo University of Technology, 1404-1, Katakura, Hachioji, Tokyo 192-0982, Japan

³Queen's Square Medical Center, 2-3-5, Minatomirai, Yokohama 220-6208, Japan

⁴Atom Giken Co., Ltd., 92-2, Katase, Fujisawa, Kanagawa 251-0032, Japan

⁵Niigata University, 8050 Ikarashi-2, Niigata 950-2181, Japan

Abstract— The combination of light and chemicals to treat skin diseases is widely practiced in the field of dermatology, and has led to the concept of photodynamic therapy in recent years. In PDT for skin cancer, 5-aminolevulinic acid is applied topically to the affected area to be absorbed percutaneously through passive diffusion, and typically requires 4–6 h before performing PDT. In this study, we attempted to reduce the absorption period in PDT by ionizing ALA using direct current pulsed iontophoresis and Bowen's disease. In all subjects, protoporphyrin IX production was confirmed after iontophoresis, and its production levels were comparable to the conventional occlusive dressing technique. Skin biopsies from the treated lesion showed the disappearance of tumour cells.

1. INTRODUCTION

In recent years, the application of optical technology to clinical medicine has been thriving. Many apparatus applying optical technology have been developed and are widely used in clinical settings; e.g., lasers have produced revolutionary results in surgery, most cases of chemical tests on specimens have been conducted using optical techniques, and automated assays have been developed, resulting in tremendous advances in patient diagnostics and medical examinations. Furthermore, a non-invasive treatment method has been recently developed, in which certain drugs given to the body are activated by light to exert their effects, and the therapeutic effects of this modality have drawn close attention. The modality is referred to as photodynamic therapy, and is based on the combined use of photosensitizers and photoradiation. That method administers a photosensitizer with affinity for the tumor cells, followed by light irradiation which results in the selective disruption of only the tumor cells in the body. Since photodynamic therapy (PDT) is less invasive than surgical therapy, it can be used in patients with serious complications and also in elderly patients, and it is being increasingly applied in many clinical fields, especially dermatology [1]. In the field of dermatology, it is widely recognized that PDT, in which an excitation light is applied to externally applied 5-aminolevulinic acid (5-ALA), a porphyrin precursor, is effective for the treatment of superficial malignant tumors of the skin. However, since the percutaneous absorption of photosensitizers is extremely low, treatment using these substances requires a long time, making it difficult to establish this method as a standard treatment modality and to apply it on an outpatient basis. In this study, PDT was optimized by introducing the photosensitizer into the skin within a short time by iontophoresis, which involves the application of a microelectric current to the skin to increase the percutaneous absorption of ionic drugs. The results of this study confirm that iontophoresis indeed enhances the percutaneous absorption of the photosensitizer within a short time, which dramatically reduces the time required for treatment. The findings of this study are reported herein. Since 5-ALA has an extremely low percutaneous absorbency, there are several methods to improve its absorption such as liposomal 5-ALA, and iontophoresis may dramatically enhance its absorption [2–4].

2. MECHANISMS OF PHOTODYNAMIC THERAPY

Photodynamic therapy is a new treatment for a wide variety of malignancies and pre-malignant dysplasias, as well as some non-cancer indications. Therapeutic response to PDT is achieved through the activation of a non-toxic photosensitizer located within the neoplastic tissue, using visible light tuned to the appropriate absorption band of the photosensitizer molecule (Table 1). This produces cytotoxic species such as singlet oxygen, which result in local photo-oxidation, cell death and destruction of the tumour. Compared with conventional treatments, such as chemotherapy, surgery

Table 1: Photosensitizer absorption spectra.

Photosensitizer	Wavelength(nm)
Hematoporphyrin derivative (HpD)	630
5-aminolevulinic acid (5-ALA)	410, 505, 540, 580, 635
Tin etiopurpurin (SnET ₂)	447, 660
N-aspartyl-chlorin e6 (NPe6)	664
Chloroaluminium phthalocyanine (AlPcS)	675
Benzoporphyrin derivative-monoacid ring A (BPD-MA)	456, 690
Lutetium texapyrin (Lu-TeX)	732

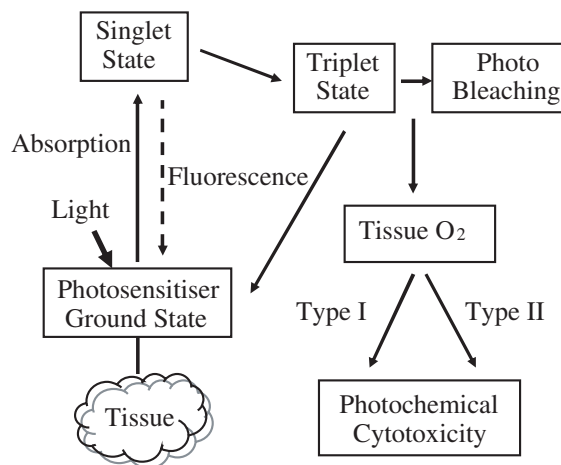


Figure 1: Mechanism of Photodynamic therapy.

or radiotherapy, PDT is relatively benign procedure, which produces good results from both a cosmetic and functional standpoint. Moreover, because it is generally well tolerated and can be repeated, PDT does not limit future treatment options. A simple diagram of PDT events is shown in Fig. 1.

The photosensitizer excited by light induces two types of reactions: A type-I reaction, which is the electron transport process and a type-II reaction which is the energy transport process. The free radicals produced by the type-I reaction react with dissolved oxygen in the tissues to produce various oxidized substances, which elicits a free-radical chain reaction. In the type-II reaction, the photosensitizer in the target cells is changed to the excited singlet state by the light energy. At that time, part of the substance returns to the ground state while emitting fluorescence, while the majority of the substance is changed to the triplet state. The triplet state returns partly to the ground state while emitting phosphorescence, however, the remaining converts energy to dissolved oxygen in the target tissues. The oxygen supplied with energy is excited and changes to singlet oxygen, which causes degenerative necrosis of the target cells. The therapeutic effect of PDT is mainly the result of the type-II reaction, but the effect varies with the type of photosensitizer used.

One of the most problematic aspects of PDT using HpD is that these agents exhibit a relatively slow rate of clearance from the skin. Consequently, patients receiving either drug systemically are rendered photosensitive and must remain out of sunlight or strong artificial light for 6 to 10 weeks after treatment to avoid severe sunburn. This problem seriously reduces the acceptability of this form of therapy, especially when other treatments are available and when the aim of the therapy is palliation rather than cure. This is achieved by the administration of 5-aminolaevulinic acid (5-ALA), the first precursor of haem after the feedback control point. Because the resulting accumulation of PpIX is relatively short-lived, any skin photosensitivity which may occur is resolved by 24 hours point treatment. An attractive and proven PDT procedure for treating superficial is the topical application of the haem precursor in the form of a cream emulsion 4–6 hours prior to light treatment. ALA applied topically passes rapidly through abnormal epidermis, or normal skin tripped of 15 μm thick stratum corneum layer and, bypassing the feedback inhibition, is converted

within the mitochondria to Protoporphyrin IX (PpIX). The fluorescent and photodynamically active substance Protoporphyrin IX is synthesized via the haem cycle in cells exposed to ALA. Once the sensitizer has been taken up by the cells in the target tissue, they are activated by a precise wavelength of non-thermal light. The sensitizer molecules become excited and in turn excite tissue oxygen to a highly toxic, but short lived singlet oxygen species. The singlet oxygen attacks the cellular membrane resulting in phototoxic damage and cell death. Toxicity occurs either as a result of direct cell kill or by attacking the endothelial layer of blood vessels thus causing vascular shutdown which starves all tissue downstream of nutrients. The body then naturally removes the dead tissue leaving the wound to heal uniquely via tissue regeneration as opposed to the normal fibrotic scarring.

3. IONTOPHORESIS MECHANISM AND DEVICES

Trans-dermal administration of drug is assuming an important place in modern drug therapy. It is used for non-ionized drugs required in a small dosage. Transdermal administration can be passive or facilitated. In passive administration, the non-ionized drug traverses the skin through the stratum corneum. The skin, being a semi-permeable membrane, allows only a small amount of any drug molecule to passively penetrate the skin. Ionized drugs do not easily penetrate this barrier and are not suitable for routine trans-dermal delivery unless an external source of energy is provided to drive the drug across the skin. Facilitated diffusion can utilize either phonophoresis or electrical (iontophoresis) energy. Iontophoresis increases the penetration of electrically charged drugs into surface tissues by the application of an electric current. Electrical energy assists the movement of ions across the stratum corneum according to the basic electrical principle of “like charges repel each other and opposite charges attract”. The drug is applied under an electrode of the same charge as the drug, and a return electrode opposite in charge to the drug is placed at a neutral site on the body surface. The operator then selects a current below the level of the patient’s pain threshold and allows it to flow for an appropriate length of time. The electrical current significantly increases the penetration of the drug into surface tissues by repulsion of like charges and attraction of opposite charges. The two classically considered prerequisites for iontophoretic treatment are that the drug must be charged (or modified to carry a charge) and that the disease process must be at or near a body surface. A typical iontophoresis device consists of direct current pulsed type delivery system and electrodes. Wires are then connected between the unit and the active and passive electrodes, and the unit set for current and time. In the iontophoresis process, the current, beginning at the device, is transferred from the electrode through the ionized drug solution as ionic flow. The drug ions are moved to the skin where the repulsion continues moving the drug through the trans-appendageal structures and stratum corneum interstices via the aqueous pores. The larger the electrode surface, the greater the current the device must supply to provide a current density for moving the drug. Iontophoresis enhances transdermal drug delivery by three mechanisms: (a) Ion-electric field interaction provides an additional force that drives ions through the skin, (b) the flow of electric current increases the permeability of the skin, and (c) electro-osmosis produces bulk motion of solvent that carries ions or neutral species with the solvent stream. Electroosmotic flow occurs in a variety of membranes and is in the same direction as the flow of counter-ions. It may assist or hinder drug transport. Since human skin is negatively charged above pH 4, counter ions are positive ions and electro-osmotic flow occurs from anode to cathode. Thus, anodic delivery is assisted by electro-osmosis but cathodic delivery is retarded. Because of the electro-osmotic flow, transdermal delivery of a large anion (negatively charged protein) from the anode compartment is more effective than that from the cathode compartment. The drug reservoir consists of a gauze/cloth or gel pad to which the solution is applied or the solution is injected through a port into the reservoir electrode combination. Wires are connected between the microprocessor unit and the active and passive electrodes.

4. SUBJECTS AND EXPERIMENTAL METHODS

Five patients who were diagnosed with actinic keratosis (two men and three women in ages ranging from 49 to 94 years, with an average of 79.6 years) and Bowen’s disease at the outpatient clinic of the Department of Dermatology, Aichi Medical University, attended this study. Informed consent was obtained from all patients following a full written and oral explanation.

Iontophoresis used in the present study (TransDermaionto System, Atom Giken Co., Ltd., Kanagawa, Japan) was a direct-current pulsed type [5]. For iontophoresis, 20% ALA was dissolved in distilled water, and then current was adjusted based on the area of the functional electrode between



Figure 2: (a) Iontophoretic delivery devices, (b) drug is placed on the skin under the active electrode, with the indifferent electrode positioned elsewhere on the body.

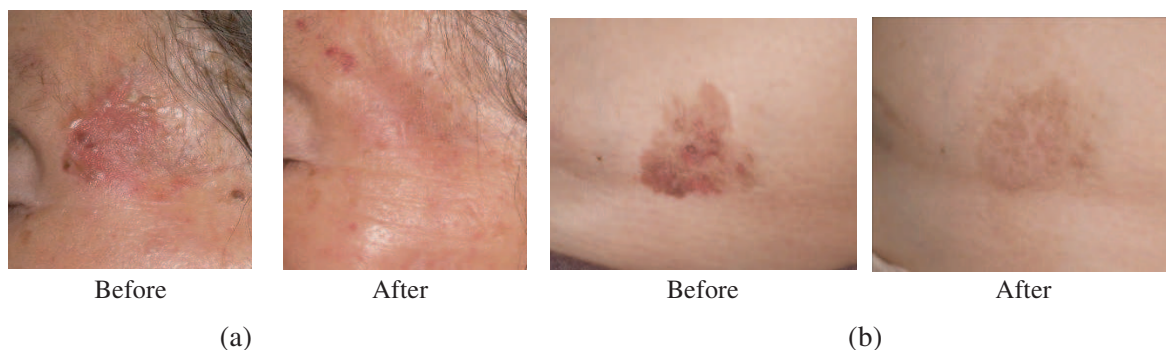


Figure 3: Clinical appearance before PDT and clinical appearance 3 weeks after PDT, (a) Actinic keratosis and (b) Bowens disease.

0.25 and 0.50 mA/cm². In all subjects, the pulse wave was set at 50 kHz, and ALA was applied to lesion for 10 min. The principal of iontophoresis is shown in Fig. 2. After application, the affected area was washed using distilled water and was shielded from light. One hour after ALA application, a fluorescent spectrometer was used to measure protoporphyrin IX (PpIX) photosensitizer production. PDT was performed by excimer dye laser and emits 630 nm with pulsed light irradiation at 50 J/cm² per session. PDT was repeated three times, weekly (total dose: 150 J/cm²). One week after the last PDT, a skin biopsy was performed in order to assess the therapeutic effects.

5. RESULTS AND DISCUSSION

In topical 5-ALA-PDT, sufficient PpIX accumulation in tumour cells by 5-ALA diffusion is necessary. With regard to the length of the topical ALA application time, the British guidelines [6] for topical PDT recommend 4–6 hours, but it has been clarified that because of superior permeability, sufficient effects can be obtained in about 3 hour with methyl 5-ALA. To reduce these procedures, application of 5-ALA using iontophoresis has been studied. Figure 3 shows an example of the therapeutic effect. In this study, only 10 minutes of application of 5-ALA and a 1 hour follow-up showed the PpIX positive reaction within the target.

With iontophoresis, it took one hour for the entire treatment, ranging from the delivery of 5-ALA to the end of the treatment. Thus, the time needed for treatment can be drastically shortened with iontophoresis. Table 2 summarizes the clinical features of patients. When compared with previous studies, our direct-current pulsed iontophoresis had a higher charge because the concentration of ALA was higher at 20% solution. With the equipment used in the present study, the pulse mode makes it possible to avoid the functional electrode depolarization associated with direct current iontophoresis, and ALA can be efficiently applied. In our study, there were no marked differences in the average PpIX production between 1 h after iontophoresis and > 4 h after occlusive dressing technique. We think that ALA was apparently able to penetrate tumour cells faster with direct-current pulsed iontophoresis when compared with percutaneous absorption based on passive diffusion. Rapid ALA diffusion into cells also quickly depleted the rate-limiting enzyme, thus accumulating PpIX inside tumour cells. The pain varies with the sites and the sizes of lesions and also the light source, but it is thought that the pain can mainly be attributed to the tissue damage caused by the thermal radiation accompanying the photoradiation and by the stimulation of nerve

Table 2: Summary of the comparison of iontophoretic PDT and external PDT.

	Iontophoretic PDT		External PDT	
Time from ALA to cure	1 hour		4 ~ 6 hours	
Quantity PpIX	AK	2.88 ($n = 5$)	AK	5.54 ($n = 39$)
	BD	15.34 ($n = 2$)	BD	6.68 ($n = 28$)

fibers by 5-ALA. Local anesthesia may need to be considered in some patients. From such a viewpoint, the delivery of 5-ALA within a short time by iontophoresis is useful, also in terms of shortening the treatment time.

6. CONCLUSION

Along with the increase in the number of elderly patients, the number of patients with superficial malignant tumors of the skin also seems to be on the increase. Under this circumstance, the need for the non-invasive modality of PDT is also increased. Since 5-ALA, a photosensitizer with high tumor affinity, is hardly absorbed percutaneously under normal circumstances, the effect of iontophoresis in enhancing the absorption within a short period of time is useful from the viewpoint of improving the quality of the PDT. In conclusion, our data suggested that when compared with conventional occlusive dressing technique, PDT could be performed much more rapidly with iontophoresis, resulting in lower a patient burden.

ACKNOWLEDGMENT

This research was supported by the Department of Dermatology, Aichi Medical University.

REFERENCES

1. Kalka, K., H. Merk, and H. Mukhtar, "Photodynamic therapy in dermatology," *J. Am. Acad. Dermatol.*, Vol. 42, 389–413, 2000.
2. Rhodes, L. E., M. M. Tsoukas, R. R. Anderson, and N. Kollias, "Iontophoretic delivery of ALA provides a quantitative model for ALA pharmacokinetics and PpIX phototoxicity in human skin," *J. Invest. Dermatol.*, Vol. 108, 87–91, 1997.
3. Kumar, R. and A. Philip, "Modified transdermal technologies: Breaking the barriers of drug permeation via the skin," *Trop. J. Pharm. Res.*, Vol. 6, 633–644, 2007.
4. Merclin, N., T. Bramer, and K. Edsman, "Iontophoretic delivery of 5-aminolevulinic acid and its methyl ester using a carbopol gel as vehicle," *J. Control Release*, Vol. 98, 57–65, 2004.
5. Akimoto, M., M. Kawahara, M. Matsumoto, and H. Matsubayashi, "Development of the pulsed direct current iontophoresis and its clinical application," *PIERS Online*, Vol. 2, No. 2, 157–162, 2006.
6. Morton, C. A., S. B. Brown, S. Collins, et al., "Guidelines for topical photodynamic therapy: Report of a workshop of the British photodermatology group," *Br. J. Dermatol.*, Vol. 146, 552–567, 2002.

Developments of Transdermal Transport System during Skin Iontophoresis and Electroporation

Tomonori Nishimura¹, Makio Akimoto², Michio Miyazaki²,
Mayumi Nomoto³, and Michio Miyakawa⁴

¹Atom Giken Co., Ltd., 92-2, Katase, Fujisawa-city, Kanagawa 251-0032, Japan

²Kanto Gakuin University, 1-50-1, Mutsuurahigashi, Kanazawa-ku, Yokohama 236-8501, Japan

³Nomoto Mayumi Skincare Clinic, 1-3-7, Bandai, Chuo-ku, Niigata 950-0088, Japan

⁴Niigata University, 8050 Ikarashi-2, Niigata 950-2181, Japan

Abstract— Transdermal drug delivery offers a non-invasive route of drug administration, although its applications are limited by low skin permeability. Various enhancers including iontophoresis, chemicals, ultrasound, and electroporation have been shown to enhance transdermal drug transport. Iontophoresis is the process of increasing the penetration of drugs into the skin by application of an electric current. The drug is applied under an electrode of the same charge as the drug, and a return electrode opposite in charge to the drug is placed at a neutral site on the body surface. Electrical energy assists the movement of ions across the skin using the principle “like charges repel each other and opposite charges attract”. In this article, we discuss the iontophoresis and electroporation on the stratum corneum of the skin and its application for dermatological conditions.

1. INTRODUCTION

Transdermal drug delivery offers several advantages over traditional drug delivery systems such as oral delivery and injection including elimination of first pass metabolism, minimization of pain, and possible sustained release of drugs. However, transdermal transport of molecules is slow due to low permeability of stratum corneum, the uppermost layer of the skin. Various physico-chemical penetration enhancers including ultrasound, chemical enhancers iontophoresis, and electroporation have been used for enhancing transdermal drug transport. These enhancers increase transdermal transport through one or more of the following mechanisms: i) Increased drug solubility (chemical enhancers), ii) increased diffusion coefficients (chemical enhancers, ultrasound, and electroporation), and iii) provision of additional driving forces (ultrasound, iontophoresis, and electroporation). While all these enhancers have been individually shown to enhance transdermal drug transport, their combinations have been hypothesized to be more effective compared to each of them alone. Specifically, the following combinations have been used for transdermal drug delivery: Chemicals + Iontophoresis, Chemicals + Ultrasound, and Electroporation + Iontophoresis, see also Fig. 1. In addition to increasing transdermal transport, a combination of enhancers should also reduce the severity of the enhancers required to be induced by these enhancers depends on their strength. However, the highest strength of the enhancers that can be applied on the skin is typically limited by safety. By combining two or more enhancers, one can reduce the strength of individual enhancers required to achieve the desired enhancement. Hence, a combination of two or more enhancer may not only increase the total enhancement, but can also increase the safety of enhancers. A review literature describing synergistic combinations of various enhancers is presented in this paper. This paper focuses on the effects induced by iontophoresis and electroporation on the stratum corneum of the skin. Even though the mechanism of drug transport is believed to be different, i.e., electrophoresis for iontophoresis and creation of new aqueous pathways for electroporation, the effects on the stratum corneum detected minutes after current application are very similar.

2. PRINCIPLES OF IONTOPHORETIC TREATMENT

Iontophoresis increases the penetration of electrically charged drugs into surface tissues by the application of an electric current. Electrical energy assists the movement of ions across the stratum corneum according to the basic electrical principle of “like charges repel each other and opposite charges attract”. The drug is applied under an electrode of the same charge as the drug, and a return electrode opposite in charge to the drug is placed at a neutral site on the body surface. The operator then selects a current below the level of the patient’s pain threshold and allows it to flow for an appropriate length of time. The electrical current significantly increases the penetration of

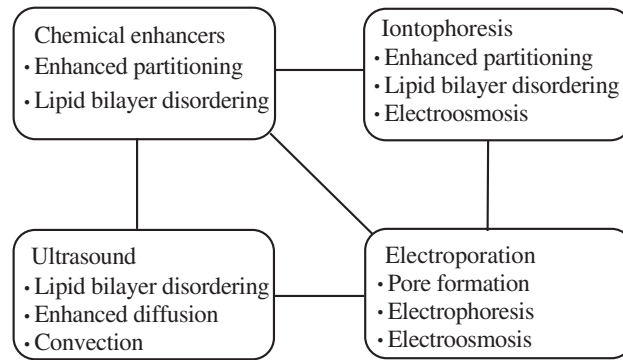


Figure 1: The figure shows possible mechanisms for the synergistic effects between various enhancers. Four enhancers, including chemical enhancers, ultrasound, iontophoresis, and electroporation are listed in each box. Mechanisms responsible for each enhancer are also listed.

the drug into surface tissues by repulsion of like charges and attraction of opposite charges. The two classically considered prerequisites for iontophoretic treatment are that the drug must be charged (or modified to carry a charge) and that the disease process must be at or near a body surface. The synergistic effect between chemical and iontophoresis may be attributed to several mechanisms, see Fig. 1.

3. IONTOPHORESIS MECHANISM AND DEVICES

A typical iontophoresis device consists of DC voltage delivery system and electrodes. Wires are then connected between the unit and the active and passive electrodes, and the unit set for current and time. In the iontophoresis process, the current, beginning at the device, is transferred from the electrode through the ionized drug solution as ionic flow. The drug ions are moved to the skin where the repulsion continues moving the drug through the trans-appendageal structures and stratum corneum interstices via the aqueous pores. The larger the electrode surface, the greater the current the device must supply to provide a current density for moving the drug. Iontophoresis enhances transdermal drug delivery by three mechanisms: (a) Ion-electric field interaction provides an additional force that drives ions through the skin, (b) the flow of electric current increases the permeability of the skin, and (c) electro-osmosis produces bulk motion of solvent that carries ions or neutral species with the solvent stream. Electroosmotic flow occurs in a variety of membranes and is in the same direction as the flow of counter-ions. It may assist or hinder drug transport. Since human skin is negatively charged above pH 4, counter ions are positive ions and electro-osmotic flow occurs from anode to cathode. Thus, anodic delivery is assisted by electro-osmosis but cathodic delivery is retarded. Because of the electro-osmotic flow, transdermal delivery of a large anion (negatively charged protein) from the anode compartment is more effective than that from the cathode compartment. The drug reservoir consists of a gauze/cloth or gel pad to which the solution is applied or the solution is injected through a port into the reservoir electrode combination. Wires are connected between the microprocessor unit and the active and passive electrodes. The theories behind iontophoresis are straightforward. Coulomb’s Law states that “like charges repel” which means that by placing a cationic solution under the anode (+), when a current is applied the positive ions will be drawn toward the cathode (–) electrode. The human body conducts electrical signals very well, as demonstrated by neuronal action. Thus, when an electrode is applied to the skin, the current flows down the path of least resistance and the ionic substance is drawn into the body. Local and systemic drug levels may be achieved when delivering drugs via iontophoresis. However, these levels depend greatly upon the solubility characteristics of each drug and local dermal blood flow. Molecules with more hydrophilic characteristics have been shown to produce systemic levels through their ability to traverse the dermis completely and enter the vasculature. However, lipophilic molecules tend to be attracted to the subcutaneous layer and thus do not move past this stage of the integument. Studies of several therapeutic classes have shown that a class can be stratified by their relative lipophilicity and that overall iontophoresis success follows that stratification. Some of these may be easily treated using iontophoresis, see Table 1. Owing to the advanced nature of transdermal iontophoretic research and development, these systems are relatively well-characterized and understood. For example, the recently developed

Table 1: Common iontophoresis drugs and their charges.

Drug	Charge	Use
Epinephrine	+	Excipient to vasoconstrict
Gentamicin	+	Ear Chondritis, Burn Infection
Hyaluronidase	+	Deep Tissue Hematomas, Edema
Hydrocortisone	+	Inflammation
Lidocaine	+	Pain
Acetic Acid	–	Calcium Deposits
Dexamethasone	–	Inflammation
Ketoprofen	–	Inflammation
Penicillin	–	Burn Infection
Sodium Salicylate	–	Pain

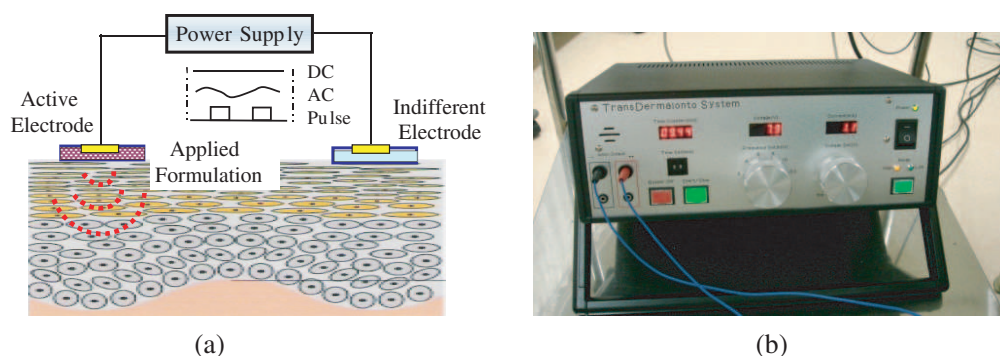


Figure 2: (a) Schematic of an iontophoretic device. An iontophoretic assembly principally consists of a pair of electrode chambers, which are placed in contact with the skin surface. When the device is powered, the passage of a small electrical current drives positively charged drugs into the skin from the anode and, likewise, negatively charged drugs from the cathode. (b) TransDermaionto System; an iontophoretic delivery system (Atom Giken Co., Ltd., Japan).

TransDermaionto System (Fig. 2; Atom Giken Co., Ltd., Japan) for dermatologic delivery offer iontophoretic platforms, which can be potentially adapted and customized to the local and systemic iontophoretic administration of drugs.

4. ELECTROPORATION MECHANISM AND DEVICES

First used for the introduction of DNA material into cells *in vitro*, the use of electroporation for transdermal delivery was suggested about 15 years ago. Unlike iontophoresis, which employs small currents (transdermal voltages ≤ 20 V) for relatively long periods of time (many minutes to hours), electroporation involves exposure of the skin to relatively high voltages (approx. 30–100 V) for short times, typically 1 to several hundred milliseconds, which in turn create intense electric fields across the thin stratum corneum. Molecular transport through transiently permeabilized skin is thought to result from a variety of mechanisms: Enhanced diffusion through the aqueous pathways produced in the lipid bilayers, electrophoretic movement (for charged species) and, to a small extent, electroosmosis. Although this mode of electrical transdermal enhancement has been shown to be more effective (at least, quantitatively) relative to iontophoresis for several molecules *in vitro*, and to produce significantly elevated levels of transport compared with passive delivery, the limited data from *in vivo* and skin toxicological studies means that its clinical value remains to be established. Owing to the advanced nature of transdermal iontophoretic research and development, these systems are relatively well-characterized and understood. For example, the recently developed Electroporation System device (Fig. 3; Atom Giken Co., Ltd., Japan) for esthetic dermatologic delivery offer electroporatic platforms, which can be potentially adapted and customized.

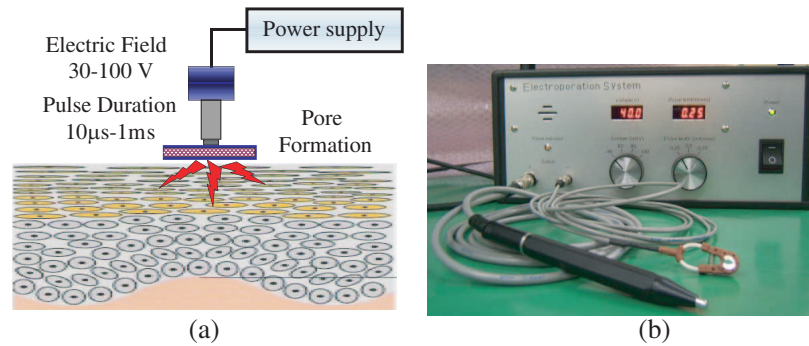


Figure 3: The basic design of electroporation delivery devices. (a) Drug is placed on the skin beneath the electroporation probe. (b) Electroporation System; electrophoretic delivery system for esthetic dermatology (Atom Giken Co., Ltd., Japan).

5. DERMATOLOGICAL APPLICATIONS

Iontophoresis has been used for the treatment of various dermatologic conditions. The most successful application of iontophoresis is for the treatment of hyperhidrosis. The basis for hyperhidrosis treatment and its practical aspects have been well described. Currently, the most commonly used conducting medium is tap water because it is safe and effective. Anticholinergic compounds have a longer lasting effect than water, but the side effects of systemic anticholinergic blockade have prevented their wide acceptance. The efficacy and safety of tap water iontophoresis is well documented, but its mechanism of action remains unknown. The most widely accepted hypothesis is that sweating is inhibited by mechanical blockage of the sweat ducts at the stratum corneum level, the depth and severity of the damage being dose-related.

Photodynamic therapy is a promising modality for the management of various tumors and non-malignant diseases, based on the combination of a photosensitizer that is selectively localized in the target and illumination of the lesion with visible light, resulting in photodamage and subsequent cell death. Moreover, the fluorescence of photosensitizing compounds is also utilized as a helpful diagnostic tool for the detection of neoplastic tissue. The two most important interactions governing the transport of light through tissue are scattering and absorption. In photodynamic therapy for skin cancer, 5-aminolevulinic acid (5-ALA) is applied topically to the affected area to be absorbed percutaneously through passive diffusion, and typically requires 4–6 h before performing PDT. In this study, we attempted to reduce the absorption period in PDT by ionizing ALA using direct-current pulsed iontophoresis to treat disease. Five patients who were diagnosed with actinic keratosis (two men and three women in ages ranging from 49 to 94 years, with an average of 79.6 years) and Bowen's disease at the outpatient clinic of the Department of Dermatology, Aichi Medical University, attended this study. Informed consent was obtained from all patients following a full written and oral explanation. Iontophoresis used in the present study was a direct-current pulsed type. When compared with conventional direct-current iontophoresis, pulsed iontophoresis was able to avoid electrode polarization, and drugs could be efficiently applied. For iontophoresis, 20% ALA was dissolved in distilled water, and then current was adjusted based on the area of the functional electrode between 0.25 and 0.50 mA/cm². In all subjects, the pulse wave was set at 50 kHz, and ALA was applied to lesion for 10 min. After application, the affected area was washed using distilled water and was shielded from light. One hour after ALA application, a fluorescent spectrometer was used to measure protoporphyrin IX (PpIX) photosensitizer production. PDT was performed by excimer dye laser and emits 630 nm with pulsed light irradiation at 50 J/cm² per session. PDT was repeated three times, weekly (total dose: 150 J/cm²). One week after the last PDT, a skin biopsy was performed in order to assess the therapeutic effects.

When compared with previous studies, our direct-current pulsed iontophoresis had a higher charge because the concentration of ALA was higher at 20% solution. With the equipment used in the present study, the pulse mode makes it possible to avoid the functional electrode depolarization associated with direct current iontophoresis, and ALA can be efficiently applied. In our study, there were no marked differences in the average PpIX production between 1 h after iontophoresis and > 4 h after occlusive dressing technique. We think that ALA was apparently able to penetrate tumour cells faster with direct-current pulsed iontophoresis when compared with percutaneous absorption based on passive diffusion. Rapid ALA diffusion into cells also quickly depleted the rate-limiting

enzyme, thus accumulating PpIX inside tumour cells. In conclusion, our data suggested that when compared with conventional occlusive dressing technique, PDT could be performed much more rapidly with iontophoresis, resulting in lower a patient burden.

6. CONCLUSION

Various enhancers including chemicals, electric fields, and ultrasound have been used to enhance transdermal drug transport. Although these enhancers have been individually shown to enhance transdermal drug transport, their combinations are significantly more effective compared to each of them alone. This paper focuses on the effects induced by iontophoresis and electroporation on the stratum corneum. Iontophoresis has been explored for many dermatologic and other medical conditions with reports of considerable success. In many conditions, however, these explorations have been limited to a single clinical trial. More rigorous studies are needed to investigate the applications of this mode of therapy.

REFERENCES

1. Langer, R., "Transdermal drug delivery: Past progress, current status, and future prospects," *Adv. Drug Deliv. Rev.*, Vol. 56, 557–558, 2004.
2. Kalia, Y. N., A. Naik, J. Garisson, and R. H. Guy, "Iontophoretic drug delivery," *Adv. Drug Deliv. Rev.*, Vol. 56, 619–658, 2004.
3. Wokovich, A. M., S. Prodduturi, W. H. Doub, A. S. Hussin, and L. F. Buhse, "Transdermal drug delivery system (TDDS) adhesion as a critical safety, efficacy and quality attribute," *Eur. J. Pharm. Biopharm.*, Vol. 64, 1–8, 2006.
4. Akimoto, M., M. Hata, and R. Sasaki, "Effect of iontophoresis on the chemical peeling with Lactic Acid," *Proceedings of 6th Meeting of the German-Japanese Society for Dermatology*, 25, Nara, Japan, 2002.
5. Akimoto, M., M. Kawahara, M. Matsumoto, and H. Matsubayashi, "Development of the pulsed direct current iontophoresis and its clinical application," *PIERS Online*, Vol. 2, No. 2, 157–162, 2006.
6. Kalka, K., H. Merk, and H. Mukhtar, "Photodynamic therapy in dermatology," *J. Am. Acad. Dermatol.*, Vol. 42, 389–413, 2000.
7. Omi, T., M. Akimoto, M. Miyazaki, and S. Kawana, "Iontophoresis-enhanced cutaneous absorption of 5-amino levulinic acid shortens the incubation period in photodynamic therapy," *Laser Therapy*, Vol. 18, No. 3, 143–149, 2009.

Comparing Effects of Extremely Low Frequency Electromagnetic Fields on the Biomass Weight of C3 and C4 Plants in Early Vegetative Growth

Azita Shabrangi¹, Ahmad Majd², Masoud Sheidai³,
 Mohammad Nabyouni¹, and Davoud Dorrnian⁴

¹Department of Biological Science, Faculty of Science, Tarbiat Moalem University, Tehran, Iran

²Department of Biology, Faculty of Science, Islamic Azad University, Tehran North Branch, Tehran, Iran

³Biology Faculty, Shahid Beheshti University, Tehran, Iran

⁴Physic Plasma Research Centre, Science and Research Branch, Islamic Azad University, Tehran, Iran

Abstract— Low frequency electromagnetic fields (EMFs) are a ubiquitous factor in the Earth's environment. In this research two states of seeds (wet, dry) of *Brassica napus L* (canola) and *Zea mays L* (maize) were exposed to pulsed EMFs (15 min on, 15 min off) by magnitude of 1 to 7 mT in steps of 2 mT and the highest intensity was 10 mT for 1 to 4 hours in steps of 1 h.

In the present study all the results suggested that treated seeds of these two species react differently against EMFs as a biotic stress. EMF treatment by 10 mT intensity of wet treated seeds caused decrease in growth and both fresh and dry biomass weight of canola. The same treatment cause increase in fresh and dry biomass weight of maize. In conclusion, canola (C3 plant) tends to damage more than maize (C4 plant) exposing to EMFs.

1. INTRODUCTION

Man-made low-frequency electromagnetic fields have become a part of our biosystem, but living organisms have to adapt themselves to this new factor, which can influence some of their biological functions. Many researchers reported that EMFs have a positive effect on plant characteristics such as seed germination, seedling growth, agronomic traits and seed yield [5, 8, 16, 22]. Magnetic field were used widely as pretreatment for seeds to increase seed vigor, seedling growth and yield [5, 13]. Some researchers indicated that suitable magnetic treatment increased the absorption and assimilation of nutrients [19], and ameliorated photosynthetic activities, therefore biomass increased [9].

They also proved that a certain magnetic field strength could affect cell division, cell extension, and cell differentiation [2, 3, 9]. The ionizing radiation source could be high-energy electrons, X-rays or gamma rays, while the non-ionizing radiation is electromagnetic radiation that does not carry enough energy/quanta to ionize atoms or molecules (World Trade Organization, 2001). It was also reported that cells respond to a variety of externally applied forces and physical phenomena, such as low intensity ultrasound and various types of electromagnetic energy. The electrical component of electromagnetic energy has an effect on dipolar molecules such as enzymes, ionic pumps, nuclear material and nucleotide molecules [2, 3, 9].

Numerous studies show an association of the internal EMF of plants with many physiological processes. For example, the electric current is involved in graviperception and root growth [24]. Plants use their internal EMF for determining and controlling their physiological polarity [15] and, specifically, for setting their biological rhythms [5]. In plants More recently it has again been demonstrated that the roots of *Zea mays* and *Lepidium sativum* respond to an electric field and grow toward the cathode when the electric current is 1 V cm²¹ [10].

In this paper, the authors present some quantitative observations regarding the influence of electromagnetic field on the growth and biomass weight of *Zea mays* and *Brassica napus L* plants in early growth stages.

2. MATERIAL AND METHOD

Exposure to EMFs was performed by a locally designed EMF generator. The electrical power was provided by a 220 V, AC power supply with variable voltages and currents. This system consisted of one coil, cylindrical in form, made of polyethylene with 12 cm in diameter and 50 cm in length. The number of turns is 1000 of 0.5 mm copper wire, which were in two layers. A fan was employed to avoid the increase of temperature (22 + 1°C). Calibration of the system as well as tests for the accuracy and uniformity of EMFs (60 Hz) were performed by a tesla meter with a probe type of hall sound.

Three replicates, with 30 seeds in each one were used. They were spread in moist filter paper (for wet seeds) on Petri dishes. They were placed in the coil. Analogous groups were used as control. The wet and dry seeds of two species were exposed to pulsed EMFs (15 min on, 15 min off) by magnitude of 1 to 7 mT in steps of 2 mT and the highest intensity was 10 mT for 1 to 4 hours in steps of 1 h. Then dry seeds in Petri dishes were moistened and all Petri dishes were placed in germinator with 23 °C temperature. Three replicates of ten 7 days seedlings were randomly taken in order to measure their fresh biomass weights. The same seedlings were placed in the oven with 60 °C for 24 hours. Then dry biomass weights were measured.

3. STATISTICAL ANALYSIS

Statistical analysis of the data was performed by using ANOVA. We applied Duncan's multiple range test to compare the experimental results of groups exposed to an electromagnetic field for seed germination rate, seedling shoot and root length, fresh and dried biomass with control. For statistical evaluation of results, significance was defined by a probability level of $p < 0.05$.

4. RESULTS

Fresh biomass weight of maize seedlings grown from dry treated seeds showed increase in almost all treatments comparing to control. But we did not observe significant increase in dry biomass weight of the same seedlings except seedlings grown from 10 mT treatment. On the other hand fresh biomass weight of seedlings grown from wet treated seeds showed increase especially in 3 and 10 mT intensities for 4 hours exposure time. Dry biomass weight of the same seedlings showed an overall increase in almost all treatments. This increase in 1, 3 and 10 mT treatments were more significant. Also we observed that increase of fresh biomass weight was more than increase of dry biomass weight of the same seedlings, comparing to their corresponding control. The results were accorded to total protein amount of 7 days seedlings (Fig. 1).

We observed some different results in canola. Fresh biomass weight of canola seedlings grown from dry treated seeds showed increase in most of treatments except 1 mT intensity. Dry biomass

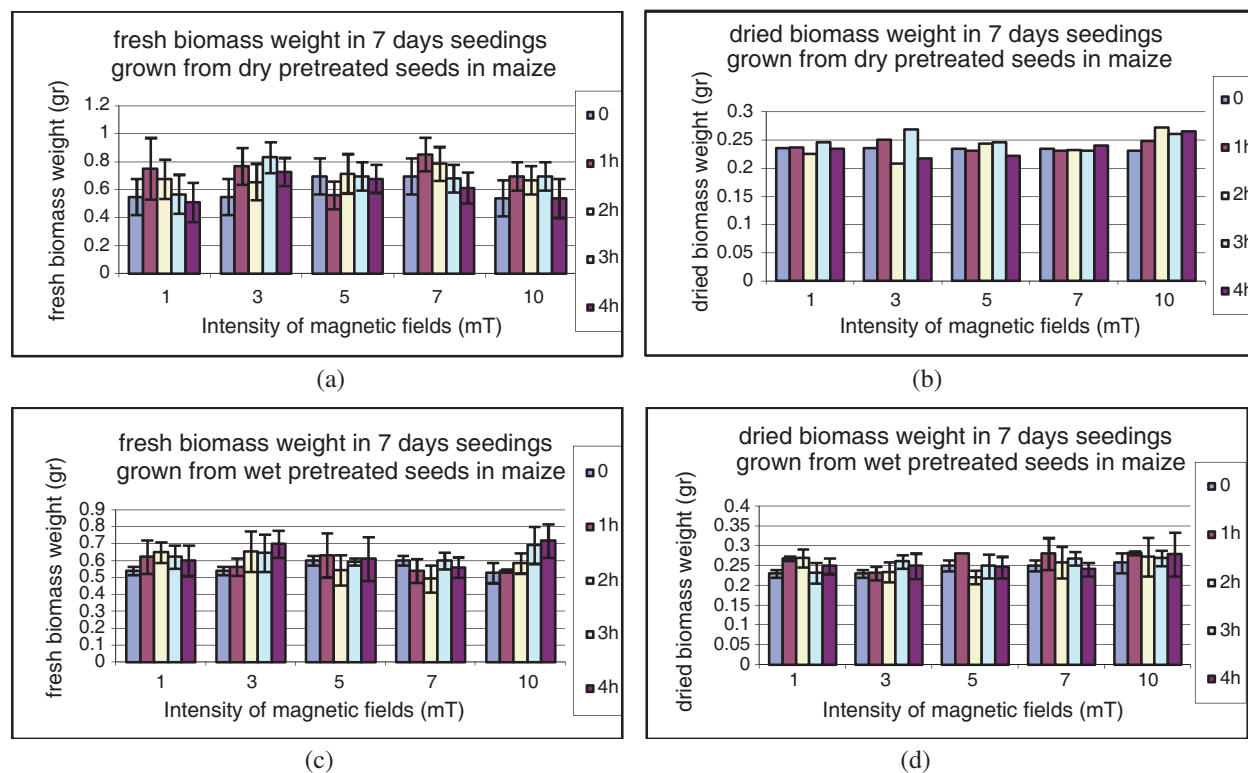


Figure 1: (a) and (c) show fresh biomass weights of 7 days seedlings under effects of EMFs. (b) and (d) show dry biomass weights of the same seedlings. Data are the means SE of experiment performed in triplicate. Fresh and dry biomass weight of each intensity in different exposure times were compared to their corresponding control in Maize We observed significant differences between plants exposed to all EMFs intensities with different exposing times and their respective control using the students t-test ($P < 0.05$).

weight of the same seedlings showed an overall increase and the most increase was observed in 1 mT intensity for 3 hour exposure time. Therefore low intensity of EMFs treatment caused augmentation in dry biomass weight in canola. We observed significant decrease in fresh biomass weight of canola seedlings grown from wet treated seeds in 10 mT intensity for different exposure time. In contrary, other treatment including 1 to 7 mT intensities caused augmentation in fresh biomass weight. Dry biomass weight of the same seedlings decreased especially in 7 and 10 mT intensities and all exposure time (Fig. 2).

All these results were in agreement with other growth parameters, including shoot and root length and seed germination rate. In maize the most significant increase of fresh biomass were observed in 7 days seedlings grown from wet treated seeds by 3 and 10 mT intensities both for 4 h exposure. Their dry biomass weight showed significant increase, too (Fig. 3). On the other hand, both fresh and dry biomass weight of 7 days canola seedlings grown from wet treated seeds by

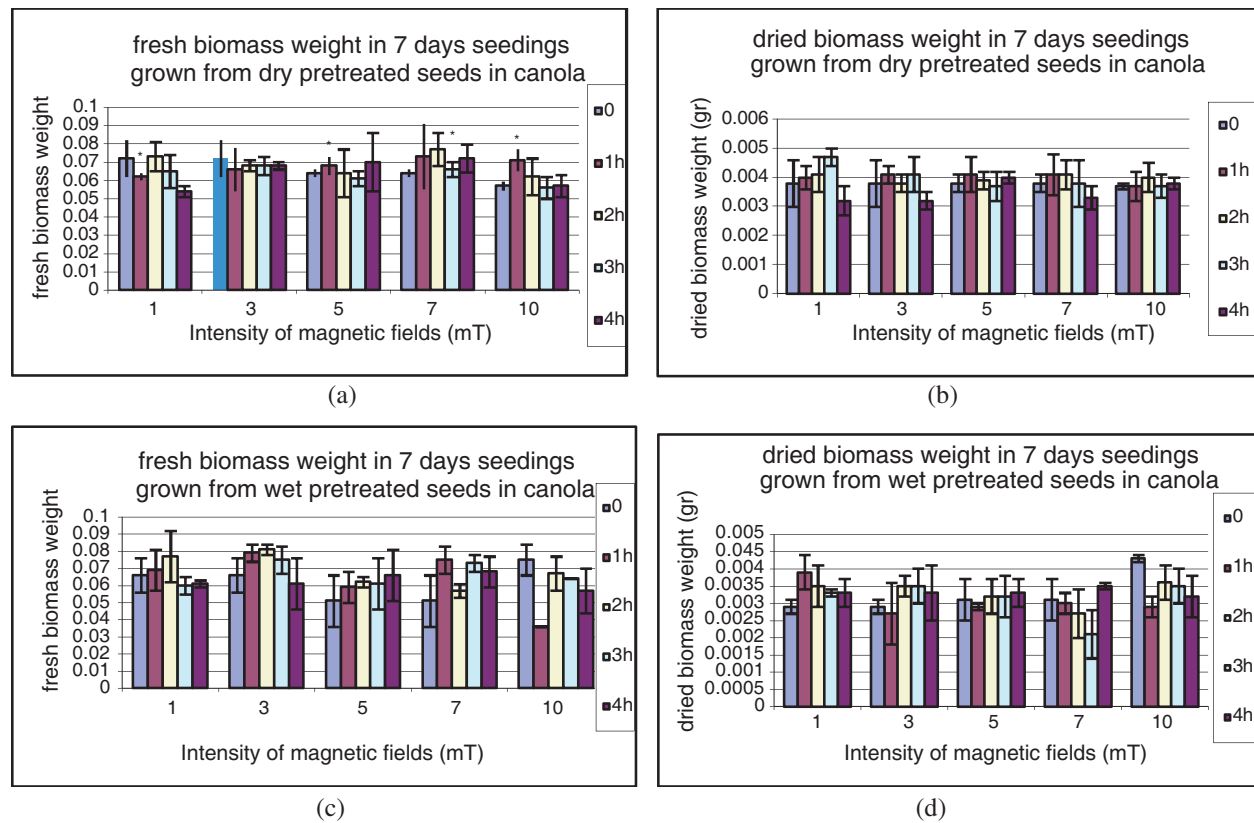


Figure 2: (a) and (c) show Fresh biomass weights of 7 days seedlings under effects of EMFs. (b) and (d) show Dry biomass weights of the same seedlings. Data are the means SE of experiment performed in triplicate. Fresh and dry biomass weight of each intensity in different exposure times were compared to their corresponding control in canola. We observed significant differences between plants exposed to their respective control in canola with different exposing times and their respective control using the students t-test ($P < 0.05$).

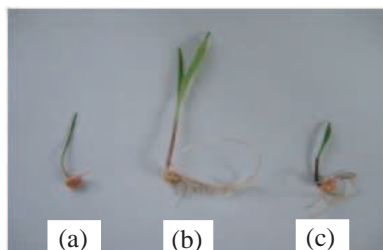


Figure 3: 7 days seedlings, (a) control, (b) wet seeds treated by 3 mT for 4 h, (c) wet seeds treated by 10 mT, 4 h.

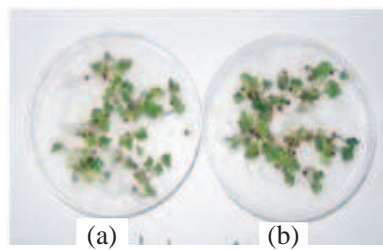


Figure 4: (a) Control, (b) 7 days seedlings grown from dry treated seeds by 10 mT intensity for 4 h exposure.

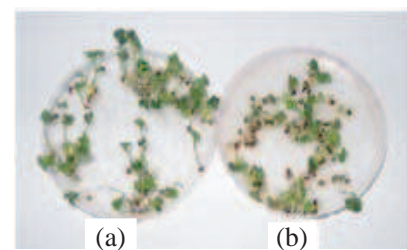


Figure 5: (a) Control, (b) 7 days seedlings grown from wet treated seeds by 10 mT intensity For 2 h exposure.

10 mT intensity for different exposure times showed significant decrease. But the same intensity on dry treated seeds showed against results and caused increase in both fresh and dry biomass weights (Figs. 4 and 5).

5. DISCUSSION

Numerous biological effects of extremely low frequency electromagnetic fields were recorded in the last decades. They were observed at various cellular or molecular levels in living tissues. However no clear interaction mechanisms yet proved [9]. Maize seedlings from electromagnetically pretreated seeds grew more than the untreated, and also biomass and root growth were significantly increased in most of intensities. Therefore, we observed an overall stimulating effects of EMFs, in the range of 1 to 10 mT, on growth and both fresh and dry biomass weight of maize as a C4 plant. This effect was accorded with other crop or horticultural species with magnetic field treatment, e.g., strawberry and wheat [16, 22]. Canola seedlings from electromagnetically pretreated seeds mostly grew more than untreated seeds. In contrary, some intensities caused decrease in growth and biomass weight of this species, which is a C3 plant. Magnetic field is known as an environmental factor, which mostly affects on gene expression [18]. Therefore by augmentation of biological reactions like protein synthesis, biomass would increase and vice versa. Biomass increasing needs metabolic changes particularly increasing protein synthesis. It is assumed that augmentation of dry biomass weight would be the result of more protein synthesis or more carbohydrate and lipid synthesis. We also believed that increase of fresh biomass weight would have the same reasons or it might be the result of more water absorption. In our studies, the ratio of fresh weight to dry weight of biomass possibly showed physiologically that nutrient element absorption was consistent with the increase in water absorption. However, further study is necessary.

It is assumed that any external field, which can cause a forced-vibration of the ions, is able to alter the function of a cell. It is well known that on both sides of every cell membrane, there are large numbers of free ions (mainly K, Na, Cl, . . .), which control the cell volume, play an important role in signal transduction processes, and create an intense electric field that exists between two sides of cell membrane [9, 25]. As mentioned before EMFs cause a forced vibration of ions'. Consequently the function of the cell would be changed. The mechanisms of interaction with the living cells are still unclear, although most seem to involve changes in the intracellular levels of Ca^{2+} [6, 7].

The cell proliferation is known to be rather sensitive to external and internal factors, whatever may be their origin is. The cell nucleus may experience the action of EMFs as a source of abnormal cellular division and, further, as putative modifier of genetic patterns [12, 20, 21]. EMFs also affects enzyme activity, gene expression, and release of calcium from intracellular storage sites, which in turn influences the membrane structure, cell growth, and cell death [14, 16]. Living organisms have developed metabolic pathways leading to the accumulation of antioxidants including enzyme system to protect cells against oxidation under conditions of various stresses like EMFs [16, 26]. Lednev [1991] and Blackman [1994] believed that the binding of Ca^{2+} and calmodulin are presumed to be affected by ELF MFs [11, 13]. Attributed to all these theories, we believe gene expression would change under effect of ELF-EMF.

In the present study, all the results suggested that treated seeds of these two species react differently against EMFs as a biotic stress. EMF treatment by 10 mT intensity of wet treated seeds caused decrease in growth and dry biomass weight in canola. The same treatment cause increase in both fresh and dry biomass weight in maize.

6. CONCLUSION

In conclusion, canola (C3 plant) tends to damage more than maize (C4 plant) against EMFs.

The results suggest that a specific combination of electromagnetic parameters of ELF MF can be explored in further studies, and this may lead to potential uses of ELF MFs for applied plant technology such as crop production.

REFERENCES

1. Berg, M. and A. M. Ros, "Treatment of psoriasis with psolarens and UVA. A double-blind comparison of 8-MOP and 5-MOP," *Life Sci.*, Vol. 53, 355–358, 1993.
2. Cadossi, R., F. Bersani, A. Cossarizza, P. Zucchini, G. Emilia, G. Torelli, and C. Franceschi, "Lymphocytes and low-frequency electromagnetic fields," *The FASEB Journal*, Vol. 6, No. 9, 2667–2674, 1992.

3. Chang, W. H., L. T. Chen, J. S. Sun, and F. H. Lin, "Effect of pulse-burst electromagnetic field stimulation on osteoblast cell activities," *Bioelectromagnetics*, Vol. 25, No. 6, 457–465, 2004.
4. Chiabrera, A., M. Grattarola, and R. Viviani, *Bioelectromagnetics*, Vol. 5, 173–191, 1984.
5. Davies, M. S., "Effects of 60 Hz electromagnetic fields on early growth in three plant species and a replication of previous results," *Bioelectromagnetics*, Vol. 17, 154–161, 1996.
6. Ekiert, H. and E. Gom'ola, "Coumarin compounds in Ammi majus L. callus cultures," *Pharmazie*, Vol. 55, No. 9, 684–687, 2000.
7. Galvanoskis, J. and J. Sandblom, "Periodic forcing of intracellular calcium oscillators. Theoretical studies of the effects of low-frequency fields on the magnitude of oscillations," *Bioelectrochem. Bioenerg.*, Vol. 46, 161–174, 1998.
8. Goldsworthy, A. and K. S. Rathore, "The electrical control of growth in plant tissue," *Oxford Journals, Journal of Experimental Botany*, Vol. 36, No. 7, 1134–1141, 1985.
9. Goodman, E. M., B. Greenebaum, and M. T. Marron, "Effects of electromagnetic fields on molecules and cells," *Int. Rev. Cytol.*, Vol. 158, 279–338, 1995.
10. Stenz, H.-C. and M. H. Weisenseel, "Electrotropism of maize (*Zea mays* L.) roots¹," *Plant Physiol.*, Vol. 101, 1107–1111, 1993.
11. Hendee, S. P., F. A. Faour, D. A. Christensen, B. Patrick, C. H. Durney, and D. K. Blumenthal, "The effects of weak extremely low frequency magnetic fields on calcium/calmodulin interactions," *Biophys. J.*, Vol. 70, No. 6, 2915–2923, Jun. 1996.
12. Ho"nes, I., A. Pospichil, and H. Berg, "Electrostimulation of proliferation of the denitrifying bacterium *Pseudomonas stutzeri*," *Bioelectrochem. Bioenerg.*, Vol. 44, 275–277, 1998.
13. Lebedev, S. I., P. I. Baranskiy, L. G. Litvinenko, and L. T. Shiyani, "Barley growth in superweak magnetic field," *Electronic Treatment of Materials*, Vol. 3, 71–73, 1977, (In Russian, with English summary).
14. Monti, L., M. S. Perneco, R. Moruzzi, P. Battini, B. Zaniol, and B. Barbiroli, "Effect of ELF pulsed electromagnetic field on protein kinase C activation processes in HL-60 leukemia cells," *J. Bioelectr.*, Vol. 12, 119–130, 1991.
15. Negishi, Y., A. Hashimoto, M. Tsushima, C. Dobrota, M. Yamashita, and T. Nakamura, "Growth of pea epicotyl in low magnetic field implication for space research," *Advances in Space Research*, Vol. 23, No. 12, 2029–2032, 1999.
16. Piacentini, M. P., D. Fraternali, E. Piatti, D. Ricci, F. Vetrano, M. Dacha, et al., "Senescence delay and change of antioxidant enzyme levels in *Cucumis sativus* L. etiolated seedlings by ELF magnetic fields," *Plant Science*, Vol. 161, No. 1, 45–53, Jun. 2001.
17. Piacentini, M. P., E. Piatti, D. Fraternali, D. Ricci, M. C. Albertini, and A. Accorsi, "Phospholipase C-dependent phosphoinositide breakdown induced by ELF-EMF in *Peganum harmala* calli," *Biochimie*, Vol. 86, No. 4–5, 343–349, 2004.
18. Phillips, J. L., W. Haggren, W. J. Thomas, T. Ishida-Jones, and W. R. Adey, "Magnetic field-induced changes in specific gene transcription," *Biochim. Biophys. Acta*, Vol. 1132, 140–144, 1992.
19. Reina, F. G., L. A. Pascual, and L. A. Fundora, "Influence of a stationary magnetic field on water relations in Lettuce seeds. Part II. Experimental results," *Bioelectromagnetics*, Vol. 22, 596–602, 2001.
20. Scarfi, M. R., M. B. Lioi, M. Della Noce, O. Zeni, C. Franceschi, D. Monti, G. Castellani, and F. Bersani, "Exposure to 100 Hz pulsed magnetic fields increases micronucleus frequency and cell proliferation in human lymphocytes," *Bioelectrochem. Bioenerg.*, Vol. 43, 77–81, 1997.
21. Schimmelpfeng, J. and H. Dertinger, "The action of 50 Hz magnetic and electric fields upon cell proliferation and cyclic AMP content of cultured mammalian cells," *Bioelectrochem. Bioenerg.*, Vol. 30, 143–150, 1993.
22. Soja, G., B. Kunsch, M. Gerzabek, T. Reichenauer, A. M. Soja, G. Rippar, et al., "Growth and yield of winter wheat (*Triticum aestivum* L.) and corn (*Zea mays* L.) near a high voltage transmission line," *Bioelectromagnetics*, Vol. 24, 91–102, 2003.
23. Tsang, E. W. T., C. Bowler, D. He'rouart, W. Van Camo, R. Villarroel, C. Genetello, M. Van Montagu, and D. Inze, "Differential regulation of superoxide dismutase in plants exposed to environmental stress," *Plant Cell*, Vol. 3, 783–792, 1991.
24. Wawrecki, W. and B. Zagórska-Marek, "Influence of a weak DC electric field on root meristem architecture," *Annals of Botany*, 1–6, 2007.

25. Xie, T. D., Y. D. Chen, P. Marszalek, and T. Y. Tsong, “Fluctuation-driven directional flow in biochemical cycle: Further study of electric activation of Na, K pumps,” *Biophys. J.*, Vol. 72, 2496–2502, 1997.
26. Yalcili, O. and S. Alikamanoglu, “The effect of magnetic field on Paulownia tissue cultures,” *Plant Cell Tissue Org Cult*, Vol. 83, 109–114, 2005.

Measurement of Complex Permittivity of Biological Tissues

J. Vorlíček, L. Oppl, and J. Vrba

Dept. of Electromagnetic Field, Czech Technical University, Czech Republic

Abstract— This paper describes and evaluates a method for determining complex permittivity, and presents results of permittivity measurement of agar phantom of biological tissue. A nondestructive and non-invasive method based on reflection coefficient measurement of an open-ended coaxial line attaching the material under test is used. Vector measurement of the reflection coefficient on the interface between probes and measured samples is performed with the aid of network analyzer in the frequency range from 300 kHz to 3 GHz. The results indicate that using the coaxial probe with dimensions of N connector is suitable in the frequency range approximately from 30 MHz to 1 GHz.

1. INTRODUCTION

Relative permittivity, loss factor and conductivity are basic parameters for electromagnetic field modeling and simulations. Although for many materials these parameters could be found in the tables, very often their experimental determination is necessary. Dielectric properties of biological tissues are determining factors for the dissipation of electromagnetic energy in the human body and therefore they are useful in hyperthermia cancer treatment. Measurement of the dielectric parameters of biological tissues is also a promising method in the medical diagnostics and imaging. Knowledge of the complex permittivity in an treated area, i.e., knowledge of the complex permittivity of healthy and tumor tissue, is very important for example in the diagnosing of tumor regions in the human body or in the design of thermo-therapeutic applicators which transform electromagnetic energy into thermal energy in the tissue. Permittivity is known as

$$\varepsilon = \varepsilon_0 \varepsilon_c \quad (1)$$

where ε_0 is free space permittivity and ε_c is complex relative permittivity. Complex relative permittivity can be written as

$$\varepsilon_c = \varepsilon_r - j\varepsilon_r \tan \delta \quad (2)$$

where ε_r is real part of complex relative [1] permittivity and $\tan \delta$ is loss factor. For purely conductive losses we will obtain the following equation where σ is the material conductivity.

$$\tan \delta = \frac{\omega}{\omega \varepsilon_0 \varepsilon_r} \quad (3)$$

2. PRINCIPLE OF REFLECTION METHOD

The reflection method means measurement of reflection coefficient on the interface between two materials, on the open end of the coaxial line and the material under test. It is a well-known method for determining the dielectric parameters [2]. This method is based on the fact that the reflection coefficient of an open-ended coaxial line depends on the dielectric parameters of material under test which is attached to it. For calculating the complex permittivity from the measured reflection coefficient it is useful to use an equivalent circuit of an open-ended coaxial line. The probe translates changes in the permittivity of a material under test into changes of the input reflection coefficient of the probe. The surface of the sample of material under test must be in perfect contact with the probe. The thickness of a measured sample must be at least twice an equivalent penetration depth of the electromagnetic wave. This assures that the waves reflected from the far material under test interface are attenuated.

3. MEASUREMENT PROBE

For this measurement method we have adapted the standard N connectors from which the parts for connecting to a panel were removed. The measurement probe can be described by the equivalent circuit consisting of the coupling capacitance [3] between the inner and outer conductor out of the coaxial structure and radiating conductance which represents propagation losses. These capacitance and conductance are frequency and permittivity dependent and also dependent on the dimensions of the probe. Finally we constructed three N-connector based probes which differs in the diameter of the reflection plate.

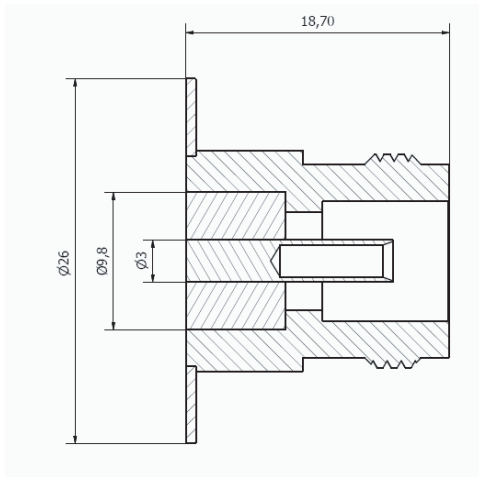


Figure 1: Basic scheme of the probe's dimensions.

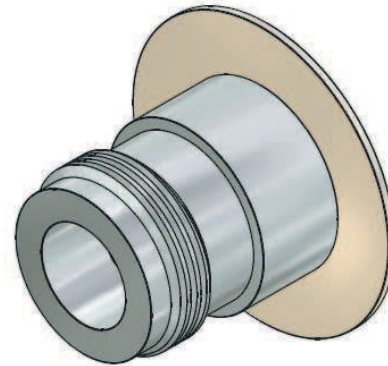


Figure 2: N-connector based probe.

4. MEASUREMENT SETUP

A typical measurement setup using the reflection method [2] on an open-ended coaxial line consists of the network analyzer, the coaxial probe and software. Our measurements were done with the aid of Agilent 6052 network analyzer in the frequency range from 300 kHz to 3 GHz.

The coaxial probe (in Fig. 3) is placed in contact with a material under test. Complex permittivity measurement proceeds through three steps. First the calibration of the vector network analyzer is performed. Then the calibration using a reference material is done. And last the reflection coefficient of material under test is measured. The complex permittivity of material under test is evaluated with the aid of MATLAB.

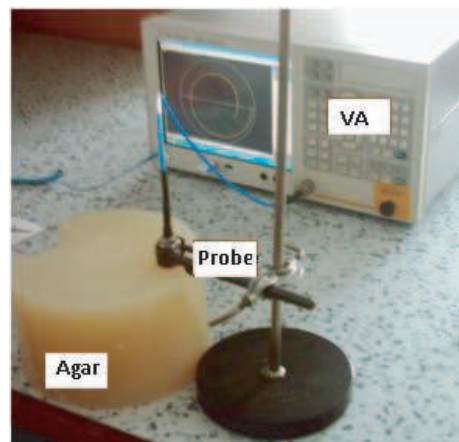


Figure 3: Measurement setup.

Table 1: Results of the measurement of complex permittivity of the agar phantom.

\varnothing of reflection area [mm]	f [MHz]	85	425	935
[16 mm]	$\varepsilon_r[-]$	65,47	60,34	50,76
	$\tan(\delta)$	0,343	0,158	0,28
[21 mm]	$\varepsilon_r[-]$	65,75	61,33	51,67
	$\tan(\delta)$	0,344	0,151	0,28
[26 mm]	$\varepsilon_r[-]$	66,31	61,82	52,59
	$\tan(\delta)$	0,345	0,149	0,286

5. RESULTS

Relative permittivity of lossy materials is a heavily [4] frequency-dependent quantity. Because of decreasing ability of particles to follow fast changes of electrical field, the relative permittivity decreases with the increasing frequency. The frequencies in following tables are chosen from the probes operating range.

6. CONCLUSION

The complex permittivity determination based on reflection coefficient measurement is suitable for the determination of dielectric parameters of biological materials in wide band due to its non invasive nature. Coaxial probes were described with the equivalent circuit as an antenna in lossy medium respecting the radiation effects at higher frequencies. Complex permittivity of a phantom of biological tissue was measured. Experiments with the modifications of the measurement's probe were done, but as can be seen from Table 1 adding the reflection plate to the probe doesn't have a significant effect on the measurement.

ACKNOWLEDGMENT

Research described in the paper was financially supported by Grant Agency of the Czech Republic, project: "Non-standard application of physical fields — analogy, modeling, verification and simulation" (102/08/H081).

REFERENCES

1. Novotný, K., *Theory of Electromagnetic Field*, Press CTU in Prague, 1997 (in Czech).
2. Stuchly, M. A., et al., "Measurement of radio frequency permittivity of biological tissues with open-ended coaxial line," *IEEE Trans. Microwave Theory Tech.*, Part I, Vol. 30, 82–92, 1982.
3. Oppl, L., "Measurement of dielectric properties," Dissertation Thesis, CTU in Prague, Dept. of EM field, 2001 (in Czech).
4. Zajíček, R., "Application of complex permittivity measurement in medical diagnostics and imaging," Dissertation Thesis, CTU in Prague, Dept. of EM field, 2009 (in Czech).

A Feasibility Study of Land CSEM Reservoir Monitoring: The Effect of the Airwave

Marwan Wirianto¹, Wim A. Mulder², and Evert C. Slob¹

¹Delft University of Technology, Delft, The Netherlands

²Shell International Exploration and Production B.V., Rijswijk, The Netherlands

Abstract— The displacement of oil with saline water creates a resistivity change that might be detectable by time-lapse CSEM measurements. Because the difference in measured EM signals before and after production is small, acquisition design plays an important role. We carried out numerical experiments to understand how to optimize the acquisition to best capture the time-lapse signal. Our study shows that exciting a VED source at some distance away from the target would be an attractive choice, as a HED source induces strong airwave energy masking the anomalous signal.

1. INTRODUCTION

Over the last decade, the controlled-source electromagnetic (CSEM) method has established its position as a tool for detecting and evaluating hydrocarbon reservoirs [1]. The method is mainly applied for derisking potential prospects, complementary to seismics. Another potential application is hydrocarbon reservoir monitoring during production. Water flooding or steam injection for oil production creates a resistivity change that may be detectable by time-lapse EM measurements. The main question is whether or not such a change is detectable and if EM can do better than time-lapse seismics. The latter requires a porosity greater than 30% to have a significant velocity difference between a water- and hydrocarbon-bearing reservoir. With EM, the resistivity difference between rock containing hydrocarbons or saline water can be two or three orders of magnitude, making CSEM method potentially more suitable if this difference can be detected in the presence of repeatability errors and noise.

Several authors have investigated the feasibility of CSEM monitoring [2–5]. The first and second groups employed a 3D integral-equation method to model the time-lapse effect due to the flooding front during water injection into an oil reservoir, whereas [4] used an accurate 2D finite-element modeling code to study several scenarios for reservoir depletion, including lateral and bottom flooding, stacked reservoirs, and partial depletion. [5] used a 3D multigrid modeling code of [6] to study the effect of vertically piston-like reservoir depletion in a land setting. To indicate the time-lapse resistivity changes, the authors frequently used both the time-lapse difference as well as the ratio of the recorded EM data before and after production, when part of the oil has been replaced by saline water. In some cases, the data comparison provided direct geometrical information about the depleted zone, whereas in others, more advanced data processing was required. However, the comparison of data recorded at the receivers offers little insight in how the EM fields interact with the depleted zone before and after production. Consequently, a direct interpretation remains difficult even if the time-lapse signals show up clearly.

Here, we present a modeling exercise investigating the interaction between excited low-frequency EM signals and the depleted zone in more detail. We use 2D vector plots of the current density generated by a harmonic electric dipole source in a simple half-space background. The patterns of current distributions are analyzed for two models that represent the resistivity before and after oil production with a water drive. We consider two sources: a surface horizontal electric dipole (HED) source and a vertical electric dipole (VED) source in a well. Understanding how the EM fields interact with the depleted zone can help us to optimize acquisition design.

We first review the basic concept of the CSEM method in the context of the monitoring problem, then present the numerical experiments, and finally discuss our findings.

2. PRIMARY-SECONDARY FORMULATION

To illustrate the concept of the CSEM method for reservoir monitoring, we begin with a simple survey layout. A typical field deployment with a horizontal electric dipole (HED) is sketched in Figure 1. During a survey, a source is employed to excite electromagnetic fields that penetrate through the background medium and illuminate the target, in our case the depleted zone (Figure 1(a)). EM

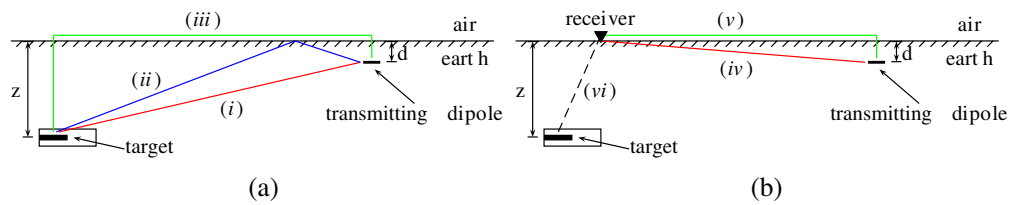


Figure 1: (a) Paths of the EM fields at the depleted zone (target) from a HED source, consisting of the direct field (i), the reflected field (ii), and the airwave (iii). (b) Paths of EM fields at receivers, consisting of the direct field (iv), the direct airwave (v) and the time-lapse field (vi).

receivers are placed on the surface, typically measuring the horizontal electric currents and the three components of the magnetic field. The interaction between the excited low-frequency EM signals and the conductive target zone then results in a secondary field that can be detected with receivers on the surface in addition to the response of the background field (Figure 1(b)). The response of the background field is the EM response that would be excited by the same source in the absence of the target body. The presence of a target body is usually analyzed by comparing the EM response of the target to the response for the background without the target.

The concept of the CSEM method for the monitoring problem is the same as for the exploration problem, but with a different target body and background fields. For exploration, the target body is the resistive hydrocarbon-bearing reservoir and the background field is the response for a background medium without the reservoir. For monitoring, the target body is the depleted zone and the background field is the response for the initial configuration, before oil production started. Although the concepts are similar, the analysis for the monitoring problem differs from that for the exploration case. For exploration, the analysis is frequently done by comparing the EM response of a hydrocarbon-bearing reservoir to the response for a horizontally layered background without the reservoir. The layered background model is used for computational speed and lateral variations are usually accommodated for by locally gluing 1D models together. Because the hydrocarbon reservoir is more resistive than the surrounding background, its presence causes the electromagnetic field to be reflected. It then diffuses back to the receivers at the sea bottom or, in our case, on the land surface, where it can be detected as an anomalous signal. In contrast to data analysis for the exploration problem, the analysis for the monitoring problem usually involves the EM responses for two different states with oil present in both. After production, there still may be oil on top of the water-flooded area. The existence of this highly resistive body may prevent the depleted zone from being “illuminated” by the source and therefore the time-lapse difference in the EM signal may be too weak to be reliably measured. In that case, acquisition design will play an important role in capturing the time-lapse variations. In the next section, we consider some numerical experiments to investigate the acquisition design that captures the time-lapse signal best, considering two types of setups, namely a surface-to-surface and a borehole-to-surface configuration.

3. NUMERICAL EXPERIMENTS

Before considering a monitoring example, we start with a simple half-space configuration. Figure 2 shows vector plots of the current density for an x -directed point source (HED) in a vertical section of

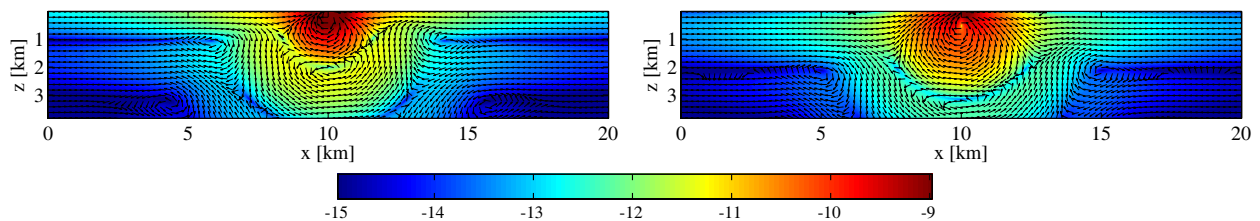


Figure 2: Current-density vector plots for a 2 Ohm-m half-space model. All panels show the x , z -plane at $y = 0$ km. A harmonic x -directed point dipole source (HED) is located at (10, 0, 0) km. The source frequency is set to 1 Hz. The background color represents the amplitude of the current density on a logarithmic scale and the black arrows mark the directions of the current-density vectors. The left panel displays the real part of current density, whereas the right panel shows its imaginary part.

a homogeneous Earth model with a resistivity of 2 Ohm-m. The source is located at (10, 0, 0) km, just below the air-earth interface, and operates at 1 Hz. The images illustrate the background current-density distribution. The color shows the magnitude of current density, overlaid by the black arrows that point in the direction of current-density vectors. The left panel shows the real part of current density, the right its imaginary part. In both panels, we see that the current-density distribution excited by a 1 Hz HED source rapidly decays away from the source. This clearly shows the diffusive character of EM fields generated by a low-frequency source. At shallow depth, both the real and imaginary parts of the current density are decaying less in the lateral direction. This fact is due to the so-called airwave, which is the electromagnetic field that propagates in the air with the speed of light. The part that propagates along the surface is called a lateral wave and it sends an electromagnetic field into the ground with an almost vertical diffusion direction [7]. A similar effect can be observed for a source at the interface between two conducting layers, where the fast diffusive medium (low conductivity) generates a field in the slow diffusive medium (high conductivity) that diffuses in the direction normal to the interface. The last case bears some resemblance to the refraction of seismic waves, where waves in the fast medium send energy back into the slow medium at the critical angle. A different pattern for the current-density distribution is obtained with a VED source, as shown in Figure 3. Here, we repeated the experiment but now with a z -directed point dipole source located at (10, 0, 0.5) km. Unlike in the case of the HED source, the lateral wave is absent and the EM signals comprise only the direct field and the reflected fields due the air-earth interface, which acts as a perfect reflector [7]. If \mathbf{E}^d denotes the direct EM field and \mathbf{E}^{aw} the field related to the airwave, the HED source generates a field $\mathbf{E}^d + \mathbf{E}^{aw}$, whereas with a VED source only produces \mathbf{E}^d .

Next, we include a reservoir under production. We take the same half-space model as before and insert a 300-m thick resistive hydrocarbon-bearing layer at 1 km depth with a resistivity of 100 Ohm-m and a 200-m thick conductive water-bearing layer with a resistivity of 3 Ohm-m. The sketch of the reservoir is shown in Figure 4. For the monitoring study, we assume the reservoir is flooded by saline water from the top left, creating a small, 100-m thick, box-shaped depleted zone in the corner of the hydrocarbon-bearing layer.

The first experiment is with surface-to-surface configuration, placing a HED source on the surface and measuring the response with receivers also on the surface. The center panel of Figure 5 displays the amplitude behavior of time-lapse difference for the in-line electric field measured on the surface, excited by a HED point source located at (11, 9.5, 0) km and operating at 1 Hz, as before. In this case, we assume the difference is entirely due the resistivity change in the reservoir.

Clearly, the result of the time-lapse difference is laterally confined to the location of resistivity change. However, if we compare the amplitude of time-lapse difference to its signal strength as shown in the left panel of Figure 5, we observe that the time-lapse signal is much weaker, below 1%

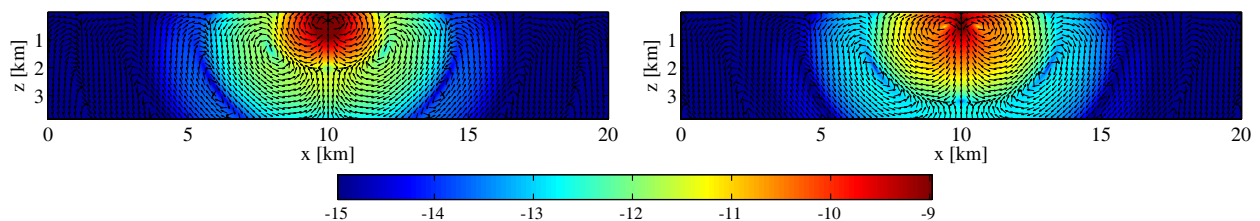


Figure 3: As Figure 2, but now for a z -directed point dipole source (VED), located at (10, 0, 0.5) km.

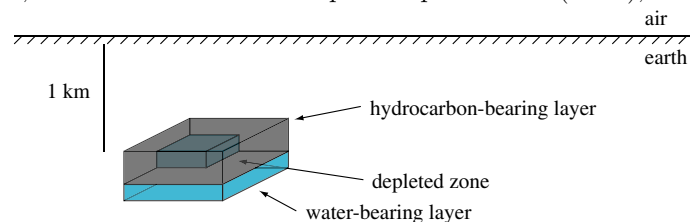


Figure 4: The reservoir has a dimension of 2 km by 2 km by 0.5 km, divided into two parts for oil-bearing reservoir and water-bearing reservoir. Before production, oil layer are assumed perfectly on top of water layer. During production, a part of oil layer is replaced by saline water creating a depleted zone in the top-left corner.

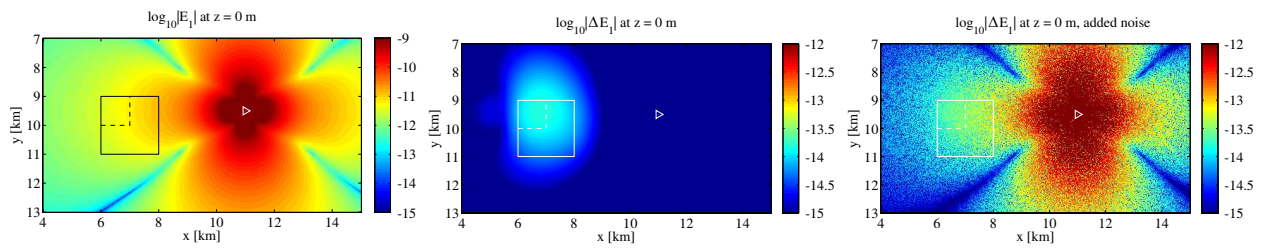


Figure 5: The left panel displays the x -directed electric field observed on the surface (top view), computed for the configuration that represents the resistivity before production. The center panel displays the time-lapse difference of the x -directed electric field observed on the surface (top view). The right panel displays the time-lapse difference with added noise. The solid white box indicates the lateral position of the reservoir and the dashed white line indicates the lateral position of the oil-water interface after flooding. The small white triangle marks the lateral location of the HED source.

of the signal strength. Consequently, the time-lapse difference may suffer from the multiplicative noise that would easily happen as a result of repeatability measurements. Frost, for instance, will increase the resistivity of the top soil and affect the time-lapse EM measurements. To illustrate the effect of this type of noise, we added a random number with a maximum amplitude of 1% relative to signal strength at each receiver, shown in the right panel of Figure 5. Here, we observed that the noise due the repeatability error dominates the time-lapse signal and imposes a strong source-imprint.

The multiplicative noise caused by repeatability errors can be described as follows. With time-lapse measurements, we collect two data sets, before and after production. The one obtained after production can be expressed as $\mathbf{E}^d + \mathbf{E}^{aw} + \mathbf{E}^{d;sc} + \mathbf{E}^{aw;sc}$. The first two terms denote the incident fields, consisting of a direct field and one due to the airwave. The last two scattering terms describe the time-lapse change. If we assume the time-lapse change is entirely due to the resistivity change in the reservoir, the component $\mathbf{E}^d + \mathbf{E}^{aw}$ will completely cancel out when considering the time-lapse difference. In the presence of multiplicative noise, however, the time-lapse difference will become $\alpha(\mathbf{E}^d + \mathbf{E}^{aw}) + \mathbf{E}^{d;sc} + \mathbf{E}^{aw;sc}$, where the factor α models the repeatability errors. The noise becomes a problem if $|\mathbf{E}^{d;sc} + \mathbf{E}^{aw;sc}|$ is much smaller than $|\alpha(\mathbf{E}^d + \mathbf{E}^{aw})|$, as happens in Figure 5. In that case, the airwave, \mathbf{E}^{aw} , appears as the predominant signal.

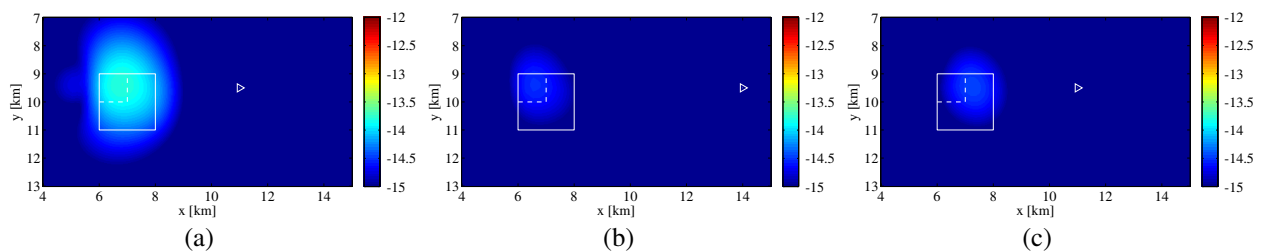


Figure 6: All panels show $\log_{10} |\Delta E_1|$ at $z = 0$ km (top view). The leftmost panel displays the amplitude behavior of time-lapse difference when the resistivity change is illuminated by the direct field and the airwave. The center panel corresponds to illumination by only the airwave, and the rightmost panel by only the direct field.

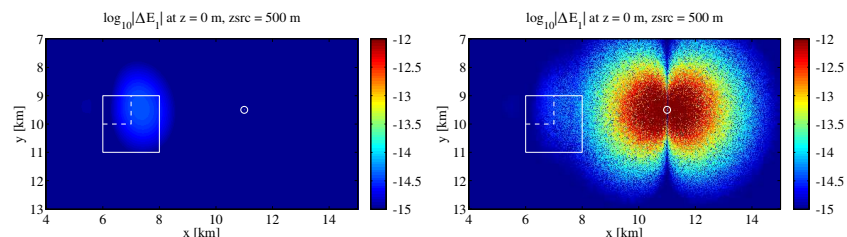


Figure 7: The left panel displays the time-lapse differences of the electric component E_1 observed on the surface (top view). The right panel displays the time-lapse difference of the electric component E_1 with added noise.

Let us assume that the time-lapse difference is entirely due the resistivity changes in the reservoir, so that it can be written as $\mathbf{E}^{d;sc} + \mathbf{E}^{aw;sc}$. We want to determine which of the two incident fields, \mathbf{E}^d or \mathbf{E}^{aw} , most affects the time-lapse signal. To reduce the contribution of the direct field, we placed the source further away from the target, whereas to reduce the contribution of the airwave, we repeated the experiment in a fully homogeneous background, without an air-earth interface. Figure 6 shows the results. The leftmost panel displays the time-lapse difference when we have the contributions of both the direct field and the airwave. The center panel shows the time-lapse difference when we have only the airwave contribution and the rightmost with only the direct field. Clearly, the time-lapse signal due to the incident field generated by the airwave provides the best result. We also observe that the time-lapse difference measured on the surface is laterally confined to the location of resistivity changes in that case. Therefore, the presence of the airwave is beneficial, because it illuminates the depleted zone even if the source is not close to the target. In the presence of repeatability errors, however, the strong currents induced by the incident airwave cannot be fully subtracted and the multiplicative noise will start to dominate the time-lapse signals, making them difficult to detect.

As an alternative, we considered a vertical dipole source located in a well. The left panel of Figure 7 displays the amplitude behavior of time-lapse differences for the in-line electric field measured on the surface, excited by a VED point source located at (11, 9.5, 0.5) km and operating at 1 Hz, as before. The right panel of Figure 7 displays the same response, but after adding random noise with a maximum amplitude of 1% relative to the signal strength at each receiver. The time-lapse differences can still be recognized, although not easily.

4. CONCLUSIONS

With the HED source, the airwave appears as the predominant signal. It propagates in the air and the part that propagates parallel to the surface has a geometrical spreading function inversely proportional to distance squared. This part generates a diffusive electromagnetic field that diffuses almost vertically down into the Earth. The presence of the airwave can be beneficial for the monitoring problem, because it provides illumination of the depleted zone even if the source is not close to the target. However, at the same time, the strong currents induced by the airwave also dominate the time-lapse signals. In the presence of repeatability errors, this will make it difficult to recognize the signals due to time lapse changes in the presence of repeatability errors. However, a HED source could still be useful if the airwave can be eliminated or at least be reduced. Otherwise, placing the source in a vertical well is the preferred option, in spite of the higher cost.

ACKNOWLEDGMENT

Marwan Wirianto received financial support from the sponsors of the Delphi consortium.

REFERENCES

1. Constable, S. and L. J. Srnka, "An introduction to marine controlled-source electromagnetic methods for hydrocarbon exploration," *Geophysics*, Vol. 72, No. 2, WA3–WA12, 2007.
2. Black, N. and M. S. Zhdanov, "Monitoring of hydrocarbon reservoirs using marine CSEM method," *SEG Technical Program Expanded Abstracts: 79th Annual International Meeting*, 850–854, Houston, USA, October 2009.
3. Lien, M. and T. Mannseth, "Sensitivity study of marine CSEM data for reservoir production monitoring," *Geophysics*, Vol. 73, No. 4, F151–F163, 2008.
4. Orange, A., K. Key, and S. Constable, "The feasibility of reservoir monitoring using time-lapse marine CSEM," *Geophysics*, Vol. 74, No. 2, F21–F29, 2009.
5. Wirianto, M., W. A. Mulder, and E. C. Slob, "A study of land CSEM reservoir monitoring in a complex 3D model," *71st EAGE Conference & Exhibition Incorporating SPE EUROPEC 2009, Extended Abstract*, X020, Amsterdam, 2009.
6. Mulder, W. A., "A multigrid solver for 3D electromagnetic diffusion," *Geophysical Prospecting*, Vol. 54, No. 5, 633–649, 2006.
7. King, R. W., M. Owens, and T. Wu, *Lateral Electromagnetic Waves: Theory and Applications to Communications, Geophysical Exploration, and Remote Sensing*, Springer-Verlag, Inc., New York, 1992.

3D Modeling of Novel Focused Source EM Survey versus the Standard CSEM

S. Davydycheva¹ and N. I. Ryhklinski²

¹3DEM Consulting, USA

²Institute of Innovative Methods of Geophysics, Russia

Abstract— We present a novel Focused Source Electromagnetic (FSEM) method that exploits an idea of focusing the EM field in the vertical direction to provide deep-reading resistivity data. The focusing technique increases the spatial resolution and the depth of investigation of land and marine EM survey, as compared to the conventional Controlled Source EM (CSEM) method. We demonstrate the high efficiency of the focusing principle on challenging 3D models of the geological formation simulating seafloor bathymetry and other complicated shallow effects, which can mask the deeper reservoir response. The focusing reduces the distorting effect of shallow structures dramatically. The idea of the vertical focusing of the EM field have been developed from Laterolog resistivity well logging principle. Laterolog is known to eliminate the axial borehole current at the receiver, reducing the effects of the conductive borehole and of the shoulder beds. However, Laterolog requires an automatic feedback loop to cancel the borehole axial current. It would be hardly feasible to apply such a feedback system on the earth's surface. We suggest a focusing procedure, which is rather based on software, than on hardware solution; still, it is an active focusing system giving results practically equivalent to the physical feedback-loop focusing. Combining together the power of our focusing technique and the power of our 3D numerical modeling method, we handle exceptionally challenging test cases and show that FSEM allows simple visual interpretation of deep reservoir responses and automatic cancelling unwanted shallow effects in cases when the standard CSEM requires full 3D inversion for wide band of frequencies or measurement times. We show that FSEM has an advantage as compared to the standard CSEM in anisotropic formations as well.

1. INTRODUCTION

We suggest a transient EM survey technique based on electric dipole-dipole and dipole-quadrupole measurement. The method utilizes the complete elimination of the axial horizontal current at the grounded electric quadrupole receiver situated between two or four horizontal grounded electric dipole transmitters (Figure 1). Such a setup directs the exciting current under the receiver vertically downward, increasing the sensitivity to a relatively narrow column of rocks directly below the receiver. The focusing dramatically reduces the distorting effect of unwanted shallow structures: Paper [4] shows that whereas separate responses of the receiver to each transmitter are noisy and spiky above a zone of shallow heterogeneities, a combination of these responses — with proper weights to cancel the shallow effects — becomes a smooth function bearing information about deeper structures. Thus, the focusing provides accurate deep-reading resistivity data.

Vertical focusing of the EM field has been developed in earlier Russian publications (for example, [7]) and originates from the resistivity well logging principle used in Laterolog [1]. The Laterolog well logging tool eliminates the axial borehole current at the receiver, thereby reducing the effects of the conductive borehole and shoulder beds. However, Laterolog requires an automatic feedback loop to cancel the borehole axial current, which is not feasible on the earth's surface. Our focusing takes a linear combination of measurements obtained with different grounded dipole transmitters, situated on different sides of the receiver. It is based on software, rather than a difficult hardware solution, yet grants results practically equivalent to the Laterolog-type physical feedback-loop focusing.

The theory behind the technique was developed in [4] assuming that the current on the x -axis between two grounded x -directed electric dipole transmitters (Figure 1(a)) is also x -directed: The technique eliminates the effect of this x -directed current assuming that the y -directed current is negligible, which holds true for most geological formations. However, strong local heterogeneities may occasionally cause perpendicular current leakage in very complex 3D formations. The latest version of FSEM develops the general theory of complete focusing and suggests an advanced setup, eliminating all horizontal currents at the receiver. The FSEM measurement setup automatically cancels many unwanted effects and obtains smooth responses along the measurement profile even

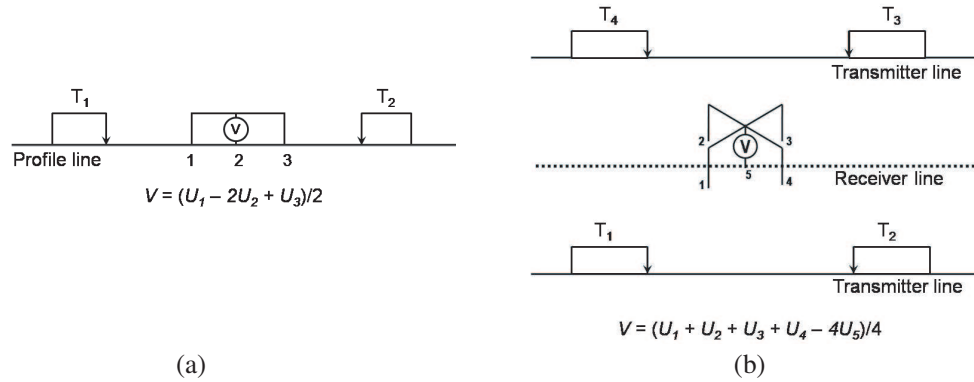


Figure 1: Setup schemes: (a) for incomplete axial focusing; (b) advanced setup for novel complete focusing: four horizontal electric dipole transmitters and a five-electrode quadrupole receiver. The x - and y -coordinates of the receiver: (0, 0); the coordinates of the transmitters (in km): (−5.2, −0.8); (5.2, −0.8); (5.2, 0.8) and (−5.2, 0.8).

in the presence of various shallow heterogeneities, which may strongly affect traditional dipole-dipole measurement data. We suggest an active focusing system which ensures elimination of the horizontal current at the receiver, no matter how complex the surrounding medium is.

2. SETUP SCHEME

Figure 1 shows two setup schemes consisting of two (a) or four (b) grounded horizontal electric dipole transmitters and a five-electrode quadrupole receiver. If U is the potential of the electric field, then the depicted voltmeter (in the receiver depicted in Figure 1(b)) measures the voltage

$$V = d^2U = (U_1 - 2U_5 + U_3 + U_2 - 2U_5 + U_4)/4 \quad (1)$$

which is nothing but the sum of two second differences of the electric potential between the electrodes 1, 5, 3, and 2, 5, 4, respectively, divided by four (or, the circular second difference of the electric potential). Thus, the depicted receiver is in effect a combination of two quadrupoles having negative (internal) co-located poles.

Each transmitter excites the geological formation by repeating low-frequency square pulses of the electromagnetic field. When the current is on, the geometrical DC sounding is performed in a wide range of the setup offsets, which provides preliminary data on the formation resistivity. It may reflect the presence of hydrocarbon-bearing rocks, which are often more resistive than surrounding rocks. The transient response of the formation is measured during the off-time. We employ the square pulses of alternating polarity to remove static and magnetotelluric noise. When using the simplified axial setup (Figure 1(a)) we analyze two ratios of dipole and quadrupole measurements from each transmitter at work, or ratios of the first and the second differences of the electric potential. Taking a particular linear combination, R_x , of these two measurements at the receiver provides vertical focusing of the electric current and elimination of the influence of x -directed axial current at the receiver. When using the advanced setup (Figure 1(b)) we analyze four ratios of dipole and quadrupole measurements from each transmitter at work. Taking a particular linear combination of these four measurements at the receiver, R_{xy} , provides a complete vertical focusing of the electric current and elimination of the influence of both x - and y -directed axial current at the receiver. The proper weights are obtained from the condition of equal potentials in the electrodes 1, 2, 3 and 4, if all transmitters would be excited simultaneously. This solution is equivalent to creating an equal-potential surface around the electrodes 1, 2, 3 and 4 by means of the automatic feedback loop.

Apparently, in homogeneous space or in a horizontally-layered 1D medium this technique results in equal weights of all four measurements. The response from a single transmitter in a 1D medium is identical to the response from the combination of the transmitters shown in Figure 1. In arbitrary 3D mediums all four resulting coefficients or weights may be different to compensate for the distorting effects of various shallow lateral heterogeneities. This makes the method insensitive to unwanted lateral effects and sensitive to a relatively narrow column of rocks situated directly below the receiver.

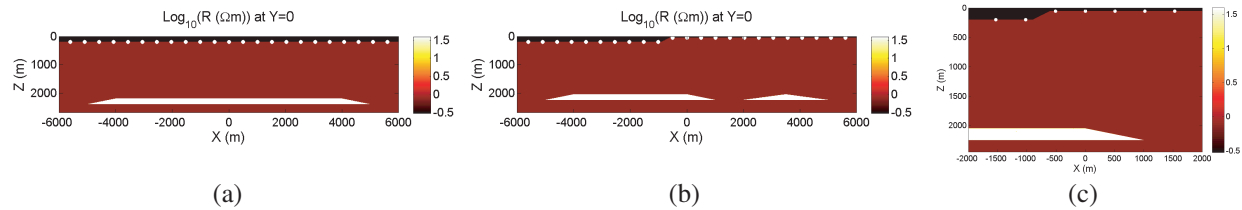


Figure 2: (a) Model 1, one 10×10 km reservoir is situated 2 km below the 50-m-deep seafloor line, and (b) Model 3, bathymetry case: Two deep reservoirs are situated 2 km below the 50-m-deep seafloor line; water depth varies from 200 to 50 m. White dots signify sea-bottom receivers.

On land the method requires three parallel measurement profiles, as depicted in Figure 1(b). In marine application the receivers are typically stationary and situated on the seafloor, and the transmitters are towed above the receivers. A large array of data is typically taken: All sea-bottom receivers register signals from the transmitter in all positions of the sea vessel moving along a few parallel profiles above the receiver line under GPS control. Since the vessel moves, the effective length of the exciting dipole may be longer than the physical transmitter length and depends on the vessel's speed. Thus, varying the speed allows improving signal-to-noise ratio.

The standard CSEM [6] acquires a large array of data as well: Data are typically registered in all sea-bottom receivers for all available transmitter positions. Later they are used in 2D or 3D inversion, which is usually necessary to interpret the data (below we show why). However, FSEM does not typically require a cumbersome 2D-3D inversion: Due to vertical focusing and removal of lateral effects, a simple 1D inversion for 1D layered model parameters or even visual data interpretation allows interpreting data taken at a single receiver. Below we demonstrate this on 3D examples. Thus, a qualified geophysicist or engineer needs only to select the proper measurements from the array of data and simply post-process them to apply the focusing technique. Data from each receiver are processed independently of other receivers, increasing efficiency of the method.

3. MODELING EXAMPLES

We use a fast 3D finite-difference (FD) modeling method developed in [2]. We consider the following models:

- Model 1: 2-km-deep 50- Ωm -resistive reservoir in 1- Ωm formation depicted in Figure 2(a). The plan view dimensions of the reservoir are 10×10 km, and the water depth is 0.2 km.
- Model 2: Two 2-km-deep 50- Ωm -resistive reservoirs in a 1- Ωm formation; their dimensions, in km, follow: (1) Larger prism has vertices at $x_1 = -5, z_1 = 2.25; x_2 = -4, z_2 = 2.05; x_3 = 0, z_3 = 2.05, x_4 = 1, z_4 = 2.25; -3 < y < 3$; (2) smaller prism: $x_1 = 2, z_1 = 2.25; x_2 = 3.5, z_2 = 2.05, \text{ and } x_3 = 5, z_3 = 2.25; -1.5 < y < 1.5$; water depth is 0.2 km; water depth is 0.2 km.
- Model 3: bathymetry case, two 2-km-deep 50- Ωm -resistive reservoirs in a 1- Ωm isotropic formation, with properties of Model 2; water depth varies from 0.2 to 0.05 km (Figures 3(b)–(c)).

Figures 3(a)–(b) models the standard dipole-dipole CSEM measurements in both frequency and time-domain in a wide range. We model responses of sea-bottom receivers to a moving x -directed dipole transmitter situated 0.03 km above the receiver line. For simplicity of representation, we vary the x -coordinate of the receiver, keeping the offset (transmitter-receiver distance) a constant 5.2 km. Our choice of the offset was based on previous studies (for example, [5]). We show relative or normalized responses for the sake of simpler representation and analysis, i.e., the electric field $E_x(x)$ divided by the response measured at a reference point situated far enough from the reservoir (the first or the last point on the receiver line). The absolute responses are shown as well on the bottom.

Figure 3(c) shows time-domain FSEM modeling for the same offset of 5.2 km. The curves depicted in the pictures show the ratios R_{xy} (top) and R_x (bottom) measured by the receiver which is excited by four of two transmitters situated 0.03 km above the seafloor (Figures 1(a), (b)),

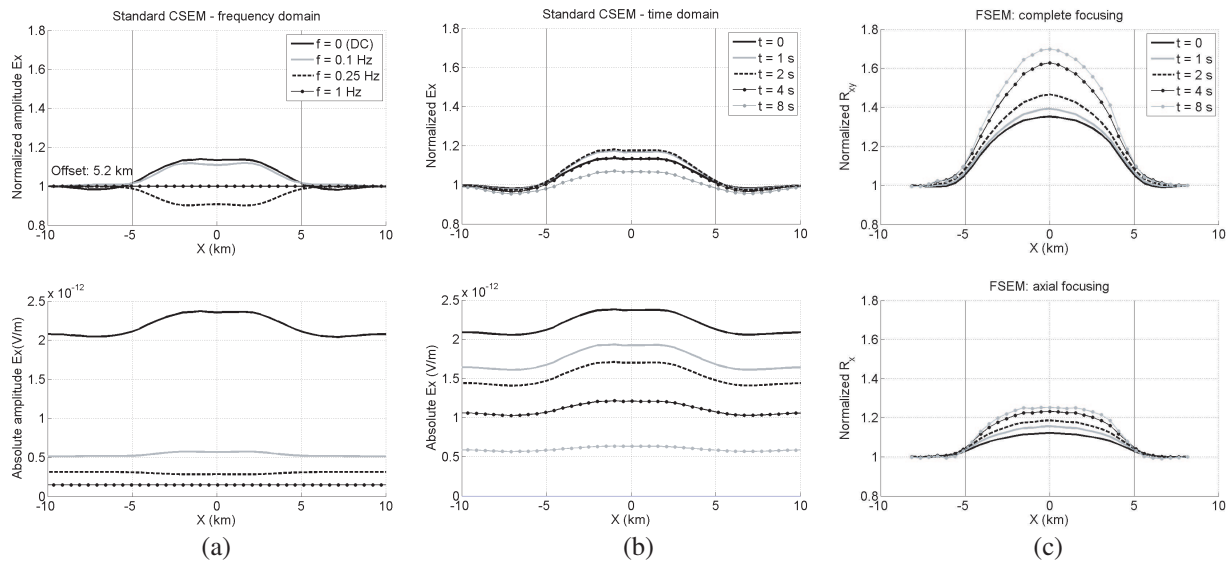


Figure 3: Synthetic responses to Model 1 (see Figure 2(a)): (a) Frequency-domain CSEM, (b) time-domain CSEM and (c) FSEM responses. Thin vertical lines signify the reservoir edges.

normalized to be equal to 1 far enough from the reservoirs — For simplicity of analysis. It is easy to see that the FSEM provides stronger reservoir response than both frequency- and time-domain CSEM, which provide the anomaly above the reservoir on the boundary of detectability level (20% from the background level), and the frequency and time variation does not really help make the relative reservoir response stronger.

Figure 4 shows the responses to Model 2 (two reservoirs) and to Model 3 (two reservoirs with complex sea-floor bathymetry). The standard CSEM response to Model 2 does not allow distinguishing between the larger and the smaller reservoir responses: If the anomaly above the larger reservoir exceeds 30% for both frequency- and time-domain CSEM, the smaller reservoir response is not detectable. In our shallow-water cases non-zero frequency/time does not seem to provide any additional information or any higher spatial resolution, and only reduces the CSEM reservoir anomalies compared to the DC response due to the airwave and the skin-effect. The spatial resolution of the standard CSEM is restricted by $\min(\text{offset}, \text{wavelength})$. For example, in the DC case (infinite wavelength) the resolution is determined by the offset only. At the standard 0.25-Hz frequency the wavelength in the seafloor is 6.3 km, which is longer than the offset of 5.2 km. So, the resolution is again restricted by the offset. At 1 Hz the wavelength is 3.2 km, but the reservoir responses are weak (almost absent) since they are dominated by the airwave. On the contrary, FSEM provides detectable anomalies above the both reservoirs, with a clear separation between them. Due to the focusing, the spatial resolution of FSEM is not restricted by the offset: we can successfully resolve the smaller target whose diameter is about twice as small as the offset (5.2 km).

The standard CSEM response to the bathymetry model (Figures 4(d)–(e)) is completely different from the CSEM response without the bathymetry (Figures 4(a)–(b)). Both frequency-domain (d) and time-domain (e) curves show a strong double elevation: First when the receiver arrives at the shallow zone and second when the transmitter passes over this zone. The bathymetry distorts the CSEM response of the reservoir beyond recognition. This case requires a full 3D inversion to extract reservoir parameters; it is questionable if this information can be reliably extracted in principle. However, the FSEM response with the bathymetry is distorted only above the steep part of the seafloor and in its close vicinity. Beyond this zone the FSEM curves (Figure 4(f)) look nearly identical to the respective curves without the bathymetry (compare with Figure 4(c) — Constant water depth of 200 m). This creates a possibility of a simple visual interpretation even in this exceptionally challenging case, since we can observe a clear elevation of the FSEM response directly above each of two reservoirs, with a clear separation between them, independent of the seafloor shape. A simple 1D inversion could also provide a reasonable solution in all receivers, perhaps excepting the case of a receiver situated right on the edge of the shallow zone. [It would be difficult either to reliably acquire or model data in this receiver; this prevents us from showing the result].

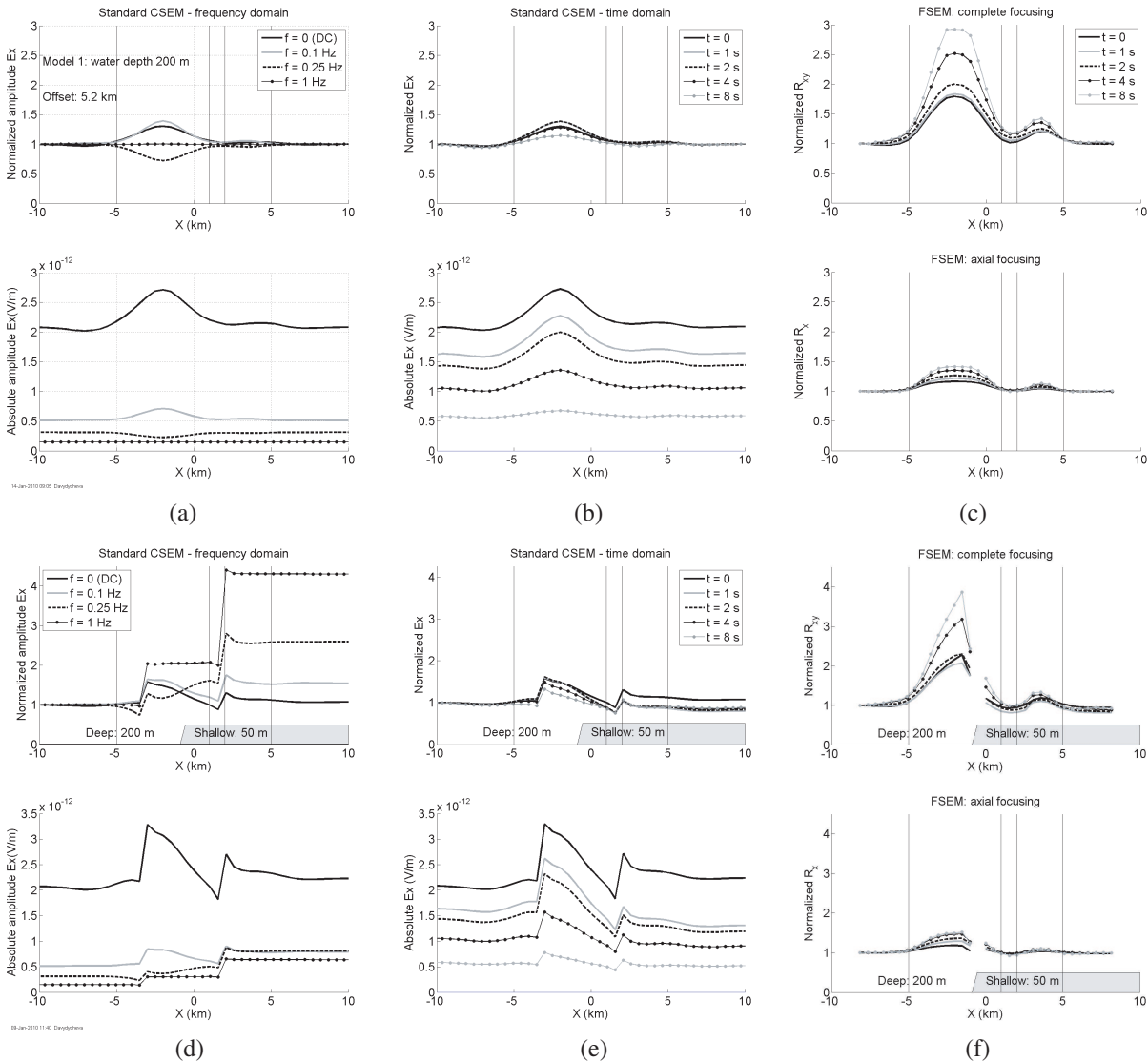


Figure 4: Synthetic responses to Model 2, two reservoirs situated 2 km below the 200-m-deep seafloor line (see Figures 2(b)–(c)): (a) Frequency-, (b) time-domain CSEM and (c) FSEM responses; in the bottom the corresponding case without the bathymetry is shown (depth varies from 200 to 50 m): (d) Frequency-, (e) time-domain CSEM and (f) FSEM responses. Thin vertical lines signify the reservoir edges.

4. CONCLUSION

We developed a novel FSEM method and showed that it has a potential for revealing and delineating deep hydrocarbon reservoirs in challenging cases where the standard marine or land CSEM method fails to provide reliable results. Our method enables directing the EM energy deep into the geological formation based on the focusing principle. We suggest a simple implementation of the focusing technique and demonstrate its successful application on complex 3D modeling examples. The new method provides great depth of investigation. It allows simple visual interpretation even in exceptionally challenging cases of the 2-km deep reservoirs in shallow water, in the presence of the sea-floor bathymetry. The data obtained in each receiver can be processed independently of the other receivers, so a simple point-by-point 1D inversion can be promising.

The focusing technique has been developed based on a similar principle used in resistivity well logging tools like the Laterolog. However, the Laterolog logging method requires an automatic feedback loop to remove the borehole axial current. This makes its on-land or marine application difficult. We have developed a simple but successful implementation of the focusing idea for both land and marine applications.

Successful field examples can be found in [3, 4].

ACKNOWLEDGMENT

We appreciate valuable help of Leonid Knizhnerman and Svetlana Schedrina (CGE, Moscow).

REFERENCES

1. Doll, H. G., “Laterolog: A new resistivity logging method with electrodes using an automatic focusing system,” *Journal of Petroleum Technology*, 1951.
2. Davydycheva, S. and V. Druskin, “Staggered grid for Maxwell’s equations in arbitrary 3-D inhomogeneous anisotropic media,” *Oristaglio, M., and Spies, B., Eds., Three-dimensional Electromagnetics: SEG*, 119–137, 1999.
3. Davydycheva, S. and N. Rykhliniski, “Focused source EM survey versus time-domain and frequency-domain CSEM,” *The Leading Edge*, No. 8, 944–949, 2009.
4. Davydycheva, S., N. Rykhliniski, and P. Legeydo, “Electrical-prospecting method for hydrocarbon search using the induced polarization effect,” *Geophysics*, Vol. 71, G179–G189, 2006.
5. Frenkel, M. and S. Davydycheva, “A modeling study of low-frequency CSEM in shallow water,” European Association of Geophysicists and Engineers, Extended abstract, Amsterdam, 2009.
6. Johansen, S. E., H. E. F. Amundsen, T. Røsten, S. Ellingsrud, T. Eidesmo, and A. H. Bhuyian, “Subsurface hydrocarbons detected by electromagnetic sounding,” *First Break*, Vol. 23, No. 3, 31–36, 2005.
7. Rykhliniski, N. I., S. Davydycheva, A. S. Kashik, V. L. Druskin, P. Y. Legeido, and V. I. Dmitriev, “A method of surface electromagnetic survey to investigate 3D formations,” Patent USSR 1454101, 1986.

Inversion of 3D Marine CSEM Data Using Seed-type Initial Models

Michael A. Frenkel
EMGS, USA

Abstract— The marine Controlled-Source Electromagnetic (CSEM) method has been evolving into a subsurface resistivity imaging tool for increasingly complex geological settings. The measured EM field needs to be inverted to obtain accurate formation resistivity volumes. This information can be used to find reservoirs and determine hydrocarbon saturations. An important step in the resistivity interpretation process is the inclusion of constraints to guide inversion and reduce its non-uniqueness. In this paper, we use 2.5D and 3D synthetic models to investigate the accuracy of the subsurface resistivity reconstruction using additional information about the target body’s position. We show that application of seed-type initial models leads to a significantly improved inversion-based CSEM resistivity interpretation.

1. INTRODUCTION

The value of subsurface resistivity data has never been in doubt in the exploration community. In the past, this information only came from well logs. Now, electromagnetic survey methods can acquire subsurface resistivity data without drilling. The marine CSEM method, which relies on a horizontal electric dipole emitting a predefined low-frequency spectrum, and the EM fields recorded by ocean bottom receivers, has been used commercially in hydrocarbon exploration since 2002 [4]. Since then, the oil and gas industry has gained experience with the method and the EM surveying technique are now used routinely by major operators in many offshore basins around the world [1–16]. Some CSEM surveys are performed before drilling to predict the presence of hydrocarbons. Others are performed after drilling to calibrate the technique [e.g., 2, 7, 8, 14]. In some cases with simple subsurface resistivity structure, stand-alone EM survey data can be sufficient for identifying the presence of resistive hydrocarbons. In complex situations, integration with available seismic and log data is required to increase reliability of CSEM resistivity interpretation.

3D inversion accommodates detailed resistivity variations in the subsurface and is well-suited for analysis of CSEM datasets. The vast majority of commercially viable solutions for 3D inversion imaging of the subsurface rely on a gradient-based, iterative inversion approach in which the full set of Maxwell’s equations is solved on a finite grid during each iteration step [e.g., 1, 15]. The model change after each step is determined from the gradient $g = \partial\varepsilon/\partial\sigma_i$ of a misfit functional ε with respect to the conductivities in a discretized model σ_i .

It is known that even a carefully executed inversion-based interpretation yields several different results, only one of which best reflects the true subsurface resistivity. With sufficient information and experience, it should, in principle, be possible to identify the most plausible result, but as in all geophysical interpretations, this very much depends on the ability of the interpreter. In this paper, we discuss a possible way to make inversion-based interpretation process more data and information-driven and less interpreter-driven. Our approach is based on the concept of seed inversion, which uses limited additional information (e.g., from logs) to build a more reliable starting model.

2. MODELING AND INVERSION METHODS

In this paper, we use the fast finite-difference time-domain method to simulate synthetic CSEM data. The code permits modeling of the electromagnetic field for arbitrarily placed sources and receivers with high accuracy [10]. For data inversion, we use 2.5D and 3D inversion programs. The 2.5D inversion algorithm is based on an iterative Gauss-Newton model update [6], and the 3D inversion algorithm uses a Quasi-Newton, gradient-based model update [15]. Important features of the inversion tools include: ability to use soft structural constraints from seismic through tear surfaces, a priori models, and the initial models. A wide range of regularization options to limit the model space, such as minimum total variation, minimum gradient support, and minimum anomaly, is also available.

In practice, for 3D inversion we employ an integrated approach to building initial models using prior knowledge from seismic and well logs in combination with resistivity information from lower dimensional inversion schemes (e.g., 1D and 2.5D) that require less computational time. If prior knowledge is limited, we use simple half-space starting models.

3. MODELING SETTINGS

The electromagnetic field is excited by the Horizontal Electric Dipole source that is towed at a fixed 30 m distance from the seafloor. The bottom panel of Figure 1 shows the XZ cross-section of the model used in this study. The 3D reservoir has dimensions $(X \times Y \times Z) = (6.0 \times 6.0 \times 0.2)$ km, while in the 2.5D case, the model properties are Y -invariant. In both 2.5D and 3D cases, the reservoir thickness in the Z -direction is 0.2 km and the top of the reservoir is located 1.5 km below the seafloor. The 2.5D and 3D models we used in tests are isotropic. The resistivities of the water, background, and target are 0.3, 1.0, and $20 \Omega\cdot\text{m}$, respectively. The 3D synthetic grid consisting of five lines (Tx01–Tx05) is shown in the top panel of Figure 1. We simulated CSEM data for the frequencies ranging from 0.05 to 2 Hz.

4. SYNTHETIC DATA INVERSION TESTS

An important step in the resistivity interpretation process is the inclusion of constraints from seismic and well log data to guide CSEM inversion and reduce its non-uniqueness. In this section, we introduce the seed-type initial models generated using a small region within the target body, and investigate the accuracy of the subsurface resistivity reconstruction using these types of initial models.

2.5D Tests. We tested the half-space and three-layer starting models. In both cases, the background resistivity is set to its true value of $1 \Omega\cdot\text{m}$. In the three-layer initial model, the resistivities of the layers located below the seafloor are 1, 5, and $1 \Omega\cdot\text{m}$; the Z -position and thickness of the second layer coincide with the corresponding local target parameters.

The results of inversion shown in Figure 2 indicate that the three-layer seed initial model yields a much sharper image of the target, i.e., the recovered resistivity is close to the accurate target resistivity, and the image indicates almost accurate vertical and lateral boundaries of the target. The convergence of inversion is faster when the three-layer seed model is used.

3D Tests. We tested the half-space and 3D smoothed local seed starting models. In both cases, the background resistivity was set to its true value of $1 \text{ Ohm}\cdot\text{m}$. In the smoothed model case, we used a small body of $1 \times 1 \times 0.2$ km size and $10 \Omega\cdot\text{m}$ resistivity. However, after resistivity smoothing, the maximum value of resistivity was $\sim 2 \Omega\cdot\text{m}$.

The results of inversion shown in Figure 3 indicate that the seed smooth initial model yields a much sharper, artifact-free resistivity image of the subsurface and the target, i.e., the recovered

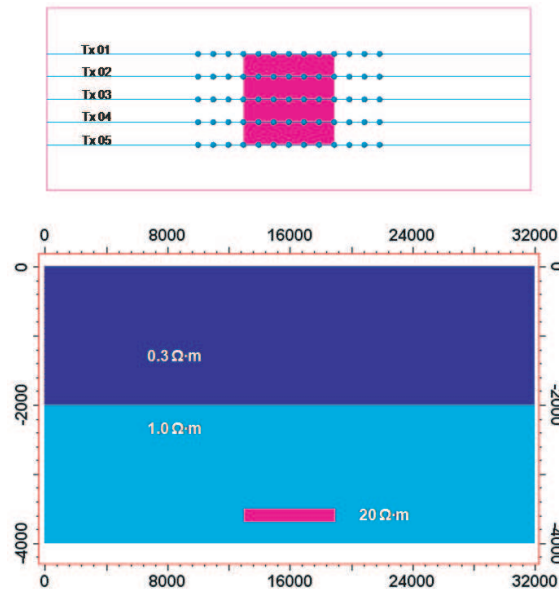


Figure 1: Model Settings (not to scale). Top — the 3D acquisition grid, the inline receiver spacing and the distance between the lines are 1.0 and 1.5 km, respectively. Bottom — XZ cross-section of the model used in this study. The reservoir has dimensions $(X \times Y \times Z) = (6 \times 6 \times 0.2)$ km. In both the 2.5D and 3D cases, the top of the reservoir is located 1.5 km below the seafloor. The model is isotropic and the resistivities of the water, background, and target are 0.3, 1.0, and $20 \Omega\cdot\text{m}$, respectively.

resistivity is closer to the accurate target resistivity and the image indicates a more accurate vertical position of the target body.

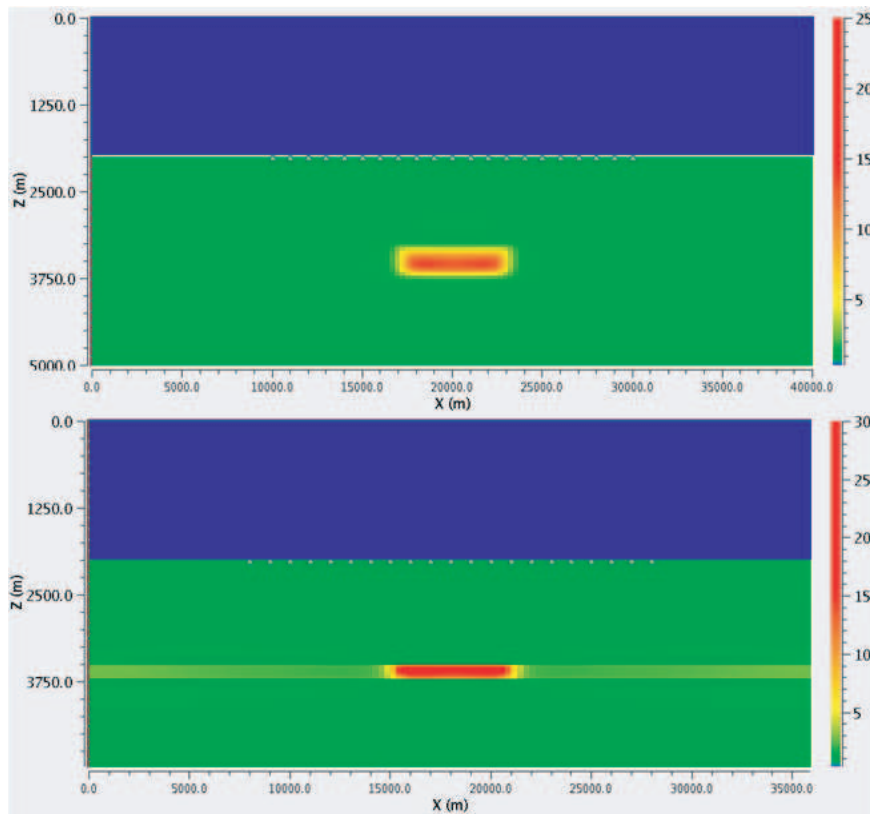


Figure 2: Top — 2.5D inversion results obtained using $1 \Omega\cdot\text{m}$ half-space starting model. Bottom — 2.5D inversion results obtained using the three-layer seed starting model of 1, 5, and $1 \Omega\cdot\text{m}$.

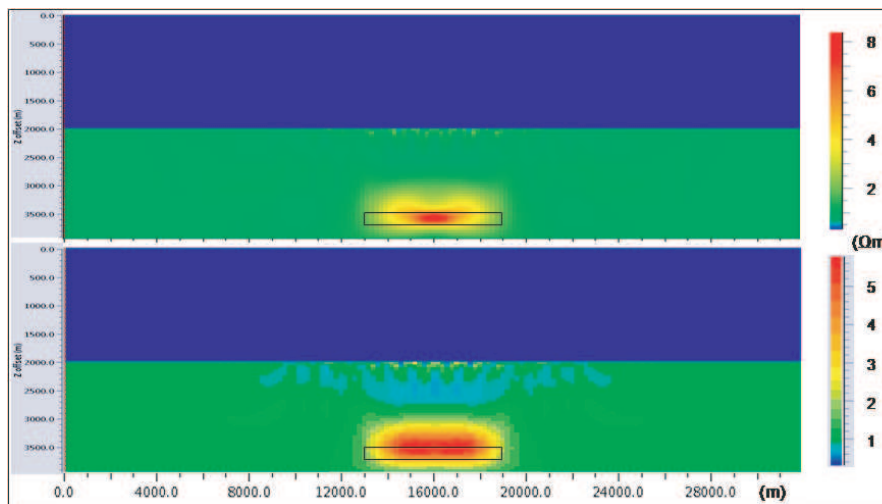


Figure 3: The two panels show the vertical (XZ) cross-sections of 3D inversion cubes for line Tx03 obtained using two starting models. Bottom — 3D inversion results obtained using $1 \Omega\cdot\text{m}$ half-space starting model. Top — 3D inversion results obtained using the smooth $1.0 \times 1.0 \times 0.2 \text{ km}$ seed starting model. The black box shows the target outline.

5. CONCLUSION

Using simple 2.5D and 3D synthetic CSEM models we found that seed-type initial models provide faster convergence and more focused (accurate) resistivity inversion results. Model tests showed

that the most important parameter to build valid 3D seed initial models to guide inversion in the correct direction is the location of the hydrocarbon target center, while the initial resistivity level is less important. Additional tests of the 3D CSEM seed inversion approach using more complicated anisotropic models and field data are being performed.

ACKNOWLEDGMENT

The author would like to thank A. Kumar and S. Sun for performing calculations.

REFERENCES

1. Abubakar, A., T. M. Habashy, V. L. Druskin, L. Knizhnerman, and D. Alumbaugh, "2.5D forward and inverse modeling for interpreting low-frequency electromagnetic measurements," *Geophysics*, Vol. 73, No. 4, F165–F177, 2008.
2. Darnet, M., M. C. K. Choo, R.-E. Plessix, M. L. Rosenquist, K. Y. Cheong, E. Sims, and J. W. K. Voon, "Detecting hydrocarbon reservoirs from CSEM data in complex settings: Application to deepwater Sabah, Malaysia," *Geophysics*, Vol. 72, No. 2, WA97-103, 2007.
3. Dell'Aversana, P., M. Vivier, and A. Tansini, "Expanding the frequency spectrum in marine CSEM applications," *EGM International Workshop*, Capri, Italy, 2007.
4. Eidesmo, T., S. Ellingsrud, L. M. MacGregor, S. Constable, M. C. Sinha, S. Johansen, F. N. Kong, and H. Westerdahl, "Seabed logging (SBL), a new method for remote and direct identification of hydrocarbon filled layers in deepwater areas," *First Break*, Vol. 20, 144–152, 2002.
5. Gribenko, A. and M. S. Zhdanov, "Rigorous 3D inversion of marine CSEM data based on the integral equation method," *Geophysics*, Vol. 72, WA73–WA84, 2007.
6. Hansen, K. R. and R. Mittet, "Incorporating seismic horizons in inversion of CSEM data," *79th Annual International Meeting, SEG, Expanded Abstracts*, 694–698, Houston, TX, 2009.
7. Harris, P., Z. Du, L. MacGregor, W. Olsen, R. Shu, and R. Cooper, "Joint interpretation of seismic and CSEM data using well log constraints: an example from the Luva field," *First Break*, Vol. 5, 73–81, 2009.
8. Hesthammer, J., A. Stefatos, M. Boulaenko, S. Fanavoll, and J. Danielsen, "CSEM performance in light of well results," *The Leading Edge*, No. 1, 258–264, 2010.
9. Jing, C., K. Green, and D. Willen, "CSEM inversion: Impact of anisotropy, data coverage, and initial models," *78th Annual International Meeting, SEG, Expanded Abstracts*, Las Vegas, NV, 2008.
10. Maaø, F. A., "Fast finite-difference time-domain modeling of marine-subsurface electromagnetic problems," *Geophysics*, Vol. 72, No. 2, A19–A23, 2007.
11. Newman, G. A., M. Commer, and J. J. Carazzone, "Imaging CSEM data in the presence of electrical anisotropy," *Geophysics*, Vol. 75, No. 2, F51–F61, 2010.
12. Smit, D. and R. P. Wood, "Experience is crucial to expanding CSEM use," *World Oil*, Vol. 9, 37–43, 2006.
13. Srnka, L. J., J. J. Carazzone, M. S. Ephron, and E. A. Eriksen, "Remote reservoir resistivity mapping," *The Leading Edge*, Vol. 25, 972–975, 2006.
14. Yuan, H., T. Pham, J. J. Zach, M. A. Frenkel, and D. Ridyard, "Exploration case studies in mature Gulf of Mexico basins using 3D marine CSEM," *Proceedings of Annual Meeting, SEG*, Houston, TX, 2009.
15. Zach, J. J., A. K. Bjørke, T. Støren, and F. Maaø, "3D inversion of marine CSEM data using a fast finite-difference time-domain forward code and approximate Hessian-based optimization," *SEG, Expanded Abstracts*, Vol. 27, 614, 2008.
16. Zach, J. J. and M. A. Frenkel, "3D inversion-based interpretation of marine CSEM data," *Offshore Technology Conference*, 20289, Houston, TX, 2009.

Simultaneous Joint Inversion of Seismic and Magnetotelluric Data for Complex Sub-salt Depth Imaging in Gulf of Mexico

M. Viriglio, M. De Stefano, S. Re, F. Golfrè Andreasi, and F. F. C. Snyder
WesternGeco, Italy

Abstract— We present the first application of the 3D simultaneous joint inversion (SJI) between seismic and marine magnetotelluric data over the northern Gulf of Mexico. Interpreting the complex salt structures is a key to understand and create accurate tomographic velocity models, which in turn, are necessary to properly position and image the subsalt targets in the framework of the geophysical exploration. SJI collects seismic and non-seismic information into a single-objective function to be inverted, as opposed to the multiple functions inverted by both single-domain approaches. SJI enhances the ambition of improving the existing velocity models for prestack depth migrations and the consistency of seismic and non-seismic representations of the subsurface in complex salt geometries.

1. INTRODUCTION

Various approaches have been proposed ([1–3]) for multidomain and multimeasurement integration, both in processing and interpretation. As a general view, integration can take place at different levels of an exploration workflow: to constrain processing, inversion, or simply when comparing interpretations or co-rendering them. Nowhere is this approach more important than in the Green Canyon-Garden Banks-Keathley Canyon-Walker Ridge areas where salt complexity is challenging, even with the latest wide-azimuth acquisition and processing methods.

Properly interpreting the numerous coalescing allochthonous salt canopies that cover potential reservoir structures is a key to understand and create accurate tomographic velocity models. The salt structures are particular challenges to deepwater exploration in this part of northern Gulf of Mexico and in order to properly position the subsalt targets for geophysical exploration, a consistent representation of the velocity model is the most important requirement for depth imaging.

2. SIMULTANEOUS JOINT INVERSION: THE METHOD

Simultaneous Joint Inversion (SJI) is a robust and integrated process to invert multiple geophysical parameters within one unique cost function. Beyond the algorithm, this requires integrated workflows across traditionally distinct geophysical domains (Seismic, Gravity, and Electromagnetics).

The SJI workflow presented here combines MMT and seismic measurements integrated within the inversion phase: in SJI inversion, one single objective function is inverted, as opposed to the multiple functions inverted in the single domains approach ([1, 2]). The kernel of the objective function is built by three different elements as displayed in Equation (1) ([1]): residual collection from different domains (ϕ_{d1} , ϕ_{d2}), single domain constraints (ρ_{m1} , ρ_{m2}) and several interdomain constraints (ξ_i). From this point of view, the role of SJI is to combine the residuals, collate the constraints for single domain models, set the constraints between the models of different domains, and finally invert for the two models involved.

In this contest, SJI uses the same regularization and preconditioning that the single domains use for standard inversion. This is one of the key benefits provided by the SJI: each domain is regularized (and/or preconditioned) as in single domain inversions. First order (Gradient filters) or second order (Laplacian filters) have been tested and used, but in general any regularizer could be used in order to drive the coherence between adjacent cells of the same model. Laplacian filters for both seismic and MMT have been used in the following examples.

The algorithm inverts for all the models providing updates for the different domains. From the inversion point of view, the SJI is fully described by the single objective function β in Equation (1) where we used a summation of different costs as opposite of [2] where multiplication has been used:

$$\beta(m_1, m_2) = \lambda_1 \phi_{d1}(r_1) + \lambda_2 \phi_{d2}(r_2) + \lambda_3 \rho_{m_1}(m_1) + \lambda_4 \rho_{m_2}(m_2) + \sum_{i=0}^n \xi_i(m_1, m_2) \quad (1)$$

β is the unique function to minimize
 m_i are the models to invert

ϕ_i are the contributes from the residuals
 ρ_i are the contributes from the regularizations
 $\xi_1, \xi_2, \dots, \xi_n$ are the cross-links between unknowns
 λ_i are the weights for each component

3. THE MT SIGNAL AND DATA PROCESSING

The electromagnetic source for magnetotellurics is the natural time-varying geomagnetic field. A useful measure of its level is the Ap index. It is a measure of the general level of geomagnetic activity over the globe for a given day. It is derived from measurements made at a number of stations world-wide of the variation of the geomagnetic field due to currents flowing in the earth's ionosphere and, to a lesser extent, in the earth's magnetosphere. The strength of solar activities affects the quality of MT signal. The quality of the MT response has a correlation with the good MT source signal. Although solar activity is generally not predictable, the geomagnetic amplitude pulsed at a frequency of approximately 6–9 days. A longer recording window can increase the likelihood of capturing peak MT pulses. Another benefit of a longer recording window is increasing the stacking. Stacking can reduce the random (incoherent) noise and improve the signal-to-noise ratio. The receivers have some common noisy segments, e.g., instrument deployment and recovery. There are also some noise sources which can affect the receivers in different ways, e.g., complicated ocean environment, motional noise, spikes from the atmosphere and ionosphere, pipe lines etc. These noisy segments of data were cut off from the time series and the “quietest” segments of data were then used for processing.

A robust remote reference processing approach [4] was used to calculate the MT impedance tensor from the time series data. The use of a remote reference receiver is the usual way to reduce the incoherent noise in the time series and therefore to improve the data quality.

4. SUBSALT IMAGING

Subsalt seismic imaging is a very common problem due to complex lateral and vertical velocity variations, scarce penetration of seismic energy, wavefield scattering, multiples, conversions, strong ray-path distortion, and irregular illumination with multipath. Solving for complex velocity models is the first goal of the SJI technology when integrated with MMT domain.

MMT measurements provide additional data on the high resistive anomaly of the salt. MMT is suited to investigate within and below the salt formation which provides a strong resistive effect both on apparent resistivity and phase but more importantly MMT is an inductive method capable of detecting the resistivity contrast at the base of salt and it provides a key benefit for velocity model building within and below basalt.

5. SYNTHETIC MODELS

The synthetic tests are based on the standard SEG 3D synthetic model and have three different elements: a water layer, a space variant background velocity (sediments), and the salt formation with constant velocity. We built a proper resistivity model [$\Omega \cdot m$] using well logs information populating the seismic structural framework, and we inverted velocities and resistivities with SJI. In this way, we emulate the common case of very fast and resistive salt structure with different dips and depths, one of the main challenges for today marine applications. Figure 1 shows the velocity and the resistivity models: the two domains use different grids according to the resolution of the measurement. SJI provides a better inversion of the salt anomaly, and a more stable velocity of the background; the SJI velocity model is also more accurate below the bottom of the salt.

6. REAL DATA APPLICATION IN WALKER RIDGE — NORTHERN GULF OF MEXICO

Since the formation of the Jurassic Louann salt during continental crust pre-breakup and subsequent early salt movement due to gravity spreading toward the cooling and sinking oceanic plate, the Gulf of Mexico has been destined as a tectonically favorable exploration province, albeit in places very complex. This complexity comes in part from the repeated and diverse salt movement episodes and the resulting deep water allochthonous canopies; our remote sensing attempts to image favorable hydrocarbon-bearing structures beneath. Properly imaging and interpreting the salt and substructures are primary tools to understanding and creating accurate geologically driven tomographic velocity models, which in turn, are necessary to properly position and image these subsalt targets.

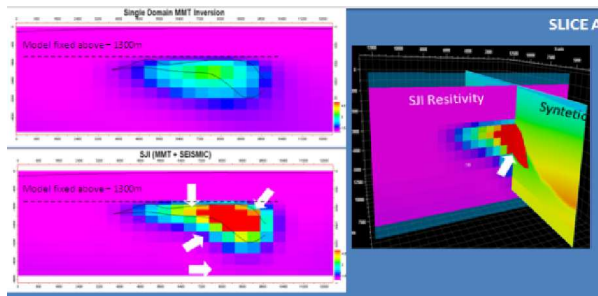


Figure 1: LHS: Comparisons between single domain inversions (top left) and SJI models (bottom left): SJI improves the focusing of the MMT inversions of the salt formation (black line). RHS: Match of SJI base of salt and synthetic one. Proper model the base of salt is a key for enhancing the subsalt depth migrations.

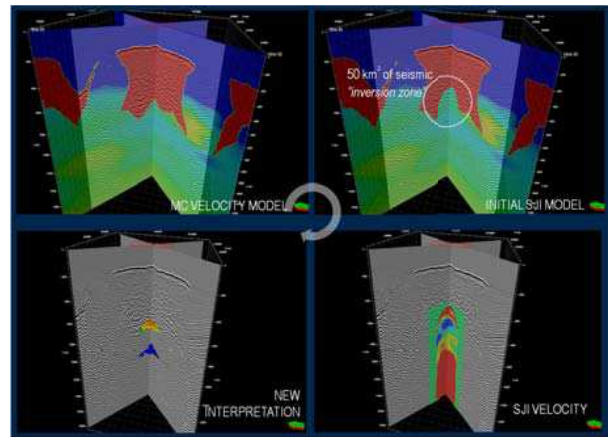


Figure 2: Workflow for the SJI. Clockwise from top left: initial structural framework, salt removal, SJI inversion, and SJI interpretation.

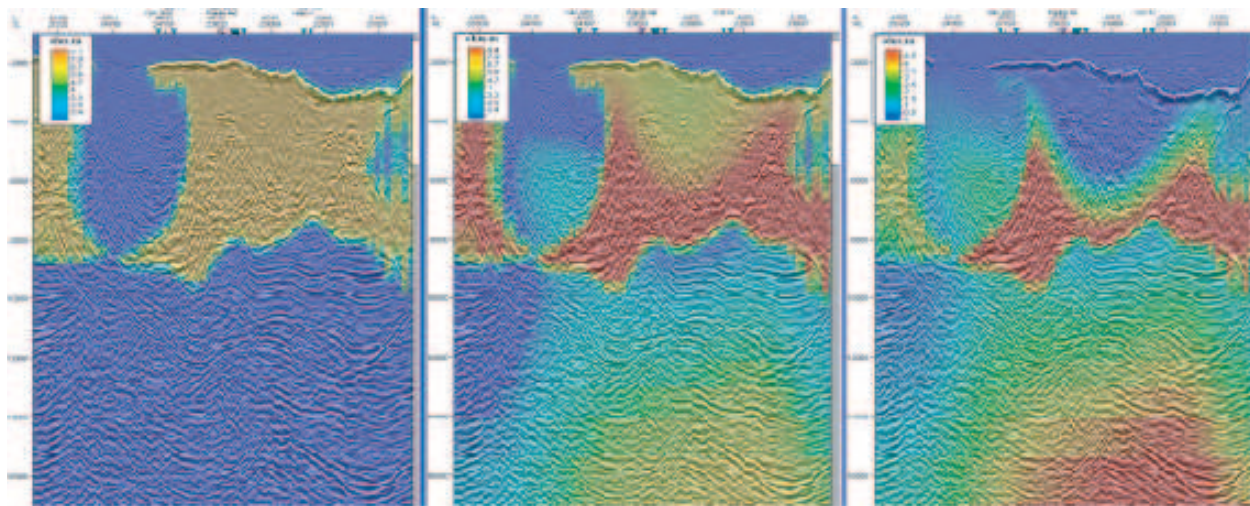


Figure 3: Left: Initial resistivity model. Middle: SJI inverted resistivity. Right: SJI resistivity update.

A robust approach involving seismic and non seismic measurements is very important in the Green Canyon-Garden Banks-Keathley Canyon-Walker Ridge areas because the salt complexity is extremely challenging, even with the latest seismic acquisition methods. Using geological information and multidomain integration to augment seismic data is proving successful. These methods help better facilitate interpreting the entire salt, which is important not only for a better salt model and reservoir image, but also to better understand possible reservoir compartmentalization mechanisms, abnormal pressure cells, and other exploration risks.

Figure 3 shows the SJI resistivity results: inverting MMT data together with seismic reflections helped to detect/confirm the base of allochthonous salt at the macro-scale, and also the top of the deeper and resistive autochthonous salt. Given the high-resolution of the seismic migration, the new bottom of the salt has been interpreted using the seismic velocity and migration.

Figure 2 shows some 3D views of velocities (colored) and seismic (black and white) overlays. For the 3D SJI proof of concept, we started from an existing seismic reflection tomographic model (top left) from which we removed a portion of the salt (top right) obtaining the initial velocity model and ran several iterations of targeted 3D SJI with reflection seismic and MMT data, obtaining the final SJI velocity model (bottom right). The bottom left image shows how the 3D SJI has led to a new 3D interpretation of the allochthonous salt base (colored) and positioning of the autochthonous

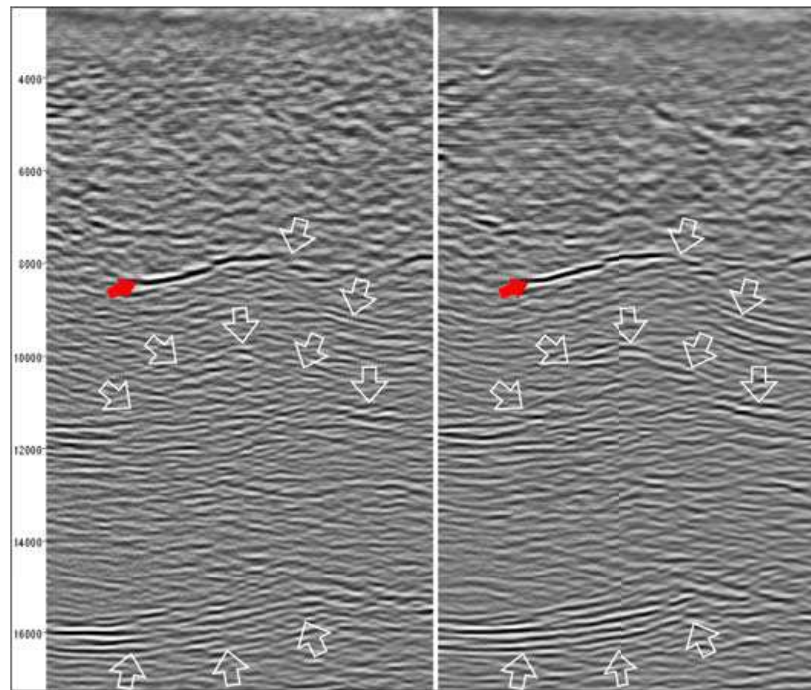


Figure 4: Subsalt zoom of the PSDM sections using single domain velocity model (LHS) and SJI velocity model (RHS). Red arrows points to the base of the salt. White arrows point to the improved subsalt migrated events.

top salt (blue). The new interpretations have been used for new depth migrations to confirm the improvements in the new SJI model.

The SJI results are shown in Figure 4 by means of 3D depth migrations. SJI provides a more focused base of the salt, enhancing the quality of the subsalt migrated events.

7. CONCLUSIONS

We integrated the inversion of seismic and MMT data with the 3D simultaneous joint inversion, showing an application in the northern Gulf of Mexico, and producing new interpretations of the allochthonous and autochthonous salt and thus an improved imaging with new depth migrations. SJI enhances the quality of the seismic migrations, reduces the inversion uncertainties, and most importantly defines a new strategy for subsalt interpretation, thereby enhancing the role of non-seismic methods.

ACKNOWLEDGMENT

The authors would like to thank Stephen Alwon, Michael O'Briain, Don Watts, and Marta Woodward for their advice and help for the project, Luca Masnaghetti for the internal review of this paper, and WesternGeco GeoSolutions and Electromagnetic divisions for the seismic, gravity, and electromagnetic dataset.

REFERENCES

1. De Stefano, M. and D. Colombo, "Pre-stack depth imaging via simultaneous joint inversion of seismic, gravity and magnetotelluric data," *69th EAGE Conference and Exhibition*, 2007.
2. Gallardo, L. A. and M. A. Meju, "Joint two-dimensional DC resistivity and seismic travel time inversion with cross-gradients constraints," *Journal of Geophysical Research*, Vol. 109, No. 10, B03311, 2004.
3. Gamble, T. D., W. M. Goubau, and J. Clarke, "Magnetotellurics with a remote reference," *Geophysics*, Vol. 54, 53–68, 1979.
4. Wenyi, H., A. Abubakar, and T. M. Habashy, "Joint electromagnetic and seismic inversion using structural constraints," *Geophysics*, Vol. 74, No. 6, 99–109, 2009.

Closed-form, Bistatic, 3D Scattering Solution for a Dihedral Corner Reflector

Julie Ann Jackson

Air Force Institute of Technology, USA

Abstract— We use a hybrid geometric optics and physical optics approach to derived a closed-form solution for bistatic scattering in three-dimensions from a right-angle dihedral. The resulting analytic model may be used to efficiently estimate dihedral features in measured radar data. The derived model equations are shown to have excellent agreement with numerical shooting and bouncing rays predictions.

1. INTRODUCTION

Scattering prediction models may be used to extract features of interest in measured synthetic aperture radar (SAR) data. Closed-form scattering models allow for scattering predictions to be computed more efficiently than with numerical electromagnetic prediction codes. Such models are feasible for simple features, such as a dihedral. Thus, we derive a three-dimensional (3D) bistatic scattering model for the right-angle dihedral.

A variety of approaches, including geometric optics (GO), physical optics (PO), physical theory of diffraction (PTD), and uniform theory of diffraction (UTD), have been used to derive scattering from a two-dimensional corner mechanism for both the monostatic and bistatic cases [1–5]. For monostatic radar the 2D problem is of most interest since backscatter is greatly reduced for angles away from the plane of the corner. Bistatic antenna configurations are able to capture specular returns for 3D antenna geometry. Thus, 3D bistatic scattering predictions are desired. We extend the monostatic works to derive in closed-form the 3D bistatic scattering predictions for a PEC, right-angle, rectangular dihedral. We use a hybrid approach, tracing ray reflections with GO and evaluating the PO integral in closed-form, to predict the scattered field. We validate the resulting dihedral model equations with numerical shooting and bouncing rays (SBR) predictions.

2. SCATTERING MODEL DERIVATION

We consider scattering from the interior of the right-angle dihedral depicted in Figure 1. The incident and scattered wave direction vectors are depicted in Figure 2 and are written in Cartesian coordinates as

$$\hat{i} = -(\hat{x} \cos \phi_t \sin \theta_t + \hat{y} \sin \theta_t \sin \phi_t + \hat{z} \cos \theta_t) \tag{1}$$

$$\hat{s} = \hat{x} \cos \phi_r \sin \theta_r + \hat{y} \sin \theta_r \sin \phi_r + \hat{z} \cos \theta_r \tag{2}$$

Dihedral scattering is comprised of single and double-bounce components. The single-bounce scattering from each dihedral plate is computed by solving the PO integral [6]

$$\vec{E} = \frac{-jkZ_0}{4\pi} \int_{S'} \hat{s} \times \left[\hat{s} \times \left(2\hat{n} \times \vec{H}_i \right) \right] e^{-jk\vec{r}' \cdot (\hat{i} - \hat{s})} dS' \tag{3}$$

for scattering from surface S' , where \vec{H}_i is the incident magnetic field, \vec{r}' is a vector from the origin to a point on the surface S' , and \hat{n} is the unit vector normal to the surface S' . Second order scattering is computed as in [1, 7] using GO to trace ray reflection from the first plate to the second plate and then solving the PO integral over the second plate.

2.1. First Order Scattering

From Equation (3), the first order scattering from the plate in the x - z plane (plate xz) is

$$\vec{E}_{xz^1} = \frac{-jkZ_0}{4\pi} \hat{s} \times \hat{s} \times \left[2\hat{y} \times \vec{H}_i \right] \int_{-\frac{L}{2}}^{\frac{L}{2}} \int_0^a e^{-jk\vec{r}'(y'=0) \cdot (\hat{i} - \hat{s})} dx' dz' \tag{4}$$

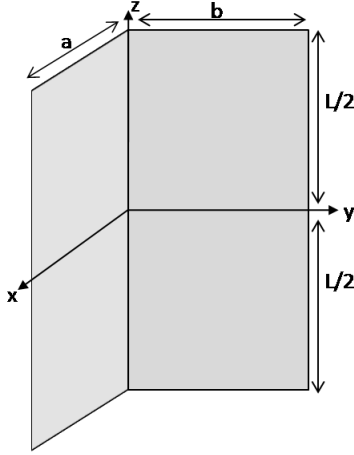


Figure 1: Dihedral corner reflector.

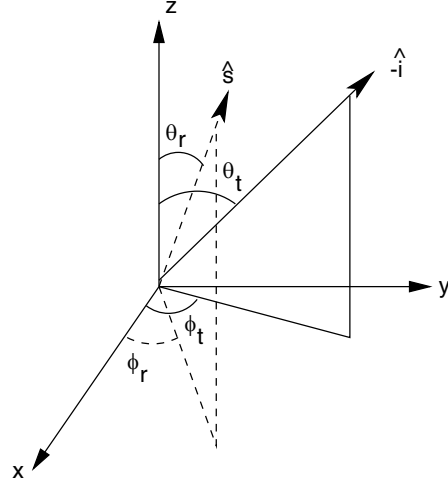


Figure 2: Bistatic spherical coordinate geometry.

For incident electric field $\vec{E}_i = E_\theta \hat{\theta}_t + E_\phi \hat{\phi}_t$, the incident magnetic field is $\vec{H}_i = \frac{-1}{Z_0} (E_\theta \hat{\phi}_t - E_\phi \hat{\theta}_t)$ and (4) becomes

$$\begin{aligned} \vec{E}_{xz^1} = & \frac{jk}{2\pi} \left(\hat{\theta}_r (E_\theta \sin \theta_r \sin \phi_t - E_\phi (\cos \theta_r \cos \phi_r \sin \theta_t - \cos \theta_t \cos \phi_t \sin \theta_r)) + \hat{\phi}_r E_\phi \sin \theta_t \sin \phi_r \right) \\ & \cdot aL \text{sinc} \left(k \frac{L}{2} (\cos \theta_t + \cos \theta_r) \right) \text{sinc} \left(k \frac{a}{2} (\cos \phi_t \sin \theta_t + \cos \phi_r \sin \theta_r) \right) e^{jk \frac{a}{2} (\cos \phi_t \sin \theta_t + \cos \phi_r \sin \theta_r)} \end{aligned} \quad (5)$$

Similarly, the first-order scattering from the plate in the y - z plane (plate yz) is

$$\begin{aligned} \vec{E}_{yz^1} = & \frac{jk}{2\pi} \left(\hat{\theta}_r (E_\theta \sin \theta_r \cos \phi_t - E_\phi (\cos \theta_t \sin \phi_t \sin \theta_r - \cos \theta_r \sin \phi_r \sin \theta_t)) + \hat{\phi}_r E_\phi \sin \theta_r \cos \phi_r \right) \\ & \cdot bL \text{sinc} \left(k \frac{L}{2} (\cos \theta_t + \cos \theta_r) \right) \text{sinc} \left(k \frac{b}{2} (\sin \theta_t \sin \phi_t + \sin \theta_r \sin \phi_r) \right) e^{jk \frac{b}{2} (\sin \theta_t \sin \phi_t + \sin \theta_r \sin \phi_r)} \end{aligned} \quad (6)$$

2.2. Second Order Scattering

First, we consider the case when the transmitted wave is incident on plate yz . Plate yz reflects the wave to plate xz , and the field scattered by plate xz to the receiver is given by the PO integral

$$\vec{E}_{xz^2} = \frac{-jkZ_0}{4\pi} \hat{s} \times \hat{s} \times \left[2\hat{y} \times \vec{H}_{yz} \right] \int_{S_{xz}} e^{-jk\vec{r}' \cdot (y'=0) \cdot (\hat{s}_{yz} - \hat{s})} dS_{xz} \quad (7)$$

where

$$\hat{s}_{yz} = \hat{x} \sin \theta_t \cos \phi_t - \hat{y} \sin \theta_t \sin \phi_t - \hat{z} \cos \theta_t \quad (8)$$

is the direction of the reflection from plate yz that is incident on plate xz and

$$\vec{H}_{yz} = \frac{\hat{x}}{Z_0} (-E_\theta \sin \phi_t - E_\phi \cos \theta_t \cos \phi_t) + \frac{\hat{y}}{Z_0} (-E_\theta \cos \phi_t + E_\phi \cos \theta_t \sin \phi_t) + \frac{\hat{z}}{Z_0} (-E_\phi \sin \theta_t) \quad (9)$$

is the magnetic field reflected from plate yz that is incident on plate xz . Substituting (8) and (9) in (7), the PO scattered field from plate xz is

$$\vec{E}_{xz^2} = \frac{-jk}{2\pi} \left(\hat{\theta}_r (E_\theta \sin \theta_r \sin \phi_t + E_\phi \sin \theta_r \cos \theta_t \cos \phi_t + E_\phi \sin \theta_t \cos \theta_r \cos \phi_r) - \hat{\phi}_r E_\phi \sin \theta_t \sin \phi_r \right) \mathcal{I}_{xz} \quad (10)$$

where we have defined the integral term in (7) as \mathcal{I}_{xz} . The limits of integration for \mathcal{I}_{xz} depend on the dihedral plate sizes and the transmitted field angle of incidence. We define \mathcal{I}_{xz} for the different illumination cases in Table 1.

Table 1: Second-order PO integral terms \mathcal{I}_{xz} and \mathcal{I}_{yz} for three illumination cases, using notation $\psi_x = \cos \phi_t \sin \theta_t - \cos \phi_r \sin \theta_r$, $\psi_y = \sin \phi_t \sin \theta_t - \sin \phi_r \sin \theta_r$, and $\psi_z = \cos \theta_t + \cos \theta_r$.

<ul style="list-style-type: none"> • Case I: $\tan \phi_t \geq \frac{b}{a}$ and $\cot \theta_t \leq \frac{L}{b} \sin \phi_t$ $\mathcal{I}_{xz}^I = \frac{e^{-jk\frac{b}{2}\psi_x \cot \phi_t}}{jk\psi_z} b \cot \phi_t \left(e^{jk\frac{L}{2}\psi_z} e^{-jk\frac{b}{2}\frac{\cot \theta_t}{\sin \phi_t}\psi_z} \text{sinc} \left(k\frac{b}{2} \cot \phi_t \left(\psi_x + \frac{\cot \theta_t}{\cos \phi_t} \psi_z \right) \right) - e^{-jk\frac{L}{2}\psi_z} \text{sinc} \left(k\frac{b}{2} \psi_x \cot \phi_t \right) \right) \quad (11)$ $\mathcal{I}_{yz}^I = \frac{e^{-jk\frac{b}{2}\psi_y}}{jk\psi_z} b \left(e^{-jk\frac{b}{2}\left(\frac{\cot \theta_t}{\sin \phi_t}\psi_z\right)} e^{jk\frac{L}{2}\psi_z} \text{sinc} \left(k\frac{b}{2} \left(\psi_y + \frac{\cot \theta_t}{\sin \phi_t} \psi_z \right) \right) - e^{-jk\frac{L}{2}\psi_z} \text{sinc} \left(k\frac{b}{2} \psi_y \right) \right) \quad (12)$
<ul style="list-style-type: none"> • Case II: $\tan \phi_t \leq \frac{b}{a}$ and $\cot \theta_t \leq \frac{L}{b} \sin \phi_t$ $\mathcal{I}_{xz}^{II} = \frac{ae^{-jk\frac{a}{2}\psi_x}}{jk\psi_z} \left(e^{-jk\frac{a}{2}\left(\frac{\cot \theta_t}{\cos \phi_t}\psi_z\right)} \text{sinc} \left(k\frac{a}{2} \left(\psi_x + \frac{\cot \theta_t}{\cos \phi_t} \psi_z \right) \right) - e^{-jk\frac{L}{2}\psi_z} \text{sinc} \left(k\frac{a}{2} \psi_x \right) \right) \quad (13)$ $\mathcal{I}_{yz}^{II} = \frac{e^{-jk\frac{a}{2}\psi_y \tan \phi_t}}{jk\psi_z} a \tan \phi_t \left(e^{jk\frac{L}{2}\psi_z} e^{-jk\frac{a}{2}\frac{\cot \theta_t}{\cos \phi_t}\psi_z} \text{sinc} \left(k\frac{a}{2} \tan \phi_t \left(\psi_y + \frac{\cot \theta_t}{\sin \phi_t} \psi_z \right) \right) - e^{-jk\frac{L}{2}\psi_z} \text{sinc} \left(k\frac{a}{2} \psi_y \tan \phi_t \right) \right) \quad (14)$
<ul style="list-style-type: none"> • Case III: $\cot \theta_t \geq \frac{L}{b} \sin \phi_t$ and $\cot \theta_t \geq \frac{L}{a} \cos \phi_t$ $\mathcal{I}_{xz}^{III} = \frac{e^{-jk\frac{L}{2}\psi_x \cos \phi_t \tan \theta_t}}{jk\psi_z} L \cos \phi_t \tan \theta_t \left(\text{sinc} \left(k\frac{L}{2} \cos \phi_t \tan \theta_t \left(\psi_x + \frac{\cot \theta_t}{\cos \phi_t} \psi_z \right) \right) - e^{-jk\frac{L}{2}\psi_z} \text{sinc} \left(k\frac{L}{2} \cos \phi_t \tan \theta_t \psi_x \right) \right) \quad (15)$ $\mathcal{I}_{yz}^{III} = \frac{e^{-jk\frac{L}{2}\psi_y \sin \phi_t \tan \theta_t}}{jk\psi_z} L \sin \phi_t \tan \theta_t \left(\text{sinc} \left(k\frac{L}{2} \sin \phi_t \tan \theta_t \left(\psi_y + \frac{\cot \theta_t}{\sin \phi_t} \psi_z \right) \right) - e^{-jk\frac{L}{2}\psi_z} \text{sinc} \left(k\frac{L}{2} \sin \phi_t \tan \theta_t \psi_y \right) \right) \quad (16)$

Table 2: Bistatic, polarimetric scattering equations for the dihedral Figure 1 (\mathcal{I}_{xz} , \mathcal{I}_{yz} defined in Table 1).

$\vec{E}_{\text{total}}^{\text{VV}} = \frac{jkL}{2\pi} E_\theta \hat{\theta}_r \sin \theta_r \text{sinc} \left(k\frac{L}{2} (\cos \theta_t + \cos \theta_r) \right) \left(a \sin \phi_r \text{sinc} \left(k\frac{a}{2} (\cos \phi_t \sin \theta_t + \cos \phi_r \sin \theta_r) \right) e^{jk\frac{a}{2} (\cos \phi_t \sin \theta_t + \cos \phi_r \sin \theta_r)} \right. \\ \left. + b \cos \phi_r \text{sinc} \left(k\frac{b}{2} (\sin \theta_t \sin \phi_t + \sin \theta_r \sin \phi_r) \right) e^{jk\frac{b}{2} (\sin \theta_t \sin \phi_t + \sin \theta_r \sin \phi_r)} \right) - \frac{jk}{2\pi} E_\theta \hat{\theta}_r \sin \theta_r (\mathcal{I}_{xz} \sin \phi_t + \mathcal{I}_{yz} \cos \phi_t) \quad (17)$
$\vec{E}_{\text{total}}^{\text{HV}} = 0 \quad (18)$
$\vec{E}_{\text{total}}^{\text{VH}} = \frac{-jkL}{2\pi} E_\phi \hat{\theta}_r \text{sinc} \left(k\frac{L}{2} (\cos \theta_t + \cos \theta_r) \right) \left(a (\cos \theta_r \cos \phi_r \sin \theta_t - \cos \theta_t \cos \phi_t \sin \theta_r) \right. \\ \cdot \text{sinc} \left(k\frac{a}{2} (\cos \phi_t \sin \theta_t + \cos \phi_r \sin \theta_r) \right) e^{jk\frac{a}{2} (\cos \phi_t \sin \theta_t + \cos \phi_r \sin \theta_r)} \\ \left. + b (\cos \theta_t \sin \phi_t \sin \theta_r - \cos \theta_r \sin \phi_r \sin \theta_t) \text{sinc} \left(k\frac{b}{2} (\sin \theta_t \sin \phi_t + \sin \theta_r \sin \phi_r) \right) e^{jk\frac{b}{2} (\sin \theta_t \sin \phi_t + \sin \theta_r \sin \phi_r)} \right) \\ - \frac{jk}{2\pi} E_\phi \hat{\theta}_r (\sin \theta_t \cos \theta_r (\mathcal{I}_{xz} \cos \phi_r - \mathcal{I}_{yz} \sin \phi_r) + \sin \theta_r \cos \theta_t (\mathcal{I}_{xz} \cos \phi_t - \mathcal{I}_{yz} \sin \phi_t)) \quad (19)$
$\vec{E}_{\text{total}}^{\text{HH}} = \frac{jkL}{2\pi} E_\phi \hat{\phi}_r \sin \theta_r \text{sinc} \left(k\frac{L}{2} (\cos \theta_t + \cos \theta_r) \right) \left(a \sin \phi_r \text{sinc} \left(k\frac{a}{2} (\cos \phi_t \sin \theta_t + \cos \phi_r \sin \theta_r) \right) e^{jk\frac{a}{2} (\cos \phi_t \sin \theta_t + \cos \phi_r \sin \theta_r)} \right. \\ \left. + b \cos \phi_r \text{sinc} \left(k\frac{b}{2} (\sin \theta_t \sin \phi_t + \sin \theta_r \sin \phi_r) \right) e^{jk\frac{b}{2} (\sin \theta_t \sin \phi_t + \sin \theta_r \sin \phi_r)} \right) + \frac{jk}{2\pi} E_\phi \hat{\phi}_r \sin \theta_r (\mathcal{I}_{xz} \sin \phi_r + \mathcal{I}_{yz} \cos \phi_r) \quad (20)$

Next, we consider the case when the transmitted wave is incident on plate xz . Plate xz reflects the wave to plate yz , and the field scattered by plate yz to the receiver is given by the PO integral

$$\vec{E}_{yz^2} = \frac{-jkZ_0}{4\pi} \hat{s} \times \hat{s} \times \left[2\hat{x} \times \vec{H}_{xz} \right] \int_{S_{yz}} e^{-jk\vec{r}' \cdot (\hat{s}_{xz} - \hat{s})} dS_{yz} \quad (21)$$

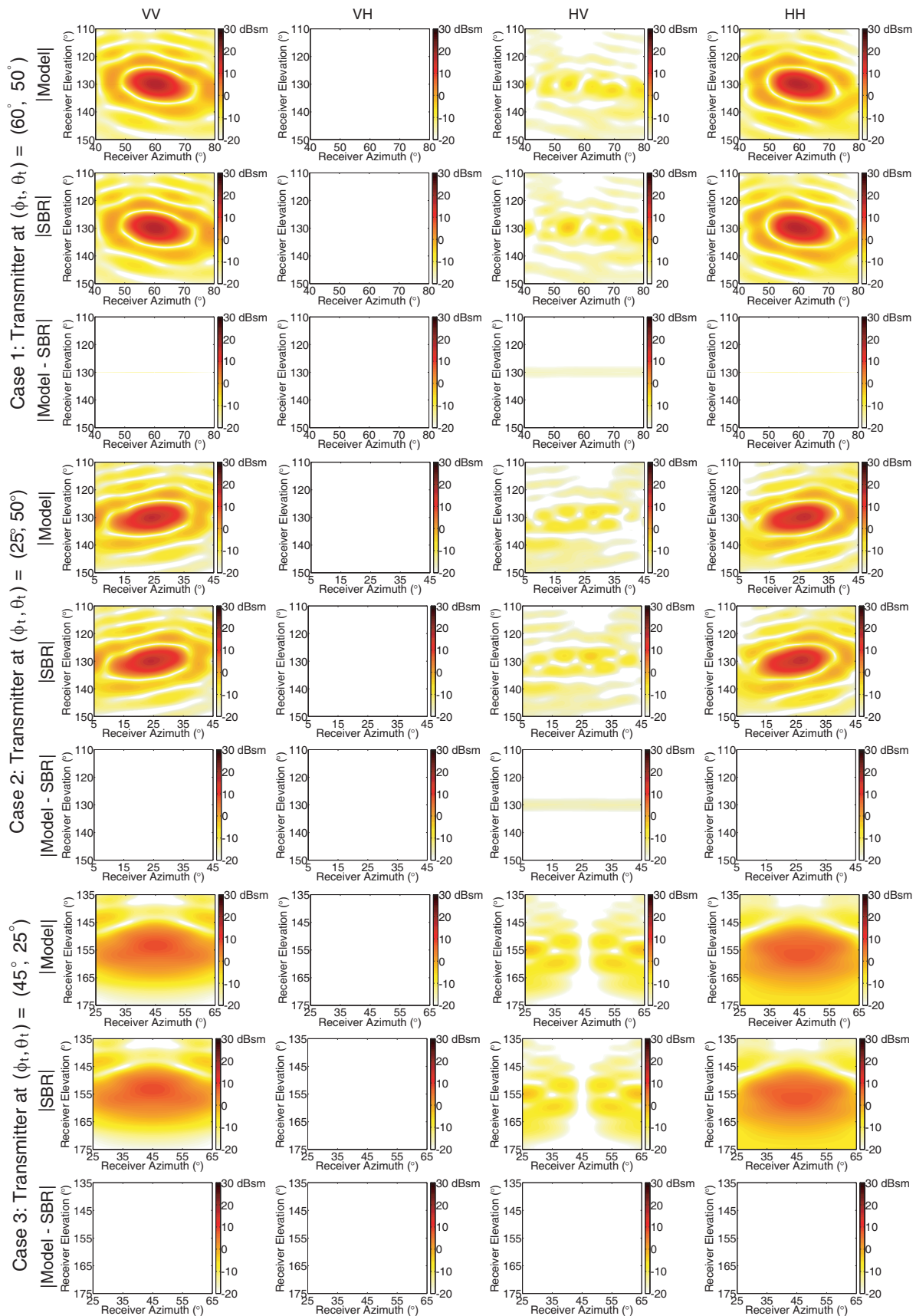


Figure 3: Comparison of bistatic dihedral response for the analytic dihedral model in Table 2 and a shooting and bouncing rays prediction for three illumination cases.

where

$$\hat{s}_{xz} = -\hat{x} \sin \theta_t \cos \phi_t + \hat{y} \sin \theta_t \sin \phi_t - \hat{z} \cos \theta_t \quad (22)$$

is the direction of the reflection from plate xz that is incident on plate yz and

$$\vec{H}_{xz} = \frac{1}{Z_0} (\hat{x}(E_\theta \sin \phi_t + E_\phi \cos \theta_t \cos \phi_t) + \hat{y}(E_\theta \cos \phi_t - E_\phi \cos \theta_t \sin \phi_t) - \hat{z}E_\phi \sin \theta_t) \quad (23)$$

is the magnetic field reflected from plate xz that is incident on plate yz . Substituting (12) and (13) in (11), the PO scattered field from plate xz is

$$\vec{E}_{yz^2} = \frac{-jk}{2\pi} \left(\hat{\theta}_r (-E_\phi \cos \theta_t \sin \phi_t \sin \theta_r - E_\phi \cos \theta_r \sin \phi_r \sin \theta_t + E_\theta \cos \phi_t \sin \theta_r) - \hat{\phi}_r E_\phi \sin \theta_t \cos \phi_r \right) \mathcal{I}_{yz} \quad (24)$$

where we have defined the integral term in (11) as \mathcal{I}_{yz} . \mathcal{I}_{yz} is also defined in Table 1.

2.3. Superposition of Scattering Terms

The total field scattered by the dihedral is given by the sum of first and second-order scattering:

$$\vec{E}_{\text{total}} = \vec{E}_{yz^1} + \vec{E}_{xz^1} + \vec{E}_{yz^2} + \vec{E}_{xz^2} \quad (25)$$

where the second order terms depend on the illumination cases defined in Table 1. Parsing the superposition into terms corresponding to horizontal and vertical transmit and receive polarizations, we obtain the model equations listed in Table 2 for the total dihedral scattering.

3. MODEL VALIDATION

We compare the analytical solution derived above to numerical results produced by shooting and bouncing rays (SBR) computation. We test a dihedral with dimensions $L = 0.45$ m and $a = b = 0.22$ m for the three double-bounce illumination cases. The phase histories shown in Figure 3 have excellent agreement between the derived solution and SBR predictions.

4. CONCLUSION

We have derived a closed-form, polarimetric, bistatic solution for dihedral scattering in three-dimensions using a hybrid GO-PO approach. The resulting phase history matches that obtained using numerical SBR prediction while being computationally efficient.

ACKNOWLEDGMENT

The views expressed in this article are those of the author and do not reflect the official policy or position of the United States Air Force, Department of Defense, or the U.S. Government. Approved for public release #88ABW-2010-0672.

REFERENCES

1. Griesser, T. and C. A. Balanis, "Backscatter analysis of dihedral corner reflectors using physical optics and physical theory of diffraction," *IEEE Transactions on Antennas and Propagation*, Vol. 35, No. 10, 1137–1147, October 1987.
2. Michaeli, A., "A closed form physical theory of diffraction solution for electromagnetic scattering by strips and 90° dihedrals," *Radio Science*, Vol. 19, No. 2, 609–616, March–April 1984.
3. Ruck, G. T., Ed., *Radar Cross Section Handbook*, Plenum Press, New York, 1970.
4. Cripin, Jr., J. W. and K. M. Siegel, *Methods of Radar Cross-Section Analysis*, Academic Press, New York, 1968.
5. Akhter, N., "Far zone electromagnetic scattering from complex shapes using geometrical theory of diffraction," Ph.D. Dissertation, The Ohio State University, 1993.
6. Knott, E. F., J. F. Shaeffer, and M. T. Tuley, *Radar Cross Section*, 2nd Edition, Artech House, Boston, 1993.
7. Gerry, M., "Two-dimensional inverse scattering based on the GTD model," Ph.D. Dissertation, The Ohio State University, 1997.

New Scheme for Radar Target Identification via Target's Internal Modes

Haythem H. Abdullah¹, Khalid F. A. Hussein¹, Mostafa El-Said², and Essam A. Hashish²

¹Electronics Research Institute, Egypt

²Faculty of Engineering, Cairo University, Egypt

Abstract— The extension of the abilities of human senses using synthetic devices or systems is of main concern for long time. So, the trend of developing remote sensing systems has attracted attention of electromagnetic researchers for its important applications such as Air-traffic control, Air defense, exploration geophysics, and several important applications in medicine. In this paper, the target identification of the conducting objects that have cavities with small apertures is considered. These apertures act as coupling windows. If the aperture couples waves to any cavity structure, for example the fuel tanks, internal resonant fields will be excited. The internal resonant fields appear as slowly damped sinusoidal signals in the late time. The internal modes are almost dominated over the target natural modes in the very late time. In this paper, a new scheme is proposed to identify targets via these internal modes. The validation of the algorithm is done using the backscattered signal from conducting structures simulated using our home made Moment Method software.

1. INTRODUCTION

The impulse response of the conducting targets always exhibit two distinct regions; the early time, forced component, representing the backscattered fields excited by currents during the time when the impulse is traversing the target T , and the late time where the target can be discriminated. If the target is closed, then a free oscillating damped signal will appear as a sum of constant amplitude natural modes and exist for all time $t > 2T$. These types of targets can be discriminated using techniques such as, the K pulse technique [1], the modified Prony's method or the E pulse techniques [2–6]. But in cases where small apertures exist, internal resonances will take place. The conventional techniques that can be applied to discriminate targets via its natural modes will fail to deal with the target backscattered response since it succeeds in case of the dominance of the natural modes where the backscattered signal is highly damped sinusoids.

2. THE DISCREMINATION ALGORITHM

In the very late time where the internal modes dominate, one can assign a sampling window for the analysis. The scheme can be described in the following few words; the sampling window takes samples from the back scattered signal starting in the very late time and lasts for sufficient number of cycles for the analysis, say more than 10 cycles of the signal fundamental frequency. The sampled signal is normalized to its maximum value. The normalized signal is fed to a bank of band pass filters. The central frequencies of the filters are assigned according to a data base containing the resonant frequencies of each target. The outputs of the filters are summed. The normalized signal is correlated with the summed signal. There are two cases for the output of the correlator. If the assigned resonant frequencies assigned to the filters are in consistence with those resonant frequencies corresponding to the existing target then the maximum output of the correlator will be the greater one. In this case, the index of the target is taken from the data base and the target is detected. On the other case where the output of the correlator is not the maximum, then the index of the data base targets is incremented. The process will be repeated till the correlator maximum output will be the greater one. At this time the index of the target will be known and the target is detected according to its internal modes. A block diagram illustrating this discrimination algorithm is depicted in Figure 1.

In the following subsections, a description for both the bank of filters and the correlator is introduced followed by illustrative examples for the algorithm.

2.1. FIR Filter Design

The bank of band pass filters can be designed according to the following transfer function

$$H(S) = \frac{kS}{S^2 + \beta S + \omega_0^2} \quad (1)$$

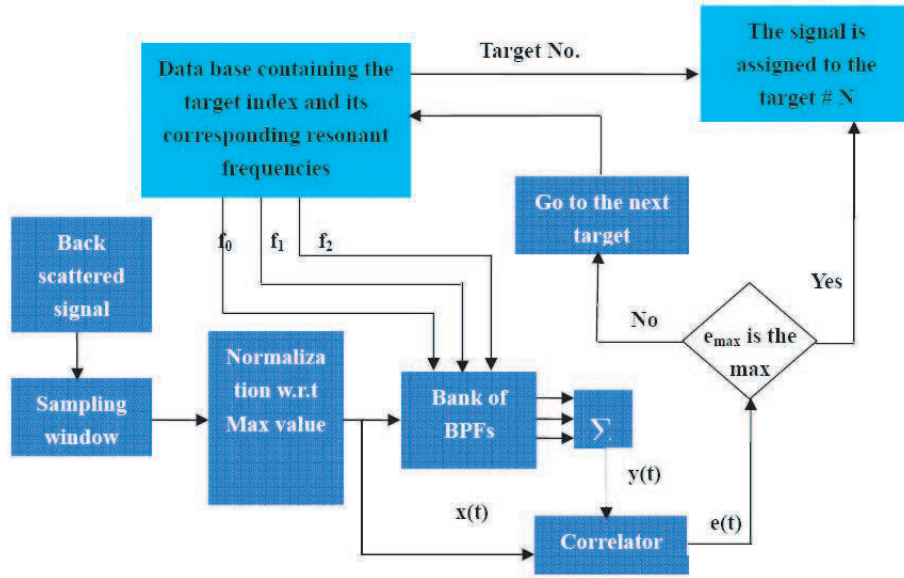


Figure 1: The block diagram explaining the discrimination algorithm.

where: ω_0 is the resonant frequency, β is the 3 dB bandwidth, k is the filter gain, and S is the complex frequency.

In order to transform the transfer function from the S domain (Laplace domain) to the Z -domain, one can use the bilinear transformation for S where

$$S = \frac{2}{\Delta t} \frac{1 - Z^{-1}}{1 + Z^{-1}} \quad (2)$$

Substituting from (2) into (1), and transforming the resultant equation into the discrete time domain taking into consideration the fact that the multiplication by Z^{-1} is corresponding to a time delay of one time step in the discrete time domain. Then the output of the filter can be using the following equation;

$$y(n) = \left(\frac{k}{A}\right) (x(n) - x(n-2)) - \left(\frac{B}{A}\right) y(n-1) - \left(\frac{C}{A}\right) y(n-2) \quad (3)$$

where $x(n)$ and $y(n)$ are the input and the output signals respectively in the discrete time domain.

Note that $x(n)$ is an abbreviation for $x(n\Delta t)$, where Δt is the discretization time step.

Where

$$\left. \begin{aligned} A &= \frac{2}{\Delta t} + \beta + \frac{\omega_0^2 \Delta t}{2} \\ B &= \omega_0^2 \Delta t - \frac{4}{\Delta t} \\ C &= \frac{2}{\Delta t} - \beta + \frac{\omega_0^2 \Delta t}{2} \end{aligned} \right\} \quad (4)$$

2.2. The Correlator Design

Suppose that, the output of the filters is

$$y = y_1 + y_2 + y_3 + y_4 \quad (5)$$

where y_1, y_2, y_3, y_4 are the outputs from each filter of the filters bank. Suppose also that the backscattered signal normalized to its maximum value in the late time be x .

Assume that $x(n)$ is an array containing N samples from the late time, and $y(n)$ is the same number of samples extracted by the filter banks after summing by the summer. The discrete correlation function $e(t)$ can be defined by

$$e(n\Delta t) = \frac{5}{N} \sum_{k=1}^N y(k\Delta t) x((k+n)\Delta t). \quad (6)$$

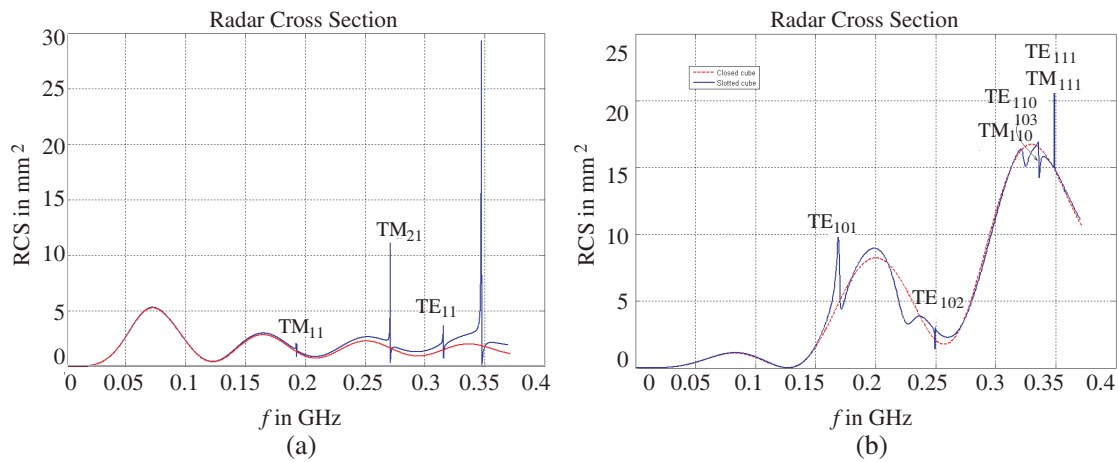


Figure 2: (a) Radar cross section of an open sphere (the blue line) compared to the radar cross section of the closed one (the red one). (b) Radar cross section of a slotted rectangular cavity (the blue line) compared to the radar cross section of the closed one (the red one).

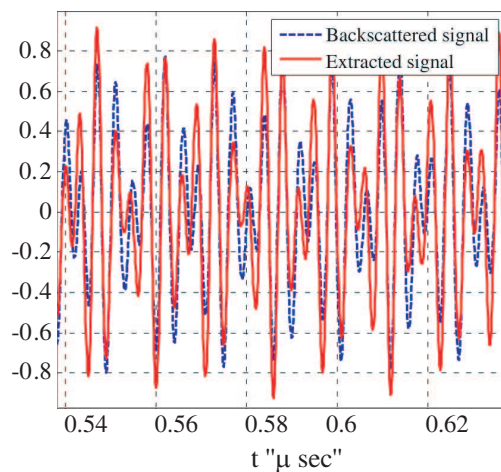


Figure 3: Comparison between the normalized backscattered signal and the extracted signal using the bank of filters that corresponds to the target resonance frequencies.

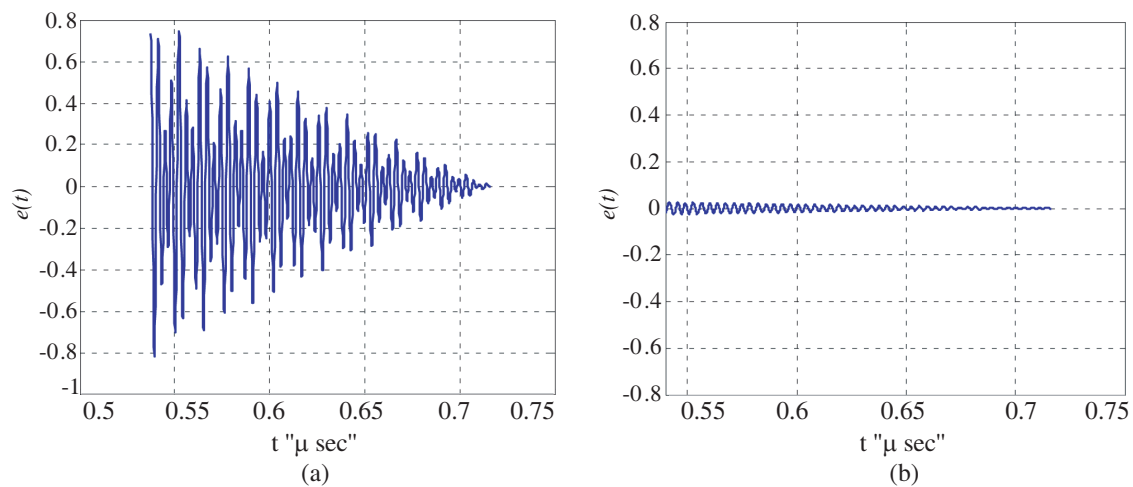


Figure 4: The correlation between the normalized backscattered signal and the extracted signal using the bank of filters associated with (a) the spherical shape. (b) The cubical shape.

3. RESULTS AND DISCUSSIONS

Suppose that there are two targets to be discriminated from each other. In our example we choose targets with small apertures to ensure the existence of sharp peaks in the frequency domain impulse response. The two targets are open sphere, and slotted rectangular box. The simulation of the scattering problem is done using our home-made Moment Method. The software is done according to the analysis described in [7,8]. The triangular patches are used to model the targets. The sphere has a 0.5 m radius and modeled using 1980 triangular patches, the sphere has a circular aperture that makes an angle of 10° from the center of the sphere. The cube dimensions are $0.5\text{ m} \times 1\text{ m} \times 1.5\text{ m}$. The cube is modeled using 1494 triangular patch and total of 2233 shared edges. The slot length is 0.5 m and width is 0.025 m.

Each target has its own internal resonances, so there is a need to design a bank of band pass filters that has center frequencies corresponding to the internal resonances of each target. The Radar Cross Section (RCS) of each of the two targets is depicted in Figure 2.

Figure 3 shows the original backscattered signal from the sphere compared to the extracted signal using the sphere bank of filters. It is noticed that the extracted signal has a similar behavior when the filters central frequencies are those corresponding to the resonance frequencies of the illuminated object. The extracted signal has a slightly different phase and magnitude than the original one due to the filters delays and gains. Also, one can note from the correlation functions depicted in Figures 4(a) and 4(b) that the correlation function has a maximum behavior when the central frequencies of the filters are matched with the resonance frequencies of the illuminated object.

4. CONCLUSION

The coupling of electromagnetic energy inside a closed object that has small coupling apertures in its body will provide the radar target identification designer with important information about the target. This is due to the re-radiation of the stored energy in the form of continuous wave that has enough information for the identification process to take place. This continuous wave is the summation of the contribution of the internal resonances which is unique for each target.

REFERENCES

1. Kennaugh, E. M., "The K-pulse concept," *IEEE Trans. Antennas Propagat.*, Vol. 29, No. 2, 327–331, Mar. 1981.
2. Lui, H.-S. and V. Z. S. Nicholas, "Radar target identification using a banded E-pulse technique," *IEEE Trans. Antennas Propagat.*, Vol. 54, No. 12, 3874–3881, 2006.
3. Morales, J. D., B. David, P. R. Diego, and C. C. Maria, "Radar target identification via exponential pulse synthesis," *IEEE Trans. Antennas Propagat.*, Vol. 55, No. 7, 2064–2072, 2007.
4. Rothwell, E., D. P. Nyquist, K. M. Chen, and B. Drachman, "Radar target discrimination using the extinction-pulse technique," *IEEE Trans. Antennas Propagat.*, Vol. 33, No. 9, 929–937, 1985.
5. Rothwell, E., K. M. Chen, and D. P. Nyquist, "Extraction of the natural frequencies of a radar target from a measured response using E-pulse technique," *IEEE Trans. Antennas Propagat.*, Vol. 35, No. 5, 715–720, 1987.
6. Yingbo, H. and T. K. Sarkar, "A discussion of E-pulse method and Prony's method for radar target resonance retrieval from scattered field," *IEEE Trans. Antennas Propagat.*, Vol. 37, No. 7, 944–946, 1989.
7. Abdullah, H. H., J. Y. Yang, N. Bagherzadeh, and K. F. Hussein, "Parallel electric field integral equation solver for arbitrary shaped conducting bodies," *PIERS Proceedings*, 1661–1666, Beijing, China, Mar. 23–27, 2009.
8. Rao, S. M., D. R. Wilton, and A. W. Glisson, "Electromagnetic scattering by surfaces of arbitrary shape," *IEEE Trans. Antennas Propagat.*, Vol. 30, No. 5, 409–418, 1982.

Multi-temporal Hyperspectral Images Unmixing and Classification Based on 3D Signature Model and Matching

I. R. Farah^{1,2}, S. Hmissi^{1,2}, K. Saheb Ettabaa^{1,2}, and B. Souleiman²

¹RIADI-GDL, ENSI, Tunis, Tunisia

²Télécom Bretagne, Dép. ITI, Technopôle Brest-Iroise-CS 83818, 29238 BREST CEDEX 3, France

Abstract— Land cover and land use types are challenged to access real-time and precise information of interest. The recent advent of sophisticated sensors permits to exploit independent observations of a phenomenon and to extract more detailed information and performs a decision level for scene interpretation. In this paper, we propose a new approach for multi-temporal hyperspectral images processing based on multi-temporal spectral signature representation. The 3D model characterizes all the pixels in a scene by considering their reflectance values as a function of time of imaging and spectral waveband. We showed the use of such modeling strategies in overcoming the dimensionality problem and improving both multi-temporal classification and unmixing problems associated with hyperspectral data. A case study was conducted on multi-temporal Hyperion series located in southern Tunisia. The obtained results showed good accuracies.

1. INTRODUCTION

Land cover and land use types are challenged to access real-time and precise information of interest. Remote sensing has been used to observe, to model and to provide input data by aerial measurements for many applications, including flood monitoring, surface deformation and land cover variations [1]. Nowadays, processing remote sensing data, as a forecasting tool for land surface study, allows a real time object detection or a-posteriori evaluation of damaged areas, on a case-to-case basis by providing thematic products. However, traditional products (e.g., aerial photographs, mono-date images) are not able to cover wide enough areas [2]. The effective use of remotely sensed data for classification and unmixing cases stills a difficult task due to some limitations associated with the data resolution, processing, and costs. Recently, the advent of hyperspectral data provides hundreds of relatively narrow (≤ 10 nm), contiguous bands that may be useful for extracting land-use information and identifying the constituents of ground materials i.e., Endmember in the image pixel.

Thus, dynamic object analysis by satellite observation and multi-temporal images processing could become a necessity. It is imperative for remote sensing community to expand their approaches boundaries to incorporate multi temporal images processing specially hyperspectral ones, since these kinds of images can provide a much better results for large areas. Therefore, multi-temporal data may improve accurate image analysis in situations where data is coming from a single sensor lack fidelity in the spectral or/and spatial domains [3].

2. RELATED WORKS

The problems of multi-temporal image classification are highly relevant in most remote sensing study [4]. To address the problem of multi-temporal images analysis, a range of image processing techniques has been greatly expanded. Such as in [5], Prasad and al. proposed a framework in which they incorporate a subspace identification procedure to divide the hyperspectral space into multiple contiguous subspaces, and then a decision fusion mechanism was employed to melt local classification resulting from each subspace. In [6], the authors proposed a new method to combine original spectral information with multi-temporal texture extracted by the Pseudo Cross Variogram algorithm (PCV). Several other approaches using neural networks or SVM have been proposed.

However, several problems are identified in the presented approaches. First, classifiers are, in general, sensitive to the high dimension of pixels in hyperspectral images or to higher dimensional feature space generated by putting together multi-dates features. Second, the learning of most proposed classifiers is based on different temporal data sets, i.e., a pixel group for each date. Nevertheless, at different time instants each pixels sample present distinctive characteristics due to differences in atmospheric conditions, sensor drifts, etc. Hence, the learning paradigm, investigated on data coming from different distributions, is violated. It does not respect the independence of features over different temporal data sets and the non-linear cross information among pixels at different temporal dates [7].

3. OVERVIEW OF THE PROPOSED APPROACH

On the attempt of multi-temporal hyperspectral images classification, we outline in this research an approach including several stages. Figure 1 depicts the proposed 3D model and its application for images classification and unmixing task. The first stage is “off-line” and consists on building a 3D hyperspectral library from field missions and In-Situ data collected using a spectro-radiometer. Other stages are on-line and include several steps. The block-diagram of the “on-line” 3D model spectral matching system is depicted using the processing chain shown in Figure 1(a).

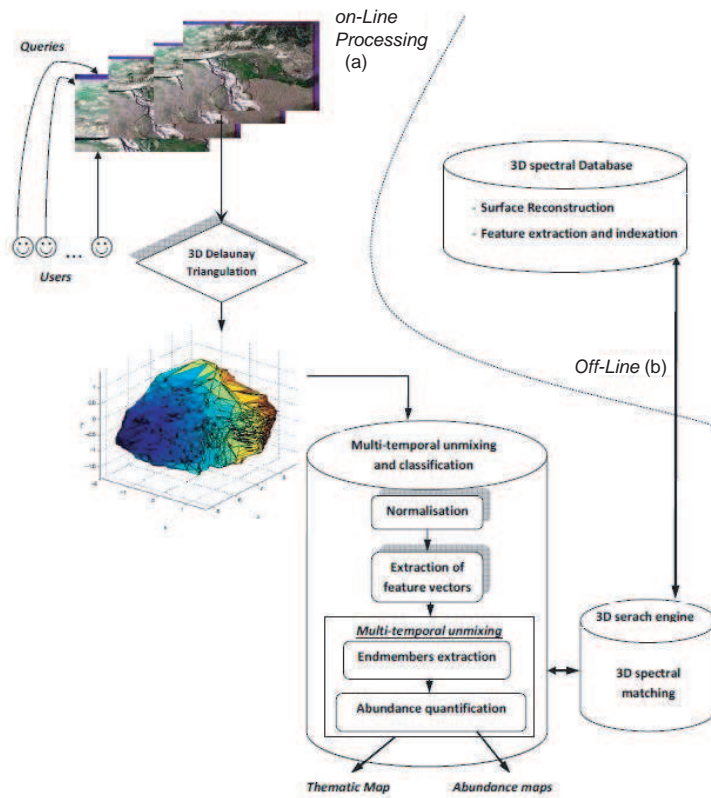


Figure 1: Proposed approach.

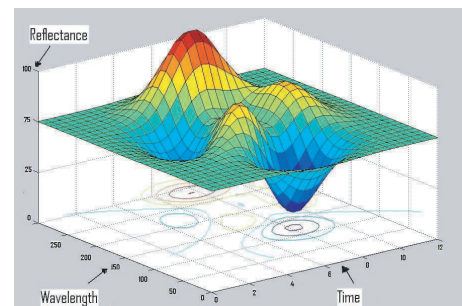


Figure 2: Proposed multi-temporal spectral signature model.

The first module inside the chain is normalization and is used to guarantee invariance with respect to rotation, translation and scaling. Indeed, different 3D spectral signature could have considerably similar shape, but different scale, orientation, and position in the 3D space. The motivation of this step can be depicted by finding a canonical position and normalized orientation for the 3D model.

Then, an analytical 3D surface is generated for each pixel, Delaunay triangulation was used to generate and parameterize the obtained mesh. The respective shape descriptors will be introduced to 3D spectral search engine. The next step consists of finding the highest match score between pixels surface in the image and the surfaces stored in our 3D spectral library, a shape differentiation of meshes using a similarity measure was used. Finally, we use the spectral distance calculated between surfaces for the classification and unmixing task.

3.1. Multi-temporal Spectral Signature

In this paper, we propose a 3D model that characterizes all the pixels in a scene by considering their reflectance values as a function of imaging time and spectral waveband.

To achieve this goal, we propose a new approach for designing multi-temporal spectral signature as a three dimensional function (time, reflectance, and wavelength band). Hence for each pixel, we generated a surface which generalizes the usual signature by adding a time dimension. Despite classical bi-dimensional spectral representation, we call this new representation the *multi-temporal spectral signature*.

Thus, the proposed model is based on a view of multi-sources and multi-temporal hyperspectral

imagery represented in a three-dimensional space (Eq. (1)), the axes of which are wavelength band (x), reflectance (y) and time (z). Multi-temporal measurement taken from different hyperspectral sensors can be plotted in this space.

$$Reflectance_{Pixel(i,j)} = f(Wavelength, time) \quad (1)$$

4. OFFLINE STAGE: SPECTRAL BASE AND SURFACE RECONSTRUCTION

The objective of this research is to provide a multi-temporal hyperspectral data classification based on 3D spectral signature matching. Before this, Endmember surface should be built according to described model. For our 3D spectral data base implementation, we opted initially for a multi-temporal construction based on spectrum probing. To achieve this goal, we collected a set of multi-temporal spectra for each Endmember from various on line spectral databases (Hyperspectral. info, DLR, ASTER Spectral Library, USGS Digital Spectral Library, Johns Hopkins University Spectral Library, SPECCHIO, etc). Then, we constructed from single-date collected spectrums the multi-temporal spectral signature by integrating the time component. We are currently working on to build the 3D spectral data base from real ground measurements.

Endmember surface construction consists to translate the point cloud collected multi-temporal spectrum into a continuous 3D surface, through *surface reconstruction*. Surface reconstruction provides a powerful concept for modeling shapes from samples. Delaunay based surface reconstruction algorithms showed good performances either in theory or practice for point cloud data with only geometric coordinates as input.

Assuming we are given a cloud point set P sampling an unknown pixel or Endmember surface and that the given sampling is dense enough. We used The *SuperCocone* algorithm [8] based on *Divide to conquer* paradigm. It demands only the computation of the Delaunay triangulation $D(P)$.

5. ONLINE STAGE: MULTI-TEMPORAL IMAGES UNMIXING AND CLASSIFICATION

This module allows two principals tasks: Spectral unmixing and hard classification.

Spectral unmixing is a quantitative analysis used to recognize ground cover materials to obtain their mixing proportions (or abundances) from a mixed pixel. The measured mixed spectrum is decomposed into a set of endmembers and their corresponding fractional abundances within the pixel. In order to reliably estimate these maps several steps are conducted:

- **Endmember extraction:** Endmember identification from a set of multi-temporal hyperspectral images was done by expert. Then, in order to label each Endmember, a 3D spectral matching was performed between each multi-temporal surface pixel and 3D spectral library ones.

- **3D spectral matching:** After generating the triangular mesh, we turn now to the spectral similarity stage. The 3D spectral matching which will take place between the built surface for each pixel with each of the surfaces stored in the 3D spectral signature. To achieve this goal, we based on the following 3D shape descriptors:

Cords-Based Descriptor combining the spatial extent information and the orientation of 3D object. For all object faces, a cord is defined and constructed as a vector that runs from an object's center to the centroid of a face.

Shape Distribution describing the geometric properties of the object as a probability distribution sampled from a shape function. Because there is no optimal way of describing a 3D object, the most important requirements in choosing 3D shape descriptors are: the static dimension of feature vectors and the robustness of fundamentally chosen descriptors.

The search engine (application) is based on the previous description scheme. These descriptors were chosen because they work on the mesh-domain. The first adopted similarity metric for calculating the distance and the similarity between two descriptors f' , f'' is the *plain Euclidean*:

$$diff(f', f'') = \sqrt{\sum_i (f', f'')^2} \quad (2)$$

Moreover, we used the *Bhattacharyya* distance defined by:

$$D = 1 - \sum_i \sqrt{Q_i} \sqrt{V_i} \quad Q \text{ et } V \text{ are the calculated histograms} \quad (3)$$

- **Abundance quantification:** The main goal of this step is to obtain an optimum and unique estimate value for the abundances α , for a given mixed pixel surface X and Endmember surface

M. Thus, this step is commonly used to measure similarity between any two surfaces. Finally, the hard classification task can be performed by choosing the highest score among Endmember 3D spectral matching.

6. VALIDATION

In the present section, we describe the experiments conducted during the research and studies made for the development of the proposed approach. The experiments are conducted using MATLAB and IDRISI. The study area was located near the town of Gabes, southern Tunisia. Twenty four remotely sensed Hyperion images acquired throughout 2007 and 2008 were used for analysis. 180 spectral wavebands of Hyperion imagery were used. In addition, some field measurements were collected and used to generate a ground reference data set. The registration of all images was performed using 17 ground control points and nearest neighbor re-sampling, since this technique maintained the original pixel values. In each case, the root-mean-square error associated with registration was less than 0.5 pixels. Atmospheric correction was performed to account for atmospheric differences between multi-temporal images.

The results of RMSE for each method were given in Table 1. As Table 1 has shown, the proposed approach gets the lowest RMSE among tested techniques, which means that it owns the highest accuracy.

On the other hand, to evaluate the classification accuracy improvement involved by the incorporation of the multi-temporal model matching into hyperspectral data classification process, several multi-temporal approaches have been used to perform the accuracy assessment task. Then, standard accuracy measures derived from a hard classification were computed. The measures based on the confusion matrix were overall accuracy, individual class accuracy, producer’s accuracy and user’s accuracy. The pixels received the label of the output class having the highest probability. Both classification accuracies for the 4 class using are presented in Table 2. Individual classification accuracy for each land cover type, the value of the Kappa coefficients and overall accuracy are reported in this table.

Table 1: RMSEs for unmixing accuracy assessment.

Land cover type	Proposed multi-temporal unmixing	Multi-temporal LSMA
Water	0.26	0.31
Vegetation	0.15	0.22
Urban	0.11	0.10
Wheats	0.41	0.48

Table 2: Classification accuracies.

Land cover type	Neural Networks	Linear Regression	Proposed approach	
			<i>Euclidan</i>	<i>Bhattacharyya</i>
Water	67.3	69.6	71.5	73.6
Vegetation	77.5	80.1	78.8	82.3
Urban	65.9	63.5	70.0	75.1
Wheats	64.5	73.6	73.2	79.4
Overall (%)	68.8	71.7	73.37	77.6
Kappa	0.67	0.69	0.71	0.78

All classification accuracies are significant better than 70% considered as a confidence level. Moreover, the level of accuracy was gradually improved by employing the 3D similarity matching for multi-temporal hyperspectral images interpretation.

7. CONCLUSION

The basic assumption of the approach is that spectral signature is changing over time, which can be modeled through 3D surface by adding the time dimension. This investigation has been shown to be effective in identifying land surface classes. Hence, data points obscured by noise and perturbations can be filtered out throughout Delaunay triangulation and interpolation. Moreover, the overall spectral variation of a given Endmember over the time is captured by a set of shape descriptors.

REFERENCES

1. Holter, M. R., "Remote sensing: The next 50 years," *IEEE Transactions on Aerospace and Electronic Systems*, Vol. 20, No. 4, 316–324, July 1984.
2. Berni, J. A. J., P. J. Zarco-Tejada, L. Suarez, and E. Fereres, "Thermal and narrowband multispectral remote sensing for vegetation monitoring from an unmanned aerial vehicle," *IEEE Transactions on Geoscience and Remote Sensing*, Vol. 47, No. 3, 722–738, 2009.
3. Bruzzone L., P. C. Smits, and J. C. Tilton, "Foreword special issue on analysis of multitemporal remote sensing images Bruzzone," *IEEE Transactions on Geoscience and Remote Sensing*, Vol. 41, No. 11, 2419–2422, 2003.
4. Jeon, B. and D. A. Landgrebe, "Decision fusion approach for multitemporal classification," *IEEE Transactions on Geoscience and Remote Sensing*, Vol. 37, No. 3, 1227–1233, May 1999.
5. Radke, R. J., S. Andra, O. Al-Kofahi, and B. Roysam, "Image change detection algorithms: A systematic survey," *IEEE Trans. Image Process*, Vol. 14, No. 3, 294–307, March 2005.
6. Du, Q., L. L. Wasson, and R. King, "Unsupervised linear unmixing for change detection in multitemporal airborne hyperspectral imagery," *Proceedings of the 3rd International Workshop on the Analysis of Multi-Temporal Remote Sensing Images*, Biloxi, MS, 2005.
7. Camps-Valls, G., L. Gómez-Chova, J. Muñoz-Marí, J. L. Rojo-Álvarez, and M. Martínez-Ramón, "Kernel-based framework for multitemporal and multisource remote sensing data classification and change detection," *IEEE Transactions on Geoscience and Remote Sensing*, Vol. 46, 2008.
8. Dey, T. K., J. Giesen, and J. Hudson, "Delaunay based shape reconstruction from large data," *IEEE Symposium on Parallel and Large-data Visualization and Graphics*, Vol. 4, 19–146, 2001.

A Telemetry Antenna System for Unmanned Air Vehicles

M. Dogan^{1,2} and F. Ustuner¹

¹TUBITAK, UEKAE, Kocaeli, Turkey

²Sabanci University, Istanbul, Turkey

Abstract— This paper presents a low VSWR high gain telemetry antenna system manufactured for UAVs that provides 360° coverage in the roll plane of the UAV. Proposed telemetry antenna system includes four telemetry antennas, one power divider that has one input and four output terminals which feeds the telemetry antennas with equal magnitude and phase. Proposed high gain telemetry antennas are based on the feeding of the microstrip patch antenna via aperture coupling. Full coverage in the roll plane of the UAV is obtained by using circular array configuration of telemetry antennas. RF power divider is designed by using couple of Wilkinson power dividers with equal line lengths and impedance sections from input terminal to the all four output terminals.

1. INTRODUCTION

Telemetry systems are used for remote data measurement, collection and evaluation of the collected data. Data transfer is done in wireless means. Telemetry systems have been used in several areas such as agriculture, defense, medicine ...etc. Typically, telemetry systems are used on moving objects such as cars, aircrafts and missiles. Airborne telemetry systems are used for remote monitoring the temperature, pressure, vibration and acceleration variations of the UAV during the flight time. The complete structure of a telemetry system includes sensors and transducers, signal conditioners, RF circuits and the transmitter [1].

Telemetry transmitter is mainly composed of telemetry antenna(s) and suitable feeding system of the antenna(s). In the application of flying object which moves very fast and may rotate around its roll axis rapidly, fully coverage in roll plane is required for continuous data transfer. Hence, as shown in Figure 1, telemetry transmitter system requires four telemetry antennas and one RF power divider to feed the antennas with equal magnitude and phase. In this paper, designed antennas and power divider are presented with the simulation and measurement results in the desired frequency range. At the end, VSWR measurement results of the complete telemetry antenna system will be given.

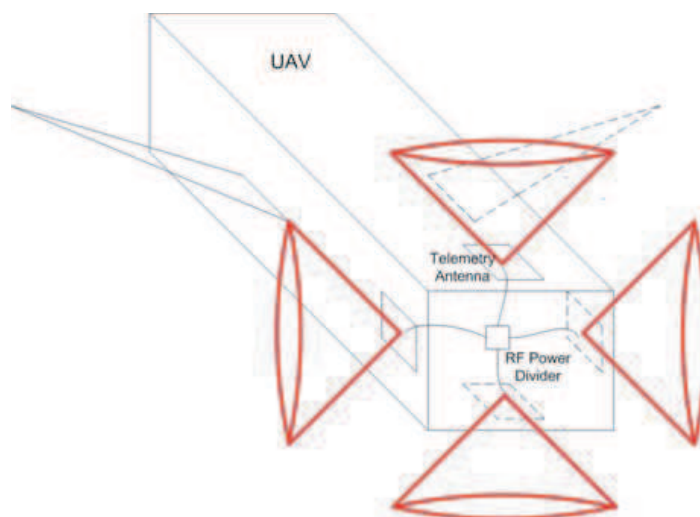


Figure 1: Full coverage in the roll axis of the UAV.

2. TELEMETRY ANTENNA

Proposed telemetry antenna system has four antennas and one RF power divider. Aperture coupled microstrip patch antennas [2] are preferred due to their high gain and wide impedance bandwidth.

Antennas are designed by using HFSS. Antenna optimizations are performed via HFSS Optometric and further optimization is performed with MATLAB Optimization Toolbox. Antennas are printed on ROGERS 4003C substrate due to its low loss characteristics at higher frequencies and its ruggedness. Upper “Air” layer is the patch substrate and the upper ROGERS 4003 layer is used as a radome material. Optimized antenna dimensions are given in Figure 2.

Antenna design and optimization is based on the antenna VSWR value (< 1.5) and the antenna gain (> 8 dBi). Both simulations and measurements are performed on telemetry antennas. Comparison of simulated and measured VSWR and gain values are depicted in Figure 3. Measurements are performed in anechoic chamber of TUBITAK — UEKAE EMC Division with Agilent E8362B Precision Network Analyzer in 2.2–2.4 GHz frequency band. The antenna gain is obtained by using three antenna method and applying Friis [3] equation. Additional measurements are performed to obtain half-power beam width (HPBW), cross-polarization ratio (CPR) and also front-to-back ratio (FBR) at center frequency which is 2.3 GHz and the measurement results are tabulated in Table 1.

3. RF POWER DIVIDER

Telemetry system will consist of four telemetry antennas that should be fed with the same amplitude and the phase. This requires a well designed 1-to-4 power divider to keep the phase and amplitude variations as minimum as possible in the given frequency range. Designed power divider is composed

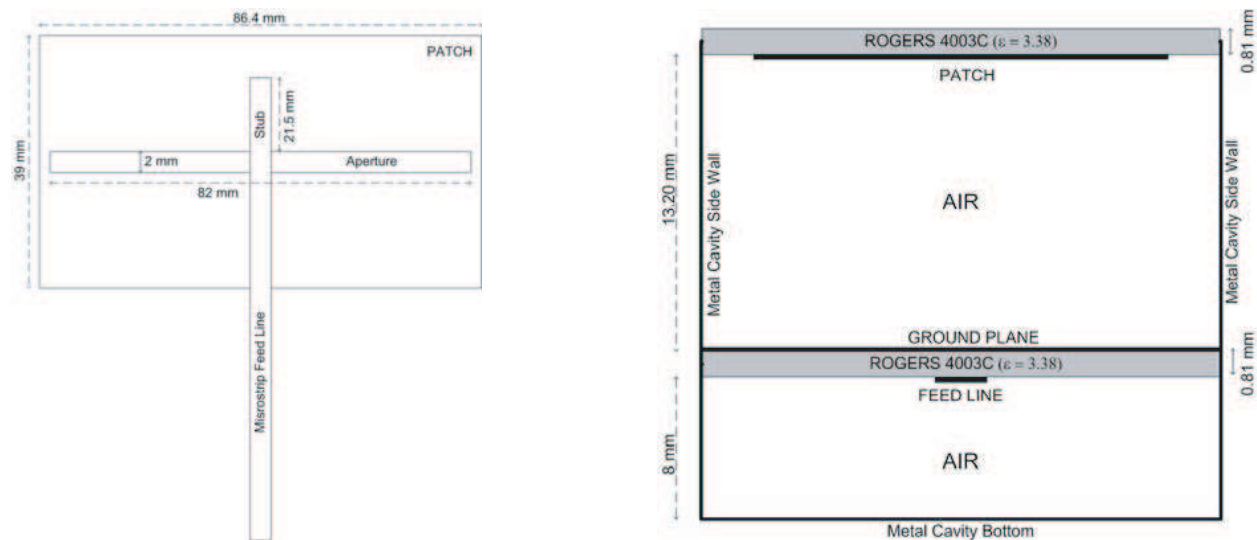


Figure 2: Telemetry antenna bottom view (left), side view (right) with corresponding dimensions.

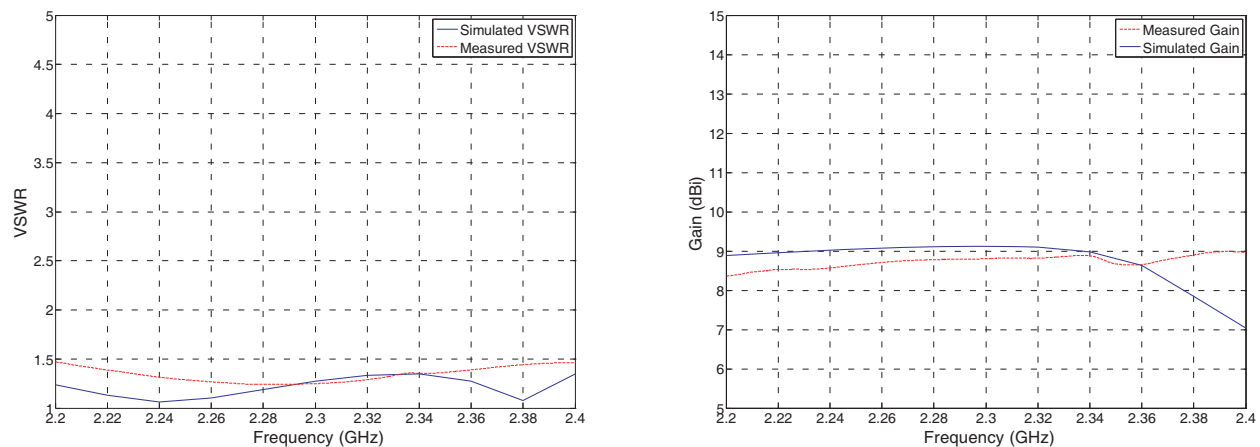


Figure 3: Comparison of simulated/measured VSWR (left) and antenna gain (right).

Table 1: Measured HPBW, CPR and FBR values of manufactured antenna at $f = 2.3$ GHz.

Half-Power Beam Width ($^\circ$)	60°
Cross-Polarization Ratio (dB)	≥ 25 dB
Front-to-Back Ratio (dB)	≥ 25 dB

of three cascaded Wilkinson Dividers [4] as shown in Figure 4. In order to have well isolated output ports we used 100- Ω resistors between the separate arms. Quarter wave section which has 70.7- Ω impedance is in circular geometry in order to have smooth transition from input to the output. Power divider is also printed on the ROGERS 4003C substrate. Simulation results depict that power divider has a VSWR below 1.25 (Figure 5), insertion losses below 6.2 dB (Figure 7). VSWR, insertion loss and port isolation measurements are also performed in the desired frequency range and results are depicted in Figures 5, 6, and 8 respectively.

One important measurement that has to be performed on RF power divider is the phase delay measurements. According to the array configuration of telemetry antennas, all four antennas should be in phase. Thus, there should be no phase difference between the four output terminals of the power divider, unfortunately in practice it is impossible to obtain the same phase but one may keep variations in acceptable range. The measured phase delays which are tabulated in Table 2, predict that phase variation is small enough to tell that all output ports are in phase.

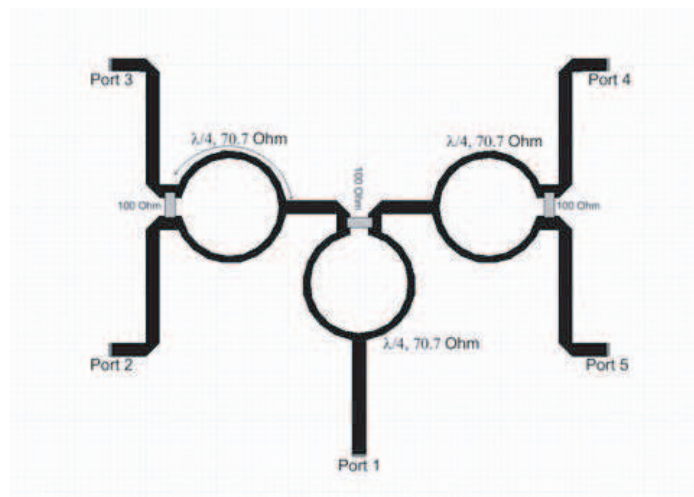


Figure 4: Telemetry system, 1-to-4 RF power divider.

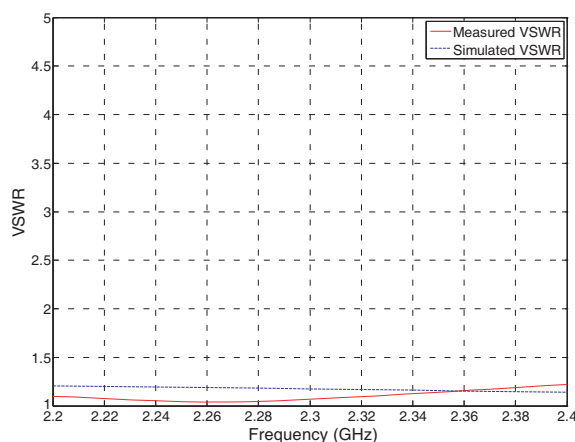


Figure 5: Measured and simulated VSWR of RF power divider.

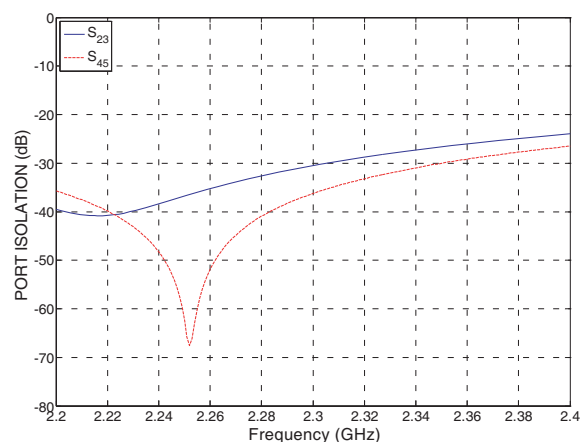


Figure 6: Measured port isolation results of power divider.

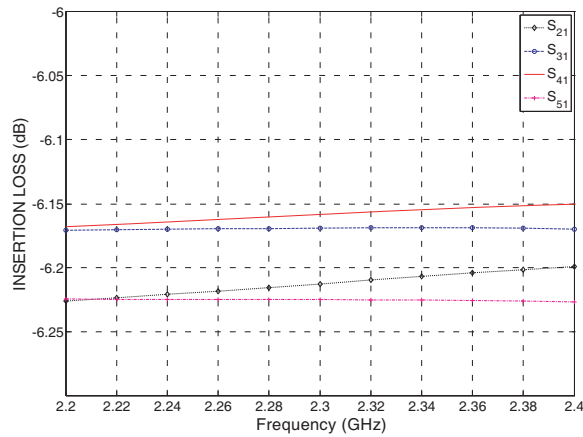


Figure 7: Simulated insertion loss.

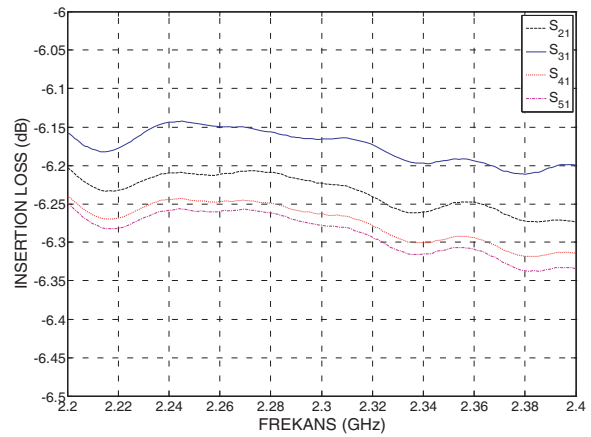


Figure 8: Measured insertion loss.

Table 2: Measured phase delays of RF power divider at different frequencies.

	PHASE (°)		
	2.2 GHz	2.3 GHz	2.4 GHz
S_{21}	-78.005	-98.538	-118.97
S_{31}	-76.372	-96.738	-117.14
S_{41}	-77.625	-98.040	-118.45
S_{51}	-77.556	-98.042	-118.44

4. TELEMETRY ANTENNA SYSTEM

In this context, telemetry system is the combination of RF power divider and the telemetry antennas. Individually, antennas and the power divider work pretty well but the overall system behavior is the most important one. In previous section, we made the insertion loss measurement between port 1 and port 2 by loading the port 3, 4 and 5 with 50 Ohm. In telemetry system all ports see the corresponding telemetry antennas as loads which have VSWR value of 1.5. Therefore the overall system VSWR value will vary as expected which should be below 2 at the end.

We performed VSWR measurements on telemetry system. Measurement setup and the VSWR results are given in Figures 9 and 10 respectively. Measured VSWR values are well below the tolerable value and at the center frequency it is still below 1.5.

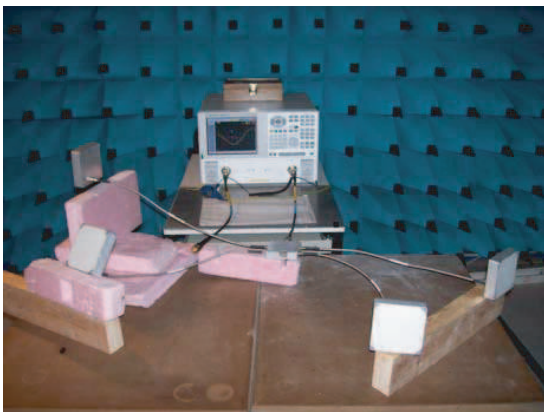


Figure 9: Telemetry system VSWR measurement setup.

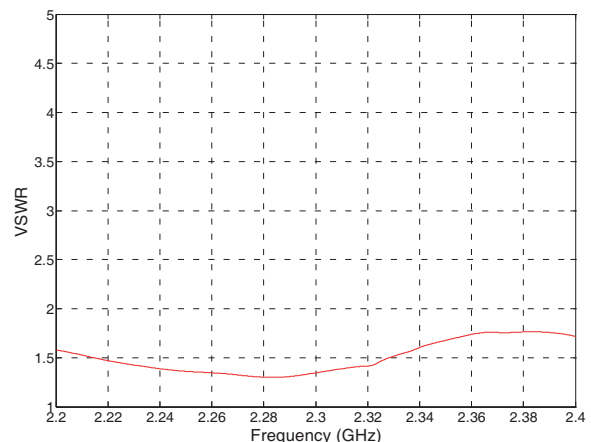


Figure 10: Telemetry system VSWR results.

5. CONCLUSION

In this paper, a proposed telemetry antenna system is investigated in detail with its antennas and RF power divider. Telemetry antennas and RF power divider meet the requirements and demonstrate very good performance individually. Telemetry system performance is also in acceptable range. On the other hand, the system needs some further improvements. Telemetry antennas are very critical here. Telemetry antenna needs very good grounding and it is very sensitive to the stub length, therefore manufacturing process should be very accurate and it should have high repeatability. RF power divider demonstrates very good performance, S_{21} and S_{51} values are 0.1–0.2 dB below from the remaining insertion loss values. There are two regions that the quarter wave circular sections of Wilkinson dividers get closer to each other. One of them is on the path from port-1 to port-2 and one of them is on port-1 to port-5. These regions are the possible cause of the insertion loss difference.

REFERENCES

1. Carden, F., R. P. Jedlicka, and R. Henry, *Telemetry Systems Engineering*, Artech House Inc., Norwood, MA, 2002.
2. Pozar, D. M., "A microstrip antenna aperture coupled to a microstrip line," *Electronics Letters*, Vol. 21, 49–50, January 17, 1985.
3. Balanis, C. A., *Antenna Theory Analysis and Design*, 2nd Edition, John Wiley & Sons Inc., Canada, 1997.
4. Pozar, D. M., *Microwave Engineering*, 3rd Edition, John Wiley & Sons Inc., 2005.

Defected Ground Structure for Coupling Reduction between Probe Fed Microstrip Antenna Elements

C. Vázquez, G. Hotopan, S. Ver Hoeye, M. Fernández, L. F. Herrán, and F. Las-Heras

Area of Signal Theory and Communications, Universidad de Oviedo

Edificio Polivalente de Viesques, Módulo 8, planta 1, Campus de Viesques, E-33203, Gijón, Spain

Abstract— The mutual coupling between elements of a microstrip antenna design based on stacked patches has been studied in an array configuration. In order to mitigate the mutual coupling, a defected ground structure based on narrow, closely spaced rectangular slots has been proposed. Two arrangements with three and five slots have been studied and optimised in an array configuration with $0.7\lambda_0$ element separation. For the experimental validation of the simulated results, prototypes of two element antenna arrays with both DGS designs, as well as without DGS, have been manufactured and measured.

1. INTRODUCTION

In recent years, microstrip antennas have become a widespread choice for a great variety of applications, due to their well-known attractive features, such as low profile, light weight and low production cost. These properties, together with the capability to integrate the feeding networks, tuning devices or other kind of auxiliary circuitry on the same substrate, make this technology an interesting option for antenna array implementations.

Different topologies of antenna arrays can be found in the literature, taking advantage of their beamforming [1], conformation [2] and pattern nulling [3] possibilities. Additionally, the behaviour of the array can be modified in real time by separately tuning the feeding signals of the different individual radiators, providing adaptive solutions [4, 5]. For this kind of applications, in which the feeding signals of the radiating elements must be separately controlled, these signals must be individually conducted from each of the tuning circuits to its corresponding radiating element, which can become a challenging task in large two dimensional arrays [6]. This has been overcome with topologies in which the tuning circuits for each row of the array are placed in a perpendicular plane, using quasi Yagi [7] or probe fed microstrip antennas [8].

The mutual coupling between elements of antenna arrays is a critical aspect that must be conveniently taken into account in the design process, as it can lead to severe degradations in the overall performance. Many different methods for the reduction of mutual coupling between antenna array elements have been proposed in the literature. An array of shorting pins between the patch and the ground plane is introduced in [9], leading to substantially decreased coupling levels. Other works focus on suppressing the surface wave generation by optimising the antenna dimensions [10], using silicon micromachined substrate structures [11], or introducing superstrates [12]. Different approaches have been proposed with Electromagnetic Band Gap (EBG) structures using either shorted [13] or floating [14] elements.

Defected Ground Structures (DGS) are implemented by etching slots of different shapes in the ground planes. They have been employed to improve the performance in multiple applications such as filters, couplers or dividers, as well as to reduce the mutual coupling between elements of antenna arrays [15].

In this work, the mutual coupling between two probe fed microstrip antennas based on stacked patches, like those presented in [8], working around 10 GHz and aligned collinearly along their E -plane, is analysed. In Section 2, the behaviour of the array is studied through electromagnetic simulations, both versus frequency and versus element separation. In Section 3, a simple defected ground structure for mutual coupling reduction is introduced. Two optimised designs based on 3 and 5 narrow, closely spaced, rectangular slots are presented and analysed through electromagnetic simulations. For the experimental validation of the simulated results, prototypes of two element antenna arrays with both DGS designs have been manufactured and measured. The experimental results are commented in Section 4.

2. ANTENNA PERFORMANCE

2.1. Microstrip Antenna Design

The antenna design used in this work was presented in [8]. The coaxial SMA connector is soldered to the bottom layer of a 0.762 mm thick ARLON 25N substrate ($\epsilon_r = 3.38$ and $\tan \delta = 0.0025$ at 10 GHz) and the probe is connected to the specified feeding point in the first patch (Fig. 1), edged on the top layer of this substrate. The second patch is placed on top of a double layer of ARLON 25N (1.524 mm). The design was optimised to increase the impedance bandwidth.

2.2. Mutual Coupling

The mutual coupling between elements is a key parameter in the design process of antenna arrays, as it can lead to severe degradations in the overall performance. The antenna design described in the previous section has been analysed through Method of Moments (MoM) electromagnetic simulations (carried out using Advanced Design System). Two radiating elements, collinearly arranged along the x axis (Fig. 1), have been simulated by placing ports in the specified feeding points of the internal patches. The simulated results for different values of the separation between elements, d , from $\lambda_0/2$ to λ_0 in steps of $\lambda_0/30$ ($\lambda_0 = 30$ mm is the free space wavelength at 10 GHz), are shown in Fig. 2.

The return loss of the antenna is not substantially affected by the element spacing (Fig. 2(a)). For the studied values, an impedance bandwidth ($|S_{11}| < -10$ dB) greater than 1.12 GHz is observed. The S_{22} parameter presents analogous properties and, therefore, it has not been displayed.

The mutual coupling is progressively reduced as the separation between elements increases (Fig. 2(b)). The first three of the studied values ($d = 15, 16$ and 17 mm), which show a slightly different variation patterns, have been represented with a different trace type and indicated in the legend.

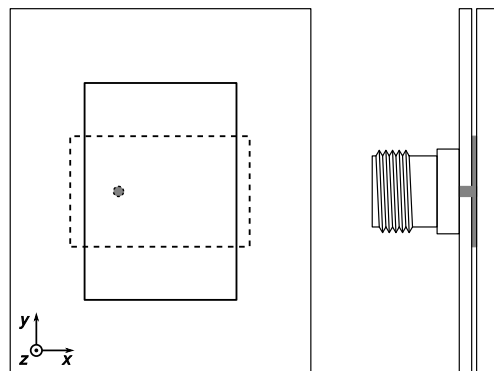


Figure 1: Outline of the probe fed microstrip antenna based on stacked patches, as presented in [8].

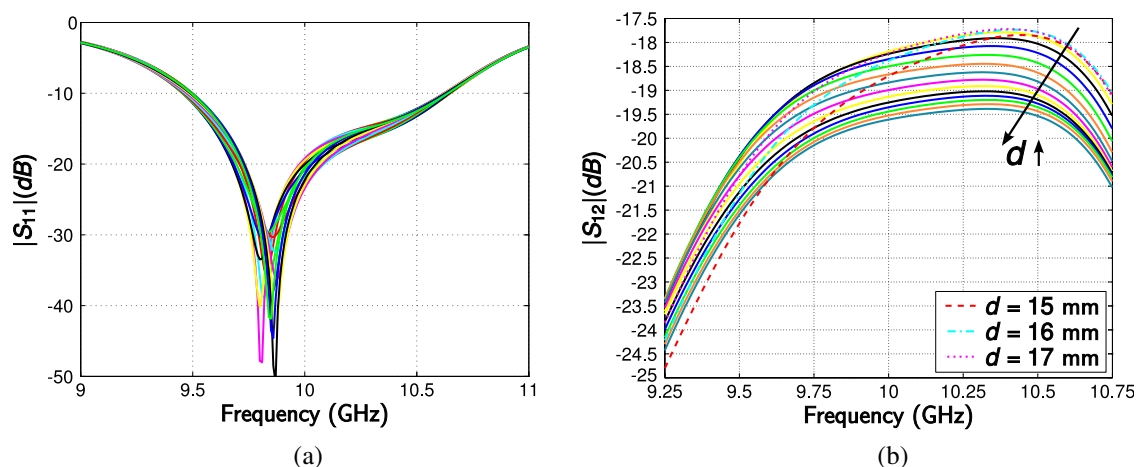


Figure 2: Simulated scattering parameters for different values of the separation between elements d (from $\lambda_0/2 = 15$ mm to $\lambda_0 = 30$ mm in steps of $\lambda_0/30 = 1$ mm). (a) $|S_{11}|$. (b) $|S_{12}|$.

3. DEFECTED GROUND STRUCTURE

3.1. Proposed Design

The defected ground structure proposed in this work is based on rectangular slots, as shown in Fig. 3(a), where the design parameters are the length and width of the slots, l_i and w_i , $i = 1, \dots, 5$, and the separation between them, $d_{i-1,i}$, $i = 2, \dots, 5$. The structure is centred between two antenna elements separated $0.7\lambda_0 = 21$ mm (Fig. 3(b)), and optimised to reduce the mutual coupling. Two different arrangements with three and five slots have been studied.

The optimisation process is carried out using ADS MoM electromagnetic simulations. An effective reduction of the mutual coupling is achieved using narrow, closely spaced slots. The optimised dimensions of the 3 and 5 slot structures are specified in Table 1.

The simulated performance of the final DGS designs is presented in Fig. 4. The mutual coupling has been reduced throughout an important fraction of the antenna operating bandwidth. A greater reduction has been attained with the five slot design (around 11 dB with respect to the results without DGS), although a slightly narrower bandwidth is observed. The three slot design presents a smoother frequency variation, with a maximum mutual coupling reduction of around 9 dB.

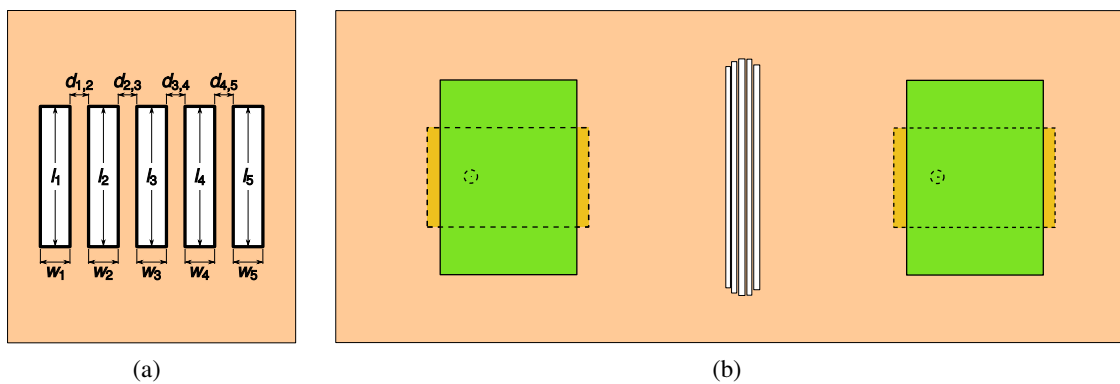


Figure 3: (a) Outline (not to scale) of the proposed defected ground structure with its design parameters. (b) Two element antenna array with the 5 slot DGS design.

Table 1: Dimensions, in μm , of the optimised defected ground structures.

(μ)m	l_1	w_1	$d_{1,2}$	l_2	w_2	$d_{2,3}$	l_3	w_3	$d_{3,4}$	l_4	w_4	$d_{4,5}$	l_5	w_5
3 slots	—	—	—	10 348	223	91	10 613	201	112	10 380	222	—	—	—
5 slots	10 075	233	87	10 398	234	79	10 619	226	114	10 329	222	74	9 939	268

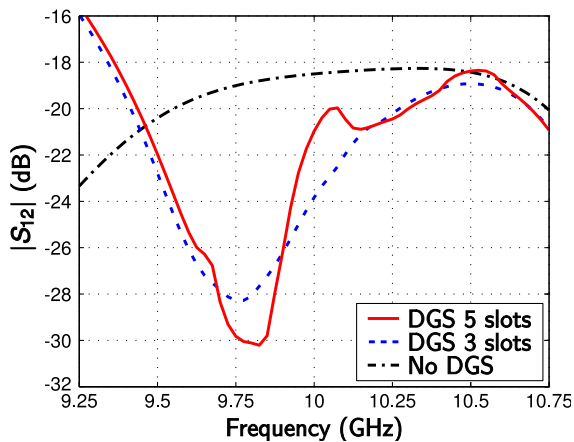


Figure 4: Simulations of the S_{12} parameter of the optimised DGS designs, compared to the results without DGS.

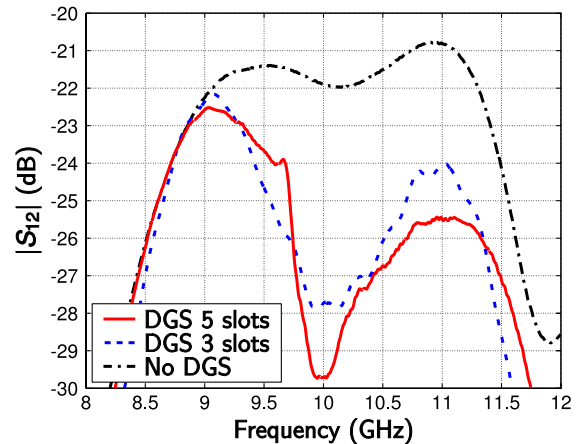


Figure 5: Measurement of the S_{12} parameter of the manufactured DGS designs, compared to the measurement without DGS.

4. EXPERIMENTAL RESULTS

For the experimental validation of the simulated results, prototypes of the two element antenna array with both optimised DGS designs have been manufactured. The results are compared to the performance of the array without DGS in Fig. 5.

The minimum of the mutual coupling with both DGS designs takes place at around 10 GHz, which represents a slight frequency shift with respect to the simulated results. Minima of around -28 dB and -30 dB have been achieved, with the three and five slot designs respectively. A wider bandwidth has been obtained with the five slot design. Therefore, as the manufacturing complexity of both designs is very similar, the five element version is more effective for the mitigation of the detrimental mutual coupling.

5. CONCLUSION

The mutual coupling between elements of a microstrip antenna design has been studied in an array configuration, both versus frequency and element spacing. A defected ground structure based on narrow, closely spaced rectangular slots has been proposed for mutual coupling reduction. Two different arrangements with 3 and 5 slots have been studied and optimised in an array configuration with $0.7\lambda_0$ element separation. For the experimental validation of the simulated results, prototypes of antenna arrays without DGS and with both optimised designs have been manufactured. The mutual coupling has been reduced to a minimum of about -28 dB with the 3 slot design. A wider bandwidth has been observed in the 5 slot version, with a minimum coupling of around -30 dB, which makes this design more effective for mutual coupling reduction in array topologies.

ACKNOWLEDGMENT

This work was supported by the “Ministerio de Ciencia e Innovación” of Spain and “FEDER”, under projects TEC2008-01638/TEC (INVEMTA) and CONSOLIDER-INGENIO CSD2008-00068 (TERASENSE), by the “Gobierno del Principado de Asturias” under the “Plan de Ciencia y Tecnología (PCTI)”/“FEDER-FSE” by the grant BP08-082, the projects EQP06-015, FC-08-EQUIP-06, PEST08-02 and IB09-081, and by the “Cátedra Telefónica” Universidad de Oviedo and “Fundación CTIC”.

REFERENCES

1. Li, Y., Y.-J. Gu, Z.-G. Shi, and K. S. Chen, “Robust adaptive beamforming based on particle filter with noise unknown,” *Progress In Electromagnetics Research*, PIER 90, 151–169, 2009.
2. Xu, Z., H. Li, Q.-Z. Liu, and J.-Y. Li, “Pattern synthesis of conformal antenna array by the hybrid genetic algorithm,” *Progress In Electromagnetics Research*, PIER 79, 75–90, 2008.
3. Mismar, M. J. and T. H. Ismail, “Pattern nulling by iterative phase perturbation,” *Progress In Electromagnetics Research*, PIER 22, 181–195, 1999.
4. Fakoukakis, F. E., S. G. Diamantis, A. P. Orfanides, and G. A. Kyriacou, “Development of an adaptive and a switched beam smart antenna system for wireless communications,” *Journal of Electromagnetic Waves and Applications*, Vol. 20, 399–408, 2006.
5. Mouhamadou, M., P. Vaudon, and M. Rammal, “Smart antenna array patterns synthesis: Null steering and multi-user beamforming by phase control,” *Progress In Electromagnetics Research*, PIER 60, 95–106, 2006.
6. Kabacik, P., “Active microstrip array for satellite communication applications,” *1995 SBMO/IEEE MTT-S International Microwave and Optoelectronics Conference, 1995 Proceedings*, Vol. 2, 626–631, Jul. 1995.
7. Deal, W., N. Kaneda, J. Sor, Y. Qian, and T. Itoh, “A new quasi-yagi antenna for planar active antenna arrays,” *IEEE Transactions on Microwave Theory and Techniques*, Vol. 48, No. 6, 910–918, Jun. 2000.
8. Vázquez, C., G. Hotopan, S. Ver Hoeye, M. Fernández, L. F. Herrán, and F. Las-Heras, “Microstrip antenna design based on stacked patches for reconfigurable two dimensional planar array topologies,” *Progress In Electromagnetics Research*, PIER 97, 95–104, 2009.
9. Nikolic, M., A. Djordjevic, and A. Nehorai, “Microstrip antennas with suppressed radiation in horizontal directions and reduced coupling,” *IEEE Transactions on Antennas and Propagation*, Vol. 53, No. 11, 3469–3476, Nov. 2005.

10. Bhattacharyya, A., D. Jackson, J. Williams, and R. Smith, “Microstrip patch designs which do not excite surface waves,” *Antennas and Propagation Society International Symposium, AP-S Digest*, Vol. 1, 68–71, Jun. 1991.
11. Yook, J.-G. and L. Katehi, “Micromachined microstrip patch antenna with controlled mutual coupling and surface waves,” *IEEE Transactions on Antennas and Propagation*, Vol. 49, No. 9, 1282–1289, Sep. 2001.
12. Alexopoulos, N. and D. Jackson, “Fundamental superstrate (cover) effects on printed circuit antennas,” *IEEE Transactions on Antennas and Propagation*, Vol. 32, No. 8, 807–816, Aug. 1984.
13. Fu, Y. Q., Q. R. Zheng, Q. Gao, and G. H. Zhang, “Mutual coupling reduction between large antenna arrays using electromagnetic bandgap (EBG) structures,” *Journal of Electromagnetic Waves and Applications*, Vol. 20, No. 6, 819–825, 2006.
14. Rajo-Iglesias, E., O. Quevedo-Teruel, and L. Inclan-Sanchez, “Mutual coupling reduction in patch antenna arrays by using a planar EBG structure and a multilayer dielectric substrate,” *IEEE Transactions on Antennas and Propagation*, Vol. 56, No. 6, 1648–1655, Jun. 2008.
15. Zulkifli, F. Y., E. T. Rahardjo, and D. Hartanto, “Mutual coupling reduction using dumbbell defected ground structure for multiband microstrip antenna array,” *Progress In Electromagnetics Research Letters*, Vol. 13, 29–40, 2010.